EVALUATION OF DROP BREAK-UP AFTER IMPINGEMENT ON HORIZONTAL SLAT GRIDS AND THE EFFECT OF DROP SIZE OF COOLING TOWER RAIN ZONE PERFORMANCE

by
Riaan Terblanche

Dissertation presented for the degree of Doctor of Philosophy in the Faculty of Engineering at the University of Stellenbosch

Promoter: Prof. Hanno Carl Rudolf Reuter
Faculty of Engineering
Department of Mechanical and Mechatronic Engineering

December 2011

DECLARATION

By submitting this dissertation electronically, I declare that the entirety of the work contained therein is my own, original work, that I am the sole author thereof (save to the extent explicitly otherwise stated), that reproduction and publication thereof by Stellenbosch University will not infringe any third party rights and that I have not previously in its entirety or in part submitted it for obtaining any qualification.

Signature:……

Date:…22 August 2011…

ABSTRACT

Natural draught wet-cooling tower rain zone performance can be significantly enhanced by reducing the mean drop size in the rain zone with the installation of specially designed grids below the cooling tower fill. Drops enter the rain zone in the form of a polydisperse drop distribution, dripping from below the cooling tower fill, comprising relatively large drops. In order to design and optimize a grid for breaking up these drops, the mechanisms of drop break-up after impingement on the grid surface, referred to as splashing, straddling and dripping, need to be clearly understood. Two of these mechanisms, splashing and straddling, are therefore investigated experimentally using high speed video cameras to measure initial drop sizes, mass fractions and drop size distributions after impingement on different horizontal slats covered with a thin layer of water. The following parameters are varied independently for these experiments: drop fall distance, initial drop size, slat width and the water film thickness on the slats. Dripping from below the grid, is investigated theoretically. The effect of drop interaction on the drop size distribution in the rain zone is also investigated experimentally by measuring the drop distributions at the top and bottom of rain zones with a height of approximately 7.05 m to 7.65 m for different inlet distributions. The experimental drop break-up data, numerically obtained splash drop trajectory data and drop interaction data found in literature are used to develop a theoretical model of a purely counter flow cooling tower rain zone with and without installed grids. The model is compared to experimental data and theoretical data from literature and the predicted thermal and dynamic behaviour of the rain zone are generally found to be in good agreement with these results. Ultimately, this model is used for the optimization of the grid layout in terms of variables such as distance between the grid and the fill, slat width, slat spacing and slat height. It is found that the best drop break-up is achieved for grids comprising narrower slats with lower grid porosities as opposed to grids comprising wider slats. For the determined optimal grid layout it is found that a significant improvement in cooling tower performance can be achieved.

SAMEVATTING

Nat-koeltoringreënsonevermoë kan aansienlik verhoog word deur die druppelgrootte in hierdie gebied te verklein deur roosters, wat spesifiek vir hierdie doel ontwerp is, onder die pakkingsmateriaal te installeer. Die inlaatdruppelverdeling aan die bokant van die reënsone bestaan uit ‘n verdeling van relatief groot druppels wat drip van die onderkant van die pakkingsmateriaal. Ten einde ‘n rooster te ontwerp en te optimeer wat hierdie druppels kan opbreek moet die meganismes van druppelopbreking, bekend as spatting, vurking en drip goed verstaan word. Spatting en vurking is om hierdie rede eksperimenteel ondersoek, met behulp van hoëspoed videokameras. Die volgende veranderlikes is onafhanklik verander tydens hierdie eksperimente: valafstand van die druppel, aanvanklike druppelgrootte, latwydte en die dikte van die lagie water bo-op die lat. Die dripmeganisme aan die onderkant van die rooster is slegs teoreties ondersoek. Die effek wat druppelinteraksie in die reënsone het op die druppelgrootte is ondersoek deur die druppelgroottes aan die bo- en onderkant van ‘n 7.05 m tot 7.65 m reënsone te meet vir verskillende druppelinlaatverdelings. Die eksperimentele druppeldata, sowel as numeries berekende data wat die snelheid en trajek van spatdruppels beskryf, tesame met data vir druppelinteraksies wat uit die literatuur verkry is word gebruik om ‘n teoretiese model te ontwikkel vir ‘n suiwer teenvloei koeltoringreënsone met en sonder roosters. Hierdie model word vergelyk met eksperimentele data en data wat uit die literatuur verkry is en daar is gevind dat daar oor die algemeen ‘n goeie ooreenstemming is tussen die voorspelde en gemete termiese en dinamiese gedrag van die reënsone. Uiteindelik word die model gebruik vir die optimering van die rooster in terme van die volgende veranderlikes: afstand tussen rooster en pakkingsmateriaal, latwydte, latspasiëring en lathoogte. Daar word gevind dat beter druppelopbreking verkry word deur gebruik te maak van smaller latte en ‘n laer roosterporeusiteit. Daar is gevind dat die bepaalde optimale roosteruitleg in die reënsone van ‘n koeltoring ‘n wesenlike verbetering in koeltoringvermoë tot gevolg kan hê.

Dedicated to my wife,

Anneke

and my parents,

Anton and Hester Terblanche

ACKNOWLEDGEMENTS

Thanks to my Lord for carrying me through the hard times and giving me the strength and the will to persevere. You are my guiding star that gives direction to my life.

Thanks to Professor. Reuter, my promoter, for the contribution he has made to my career by teaching me discipline and inspiring me to try harder and be better. We came a long way since I first stepped into your office at the end of 2004 as a third year student and I will always be grateful for the chance you have given me to work with you.

Thank you to Professor Kröger for his interest and guidance in this project.

Thank you to all the SMD personnel for their help with my experimental equipment.

Thank you to my lovely wife, Anneke, who inspires and encourages me every day. Thank you for dreaming with me and brightening my days with your smiles. I am truly blessed to have you as my wife and love you very much.

Thank you to my parents for all their help and support throughout my life. You are the best parents that anyone can ask for and you still inspire me everyday to be the best I can be with your positive attitude towards life and all its obstacles. I love you very much.

TABLE OF CONTENTS

LIST OF FIGURES

LIST OF TABLES

List of symbols

A	Area, m^2, Amplitude
a_{fi}	Area to volume ratio, m^{-1}
C	Non-dimensional drop size,-
C_D	Drag coefficient, -
c_F	Friction factor
c_p	Specific heat at constant pressure, J/kgK
c_v	Specific heat at constant volume, J/kgK
D_{AB}	Diffusion coefficient, m^2/s
D_s	Splash diameter, m
d	Diameter, m or mm
d_m	Maximum stable drop diameter, m or mm
d_{RR}	Rosin-Rammler parameter, m or mm
d_{32}	Sauter mean drop diameter, m or mm
d_{50}	Mass mean diameter, m or mm
E	Drop deformation ratio, -
F	Force, N
f	Mass fraction, -
G	Mass velocity, kg/m^2s
g	Gravitational acceleration, m/s^2
g_{YS}	Correction factor, -
H	Height, m
h_c	Convection heat transfer coefficient, W/m^2K
h_D	Mass transfer coefficient, m/s
h_d	Mass transfer coefficient, kg/m^2s
i	Enthalpy, J/kg
K	Pressure loss coefficient, -
KE	Kinetic energy, J
k	Thermal conductivity, W/mK
L_{fi}	Fill height, m
M	Mass, kg, Mass fraction, - , Molecular weight, g/mol
m	Mass flow rate, kg/s
N	Number, -

n	Number of drops, -
$\dot{n}$	Number rate of drops, s^{-1}
n_{RR}	Spread diameter, mm
n_{RT}	Straddle distribution parameter, -
P_t	Fill element pitch, m, Slat tooth pitch, mm
P	Pressure, Pa, Momentum, kg·m/s
Q	Heat transfer rate, W
R	Gas constant, J/kgK, Cumulative mass fraction
S	Shape factor, -, or slat spacing, m or mm
S_P	Drip characteristic length, m
s	Distance, m
T	Temperature, K
t	Time, s
U	Total internal energy, J
v	Velocity, m/s
w	Humidity ratio, kg/kg dry air
W	Slat width, mm
x	Drop collision impact parameter, -
X	Drop collision impact parameter, m
z	Height, m

List of Greek symbols

β	Grid porosity, -
γ	Collision drop diameter ratio, -
Δ	Differential
δ	Water film thickness on slat, mm
η	Angle, °
θ	Angle, °
λ	Displacement between drop and slat centre, -
μ	Dynamic viscosity, kg/ms
ρ	Density, kg/m^3
σ	Surface tension, N/m
τ	Shear stress, N/m^2

ϕ	Splash mix ratio, -

List of subscripts

a	Air
atm	Atmosphere
B	Buoyancy
b	Break
bot	Bottom of slat
c	Critical, cutting, straddling
coal	Coalescence
coll	Collisions
conv	Convection
ct	Cooling tower
D	Drag
d	Drop, dripping below slats
e	Evaporate, e-NTU
f	Fluid, frontal, film
F	Fill
fr	Frontal based on rain zone
G	Grid
g	Gas
h	Hydraulic
i	Inlet, initial
l	Large
M	Merkel
m	Mean
n	Normalised
o	Outlet
P	Poppe
p	Primary drip drop, particle
pr	Projected
R	Resultant
RR	Rosin-Rammler

ref	Reference
rz	Rain zone
s	Small, splash, satellite, saturated, splash drop, surface
T	Terminal velocity
v	Vapour or vertical
w	Water, wire
wb	Wet bulb
∞	Far field

Dimensionless groups

Eo	Eotvos number,	$\frac{gd^2(\rho_p - \rho_f)}{\sigma}$
Le$_f$	Lewis factor,	$\frac{h_c}{h_d c_p}$
Nu	Nusselt number,	$\frac{h_c d}{k} = f(Re, Pr)$
Oh	Ohnesorge number,	$\frac{\sqrt{We}}{Re} = \frac{\mu}{(\rho\sigma d)^{0.5}}$
Pr	Prandtl number,	$\frac{c_p \mu}{k}$
Re	Reynolds number,	$\frac{\rho v d}{\mu}$
Sc	Schmidt number,	$\frac{\mu}{\rho D}$
Sh	Sherwood number,	$\frac{h_D d}{D} = f(Re, Sc)$

We	Weber number,	$\frac{\rho v^2 d}{\sigma}$
Me	Merkel number,	$\frac{h_d a_{fi}}{G_w}$

Abbreviations

SPSIM	Splash pack simulation program
STP	Standard temperature and pressure, 20°C and 101 325 Pa
NDWCT	Natural draught wet-cooling tower

1

INTRODUCTION

In this chapter a short background is given to show how this thesis aims to benefit the power generation sector, followed by the project motivation, objectives and scope, with a thesis summary at the end.

1.1 Background

Industrial thermal systems like power plants and petrochemical plants can reject waste heat to the atmosphere by means of natural draught wet-cooling towers (NDWCTs). These towers are currently employed at numerous power plants worldwide and there is a need for the improvement of these cooling towers in order to reduce life cycle costs of these power plants. Increased cycle efficiencies due to improved cooling towers will also be beneficial to the environment due to reduced emissions of greenhouse gases.

Figure 1.1 shows a diagram of a NDWCT. When the hot cooling water leaves the condenser it is pumped to the water distribution system inside the cooling tower from where the water is distributed onto the fill by means of spray nozzles. The hot water then passes through the fill zone where convection heat- and mass transfer to the air is enhanced by maximizing the air to water interface area. Below the fill region the water passes through the rain zone in the form of drops with a polydisperse size distribution before ending up in the pond from where it is pumped back to the condenser.

Cold air enters from the bottom of the cooling tower and becomes buoyant as heat and mass is transferred to the air stream in the rain- , fill- , and spray zone which reduces the density of the air to induce a natural draught inside the cooling tower.

The mechanism for drop formation below the fill region in a NDWCT is mainly dripping causing the formation of relatively large drops which have a Sauter mean drop diameter of approximately d_{32} = 5 to 5.5 mm according to Terblanche *et al.* (2009). These drops accelerate under gravity thus converting potential energy to kinetic energy while the average drop size may change significantly over the fall distance due to drop collisions and aerodynamic forces breaking up the larger drops.

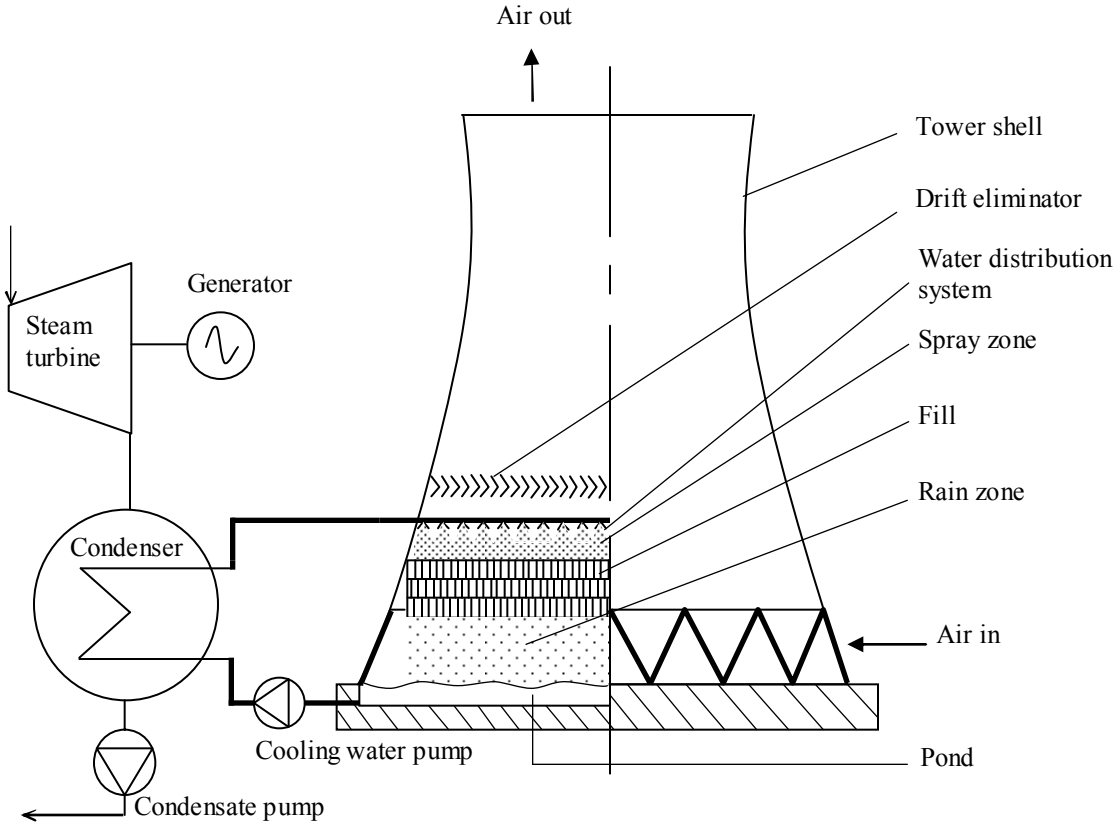

Figure 1.1: Counter flow natural draught wet-cooling tower.

According to Kröger (2004) and Reuter (2010) 10 – 20 % of a NDWCT's heat is rejected in the rain zone. A significant improvement in this region will therefore lead to a significant improvement in the overall NDWCT's performance that is currently not fully exploited. Kröger (2004) and Reuter (2010) show that the performance of a NDWCT is significantly influenced by the Sauter mean drop diameter in the rain zone and that a reduction of the initial drop size can significantly improve the overall performance of the NDWCT. Hollands (1974) recommended a uniform drop size between d_d = 1 and 2 mm in diameter for the rain zone because drops of this size cool relatively fast and their uniform size distribution means that collisions that can lead to coalescence between the drops are negligible in many cases.

Figure 1.2 shows the sensitivity of the cooling tower inlet water temperature change and tower Merkel number to the Sauter mean drop diameter in the rain zone. This is calculated with the full scale cooling tower model of Kröger (2004) for two types of fill packing, namely a Type 9 fibre cement fill (Kröger, 2004), consisting of vertical plates spaced 0.0254 m apart, and the expanded metal fill of Kröger (2004). The figure shows that the model of Kröger (2004) predicts a significant reduction in the inlet water temperature with a reduction in the rain zone Sauter mean drop diameter,

even under the fibre cement fill which is a relatively high performing fill compared to the expanded metal fill.

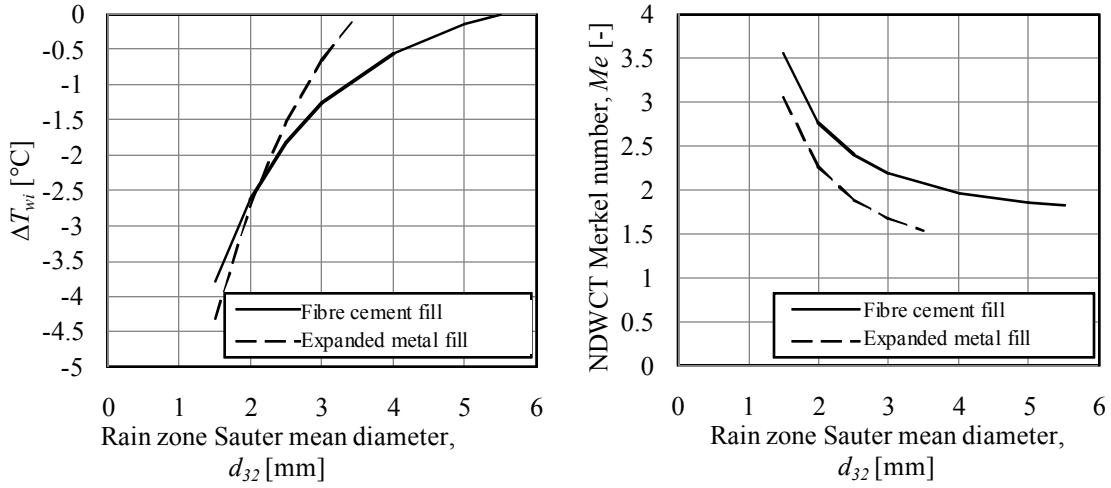

a) Inlet water temperature change b) NDWCT Merkel number

Figure 1.2: Inlet cooling water temperature change and NDWCT Merkel number as a function of rain zone drop size.

Dreyer (1994), Oosthuizen (1995) and Terblanche (2008) showed that the average drop size in the rain zone can be significantly reduced with the installation of splash grids below the fill. The aim is to design a grid in which an optimum is determined between variables such as grid porosity, slat width, slat height, slat bottom profiles and the distance between the fill and the grid.

1.2 Motivation

Improving the performance of the NDWCT means that heat can be transferred to the environment at lower cooling water temperatures which reduces the back pressure on the turbine (Figure 1.1) and increases power output; leading to improved cycle efficiency. Reuter (2010) estimates that a 3 °C reduction in cooling water temperature of a NDWCT leads to an approximate 1 % increase in power plant cycle efficiency and that a significant reduction in cooling water temperature may potentially be achieved by reducing the drop sizes in the rain zone, while still reducing the life cycle cost of the power plant.

1.3 Objectives

The objectives for this project are as follows:

a) Quantify the reduction in cooling water temperature of the cooling tower when the rain zone performance is improved.
b) Determine the drop size reduction capability of existing splash grids.
c) Determine the drop interactions in the free fall zone below cooling tower fill and drop size reduction grids installed below the fill.
d) Determine the mechanisms of drop break-up when drops impinge onto the surfaces of splash grids.
e) Quantify each drop break-up mechanism in terms of mass and drop size distribution.
f) Determine the expected increase in rain zone performance when splash grids are installed.
g) Measure the increase in rain zone performance when splash grids are installed.
h) Optimize the grid geometry.

1.4 Scope of the work

The scope of work needed to fulfil the above objectives is summarised as follows:

a) Investigate the effect of rain zone drop size on the performance of different cooling towers, using the model of Kröger (2004).
b) Measure the drop sizes below existing splash grids as well as experimental grids by using the photographic technique and equipment described in Terblanche *et al.* (2009).
c) Measure the initial drop sizes at the top of free fall zones with different drop inlet distributions and then again at a distance of approximately H_{rz} = 7 to 7.7 m further down and compare the drop distributions.
d) Investigate drop break-up after impingement on slats by taking sequential photographs with high speed video cameras, varying drop diameter, fall distance, slat width and water film thickness on the slat.
e) Distinguish between the different drop break-up mechanisms and quantify the mass as well as the drop distribution associated with each mechanism and correlate the results.
f) Develop a theoretical model to predict the drop size reduction of splash grids, the rain zone performance and pressure difference when such grids are installed.

g) Measure the performance of a cross flow rain zone and compare the performances of these rain zones with and without installed splash grids.
h) Use the theoretical model to optimize grid geometry.

1.5 Thesis summary

In this section a summary of each chapter is provided by giving a brief description of the content in each chapter.

CHAPTER 1. INTRODUCTION

This chapter provides the background to the project and shows how it aims to benefit the power generation sector. A motivation, objectives and scope of work of the project are provided. Finally a summary of the thesis is provided where each chapter is briefly discussed.

CHAPTER 2. LITERATURE SURVEY

This chapter discusses the relevant literature necessary to model counter flow rain zone performance. It includes many of the current correlations for predicting drop drag, aerodynamic drop break-up, drop coalescence upon collision and drop heat and mass transfer in the free fall zone. The interaction of drops with a splash grid is discussed by referring to the mechanisms (splashing, cutting and dripping) of drop break-up and the current correlations used to quantify the effect of each mechanism on the overall drop distribution in the rain zone. Rain zone transfer characteristic and pressure drop are also discussed.

CHAPTER 3. A THEORETICAL MODEL FOR PREDICTING THE PERFORMANCE OF A COUNTER FLOW COOLING TOWER RAIN ZONE WITH HORIZONTAL LAYERS OF SPLASH GRIDS INSTALLED IN IT.

This chapter discusses the development of a theoretical model for predicting counter flow rain zone performance with and without installed splash grids. It is based on current correlations and equations found in literature as well as new correlations proposed in this thesis. For free fall zone modelling, analytical equations are proposed for drop velocity, trajectory and temperature. For the grid interaction zone, equations are proposed for predicting the amount of splashing and straddling when drops impinge onto grid surfaces as well as for predicting the distribution of the drops due to splashing and straddling. An analytical equation is also developed for predicting the sizes of drops dripping from various slat geometries. Lastly, simplified equations for predicting the interaction between splash drops and other falling drops

above the grid as well as between splash drops and the grid itself are developed from numerical results.

CHAPTER 4. COMPARISON BETWEEN THE THEORETICAL RAIN ZONE MODEL AND EXPERIMENTAL DATA

In this chapter the theoretical model developed in the previous chapter is compared to the measured data obtained in this thesis as well as data from literature.

CHAPTER 5. SPLASH GRID OPTIMIZATION

This chapter discusses the drop size reduction trends associated with the main grid variables such as distance between the fill and grid, number of grid layers, slat width, slat spacing, slat height, geometry on the bottom of the slat and aims to provide the optimum splash grid layout inside a rain zone.

CHAPTER 6. CONCLUSIONS

This chapter provides a short summary of the thesis and discusses the main conclusions that are drawn from the work done in this thesis.

APPENDICES

The appendices contain detailed descriptions of the experimental, theoretical, numerical and analytical procedures conducted in this dissertation and they are referred to in the main chapters.

2

LITERATURE SURVEY

2.1 Introduction

Performance enhancement of natural draught wet-cooling towers may involve the installation of additional performance enhancing devices (e.g. drop size reduction grids in the rain zone or wind break walls) or the modification or replacement of existing internals with more efficient ones (e.g. drift eliminators, sprayers, fill). Performance enhancement can also be achieved with good maintenance to ensure that the performance deterioration over time of the cooling tower is kept to a minimum. Maintenance may include good water treatment to minimize fouling and precautionary measures to prevent icing inside cooling towers that causes damage to the fill material when it breaks off and falls on the fill after becoming too heavy due to ice build-up.

A very important aspect in insuring optimal cooling tower performance is an even water distribution onto the fill. The important aspects to consider when improving or designing the water distribution system are the type of nozzle, nozzle spacing, operating pressure and height between the nozzles and the fill [Kranc (1983), Kranc (1986), Chen *et al.* (2004), Viljoen (2006), Kranc (2007)]. Non-uniform spray patterns generally occur because spray nozzles that produce a circular spray pattern are positioned on a rectangular grid and can be partially corrected by overlapping spray patterns. According to the model of Kranc (1983) some degree of non-uniformity from the water distribution system can be tolerated without significantly affecting the thermal performance of the fill, but as much as 10 to15 % less than the expected heat and mass transfer may take place in a fill due to non-uniform water distribution, depending on the nozzle spacing and spray pattern. The type of nozzle as well as the operating pressure also influences the average drop size in the spray zone that significantly influences the overall performance of the cooling tower. According to Kröger (2004) up to 15 % of the cooling taking place inside a cooling tower may happen in the spray zone and the ideal would be to produce a uniform drop distribution with drop diameters between d_d = 1 and 2 mm [Hollands (1974), Bellagamba *et al.* (1988), Viljoen (2006)] so that the drops are still large enough not to be entrained in the counter flowing air.

The type of fill can also significantly influence the cooling tower's performance seeing that most of the heat and mass transfer takes place in this region. There are

three basic types of fill namely: film- , splash- and trickle fill. Trickle fill generally performs the best followed by film- and splash fill. According to Kröger (2004) the disadvantages of trickle fills are that they tend to clog more easily due to their fine mesh and they have greater pressure drops, while film type fills are more prone to fouling and therefore water quality becomes important. When water quality is good film- and trickle fills are generally preferred to splash fills because they are more compact and therefore require less pumping power and also less material. Cooling towers fitted with splash fills may require extra fan power due to increased resistance which means that operating cost increases. When deciding on the type of fill to be used in a cooling tower the main considerations according to Mohiuddin and Kant (1996) are the heat transfer performance, pressure drop, cost and durability of the fill. Surface roughness and free energy of the fill surface together with the pitch and layout of the fill elements can significantly influence the fill performance characteristics [Goshayshi and Missenden (2000), Gharagheizi *et al.* (2007)]. Williamson *et al.* (2008b) concluded from their 2D study of a natural draught wet-cooling tower that for optimal performance the depth of film type fills as well as the water mass velocity should decrease towards the centre of the tower where the air is warmer, but shows that the expected performance increase is very low. Reuter (2010) concluded that fill type must be taken into account when optimising fill layout and water load inside a cooling tower and showed numerically that a layout that leads to an increase in cooling range for an expanded metal fill can have the opposite effect when a trickle fill is used.

Poor water quality inside the cooling tower can cause fouling which can be defined as the deposition of foreign matter, including bio-growth, on the water film flow area [Khan *et al.* (2004)]. Qureshi and Zubair (2006) quoted experimental data from Michael *et al.* (1993) that shows tower characteristics reducing to 18 % of the clean tower values due to fouling, but states that the decrease in performance characteristics stopped here although fouling continued further.

According to Kröger (2004), Williamson *et al.* (2008a) and Reuter (2010) 10 - 20 % of the total heat can be rejected in the wet-cooling tower rain zone and the total performance can be significantly increased by installing drop size reduction devices inside the rain zone [Oosthuizen (1995), Terblanche (2008)] in order to maximize the air-water interfacial area.

The performance of the cooling tower in cross wind conditions can be improved by the shape of the cooling tower or through the installation of wind break walls. These walls can be installed below the wet-cooling tower fill or outside the cooling tower to improve the air inlet of the cooling tower. Al-Waked and Behnia (2007) suggested the installation of porous walls inside and outside the rain zone and claimed a reduction in cooling water temperature of between 0.5 and 1°C for cross-wind velocities up to 16 m/s. Wang *et al.* (2010) found that wet-cooling tower performance

increases remarkably when the inlet air is directed by means of vertical guide vanes around the circumference of the rain zone and proposed an optimum vane angle of 70° (relative to the tangent on the circumference) which is independent of the amount of vanes used. Ruscheweyh (1982) showed how a diverging outlet shape may improve air flow through the cooling tower under cross wind conditions.

General aerodynamic improvements can include solid walkways around the upper rim of the air inlet section and rounded air inlets, according to Reuter (2010), as well as the initial placement of the tower relative to other buildings and cooling towers [Niemann and Köpper (1998) and Orlando (2001)]. Reuter (2010) stressed the importance of optimising on a case by case basis and showed that the optimal radial varying water and fill distributions inside a NDWCT can vary for different fill types, as mentioned earlier.

Aerodynamically well designed drift eliminators, according to Yao and Schrock (1976a), can also lead to improved air flow through the cooling tower and therefore enhance overall performance. Becker and Burdick (1993) showed the importance of evaluating cooling tower components such as drift eliminators in the context of the total cooling tower system when deciding between different options.

In this thesis the focus is on developing a performance enhancement grid for natural draught wet-cooling towers which improves the rain zone. The rest of this chapter focus on the literature associated with the rain zone and discusses the available theory on the different aspects of rain zone performance prediction.

2.2 Drop drag

In order to predict drop motion in the rain zone accurately, it is necessary to predict the drop drag accurately since it directly influences the drop velocity which in turn influences drop cooling, drop interaction, aerodynamic drop break-up and drop break-up caused by impingement of drops onto splash grid surfaces.

$$F_D = C_D \rho_a \frac{{v_d}^2}{2} A_f \tag{2.1}$$

Drag force, $F_{D,}$ on a drop can be expressed by Equation (2.1) where the force acting on the drop due to air resistance is expressed in terms of a drag coefficient (C_D). The drag coefficients for spheres have in the past been investigated by numerous researchers who obtained their results experimentally, numerically or analytically and a few of the proposed drag coefficients are listed in Table 2.1 and plotted in Figure 2.1. It can be seen in Figure 2.1 that within the applicable range for falling drops the

difference between the models are negligible and in this thesis the sphere drag coefficient of Turton and Levenspiel (1986) is used, the same as Dreyer (1994).

A sphere drag coefficient is often not accurate enough, especially if the Eotvos number exceeds 0.15 (Clift *et al.*, 1978) and secondary effects like drop oscillations, drop deformation and internal circulation becomes significant. According to Clift *et al.* (1978) falling drops can also experience further secondary effects like side to side rocking or the following of a zig-zag or spiral trajectory. It can be concluded from the work done by LeClair *et al.* (1972) and Pruppacher and Klett (1978) that drop oscillations and internal circulation have a negligible effect on drop drag and are at least partially damped out by surface active contaminants according to Clift *et al.* (1978).

Table 2.1: Correlations for the drag coefficients of spherical bodies.

Researcher	Drag coefficient formula	
Schiller and Nauman (1933)	$C_D = \frac{24}{Re}(1 + 0.15Re^{0.687})\ for\ 2 < Re \leq 800$	(2.2)
Torobin and Gauvin (1959)	$C_D = \frac{24}{Re}(1 + 0.197Re^{0.63} + 0.0026Re^{1.38})\ for\ 1 < Re < 100$	(2.3)
Clift *et al.* (1978)	$C_D = \frac{24}{Re}(1 + 0.15Re^{0.687}) + \frac{0.42}{1 + 42500Re^{-1.16}}\ for\ Re \leq 2 \cdot 10^5$	(2.4)
Concha and Barrientos (1982)	$C_D = \frac{0.284153}{Re^2}\left(1 + \frac{9.04}{\sqrt{Re}}\right)^2 (0.9620833Re^2 + 2.736461 \cdot 10^{-5}Re^3 - 3.938611 \cdot 10^{-10}Re^4 + 2.476861 \cdot 10^{-15}Re^5 - 7.159345 \cdot 10^{-21}Re^6 + 7.437237 \cdot 10^{-27}Re^7)$ $for\ Re < 3 \cdot 10^6$	(2.5)
Flemmer and Banks (1986)	$C_D = \frac{24}{Re}10^E\ where$ $E = 0.261Re^{0.369} - 0.105Re^{0.431} - \frac{0.124}{1 + (\log Re)^2}\quad for\ Re < 10^5$	(2.6)
Turton and Levenspiel	$C_D = 24\frac{(1 + 0.173Re^{0.657})}{Re} + \frac{0.413}{(1 + 16300Re^{-1.09})}\ for\ Re \leq 2 \cdot 10^5$	(2.7)

Researcher	Drag coefficient formula	
(1986)		
Hesketh *et al.* (1991)	$C_D = 1 - 0.5exp(0.182) + 10.11Re^{-\frac{2}{3}}exp\left(0.952Re^{-\frac{1}{4}}\right) - 0.03859Re^{-\frac{4}{3}}exp\left(1.3Re^{-\frac{1}{2}}\right) + 0.037 \cdot 10^{-4}Re \cdot exp(-0.125 \cdot 10^{-4}Re) - 0.116 \cdot 10^{-10}Re^2exp(-0.444 \cdot 10^{-5}Re)$ $for\ 0.1 < Re < 10^6$	(2.8)
Ceylan *et al.* (2001)	$C_D = K_1(Re,n) + K_2(Re,n)\ where$ $K_1(Re,n) = 1 - 0.5exp(0.182) + 10.11Re^{-\frac{2}{3}}exp\left(0.952Re^{-\frac{1}{4}}\right) - 0.03859Re^{-\frac{4}{3}}exp\left(1.30Re^{-\frac{1}{2}}\right)$ $K_2(Re,n) = 0.037 \cdot 10^{-4}Re \cdot exp(-0.125 \cdot 10^{-4}Re) - 0.116 \cdot 10^{-10}Re^2exp(-0.444 \cdot 10^{-5}Re)$	(2.9)
Feng and Michaelides (2001)	$C_D = \frac{24}{Re}\left(1 + \frac{Re^{\frac{2}{3}}}{6}\right)\ for\ Re \leq 10^3$	(2.10)
Brown and Lawler (2003)	$C_D = \frac{24}{Re}(1 + 0.15Re^{0.681}) + \frac{0.407}{1 + 8710/Re}\ \ for\ Re < 2 \cdot 10^5$	(2.11)
Almedeij (2008)	$C_D = \left[\frac{1}{(\varphi_1 + \varphi_2)^{-1} + \varphi_3{}^{-1}} + \varphi_4\right]^{\frac{1}{10}}\ \ for\ Re < 10^6$ where $\varphi_1 = (24/Re)^{10} + (21/Re^{0.67})^{10} + (4/Re^{0.33})^{10} + 0.4^{10}$ $\varphi_2 = \frac{1}{(0.148Re^{0.11})^{-10} + 0.5^{-10}}$, $\varphi_3 = (1.57 \cdot 10^8/Re^{1.625})^{10}$ $\varphi_4 = \frac{1}{(6 \cdot 10^{-17}Re^{2.63})^{-10} + 0.2^{-10}}$	(2.12)
Cheng (2009)	$C_D = \frac{24}{Re}(1 + 0.27Re)^{0.43} + 0.47[1 - exp(-0.04Re^{0.38})]$ $for\ Re \leq 2 \cdot 10^5$	(2.13)

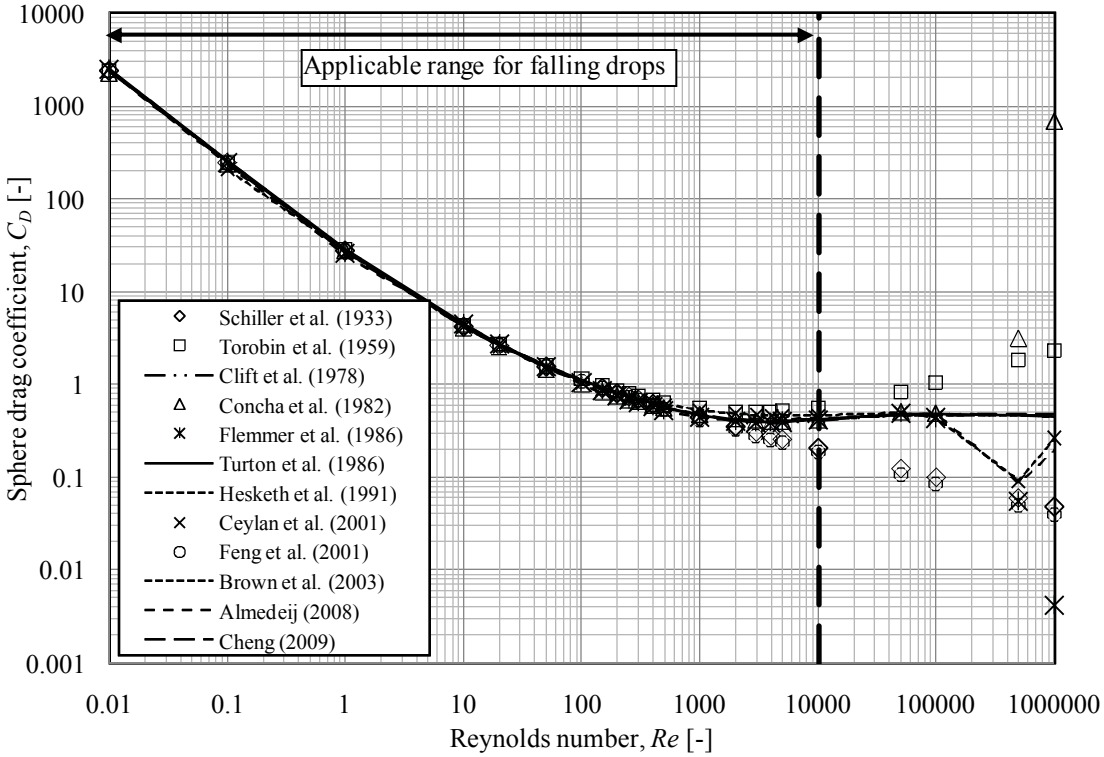

Figure 2.1: Comparison between different sphere drag coefficient correlations.

Drop deformation causes a significant increase in drop drag for drops with Eotvos numbers larger than 0.15 and Dreyer (1994) proposed a correlation for the ratio between the drag coefficient of a deformable drop and a corresponding sphere that is given by

$$\frac{C_D}{C_{D,sphere}} = 1 - 0.17185(1-E) + 6.692(1-E)^2 - 6.605(1-E)^3 \tag{2.14}$$

where the aspect ratio of the drop is also given by Dreyer (1994) as

$$E = 1 - \left(\frac{v_d}{v_T}\right)^2 (1 - E_T) \tag{2.15}$$

Table 2.2 shows equations for predicting the aspect ratios of drops falling at terminal velocity as proposed by previous researchers. The aspect ratios are expressed in terms of the Eotvos number given by

$$Eo = \frac{g{d_d}^2(\rho_d - \rho_{av})}{\sigma_d} \tag{2.16}$$

Table 2.2: Deformed drop aspect ratio at terminal velocity.

Researcher	Deformed drop aspect ratio	
Pruppacher and Beard (1970)	$E_T = 1.03 - 0.062 d_d \ for \ 1.0 < d < 9.0 \ mm$	(2.17)
Clift *et al.* (1978)	$E_T = [1 + 0.18(Eo - 0.5)^{0.8}]^{-1} \ for \ 0.5 < Eo < 8$	(2.18)
Srikrishna *et al.* (1982)	$E_T = (0.146Eo + 1)^{-1}$	(2.19)
Dreyer (1994)	$E_T = (1 + 0.148Eo^{0.85})^{-1}$	(2.20)

Figure 2.2(a) shows the ratio between the drag coefficient of a deformable drop and a corresponding sphere (Equation 2.14) and Figure 2.2(b) shows the predicted aspect ratios of drops at terminal velocity according to the Equations (2.18 – 2.20) listed in Table 2.2.

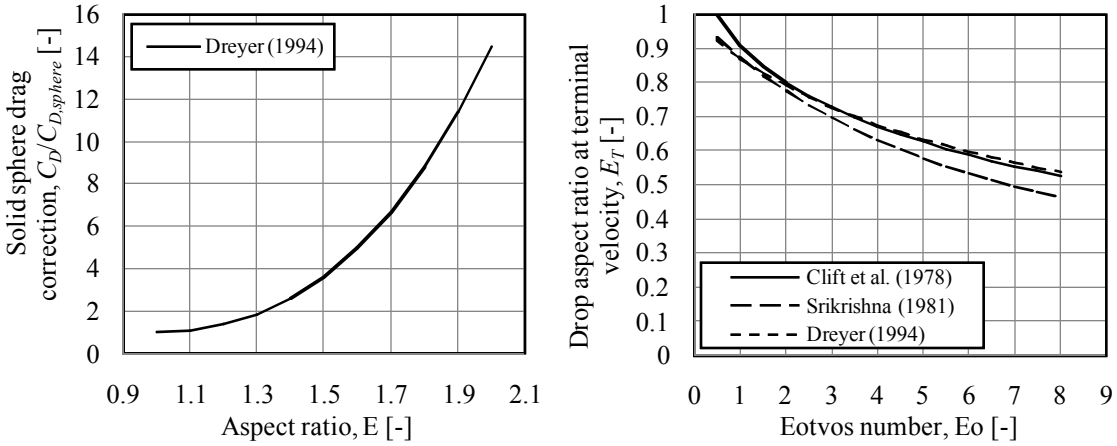

a) Sphere drag coefficient correction b) Aspect ratio at terminal velocity

Figure 2.2: Correction parameters for converted sphere drag coefficients to accelerating deformed drop drag coefficients.

Drag coefficients of spheres or drops might be influenced by other spheres or drops that are in close proximity and a number of researchers investigated this effect on spheres [Zhu *et al.* (2003), Maheshwari *et al.* (2006), Kishore *et al.* (2008)] in power law fluids. The relationship between shear stress and the velocity gradient in power law fluids is given by the following generalised equation

$$\tau = K\left(\frac{\partial v}{\partial y}\right)^n \tag{2.21}$$

where K = μ and n = 1 for Newtonian fluids and ∂v/∂y is perpendicular to the flow direction.

According to Hollands (1974) the void factions between drops in a spray cooling tower, similar to a rain zone, are very large especially closer to the bottom where drop velocities are relatively high. One can therefore assume that drops in a rain zone have a negligible effect on each other in terms of drag due to air resistance.

Turbulence may also affect drop drag in the rain zone. Brucato *et al.* (1998) measured a significant increase in particle drag coefficient with increased turbulence for small particles at Reynolds numbers up to 1000 (d_p < 0.5 mm), but mentions that the reason for this is unclear. Moradian *et al.* (2009) measured a reduction in sphere drag coefficient with increasing turbulence intensity at Reynolds numbers ranging from Re = $2.2{\cdot}10^4$ to $8{\cdot}10^4$ (20 mm < d_{sphere} < 102 mm). Neve and Shansonga (1989) showed contour plots for sphere drag coefficients for different combinations of turbulence intensity and length scale to sphere diameter ratios and shows that drag coefficient can increase or decrease with increasing turbulence depending on the combination of length scale to sphere diameter ratio and turbulence intensity. The effect of turbulence on drop motion is however assumed negligible in this project as was done by Dreyer (1994) in his splash pack simulation program (SPSIM).

2.3 Aerodynamic drop break-up

Aerodynamic drop break-up occurs when the ratio of the disruptive hydrodynamic forces (drag force and viscous stresses inside the drop caused by drop deformation) to the stabilizing surface tension forces, quantified by the Weber number, exceeds a critical value. When this happens it leads to the formation of two or several smaller drops. Aerodynamic drop break-up becomes important for relatively large drops, typically exceeding d_d = 5.5 mm in diameter (List *et al.*, 1970), at fall distances of approximately H_{rz} = 5 to 7 m in the rain zones of wet-cooling towers. Although the expected effect on cooling tower performance may be small, but still significant, it is included in the rain zone analysis of the next chapter.

Table 2.3: Criteria for different drop break-up regimes given by Pilch *et al.* (1988).

Drop break-up regime	Criteria
Vibrational break-up	$We \leq 12$

Drop break-up regime	Criteria
Bag break-up	$12 \leq We \leq 50$
Bag-and-stamen break-up	$50 \leq We \leq 100$
Sheet stripping	$100 \leq We \leq 350$
Wave crest stripping followed by catastrophic break-up	$We > 350$

Five different types of break-up, depending on the Weber number (Table 2.3), have been observed in the literature and they are:

1) Simple or vibrational break-up in which the drop divides into smaller equally sized drops (never more than four) due to the development of oscillations at the natural frequency of the drop [Borisov *et al.* (1981), Pilch and Erdman (1988), Wierzba (1990)].
2) Parachute or bag break-up in which the drop initially flattens before deforming into a bag in the downstream air direction, anchored to a rim, that eventually breaks up into fine drops leaving a torus that breaks up a short time later in the form of a small number of larger fragments [Lane (1951), Borisov *et al.* (1981), Pilch and Erdman (1988), Wierzba (1990)].
3) Bag-and-stamen break-up is similar to bag break-up, but is accompanied by the formation of a liquid column (stamen) along the drop's central axis parallel to the flow. The bag bursts, followed by the disintegration of the stamen [Pilch and Erdman (1988)].
4) Stripping in which thin sheets of the flattened drop are torn away around its periphery to disintegrate a short distance downstream in the form of small drops [Borisov *et al.* (1981), Pilch and Erdman (1988)].
5) Wave crest stripping followed by catastrophic break-up happens when small wavelength, large-amplitude waves are formed on the surface of the drop while the wave crests are continuously eroded by the air stream (wave crest stripping). Ultimately the drop is penetrated by large-amplitude long-wavelength waves to break up into fragments that are further subjected to catastrophic break-up in the air stream [Borisov *et al.* (1981), Pilch and Erdman (1988)].

Lane (1951) gives a relation (Equation 2.22) in terms of critical Weber number at which a drop will break up due to the bursting bag process in an air stream, but found that the experimental critical Weber number is closer to We_c = 10, compared to a maximum possible Weber number in the rain zone of $We_{rz,max}$ = 15.5. It is observed in this thesis that at H_{rz} = 7 to 7.7 m below a trickle fill (still air) significant break-up, that resembles stripping (Figure G.6), happens at a Weber number of approximately We_c = 10.5.

$$We_c = \frac{\rho_{av}(v_a - v_d)^2 d_d}{\sigma_d} = \frac{8}{C_D} \approx 20 \tag{2.22}$$

The following empirical correlation is provided by Pilch and Erdman (1988) for the critical Weber number at which drop break-up is initiated.

$$We_c = 12(1 + 1.077Oh^{1.6}) \tag{2.23}$$

where

$$Oh = \frac{\mu_d}{(\rho_d d_d \sigma_d)^{0.5}} \tag{2.24}$$

Wierzba (1990) conducted experiments in which water drops with diameters of d_d = 2.22, 2.60 and 3.90 mm respectively where injected vertically downwards in a horizontal flowing air stream with Weber numbers ranging from We = 11 to 14. Wierzba (1990) suggested that the critical Weber number should be the one where break-up occurs for 100% of the drops and for his experiments this value ranged from We_c = 13.7 to 14.07.

In the 2-D simulation of Duan *et al.* (2003) the critical Weber number for a uranium dioxide drop in water were found to be We_c = 13, which is in agreement with the observations of Wierzba (1990) for water drops.

2.4 Drop-drop collisions

Rain zone performance may be improved by using grids to reduce the average drop size in this region. However, in the free fall zone below such a grid the Sauter mean drop diameter may tend to increase significantly over a distance of H_{rz} = 7 to 10 m as a result of drop coalescence due to collisions. It is estimated in this thesis that the Sauter mean drop diameter below a newly designed grid can increase from d_{32} = 2 to 2.6 mm over a $H_{rz} \approx$ 9 m fall distance below the grid, which shows that the effect of drop collisions on the rain zone performance can be significant.

Drops may fall at different velocities in a rain zone due to size differences or splash grid interaction. This can lead to many drop collisions, especially at relatively high rain densities. When collisions happen the drops can either shatter, bounce apart, coalesce permanently or coalesce temporary before separating into drops that are similar to the initial drops, accompanied by much smaller satellite drops [Brazier-Smith *et al.* (1972), Ashgriz and Poo (1990), Jiang *et al.* (1992), Qian and Law (1997)].

In order for drops to coalesce after colliding, the coalesced drop must be able to withstand the dynamic forces created inside the drop and dissipates the collision energy (kinetic and surface energy) by deforming (increased drag and internal viscous dissipation), by oscillating, by spinning or through surface waves [Adam *et al.* (1968), Low and List (1982)]. According to Ashgriz and Poo (1990) the viscous dissipation inside the drops only becomes significant at large Laplace numbers [$Lp = We/Re^2 = \mu^2/(\rho_d d_d \sigma)$], which indicate the ratio of viscous effects to surface tension effects.

Drop separation after temporary coalescence can occur when the dynamic forces, due to the collision energy and impact parameter (Figure 2.3a), overcome the stabilizing surface tension forces. When this happens the coalesced drop separates into primary drops, similar to the initial drops, and a multitude of smaller satellite drops [List *et al.* (1970), McTaggart-Cowan and List (1975), Bradley and Stow (1978), Bradley and Stow (1979), Qian and Law (1997)]. Cases do also exist where the integrity of the initial drops is completely lost and they aren't recognisable in the collision products [McTaggart-Cowan and List (1975), Ashgriz and Poo (1990)]. Figure 2.3(b) shows the various collision regimes of water drops in atmospheric air as given by Qian and Law (1997).

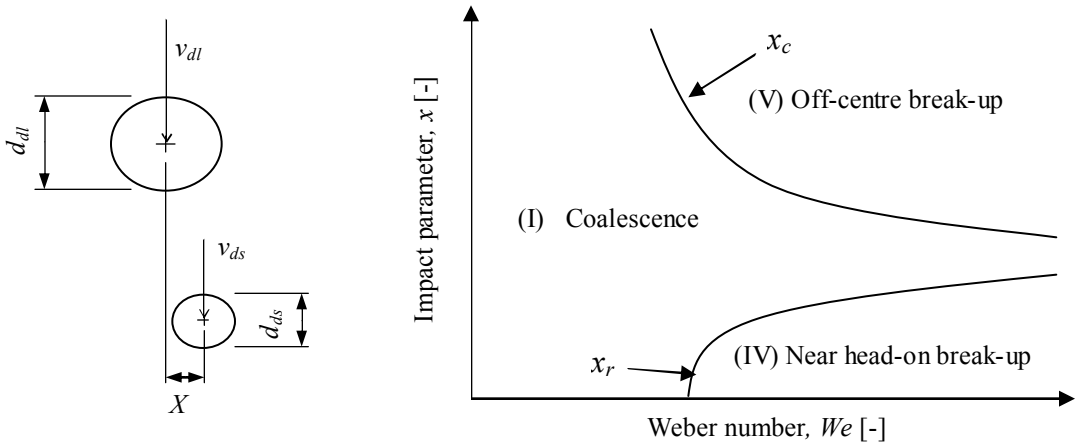

a) Impact parameter (X) b) Drop collision regimes in atmospheric air (Qian *et al.* (1997)

Figure 2.3: Impact parameter (X) and collision regimes of colliding drops.

Some of the first researchers who developed criteria for the coalescence and separation of colliding drops were Adam *et al.* (1968). They investigated the collisions between equally sized drops ranging from d_d = 0.12 to 1 mm in diameter, colliding at relative velocities of up to v_{dls} = 8 m/s. They found that coalescence and separation after drop collisions can be linked to an impact parameter X (Figure 2.3a) and that drop coalescence usually takes place below a certain critical value, X_c, given

a certain relative velocity $v_{dls} = v_{dl} - v_{ds}$. Adams *et al.* (1968) also found that with increasing relative velocity (v_{dls}) the critical impact parameter X_c decreased.

Table 2.4 presents some of the proposed equations found in literature for the dimensionless critical impact parameter (x_c) in terms of the collision Weber number and drop diameter ratio (γ). The dimensionless critical impact parameter is given by

$$x_c = \frac{2X_c}{d_{dl} + d_{ds}} \tag{2.25}$$

The collision Weber number is given by

$$We = \frac{\rho_{av}(v_{dl} - v_{ds})^2(d_{dl} + d_{ds})}{2\sigma} \tag{2.26}$$

and the drop diameter ratio is given by

$$\gamma = \frac{d_{ds}}{d_{dl}} \tag{2.27}$$

Park (1970) derived Equation (2.28), for the boundary between coalescence (Regime I) and stretching separation (Regime V), by balancing the centrifugal forces of the rotating coalesced drop with the surface tension forces in the region of contact.

Table 2.4 : Critical impact parameters for drop collisions (Regime V).

Researcher	Dimensionless critical impact parameter	
Park (1970)	$x_c = \left(\frac{6}{\pi}\right)^{\frac{1}{2}} \frac{[(1+\gamma)(\gamma^2-\gamma+1)]^{\frac{1}{2}}}{\gamma^{\frac{3}{2}} We^{\frac{1}{2}}} \left[\frac{(1+\gamma^5)(\gamma^2-\gamma+1)}{5\gamma^3} + \frac{(1+\gamma)}{2}\right] \left[4 - \left(x_c(1+\gamma) - \frac{(1-\gamma)}{x_c}\right)^2\right]^{\frac{1}{4}}$	(2.28)
Brazier-Smith *et al.* (1972)	$x_c = \left(\frac{12}{5We}\right)^{\frac{1}{2}} \frac{(1+\gamma^3)^{\frac{11}{6}}}{(1+\gamma)\gamma^3} \left[(1+\gamma)\left(1+\gamma^2-(1+\gamma^3)^{\frac{2}{3}}\right)\right]^{\frac{1}{2}}$	(2.29)
O'Rourke (1981)	$x_c = \sqrt{\frac{2.4(\gamma^{-3} - 2.4\gamma^{-2} + 2.7\gamma^{-1})}{We}}$	(2.30)

Researcher	Dimensionless critical impact parameter	
Low and List (1982)	$x_c = \left[0.778(1+\gamma)^{-2} exp\left\{-\frac{2.61 \times 10^6 {E_T}^2}{\pi\left({d_{dl}}^3 + {d_{ds}}^3\right)^{2/3}}\right\}\right]^{\frac{1}{2}} \quad for\ E_T < 5.0\mu J$ $E_T = \left(\frac{\rho_d \pi}{12}\right)\frac{{d_{dl}}^3 {d_{ds}}^3}{{d_{dl}}^3 + {d_{ds}}^3}(v_{dl} - v_{ds})^2 + \pi\sigma\left({d_{dl}}^2 + {d_{ds}}^2\right) - \pi\sigma\left({d_{dl}}^3 + {d_{ds}}^3\right)^{2/3}$	(2.31)
Arkhipov *et al.* (1983)	$x_c = \frac{1}{\gamma^3}\left[\frac{3(1+\gamma^3)(1+\gamma)}{\gamma We}\right]^{\frac{1}{2}}$	(2.32)
Ashgriz and Poo (1990)	$We = \frac{2(1+\gamma)(1+\gamma^3)^2[3(1+\gamma)(1-x_c)(\gamma^3\phi_s + \phi_l)]^{\frac{1}{2}}}{\gamma^3[(1+\gamma^3) - (1-{x_c}^2)(\phi_s + \gamma^3\phi_l)]}$ $\phi_s = \begin{cases} 1 - \frac{1}{4\gamma^3}(2\gamma - \tau)^2(\gamma + \tau) & for\ h > \frac{1}{2}d_{ds} \\ \frac{\tau^2}{4\gamma^3}(3\gamma - \tau) & for\ h < \frac{1}{2}d_{ds} \end{cases}$ $\phi_l = \begin{cases} 1 - \frac{1}{4}(2-\tau)^2(1+\tau) & for\ h > \frac{1}{2}d_{dl} \\ \frac{\tau^2}{4}(3-\tau) & for\ h < \frac{1}{2}d_{dl} \end{cases}$ $h = \frac{1}{2}(d_{dl} + d_{ds})(1 - x_c)\ and\ \tau = (1 - x_c)(1+\gamma)$	(2.33)
Jiang *et al.* (1992)	$x_c \approx We^{-\frac{1}{2}}\left[1 + k\frac{\mu_d}{\sigma_d}\left(\frac{\rho_d d_d}{2\sigma_d}\right)^{\frac{1}{2}}\right]$	(2.34)

Brazier-Smith *et al.* (1972) conducted collision experiments on drops of different sizes, ranging from d_d = 0.3 to 1.5 mm in diameter with relative velocities ranging from $|v_{dl} - v_{ds}|$ = 0.3 to 3 m/s. They also argued that for a temporary coalesced drop to break up the rotational energy of the drop must be equal to the stabilizing surface energy of the drop and derived Equation (2.29) for predicting the impact parameter boundary between coalescence (Regime I) and stretching separation (Regime V). They showed that coalescence efficiency increases with the drop diameter ratio (γ) due to less rotational energy upon impact and decreases with increasing relative velocity and impact parameter. Coalescence efficiency (Equation 3.6) was found to be between 0.1 and 0.4 for γ = 1 and between 0.2 and 0.6 for γ = 0.5 and it is reported that coalescence efficiencies is approximately unity for γ < 0.5. This model is the model of choice in StarCD®.

FLUENT® 6.2.16 uses Equation (2.30), proposed by O'Rourke (1981), for the critical impact parameter between two colliding drops of different diameters (boundary between Regime I and V). O'Rourke obtained his results by looking at drop collisions in Diesel sprays.

Low and List (1982) investigated the collisions between drops of different sizes travelling at terminal velocity with diameters ranging from d_d = 0.395 mm to 4.4 mm. They obtained a semi-empirical correlation (Equation 2.31), involving collision kinetic energy and surface energy for predicting the coalescence boundary between Regimes I and V.

Arkhipov *et al.* (1983) used the minimum-potential-energy variational principal and obtained a relation (Equation 2.32) for predicting the boundary between coalescence (Regime I) and stretching separation (Regime V).

Ashgriz and Poo (1990) investigated the collisions between drop pairs with size ratios of γ = 1, 0.75 and 0.5 and collision Weber numbers, based on the diameter of the smallest drop, ranging from $We = \rho_{av} d_{ds} (v_{dl} - v_{ds})^2/\sigma$ = 1 to 100. They distinguished between four main collision events which were bouncing, reflexive separation (Regime IV), coalescence (Regime I) and stretching separation (Regime V). Reflexive separation occurs at high relative velocities and head-on or near head-on collisions ($X < X_r$), while stretching separation occurs at higher impact parameters ($X > X_c$) with coalescence occurring between X_r and X_c. They argued that drop separation after temporary coalescence is due to internal flow and proposed Equation (2.35) for predicting the impact parameter boundary between coalescence (Regime I) and reflexive separation (Regime IV) and Equation (2.33) for predicting the boundary between coalescence and stretching separation (Regime V), based on the assumption of inviscid flow within the drops. Ashgriz and Poo (1990) concluded from their experimental results that stretching separation occurs long before any significant rotation can be induced and therefore angular momentum is not the cause of drop separation after temporary coalescence in off-centre collisions, as proposed by earlier researchers [Park (1970), Brazier-Smith *et al.* (1972)].

$$\frac{2We}{(1+\gamma)(1+\gamma^3)^2}(\gamma^6\eta_1 + \eta_2) + 3\left[4(1+\gamma^2) - 7(1+\gamma^3)^{\frac{2}{3}}\right] = 0 \qquad (2.35)$$

where

$$\eta_1 = 2(1-\xi)^2(1-\xi^2)^{\frac{1}{2}} - 1 \qquad (2.36)$$

$$\eta_2 = 2(\gamma-\xi)^2(\gamma^2-\xi^2)^{\frac{1}{2}} - \gamma^3 \qquad (2.37)$$

$$\xi = \frac{1}{2}X_r(1+\gamma) \qquad (2.38)$$

Jiang *et al.* (1992) investigated drop collisions between equally sized water and hydrocarbon drops respectively and showed that viscous dissipation can't be ignored for high collision velocities. They showed that roughly half of the initial drop kinetic energy is dissipated by means of viscous action inside the coalesced drop after head-on collisions. They found that drop separation after grazing off-centre collisions (Regime V with high impact parameter) is mainly due to shearing and that rotational motion is minimal in these cases. For these grazing off-centre collisions the temporary coalesced drop generally separated into larger primary drops accompanied by 5 satellite drops. At smaller impact parameters the collisions are similar to head-on collisions, but a definitive rotating component is introduced to the coalesced drop (Regime V just above transition boundary) with only one satellite drop forming after break-up. Qian and Law (1997) made some photographic observations in this region and observed that the coalesced drop rotated 180° in 2.21 ms (approx. 1421.5 rad/s), which means that rotation presumably have a significant influence on the drop break-up. Furthermore Jiang *et al.* (1992) concluded that water drops always coalesce for head-on or near head-on collisions (Regime I) in the Weber range they investigated (We < 40) and proposed Equation (2.34) for predicting the boundary between temporary (Regime V) and permanent coalescence (Regime I) based on a shearing mechanism for separation after the collision of equally sized drops.

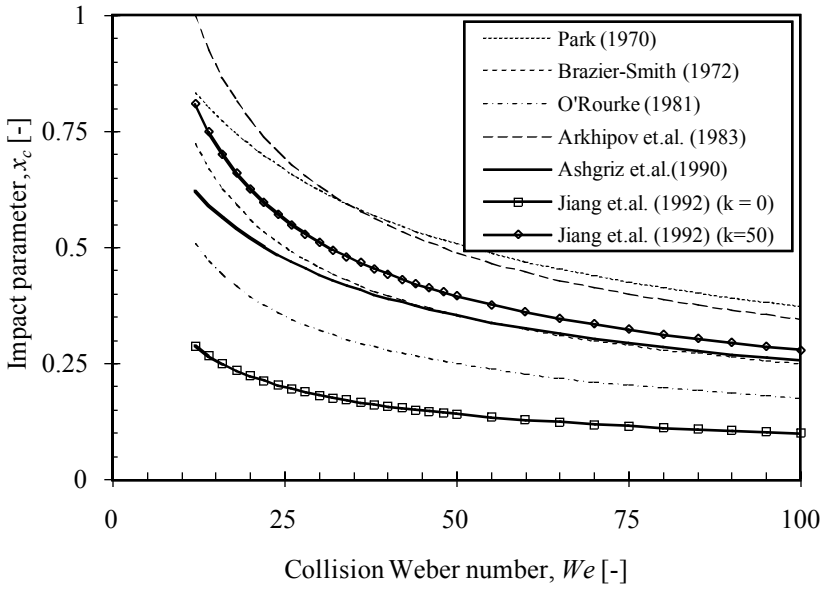

Figure 2.4: Comparison of the different critical impact parameter relations in Table 2.4 ($\gamma = 1$).

Figure 2.4 presents the predicted dimensionless critical impact parameters according to the equations listed in Table 2.4.

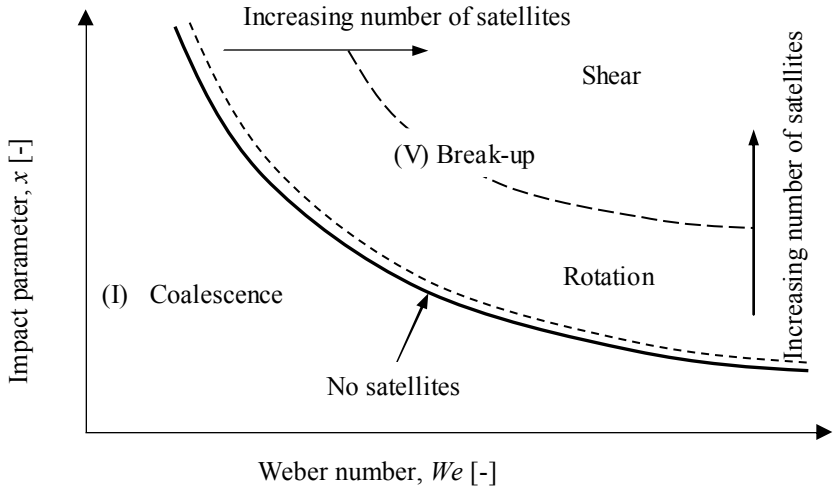

Figure 2.5: Break-up physics for collisions of water drops in Regime V at atmospheric pressure.

Taking the findings on drop collisions by the different researchers into account this author speculates that Regime V may be subdivided into two regions i.e. one where break-up is mainly due to rotation and one where break-up is mainly due to shearing (Figure 2.5) as the impact parameter is increased.

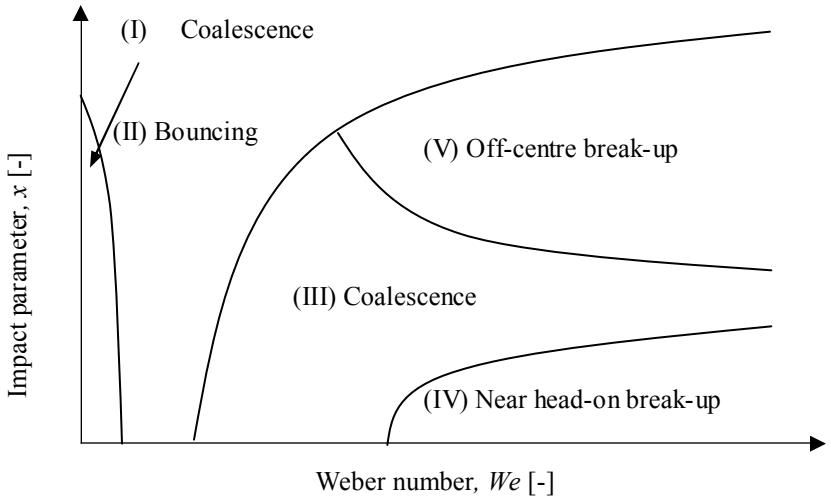

Figure 2.6: Schematic of collision regimes for water drops at an elevated air pressure of 20 MPa (Qian and Law, 1997).

Figure 2.6 shows the collision regimes for water drops at an air pressure of 20 MPa. Qian and Law (1997) investigated the collisions between water and hydrocarbon

drops respectively and found that the properties of the air may be significant in the coalescence of drops. Colliding water drops showed more bouncing with increasing air pressure which is uncommon for collisions at atmospheric pressure.

Estrade *et al.* (1999) investigated the collisions of ethanol drops in atmospheric air, which showed the same collision regimes as water drops in an elevated pressure environment (Qian *et al.*, 1997). Estrade *et al.* (1999) observed the same collision regimes as previous researchers, but categorized the separation of Regime V in terms of the number of satellite drops that formed. In equal-sized drop collisions ($\gamma = 1$) as much as 9 satellite drops were observed and a maximum of 4 satellite drops were observed for a collision drop size ratio of $\gamma = 0.5$. In a narrow range above the boundary of Regime V there were no observed satellite drops which is consistent with the observations made by Brazier-Smith *et al.* (1972). Figure 2.5 shows schematically how this satellite drop formation increases in Regime V with increasing impact parameter and Weber number.

2.5 Heat and mass transfer from drops

Many researchers have investigated heat and mass transfer from drops and have proposed empirical relations for Nusselt and Sherwood numbers. Frössling (1938) and Ranz and Marshall (1952) proposed similar relations while other researchers proposed modified versions of the Ranz and Marshall (1952) correlation to make provision for secondary effects such as drop oscillation, deformation and internal circulation. Some of the relations found in literature are listed in Table 2.5.

Table 2.5 : Empirical relations for heat and mass transfer.

Researcher	Correlation	
Frössling (1938)	$Sh = 2 + 0.552Sc^{\frac{1}{3}}Re^{\frac{1}{2}} \quad for\ 2 < Re < 800\ and\ 0.2 < d_d < 1.8\ mm$ $Nu = 2 + 0.552Pr^{\frac{1}{3}}Re^{\frac{1}{2}} \quad for\ 2 < Re < 800\ and\ 0.2 < d_d < 1.8\ mm$	(2.39)
Ranz and Marshall (1952)	$Sh = 2 + 0.6Sc^{\frac{1}{3}}Re^{\frac{1}{2}} \quad for\ 2 < Re < 800\ and\ 0.6 < d_d < 1.1\ mm$ $Nu = 2 + 0.6Pr^{\frac{1}{3}}Re^{\frac{1}{2}} \quad for\ 2 < Re < 800\ and\ 0.6 < d_d < 1.1\ mm$	(2.40)
Yao and Schrock (1976b)	$Nu = 2 + g_{YS}\left(0.6Re^{\frac{1}{2}}Pr^{\frac{1}{3}}\right) \quad for\ Re < 2500$ where $g_{YS} = 25\left(\frac{z}{d_d}\right)^{-0.7} \quad for\ 10 < \frac{z}{d_d} < 600$	(2.41)
Srikrishna *et al.* (1982)	$Sh = 2 + 0.37Sc^{\frac{1}{3}}Re^{0.557} \quad for\ 628 < Re < 4271\ and\ 2 < d_d < 8.4\ mm$	(2.42)

Researcher	Correlation	
Mercker (1993)	$Nu = 2 + g_{YS}\left(0.6Re^{\frac{1}{2}}Pr^{\frac{1}{3}}\right)$ where $g_{YS} = 1 + 66.54{M_{\ddot{Z}}}^{0.8}\left(\frac{d_d}{d_m}\right)^{-0.1}$ $for\ M_{\ddot{Z}} = \frac{(dv_d/dt)d_d}{{v_d}^2} < 3 \cdot 10^{-3}\ and\ \ 2.5 < d_d < 6\,mm$	(2.43)
Dreyer (1994)	$Nu = 2 + g_{YS}\left(0.6Re^{\frac{1}{2}}Pr^{\frac{1}{3}}\right)$ where $g_{YS} = 0.22 + 3.15{M_{\ddot{Z}}}^{0.2}\left(\frac{d_d}{d_m}\right)^{0.2}\ for\ M_{\ddot{Z}} = \frac{(dv_d/dt)d_d}{{v_d}^2} > 5 \cdot 10^{-4}$	(2.44)
Erens *et al.* (1994)	$Nu = 2 + g_{YS}\left(0.6Re^{\frac{1}{2}}Pr^{\frac{1}{3}}\right)$ where $g_{YS} = 0.22 + 3.15\left(\frac{(dv_d/dt)d_d}{{v_d}^2 d_m}\right)^{0.2}\ for\ \ \frac{(dv_d/dt)d_d}{{v_d}^2} > 5 \cdot 10^{-4}$	(2.45)
Martin (2005)	$Nu = 2 + 0.4038(c_F Re^2 Pr)^{\frac{1}{3}}\ \ for\ \ 10^{-1} \le Re \le 10^6$ where $c_F = 16/Re + 3.73Re^{\frac{1}{2}} + 0.03$	(2.46)
Pierce (2007)	$Nu = 2 + g_{YS}\left(0.6Re^{\frac{1}{2}}Pr^{\frac{1}{3}}\right)$ where $g_{YS} = 0.68\left(\frac{C_D Re^2}{(C_D Re^2)_T}\right)^{-0.28} + \frac{0.95}{\left(1 + 1.4\left(\frac{C_D Re^2}{(C_D Re^2)_T}\right)^{-2}\right)}$	(2.47)

Mercker (1993) defined the maximum stable drop diameter used in Equations (2.44) and (2.45) as

$$d_m = \sqrt{\frac{16\sigma_d}{g(\rho_d - \rho_{av})}} \tag{2.48}$$

2.6 Drop interaction with grids

Dreyer (1994), Oosthuizen (1995) and Terblanche (2008) showed that rain zone performance can be improved by the installation of grids that reduce the drop size in the rain zone. It is therefore important to understand the mechanisms of drop break-up due to grid interaction, since drop size reduction is the main reason for achieving better rain zone performance.

Figure 2.7 shows an example of drop break-up through a combination of splashing and cutting on a slat covered by a thin water film. Splashing is characterized by small upward moving drops after drop impingement on a slat, while cutting is characterized by larger drops with downward trajectories that form when part of the initial drop is not directly above the slat upon impingement.

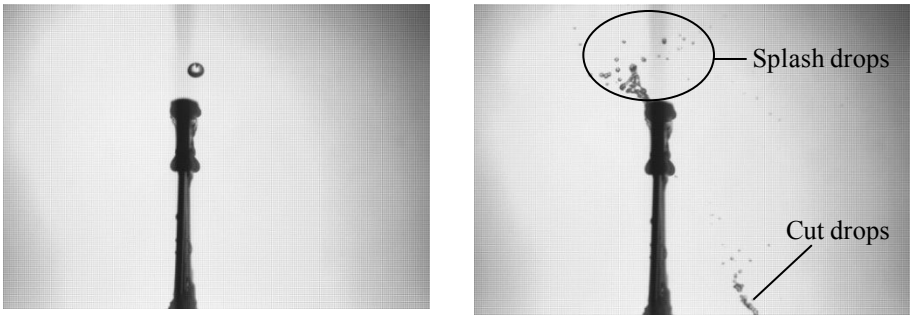

a) $t = 0$ s b) $t = 0.005$ s

Figure 2.7: Drop break-up through a combination of splashing and cutting.

Yao *et al.* (1988) investigated drop (d_i = 0.7 to 2.0 mm) impingement on thin steel strips (W = 0.33 and 0.175 mm) that was heated (red hot) beyond the Leidenfrost temperature and observed that drop break-up was due to a combinations of splashing and cutting and that splash drops were generally smaller than cut drops. Yao *et al.* (1988) proposed Equations (2.49), plotted in Figure 2.8, for predicting the Sauter mean drop diameters of the drops that formed due to a combination of splashing and cutting on the heated strips.

$$\frac{d_{32}}{d_i} = 12We^{-1} \qquad for\ \frac{d_i}{W} \approx 0 \tag{2.49a}$$

$$\frac{d_{32}}{d_i} = 1.84We^{-0.2} \qquad for\ \frac{d_i}{W} = 3.8 \tag{2.49b}$$

$$\frac{d_{32}}{d_i} = 1.21We^{-0.08} \qquad for\ \frac{d_i}{W} = 5.7 \tag{2.49c}$$

$$\frac{d_{32}}{d_i} = 0.85 \qquad for\ \frac{d_i}{W} \approx \infty \tag{2.49d}$$

where

$$We = \frac{\rho_d {v_d}^2 d_i}{\sigma_d} \tag{2.49e}$$

Dreyer (1994) also distinguished between splashing and cutting and developed correlations to predict each of these two break-up components separately, unlike

Yao *et al.* (1988). In addition to splashing and cutting , Dreyer (1994) also considered dripping below slats.

Splashing, cutting and dripping are discussed in more detail in the next three sections.

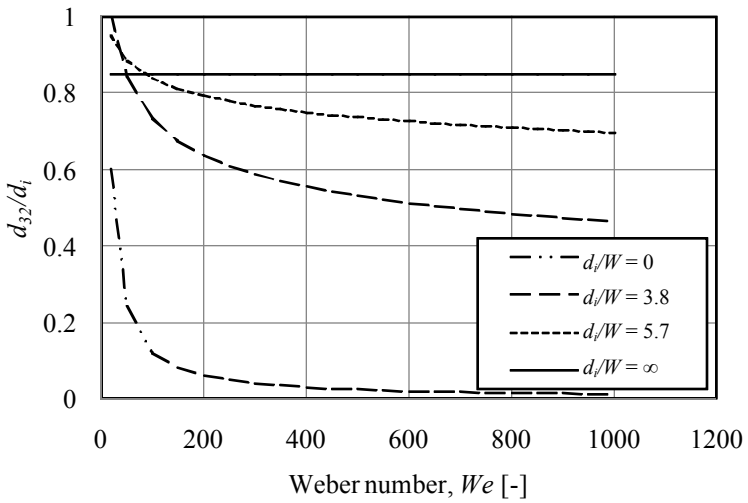

Figure 2.8: The prediction of drop size reduction by thin heated steel strips Equations (2.49).

2.6.1 Splashing on the upper surfaces of splash grids

There are a number of variables that can influence the outcome of splashing. They include surface tension, pre-existing film thickness, angle of the splash surface, surface roughness, initial drop diameter, initial drop velocity, micro-structure of the splash surface and drop oscillation before impingement on the splash surface. This section discusses the literature relating to these topics after starting out by giving a possible explanation why splash drops form in the first place.

A possible explanation for the onset of splash crown break-up, leading to the formation of splash drops, might be the instabilities at the air-water interface. Allen (1975) showed that interfacial waves develop at the rapidly decelerating air-water interface of the splash crown due to Raleigh-Taylor instability and that the amplitude of these waves can be given by

$$A = A_0 e^{nt} \tag{2.50}$$

The exponential rate of wave growth (n) can be expressed as a function of the density of the air and water respectively as well as the interfacial surface tension

$$n^2 = \frac{\rho_d - \rho_{av}}{\rho_d + \rho_{av}} a_{aw} k - \frac{\sigma k^3}{\rho_d + \rho_{av}} \tag{2.51}$$

with

$$k^3 = a_{ad}(\rho_d - \rho_{av})/3\sigma \tag{2.52}$$

where a_{ad} is the deceleration of the air-water interface.

Finger-like jets form at equally spaced locations on the upper rim of the crown due to the amplification of the surface wave amplitude that break up to form many small splash drops.

The role of surface tension in terms of the unstable interfacial waves can be seen in Equation (2.50), but the effect of surface tension on the number of splash drops was experimentally investigated by Stow and Stainer (1977), who measured a decrease in the number of splash drops with decreasing surface tension.

Rieber and Frohn (1999) studied splashing on a surface covered by a thin liquid film numerically and according to them Raleigh instability can explain the onset of the break-up of the crown at its upper rim. They also state that splashing only occurred for Weber numbers greater than $We = 200$ for their investigated film thickness to drop diameter ratios ($0.1 \leq \delta/d_i \leq 0.116$) and Ohnesorge numbers ($0.0014 \leq Oh \leq 0.0016$).

Wu (2003) predicted the probability, from a simplified theoretical analysis, of the occurrence of splash drops of a certain diameter after a drop impinges on a solid wall and proposed the following log-normal probability equation

$$L(d_d) = \frac{\sqrt{3}}{\sqrt{\pi} d} exp\left[-3\left(ln\frac{d_d}{d_s} - \frac{1}{6}\right)^2\right] \tag{2.53}$$

where d_s is the splash diameter probable to occur most often in the distribution of the splash drops that can be obtained from

$$\frac{d_s}{d_i} = 4.23\left(\sqrt{9 + \frac{2We(We+12)}{Re}} + 3\right)/(We+12) \tag{2.54}$$

Stow and Stainer (1977) also used a log-normal equation for expressing splash drop distribution.

According to Wu (2003) the theoretical equation is applicable when the target is wet or dry, but does not account for the effects of gravity and the liquid contained in the pre-existing film and only considers viscous dissipation in the crown. It may therefore only be useful in conditions where the pre-existing film is just thick enough for a crown to form. When Froude numbers are in the region of Fr =1000 or smaller the equation also tend to overestimate d_s.

Krechetnikov and Homsy (2009) experimentally investigated drop splashing on a surface covered by a thin liquid film and concluded that the initial instability of the crown may be due to Richtmyer-Meshkov instability because of the impulsive nature of the initial liquid acceleration. This instability is however further amplified by Raleigh-Taylor instability when the crown decelerates in the air to form finger-like jets on the upper rim of the crown that break up into small drops.

Huber *et al.* (1997) investigated how target characteristics like film thickness on a glass plate and the angle of the glass plate influence the mass of water that splashes and found that the splash mass generally increases with increasing liquid film thickness on the glass plate and decreases with an increasing inclination angle. Tooke (1965) reported a measured increase in fine splash if the splash surface was inclined at 15°, but reports that a corresponding improvement for inclined slats over horizontal slats wasn't found in full-scale packing.

Stow and Stainer (1977) measured splash products and found that for dry surfaces the number of splash drops increases with surface roughness, impact velocity and initial drop size. They also found that the splash drops that form after drop impingement on relatively rough and dry surfaces travel much further than the splash drops formed on smoother surfaces. Stow *et al*. (1977) also investigated splashing on surfaces covered by liquid films of different thicknesses. They measured a rapid increase in the number of splash drops for film thicknesses increasing from δ = 0.03 to 0.06 mm and an almost linear decrease in the number of splash drops for further increased film thicknesses. They also measured a decrease in the number of splash drops for increasing surface roughness at constant liquid film thicknesses.

Young (1961) investigated splashing on soaked wooden splash bars and also found that increased surface roughness reduces the amount of splashing.

Kannan and Sivakumar (2008) investigated the impingement of drops on hydrophobic surfaces and concluded that the orientation of the surface micro structure (grooves in this case) significantly influences the processes of spreading and receding. Perpendicular to the micro grooves the spreading of the drop is significantly slower than parallel to the grooves and the drops also rebounded to a larger height when they receded on a hydrophobic surface, compared to a smooth surface.

Tooke (1965) related drop oscillation before impact to the amount of splashing that happens on flooded splash bars and concluded that it may have an effect on the amount of splashing for drop fall distances up to a certain height, but that it is impractical to try and consider this effect when improving the grid layout due to the many different drop sizes impinging on splash grids and also due to the effect of counter flowing air on drop oscillation.

When drops impinge onto a relatively narrow slat a fraction of the drop mass, called the splash fraction (Equation 2.55), splashes sideways, according to Yao *et al.* (1988), and causes the formation of many small drops ranging in sizes generally smaller than d_s = 2 mm in diameter as measured by Dreyer (1994).

$$f_s = \frac{M_s}{M_i} \tag{2.55}$$

Dreyer (1994) correlated his empirical splash fraction data and proposed Equation (2.56a) for predicting the average splash fractions of drops impinging onto W = 2, W = 5 or W = 10 mm slats and Equation (2.56b) for predicting the average splash fractions of drops impinging onto a W = 25 mm slat covered by a thin layer of water.

$$\overline{f_s} = 0.01\left[c_1 + c_2\left(\frac{\delta}{W}\right)\right]\left[c_3 + c_4\left\{\left(\frac{We}{We_{ref}}\right)\left(\frac{d_i}{W}\right)^2\right\}^{c_5}\right]\left[c_6 + c_7\left(\frac{d_i}{W}\right)^{c_8}\right] \tag{2.56a}$$

$$\begin{aligned}\overline{f_s} = 0.01\Bigg[c_1 + \left(\frac{\delta}{d_i}\right)\left\{c_2 + c_3\left(\frac{We}{We_{ref}}\right) + c_4\left(\frac{We}{We_{ref}}\right)^{0.4}\right\}\Bigg] \\ \times\left[c_5 + c_6\left(\frac{We}{We_{ref}}\right)^{c_7}\right]\left[c_8 + c_9\left(\frac{\delta}{d_i}\right)^{c_{10}}\right]\end{aligned} \tag{2.56b}$$

The reference Weber number at STP defined in terms of the terminal velocity ($v_{dm,T}$) of the maximum stable drop is given by

$$We_{ref} = \frac{\rho_d {v_{dm,T}}^2 d_m}{\sigma_d} \tag{2.57}$$

where the maximum stable drop diameter (d_m) is given by Equation (2.48).

The constants for Equations (2.56a) and (2.56b) are given in Table 2.6.

Table 2.6: Constants for Equations (2.56a) and (2.56b).

Constant	25 mm slat	10 mm slat	5 mm slat	2 mm slat
c_1	-1.930	4.882	6.613	10.737
c_2	67.471	22.930	8.200	6.805
c_3	101.876	-2.301	-12.550	-12.996
c_4	-298.003	3.242	13.700	14.766
c_5	-62.009	0.05327	0.01628	0.03578
c_6	36.996	8.061	0.5506	0.1210
c_7	0.09383	2.598	12.551	15.575
c_8	0.4446	-2.977	-1.792	-2.148
c_9	-4.454	-	-	-
c_{10}	2.086	-	-	-

Dreyer (1994) also provided an empirical correlation for the cumulative splash drop mass distribution that is given by the following Rosin-Rammler equation

$$R(d_d) = 1 - exp\left[-\left(\frac{d_d}{d_{RR}}\right)^{n_{RR}}\right] \tag{2.58}$$

where

$$d_{RR} = d_{50}\left[0.6931^{-\left(\frac{1}{n_{RR}}\right)}\right] \tag{2.59}$$

and

$$n_{RR} = \left[24.532 - 75.174\left(\frac{\delta}{d_i}\right)\left(\frac{We}{We_{ref}}\right)^{0.74}\right] \times \left[0.149 + 6.801 \cdot 10^{-4}\left(\frac{KE}{KE_{ref}}\right)^{-0.76}\right] \tag{2.60}$$

The reference kinetic energy (KE_{ref}) at STP is given in terms of the terminal velocity ($v_{dm,T}$) of the maximum stable drop

$$KE_{ref} = 0.5\left(\frac{\rho_d \pi {d_m}^3}{6}\right){v_{dm,T}}^2 \tag{2.61}$$

where the maximum stable drop diameter (d_m) is given by Equation (2.48).

The mass median diameter can be obtained from the following ratio by Dreyer (1994).

$$\left(\frac{d_{50}}{d_m}\right) = 3.08 \cdot 10^{-2} + \left[-0.163 + 4.560 \cdot 10^{-2}\left(\frac{\delta}{d_m}\right)^{-0.34}\right] \left[-0.804 - 0.619\left(\frac{We}{We_{ref}}\right)^{-0.27}\right]\left[-1.738 + 1.980\left(\frac{\delta}{d_i}\right)^{-0.17}\right] \quad (2.62)$$

Oosthuizen (1995) measured the drop size reduction capability of different splash grid configurations and compared the results to the predicted results of Dreyer's model. He found that there is a significant over prediction in the number of drops with diameters smaller than d_s = 2 mm in the predicted drop distributions below the different splash grid configurations.

The mean water film thickness on slats was measured by Dreyer (1994) in an operational cooling tower and correlated by the following equation

$$\bar{\delta} = 0.315 - 1.387 \times 10^{-2} G_w - 2.550 \times 10^{-3} v_a + 1.575 \times 10^{-2} W - 3.992 \times 10^{-4} W^2 + 1.916 \times 10^{-3}(G_w W) + 2.188 \times 10^{-3}(v_a W) \quad (2.63)$$

where $\bar{\delta}$ and W are in mm, v_a is in m/s and G_w is in kg/m^{2}s

A correlation for the initial splash drop velocity to terminal velocity of the maximum stable drop ($v_{dm,T}$) ratio is given by Dreyer (1994)

$$\left(\frac{v_{s,i}}{v_{dm,T}}\right) = 1.925 \times 10^{-2} + \left[\frac{7.372 \times 10^{-3}}{(d_s/d_m) - 0.01}\right] \quad (2.64)$$

In Dreyer's sensitivity analysis of SPSIM (splash pack simulation program) the splash angle was varied from 50° to 70° (relative to horizontal) and the effect on transfer characteristic were found to be negligible.

When a drop impinges on a slat and splashes, Dreyer (1994) assumed in his model (SPSIM) that the splash drops consist partly of the water contained in the initial drop and partly of the water contained in the film on top of the slat and therefore the initial temperature of a splash drops is determined by using an arbitrary chosen mixing ratio (ϕ) in the following equation.

$$T_{s,i} = \phi T_{d,i} + (1 - \phi) T_f \quad (2.65)$$

2.6.2 Cutting of impinging drops by the slats of a splash grid

Cutting happens when part of the initial drop is not directly above the slat before impingement. This part of the drop gets sheared from the rest of the drop by the slat edge and contains drops that travel at approximately the same speed as the initial drop, according to Dreyer (1994). The cutting fraction, defined as the fraction of the initial drop that breaks up due to cutting is given by

$$f_c = \frac{M_c}{M_i} \tag{2.66}$$

Dreyer (1994) obtained a simplified analytical equation for determining the average cutting fraction when a drop impinges onto a slat that is given by

$$\bar{f_c} = \frac{\int_{-(W+\,d_i)/2}^{(W+\,d_i)/2} f_c(x)\partial x}{W\,+\,d_i} = \frac{d_i}{W\,+\,d_i} \tag{2.67}$$

Dreyer (1994) assumed that two cut drops form (one on each side of the slat) after drop impingement for cases where the drop diameter is greater than the slat width ($d_i > W$) and that their sizes depend on the location of the impingement. The mass of each drop is given by the following equation (Dreyer, 1994) of which the variables are depicted in Figure 2.9.

$$M_c = \rho_d \left[\frac{\pi {b_{A/B}}^2}{3}\left(\frac{3d_i}{2} - b_{A/B}\right)\right] \tag{2.68}$$

where

$$b_A = \left(\frac{2x - W}{2}\right) + \left(\frac{d_i}{2}\right) \tag{2.69}$$

$$b_B = \left(\frac{-2x - W}{2}\right) + \left(\frac{d_i}{2}\right) \tag{2.70}$$

Dreyer (1994) also calculated the average size of each of the two drops that form due to cutting ($d_i > W$), for drop impingements between $x = 0$ and $x = (W + d_i)/2$. The mass of these two drops ($d_i > W$) can be determined from Equation (2.68) by using the following equations for $\bar{b}_A$ and $\bar{b}_B$ instead of b_A and b_B (Equations 2.69 and 2.70).

$$\overline{b_A} = \frac{2\int_0^{\frac{W+\,d_i}{2}} b_A\,dx}{W\,+\,d_i} = \frac{3d_i}{4} - \frac{W}{4} \tag{2.71}$$

$$\overline{b_B} = \frac{2\int_0^{\frac{d_i - W}{2}} b_B \, dx}{d_i - W} = \frac{d_i}{4} - \frac{W}{4} \tag{2.72}$$

For cases where the initial drop diameter is smaller than the slat width ($d_i < W$), Dreyer (1994) assumed that a cut drop forms on only one side of the slat for drop impingements between $x = 0$ and $x = (W + d_i)/2$ and that the drop has an average diameter of $\bar{d}_c = 0.79 d_i$.

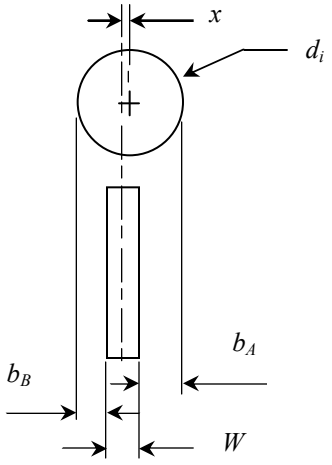

Figure 2.9: Variables for Equation (2.68).

2.6.3 Dripping below splash grids

Yung *et al.* (1980) investigated the vapour-liquid interaction in horizontal tube falling film evaporators and attributed the formation of droplets on the bottom of the tubes to a Raleigh-Taylor instability wave that forms when a heavier fluid is on top of a lighter fluid. According to Yung *et al.* (1980) these drops eventually detach from the bottom of the tube, to form the primary drop, after forming a long narrow liquid column that breaks up in the form of 4 to 5 smaller satellite drops due to Raleigh instability.

Yung *et al.* (1980) attributed the mechanism by which the liquid breaks off from the bottom of the tubes to an interaction between gravity and surface tension forces and proposed the following equation for determining the primary drop diameter

$$d_p = 3\sqrt{\frac{\sigma}{\rho_w g}} \tag{2.73}$$

with the 5 satellite drop diameters equally distributed within the following size range

$$0.24 < \frac{d_s}{d_p} < 0.46 \tag{2.74}$$

Dreyer (1994) used the following equation, similar to Equation (2.73), to quantify the primary drop diameter when dripping occurs below slats with different profiles on the bottom

$$d_p = C\sqrt{\frac{\sigma}{g(\rho_w - \rho_{av})}} \tag{2.75}$$

where C is a non-dimensional drop diameter that is given by

$$C = 2.206 + \left(\frac{0.0597}{1.1 - S}\right) \tag{2.76}$$

and the dimensionless shape factor based on an imaginary 12.5 mm in diameter sphere hanging from its centre is given by

$$S = \frac{\textit{Circumference of the vertical projection of interpenetrating line}}{\textit{Circumference of the sphere}} \tag{2.77}$$

Hung and Yao (2002) investigated the dripping when drops impinged onto horizontal wire screen meshes and found that the dripping below the wires is influenced by parameters such as wire diameter (drip drop diameters decrease with decreasing wire diameter) and the size of the mesh openings and not the velocities of the impinging drops, which were v_d = 2.8 to 7 m/s. They also showed that for a coarse mesh consisting of d_w = 1.19 mm wires with openings of 11.51 x 11.51 mm the drops that dripped from the mesh corners were generally larger than the drops dripping from single wires. Hung and Yao (2002) gave the following equation in terms of wire diameter (d_w) for the diameter of a drop dripping from below a single wire.

$$d_p = 1.813 d_w \left(\frac{d_w}{\sqrt{\sigma/\rho_w g}}\right)^{-0.786} \tag{2.78}$$

2.7 Heat transfer from the film covering the grid surface

When small drops or drops that have low velocities impinge onto the grid surface these drops may become part of the surface water that runs down the surface of the grid to form drops at the bottom of the grid that eventually detaches from the grid in the form of drip drops. The temperature change of the water contained in this water film covering the grid surface can be determined by Equation (2.79) where the initial film temperature (T_{fi}) is assumed to be the average water temperature before the water reaches the splash grid (Dreyer, 1994).

$$T_{fo} = T_{fi} - \left[\frac{hA_{slats}(i_{masw} - i_{ma})}{m_d c_{pw}}\right] \tag{2.79}$$

Gnielinski (1983) provides the following correlation for the Nusselt number based on the hydraulic diameter (d_h) of immersed complex shapes of which the correlation accuracy for different tubular shapes like cylinders, squares and T-sections was confirmed by Dreyer (1994).

$$Nu = 0.3 + \sqrt{\left(0.664\sqrt{Re}Pr^{\frac{1}{3}}\right)^2 + \left[\frac{0.037Re^{0.8}Pr}{1 + 2.443Re^{-0.1}\left(Pr^{\frac{2}{3}} - 1\right)}\right]^2} \tag{2.80}$$

The hydraulic diameter, according to Dreyer (1994), can be defined as the ratio of the total surface area of the body to the maximum perimeter perpendicular to the flow.

2.8 Pressure drop over the rain zone

With the installation of drop size reduction grids in the rain zones of cooling towers there is an increase in the pressure drop over the rain zone due to the grids, but also due to the reduced drop sizes that must be taken into account when evaluating rain zone performance.

The pressure drop over a counter flow rain zone can therefore be expressed by

$$\Delta p_{rz} = \frac{\sum F_{D,drops}}{A_{fr}} + \sum K_{grid}\,\rho_{av}\frac{{v_{av}}^2}{2} \tag{2.81}$$

Baines and Peterson (1951) investigated flow through screens and concluded from their experimental results that the loss coefficient of a screen is independent of the screen Reynolds number at high screen Reynolds numbers ($10^3 \leq Re \leq 10^4$). They expressed the loss coefficient in terms of the screen porosity and the contraction coefficient through the openings, which is a function of screen form, with the following equation.

$$K_{grid} = \left(\frac{1}{C_c \beta} - 1\right)^2 \tag{2.82}$$

Dreyer (1994) verified the results of Baines and Peterson (1951) and Miller (1990) experimentally and obtained the following equation for predicting the loss coefficient of a sharp edged grids.

$$K_{grid} = 0.78\left(\frac{1}{\beta^2} - 1\right)^{1.25} \tag{2.83}$$

2.9 Rain zone transfer characteristic

The performance of an evaporative system can be expressed by the Merkel transfer characteristic that is defined by

$$Me = \frac{h_d a_{fi} L_{fi}}{G_w} = \int_{T_{wo}}^{T_{wi}} \frac{c_{pw} \partial T_w}{(i_{masw} - i_{ma})} \tag{2.84}$$

where

$$h_d = h_D(\rho_{vsw} - \rho_{v\infty})/(w_{sw} - w_\infty) \tag{2.85}$$

The Merkel transfer characteristic for evaporative systems can be determined according to the methods of Merkel (1925), Poppe and Rögener (1991) and the *e*-NTU method of Jaber and Webb (1989).

The Merkel method is the most commonly used method for determining the Merkel transfer characteristic and assumes:

1) A Lewis (Le_f) factor of unity.
2) Saturated outlet air.
3) Negligible water mass loss due to evaporation.

The reader is referred to Kloppers (2003) for a detailed analysis into the different methods for determining the Merkel transfer characteristic of an evaporative system.

2.10 Conclusions

At the beginning of this chapter the current techniques for improving cooling tower performance are discussed with the focus shifting to rain zone performance enhancement. A detailed review of the literature associated with this region that is needed to aid in developing a model for predicting the performance of a counter flow rain zone with installed splash grids is provided.

From this literature survey enough information is obtained to model the dynamic as well as the thermal behaviour of the free fall zone, but the literature found on drop break-up (which includes the splashing, cutting and dripping processes when drops impinge on slats) has a few identified shortcomings that are given by:

1) All the researchers that investigated drop splashing in shallow films investigated it on relatively large flat surfaces where complete crown formation could be observed and where there was no influence of an adjacent edge. Even the drop distribution equations (Equations 2.58 to 2.62) proposed by Dreyer (1994) were correlated from this type of splashing were edges had no influence on the splash drop distribution. Drop splashing on relatively narrow slats therefore needs further investigation.
2) The only researcher who tried to predict the component that is cut form the initial drop by the slat edge when a drop impinges close to the edge of a slat was Dreyer (1994) and the model that was used is only a simplified analytical model that has to be verified experimentally.
3) Apart from Dreyer (1994) there seems to be no-one who investigated the layout of a splash grid and therefore the aim of this dissertation is to try and predict the optimum layout for a splash grid by incorporating current theoretical equations and new experimentally obtained equations into a theoretical model for predicting the performance of a counter flow rain zone with installed splash grids.

3

A THEORETICAL MODEL FOR PREDICTING THE PERFORMANCE OF A COUNTER FLOW COOLING TOWER RAIN ZONE WITH HORIZONTAL LAYERS OF SPLASH GRIDS INSTALLED IN IT

3.1 Introduction

In this chapter a theoretical model is developed for predicting the performance of a counter flow rain zone with horizontal layers of splash grids installed in it. This model is developed from experimental and numerical data determined for this thesis as well as from literature.

Figure 3.1 shows the layout of the theoretical model, with the free fall zones and grids, similar to the model used by Dreyer (1994).

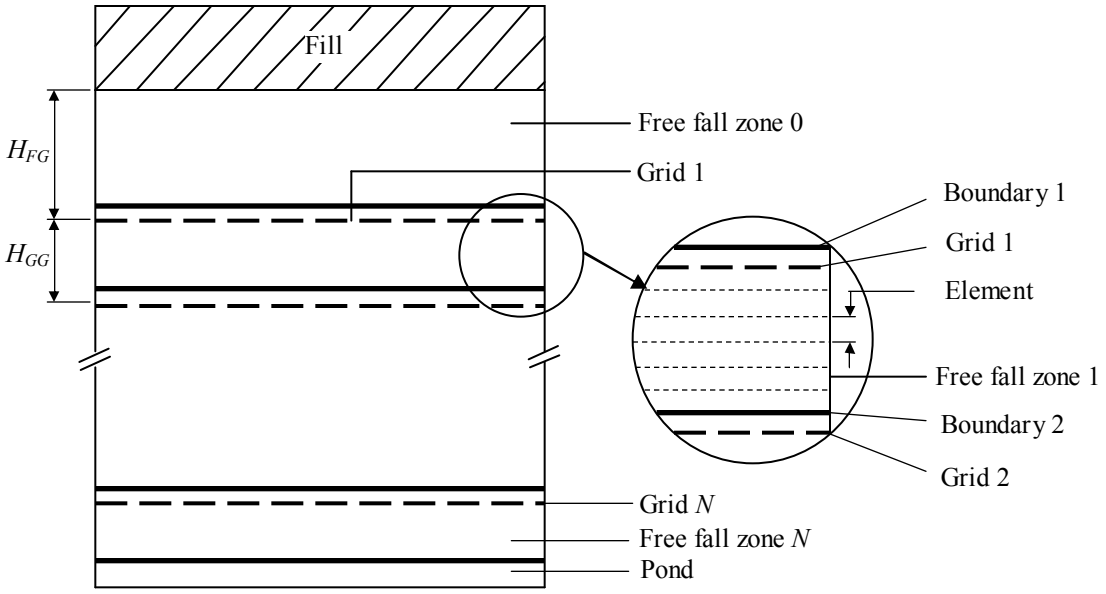

Figure 3.1: Layout of theoretical rain zone model.

In the free fall zone model, drop temperature change is determined as the drops accelerate under gravity through counter flowing air, with the larger and faster

moving drops colliding with the smaller and slower moving ones. The free-fall zone model initially (Free fall zone 0, Figure 3.1) requires an experimentally determined inlet drop distribution and initial drop speed and temperature and calculates the following for the free fall zone:

1) Drop velocity due to acceleration under gravity, taking into account the effect of drop deformation on the drag.
2) Drop break-up due to dynamic forces.
3) Collisions between drops of different sizes falling at different velocities, resulting in either coalescence of the two drops or bouncing in which the colliding drops remain unchanged.
4) The temperature of the drops.
5) Air-side temperature with the assumption that the air is always saturated at the calculated air temperature for each location over the height of the rain zone or by assuming constant wet- and dry bulb temperatures throughout the rain zone.
6) Free fall zone pressure drop.

When the counter flowing air velocity becomes larger than the terminal velocity of the smaller drops, it is assumed that these drops become entrained in the air stream and are blown out at the top; therefore subtracting their mass velocity from the total mass velocity.

The grid interaction zone is associated with a relatively large amount of drop break-up in the form of splashing, straddling and dripping below the grid. This happens when drops impinge onto the surface of the grid and leads to significant drop-drop interaction in the region just above the grid where splash drops collide with other drops. The grid interaction model calculates the following when drops from the free fall zone reach a grid:

1) The number of drops that pass through the grid unhindered.
2) Mass velocity of the water that splashes, straddles and drips from below the grid respectively.
3) Size distribution of the splash, straddle and drip drops.
4) Velocities of the newly formed drops.
5) Temperature change of the splash drops while they travel through the air above the grid.
6) The fraction of splash drops that return to the grid.
7) Collisions between splash drops and other drops resulting in coalescence or bouncing.
8) Temperature change of the water on the grid surface.
9) Pressure drop due to the grid.

In the following sections the complete rain zone model is explained by referring back to Figure 3.1.

3.2 Free fall zone

3.2.1 Initial drop distribution

Drops enter the rain zone below the fill zone of a cooling tower as a distribution of drops of different sizes. The distribution is normally a function of the fill type used in the cooling tower, with Sauter mean drop diameters generally ranging between d_{32} = 5 and 6 mm according to Kröger (2004) and Terblanche *et al.* (2009). The initial rain zone drop distribution is required as an input to the model and is obtained from the data by Terblanche (2008).

Due to the non-uniformity of the drop sizes entering the rain zone the drop size distribution is divided into parcels, similar to Dreyer (1994), based on drop diameter where the diameters of all the drops in a parcel are equal. Each parcel also contains information such as the number of drops, the velocity and the temperature of the drops in the parcel.

3.2.2 Drop velocity

As the drops accelerate under gravity, the larger drops travel faster than the smaller ones. The velocity and distance travelled by the different drops are determined by means of the analytical equations derived in Appendix I (Equations I.13 and I.24) which are used instead of a numerical integration approach to reduce computing time.

$$v_d(t) = \frac{\mu_{av} Re_T}{2a_\alpha \rho_{av} d_d}\left[\varphi tan\left\{\frac{\varphi}{2Re_T}(t - t_i) + tan^{-1}\left(\frac{2a_\alpha z_i + a_\beta}{\varphi}\right)\right\} - a_\beta\right] - v_a \tag{I.13}$$

$$s_d(t) = -\frac{\mu_{av} Re_T}{2a_\alpha \rho_{av} d_d}\left(2Re_T\, ln\left[\frac{cos\left\{\frac{\varphi}{2Re_T}(t - t_i) + tan^{-1}\left(\frac{2a_\alpha z_i + a_\beta}{\varphi}\right)\right\}}{cos\left\{tan^{-1}\left(\frac{2a_\alpha z_i + a_\beta}{\varphi}\right)\right\}}\right] + a_\beta(t - t_i)\right) - v_a(t - t_i) + s_i \tag{I.24}$$

with

$$\varphi = \left(4a_\gamma a_\alpha - a_\beta{}^2\right)^{\frac{1}{2}} \tag{I.11b}$$

The *a*- coefficients of Equations (I.13) and (I.24) are listed in Table I.1

3.2.3 Drop temperature

The drop temperature decreases as the drops pass through the free fall zone and the temperature of the drops are determined by means of the following analytical equation derived in Appendix J (Equation J.30).

$$T_d(t) = \frac{1}{2c_\alpha}\left[\psi\, tan\left\{-\frac{\psi}{2}k_5 + tan^{-1}\left(\frac{2c_\alpha T_{d,i} + c_\beta}{\psi}\right)\right\} - c_\beta\right] \tag{J.30}$$

where

$$\psi = \left(4c_\alpha c_\gamma - c_\beta{}^2\right)^{\frac{1}{2}} \tag{J.29}$$

$$k_1 = \frac{\varphi}{2Re_T} \tag{J.31}$$

$$k_2 = \tan^{-1}\left(\frac{2a_\alpha z_i + a_\beta}{\varphi}\right) \tag{J.32}$$

$$k_3 = k_1(t - t_i) + k_2 \tag{J.33}$$

$$k_4 = \frac{h_\alpha a_\beta}{2a_\alpha} - h_\beta \tag{J.34}$$

$$k_5 = \frac{D_{AB}}{d_d}\left[2(t - t_i) - 0.6Sc^{\frac{1}{3}}Re_T{}^{\frac{1}{2}}\left\{\frac{h_\alpha Re_T}{a_\alpha} ln\left(\frac{\cos k_3}{\cos k_2}\right) + k_4(t - t_i)\right\}\right] \tag{J.35}$$

The *a*-coefficients are listed in Table I.1, the *c*-coefficients given by Equations (J.24) to (J.26) and the *h*- coefficients listed in Table J.1.

3.2.4 Drop-drop collisions

As mentioned previously the drops of different sizes travel at different velocities, which means that the larger (d_{dl}), faster moving drops (v_{dl}), collide with the smaller (d_{ds}), slower moving ones (v_{ds}). These collisions are accounted for by dividing the free fall zone into elements (Figure 3.1) before determining the number of collisions on the boundary of each element. The velocities of all the drop sizes are determined at every element boundary and the number of collisions is determined based upon the drop diameters, the relative drop velocities and number of drops of each diameter.

Upon collision of two drops it is assumed that the drops may coalesce or simply bounce apart with no changes in temperature, drop diameter or velocity of the original drops. When a cloud of larger faster moving drops (e.g. parcel 1) passes through a cloud of smaller slower moving drops (e.g. parcel 2) the number of collisions that take place, as given by Dreyer (1994), is

$$\dot{n}_{coll} = \frac{\pi}{4}(d_{dl} + d_{ds})^2 |v_{dl} - v_{ds}| \eta_{coll} n_l n_s \tag{3.1}$$

where the collision efficiency (η_{coll}) is assumed to be unity for straight trajectories and the number of smaller and larger drops are respectively given by n_s and n_l where

$$n_s = \frac{\dot{n}_s}{A_{fr} v_{ds}} \quad \text{with} \quad \dot{n}_s = \frac{m_s}{\rho_w (\pi {d_{ds}}^3/6)} \tag{3.2}$$

and

$$n_l = \frac{\dot{n}_l}{A_{fr} v_{dl}} \quad \text{with} \quad \dot{n}_l = \frac{m_l}{\rho_w (\pi {d_{dl}}^3/6)} \tag{3.3}$$

The number of collisions in a volume with frontal area A_{fr} and height Δz can now be given by

$$\dot{n}_{coll,\Delta z} = \dot{n}_{coll} A_{fr} \Delta z \tag{3.4}$$

and the number of drop collisions that leads to coalescence is given by

$$\dot{n}_{coal,\Delta z} = \eta_{coal} \dot{n}_{coll,\Delta z} \tag{3.5}$$

The coalescence efficiency (η_{coal}) which is defined as the fraction of the number of collisions that leads to permanent coalescence can be expressed in terms of the critical impact parameter (Equation 3.6) that can be obtained from one of the models listed in Table 2.4. During coalescence of the drops in two different parcels, the drops involved in the coalescence are subtracted from their original parcels and a new parcel is created for the coalescence product that contains the diameter of the new drops, new drop temperature, new velocity and the number of new drops.

$$\eta_{coal} = {x_c}^2 \tag{3.6}$$

An increase in the average drop size is expected to be significant when the relative velocities between drops are relatively high and the initial distribution contains smaller to medium sized drops (distribution below a splash grid is installed below a fill). In Appendix G the drop size change over a H_{rz} = 7.05 m free fall zone is measured below a splash grid installed H_{FG} = 600 mm below a trickle fill. The Sauter

mean drop diameter increased from d_{32} = 3.06 mm to d_{32} = 3.60 mm over this fall distance (H_{rz} = 7.05 m) due to drop coalescence caused by drop collisions.

3.2.5 Aerodynamic drop break-up

Large drops can form in the rain zone due to the dripping from below the fill or splash grid or they can form due to the repeated collisions and coalescence of smaller drops. As these larger drops accelerate under gravity the dynamic forces on them increase until these forces overcome the stabilizing surface tension forces and the drop breaks up according to one of a number of break-up regimes (Table 2.3 and Figure G.3b). This is confirmed by the measurements done in Appendix H where a reduction in Sauter mean drop diameter from d_{32} = 5.092 mm to d_{32} = 4.288 mm is measured over a fall distance of H_{rz} = 7.65 m below a trickle fill. The observed form of break-up in this case is mostly something that looks like stripping, as shown in Figure G.6, where break-up leads to the formation of a relatively large number of smaller drops. Drop flattening which may be the onset of a bag type of break-up is also observed (Figure G.3b). Aerodynamic drop break-up is normally associated with a critical Weber number (Section 2.3) at which break-up is initiated. It is assumed in this model that a drop breaks up into 50 equally sized drops when a critical Weber number of We_c = 10.5 is reached. This assumption is made due to the more catastrophic break-up of drops observed in free fall (Figures G.3 and G.6).

3.2.6 Pressure drop over the free fall zone

The pressure drop over the free fall zone is determined by summation of the drag forces on all the drops present in the rain zone at one time before dividing this value by the cross-sectional area of the rain zone. Due to drop interaction in the rain zone the drop distribution may change from element to element (Figure 3.1) and therefore this calculation is done for each element where the drop velocity relative to the counter flowing air velocity over the element is used to determine the drag force for drops of a certain size. When the total pressure drop in each element is determined the pressure drop in all the elements is summed to determine the total pressure drop over the free fall zone.

The total pressure drop over the free fall zone is given by

$$\Delta p_{drops} = \left(\sum_{i=1}^{N_{elements}} \sum_{j=1}^{M_{parcels}} F_{D,i,j} \right) \Big/ A_{fr} \tag{3.7}$$

3.2.7 Reducing computing time

Due to the large number of collisions that may occur in the rain zone the model can become very slow if all these collisions are taken into account and therefore the number of collisions determined at the edge of each element must exceed a certain user-defined threshold value before it is considered to be significant; typically in the order of 1000/m^3.

When all the collision products at the edge of each element (Figure 3.1) are determined the different drop parcels can also be grouped together to form one parcel if their temperature differences, drop diameter differences and velocity differences are all within certain user-defined limits. For the analyses done in this thesis this procedure, generally executed at every fifth element, is set to group different parcels together when their temperature differences, diameter differences and velocity differences are smaller than 0.2 °C, 0.5 mm and 0.2 m/s respectively.

3.3 Grid interaction zone

When drops pass through the free fall zone and reach the grid (Figure 3.1), some of the drops pass through the openings in the grid and others will impinge onto the grid surface which cause them to break up into smaller drops (Figures 3.2 and 3.3). The fraction of drops of a certain diameter that impinges onto the grid can be given by Equation (3.8) and the drop break-up is divided into three mechanisms, similar to Dreyer (1994), called splashing, straddling (comprising cutting and deflection) and dripping. In order to determine the drop distribution below the grid, as well as the amount of water present on the grid surface, splashing and straddling is quantified experimentally in terms of their mass and drop distribution.

$$f_b = \frac{W + d_i}{W + S} \tag{3.8}$$

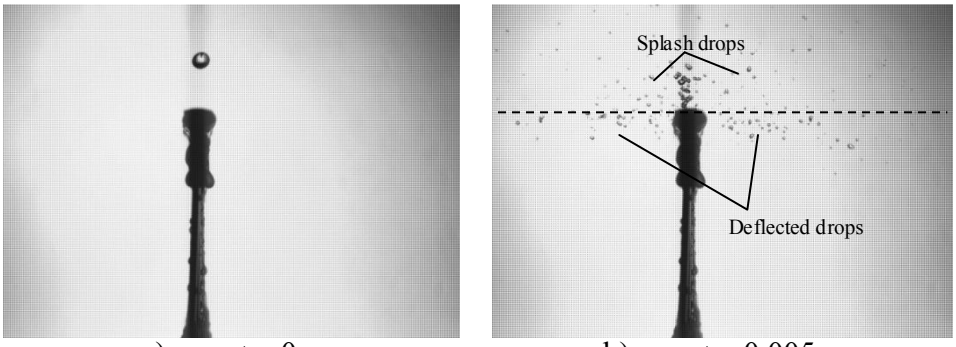

a) $t = 0$ s b) $t = 0.005$ s

Figure 3.2: Photograph of splashing together with deflective break-up.

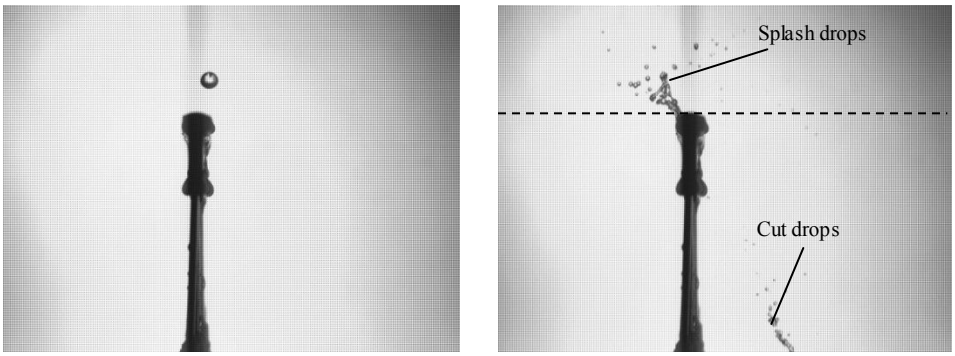

a) $t = 0$ s b) $t = 0.005$ s

Figure 3.3: Photograph of splashing together with cutting break-up.

3.3.1 Drop splashing after impingement onto a slat covered by a thin layer of water

Figure 3.4 shows a diagram of splashing on slats as considered in the theoretical rain zone model.

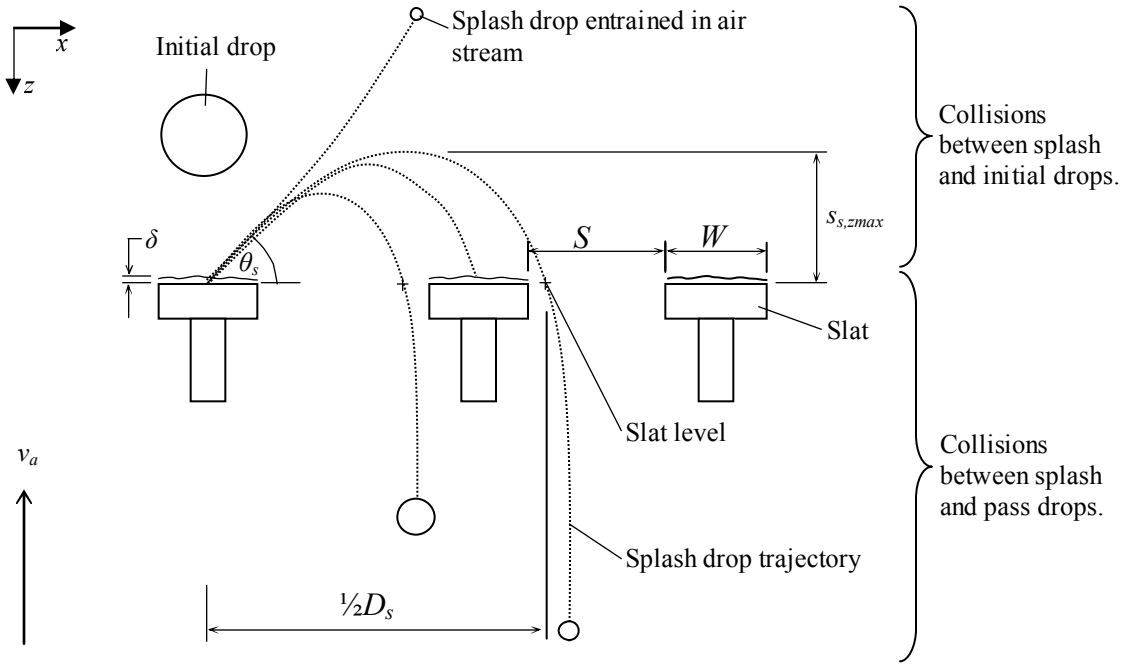

Figure 3.4: Diagram of splashing as considered in the rain zone model.

When drops impinge onto a slat the drop starts spreading out in the horizontal direction and if enough water is present on top of the slat to resist this spreading, water is forced upward in the form of a crown that breaks up to form a distribution of relatively small drops (Figures 3.2 and 3.3). The initial trajectory of the splash drop

has an assumed angle of $\theta_s \approx 60°$ relative to the top surface of the slat as shown in Figure 3.4.

In Appendix B splashing on slats covered by a thin layer of water is experimentally investigated for drops falling from different heights onto slats of different widths. The fraction of an incoming drop that splashes can be quantified in terms of the splash fraction given by

$$f_s = \frac{M_s}{M_i} \tag{2.55}$$

The following empirical equations for predicting the average splash fractions on $W = 12$ mm, $W = 6$ mm and $W = 3$ mm wide slats are respectively given by

$$\bar{f}_{s,12} = \frac{6.94\delta_n + 0.8}{\csc[\pi/(3d_n + 0.45)]} \tanh\left[\frac{(We_n - 0.11\delta_n - 0.01)\{\mathrm{sech}(16d_n - 3.3) + 0.11\}}{0.02\cos\{\pi/(15\delta_n + 2.5)\}}\right] \tag{B.7}$$

$$\bar{f}_{s,6} = \frac{1.16\delta_n + 0.41}{\csc[\pi/(2.8d_n + 0.3)]} \tanh\left[\frac{(We_n - 0.018)\{\mathrm{sech}(6.5d_n - 4.1) + 0.31\}}{0.05\cos\{\pi/(3.5\delta_n + 2.6)\}}\right] \tag{B.8}$$

$$\bar{f}_{s,3} = \frac{1.58\delta_n + 0.077}{\csc[\pi/(4d_n - 2.6)]} \tanh\left[\frac{(We_n - 0.018)\{\mathrm{sech}(2.6d_n - 1.6) + 0.08\}}{0.09\cos\{\pi/(\delta_n + 2.05)\}}\right] \tag{B.9}$$

The average splash fractions at intermediate slat widths can be obtained by interpolating the values obtained from the equations above.

Splash drops generally range in sizes below $d_s = 2.5$ mm in diameter and the cumulative drop mass distribution is expressed by a Rosin-Rammler function given by

$$R(d_d) = 1 - exp\left[-\left(\frac{d_d}{d_{RR}}\right)^{n_{RR}}\right] \tag{2.58}$$

where the average Rosin-Rammler parameters are empirically obtained in Appendix B and given by

$$\bar{d}_{RR} = 3.86{\delta_n}^R {We_n}^{0.09} \tanh\left[1.8d_n - 5.39/exp\left(6.03\frac{W}{d_m}\right)\right] exp\left(0.66\frac{W}{d_m}\right) \tag{B.13}$$

where

$$R = 0.28\left(\frac{W}{d_m}\right)^{-0.56}$$

and

$$\bar{n}_{RR} = 1.44exp\left(0.53\frac{W}{d_m}\right)\frac{\delta_n^{\,0.1exp\left(0.69\frac{W}{d_m}\right)}}{We_n^{\,0.4}} \tag{B.17}$$

The average natural film thickness of the water on the slats, as shown in Figure 3.4, can be determined with the empirical correlation of Dreyer (1994) given by

$$\bar{\delta} = 0.315 - 1.387 \times 10^{-2}G_w - 2.550 \times 10^{-3}v_a + 1.575 \times 10^{-2}W - 3.992 \times 10^{-4}W^2 + 1.916 \times 10^{-3}(G_wW) + 2.188 \times 10^{-3}(v_aW) \tag{2.63}$$

Splashing is modelled as the superposition of single drop impingements and the interaction between the crowns of adjacent drop impingements are ignored as well as the interaction between different splash drops.

Due to the large number of splash drops present in the volume above the grid, it is expected that a large number of collisions occur between the initial drops and the splash drops. A method similar to the one used in Section 3.2.4 is used in Appendix C to determine the number of drop collisions above the grid that leads to coalescence. In order to determine the height of the splash volume for each splash drop diameter the maximum height ($s_{s,zmax}$), shown in Figure 3.4, to which each splash drop diameter splashes are determined from the numerical model in Appendix C and is given by

$$s_{s,zmax} = -exp(-0.0192\theta_s - 1.5252d_s - 0.1417v_a - 2.9320) \tag{C.15}$$

The average upward (Equation C.12) and downward (Equation C.13) velocities of the splash drops over the height $s_{s,zmax}$ for each splash drop and the average horizontal (Equation C.14) splash drop velocities over the distance ½D_s above the grid are also obtained from the numerical model in Appendix C.

$$\bar{v}_{s,z-} = -exp(-0.01\theta_s - 0.6783d_s + 0.0162v_a - 0.7627) \tag{C.12}$$

$$\bar{v}_{s,z+} = exp(-0.0094\theta_s - 0.5659d_s + 0.0581v_a - 0.9099) \tag{C.13}$$

$$\bar{v}_{s,x} = exp(0.0332\theta_s - 0.4898d_s + 0.0462v_a + 1.5912) \tag{C.14}$$

With these values known the total number of collisions between a splash drop parcel and an initial drop parcel, which is the vector sum of collisions in the vertical and

horizontal directions as shown in Figure C.6, can be obtained from Equations (C.16) to (C.25).

The velocity of the splash drops as it passes the grid and enters the free fall zone below the grid is determined by assuming that the splash drop velocity is zero at the maximum displacement above the grid (Equation C.15) before using the equations for drop velocity (Equation I.13) and drop trajectory (Equation I.24) to determine the velocity of the drop as it passes the slat level on its way down. The horizontal component of the splash drop velocity below the grid is assumed negligible compared to the vertical component below the grid and is therefore not included in any further calculations.

As the splash drops return to the grid, some of them will pass through the grid and some of them will become part of the surface water when they impinge onto the grid surface due to their low kinetic energy (Figure 3.4). The fraction of the drops of a certain diameter that becomes part of the surface water (grid fraction) is estimated by Equation (C.10).

$$f_G = \frac{2(D_s + W + S)(W + d_s)}{\pi D_s (W + S)} \tag{C.10}$$

The splash diameter is given by Equation (C.11) and shown in Figure 3.4.

$$D_s = exp(0.0225\theta_s - 1.3981 d_s - 0.1191 v_a + 0.8497) \tag{C.11}$$

Some of the smallest splash drops can become entrained in the air stream when their terminal velocities are smaller than the counter flowing air velocity. When this happens it is assumed that these drops get blown out of the model at the top and their mass velocity gets subtracted from the total water mass velocity.

The initial temperature of the splash drops can be determined according to Equation (2.65) as used by Dreyer (1994), where the initial temperature is determined according to an arbitrary chosen mix ratio (ϕ) between the surface water on top of the slat and the temperature of the drop impinging onto the slat. For the initial film temperature (T_f) on top of the slat the average water temperature just before impingement onto the grid is used.

$$T_{s,i} = \phi T_{d,i} + (1 - \phi) T_f \tag{2.65}$$

From the numerical investigation in Appendix C a simplified equation is obtained that is used to determine the temperature change of the splash drops as they travel through the air above the grid that is given by

$$\Delta T_s = -exp(-0.0031\theta_s - 2.0422 d_s - 0.2974 v_a + 0.01113 T_{s,i} - 0.0099 T_{wb} - 0.0036 T_a - 4.9405 \cdot 10^{-7} P_{atm} - 28.4274) \quad \text{(C.30)}$$

3.3.2 Drop straddling after impingement onto a slat covered by a thin layer of water

Drop straddling can be divided into two regimes namely deflection (Figure 3.2) and cutting (Figure 3.3). Deflection happens when the whole drop is directly above the slat before impingement and some of the water is forced away from the slat in the horizontal direction in the form of relatively small drops. Cutting happens when a part of the drop is not directly above the slat before impingement and the slat shears off that part from the original drop to form drops that are generally larger than the drops associated with deflection.

Straddling is experimentally investigated in Appendix D when drops of different diameters impinge onto slats of different widths, covered by a thin layer of water. The fraction of an incoming drop that breaks up due to straddling when it impinges onto the grid surface is expressed in terms of the straddle fraction given by Equation (2.66).

$$f_c = \frac{M_c}{M_i} \quad \text{(2.66)}$$

The average straddle fraction is determined experimentally in Appendix D and given by

$$\bar{f_c} = 1.1 exp\left(-0.62 \frac{W}{d_m}\right) \tanh\left[10.3 \left(\frac{W}{d_m}\right)^{-0.4} exp\left(2.87 \frac{d_i}{d_m}\right) We_n\right] \quad \text{(D.5)}$$

The size distribution of the drops formed by straddling is also experimentally determined in Appendix D and given by

$$R(d) = \left(\frac{d}{d_{ref}}\right)^{n_{RT}} \quad \text{(D.2)}$$

where

$$d_{ref} = d_i \qquad for\ d_i \leq S \quad \text{(3.9)}$$

$$d_{ref} = \sqrt[3]{\frac{3 {d_i}^2 S - S^3}{2}} \qquad for\ d_i > S \quad \text{(3.10)}$$

and

$$n_{RT} = 1.35 \coth(25We_n) \tag{D.6}$$

Although the drops formed by straddling do not necessarily travel in straight vertical paths, the initial velocity of the straddled drops is assumed to be equal to the initial drop velocity in the vertical direction, with no horizontal component.

When the straddle drops are deflected by slats it may happen that these drops are deflected onto adjacent slats if the slat spacing becomes small enough. This effect is however considered negligible seeing that the straddle mass fraction is generally dominated by cutting in which the horizontal deflection of the drops from the original vertical trajectory is relatively small. It is therefore assumed that the straddled products always clear adjacent slats.

The initial temperature of the straddled drops is taken as the temperature of the initial drop just before impingement onto the slat.

3.3.3 Dripping from below slats

With the average mass fractions for straddling and splashing known, the dripping mass velocity is determined by doing a mass balance over the grid.

Dripping is theoretically investigated in Appendix E and it is assumed that dripping happens in the form of a large (or primary) drop followed by 5 satellite drops, as proposed by Yung *et al.* (1980). The diameter of the primary drop, determined from a force balance on a drop suspended below a slat, is given by

$$d_p = 1.2407 \sqrt[3]{\frac{\sigma S_P}{g(\rho_w - \rho_{av})}} \tag{E.1}$$

where the characteristic length S_p is approximated for different slat bottom profiles by the equations listed in Table E.1. The sizes of the 5 satellite drops are assumed to be equally distributed within the following size range.

$$0.24 < \frac{d_s}{d_p} < 0.46 \tag{2.74}$$

The initial velocity of the drip drops as they detach from the slat bottom is assumed to be zero.

The temperature of the surface water leaving the slat (T_{fo}) in the form of drip drops is determined by

$$T_{fo} = T_{fi} - \left[\frac{hA_{slats}(i_{masw} - i_{ma})}{m_d c_{pw}}\right] \tag{2.79}$$

where the initial temperature (T_{fi}) of the water film on top of the slat is taken as the average water temperature just before the splash grid is reached. The transfer coefficient h can be determined from

$$h = \frac{Nuk_{av}}{Le_f c_{pav} d_h} \tag{3.11}$$

with the Nusselt number based on a hydraulic diameter (d_h) given by Gnielinski (1983) and verified by Dreyer (1994) to be accurate for various slat shapes.

$$Nu = 0.3 + \sqrt{\left(0.664\sqrt{Re}Pr^{\frac{1}{3}}\right)^2 + \left[\frac{0.037Re^{0.8}Pr}{1 + 2.443Re^{-0.1}\left(Pr^{\frac{2}{3}} - 1\right)}\right]^2} \tag{2.80}$$

The hydraulic diameter (d_h) is defined as the ratio of the total surface area of the slat to the maximum slat perimeter perpendicular to the air flow.

3.3.4 Pressure drop over the grid

The pressure drop over the grids can be calculated using Equation (3.12) and the loss coefficient (Equation 2.83) proposed by Dreyer (1994) that were correlated from the data of Baines and Peterson (1951) and Miller (1990).

$$\Delta p_{grid} = \sum K_{grid}\, \rho_{av} \frac{{v_{av}}^2}{2} \tag{3.12}$$

where

$$K_{grid} = 0.78\left(\frac{1}{\beta^2} - 1\right)^{1.25} \tag{2.83}$$

3.4 Conclusions

In this chapter the development of a theoretical model (Figure 3.5) to predict the performance of a counter flow rain zone with splash grids, based on experimental and theoretical data as well as current literature is described. The major thermal and dynamic effects are taken into consideration and in the next chapter the model is compared to measured data.

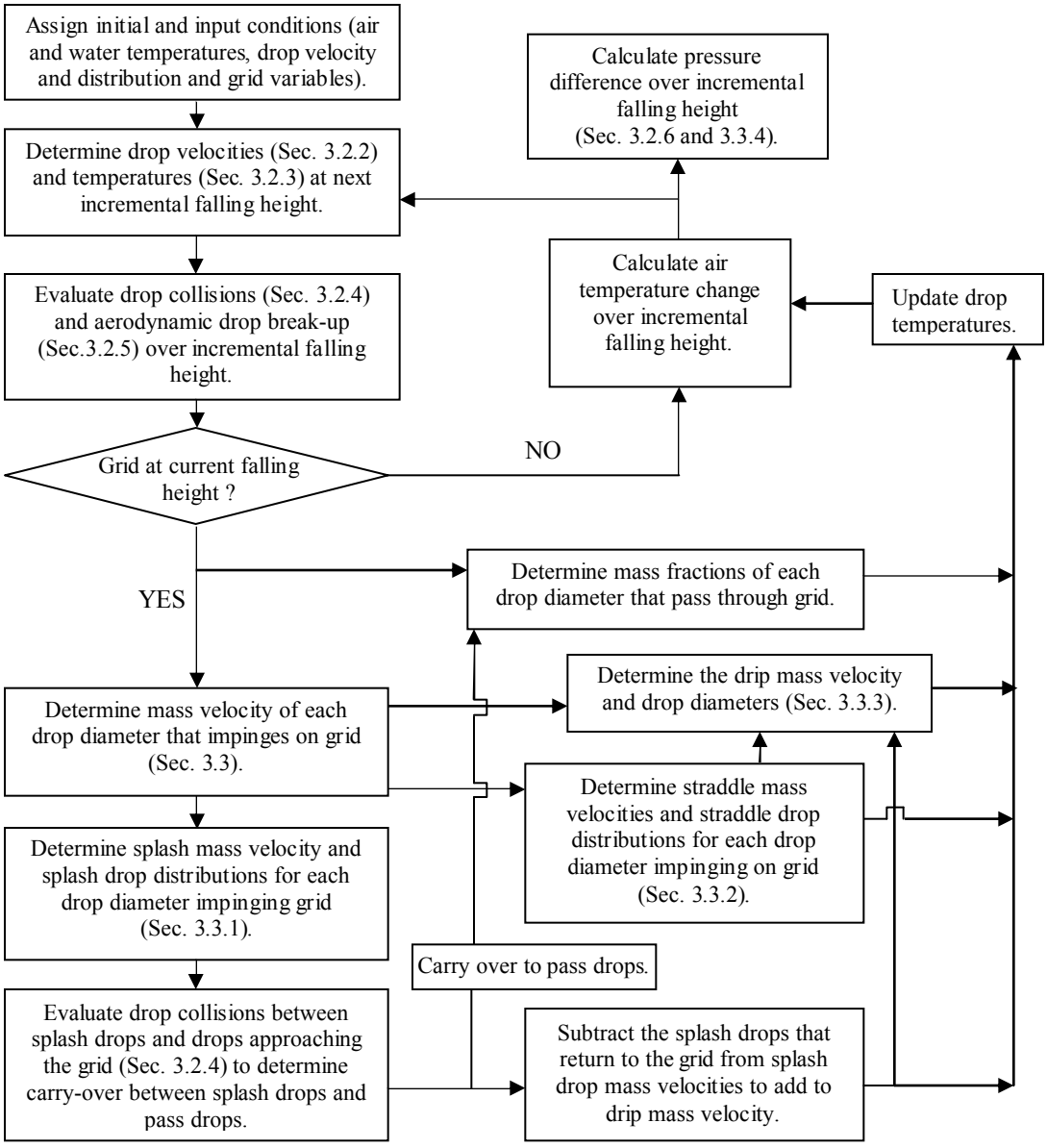

Figure 3.5: Flow chart of theoretical rain zone model.

4

COMPARISON BETWEEN THE THEORETICAL MODEL AND EXPERIMENTAL DATA

4.1 Introduction

In this chapter the results obtained with the theoretical rain zone model developed in the previous chapter are compared to the measured drop size distribution data presented in Appendices G and H and also the measured data of Oosthuizen (1995), Dreyer (1994) and Terblanche (2008). The predicted Merkel numbers and loss coefficients are compared to correlations by de Villiers, given in Kröger (2004), for a purely counter flow rain zone.

4.2 Drop distribution below different grid layouts

Figure 4.1 shows a comparison between the measured cumulative drop mass distribution below an experimental slat grid (Figure H.3) and corresponding data predicted by the theoretical model. A single layer of this grid is installed at various distances (H_{FG}) below a trickle fill and the drop distribution is measured H_{rz} = 260 mm below the grid in each case (Terblanche, 2008). The initial drop distribution measured H_{rz} = 0.26 m below the trickle fill is provided as an input to the theoretical model and the cumulative drop mass distributions are calculated at a corresponding distance below the grid and compared to the measured distributions for each case, as shown in Figure 4.1(a-e). Figure 4.1(f) compares the measured and predicted Sauter mean drop diameters for each of the cases presented in Figures 4.1(a-e). Figure 4.1 shows good agreement between the measured and predicted cumulative drop mass distributions for a single layer of the experimental slat grid (Terblanche, 2008) with deviations between the measured and predicted Sauter mean drop diameters ranging between 15.81 % (H_{FG} = 0.2 m) and 0.3 % (H_{FG} = 0.6 m).

Figure 4.2 shows mass fractions and Sauter mean drop diameters produced by the different drop break-up mechanisms when the slat grid (Figure H.3) is installed below the trickle fill. It can be seen in the figure that the Sauter mean drop diameter of the pass drops is slightly smaller that that of the initial distribution and this happens because a larger percentage of smaller drops pass through the grid openings

compared to the larger drops because they can pass closer to the slats without making contact.

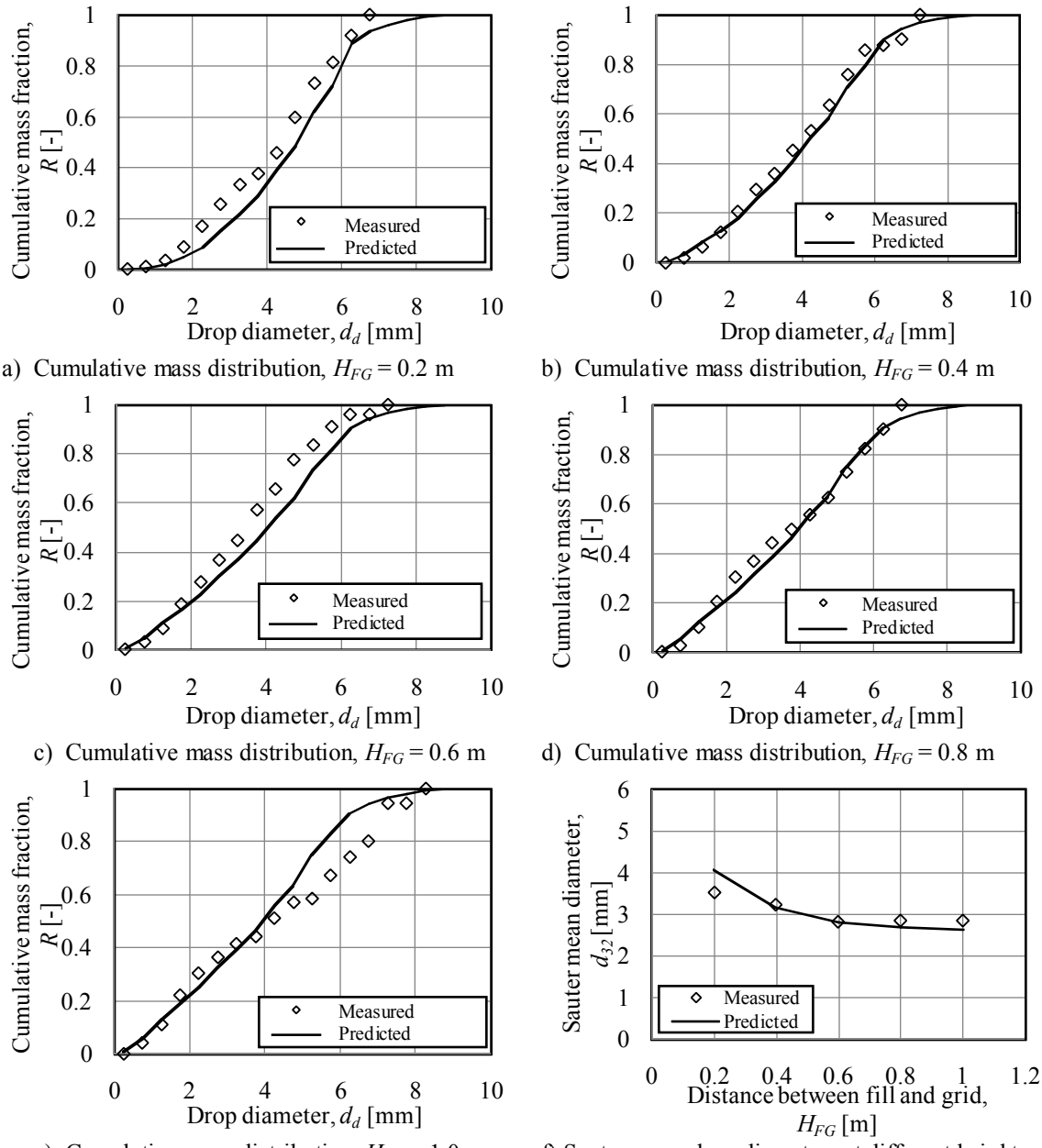

a) Cumulative mass distribution, H_{FG} = 0.2 m

b) Cumulative mass distribution, H_{FG} = 0.4 m

c) Cumulative mass distribution, H_{FG} = 0.6 m

d) Cumulative mass distribution, H_{FG} = 0.8 m

e) Cumulative mass distribution, H_{FG} = 1.0 m

f) Sauter mean drop diameters at different heights

Figure 4.1: Drop mass distributions and Sauter mean diameters produced below one layer of slat grid installed below a trickle fill (G_w = 2.84 kg/m^{2}s, G_a = 0, $d_{32,i}$ = 5.19 mm).

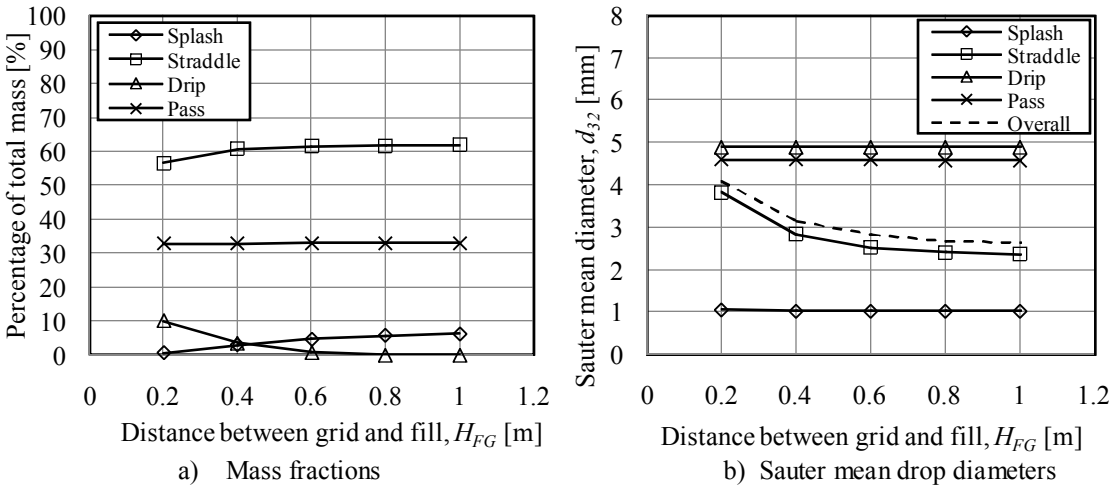

a) Mass fractions b) Sauter mean drop diameters

Figure 4.2: Contributions of different break-up mechanisms for one layer of slat grid installed below a trickle fill (G_w = 2.84 kg/m^{2}s, G_a = 0, $d_{32,i}$ = 5.19 mm).

Figure 4.3 shows a comparison between the measured and predicted cumulative mass distributions below two layers of the experimental slat grid (Figure H.3) that are installed simultaneously at heights of H_{FG} = 0.8 and H_{FG} = 1.6 m below a trickle fill (Terblanche, 2008). The drop distribution is measured H_{rz} = 200 mm below the second grid layer at counter flow air mass velocities of G_a = 0 kg/m^{2}s and G_a = 2.28 kg/m^{2}s respectively. Figure 4.4 again shows the mass fraction and drop size contributions of the different drop break-up mechanisms for each grid located H_{FG} = 0.8 m and H_{FG} = 1.6 m below the trickle fill.

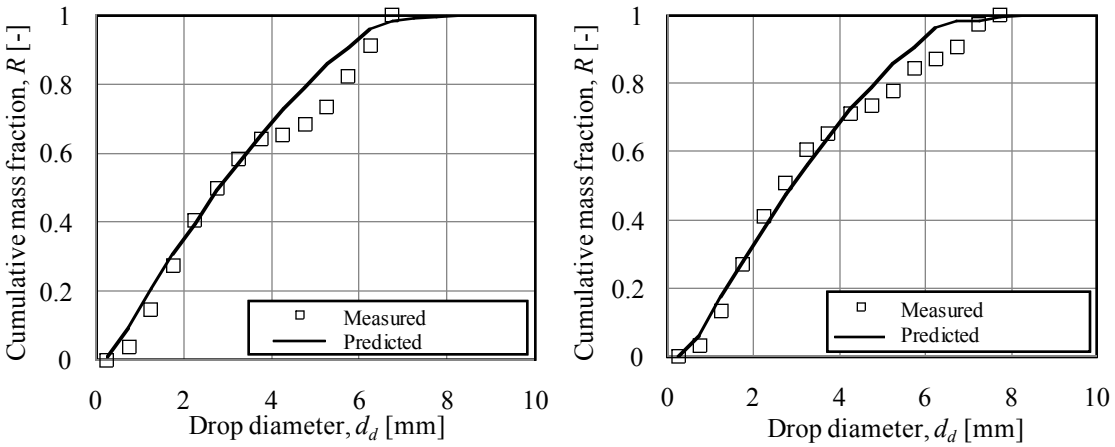

a) Cumulative mass distribution, H_{FG} = 0.8 and H_{FG} = 1.6 m, G_a = 0 kg/m^{2}s

b) Cumulative mass distribution, H_{FG} = 0.8 and H_{FG} = 1.6 m, G_a = 2.28 kg/m^{2}s

Figure 4.3: Drop mass distributions produced below two layers of slat grid, installed H_{FG} = 0.8 m and H_{FG} = 1.6 m below a trickle fill respectively (G_w = 2.84 kg/m^{2}s, $d_{32,i}$ = 5.19 mm).

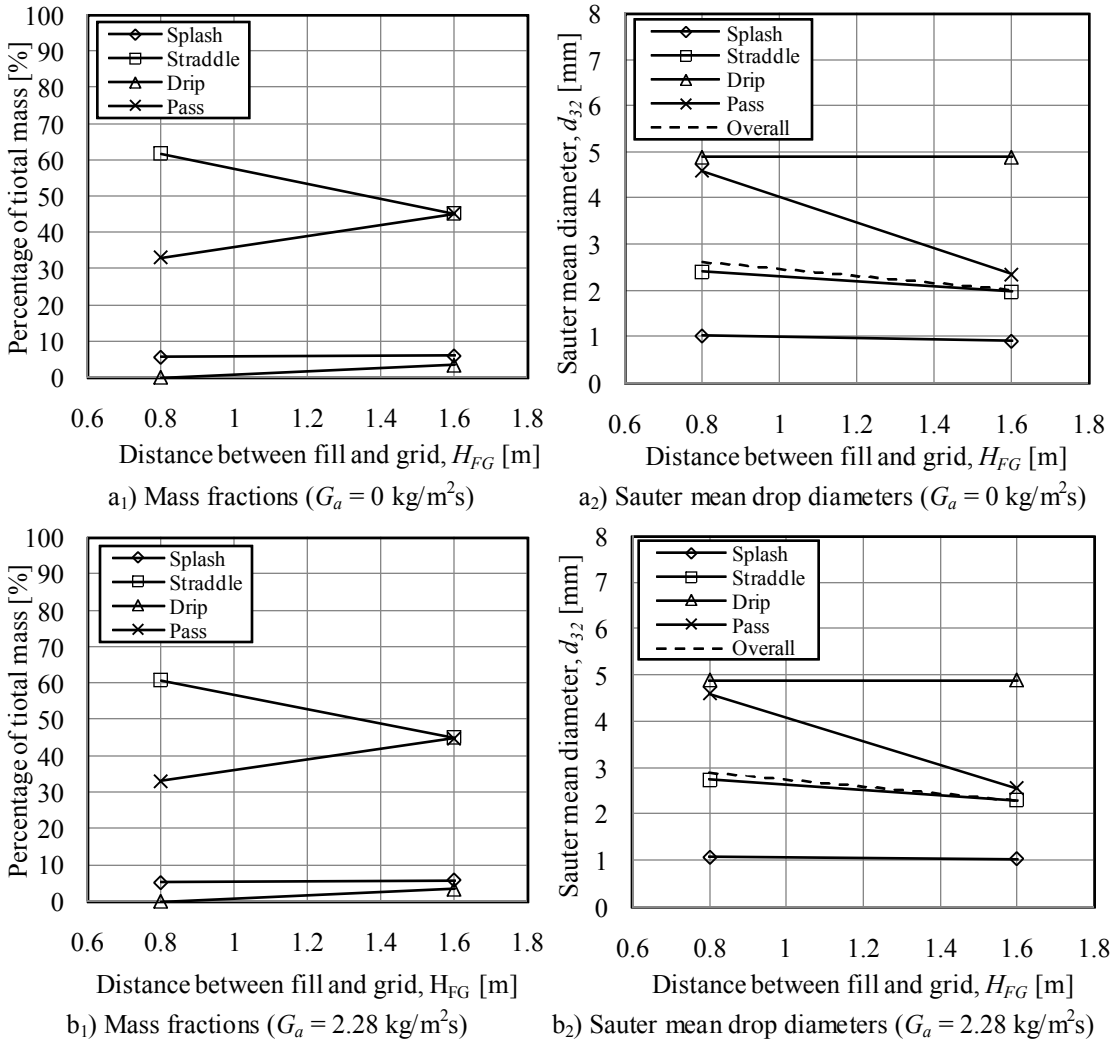

Figure 4.4: Contributions of different drop break-up mechanisms for two layers of slat grid installed H_{FG} = 0.8 and H_{FG} = 1.6 m below a trickle fill (G_w = 2.84 kg/m^{2}s, G_a = 0, $d_{32,i}$ = 5.19 mm).

Figure 4.5 shows a comparison between the measured and the predicted cumulative drop mass distributions when the experimental slat grid (Figure H.3) is installed below a spray frame (Section H.3) that produces smaller drops than a typical trickle fill, with Figure 4.6 showing the mass fraction and drop size contributions of the different drop break-up mechanisms towards the drop break-up.

Figure 4.7 shows a comparison between the measured and predicted cumulative drop mass distributions below a single layer of commercial grid (Figure H.6) installed below a spray frame (Section H.3). The model predicts similar results to the experimental splash grid, which is to be expected, since the porosities of the grids are

similar, but the measured results show negligible drop size reduction. This can be attributed to the way in which the distribution system releases the drops from distinct nodes as opposed to the release of drops at random locations below a fill. The number of drops that impinge onto the grid surface in this case is therefore also influenced by the horizontal placement of the commercial grid below the spray frame. This theory is supported by cross flow performance measurements where both grids produced similar transfer characteristics (Appendix K). This can only be attributed to similar drop size reduction since the water on the grid surface is almost negligible, as shown in Figure 4.8 where the mass fraction and drop size contributions of different break-up mechanisms are presented for the commercial grid.

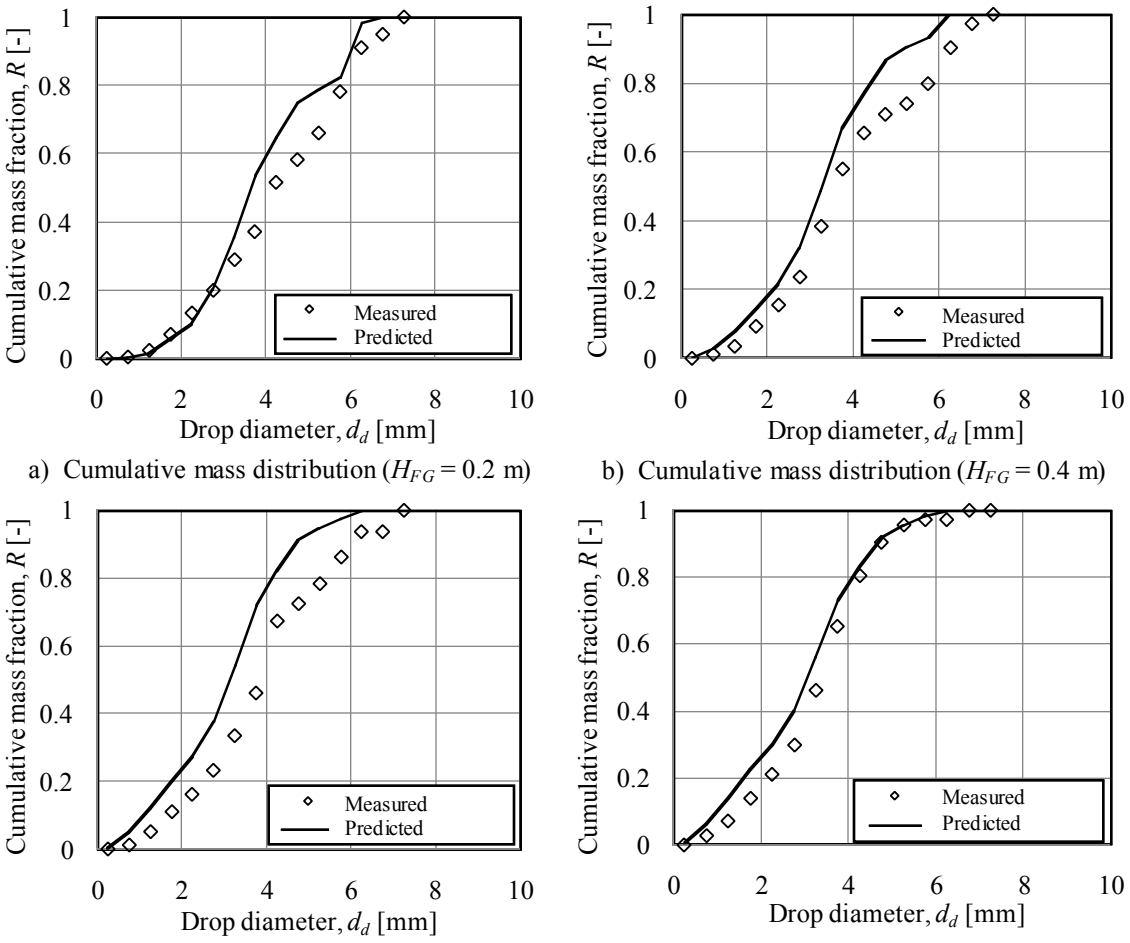

Figure 4.5: Drop mass distributions produced below one layer of the slat grid installed below the spray frame of Section H.3 (G_w = 2.84 kg/m^{2}s, G_a = 0, $d_{32,i}$ = 3.72 mm).

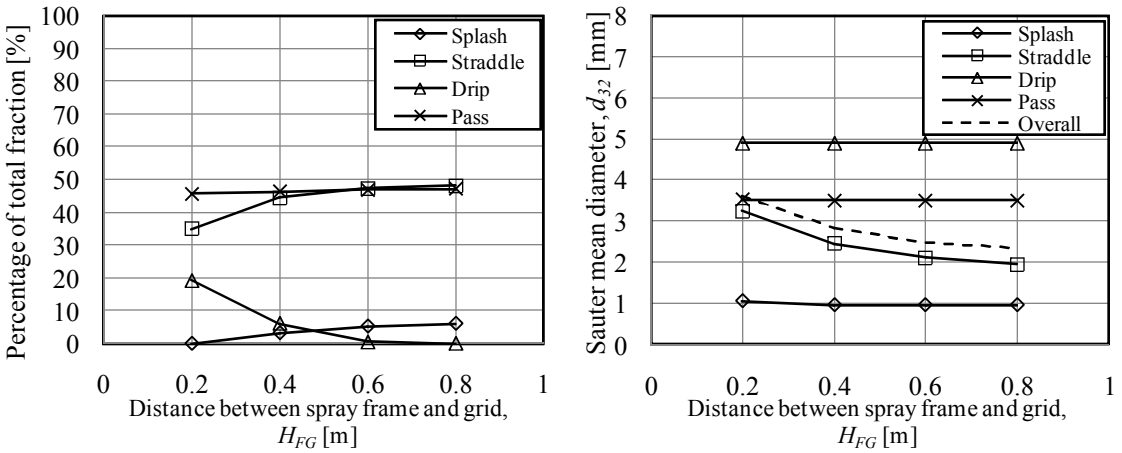

a) Mass fractions b) Sauter mean drop diameters

Figure 4.6: Contributions of the different drop break-up mechanisms for one layer of slat grid installed below the spray frame of Section H.3 (G_w = 2.84 kg/m^{2}s, G_a = 0, $d_{32,i}$ = 3.72 mm).

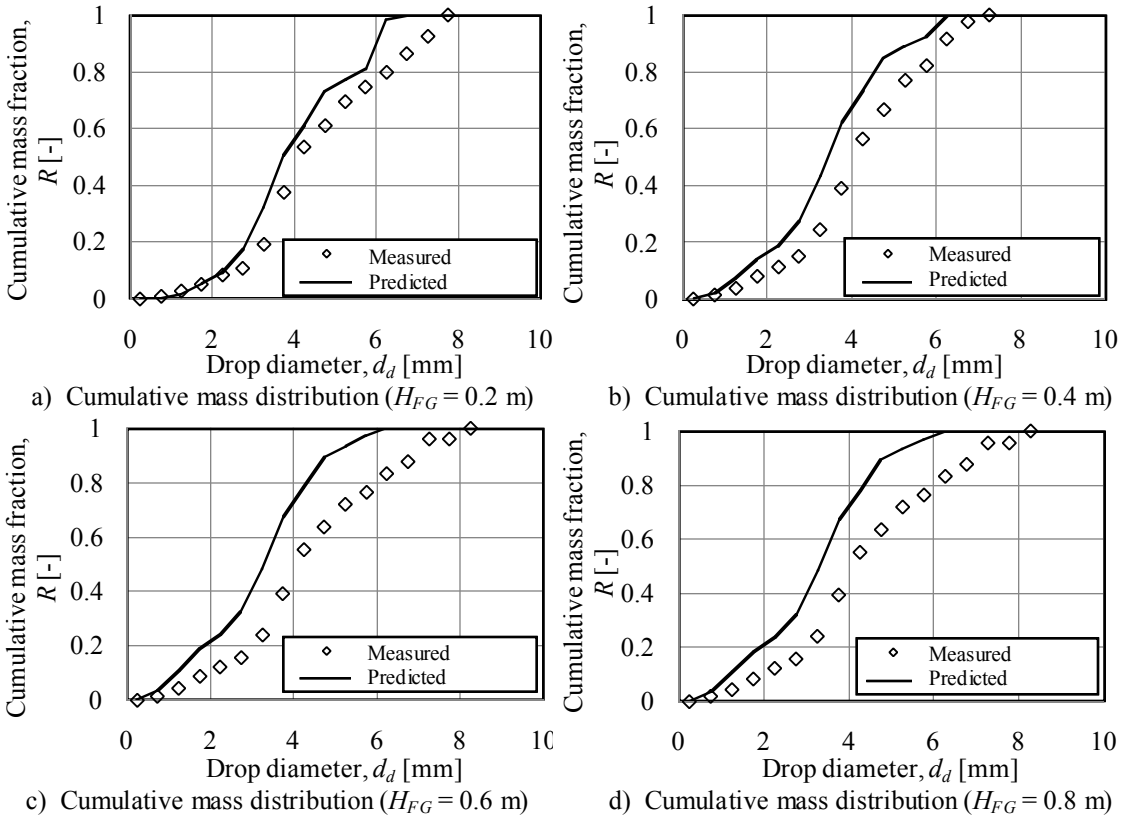

a) Cumulative mass distribution (H_{FG} = 0.2 m) b) Cumulative mass distribution (H_{FG} = 0.4 m)

c) Cumulative mass distribution (H_{FG} = 0.6 m) d) Cumulative mass distribution (H_{FG} = 0.8 m)

Figure 4.7: Drop mass distributions produced below one layer of commercial grid installed below the spray frame of Section H.3 (G_w = 2.84 kg/m^{2}s, G_a = 0, $d_{32,i}$ = 3.72 mm).

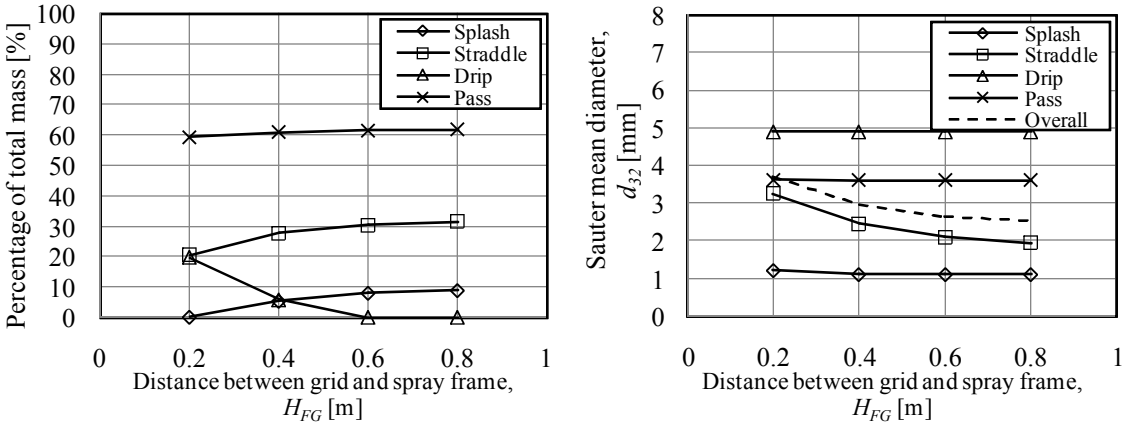

a) Mass fractions b) Sauter mean drop diameters

Figure 4.8: Contributions of different drop break-up mechanisms for one layer of commercial grid installed below the spray frame of Section H.3 (G_w = 2.84 kg/m^{2}s, G_a = 0, $d_{32,i}$ = 3.72 mm).

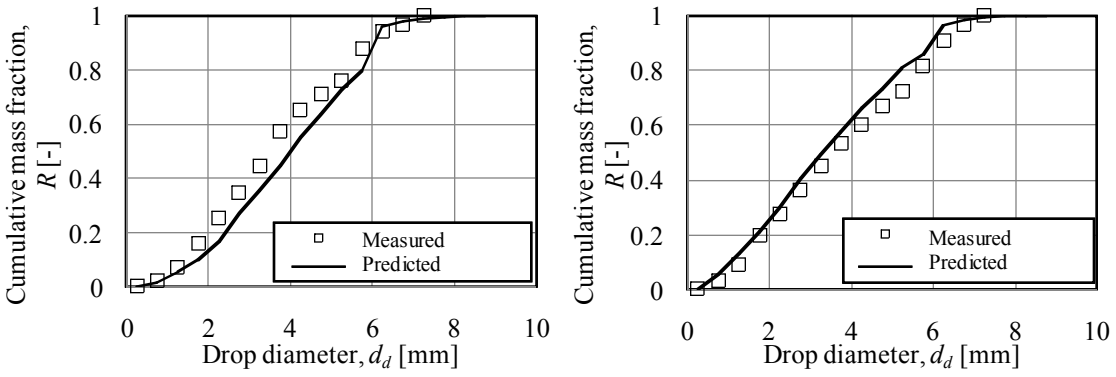

a) Cumulative mass distribution (H_{FG} = 0.2 m) b) Cumulative mass distribution (H_{FG} = 0.4 m)

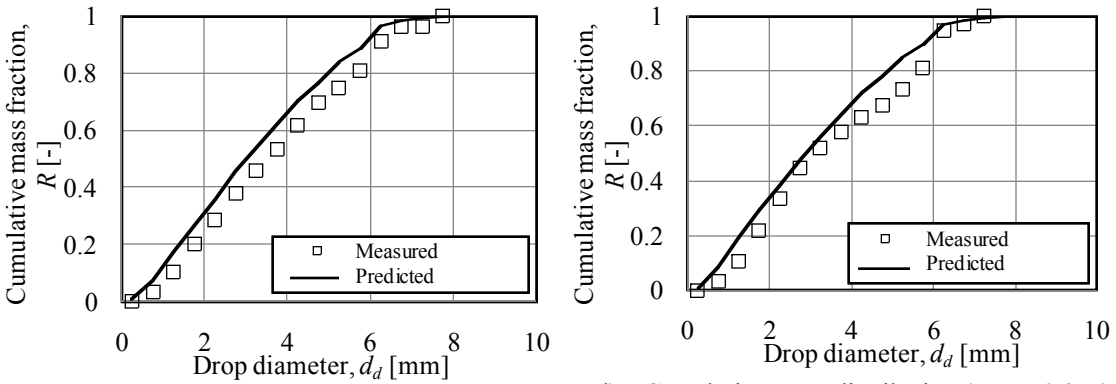

c) Cumulative mass distribution (H_{FG} = 0.6 m) d) Cumulative mass distribution (H_{FG} = 0.8 m)

Figure 4.9: Drop mass distributions produced below two layers of slat grid installed below a trickle fill with a vertical grid spacing of H_{GG} = 100 mm (G_w = 2.84 kg/m^{2}s, G_a = 0, $d_{32,i}$ = 5.19 mm).

Oosthuizen (1995) and Terblanche (2008) installed multiple layers of splash grid relatively closely below each other (H_{GG} = 100 mm) in order to enhance rain zone performance. Figure 4.9 shows a comparison between the measured results obtained by Terblanche (2008) and the results predicted by the theoretical model when two layers of the experimental slat grid (Figure H.3) are installed at a vertical grid spacing of H_{GG} = 100 mm below a trickle fill. Oosthuizen (1995) measured the drop mass distributions below two layers of relatively coarse expanded metal splash grid, with a vertical grid spacing of H_{GG} = 100 mm, installed H_{FG} = 0.57 m below a trickle fill in a counter flow rain zone test facility. Figure 4.10 shows his results compared to the predicted results obtained by the theoretical model for different air and water mass velocity ratios. The graphs show that individual measurements are scattered over a relatively wide range.

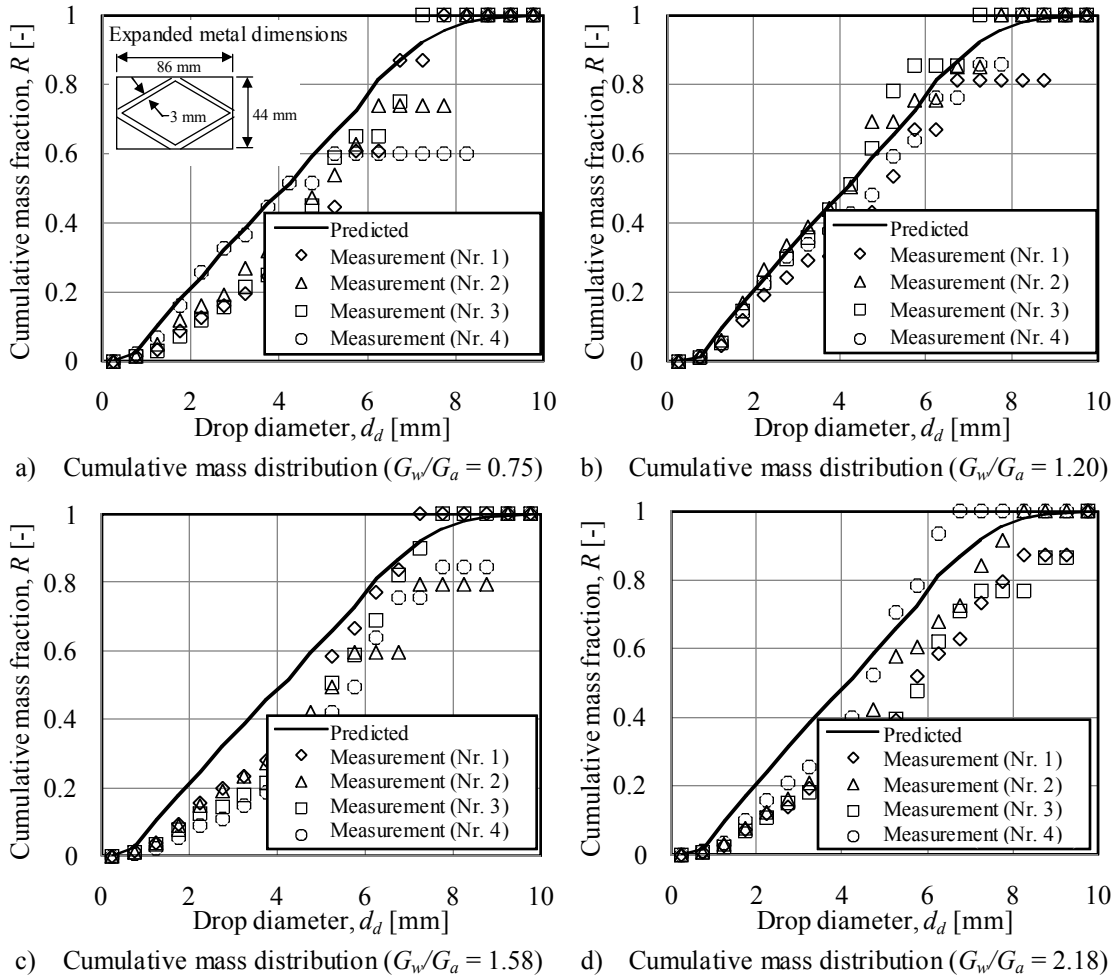

a) Cumulative mass distribution (G_w/G_a = 0.75)

b) Cumulative mass distribution (G_w/G_a = 1.20)

c) Cumulative mass distribution (G_w/G_a = 1.58)

d) Cumulative mass distribution (G_w/G_a = 2.18)

Figure 4.10: Drop mass distributions (Oosthuizen, 1995) produced below a two layers of coarse expanded metal grid installed H_{FG} = 0.57 below a trickle fill with a vertical grid spacing of H_{GG} =100 mm ($d_{32,i}$ = 5.37 mm).

Dreyer (1994) measured the drop mass distribution H_{rz} = 200 mm below ten layers (H_{GG} = 100 mm) of splash grids, comprising wooden slats with widths, heights and horizontal spacing between the slats of W = 9 mm, H_s = 22 mm and S = 73 mm respectively, installed in a counter flow cooling tower test section. Figure 4.11 shows a comparison between Dreyer's measured cumulative drop mass distribution and the drop mass distribution predicted by the theoretical model, which over predicts the splashing significantly. According to Dreyer this over prediction of the splashing may be due to interference between splash crowns, because he argued that the time between splashes is less than the life-time of a splash crown, especially at higher water flow rates where rain densities are relatively high. There may be other reasons for the decline in the expected amount of splashing when multi-layer splash grid setups are used that are shortly discussed.

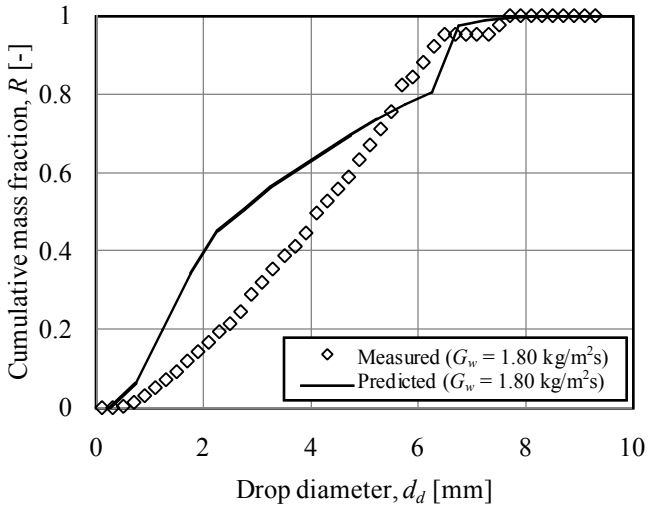

Figure 4.11: Drop mass distribution produced below multiple grids from Dreyer (1994) (N_{grids} = 10, H_{GG} = 100 mm, W = 9 mm, S = 73 mm, H_s = 22 mm).

Multiple layers of splash grids can be installed in a vertical configuration where corresponding slats in the different layers are approximately below each other or a staggered configuration where slats of two neighbouring layers are never below each other. Drops impinge the first layer/layers, depending on the configuration, with vertical trajectories (approximately) but may impinge the slats in subsequent layers at an angle (staggered configuration) or predominantly graze the slats (vertical configuration). The angle at which a drop impinges on a slat (staggered configuration) can significantly reduce the amount of splashing and instead of the water leaving a slat in the form of splash drops they leave a slat as relatively large (compared to splash drops) straddled drops. Liu *et al.* (2010) did some experiments where FC – 72 drops impinged onto a Plexiglas surface and found splashing to be much weaker at an impingement angle of 60° compared to a 90° vertical

impingement. They also found splashing to be almost negligible at an impingement angle of 45°. In a vertical configuration with a relative large horizontal spacing (S) between individual slats, like the S = 73 mm used by Dreyer, it may also be that a large number of drops pass through all ten grid layers without impinging on any of the slats or when the drops do impinge onto slats in subsequent layers they predominantly graze the slats, as mentioned earlier, resulting in negligible drop size reduction. The only significant drop size reduction therefore only happens on the first few layers.

These secondary effects are beyond the scope of this project and are therefore not included in the theoretical model.

4.3 Drop interaction in the free fall zone

Drop distributions are measured at the top and bottom of free fall zones below five different initial drop distribution arrangements (Appendix G) in order experimentally quantify the effect of drop interactions in a rain zone. In this section some of these results are compared to results predicted with the theoretical rain zone model.

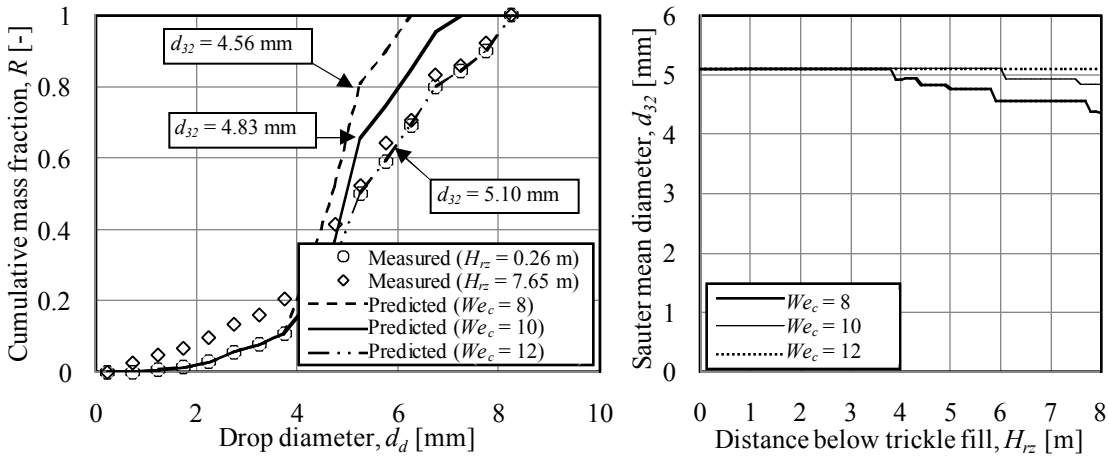

a) Measured and predicted mass distributions

b) Predicted Sauter mean drop diameters

Figure 4.12: Change in drop size distribution, due to drop collisions and vibrational break-up, for a rain zone below a trickle fill (G_w = 2.84 kg/m^{2}s, G_a = 0, $d_{32,i}$ = 5.092 mm).

Figure 4.12(a) compares the measured (Section G.4) and predicted cumulative mass distributions H_{rz} = 7.65 m below the trickle fill, and also shows the initial distribution measured H_{rz} = 0.26 m below the trickle fill. In the theoretically predicted results it is assumed that vibrational aerodynamic drop break-up happens at one of three different critical Weber numbers (We_c = 8, 10 and 12). The assumption is made that vibrational

aerodynamic break-up of a drop leads to the formation of four equally sized drops (Section 2.3) and the number of drop collisions that leads to coalescence is determined by means of the coalescence model of Brazier-Smith *et al.* (1972). Figure 4.12(a) shows that the model under predicts the number of drops smaller than d_d = 4 mm in diameter in all the cases. This happens because of the assumption that vibrational drop break-up leads to four equally sized drops while drop break-up due to aerodynamic forces are more catastrophic, leading to the formation of many small drops, as shown in Figures G.3(b) and G.6. Figure 4.12(b) shows the predicted Sauter mean drop diameter in terms of the fall distance below the trickle fill for this model.

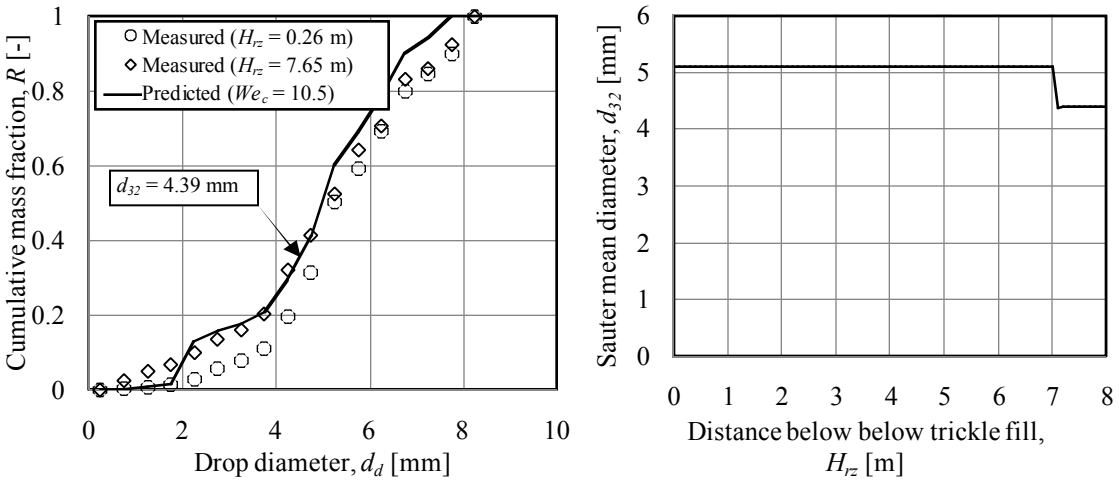

a) Measured and predicted mass distributions

b) Predicted Sauter mean drop diameters (We_c = 10.5)

Figure 4.13: Change in drop size distribution, due to drop collisions and catastrophic break-up of large drops, for a rain zone below a trickle fill (G_w = 2.84 kg/m^{2}s, G_a = 0, $d_{32,i}$ = 5.092 mm).

Figure 4.13(a) again compares the measured (Section G.4) and predicted cumulative drop mass distributions H_{rz} = 7.65 m below a trickle fill and again shows the initial distribution measured H_{rz} = 0.26 m below the trickle fill. This time the predicted drop mass distribution H_{rz} = 7.65 m below the fill is obtained by assuming that drops break up into 50 drops of equal size due to aerodynamic forces at a critical Weber number of We_c = 10.5 [similar to the catastrophic bursting bag break-up observations by Lane (1951)]. By choosing 50 break-up drops it means that the break-up drops have equal diameters of approximately d_d = 2 mm, as shown in Figure 4.13(a). In reality it is probably a distribution of drop sizes centred around $d_d \approx$ 2 mm, but this method is a relatively simple way to account for the increase in the number of small drops that form due to aerodynamic break-up. Figure 4.13(b) shows the predicted rain zone Sauter mean drop diameter in terms of the fall distance below the trickle fill for this model.

Figure 4.14 compares the measured (Section G.3) and predicted cumulative mass distribution H_{rz} = 7.65 m below a mini spray frame and also shows the distribution measured H_{rz} = 0.26 m below the spray frame. The spray frame produces an initial Sauter mean drop diameter of d_{32} = 2.325 mm and the results show negligible drop size changes due to drop interaction over the fall distance (H_{rz} = 0.26 m to H_{rz} = 7.65 m).

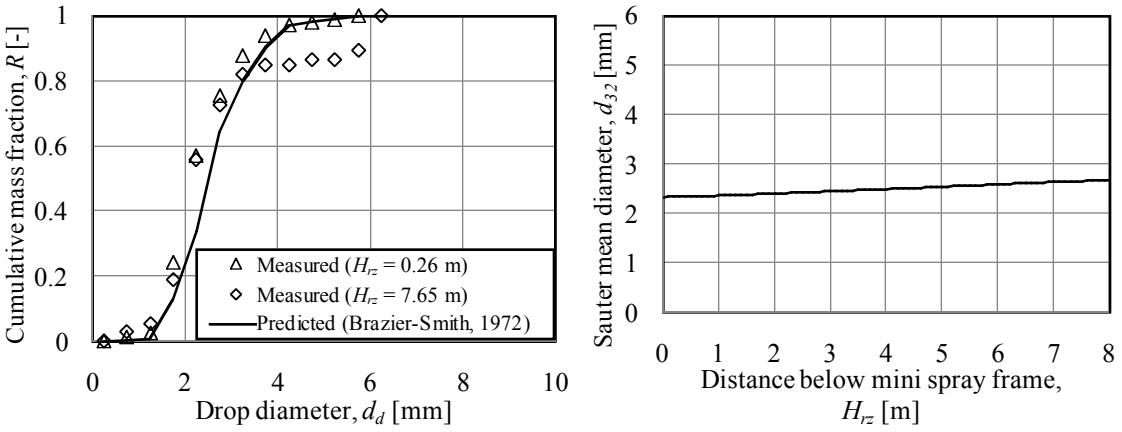

a) Mass distribution (H_{rz} = 7.65 m) b) Sauter mean drop diameters

Figure 4.14: Change in drop size distribution, due to drop collisions and aerodynamic break-up, for a rain zone below a mini spray frame (G_w = 2.84 kg/m^{2}s, G_a = 0, $d_{32,i}$ = 2.325 mm).

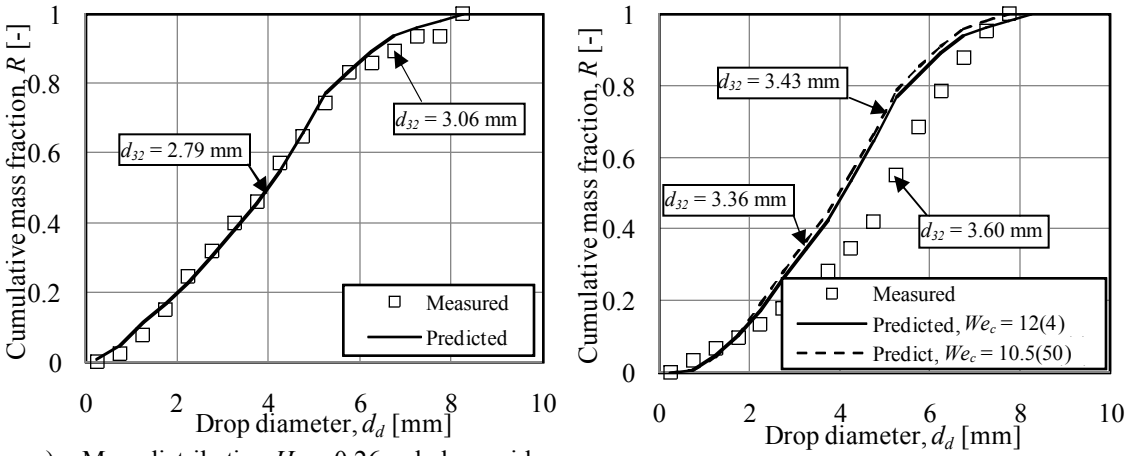

a) Mass distribution H_{rz} = 0.26 m below grid b) Mass distribution H_{rz} = 7.05 m below the grid

Figure 4.15: Change in drop distribution, due to drop collisions and aerodynamic break-up, for a rain zone below a slat grid (Figure H.9) installed H_{FG} = 0.6 m below a trickle fill (G_w = 2.84 kg/m^{2}s, G_a = 0, $d_{32,i}$ = 5.092 mm).

For the final comparison an experimental slat grid (Figure H.9) is installed below a trickle fill (Section G.5) and the measured drop mass distributions H_{rz} = 0.26 m and H_{rz} = 7.05 m below the grid are compared to the predicted results. Figure 4.15(a) shows a comparison between the measured and predicted drop mass distributions below the slat grid when the distribution measured H_{rz} = 0.26 m below the trickle fill, shown in Figure 4.12(a), is used as an input to the theoretical model. Figure 4.15(b) shows the measured and predicted drop mass distributions H_{rz} = 7.05 m below the slat grid with negligible difference between the predicted interaction for assumed critical Weber numbers of We_c = 12 (4 break-up drops form) and We_c = 10.5 (50 break-up drops form). Figure 4.15 (b) shows that the interaction is slightly under predicted and there is a significant reduction in drops ranging from d_d = 2 to 4 mm, compared to Figure 4.15 (a), that is not shown in the predicted results. The prediction of the rest of the distribution is however good; leading to similar measured and predicted Sauter mean drop diameters.

4.4 Counter flow rain zone performance

In this section the performances predicted by the theoretical rain zone model are compared to equations by de Villiers, as given in Kröger (2004), for predicting the Merkel transfer characteristic and loss coefficient of a purely counter flow rain zone. The Merkel number for a purely counter flow rain zone, given by de Villiers, is

$$\begin{aligned}\frac{h_{drz}a_{rz}H_i}{G_W} = 3.6\left(\frac{p_a}{R_v T_a \rho_w}\right)\left(\frac{D}{v_{azo}d_d}\right)\left(\frac{H_{rz}}{d_d}\right)Sc^{0.33}\left[ln\left(\frac{w_s + 0.622}{w + 0.622}\right)/(w_s - w)\right] \\ \left[5.01134a_\rho\rho_a - 192121.7a_\mu\mu_a - 2.57724\right. \\ + 23.61842\{0.2539(a_v v_{azo})^{1.67} + 0.18\}\{0.83666(a_L H_{rz})^{-0.5299} \\ \left. + 0.42\}\{43.0696(a_L d_d)^{0.7947} + 0.52\}\right]\end{aligned} \tag{4.5}$$

and the loss coefficient is given by

$$\begin{aligned}K_{rz} = a_v v_w\left[10645988a_\mu\mu_a - 130.7774a_\rho\rho_a - 32.6634\right. \\ + 888.6645\left\{2.45287\left(a_\mu v_{azo}\right)^{-1.93315}\right. \\ \left. + 0.34\right\}\{4.03861exp(-574.542a_L d_d) \\ + 0.493\}exp\{(65.26215a_L d_d \\ \left. + 0.74827)ln(6.09836exp(0.0767a_L H_{rz}) - 6.1)\}\right]\end{aligned} \tag{4.6}$$

where

$$a_\mu = 3.061 \times 10^{-6} \left[\frac{{\rho_w}^4 g^9}{\sigma_w} \right]^{0.25} \tag{4.7}$$

$$a_\rho = \frac{998}{\rho_w} \tag{4.8}$$

$$a_v = 73.298 \left[\frac{g^5 {\sigma_w}^3}{{\rho_w}^3} \right]^{0.25} \tag{4.9}$$

$$a_L = 6.122 \left[\frac{g \sigma_w}{\rho_w} \right]^{0.25} \tag{4.10}$$

These equations are valid for 1 m/s $\leq v_{azo} \leq$ 5 m/s and 0.5 m $\leq H_{rz} \leq$ 5.5 m.

Table 4.1 presents the rain zone simulation parameters for predicting the Merkel numbers of a H_{rz} = 5 m high purely counter flow rain zone. In the theoretical model the water side temperature change is determined by calculating the temperature changes of all the drop parcels contained in the distribution, of which the Sauter mean drop diameters are provided in Table 4.1, before determining the mass weighted average temperature. The Merkel number for each distribution is then determined by making use of the Chebyshev method as presented in Kröger (2004). The simulation results presented in Table 4.1 are for pure rain zones with no grids, but drop interaction and aerodynamic break-up are taken into account.

The air temperature and humidity as the air moves through the rain zone is handled in one of three ways:

1) The air wet- and dry bulb temperatures remain constant over the height of the rain zone and equal to the initial values provided in Table 4.1 (Method #1).
2) The air wet- and dry bulb temperatures remain constant over the height of the rain zone, but this time at iteratively determined mean values between the air inlet and outlet. The mean wet- and dry bulb temperatures are determined by assuming that the outlet air is saturated (Method #2).
3) The air-side temperature change is determined over each element (Figure 3.1) as the air moves through the rain zone while assuming that the air is always saturated. The initial air temperatures are provided in Table 4.1(Method #3).

Table 4.1: Simulation parameters for a H_{rz} = 5 m purely counter flow rain zone.

$d_{32,i}$ [mm]	G_a [kg/m^{2}s]	G_w [kg/m^{2}s]	T_{wi} [°C]	P_{atm} [Pa]	T_{ai} [°C]	T_{wbi} [°C]	T_{am} [°C]	T_{wbm} [°C]	Air-side method	Me [m^{-1}]	K_{rz} [m^{-1}]
5.19	2.08	1.51	30	84100	15.45	11.05	15.45	11.05	1	0.0307	0.4565
5.19	2.08	1.51	30	84100	15.45	11.05	14.54	12.34	2	0.0304	0.4564
5.19	2.08	1.51	30	84100	15.45	15.45	16.24	16.24	3	0.0297	0.4503
4.09	2.08	1.51	30	84100	15.45	11.05	15.45	11.05	1	0.0458	0.5785
4.09	2.08	1.51	30	84100	15.45	11.05	15.02	12.82	2	0.0451	0.5767
4.09	2.08	1.51	30	84100	15.45	15.45	16.47	16.47	3	0.0442	0.5702
2.97	2.08	1.51	30	84100	15.45	11.05	15.45	11.05	1	0.0703	0.8075
2.97	2.08	1.51	30	84100	15.45	11.05	15.69	13.49	2	0.0687	0.8004
2.97	2.08	1.51	30	84100	15.45	15.45	16.74	16.74	3	0.0684	0.7924
1.97	2.08	1.51	30	84100	15.45	11.05	15.45	11.05	1	0.1259	1.1664
1.97	2.08	1.51	30	84100	15.45	11.05	16.74	14.54	2	0.1223	1.1459
1.97	2.08	1.51	30	84100	15.45	15.45	17.09	17.09	3	0.1228	1.1335

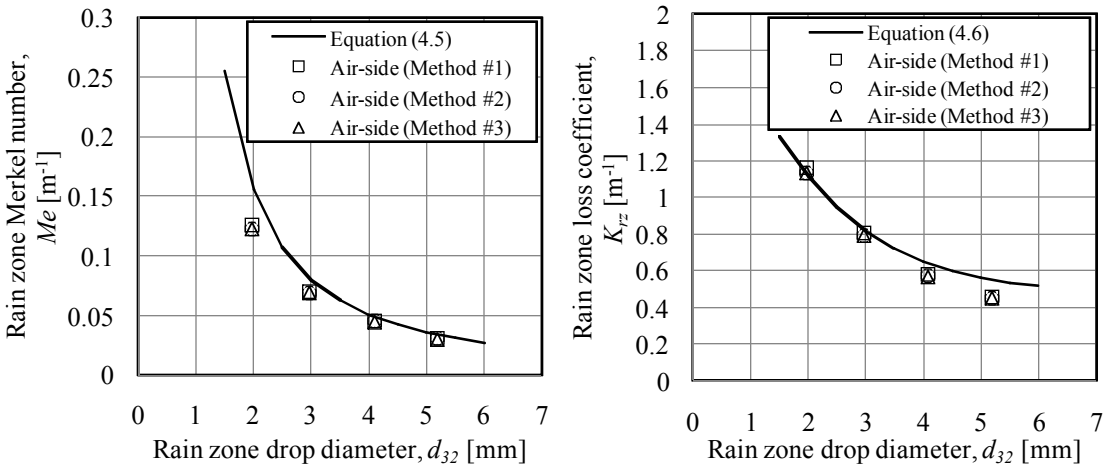

a) Merkel numbers b) Loss coefficients

Figure 4.16: Counter flow rain zone Merkel numbers and loss coefficients (H_{rz} = 5 m).

Figure 4.16 (a) shows the predicted Merkel numbers for a H_{rz} = 5 m high purely counter flow rain zone as listed in Table 4.1 and the Merkel numbers predicted by Equation (4.5). The predicted loss coefficients for each of the cases are presented in Figure 4.16 (b) as well as the loss coefficients predicted by Equation (4.6).

4.5 Conclusions

In this chapter the theoretical rain zone model developed in Chapter 3 is compared to experimental splash grid data and it is shown that the agreement between the measured and predicted drop size distributions below various grid setups are generally good. There is however a discrepancy between the measured drop size distributions of Dreyer (1994) and the predicted distribution below N_{grids} = 10 layers of his grid (Figure 4.11). This can be attributed to secondary effects associated with multiple grid layer setups that are beyond the scope of this dissertation where the aim is to use the minimum number of grid layers to reduce the drop size in the rain zone.

It is also shown that drop interaction in the rain zone below a trickle fill, with no grids, can be adequately accounted for by using a current drop coalescence model (Brazier-Smith, 1972) and by assuming that aerodynamic break-up is catastrophic, as opposed to vibrational. This break-up generally leads to the formation of a relative large number of smaller drops with diameters of approximately $d_d \approx 2$ mm. When the slat grid (Figure H.9) is installed below the trickle fill, Figure 4.15(b) shows that a catastrophic and vibrational drop break-up model predict the same drop size distribution changes over the H_{rz} = 7.05 m rain zone below the grid. A reason for this is the reduced numbers of large drops below the slat grid (Figure H.9) that are subjected to aerodynamic break-up.

There is also generally good agreement between the predicted rain zone loss coefficients and Merkel transfer characteristics and the values predicted by de Villiers (Kröger, 2004) for a purely counter flow rain zones. De Villiers do however tend to over predict the Merkel number by approximately 26 % at a rain zone Sauter mean drop diameter of $d_{32} \approx 2$ mm (Figure 4.16a).

5

SPLASH GRID OPTIMIZATION

5.1 Introduction

In this chapter the theoretical model of chapter 3 is used to investigate the effect of the grid variables on the capability of the grid to reduce the drop sizes in the rain zone when it is installed below a trickle fill that produces a Sauter mean drop diameter of d_{32} = 5.19 mm. Grid variables include the slat width (W), slat height (H_s), spacing between slats (S) and the distance between the fill and the grid (H_{FG}).

5.2 Splash grid optimization

From the work in previous chapters the following conclusions can be drawn:

1. Slat height is important for the stiffness of the grid but has a negligible effect on rain zone performance when the slats are relatively narrow and the grid is installed H_{FG} = 0.8 m below the fill. At this height the drops are relatively high in kinetic energy with most of the water leaving the grid through splashing or straddling. A negligible volume of water is left on the grid surface (Section 4.2) and therefore slat bottom profiles also become unimportant.
2. For a constant porosity, the use of wider slats leads to greater numbers of drops that pass through the grid openings.
3. When wider slats are used, splashing is the main mechanism of drop break-up and the spacing between 2 layers becomes important in order to prevent the accumulation of splash drops, coming from the bottom layer, on the surface of the top layer.
4. As the spacing between wider slats is decreased, many of the splash drops may fall back onto the slats and become part of the surface water that drips from below the slat.

Figures 5.1 to 5.4 show the predicted mass fractions and Sauter mean drop diameter contributions of the different drop break-up mechanisms below one layer of grid for different combinations of slat width (W), grid porosity (β) and distance between the fill and grid (H_{FG}). The grid porosity (β) is defined as the ratio of the open area of the

grid to the total cross sectional area of the grid. The figures also show the overall Sauter mean drop diameter for each case.

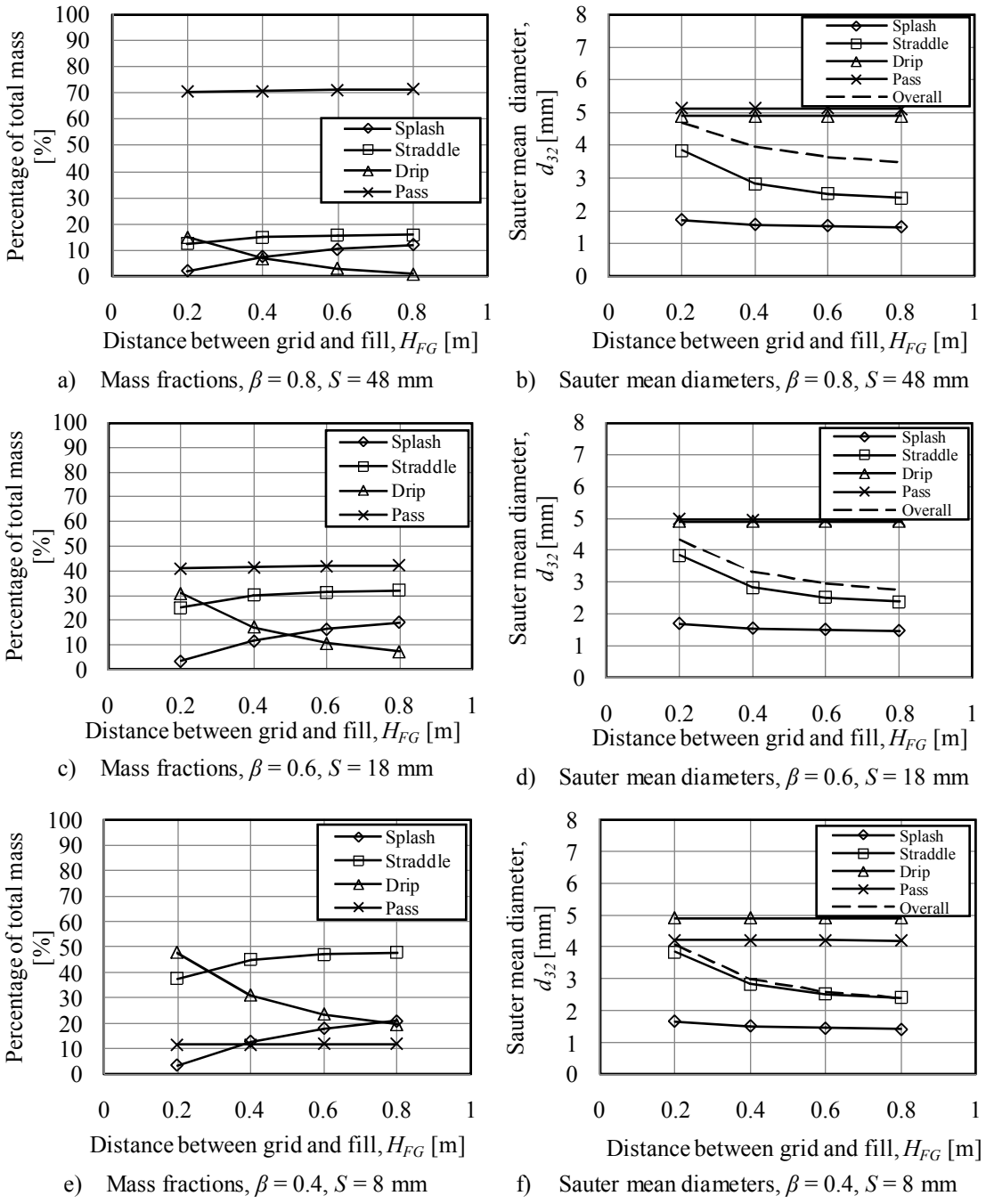

a) Mass fractions, $\beta = 0.8$, $S = 48$ mm

b) Sauter mean diameters, $\beta = 0.8$, $S = 48$ mm

c) Mass fractions, $\beta = 0.6$, $S = 18$ mm

d) Sauter mean diameters, $\beta = 0.6$, $S = 18$ mm

e) Mass fractions, $\beta = 0.4$, $S = 8$ mm

f) Sauter mean diameters, $\beta = 0.4$, $S = 8$ mm

Figure 5.1: Contribution of different drop break-up mechanisms for one layer of grid below a trickle fill (W = 12 mm, T-type slat, W_{bot} = 3 mm, $G_w = 2.84$ kg/m^{2}s, $G_a = 0$, $d_{32,i} = 5.19$ mm).

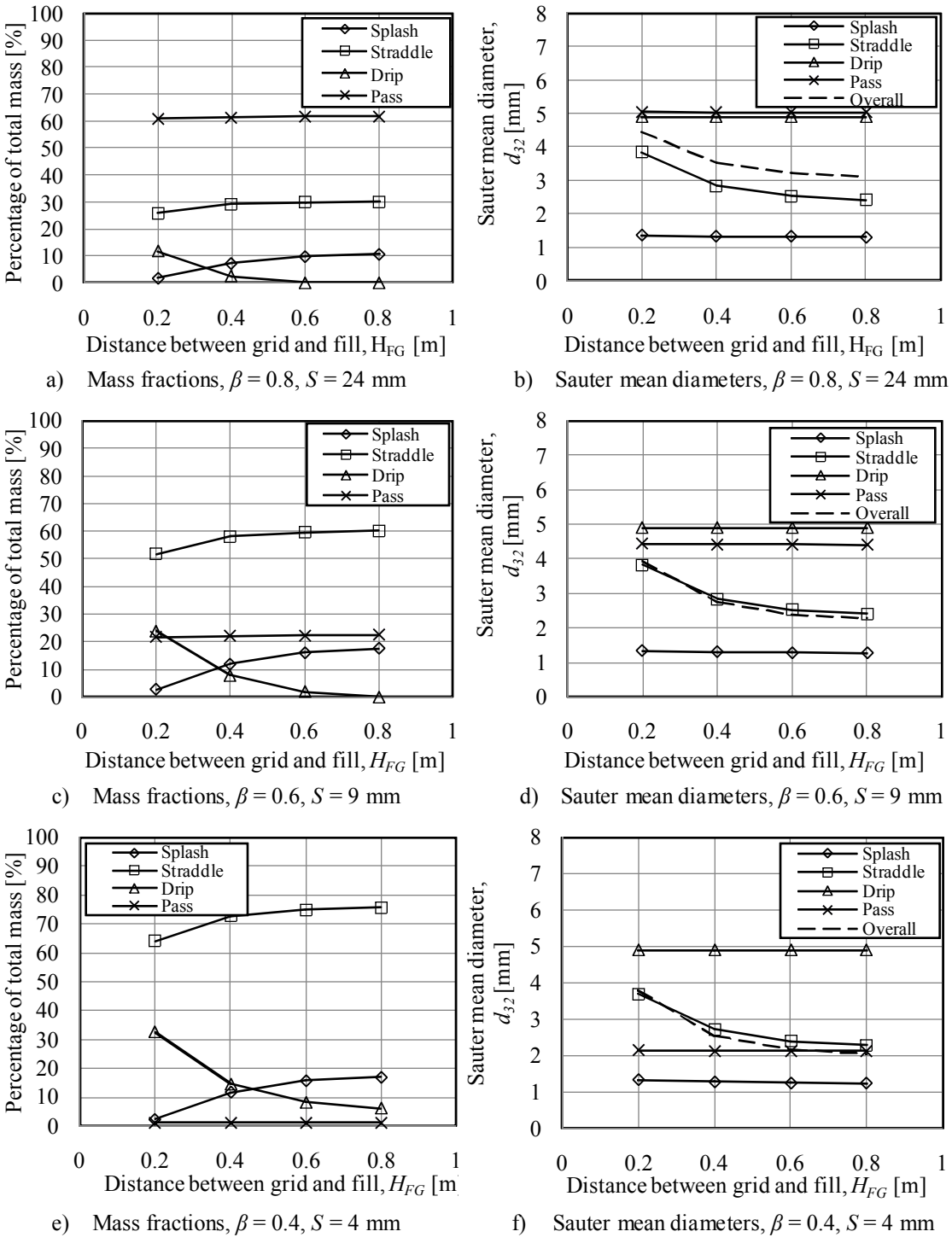

Figure 5.2: Contribution of different drop break-up mechanisms for one layer of grid below a trickle fill (W = 6 mm, T-type slat, W_{bot} = 3 mm, G_w = 2.84 kg/m^{2}s, G_a = 0, $d_{32,i}$ = 5.19 mm).

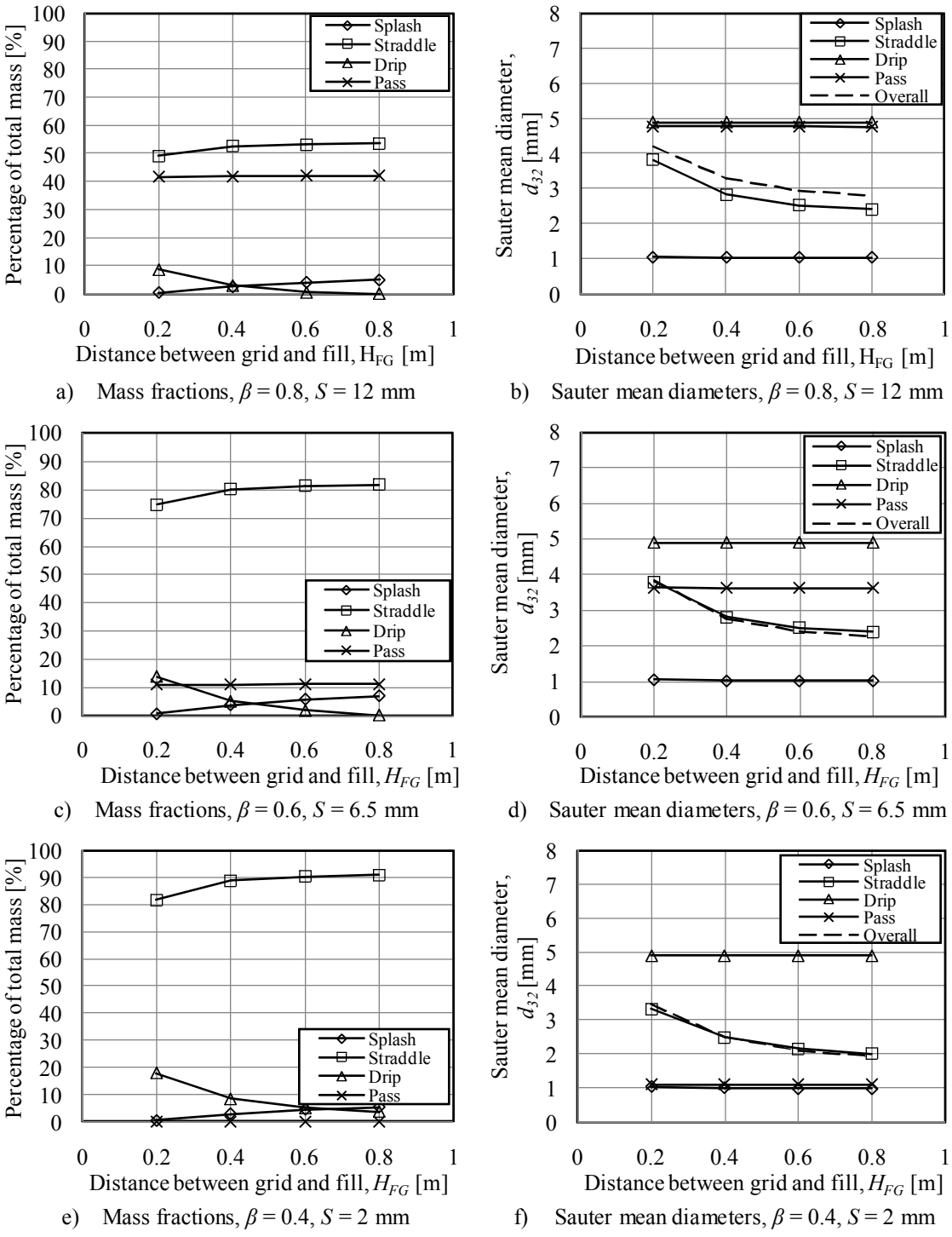

Figure 5.3: Contribution of different drop break-up mechanisms for one layer of grid below a trickle fill (W = 3 mm, G_w = 2.84 kg/m^{2}s, G_a = 0, $d_{32,i}$ = 5.19 mm).

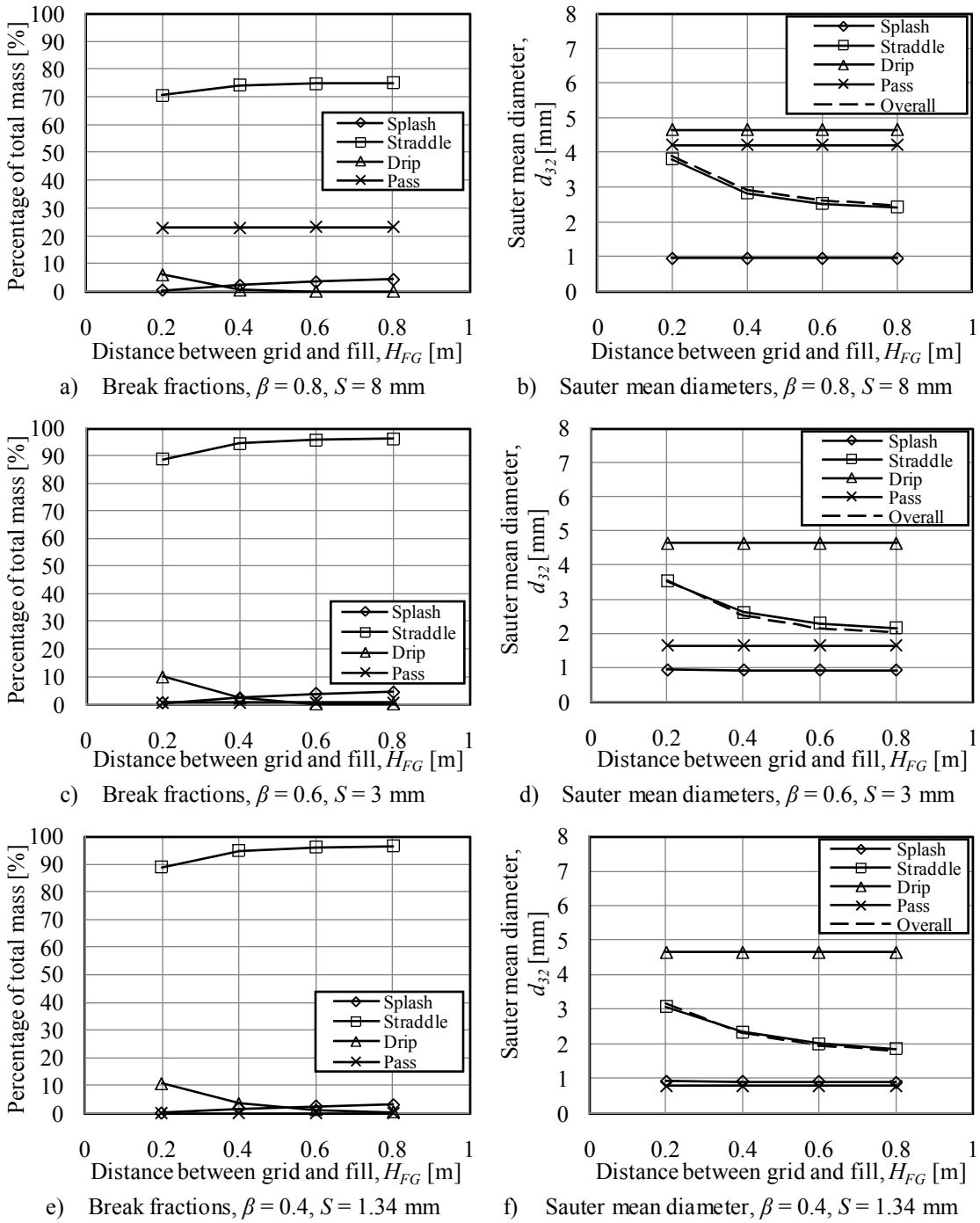

a) Break fractions, $\beta = 0.8$, $S = 8$ mm

b) Sauter mean diameters, $\beta = 0.8$, $S = 8$ mm

c) Break fractions, $\beta = 0.6$, $S = 3$ mm

d) Sauter mean diameters, $\beta = 0.6$, $S = 3$ mm

e) Break fractions, $\beta = 0.4$, $S = 1.34$ mm

f) Sauter mean diameter, $\beta = 0.4$, $S = 1.34$ mm

Figure 5.4: Contribution of different drop break-up mechanisms for one layer of grid below a trickle fill (W = 2 mm, G_w = 2.84 kg/m^{2}s, G_a = 0, $d_{32,i}$ = 5.19 mm).

The results presented in Figures 5.1 to 5.4 show that the pass fractions are significantly reduced with a reduction in the grid porosity, but that the effect on the Sauter mean drop diameters below the grid is not as significant as what might be expected. It is however theoretically possible to reduce the overall Sauter mean drop diameter to less than d_{32} = 2 mm, as shown in Figure 5.4(f) where a W = 2 mm wide slat (H_s = 2 mm) is used with a grid porosity of β = 0.4. The results for a W = 3 mm slat at the same porosity, shown in Figure 5.3(f), produce a slightly larger overall Sauter mean drop diameter below the grid.

Figure 5.5 (a) shows the predicted overall Sauter mean drop diameters below one and two layers of grid comprising W = 2 mm slats with a grid porosity of β = 0.4. The vertical spacing between the two grid layers is H_{GG} = 100 mm and the results show that the decrease in the Sauter mean drop diameter with the addition of a second layer of grid is negligible.

Figure 5.5 (b) shows the change in the Sauter mean drop diameter over a H_{rz} = 10 m rain zone as the drops go through the grids at H_{rz} = 0.8 and 0.9 and it also shows how the Sauter mean drop diameter increases due to drop collisions and coalescence below the grid.

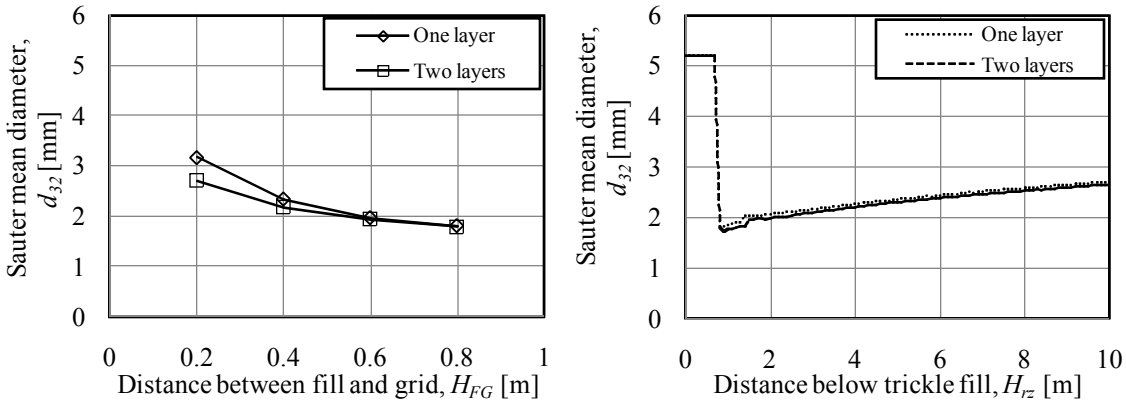

a) Sauter mean drop diameters below the grids for different grid locations below the fill

b) Sauter mean diameter change over the rain zone (H_{FG} = 0.8 m)

Figure 5.5: Sauter mean diameters below one and two layers of grid installed below a trickle fill respectively (W = 2 mm, β = 0.4, H_{GG} = 100mm, G_w = 2.84 kg/m^{2}s, G_a = 0, $d_{32,i}$ = 5.19 mm).

Figure 5.6 shows the Merkel number to loss coefficient ratio for a H_{rz} = 10 m high, purely counter flow rain zone, as a function of grid porosity for grids comprising slats of three respective widths (W = 2 mm, W = 6 mm and W = 12 mm). The drop distribution measured below a trickle fill (d_{32} = 5.19 mm) is used as an input to the theoretical model for the initial drop distribution. The analysis shown in Figure 5.6(a) assumes that the air wet- and dry bulb temperatures are constant throughout the rain

zone (Method #1, Section 4.4), while the analysis in Figure 5.6(b) calculates the air temperature changes over each element (Figure 3.1) while assuming that the air is always saturated (Method #3, Section 4.4).

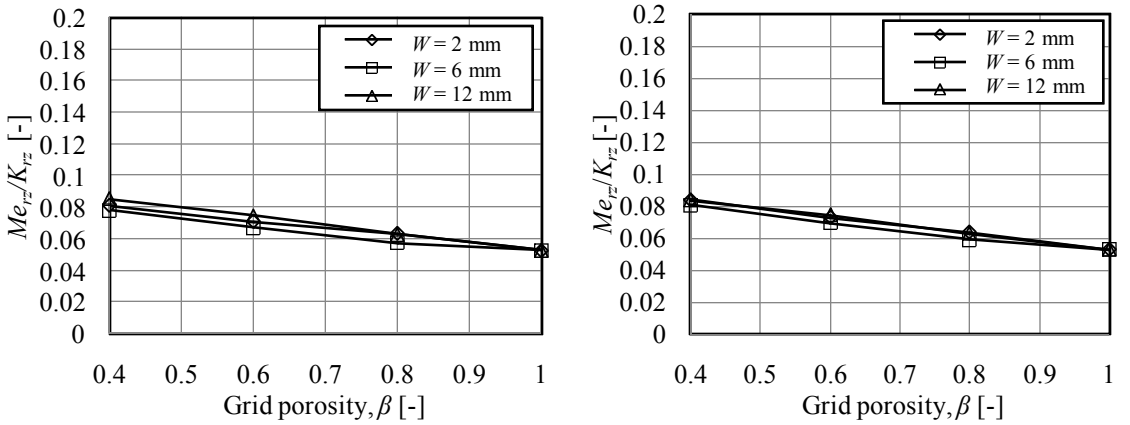

a) Constant air-side properties based on inlet conditions (Method #1, Section 4.4)

b) Changing air-side properties assuming saturation at all times (Method #3, Section 4.4)

Figure 5.6: Merkel number to loss coefficient ratio for a purely counter flow rain zone with one layer of grid (H_{FG} = 0.8 m, H_{rz} = 10 m).

The mixing ratio ($0.2 \leq \phi \leq 0.8$) and the initial splash angle ($50° \leq \theta_s \leq 70°$) generally has a negligible influence on the predicted Merkel transfer characteristic of rain zones with grids installed in it.

5.3 Approximate cost analysis for a concept drop size reduction device

All costs in this section are expressed in terms of a currency (C) that is independent of any specific currency, similar to Pretorius (2007). The capital parity ($C_{s,p}$) for a new power plant is expressed in terms of cost units (C) per kilowatt (kW) of power generation capacity (C/kW). The specific cost of performance enhancement per area ($c_{s,g}$) due to the installation of drop size reduction grids in NDWCT rain zones is defined in terms of cost units (C) per square meter (m^2) per kilowatt (kW) of additional power output gained ($\Delta P_{net,gain}$) (C/kWm^2). The specific cost of performance enhancement is given by

$$C_{s,g} = \frac{\left(C_{T,g,material} + C_{T,g,manufacturing} + C_{T,g,installation}\right)}{\Delta P_{net,gain}} = c_{s,g} A_{fr} \qquad (5.1)$$

The ratio of the specific cost of performance enhancement to capital parity is given by

$$\eta = \frac{C_{s,g}}{C_{s,p}} = \eta_{material} + \eta_{manufacturing} + \eta_{installation} \quad (5.2)$$

Figure 5.7 shows a concept drop size reduction grid that comprises two layers of Polypropylene grid that clip onto each other in such a way that the open areas of the one grid layer coincide with the slatted areas of the other grid layer. This prevents drops from passing through the grids without contact, while allowing for relatively large solid objects to fall through the grids. The slatted areas in each grid comprises W = 2 mm wide slats spaced S = 1.8 mm apart (β = 0.47). Table 5.1 shows the specifications for the drop size reduction grid shown in Figure 5.7.

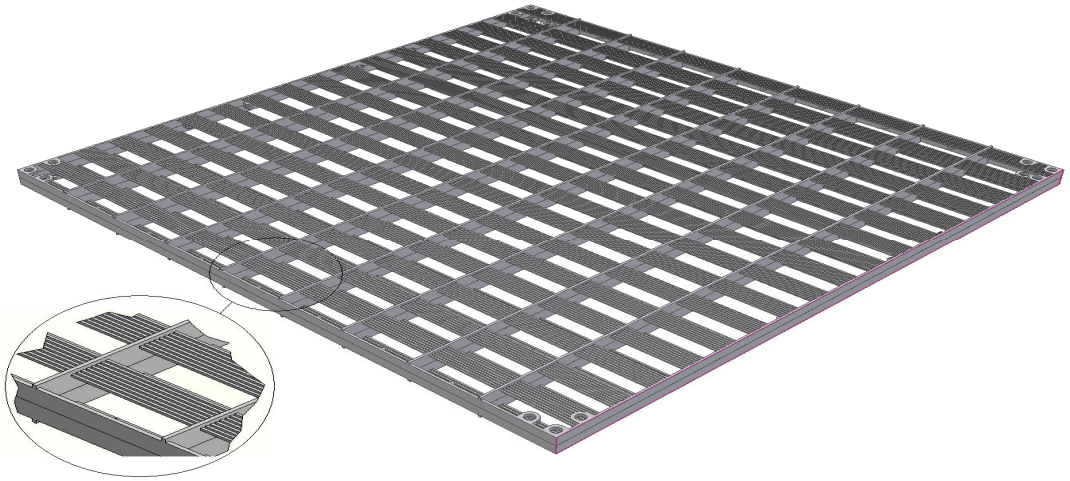

Figure 5.7: Concept for a drop size reduction grid.

Table 5.1: Specifications for drop size reduction grid.

Variables	Values
Dimensions (1 layer)	900 x 900 x 17.5 mm
Grid porosity, β (1 layer)	0.71
Grid porosity, β (2 layers)	0.47
Loss coefficient, K_{grid} (1 layer)	1.26
Loss coefficient, K_{grid} (2 layer)	2.52
Material type	Polypropylene
Material cost per weight	C 0.007 / kg
Weight (1 layer)	0.943 kg
Material cost per area covered (2 layers)	C 0.0161 / m^2

For the cost analysis in this section it is assumed that the concept drop size reduction grid is installed at a power station with a 4 500 MW output (6 units) operating at

35 % efficiency. The waste heat of each unit is rejected to the atmosphere by means of cooling towers with the dimensions shown in Table 5.2 (Kröger, 2004).

Table 5.2: Cooling tower specification for approximate cost analysis.

Variables	Values
Tower height (H_{ct})	147 m
Rain zone height (H_{rz})	10 m
Rain zone diameter (d_{rz})	104.5 m
Tower outlet diameter	60.85 m
Fill height (L_{fi})	2.504 m
Fill type	Fibre cement (Kröger, Type 9)
Water mass velocity (G_w)	1.51 kg/m^{2}s

Table 5.3 presents the change in the inlet water temperature and tower Merkel number in terms of the rain zone Sauter mean drop diameter for the NDWCT specified in Table 5.1. The values are determined with the 1-D cooling tower model of Kröger (2004). The Sauter mean drop diameter below the fibre cement fill is similar to the Sauter mean drop diameter below a trickle fill (d_{32} = 5.19 mm), according to Terblanche *et al.* (2009), and can reduce from d_{32} = 5.19 mm to approximately d_{32} = 4.39 mm (Figure 4.13, Section G.4) over a H_{rz} = 10 m high rain zone due to the aerodynamic break-up of large drops. The representative Sauter mean drop diameter for a pure rain zone with an initial Sauter mean drop diameter of d_{32} = 5.19 mm is taken as d_{32} = 4.80 mm and is the average value over the rain zone height. The drop size reduction grid (Figure 5.7) can reduce the Sauter mean drop diameter to approximately d_{32} = 2 mm when installed H_{FG} = 0.8 m below the fill, but when drop interaction is taken into account the representative Sauter mean drop diameter for the rain zone in this case is approximately d_{32} = 2.50 mm; similar to Figure 5.5. The decrease in the cooling tower inlet temperature is determined for a rain zone Sauter mean drop diameter decreasing from d_{32} = 4.80 mm to d_{32} = 2.50 mm (not from d_{32} = 5.19 mm to d_{32} = 2.00 mm). An approximated decrease of ΔT_{wi} = -1.6 °C is expected (Table 5.3) that corresponds to an increase in the total Merkel transfer characteristic of the NDWCT of 28 % and an increase in the power cycle efficiency of approximately 0.5 %. This translates to an additional power output capacity of $\Delta P_{net,gain}$ = 64 MW for a 4 500 MW (35% efficiency) power plant.

Table 5.3: Sensitivity of the NDWCT (Table 5.1) performance to rain zone drop size.

d_{32} [mm]	5.19	4.80	2.50	2.00
Me_{tower} [-]	1.838	1.870	2.396	2.772
ΔT_{wi} [°C]	0	-0.122	-1.734	-2.544

The total material cost of the grid (Figure 5.7) can be approximated from Table 5.1 to give

$$\eta_{material} = \frac{\text{C } 0.0161\ N_{ct}\ \pi\ {d_{rz}}^2}{4\Delta P_{net,gain} C_{s,p}} = 0.0130 \tag{5.3}$$

Manufacturing and installation cost is approximated at C 1737.43 to give

$$\eta_{manufacturing} + \eta_{installation} = \frac{\text{C } 1737.43}{\Delta P_{net,gain} C_{s,p}} = 0.0271 \tag{5.4}$$

The variable η is now obtained from Equation (5.2) and equals $\eta = 0.0402$.

The approximate cost analysis in this section shows that the specific cost of performance enhancement (C/kW) is approximately 4.02 % of the capital parity (C/kW) of a new power plant when a concept drop size reduction grid (Figure 5.7) is installed (H_{FG} = 0.8 m) below a fibre cement fill (Kröger, Type 9) in a NDWCT rain zone.

5.4 Conclusions

The analysis in this chapter shows that a drop size reduction grid (single layer) comprising relatively narrow slats (W = 2 mm) with a grid porosity of approximately β = 0.4 can decrease the Sauter mean drop diameter from d_{32} = 5.19 mm below the fill to approximately d_{32} = 2 mm below the drop size reduction grid [Figure 5.4(f), H_{FG} = 0.8 m]. In order to ensure that large solid objects can fall through the grid while achieving approximately the same drop size reduction, a double layer concept drop size reduction grid (Figure 5.7) is proposed with a double layer porosity of β = 0.47. Drop interaction in the rain zone below the drop size reduction grid is significant and the Sauter mean drop diameter tends to increase from d_{32} = 2 mm to approximately d_{32} = 2.5 mm before the drops fall H_{rz} = 10 m [Figure 5.5(b)]. The installation of the concept drop size reduction grid in the cooling tower rain zone (H_{FG} = 0.8 m) leads to an approximate increase in the power cycle efficiency of 0.5 % and an additional power output of $\Delta P_{net,gain}$ = 64 MW for a 4 500 MW (35 % efficiency) power plant. The specific cost (C/kW) of performance enhancement is approximately 4 % of the capital parity of a new power plant (C/kW).

6

CONCLUSIONS

There are numerous ways to enhance NDWCT performance and the methods are briefly discussed at the beginning of Chapter 2 before the focus of the thesis is shifted towards rain zone performance enhancement. The aim is to reject waste heat to atmosphere at lower cooling water temperatures (leading to higher power plant efficiency) by reducing the average drop diameter in the rain zone by means of grids while reducing the life cycle cost of the power plant.

The cooling water temperature can be reduced by reducing the Sauter mean drop diameter in the rain zone, which is between d_{32} = 5 and 6 mm directly below the fill (Kröger, 2004 and Terblanche, 2009), depending on the fill type (film or trickle type fills) used in the cooling tower. A significant reduction in the rain zone drop size may be achieved by installing grids in the rain zone below the fill, leading to faster drop cooling, longer residence times but increased pressure drop over the rain zone. Current commercial splash grids can reduce the Sauter mean drop diameter below a trickle fill from d_{32} = 5.19 mm to approximately d_{32} = 3.10 mm when installed between H_{FG} = 0.6 and H_{FG} = 0.8 m below the fill. Large openings in current commercial grids do however mean that a large number of drops can pass through one layer of grid without contact. This means there is a significant potential for further drop size reduction and therefore NDWCT performance enhancement that is currently not fully exploited.

The mechanisms of drop break-up when drops impinge onto slats are splashing (Appendices B and C) straddling (Appendix D) and dripping from below the slat (Appendix E). Splashing and straddling are investigated experimentally and numerically and quantified in terms of the mass fraction with respect to the original drop and the drop size distributions, while dripping is investigated analytically. Splash fractions and straddle fractions for individual drops generally increase significantly with drop fall distances up to H_d = 0.6 to H_d = 0.8 m, while the average splash and straddled drop sizes tend to decrease. Any further changes in splash and straddle fractions and drop sizes become insignificant beyond a drop fall distance of H_d = 0.8 m. The Sauter mean drop diameter of the splash drops when a grid is installed below a fill in a rain zone is relatively constant for different splash grid configurations and is approximately d_{32} = 1.0 to 1.5 mm (Figures 5.1 to 5.4). Splash fractions normally increase with increasing slat width while straddle fractions decrease. The amount of dripping below a grid decreases as the distance between the fill and the grid is increased and generally becomes insignificant when the grid is

placed H_{FG} = 0.6 to H_{FG} = 0.8 m below the fill (Chapters 4 and 5). This means that the need for profiles on slat bottoms to reduce the size of the drip drops can be eliminated with the correct placement of the grid below the fill.

In the free fall zone above and below a splash grid, drop-drop collisions and aerodynamic drop break-up can significantly change drop distributions. Appendix G shows that the Sauter mean drop diameter below a trickle fill reduces by approximately 1 mm over a fall distance of approximately H_{rz} = 7.65 m due to aerodynamic drop break-up and can increase by almost 0.6 mm over a fall distance of approximately H_{rz} = 7.05 m below a splash grid that is installed below a trickle fill.

A theoretical model is developed in Chapter 3, based on the previous results, that is used to investigate the effects of the following grid variables on the drop size reduction capability of a grid: 1) distance between the grid and the fill, 2) slat width and 3) grid porosity (Chapter 5). Chapter 5 (Figures 5.1 to 5.4) shows that the overall Sauter mean drop diameter below a grid ($W \leq 12$ mm) can be approximated by the Sauter mean drop diameter of the straddled drops when the fraction of the drops that pass through the grid without contact is less than 40 % of the total drop mass. It is estimated that the best drop size reduction is achieved when narrower slats of W = 2 to W = 3 mm in width are used at a grid porosity of β = 0.4. Any further decrease in the porosity would mean that the pressure drop over the grid becomes unnecessarily high and manufacturing of the grid becomes unnecessarily difficult due to the small sizes of the grid openings. By using a double layer setup with an equivalent porosity, as shown in Figure 5.7, the porosity of a single layer (β = 0.71) becomes comparable with existing commercial grids, but the double layer setup ensures better drop size reduction capability compared to current commercial grids. The optimal distance between the grid and fill is between H_{FG} = 0.6 and H_{FG} = 0.8 m. An increase in this distance leads to no further decrease in the Sauter mean drop diameter below the grid and only means that the average Sauter mean drop diameter over the height of the rain zone increases compared to the optimal placement. A reduction in the distance between the grid an the fill means that drop size reduction is significantly reduced, again leading to a larger average Sauter mean drop diameter over the height of the rain zone. The smallest estimated Sauter mean drop diameter below a single layer of grid placed H_{FG} = 0.8 m below a trickle fill is $d_{32} \approx 2$ mm (W = 2, β = 0.4, $d_{32,i}$ = 5.19 mm), compared to an estimated value of d_{32} = 3.10 mm for current commercial grids. It is found that this drop diameter can increase to approximately d_{32} = 2.6 mm over a rain zone height of H_{rz} = 7.05 m below the grid (still air) as shown in Figure 5.5(b).

Cross flow performance measurements (Appendix K) show that the installation of one and two layers of the grids, shown in Figures H.3 and H.6(a), in a H_{rz} = 2 m high cross flow rain zone ($3.72 < d_{32,i} < 4.35$ mm) leads to respective increases in the Merkel number of approximately 55 and 115%.

By installing the drop size reduction device (W = 2 mm, β = 0.4) H_{FG} = 0.8 m below a trickle or film type fill the average Sauter mean drop diameter over a H_{rz} = 10 m high rain zone reduces from approximately d_{32} = 4.8 mm to d_{32} = 2.5 mm, taking into account drop collisions and aerodynamic drop break-up. Table 5.3 shows the sensitivity [1-D model of Kröger (2004)] of the inlet water temperature of a NDWCT to the average Sauter mean drop diameter in the rain zone when a fibre cement (Type 9 film type fill), as given by Kröger (2004), is used. It shows an approximate decrease in the inlet water temperature of ΔT_{wi} = -1.6°C. If it is assumed that a ΔT_{wi} = -3°C change in the inlet water temperature leads to a 1 % increase in power plant cycle efficiency, as estimated by Reuter (2010), the expected increase in cycle efficiency due to the grid in the rain zone is approximately 0.5%

If it is assumed that a 4500 MW power plant operates at 35 % efficiency, an increase of 0.5 % in cycle efficiency leads to a capacity increase of 64 MW. At a current cost of C 1000 /MW for a new power plant and an approximated total cost (material, manufacturing and installation) for the new grid of C 428.57 per cooling tower (assuming a d_{rz} = 104.5 m rain zone diameter) the additional capacity of the power station comes at a cost of approximately C 40/MW.

REFERENCES

Adam, J. R., N. R. Lindblad and C. D. Hendricks (1968), *The Collision, Coalescence and Disruption of Water Droplets*, Journal of Applied Physics, Vol. 39(11), pp. 5173-5180.

Al-Waked, R. and M. Behnia (2007), *Enhancing Performance of Wet Cooling Towers*, Energy Conversion and Management, Vol. 48, pp. 2638-2648.

Allen, R. F. (1975), *The Role of Surface Tension in Splashing*, Journal of Colloid and Interface Science, Vol. 51(2), pp. 350-351.

Almedeij, J. (2008), *Drag Coefficient of Flow Around a Sphere: Matching Asymptotically the Wide Trend* Powder Technology, Vol. 186(3), pp. 218-223.

Arkhipov, V. A., I. M. Vasenin and V. F. Trofimov (1983), *Stability of Colliding Drops of Ideal Liquid*, Tomsk. Translated from Zh. Prikl. Mekh. Tekh. Fiz., Vol. 3, pp. 95-98.

Ashgriz, N. and J. Y. Poo (1990), *Coalescence and Separation in Binary Collisions of Liquid Drops*, Journal of Fluid Mechanics, Vol. 221, pp. 183-204.

Baines, W. D. and E. G. Peterson (1951), *An Investigation of Flow through Screens*, Transactions of ASME, Vol. 73(1), pp. 467-480.

Becker, B. R. and L. F. Burdick (1993), *Drift Eliminators and Cooling Tower Performance*, ASHRAE Journal, Vol., pp. 28-36.

Bellagamba, B., G. Dinelli, L. Tognotti and S. Zanelli (1988), *Water Distribution in Cooling Towers*, International Cooling Tower Conference, Pisa, Italy.

Borisov, A. A., B. E. Gel'fand, M.S.Natanson and O. M. Kossov (1981), *Droplet Break-up Regimes and Criteria for their Existence*, Journal of Engineering Physics, Translated from Inzhenero-Fizicheskii Zhurnal, Vol. 40(1), pp. 44-49.

Bradley, S. G. and C. D. Stow (1978), *Collisions between Liquid Drops*, Philosophical Transactions of the Royal Society of London, Vol. 287(Series A), pp. 635-675.

Bradley, S. G. and C. D. Stow (1979), *On the Production of Satellite Droplets during Collisions between Water Drops Falling in Still Air*, Journal of Atmospheric Sciences, Vol. 36, pp. 494-500.

Brazier-Smith, P. R., S. G. Jennings and J. Latham (1972), *The Interaction of Falling Water Drops: Coalescence*, Proceedings of the Royal Society of London, Vol. 326(Series A), pp. 393-408.

Brown, P. P. and D. F. Lawler (2003), *Sphere Drag and Settling Velocity Revisited*, Journal of Environmental Engineering-ASCE, Vol. 129, pp. 222-231.

Brucato, A., F. Grisafi and G. Montante (1998), *Particle Drag Coefficients in Turbulent Fluids*, Chemical Engineering Science, Vol. 53(18), pp. 3295-3314.

Ceylan, K., A. Altunbas and C. Kelbaliyev (2001), *A New Model for Estimation of Drag Force in the Flow of Newtonian Fluids around Rigid or Deformable Particles*, Powder Technology, Vol. 119, pp. 250-256.

Chen, R.-H., L. C. Chow and J. E. Navedo (2004), *Optimal Spray Characteristics in Water Spray Cooling*, International Journal of Heat and Mass Transfer, Vol. 47, pp. 5095-5099.

Cheng, N.-S. (2009), *Comparison of Formulas for Drag Coefficient and Settling Velocity of Spherical Particles*, Powder Technology, Vol. 189, pp. 395-398.

Clift, R., J. R. Grace and M. E. Weber (1978), *Bubbles Drops and Particles*, New York, Academic Press.

Concha, F. and A. Barrientos (1982), *Settling Velocities of Particulate Systems, 3.Power Series Expansion for Drag Coefficient of a Sphere and Prediction of Settling* International Journal of Mineral Processing, Vol. 9(2), pp. 167-172.

Dreyer, A. A. (1994), *Modelling of a Cooling Tower Splash Pack*, Mechanical Engineering, University of Stellenbosch, Stellenbosch, South Africa, Ph.D.

Duan, R.-Q., S. Koshizuka and Y. Oka (2003), *Two-Dimensional Simulation of Drop Deformation and Breakup at Around the Critical Weber Number*, Nuclear Engineering and Design, Vol. 225, pp. 37-48.

Erens, P. J., A. A. Mercker and A. A. Dreyer (1994), *Evaporation from Accelerating Droplets*, 10th Heat Transfer Conference, Brighton.

Estrade, J. P., H. Carentz, G. Lavergne and Y. Biscos (1999), *Experimental Investigation of Dynamic Binary Collision of Ethanol Droplets - A Model for Droplet Coalescence and Bouncing*, International Journal of Heat and Fluid Flow, Vol. 20, pp. 486-491.

Feng, Z. G. and E. E. Michaelides (2001), *Drag Coefficients of Viscous Spheres at Intermediate and High Reynolds Numbers*, Journal of Fluids Engineering, Vol. 123, pp. 841-849.

Flemmer, R. L. C. and C. L. Banks (1986), *On the Drag Coefficient of a Sphere*, Powder Technology, Vol. 48(3), pp. 217-221.

Frössling, N. (1938), *Uber die Verdunstung Fallender Tropfen*, Gerlands Beitrage Zur Geophysik, Vol. 52, pp. 170-216.

Fuller, E. N. and J. C. Giddings (1965), Journal of Gas Chromatography, Vol. 3, pp. 222.

Gharagheizi, F., R. Hayati and S. Fatemi (2007), *Experimental Study on the Performance of Mechanical Cooling Tower with Two Types of Packing*, Energy Conversion and Management, Vol. 48, pp. 277-280.

Gnielinski, V. (1983), *Heat Exchanger Handbook*, Hemisphere Publishing Corporation.

Goshayshi, H. R. and J. F. Missenden (2000), *The Investigation of Cooling Tower Packing in Various Arrangements*, Applied Thermal Engineering, Vol. 20, pp. 69-80.

Hesketh, R. P., A. W. Etchells and T. W. Russell (1991), *Bubble Breakage in Pipeline Flow*, Chemical Engineering Science, Vol. 46(1), pp. 1-1.

Hollands, K. G. T. (1974), *An Analysis of a Counter Flow Spray Cooling Tower*, International Journal of Heat and Mass Transfer, Vol. 17, pp. 1227-1239.

Huber, L., H. A. McCartney and B. D. L. Fitt (1997), *Influence of Target Characteristics on the amount of Water Splashed by Impacting Drops*, Agricultural and Forest Meteorology, Vol. 87, pp. 201-211.

Hung, L. S. and S. C. Yao (2002), *Dripping Phenomena of Water Droplets Impacted on Horizontal Wire Screens*, International Journal of Multiphase Flow, Vol. 28, pp. 93-104.

Jaber, H. and R. L. Webb (1989), *Design of Cooling Towers by the Effectiveness-NTU Method*, Journal of Heat Transfer, Vol. 111, pp. 837-843.

Jiang, Y. J., A. Umemura and C. K. Law (1992), *An Experimental Investigation on the Collision Behaviour of Hydrocarbon Droplets*, Journal of Fluid Mechanics, Vol. 234, pp. 171-190.

Kannan, R. and D. Sivakumar (2008), *Drop Impact on a Hydrophobic Grooved Surface*, Colloids and Surfaces, Vol. 317, pp. 694-704.

Khan, J.-U.-R., B. A. Qureshi and S. M. Zubair (2004), *A Comprehensive Design and Performance Evaluation Study of Counter Flow Wet Cooling Towers*, International Journal of Refrigeration, Vol. 27, pp. 914-923.

Kishore, N., R. P. Chhabra and V. Eswaran (2008), *Drag on Ensembles of Fluid Spheres Translating in a Power-Law Liquid at Moderate Reynolds Numbers*, Chemical Engineering Journal, Vol. 139, pp. 224-235.

Kloppers, J. C. (2003), *A Critical Evaluation and Refinement of the Performance Prediction of Wet-Cooling Towers*, Department of Mechanical and Mechatronic Engineering, University of Stellenbosch, Stellenbosch, South Africa, PhD.

Kranc, S. C. (1983), *The Effect of Nonuniform Water Distribution on Cooling Tower Performance*, Journal of Energy, Vol. 7(6), pp. 636-639.

Kranc, S. C. (1986), *Radial Profiles of Deposition Nozzles for High Uniformity*, Applied Mathematical Modelling, Vol. 10, pp. 429-432.

Kranc, S. C. (2007), *Optimal Spray Patterns for Counterflow Cooling Towers with Structured Packing*, Applied Mathematical Modelling, Vol. 31, pp. 676-686.

Krechetnikov, R. and G. M. Homsy (2009), *Crown-Forming Instability Phenomena in the Drop Splash Problem*, Journal of Colloid and Interface Science, Vol. 331, pp. 555-559.

Kröger, D. G. (2004), *Air-Cooled Heat Exchangers and Cooling Towers*, Pennwell Corporation.

Lane, W. R. (1951), *Shatter of Drops in Streams of Air*, Industrial and Engineering Chemistry, Vol. 43(6), pp. 1312-1317.

LeClair, B. P., A. E. Hamielec, H. R. Pruppacher and W. D. Hall (1972), *A Theoretical Study of the Internal Circulation in Water Drops Falling at Terminal Velocity in Air*, Journal of Atmospheric Sciences, Vol. 29, pp. 728-740.

List, R., C. F. MacNeil and J. D. McTaggart-Cowan (1970), *Laboratory Investigations of Temporary Collisions of Rain Drops*, Journal of Geophysical Research, Vol. 75(36), pp. 7573-7580.

Liu, J., H. Vu, S. S. Yoon, R. Jepsen and G. Aguilar (2010), *Splashing Phenomena During Liquid Droplet Impact*, Atomization and Sprays, Vol. 20(4), pp. 297-310.

Low, T. B. and R. List (1982), *Collision, Coalescence and Break-up of Rain Drops, Part 1: Experimentally Established Coalescence Efficiencies and Fragment Size Distributions in Break-up*, Journal of Atmospheric Sciences, Vol. 39, pp. 1591-1606.

Maheshwari, A., R. P. Chhabra and G. Biswas (2006), *Effect of Blockage on Drag and Heat Transfer from a Single Sphere and an In-Line Array of Three Spheres*, Powder Technology, Vol. 168, pp. 74-83.

Martin, H. (2005), *How to Predict Heat and Mass Transfer from Friction*, 4th International Conference on Heat Transfer, Fluid Mechanics and Thermodynamics, Cairo, Egypt.

McTaggart-Cowan, J. D. and R. List (1975), *Collision and Break-up of Water Drops at Terminal Velocity*, Journal of Atmospheric Sciences, Vol. 32, pp. 1401-1411.

Mercker, J. H. (1993), *Heat and Mass Transfer from Accelerating Water Drops*, Department of Mechanical Engineering, University of Stellenbosch, Stellenbosch, M.Eng.

Merkel, F. (1925), *Verdunstungskühlung*, VDI-Zeittschrift, Vol. 70(70), pp. 123-128.

Michael, M., R. Noble and R. M. Gary (1993), *Research of Fouling Film Fills*, Cooling Tower Institute Annual Meeting, New Orleans, USA.

Miller, D. S. (1990), *Internal Flow Systems*, Cranfield, BHRA (Information Services).

Mohiuddin, A. K. M. and K. Kant (1996), *Knowledge Base for the Systematic Design of Wet Cooling Towers. Part II: Fill and Other Design Parameters*, International Journal of Refrigeration, Vol. 19(1), pp. 52-60.

Moradian, N., D. S.-K. Ting and S. Cheng (2009), *The Effects of Freestream Turbulence on the Drag Coefficient of a Sphere*, Experimental Thermal and Fluid Science, Vol. 33, pp. 460-471.

Neve, R. S. and T. Shansonga (1989), *The Effects of Turbulence Characteristics on Sphere Drag*, International Journal of Heat and Fluid Flow, Vol. 10(4), pp. 318 - 321.

Niemann, H.-J. and H.-D. Köpper (1998), *Influence of Adjacent Buildings on Wind Effects on Cooling Towers*, Engineering Structures, Vol. 20(10), pp. 874-880.

O'Rourke, P. J. (1981), *Collective Drop Effects on Vaporizing Liquid Sprays*, Princeton University, Princeton, New Jersey, PhD.

Oosthuizen, H. R. (1995), *Enhancement of Cooling Tower Performance by Manipulation of Rain Zone Drop Size*, Department of Mechanical Engineering, University of Stellenbosch, Stellenbosch, South Africa, MEng (Mechanical).

Orlando, M. (2001), *Wind-Induced Interference Effects on Two Adjacent Cooling Towers*, Engineering Structures, Vol. 23, pp. 979-992.

Park, R. W. (1970), *Behaviour of Water Drops Colliding in Humid Nitrogen*, Department of Chemical Engineering, University of Wisconsin, Wisconsin, USA, Ph.D.

Pierce, D. J. (2007), *Evaluation and Performance Prediction of Cooling Tower Rain Zones*, Department of Mechanical and Mechatronic Engineering, University of Stellenbosch, Stellenbosch, South Africa, MScEng (Mechanical).

Pilch, M. and C. A. Erdman (1988), *Use of Break-up Time Data and Velocity History Data to Predict the Maximum Size of Stable Fragments for Acceleration Induced Break-up of a Liquid Drop,* International Journal of Multiphase Flow, Vol. 13(6), pp. 741-757.

Poppe, M. and H. Rögener (1991), *Berechnung von Rückkühlwerken*, VDI-Wärmeatlas, Vol., pp. Mi 1 - Mi 15.

Pretorius, J. P. (2007), *Optimization and Control of a Large-scale Solar Chimney Power Plant*, Department of Mechanical and Mechatronic Engineering, University of Stellenbosch, Stellenbosch, South Africa, PhD.

Pruppacher, H. R. and K. V. Beard (1970), *A Wind Tunnel Investigation of the Internal Circulation and Shape of Water Drops Falling at Terminal Velocity in Air*, Quarterly Journal of the Royal Meteorological Society, Vol. 96, pp. 247-256.

Pruppacher, H. R. and J. D. Klett (1978), *Microphysics of Clouds and Precipitation*, Dordrecht, Holland, D. Reidel Publishing Company.

Qian, J. and C. K. Law (1997), *Regimes of Coalescence and Separation in Droplet Collision*, Journal of Fluid Mechanics, Vol. 331, pp. 59-80.

Qureshi, B. A. and S. M. Zubair (2006), *A Complete Model of Wet Cooling Towers with Fouling in Fills*, Applied Thermal Engineering, Vol. 26, pp. 1982-1989.

Ranz, W. E. and W. R. Marshall (1952), *Evaporation from Drops*, Chemical Engineering Progress, Vol. 48(3), pp. 141-146.

Reuter, H. C. R. (2010), *Performance Evaluation of Natural Draught Cooling Towers with Anisotropic Fills*, Department Mechanical and Mechatronic Engineering, University of Stellenbosch, Stellenbosch, South Africa, PhD.

Rieber, M. and A. Frohn (1999), *A Numerical Study on the Mechanism of Splashing*, International Journal of Heat and Fluid Flow, Vol. 20, pp. 455-461.

Ruscheweyh, H. (1982), *Modelluntersuchung zum Einfluss der Kühlturm-kronenform auf das Zugverhalten grosser Naturzugkühltürme unter Querwindeinfluss*, Brennst - Wärme - Kraft, Vol. 34(7), pp. 361-369.

Schiller, L. and A. Z. Nauman (1933), *Uber die Grundlegenden Berechungen bei der Schwerkraftaufbereitung*, Ver. Deut. Ing., Vol. 77, pp. 318-320.

Srikrishna, M., K. Sivaji and G. S. R. Narasimhamurty (1982), *Mechanics of Liquid Drops in Air*, Chemical Engineering Journal, Vol. 24, pp. 27-34.

Stewart, J. (1999), *Calculus*, Pacific Grove, Brooks/Cole Publishing Company.

Stow, C. D. and R. D. Stainer (1977), *The Physical Products of a Splashing Drop*, Journal of the Meteorological Society of Japan, Vol. 55(5), pp. 518-531.

Terblanche, R. (2008), *Investigation of Performance Enhancing Devices for the Rain Zones of Wet-Cooling Towers*, Mechanical and Mechatronic Engineering, University of Stellenbosch, Stellenbosch, South Africa, MScEng (Mechanical).

Terblanche, R., H. C. R. Reuter and D. G. Kröger (2009), *Drop Size Distribution Below Different Wet-Cooling Tower Fills*, Applied Thermal Engineering, Vol. 29, pp. 1552-1560.

Tooke, S. (1965), The Impact of Water Drops on Cooling Tower Splash-Bar Packings, Central Electricity Research Laboratories, Vol. Lab. Note No. RD/L/N 108/65.

Torobin, L. B. and W. H. Gauvin (1959), *Fundamental Aspects of Solid in Gas Flow*, Canadian Journal of Chemical Engineering, Vol. 37(4), pp. 129-141.

Turton, R. and O. Levenspiel (1986), *A Short Note on the Drag Correlation for Spheres*, Powder Technology, Vol. 47, pp. 83-86.

Van der Merwe, D. (2007), *Evaluation of Natural Draught Wet-Cooling Tower Performance Uncertainties*, Department of Mechanical and Mechatronic Engineering, University of Stellenbosch, Stellenbosch, MScEng (Mechanical).

Viljoen, D. J. (2006), *Evaluation and Performance Prediction of Cooling Tower Spray Zones*, Department of Mechanical and Mechatronic Engineering, University of Stellenbosch, Stellenbosch, South Africa, MScEng (Mechanical).

Wang, K., F.-z. Sun, Y.-b. Zhao, M. Gao and L. Ruan (2010), *Experimental Research of the Guiding Channels Effect on the Thermal Performance of Wet Cooling Towers Subjected to Crosswinds - Air Guiding Effect on Cooling Tower*, Applied Thermal Engineering, Vol. 30, pp. 533-538.

Wierzba, A. (1990), *Deformation and Break-up of Liquid Drops in a Gas Stream at Nearly Critical Weber Numbers*, Experiments in Fluids, Vol. 9, pp. 59-64.

Williamson, N., S. Armfield and M. Behnia (2008a), *Numerical Simulation of Flow in a Natural Draft Wet Cooling Tower - The Effect of Radial Thermofluid Fields*, Applied Thermal Engineering, Vol. 28, pp. 178-189.

Williamson, N., M. Behnia and S. W. Armfield (2008b), *Thermal Optimization of a Natural Draft Wet Cooling Tower*, International Journal of Energy Research, Vol. 32, pp. 1349-1361.

Wu, Z.-N. (2003), *Prediction of the Size Distribution of Secondary Ejected Droplets by Crown Splashing of Droplets Impinging on a Solid Wall*, Probabilistic Engineering Mechanics, Vol. 18, pp. 241-249.

Yao, S. C., L. E. Hochreter and K. Y. Cai (1988), *Dynamics of Drops Impacting on Thin Heated Strips*, Transactions of ASME, Vol. 110, pp. 214-220.

Yao, S. C. and V. E. Schrock (1976a), *Aerodynamic Design of Cooling Tower Drift Eliminators*, Journal of Engineering for Power/Transactions of ASME, pp. 450-456.

Yao, S. C. and V. E. Schrock (1976b), *Heat and Mass Transfer from Freely Falling Drops*, ASME Journal of Heat Transfer, Vol., pp. 120-126.

Young, G. A. J. (1961), Cooling Tower Splash Packings. *Progress Report to Committee A.*, The British Hydrodynamics Research Association.

Yung, D., J. J. Lorenz and E. N. Ganic (1980), *Vapour/Liquid Interaction and Entrainment in Falling Film Evaporators*, ASME Journal of Heat Transfer, Vol. 102, pp. 20-25.

Zhu, C., K. Lam, H.-H. Chu, X.-D. Tang and G. Liu (2003), *Drag Forces of Interacting Spheres in Power-Law Fluids*, Mechanics Research Communications, Vol. 30, pp. 651-662.

A

THERMOPHYSICAL PROPERTIES

The properties listed in this appendix are as they appear in D.G Kröger's book, "Air Cooled Heat Exchangers and Cooling Towers".

A.1 Thermophysical properties of dry air from 220K to 380K at Standard Atmospheric Pressure (101325 Pa)

Density:

$$\rho_a = p_a/(287.08T), \text{ kg/m}^3 \tag{A.1}$$

Specific Heat:

$$c_{pa} = 1.045356 \cdot 10^3 - 3.161783 \times 10^{-1}T + 7.083814 \times 10^{-4}T^2 - 2.705209 \times 10^{-7}T^3, \text{ J/kgK} \tag{A.2}$$

Dynamic Viscosity:

$$\mu_a = 2.287973 \times 10^{-6} + 6.259793 \times 10^{-8}T - 3.131956 \times 10^{-11}T^2 + 8.15038 \times 10^{-15}T^3, \text{ kg/ms} \tag{A.3}$$

Thermal Conductivity:

$$k_a = -4.937787 \times 10^{-4} + 1.018087 \times 10^{-4}T - 4.627937 \times 10^{-8}T^2 + 1.250603 \times 10^{-11}T^3, \text{ W/mK} \tag{A.4}$$

A.2 Thermophysical properties of saturated water vapour from 273.15K to 380K

Vapour Pressure:

$$p_v = 10^z, \text{ Pa} \tag{A.5}$$

$$z = 10.79586\left(1 - \frac{273.16}{T}\right) + 5.02808log_{10}\left(\frac{273.16}{T}\right)$$
$$+1.50474 \times 10^{-4}\left[1 - 10^{-8.29692\left\{\left(\frac{T}{273.16}\right)-1\right\}}\right]$$
$$+ 4.2873 \times 10^{-4}\left[10^{4.76955(1-273.16/T)} - 1\right] + 2.786118312$$

Specific Heat:

$$c_{pv} = 1.3605 \times 10^{3} + 2.31334T - 2.46784 \times 10^{-10}T^{5} + 5.91332 \times 10^{-13}T^{6}, \text{J/kgK} \quad (A.6)$$

Dynamic Viscosity:

$$\mu_v = 2.562435 \times 10^{-6} + 1.816683 \times 10^{-8}T\ 2.579066 \times 10^{-11}T^{2} - 1.067299 \times 10^{-14}T^{3}, \text{kg/ms} \quad (A.7)$$

Thermal Conductivity:

$$k_v = 1.3046 \times 10^{-2} - 3.756191 \times 10^{-5}T + 2.217964 \times 10^{-7}T^{2} - 1.111562 \times 10^{-10}T^{3}\ , \text{W/mK} \quad (A.8)$$

Vapour Density:

$$\rho_v = -4.062326056 + 0.10277044T - 9.76300388 \times 10^{-4}T^{2} + 4.475240795 \times 10^{-6}T^{3} - 1.004596894 \times 10^{-8}T^{4} + 8.9154895 \times 10^{-12}T^{5}\ , \text{kg/m}^3 \quad (A.9)$$

A.3 Thermophysical Properties of Mixtures of Air and Vapour

Density:

$$\rho_{av} = (1+w)[1 - w/(w + 0.62198)]P_{abs}/(287.08T) \text{ , kg air-vapour/m}^3 \quad \text{(A.10)}$$

Specific Heat:

$$c_{pav} = \left(c_{pa} + wc_{pv}\right)/(1+w) \text{ , J/K kg air-vapour} \quad \text{(A.11)}$$

Dynamic Viscosity:

$$\mu_{av} = \left(X_a\mu_a {M_a}^{0.5} + X_v\mu_v {M_v}^{0.5}\right)/\left(X_a {M_a}^{0.5} + X_v {M_v}^{0.5}\right) \text{ , kg/ms} \quad \text{(A.12)}$$

where

M_a = 28.97 kg/mole, M_v = 18.016 kg/mole, X_a = 1/(1 + 1.608w) and

X_v = w/(w + 0.622)

Thermal Conductivity:

$$k_{av} = \left(X_a k_a {M_a}^{0.33} + X_v k_v {M_v}^{0.33}\right)/\left(X_a {M_a}^{0.33} + X_a {M_a}^{0.33}\right) \text{ , W/mK} \quad \text{(A.13)}$$

Humidity Ratio:

$$w = \left(\frac{2501.6 - 2.3263(T_{wb} - 273.15)}{2501.6 + 1.8577(T - 273.15) - 4.184(T_{wb} - 273.15)}\right) \times \left(\frac{0.62509 p_{vwb}}{P_{abs} - 1.005 p_{vwb}}\right) - \left(\frac{1.00416(T - T_{wb})}{2501.6 + 1.8577(T - 273.15) - 4.184(T_{wb} - 273.15)}\right) \text{, kg/ kg dry air} \quad \text{(A.14)}$$

Enthalpy:

$$i_{av} = \left[c_{pa}(T - 273.15) + w\{i_{fgwo} + c_{pv}(T - 273.15)\}\right]/(1 + w), \quad \text{J/kg air-vapour} \tag{A.15a}$$

Or the enthalpy of the air-vapour mixture per unit mass of dry air

$$i_{ma} = c_{pa}(T - 273.15) + w\left[i_{fgwo} + c_{pv}(T - 273.15)\right], \text{ J/kg dry air} \tag{A.15b}$$

where the specific heats are evaluated at (T + 273.15)/2 and the latent heat i_{fgwo}, is evaluated at 273.15 K according to equation (A.20) i.e. i_{fgwo} = 2.5016 x 10^6 J/kg.

A.4 Thermophysical Properties of Saturated Water Liquid from 273.15K to 380K

Density:

$$\rho_w = (1.49343 \times 10^{-3} - 3.7164 \times 10^{-6}T + 7.09782 \times 10^{-9}T^2 - 1.90321 \times 10^{-20}T^6)^{-1}, \text{ kg/m}^3. \tag{A.16}$$

Specific Heat:

$$c_{pw} = 8.15599 \times 10^3 - 2.80627 \times 10T + 5.11283 \times 10^{-2}T^2 - 2.17582 \times 10^{-13}T^6 \text{ , J/kgK.} \tag{A.17}$$

Dynamic Viscosity:

$$\mu_w = 2.414 \times 10^{-5} \times 10^{247.8/(T-140)}, \text{ kg/ms.} \tag{A.18}$$

Thermal Conductivity:

$$k_w = -6.14255 \times 10^{-1} + 6.9962 \times 10^{-3}T - 1.01075 \times 10^{-5}T^2 + 4.74737 \times 10^{-12}T^4 \text{ , W/mK.} \tag{A.19}$$

Latent heat of Vaporization:

$$i_{fgw} = 3.4831814 \times 10^{6} - 5.8627703 \times 10^{3}T + 12.139568T^{2} - 1.40290431 \times 10^{-2}T^{3} \text{ , J/kg.} \quad \text{(A.20)}$$

Critical Pressure:

$$p_{wc} = 22.09 \times 10^{6} \text{ , Pa.} \quad \text{(A.21)}$$

Surface Tension:

$$\sigma_{w} = 5.148103 \times 10^{-2} + 3.998714 \times 10^{-4}T - 1.4721869 \times 10^{-6}T^{2} + 1.21405335 \times 10^{-9}T^{3} \text{ , N/m.} \quad \text{(A.22)}$$

B

DROP SPLASHING AFTER IMPINGEMENT ON NARROW SLATS COVERED BY A THIN LAYER OF WATER

B.1 Introduction

Installation of splash grids below the fill in natural draught wet-cooling towers (NDWCTs) can enhance rain zone and therefore cooling tower performance due to the break-up of larger drops into smaller ones, herewith increasing the interfacial surface area between the water and the air and the residence time of drops in the rain zone. The mechanisms of drop break-up are splashing, straddling and dripping from below the slats. Splashing occurs when a drop impinges on the surface of a splash grid and small upward moving drops are formed when the initial drop breaks up that are thrown clear of the impinged slat, as shown in Figure B.1.

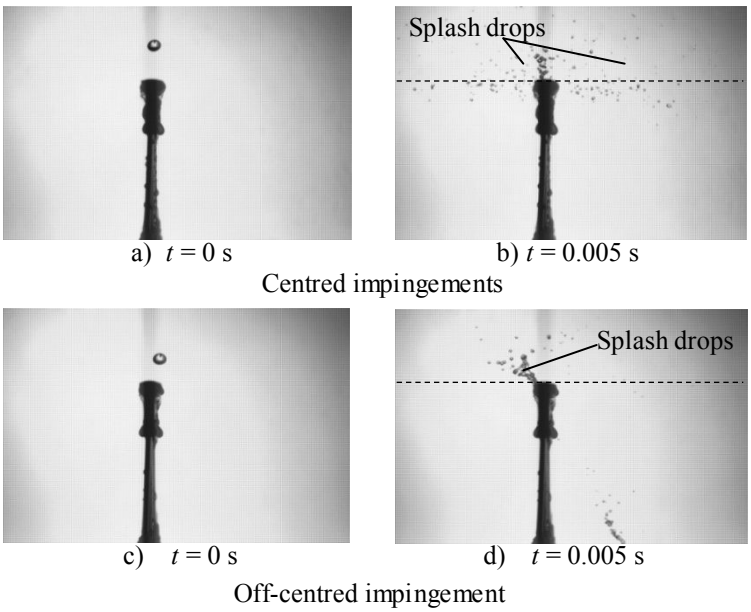

Figure B.1: Drop splashing on a slat for a centred and off-centred impingement.

In this appendix sequential photographs of drop impingement at different locations over the slat width are presented in order to quantify the average mass fractions and drop distributions associated with splashing. Results are presented for different initial drop diameters, falling heights, slat widths and water film thicknesses on the slats, before comparing the results to the data from Dreyer (1994).

B.2 Experimental setup

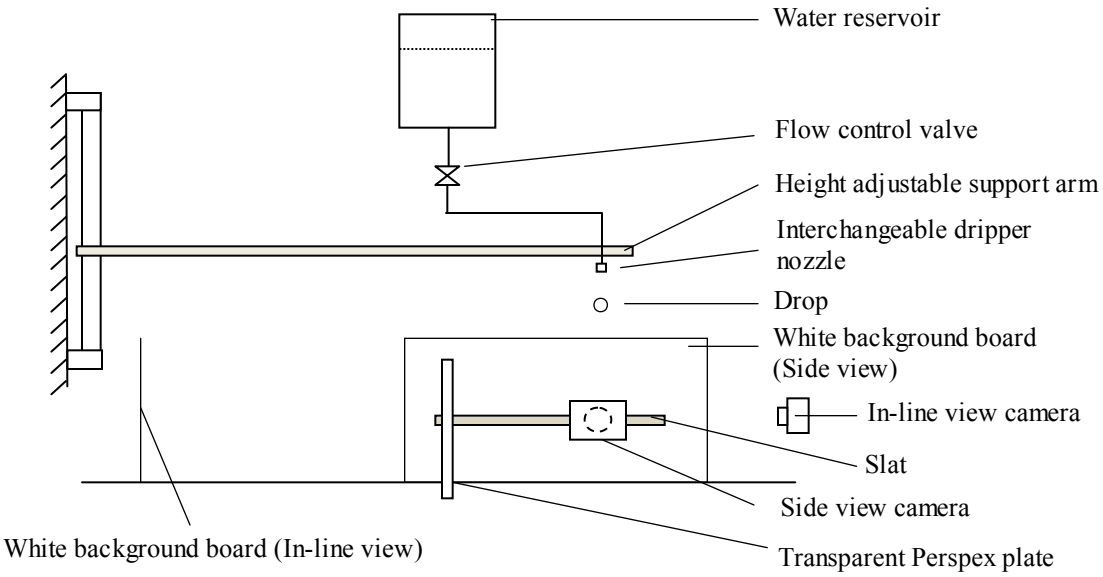

a) Schematic of the experimental setup for splash experiments.

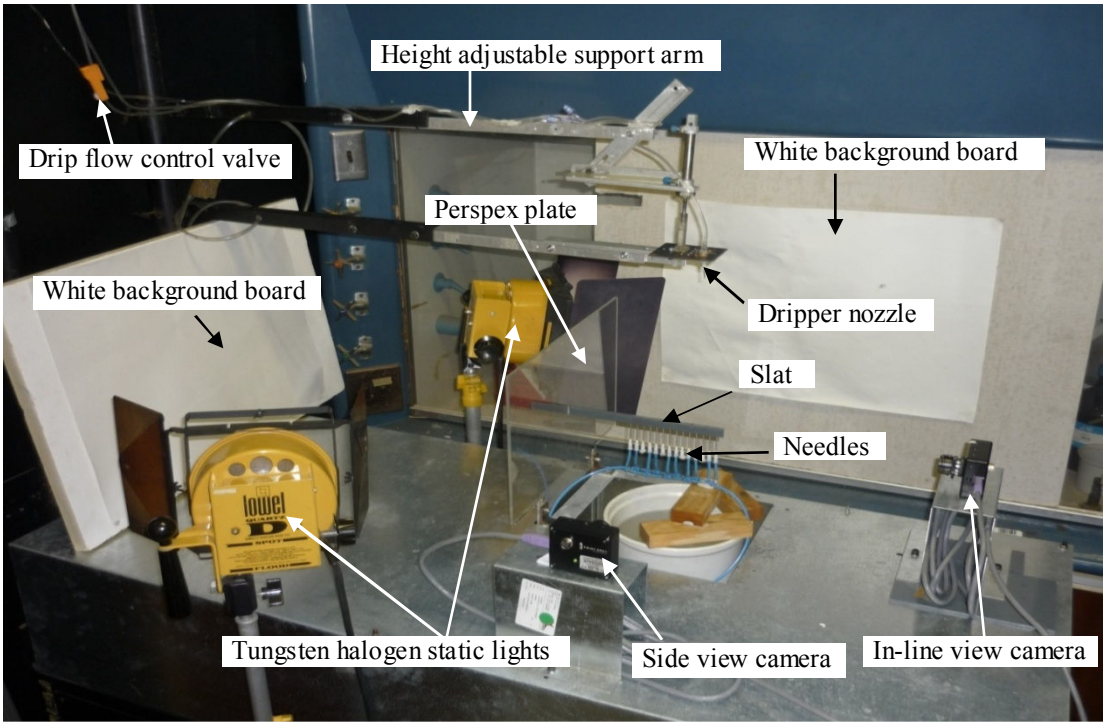

b) Photograph of experimental setup for splash experiments.

Figure B.2: Experimental setup for splash experiments.

The experimental setup can be seen in Figures B.2. A drop generator that consists of a reservoir, flow control valve and an exchangeable nozzle connected to a height adjustable support arm is used to generate drops of different sizes. The sizes of the drops can be controlled by changing the size of the nozzle. The drop frequency is controlled by the drip flow control valve and is low enough to ensure that the film on the slat has sufficient time to recover and settle between different drop impingements. The impinging drops are filmed by two synchronised high speed video cameras at a rate of 200 frames per second, from the front (in-line with the slat) and the side. Tungsten-halogen static lights are used to illuminate white background boards. Both cameras are connected to a personal computer onto which the photographs are saved before drop size data is extracted to determine the splash drop size distributions and splash fractions, as shown in Appendix F.

Figure B.3 shows how water is fed to the slat surface from a water supply by means of a set of needles protruding from the bottom of the slat, to create a water film.

Figure B.4 shows the procedure for measuring the water film thickness on a slat by means of the side view camera, making use of a software programme developed for this purpose. This program compares a photo of a slat covered by a water film (Figure B.4b) to one with no water film (Figure B.4a) and subtracts the binary images of these two photographs, obtained by a threshold procedure, to get a binary image containing only the water film (Figure B.4c). The number of pixels comprising the water film at each horizontal location is then counted and the local and average film thicknesses are obtained by multiplying the number of pixels with a calibration value (Figure B.4d). The program also tests for vertical alignment of the two images according to the holes in the slats, as seen in Figure B.4, and re-aligns the images if necessary to ensure accurate determination of the film thickness.

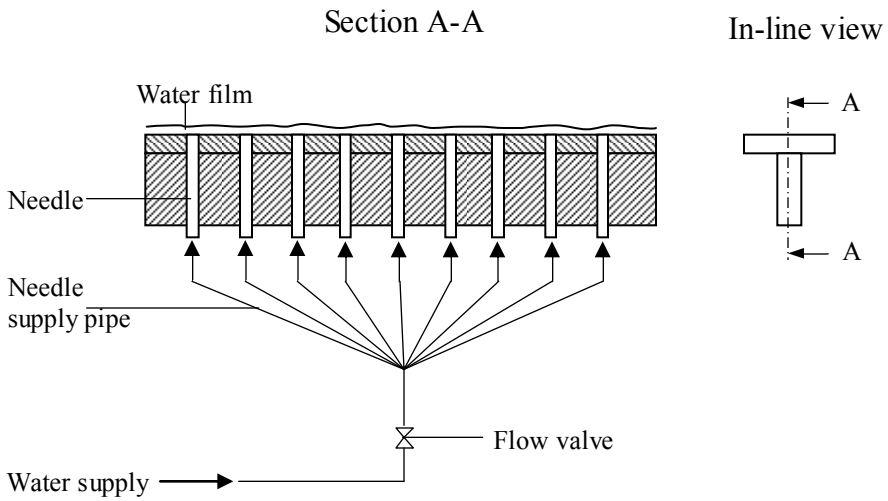

Figure B.3: Slat configuration for splash experiments.

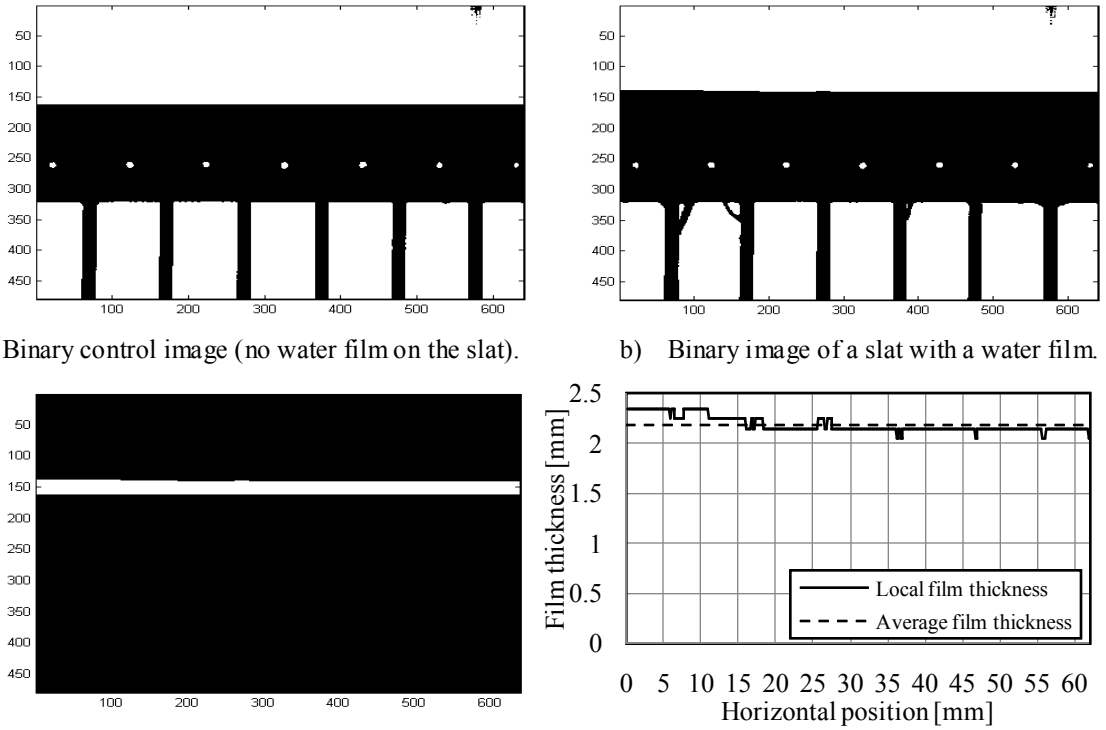

a) Binary control image (no water film on the slat).

b) Binary image of a slat with a water film.

c) Binary image of only the water film.

d) Water film thickness measurement result.

Figure B.4: Water film thickness measurement procedure on slats.

B.3 Experimental results

In this section the photographs taken for different splash experiments are presented together with plots of the locally measured Sauter mean drop diameters, splash fractions and drop distribution parameters. Table B.1 shows a summary of the experiments done in terms of the test variables and also shows the sections where the data can be found.

Table B.1: Summary of splash experiments.

Section	Initial drop diameter, d_i [mm]	Slat width, W [mm]	Film thickness on slat, δ [mm]	Drop fall distance, H_d [mm]
B.3.1	4	3, 6, 12	$0 < \delta < 2$	250
B.3.2	4	3, 6, 12	$0 < \delta < 2$	470
B.3.3	4	3, 6, 12	$0 < \delta < 2$	970
B.3.4	2.89, 5.48	3, 6, 12	$0.78 \leq \delta \leq 1.00$	250
B.3.5	2.89, 5.48	3, 6, 12	$0.78 \leq \delta \leq 1.00$	470
B.3.6	2.89, 5.48	3, 6, 12	$0.78 \leq \delta \leq 1.00$	970

The measured splash mass data are presented by the local splash fraction given by

$$f_s = \frac{M_s}{M_i} \tag{2.55}$$

The average splash fraction is given by

$$\overline{f_s} = \int_0^1 f_s(\lambda)\, \partial\lambda \tag{B.1}$$

where the dimensionless displacement, λ, is given by

$$\lambda = \frac{2x}{W + d_i} \tag{B.2}$$

with x being the displacement between the drop and slat centres and W and d_i the slat width and initial drop diameter respectively, as shown in Figure B.5.

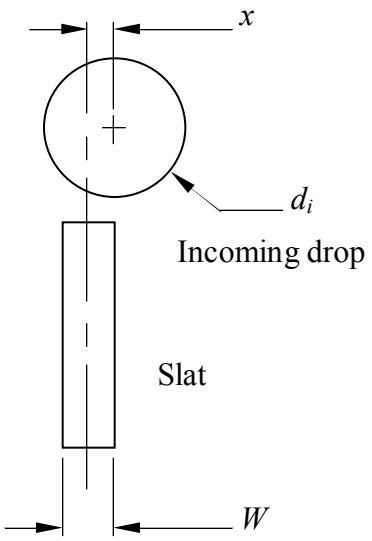

Figure B.5: Drop impingement variables.

The splash drop distribution is expressed by the Rosin-Rammler function given by

$$R(d) = 1 - exp\left[-\left(\frac{d}{d_{RR}}\right)^{n_{RR}}\right] \tag{2.58}$$

The drop distribution data are presented graphically in terms of the Rosin-Rammler parameter (d_{RR}), the spread parameter (n_{RR}) and the Sauter mean drop diameter (d_{32}).

B.3.1 Splash results (H_d = 250 mm, $d_i \approx$ 4 mm)

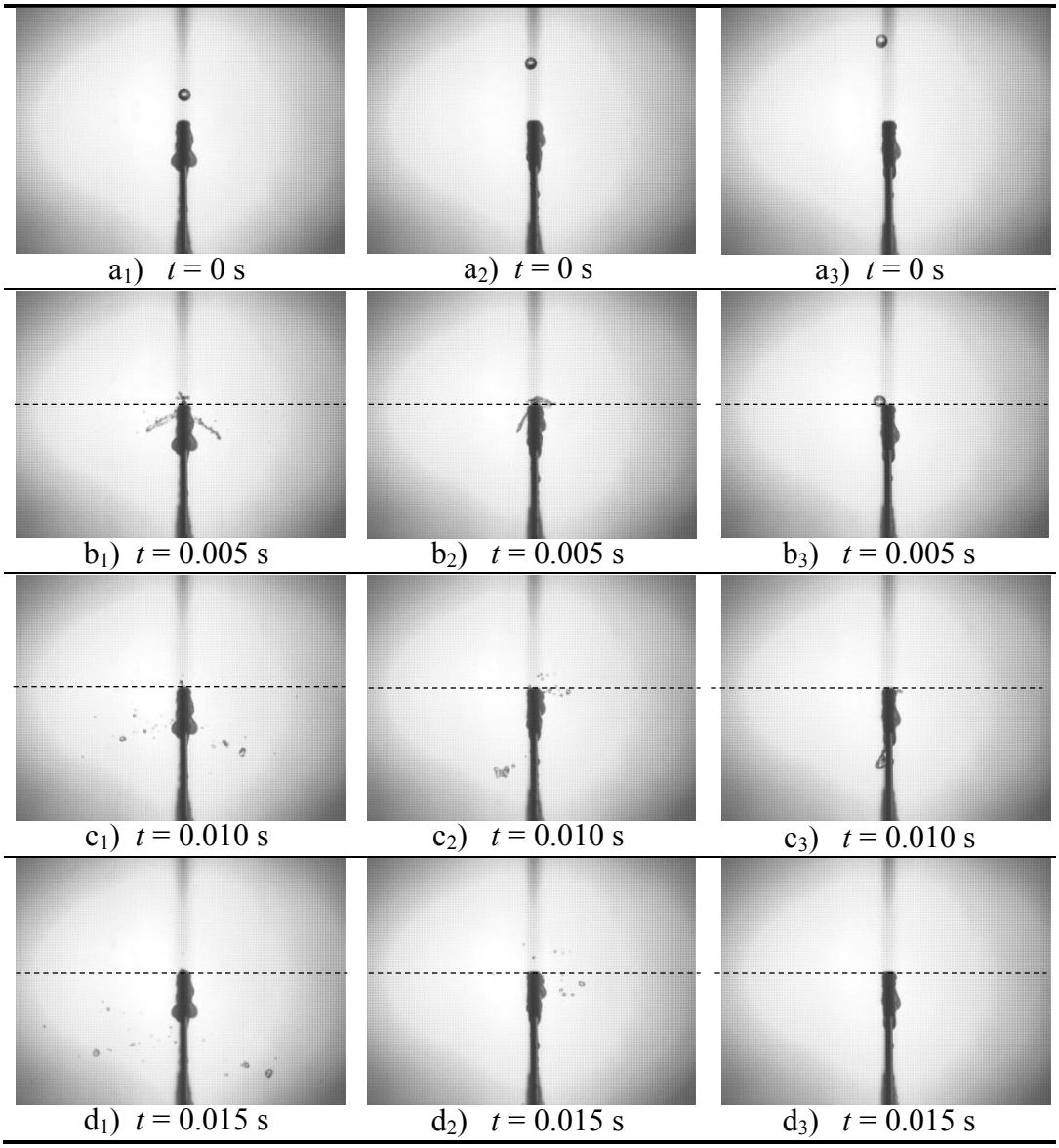

Figure B.6: Splash photographs (H_d = 250 mm, W = 3 mm, $d_i \approx$ 4 mm, $\delta = 0.43 \pm 0.09$ mm).

This section presents the splash results when a d_i = 4 mm in diameter drop falls H_d = 250 mm before it impinges onto different film covered slats. Figures B.6 to B.12 show sequential photographs of the drop impingements at different locations over the width of a slat for different slat width (W = 3, W = 6 and W = 12 mm) and film

thickness combinations and generally little to no splashing is observed. Figures B.13 and B.14 show plots of the measured local splash fractions, Sauter mean drop diameters and Rosin-Rammler parameters for each slat.

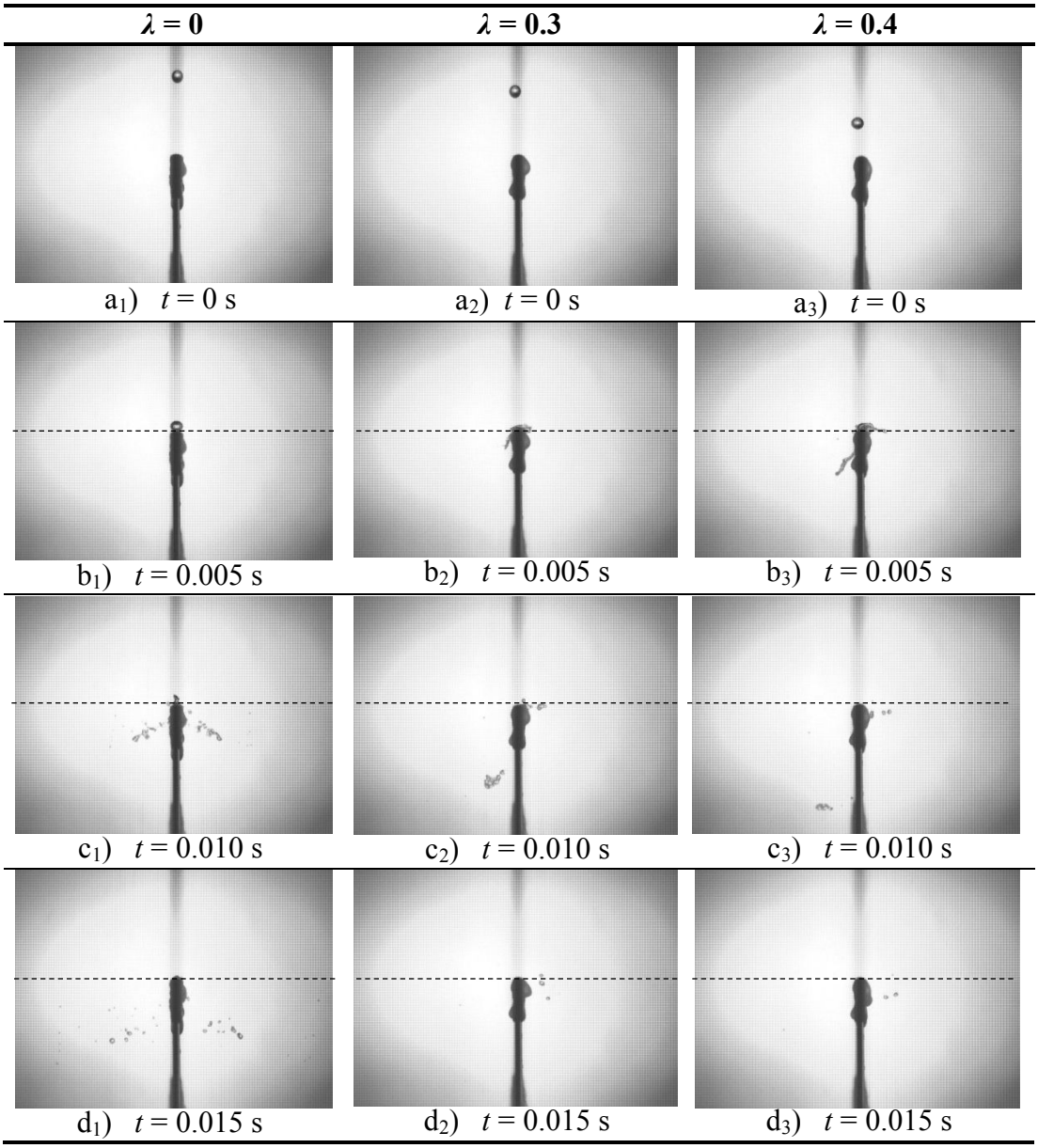

Figure B.7: Splash photographs (H_d = 250 mm, W = 3 mm, $d_i \approx$ 4 mm, $\delta = 0.78 \pm 0.05$ mm).

Figure B.7 shows two very similar break-ups at $\lambda = 0.3$ and $\lambda = 0.4$ and is an example of how splashing is identified when it is not possible to see individual drops travel

through the air above the slat. The small drops that form to the right of the slat (λ = 0.4) are considered to be splash drops due to the slight upward motion of the crown that has an arch-like shape (photo b_3) while no such arch-like shape is observed at λ = 0.3. This is also observed in Figure B.8(b_2 to d_2).

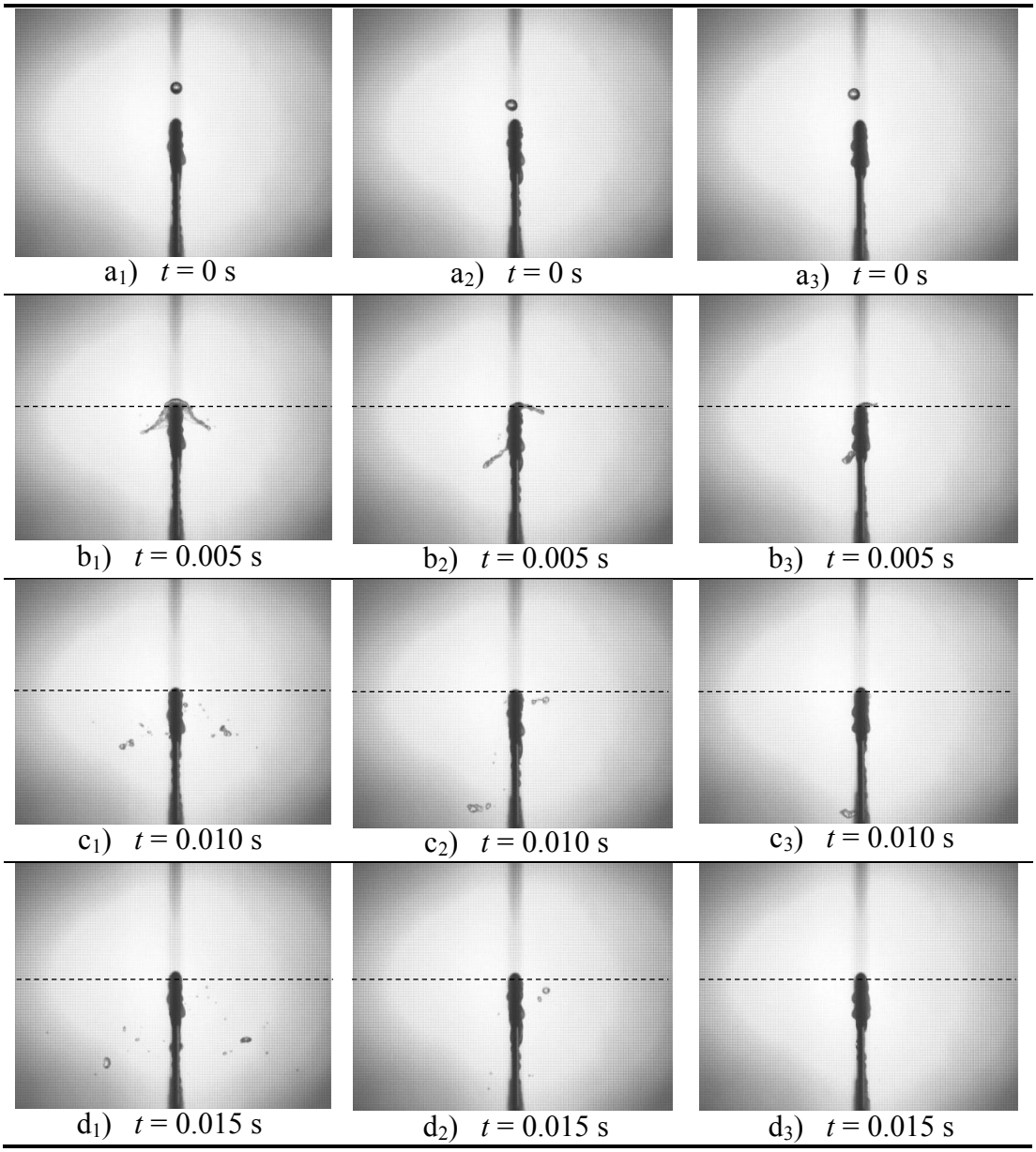

Figure B.8: Splash photographs (H_d = 250 mm, W = 3 mm, $d_i \approx$ 4 mm, δ = 1.30 ± 0.16 mm).

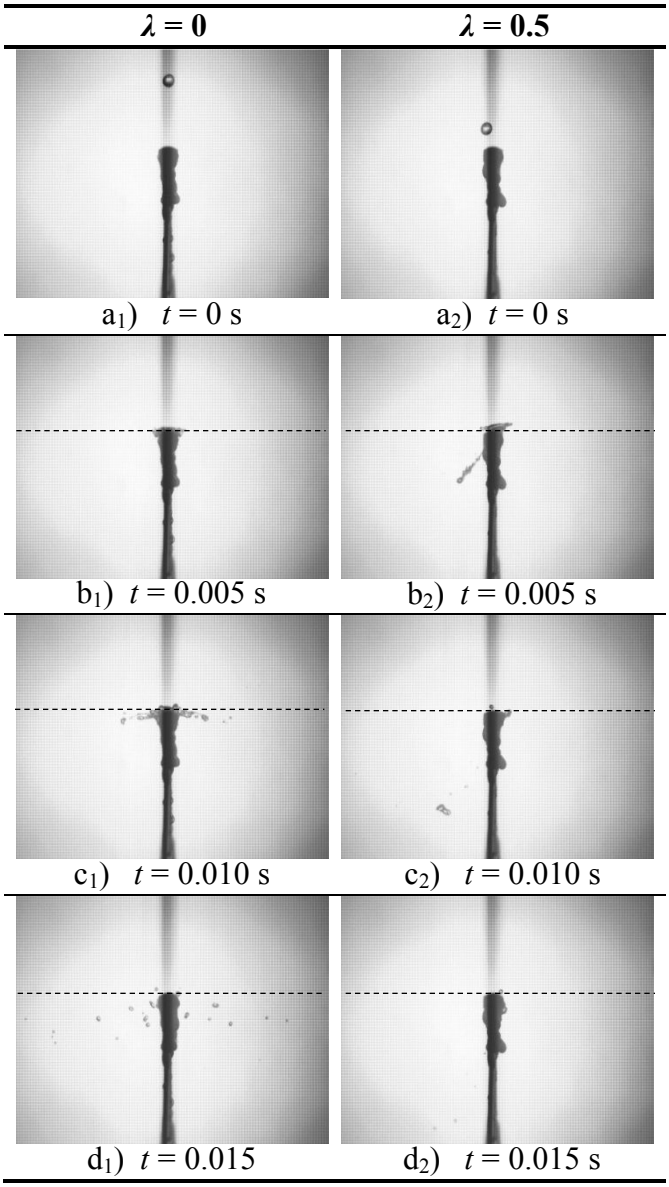

Figure B.9: Splash photographs (H_d = 250 mm, W = 6 mm, $d_i \approx$ 4 mm, $\delta = 0.85 \pm 0.15$ mm).

Drop splashing of a $d_i = 4$ mm in diameter drop on a $W = 6$ mm wide slat is shown in Figure B.9 for a film thickness on the slat of $\delta = 0.85$ mm and it can be seen that splashing is again almost negligible. This is comparable with the $W = 3$ mm wide slat where generally little to no splashing is measured at the current drop fall distance ($H_d = 250$ mm).

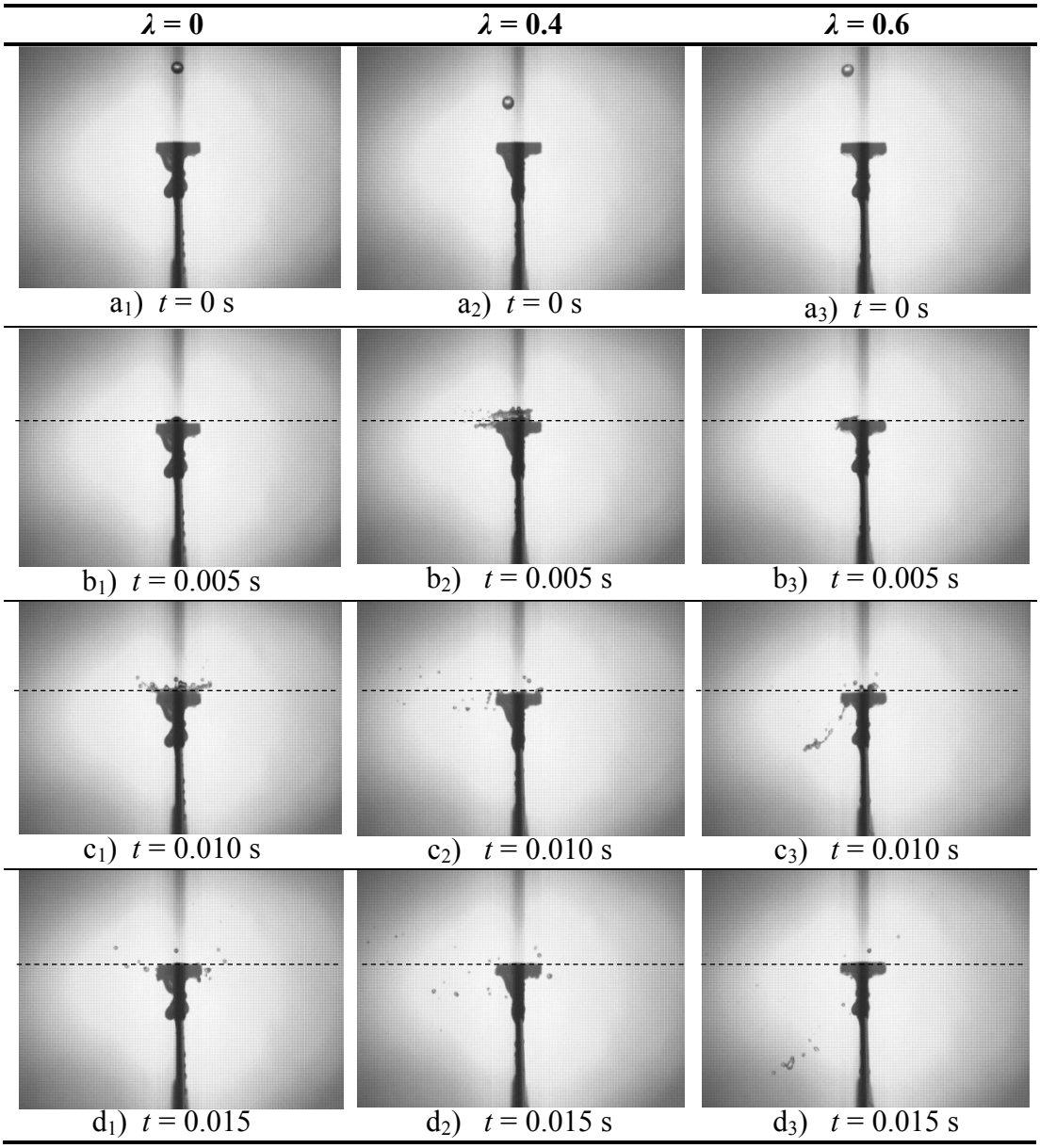

Figure B.10: Splash photographs (H_d = 250 mm, W = 12 mm, $d_i \approx$ 4 mm, $\delta = 0.36 \pm 0.04$ mm).

For a W = 12 mm wide slat it is clear that the thinnest water film causes the smallest splash drops although splashing occurs relatively seldom (28 of the 45 measured points produced no splashing). When splashing does occur it happens in the form of one or two drops of roughly the same size, meaning that a spread parameter can't always be determined.

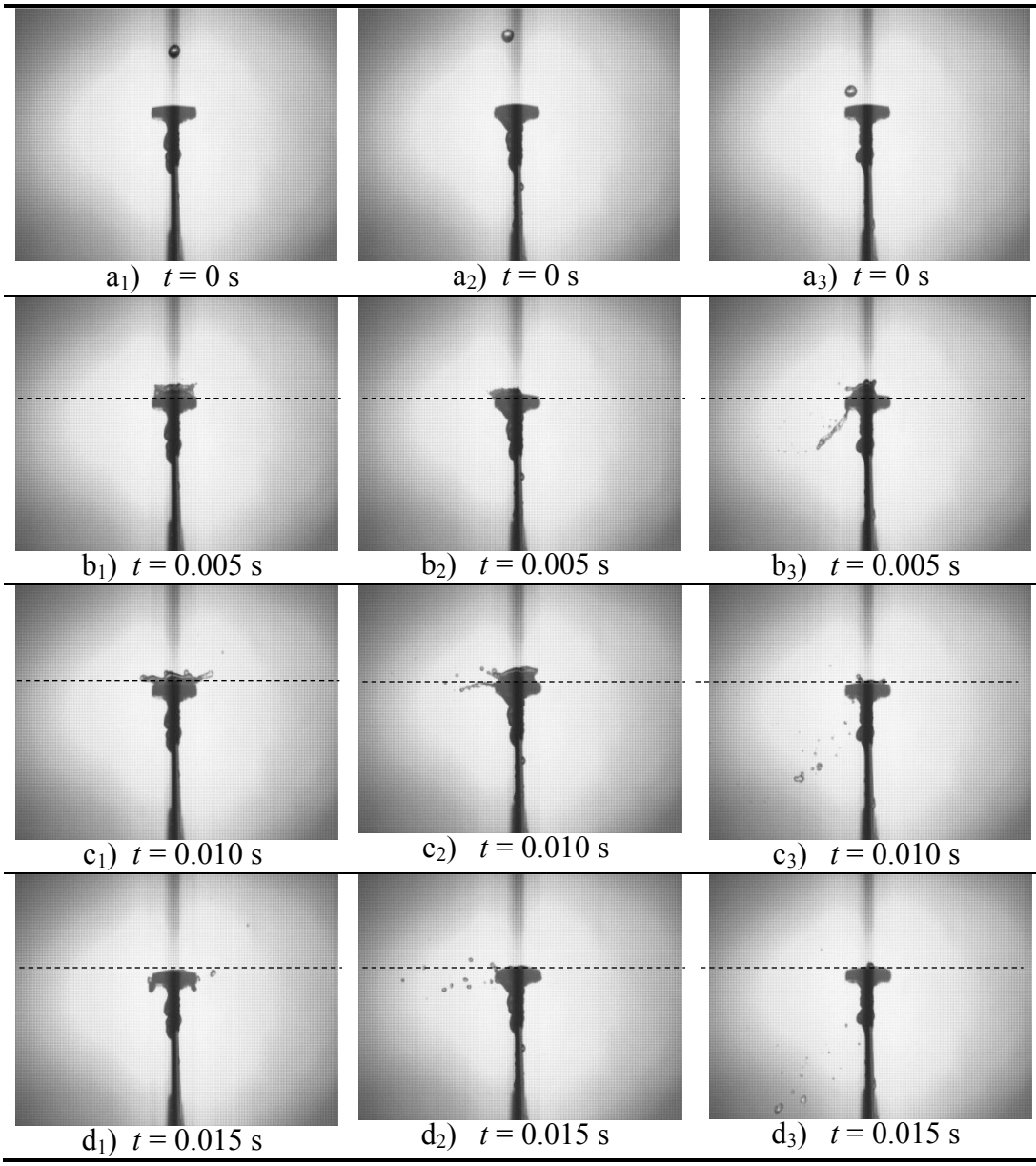

Figure B.11: Splash photographs (H_d = 250 mm, W = 12 mm, $d_i \approx$ 4 mm, $\delta = 1.00 \pm 0.12$ mm).

Although splashing on a W = 12 mm wide slat is not very significant at the current drop fall distance (H_d = 250 mm) the most splashing takes place when the film is at its thinnest.

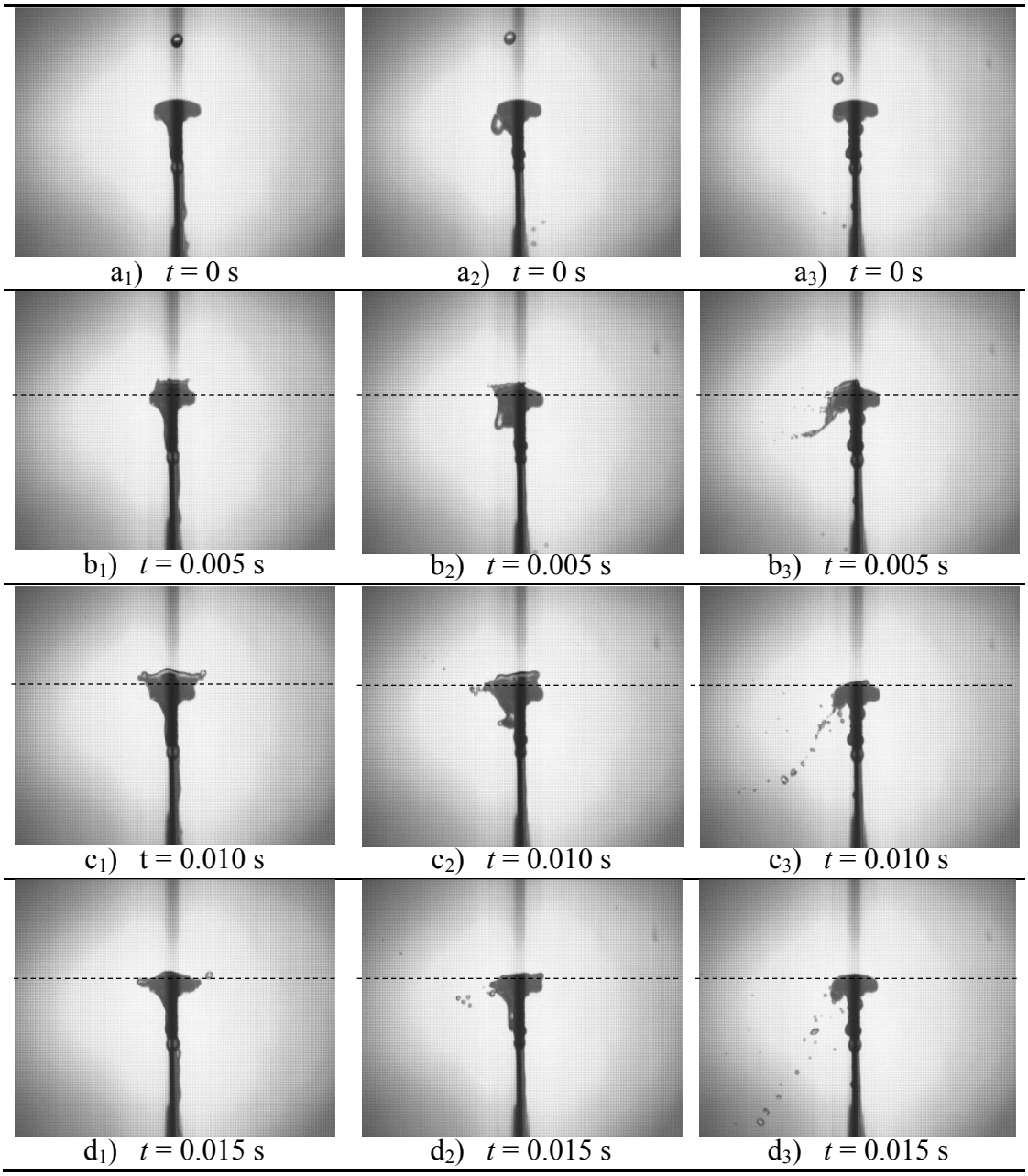

Figure B.12: Splash photographs (H_d = 250 mm, W = 12 mm, $d_i \approx$ 4 mm, δ = 1.75 ± 0.04 mm).

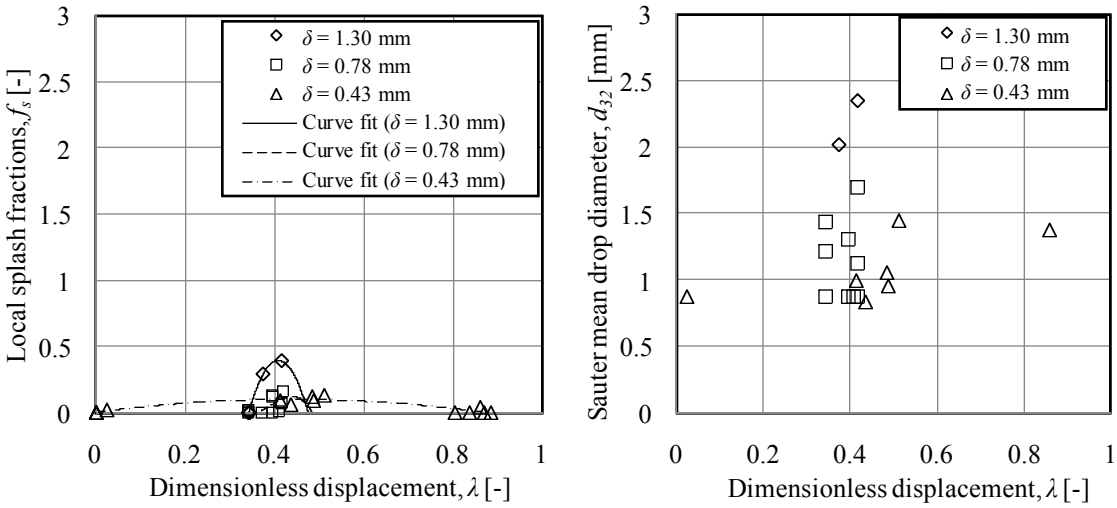

a$_1$) Local splash fractions (W = 3 mm) b$_1$) Sauter mean drop diameters (W = 3 mm)

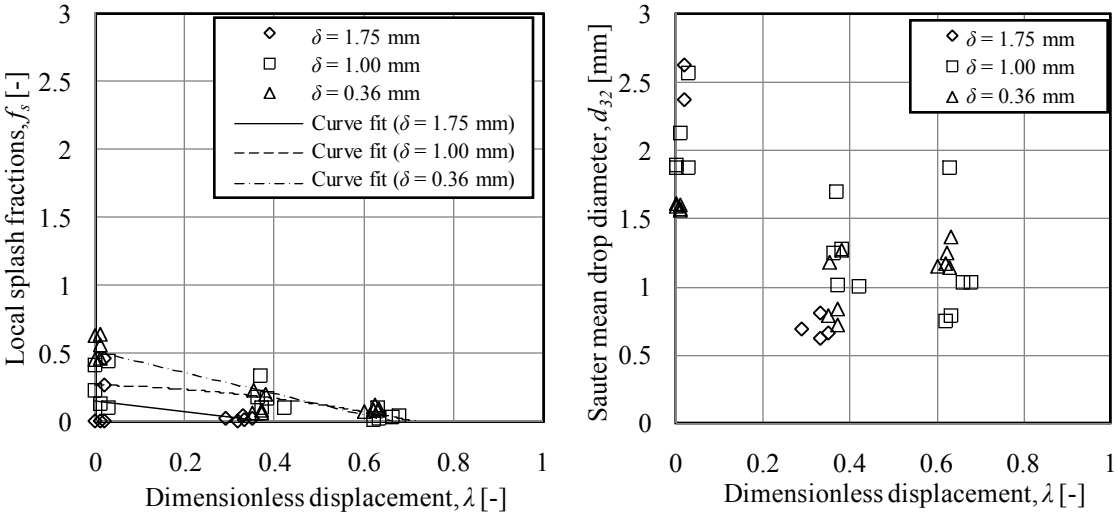

a$_2$) Local splash fraction (W = 12 mm) b$_2$) Sauter mean drop diameters (W = 12 mm)

Figure B.13: Measured splash fractions and Sauter mean drop sizes (H_d = 250 mm, $d_i \approx$ 4 mm).

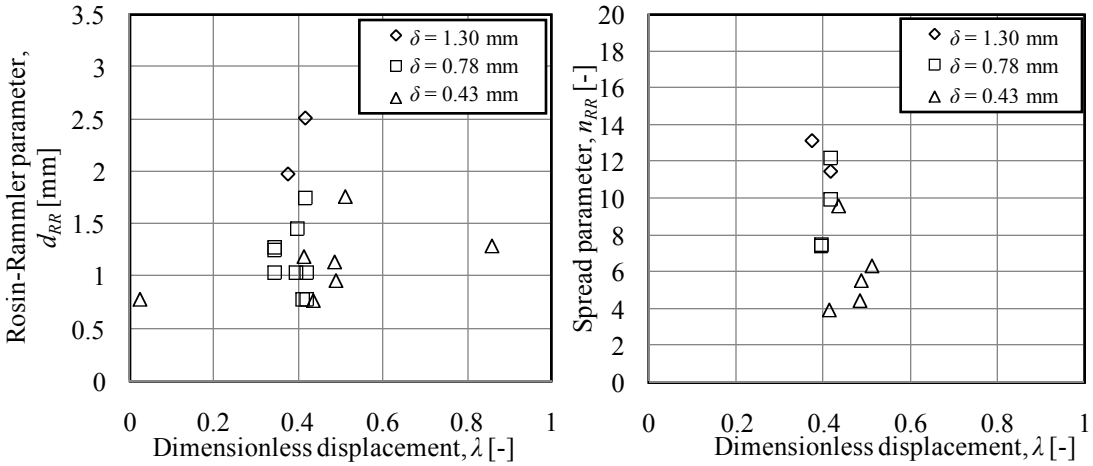

a$_1$) Rosin-Rammler parameter, d_{RR} (W = 3 mm) b$_1$) Spread parameter, n_{RR} (W = 3 mm)

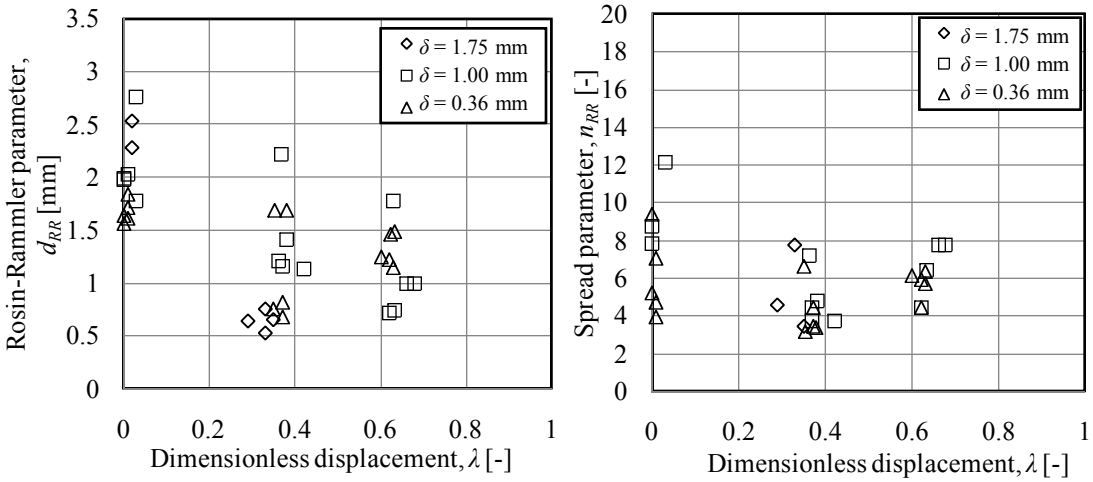

a$_2$) Rosin-Rammler parameter, d_{RR} (W = 12 mm) b$_2$) Spread parameter, n_{RR} (W = 12 mm)

Figure B.14: Measured Rosin-Rammler parameters (H_d = 250 mm, $d_i \approx$ 4 mm).

B.3.2 Splash results (H_d = 470 mm, $d_i \approx$ 4 mm)

This section presents the splash results when a d_i = 4 mm in diameter drop falls H_d = 470 mm before it impinges onto different film covered slats. Figures B.15 to B.23 show sequential photographs of the drop impingements at different locations over the width of a slat for different slat width (W = 3, W = 6 and W = 12 mm) and film thickness combinations while Figures B.24 and B.25 show plots of the measured local splash fractions, Sauter mean drop diameters and Rosin-Rammler parameters.

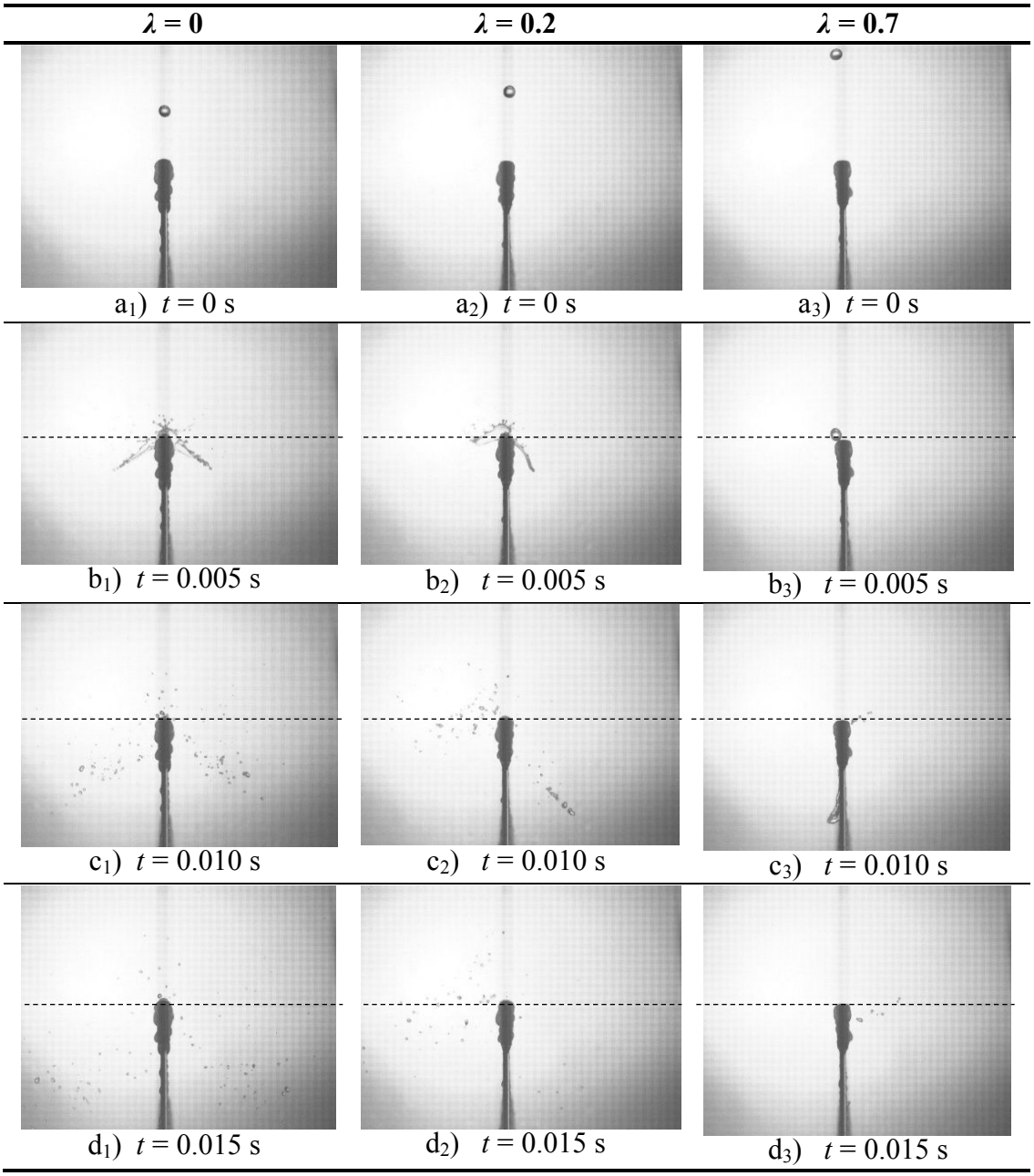

Figure B.15: Splash photographs (H_d = 470 mm, W = 3 mm, $d_i \approx$ 4 mm, $\delta = 0.35 \pm 0.1$ mm).

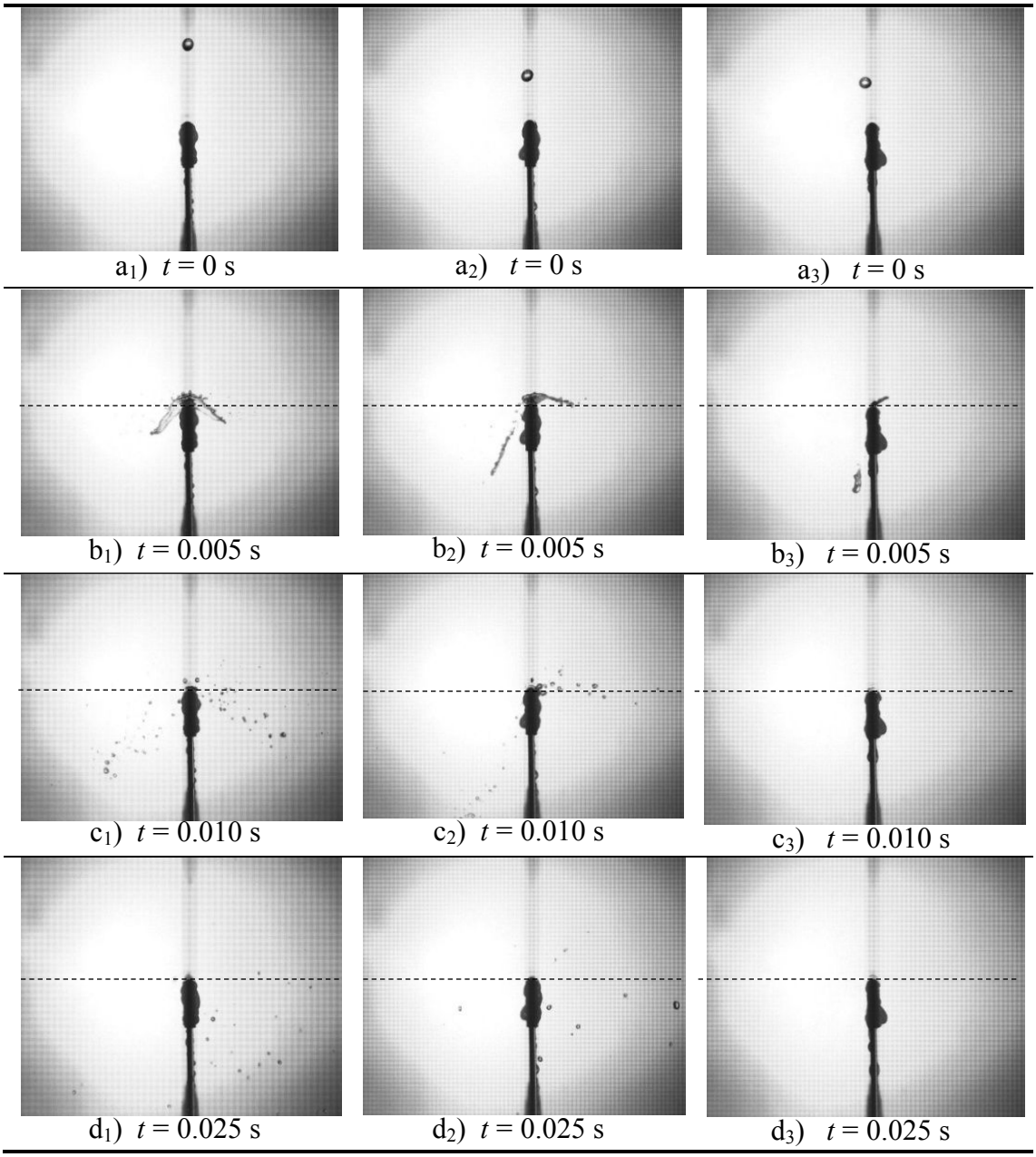

Figure B.16: Splash photographs (H_d = 470 mm, W = 3 mm, $d_i \approx$ 4 mm, $\delta = 0.95 \pm 0.15$ mm).

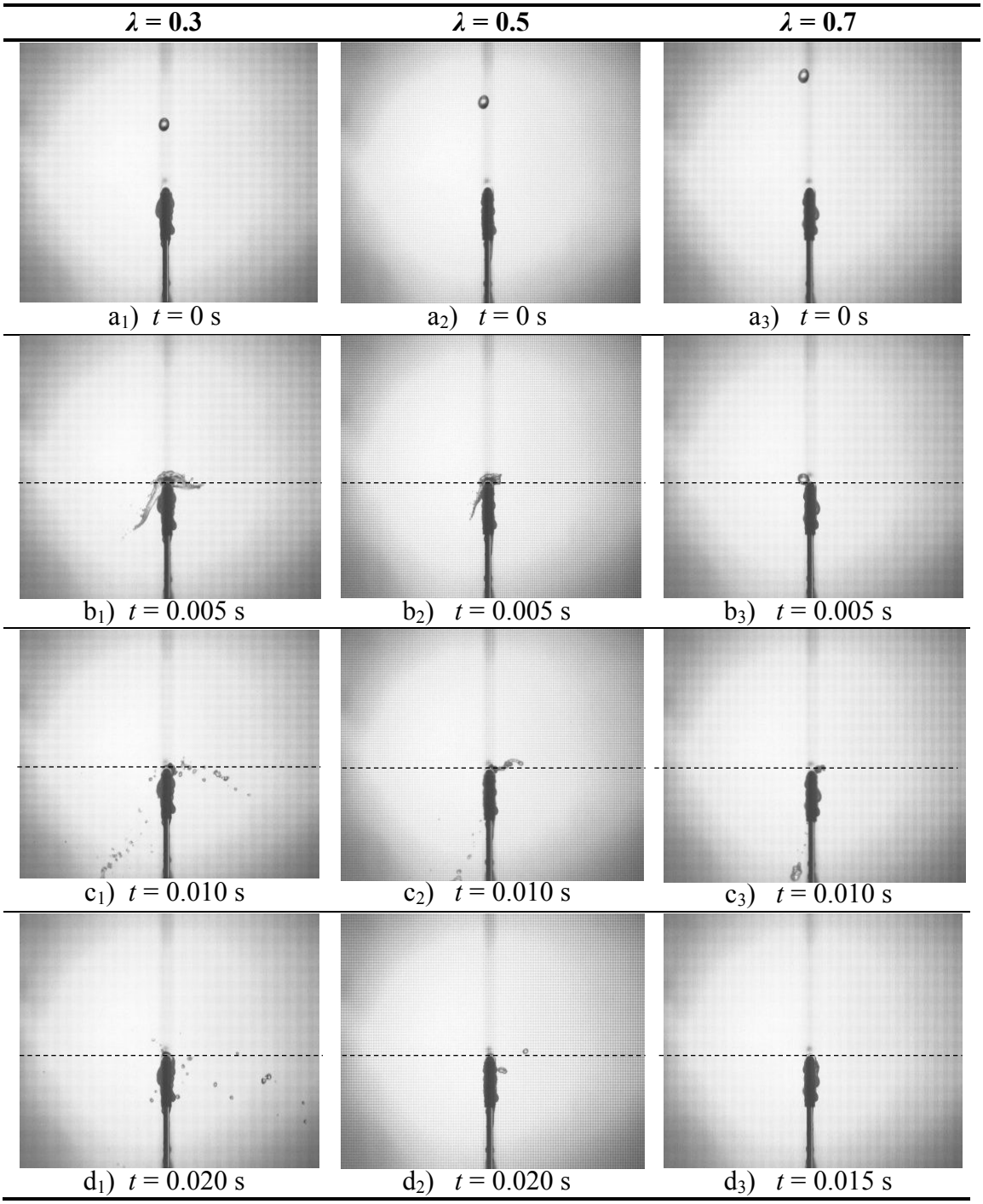

Figure B.17: Splash photographs (H_d = 470 mm, W = 3 mm, $d_i \approx$ 4 mm, δ = 1.40 ± 0.1 mm).

This section shows splashing to be much more significant at H_d = 470 mm compared to H_d = 250 mm. For the W = 12 mm slat the most splashing generally happens from centred impingements while corresponding impingements on the W = 3 mm slat lead to negligible splashing. The overall splashing also seems to be significantly lower for the cases where the slat width is smaller than the initial drop diameter.

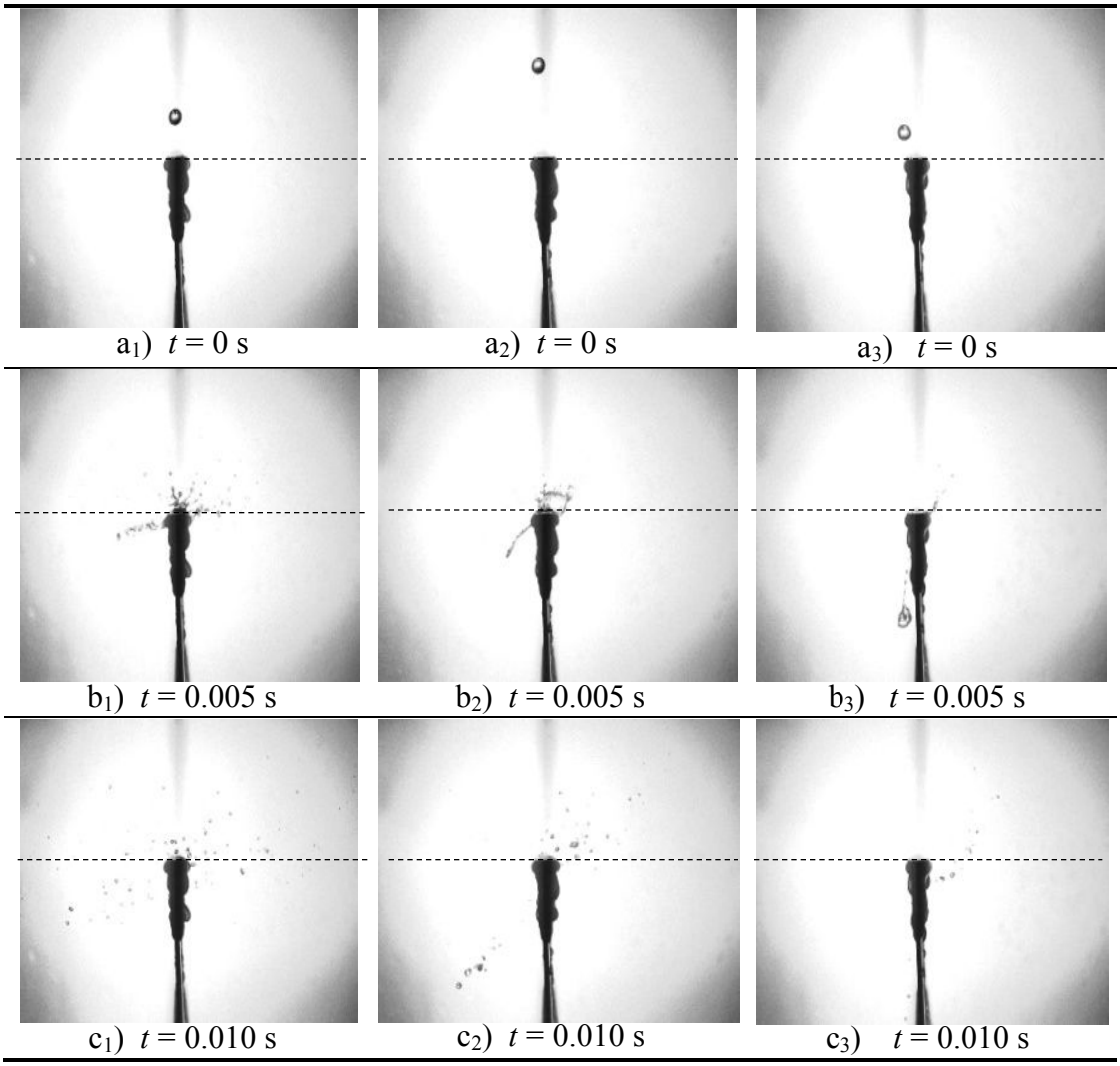

Figure B.18: Splash photographs (H_d = 470 mm, W = 6 mm, $d_i \approx$ 4 mm, δ = 0.25 ± 0.1 mm).

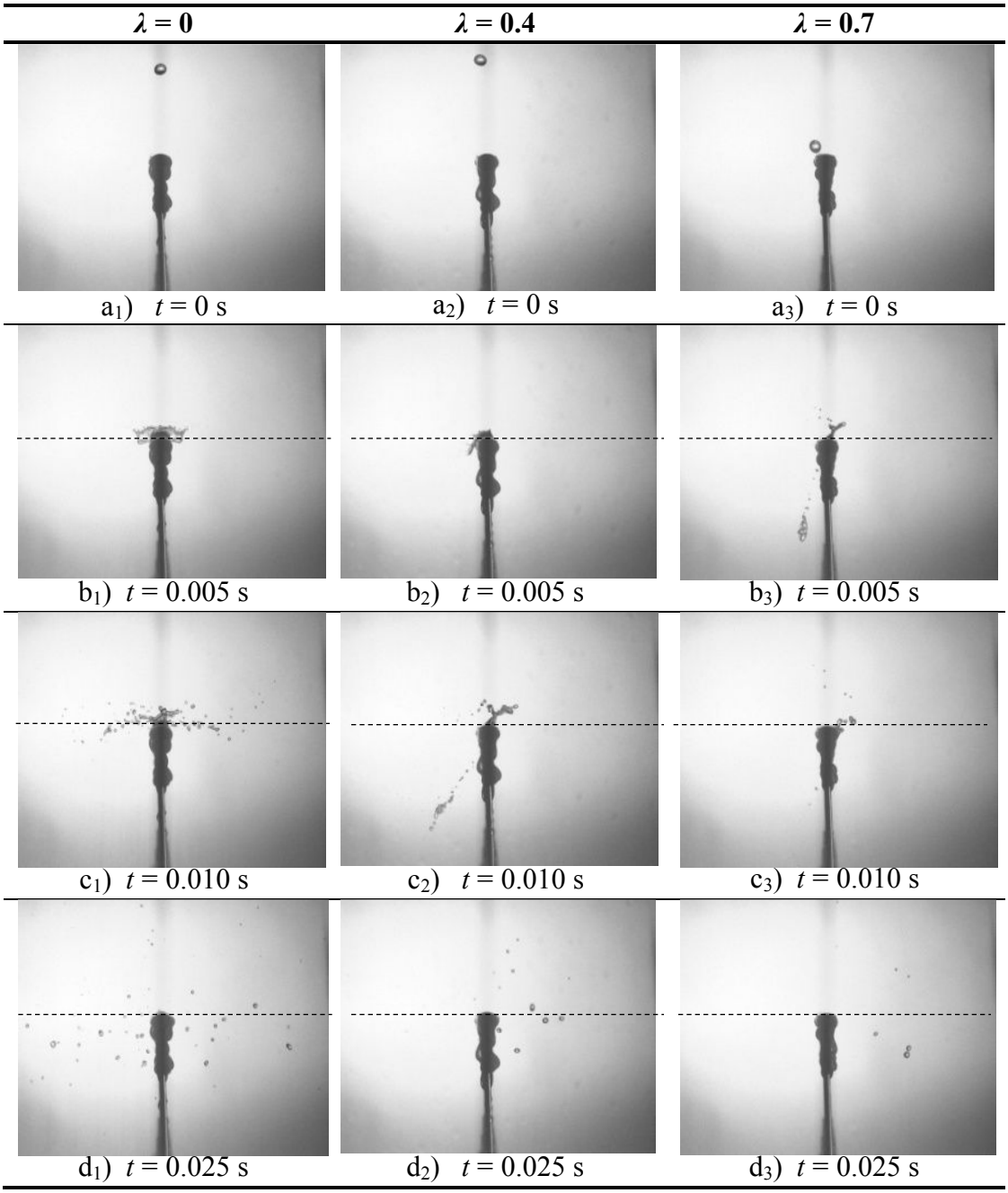

Figure B.19: Splash photographs (H_d = 470 mm, W = 6 mm, $d_i \approx$ 4 mm, $\delta = 0.85 \pm 0.1$ mm).

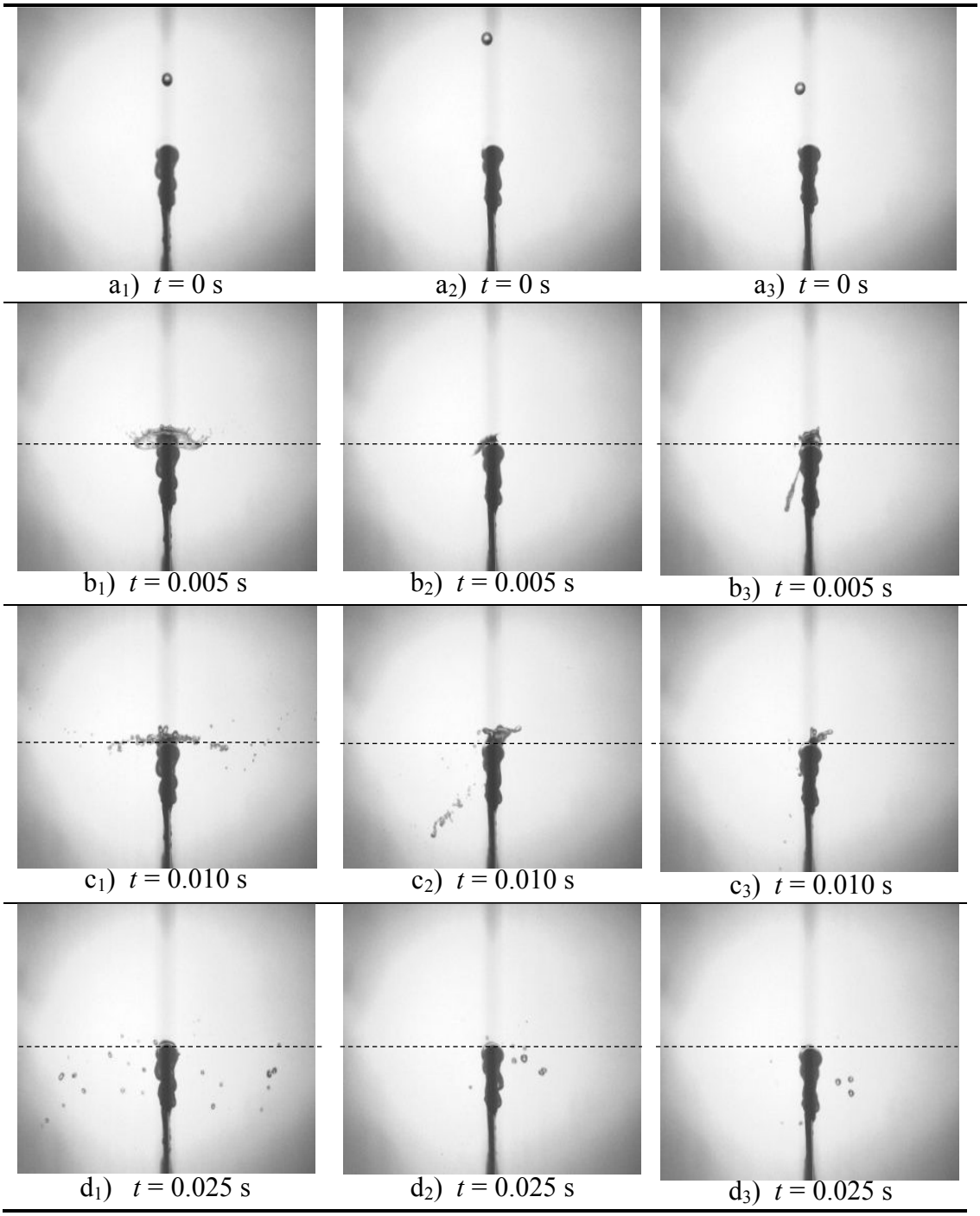

Figure B.20: Splash photographs (H_d = 470 mm, W = 6 mm, $d_i \approx$ 4 mm, δ = 1.45 ± 0.1 mm).

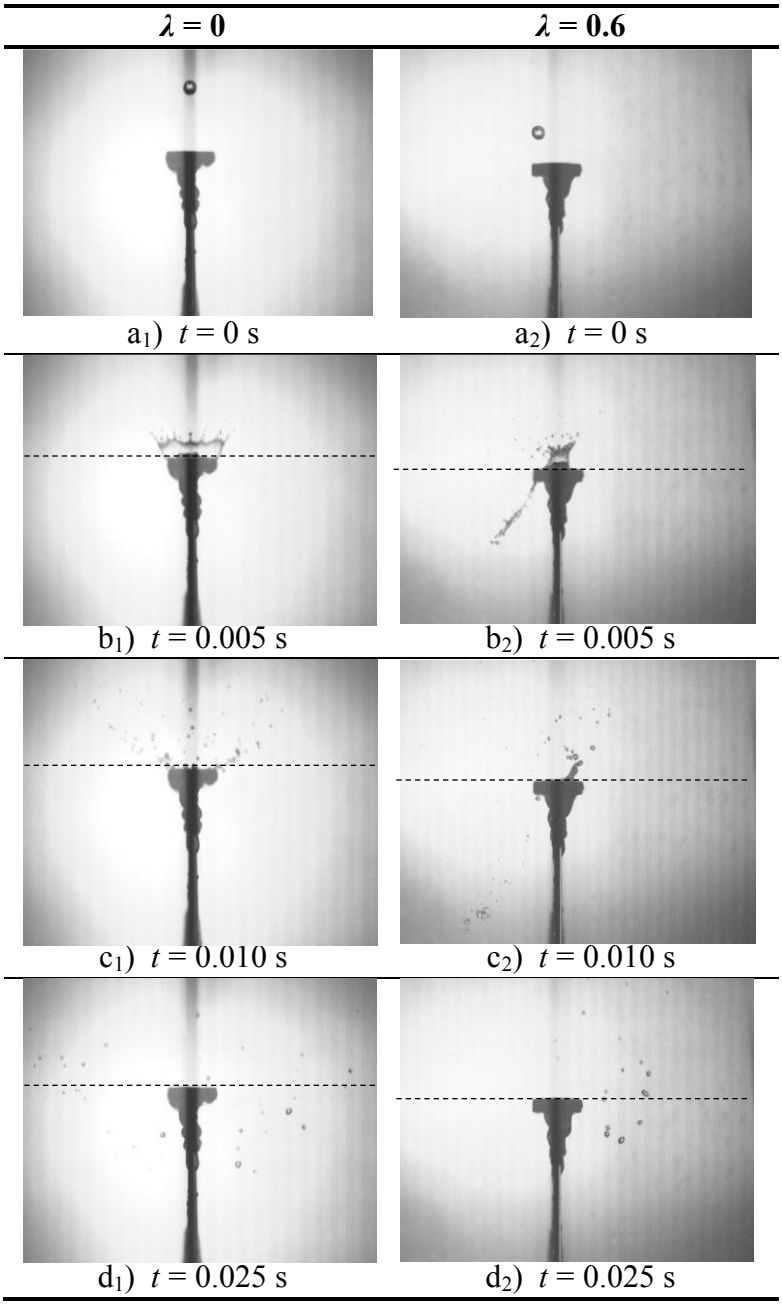

Figure B.21: Splash photographs (H_d = 470 mm, W = 12 mm, d_i = 4 mm, $\delta = 0.30 \pm 0.1$ mm).

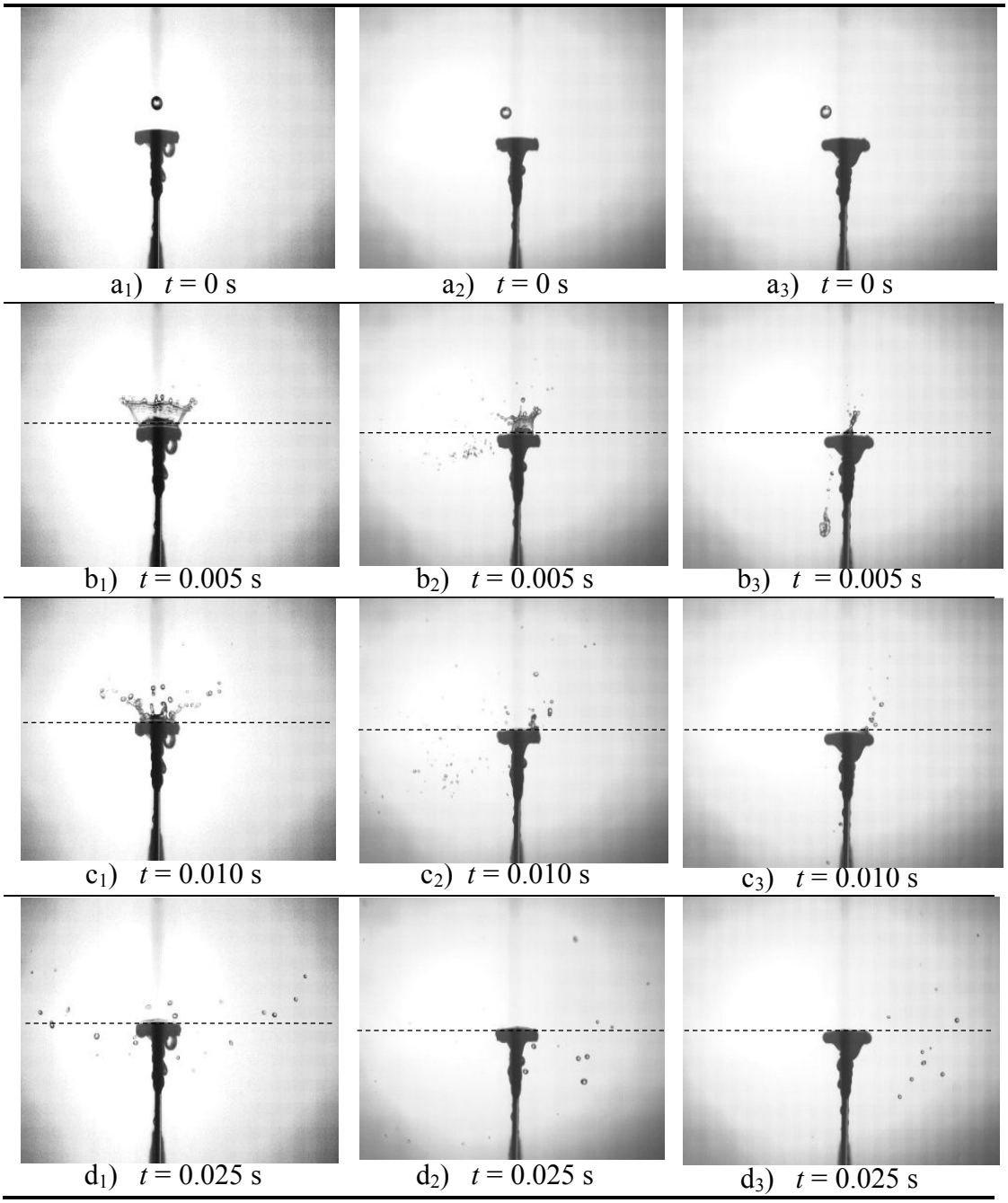

Figure B.22: Splash photographs (H_d = 470 mm, W = 12 mm, d_i = 4 mm, $\delta = 0.75 \pm 0.15$ mm).

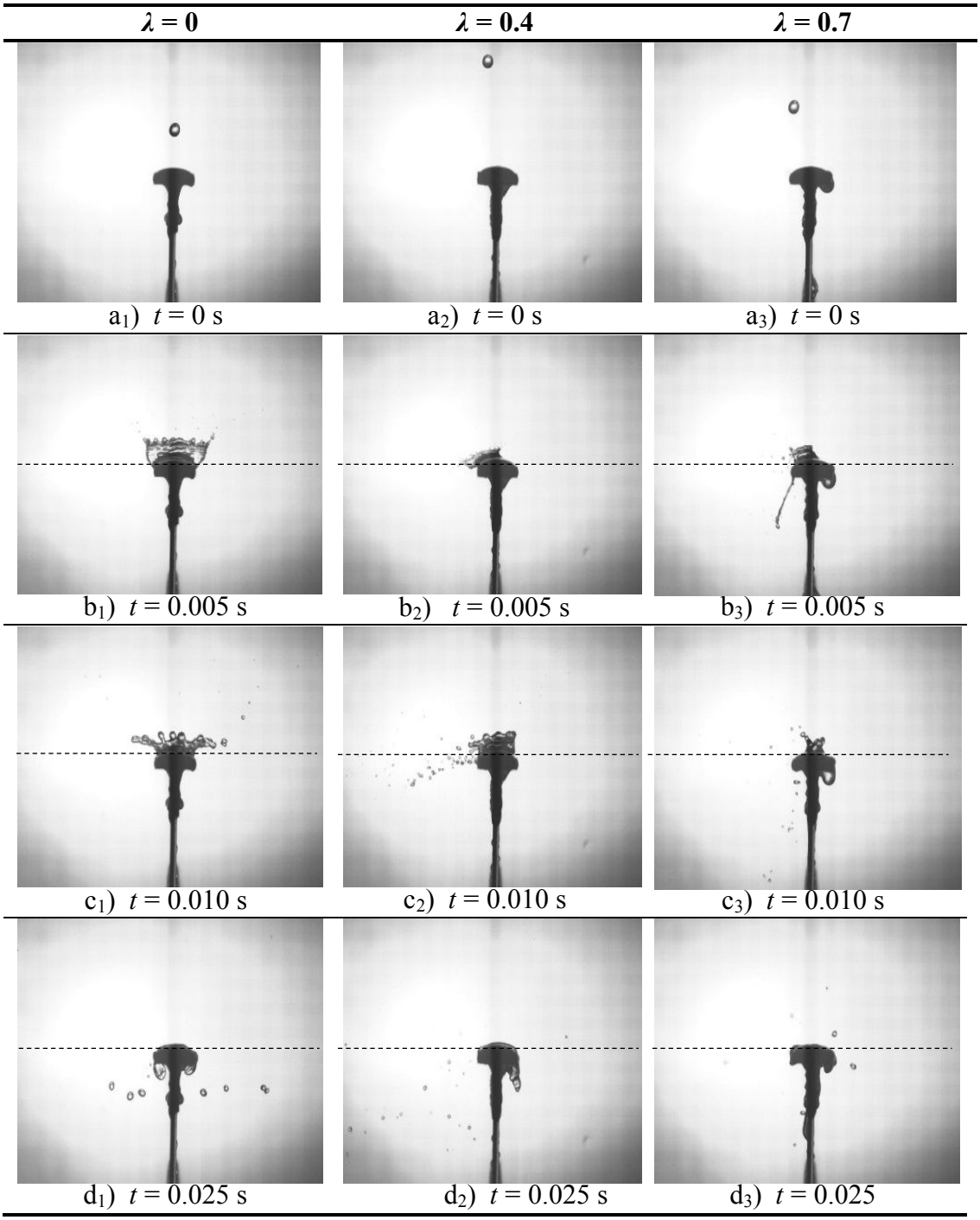

Figure B.23: Splash photographs (H_d = 470 mm, W = 12 mm, d_i = 4 mm, δ = 1.95 ± 0.1 mm).

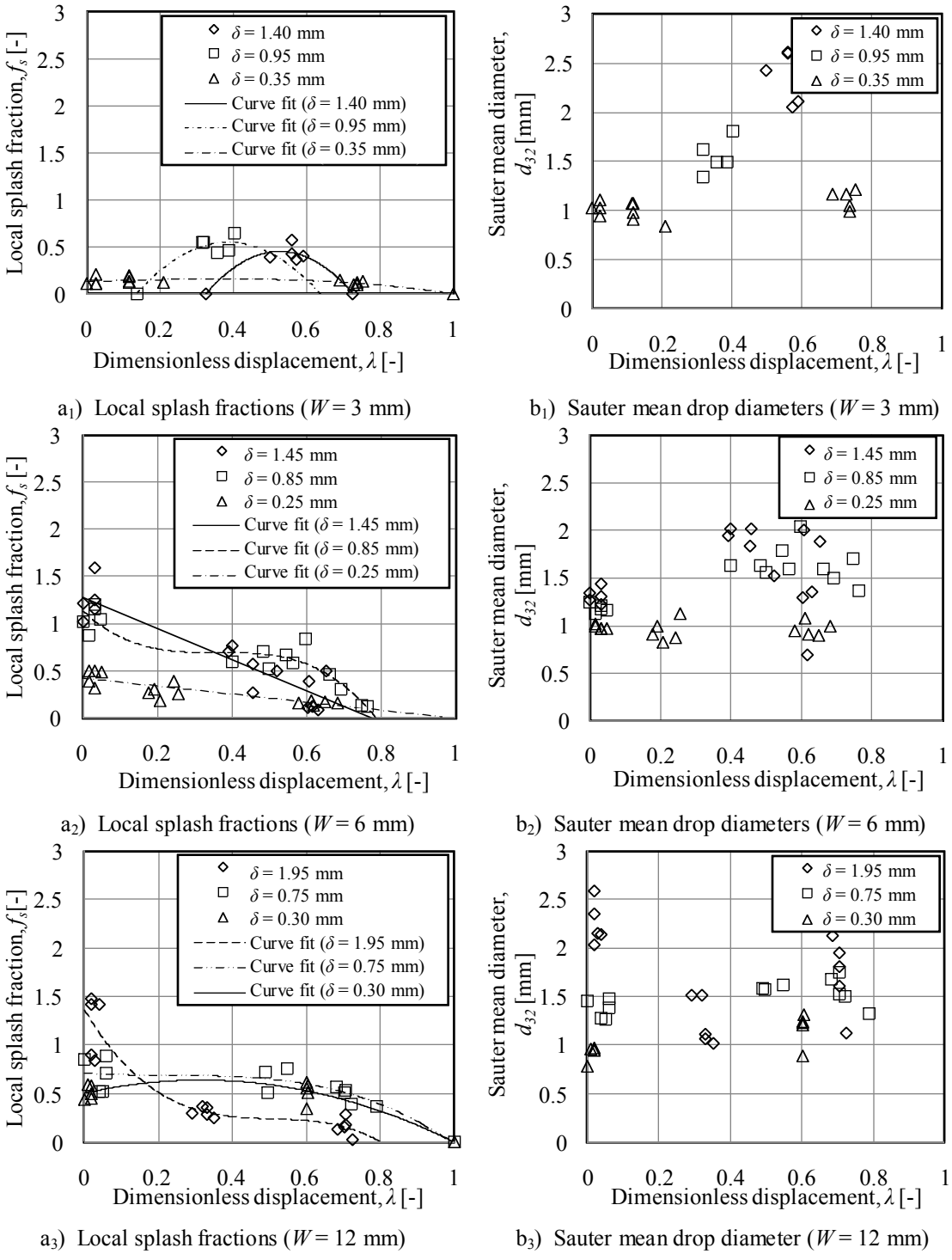

a$_1$) Local splash fractions (W = 3 mm)

b$_1$) Sauter mean drop diameters (W = 3 mm)

a$_2$) Local splash fractions (W = 6 mm)

b$_2$) Sauter mean drop diameters (W = 6 mm)

a$_3$) Local splash fractions (W = 12 mm)

b$_3$) Sauter mean drop diameter (W = 12 mm)

Figure B.24: Measured splash fractions and Sauter mean drop sizes (H_d = 470 mm, $d_i \approx 4$ mm).

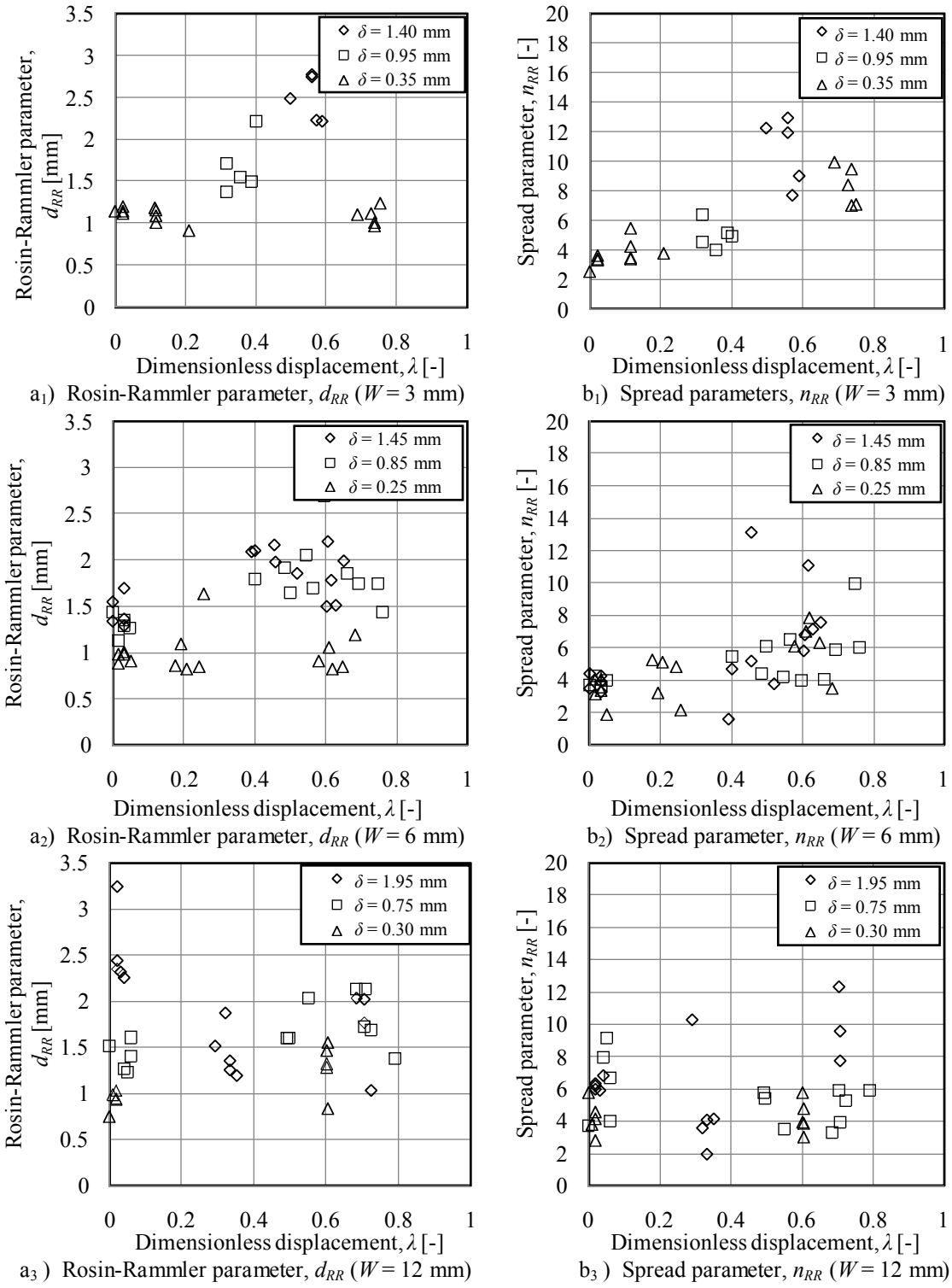

a$_1$) Rosin-Rammler parameter, d_{RR} (W = 3 mm)

b$_1$) Spread parameters, n_{RR} (W = 3 mm)

a$_2$) Rosin-Rammler parameter, d_{RR} (W = 6 mm)

b$_2$) Spread parameter, n_{RR} (W = 6 mm)

a$_3$) Rosin-Rammler parameter, d_{RR} (W = 12 mm)

b$_3$) Spread parameter, n_{RR} (W = 12 mm)

Figure B.25: Measured Rosin-Rammler parameters (H_d = 470 mm, $d_i \approx$ 4 mm).

B.3.3 Splash results (H_d = 970 mm, $d_i \approx$ 4 mm)

This section presents the splash results when a d_i = 4 mm in diameter drop falls H_d = 970 mm before it impinges onto different film covered slats. Figures B.26 to B.34 show sequential photographs of the drop impingements at different locations over the width of a slat for different slat width (W = 3, W = 6 and W = 12 mm) and film thickness combinations while Figures B.35 and B.36 show plots of the measured local splash fractions, Sauter mean drop diameters and Rosin-Rammler parameters.

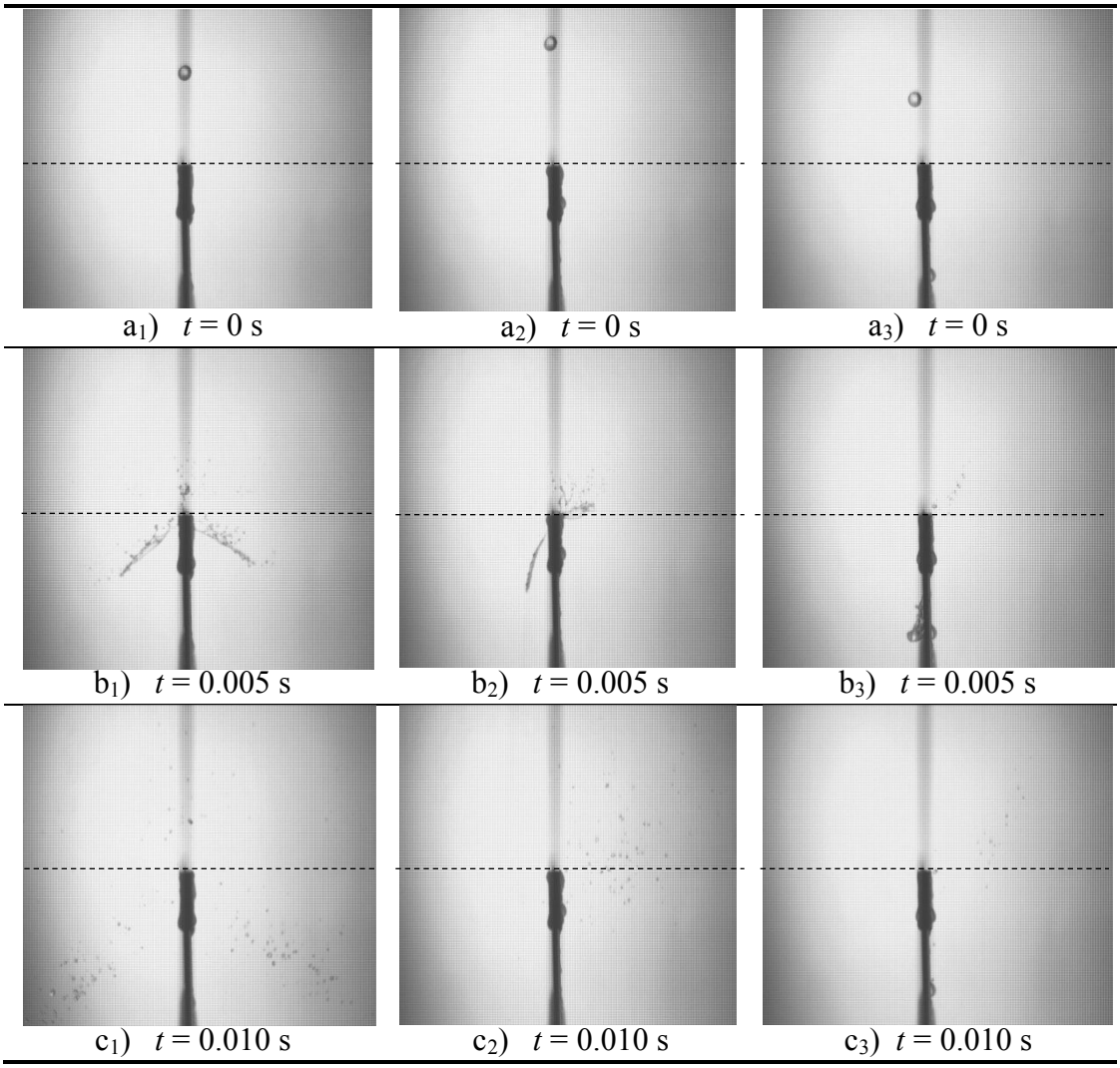

Figure B.26: Splash photographs (H_d = 970 mm, W = 3 mm, $d_i \approx$ 4 mm, δ = 0.11 ± 0.04 mm).

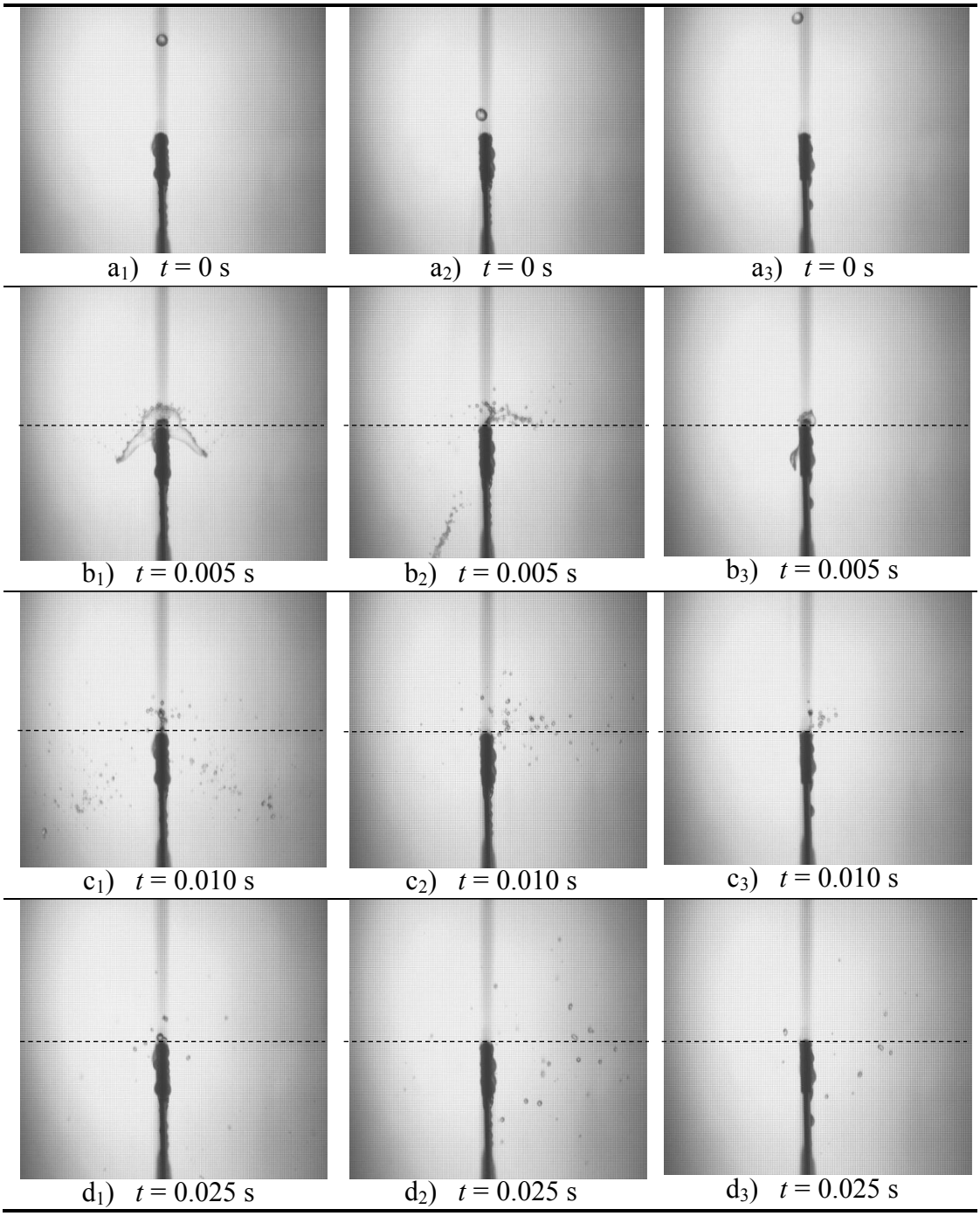

Figure B.27: Splash photographs (H_d = 970 mm, W = 3 mm, $d_i \approx$ 4 mm, $\delta = 0.85 \pm 0.1$ mm).

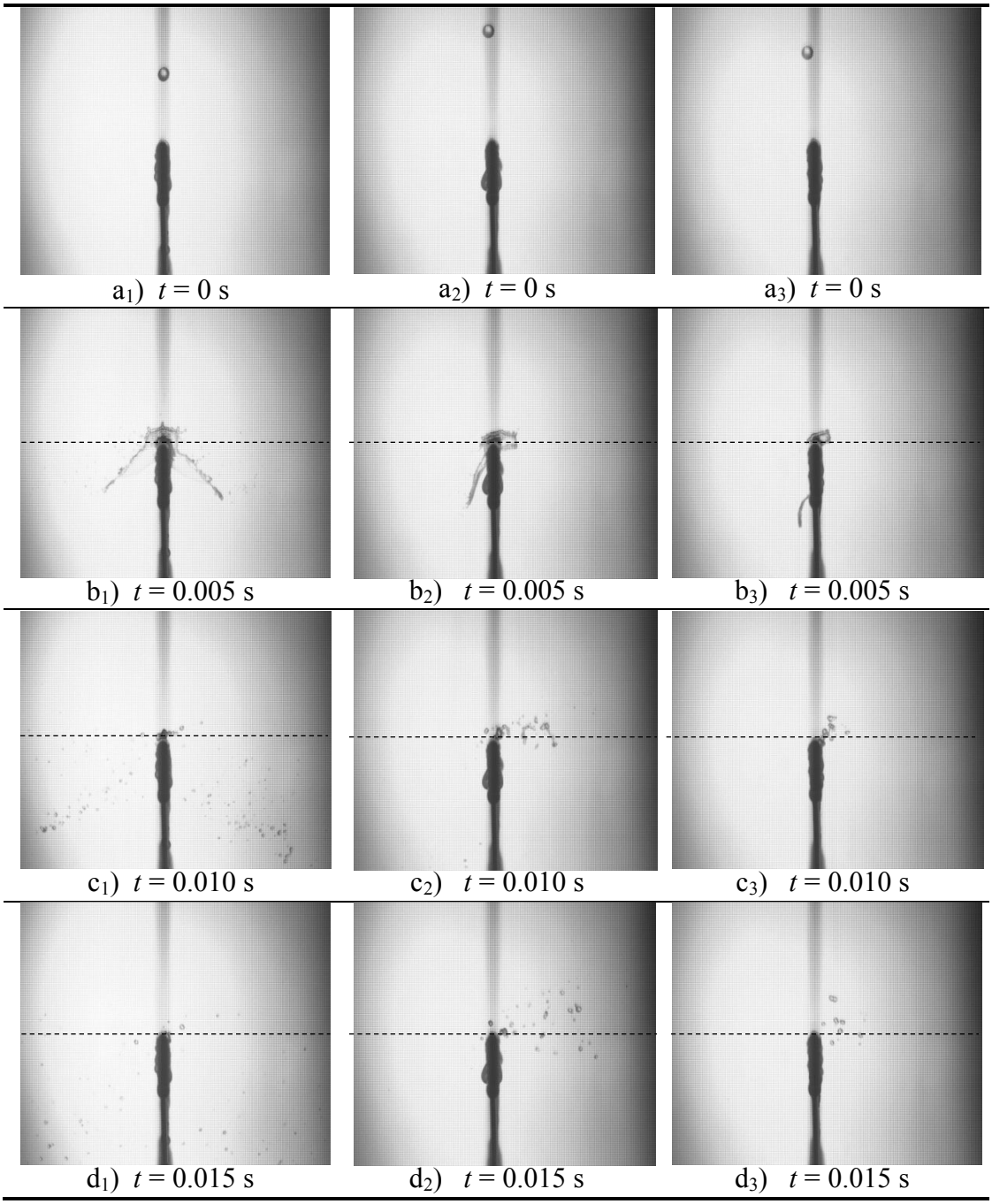

Figure B.28: Splash photographs (H_d = 970 mm, W = 3 mm, $d_i \approx$ 4 mm, $\delta = 1.32 \pm 0.15$ mm).

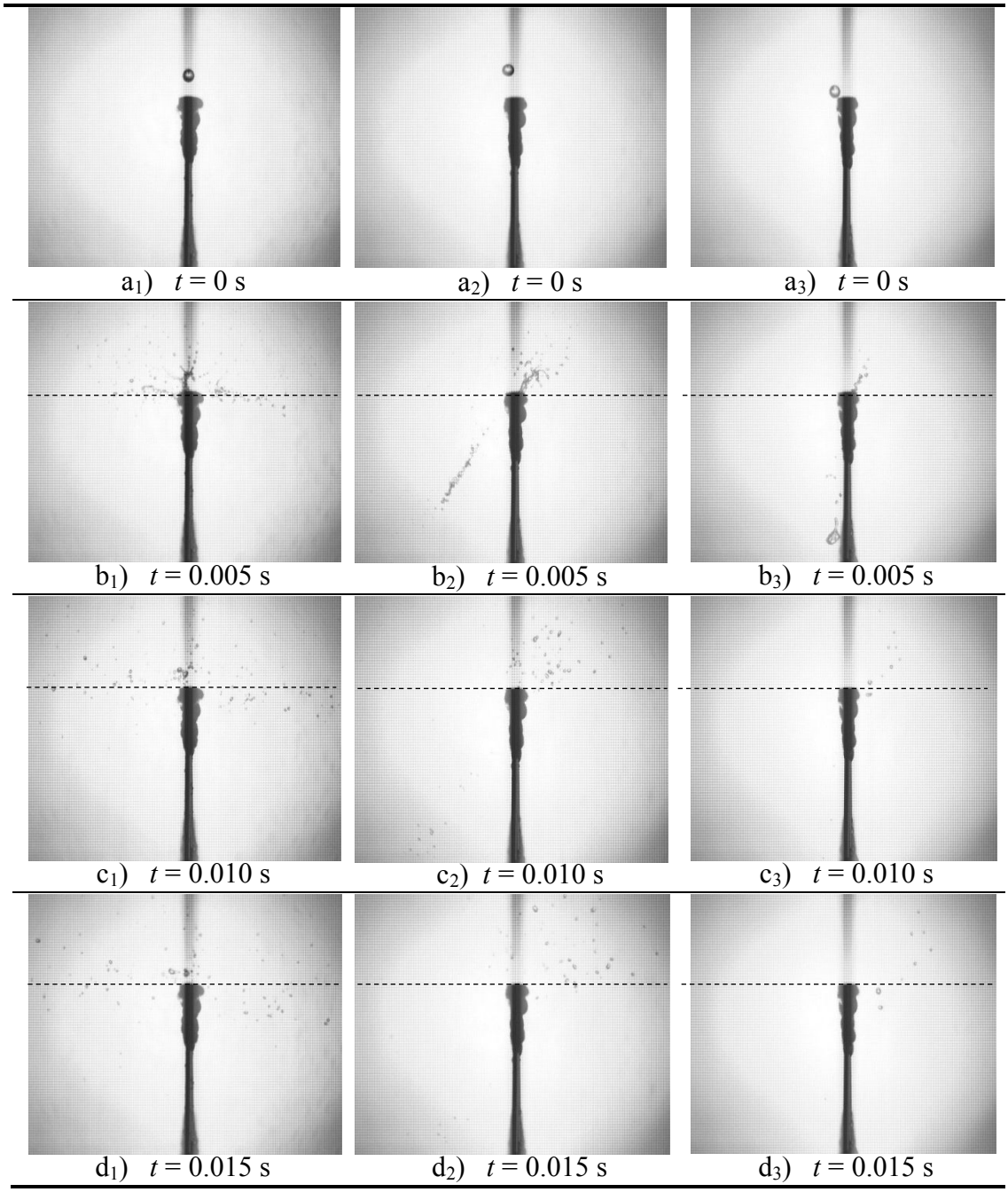

Figure B.29: Splash photographs (H_d = 970 mm, W = 6 mm, $d_i \approx$ 4 mm, $\delta = 0.50 \pm 0.12$ mm).

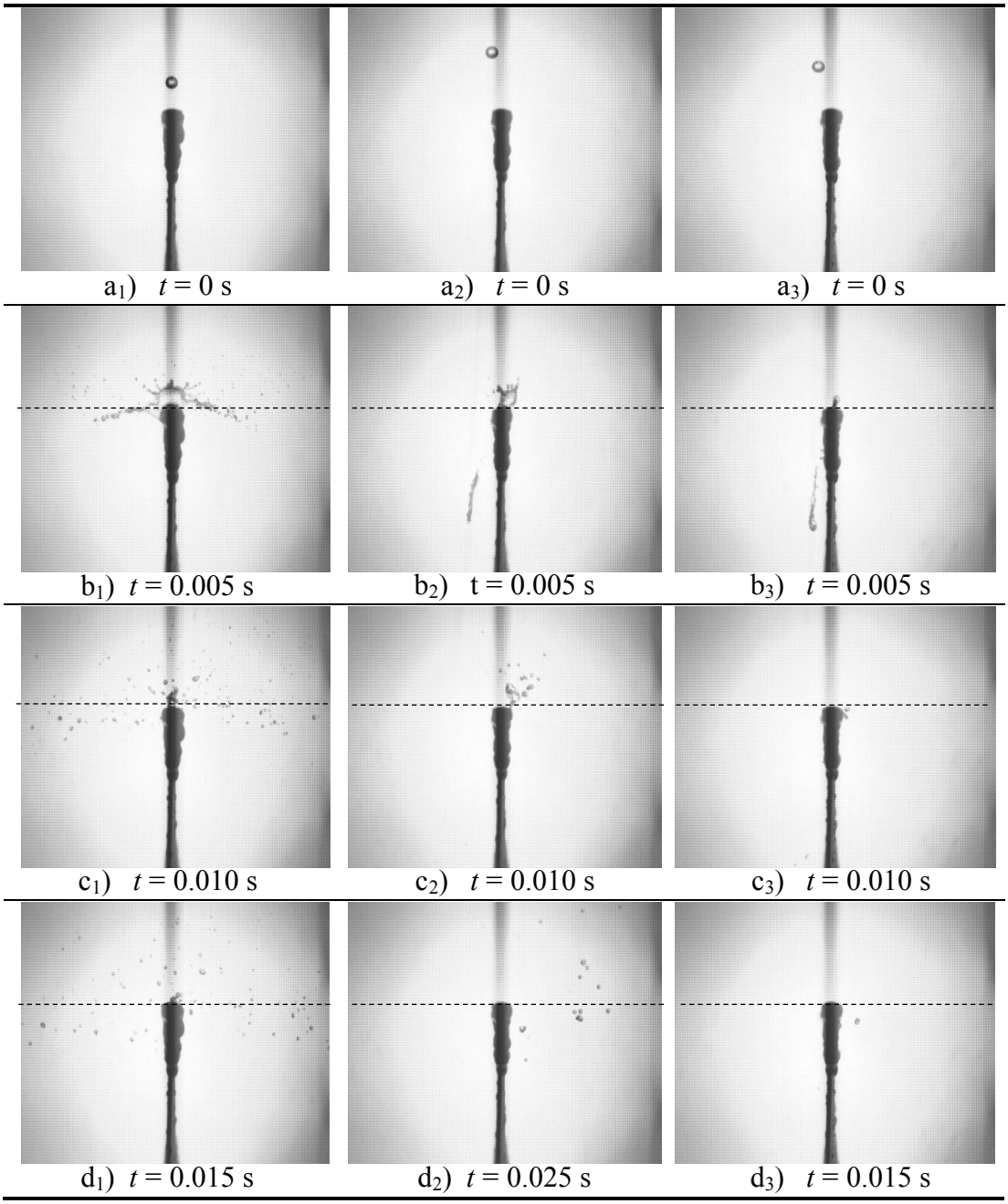

Figure B.30: Splash photographs (H_d = 970 mm, W = 6 mm, $d_i \approx$ 4 mm, $\delta = 0.84 \pm 0.10$ mm).

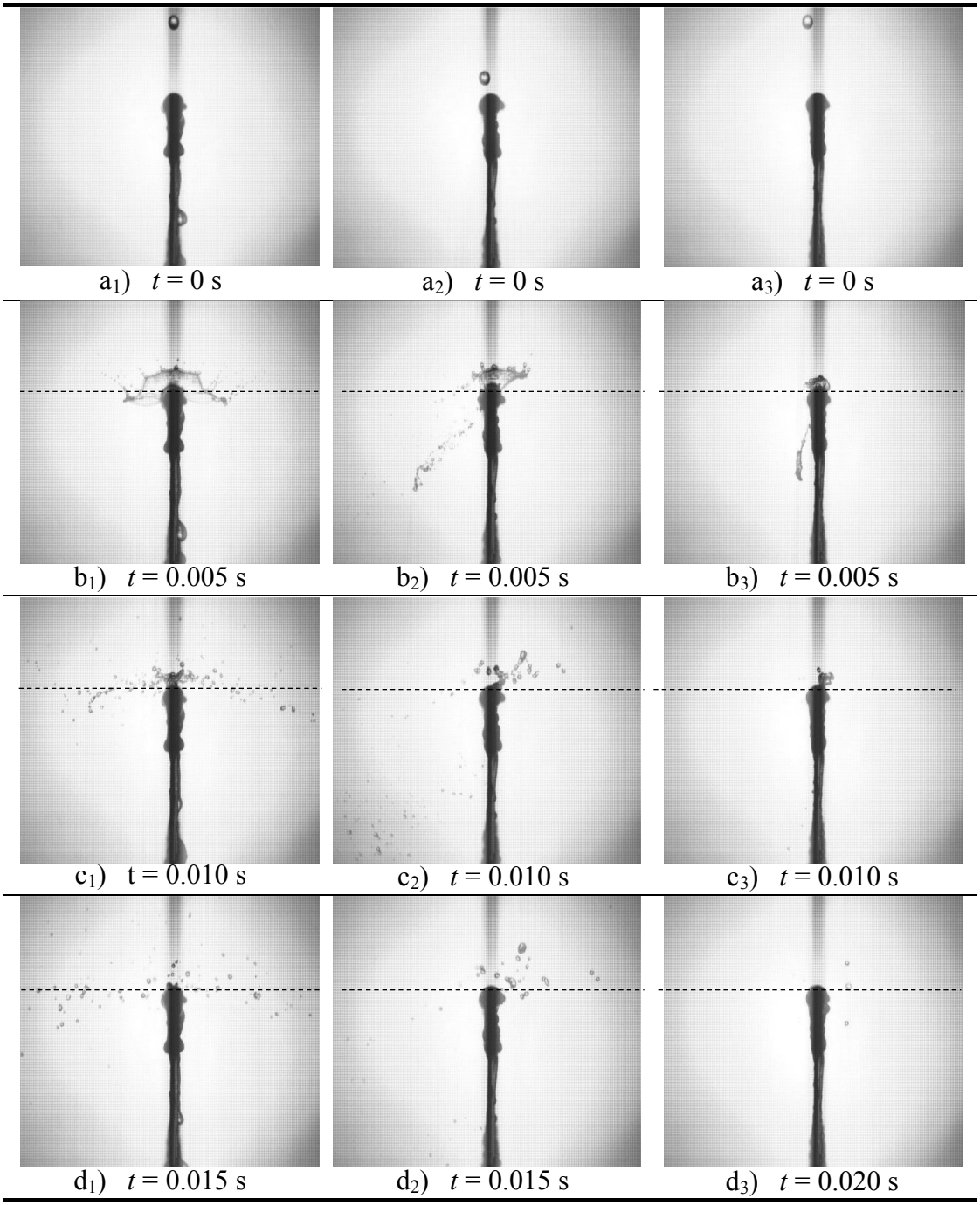

Figure B.31: Splash photographs (H_d = 970 mm, W = 6 mm, $d_i \approx$ 4 mm, $\delta = 1.43 \pm 0.10$ mm).

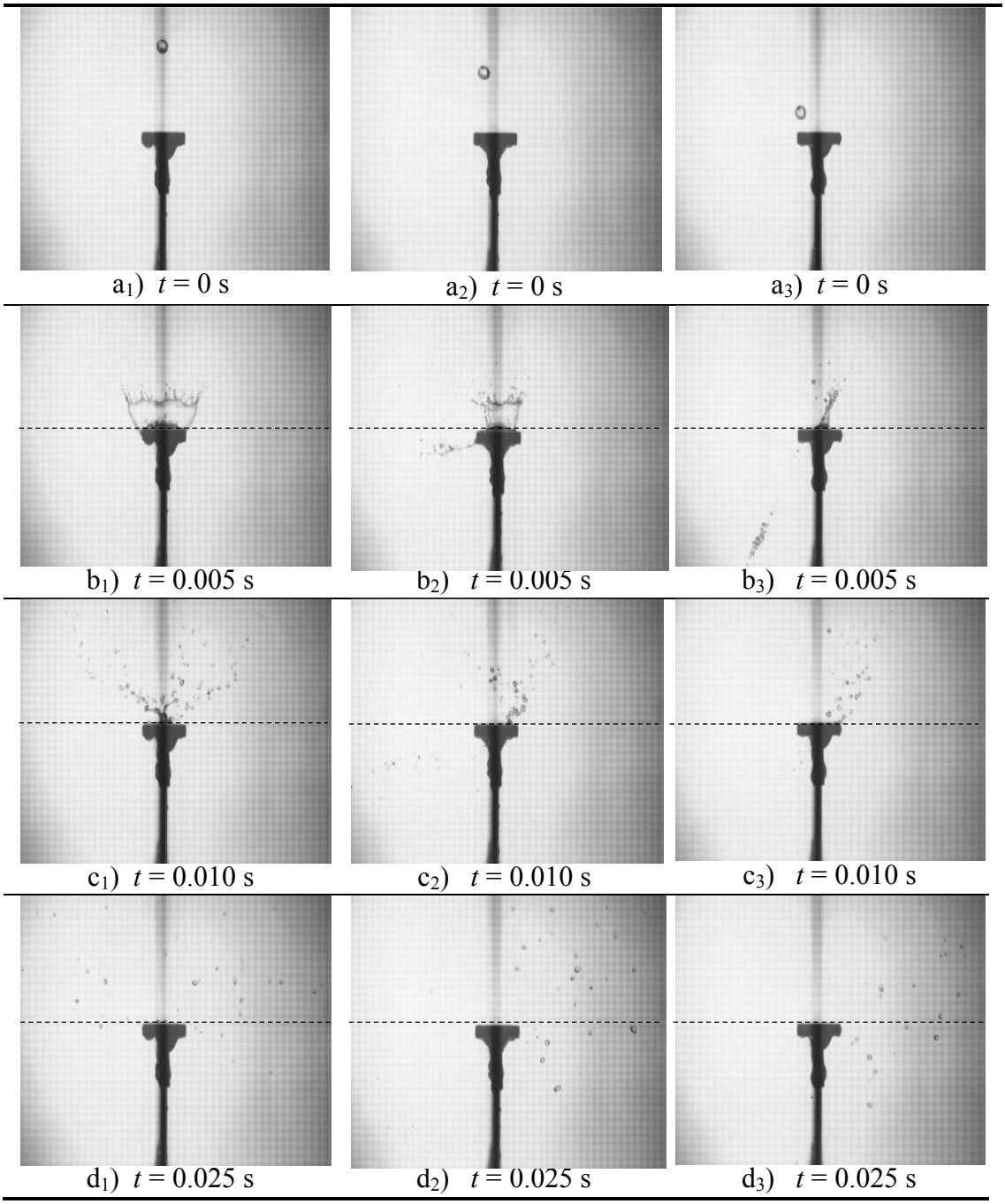

Figure B.32: Splash photographs (H_d = 970 mm, W = 12 mm, $d_i \approx$ 4 mm, $\delta = 0.21 \pm 0.15$ mm).

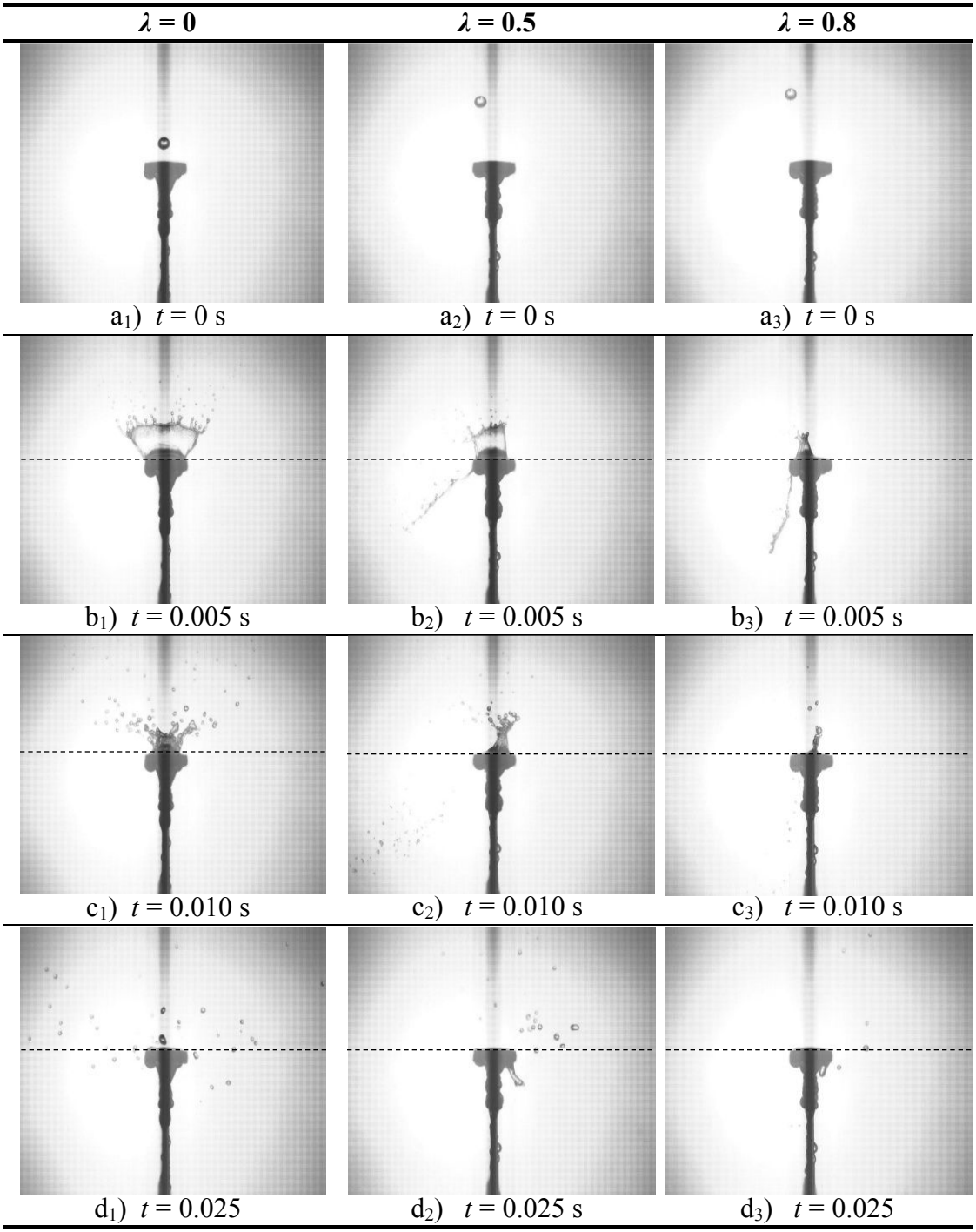

Figure B.33: Splash photographs (H_d = 970 mm, W = 12 mm, $d_i \approx$ 4 mm, $\delta = 0.95 \pm 0.15$ mm).

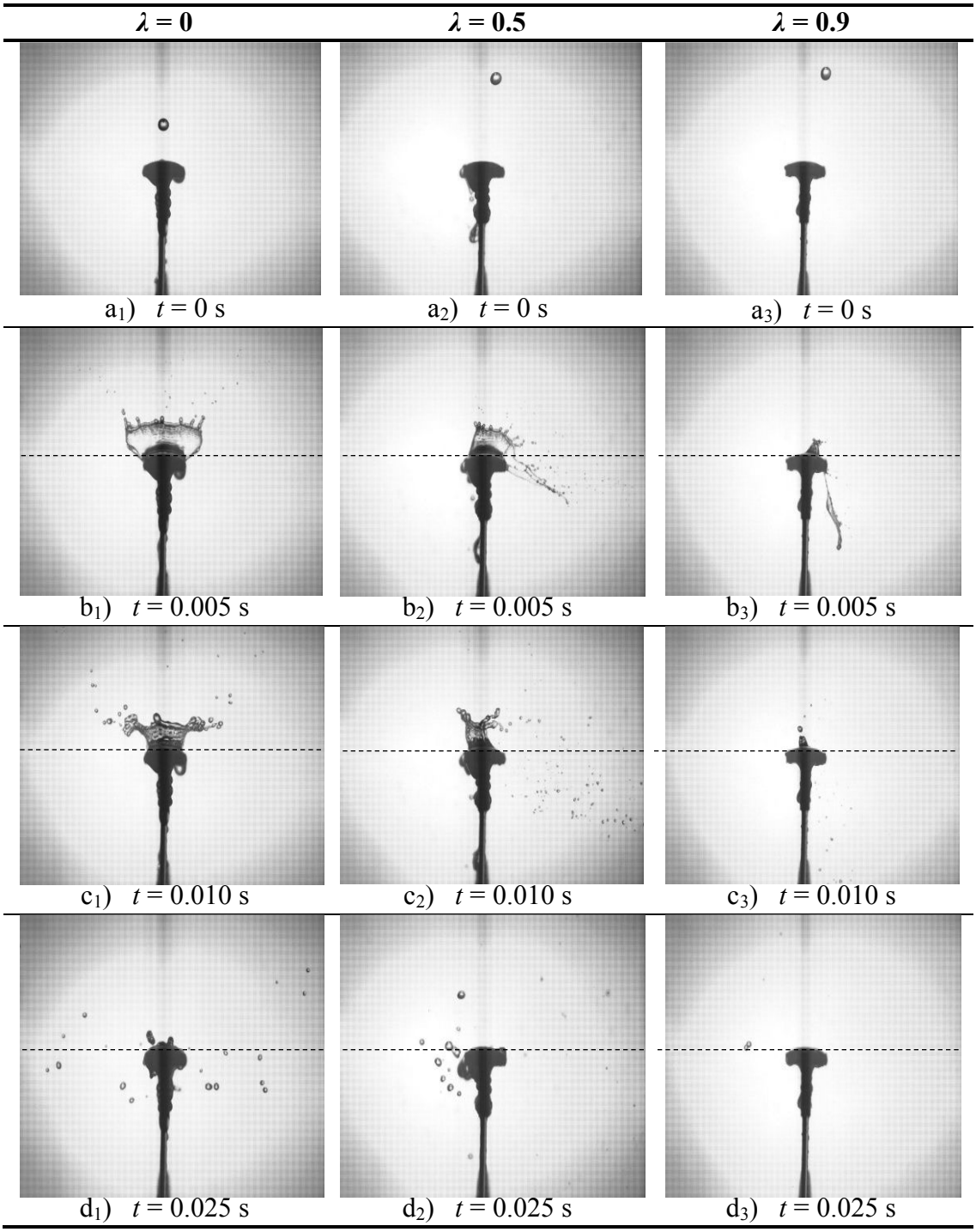

Figure B.34: Splash photographs (H_d = 970 mm, W = 12 mm, $d_i \approx$ 4 mm, δ = 1.75 ± 0.15 mm).

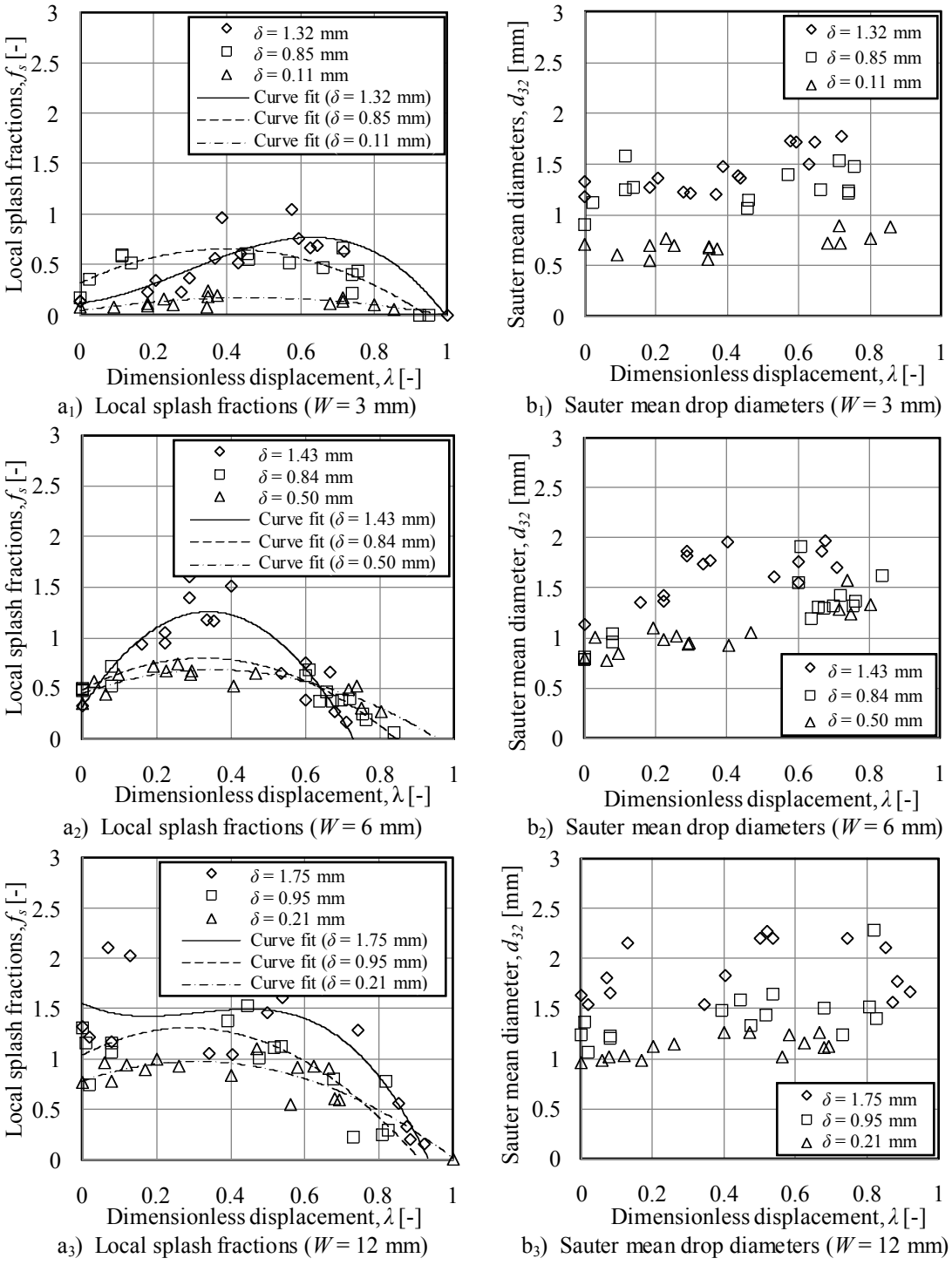

a$_1$) Local splash fractions (W = 3 mm)
b$_1$) Sauter mean drop diameters (W = 3 mm)
a$_2$) Local splash fractions (W = 6 mm)
b$_2$) Sauter mean drop diameters (W = 6 mm)
a$_3$) Local splash fractions (W = 12 mm)
b$_3$) Sauter mean drop diameters (W = 12 mm)

Figure B.35: Measured splash fractions and Sauter mean drop sizes (H_d = 970 mm, $d_i \approx$ 4 mm).

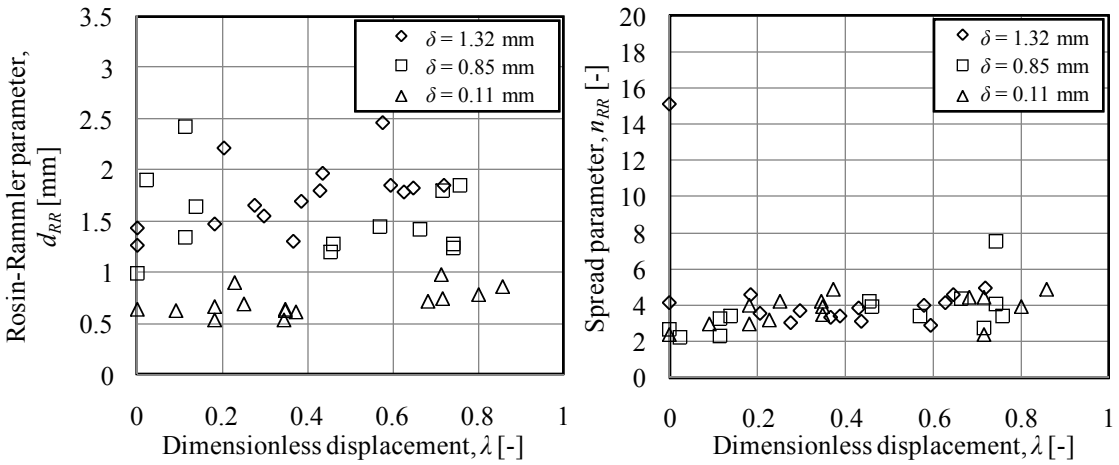

a$_1$) Rosin-Rammler parameter, d_{RR} (W = 3 mm) b$_1$) Spread parameter, n_{RR} (W = 3 mm)

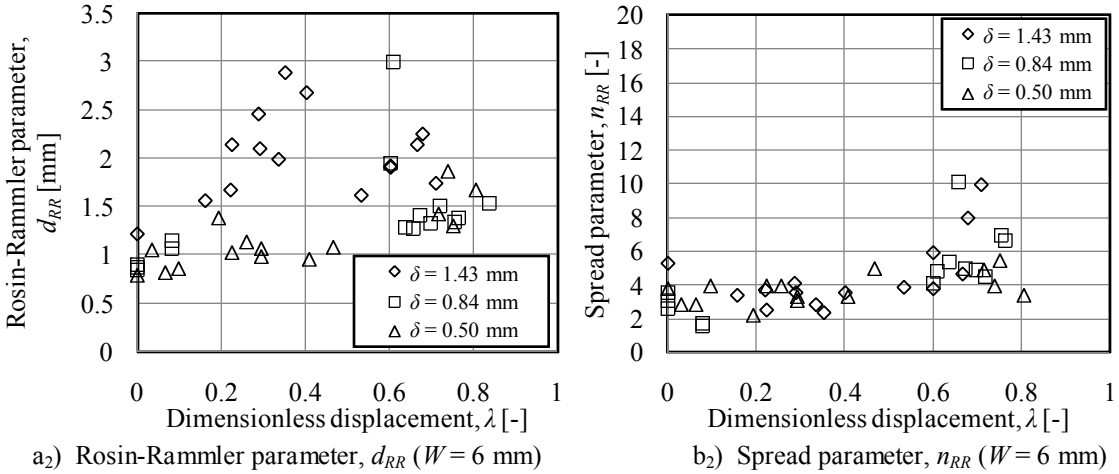

a$_2$) Rosin-Rammler parameter, d_{RR} (W = 6 mm) b$_2$) Spread parameter, n_{RR} (W = 6 mm)

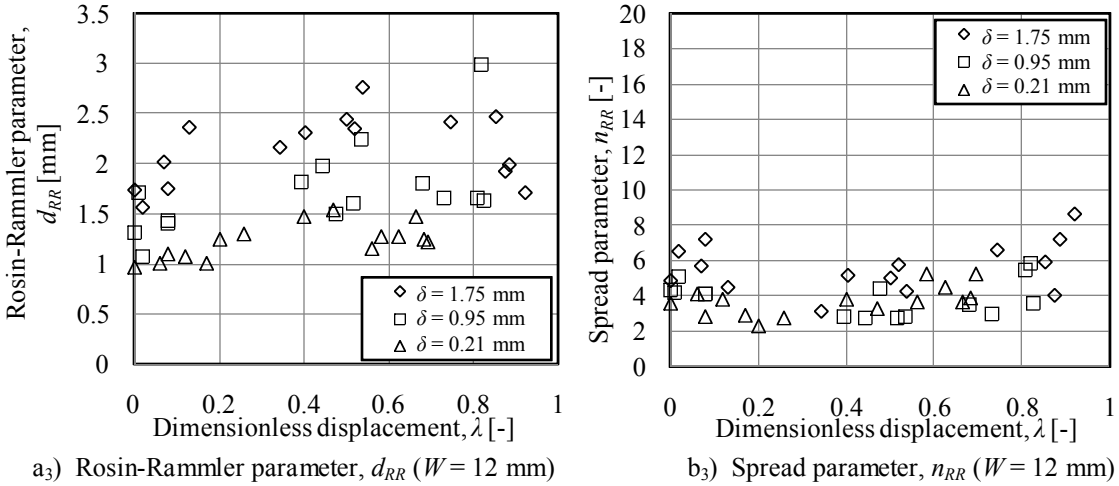

a$_3$) Rosin-Rammler parameter, d_{RR} (W = 12 mm) b$_3$) Spread parameter, n_{RR} (W = 12 mm)

Figure B.36: Measured Rosin-Rammler parameters (H_d = 970 mm, $d_i \approx$ 4 mm).

B.3.4 Splash results (H_d = 250 mm, d_i = 2.89 mm and d_i = 5.48 mm)

This section presents the splash results when a relatively small (d_i = 2.89 mm) and large drop (d_i = 5.48 mm), respectively, falls H_d = 250 mm before impinging onto different slats. Figures B.37 to B.42 show sequential photographs of drop impingements at different locations over the width of a slat for different drop size (d_i = 2.89 mm and d_i = 5.48 mm) and slat width (W = 3, W = 6 and W = 12 mm) combinations while the film thickness on each slat is constant. Figures B.43 and B.44 show plots of the measured local splash fractions, Sauter mean drop diameters and Rosin-Rammler parameters.

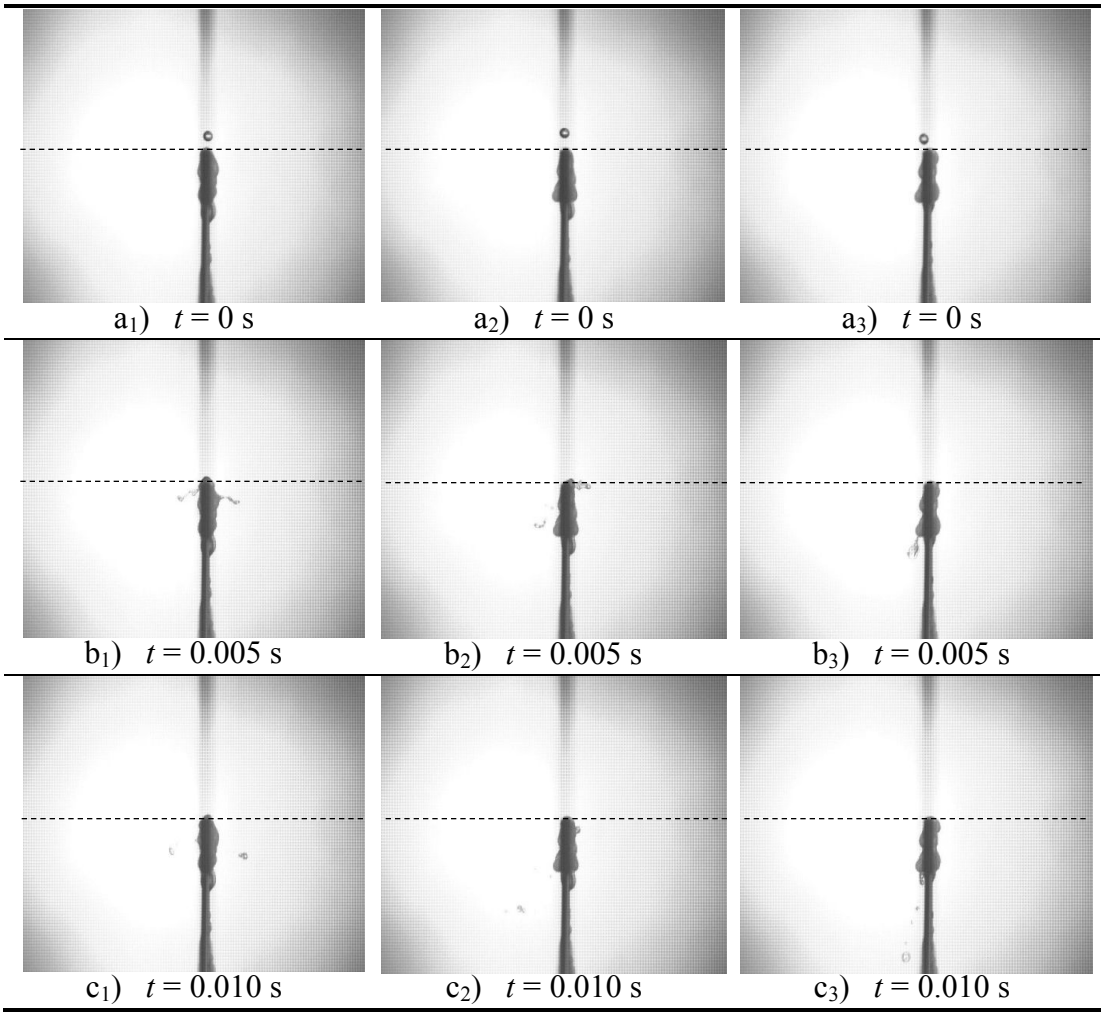

Figure B.37: Splash photographs (H_d = 250 mm, W = 3 mm, $d_i \approx$ 2.89 mm, δ = 1.00 ± 0.11 mm).

Figures B.38 and B.39 show that splashing is almost negligible on the W = 3 mm wide slat for both drop sizes at the current drop fall distance of H_d = 250 mm. For the d_i = 5.48 mm in diameter drop there seems to be an increase in splashing as the slat width increases (Figures B.40 and B.42).

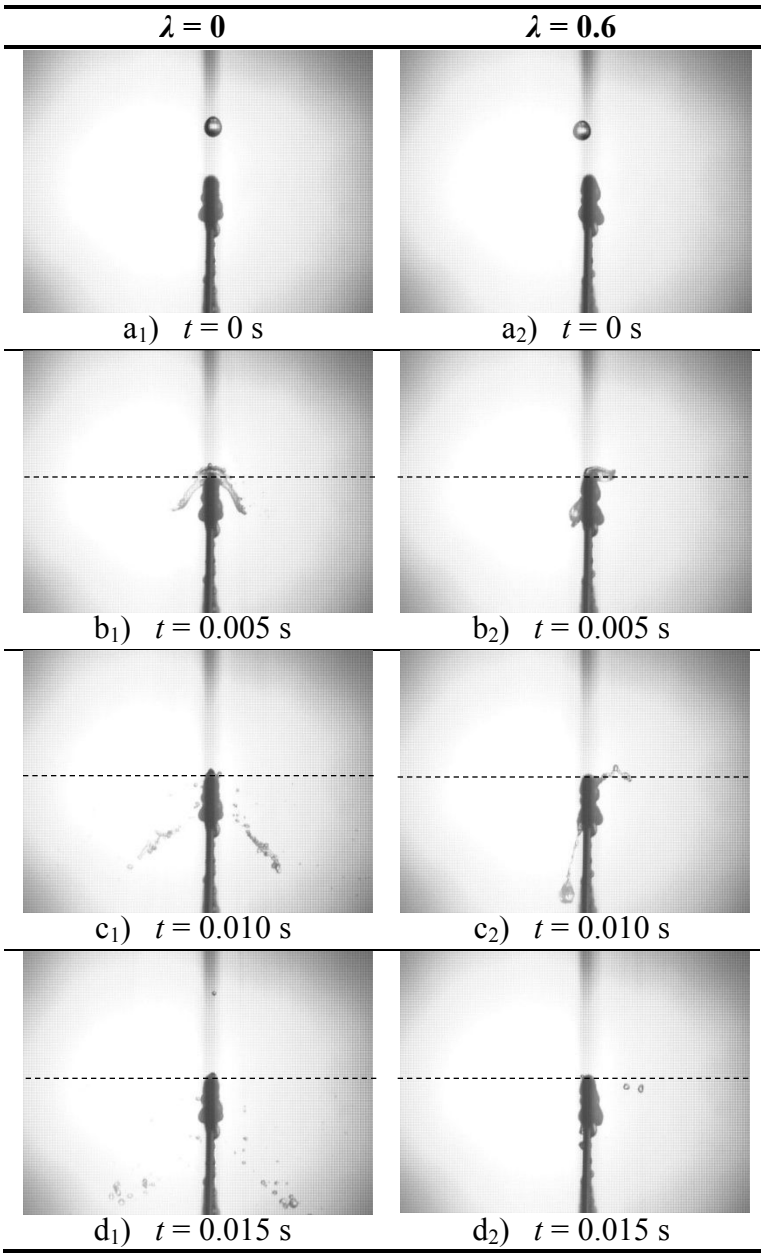

Figure B.38: Splash photographs (H_d = 250 mm, W = 3 mm, $d_i \approx$ 5.48 mm, δ = 1.00 ± 0.15 mm).

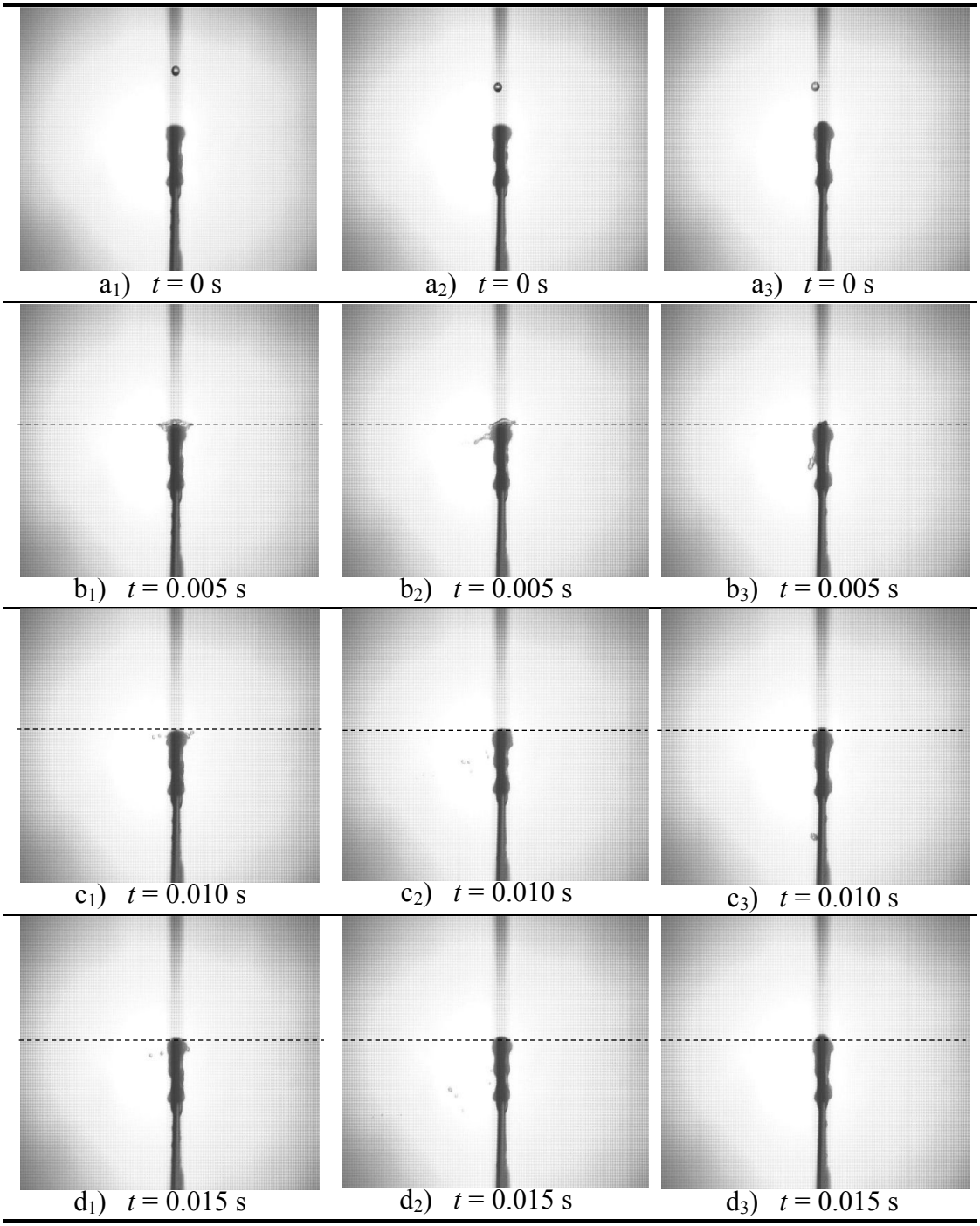

Figure B.39: Splash photographs (H_d = 250 mm, W = 6 mm, $d_i \approx$ 2.89 mm, $\delta = 0.85 \pm 0.11$ mm).

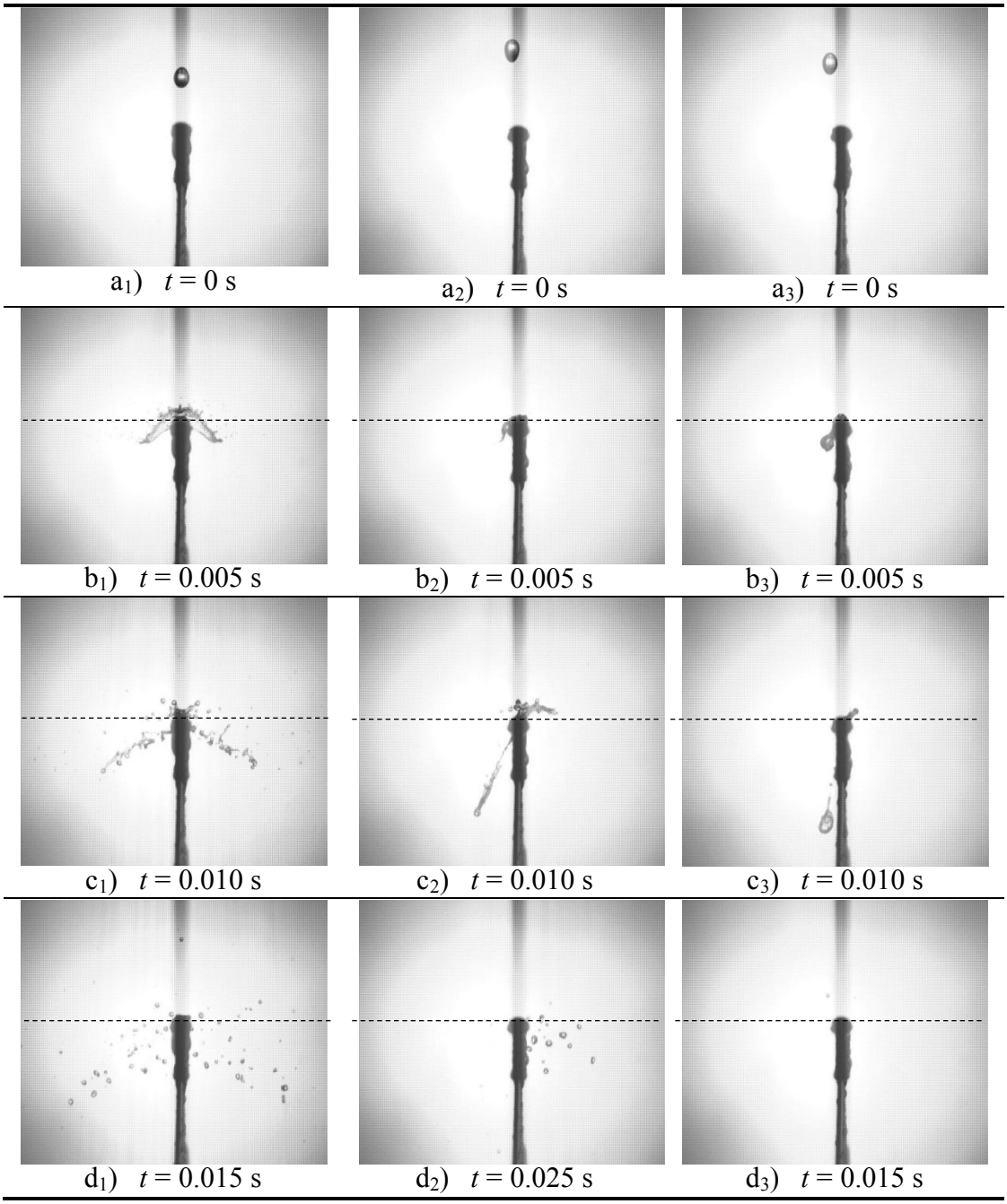

Figure B.40: Splash photographs (H_d = 250 mm, W = 6 mm, $d_i \approx$ 5.48 mm, $\delta = 0.85 \pm 0.15$ mm).

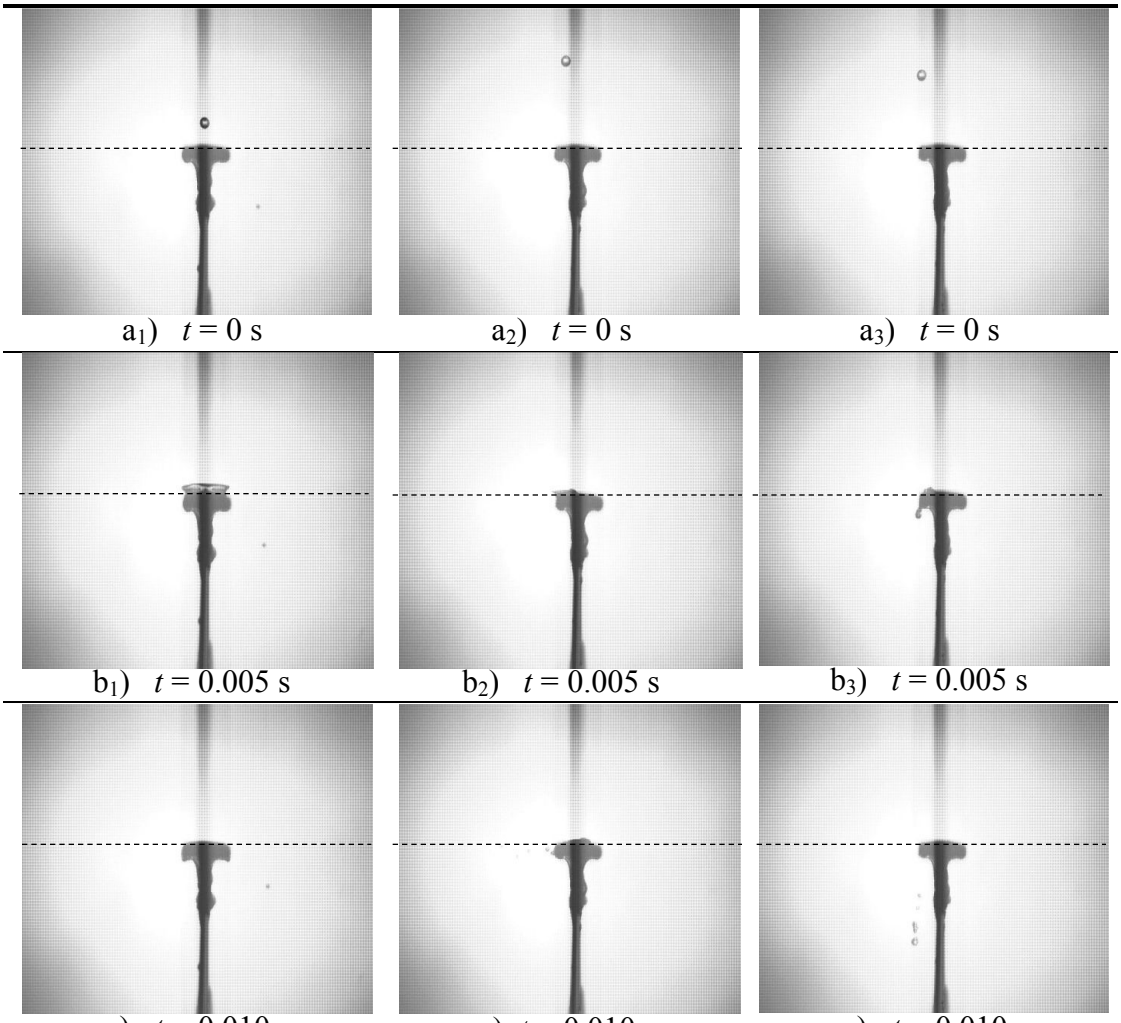

Figure B.41: Splash photographs (H_d = 250 mm, W = 12 mm, $d_i \approx$ 2.89 mm, $\delta = 0.78 \pm 0.15$ mm).

When water swings over the edge of the slat as seen in Figure B.42(d_2), but is unable to detach from the slat before it eventually detaches due to gravity at the bottom of the slat, the drops that form aren't considered to be splash drops but are associated with dripping.

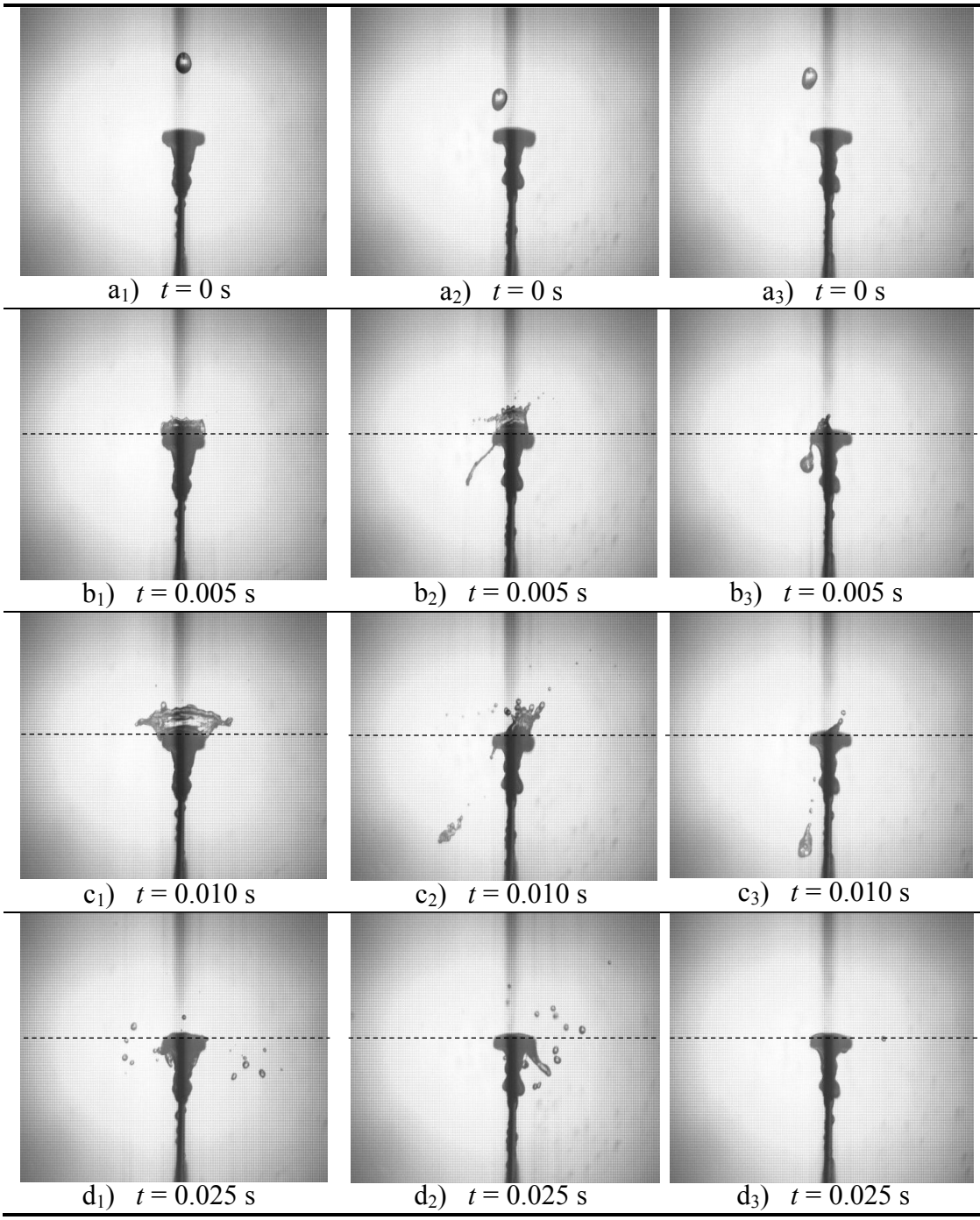

Figure B.42: Splash photographs (H_d = 250 mm, W = 12 mm, $d_i \approx$ 5.48 mm, $\delta = 0.78 \pm 0.12$ mm).

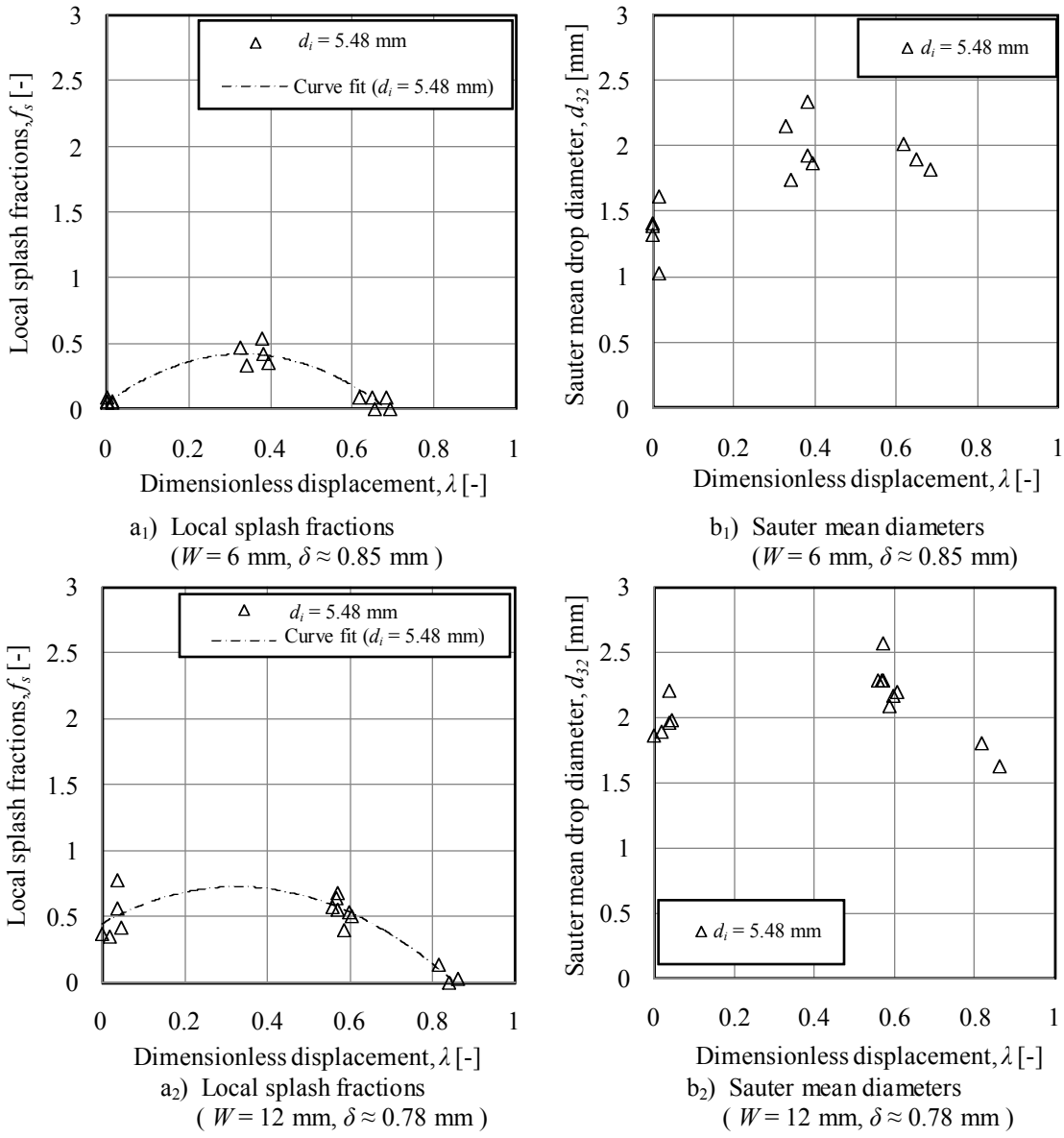

a$_1$) Local splash fractions (W = 6 mm, $\delta \approx$ 0.85 mm)

b$_1$) Sauter mean diameters (W = 6 mm, $\delta \approx$ 0.85 mm)

a$_2$) Local splash fractions (W = 12 mm, $\delta \approx$ 0.78 mm)

b$_2$) Sauter mean diameters (W = 12 mm, $\delta \approx$ 0.78 mm)

Figure B.43: Measured splash fractions and Sauter mean drop sizes (H_d = 250 mm, d_i = 2.89 mm and d_i = 5.48 mm).

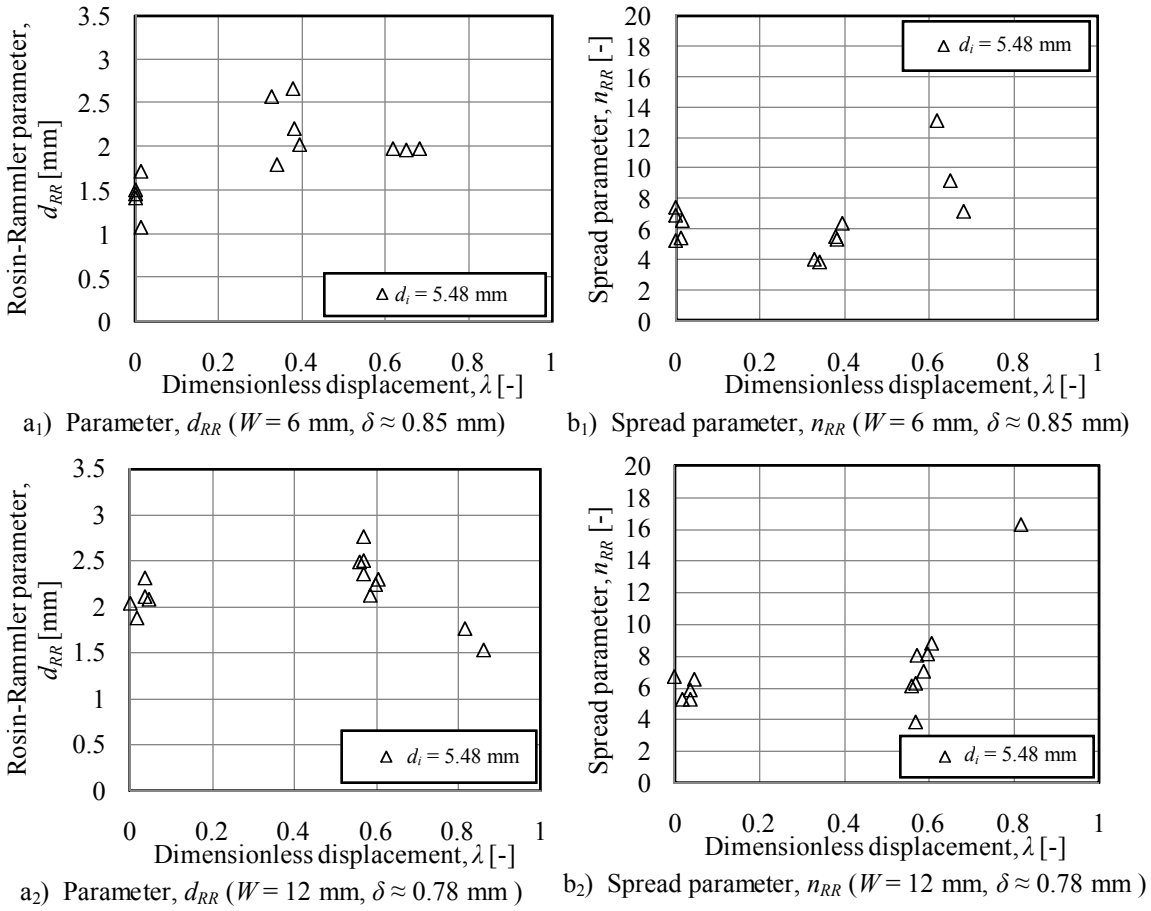

a$_1$) Parameter, d_{RR} (W = 6 mm, $\delta \approx$ 0.85 mm)

b$_1$) Spread parameter, n_{RR} (W = 6 mm, $\delta \approx$ 0.85 mm)

a$_2$) Parameter, d_{RR} (W = 12 mm, $\delta \approx$ 0.78 mm)

b$_2$) Spread parameter, n_{RR} (W = 12 mm, $\delta \approx$ 0.78 mm)

Figure B.44: Rosin-Rammler parameters (H_d = 250 mm, d_i = 2.89 mm and d_i = 5.48 mm).

B.3.5 Splash results (H_d = 470 mm, d_i = 2.89 mm and d_i = 5.48 mm)

This section presents the splash results when a relatively small (d_i = 2.89 mm) and large drop (d_i = 5.48 mm), respectively, falls H_d = 470 mm before impinging onto different slats. Figures B.45 to B.50 show sequential photographs of drop impingements at different locations over the width of a slat for different drop size (d_i = 2.89 mm and d_i = 5.48 mm) and slat width (W = 3, W = 6 and W = 12 mm) combinations while the film thickness on each slat is constant. Figures B.51 and B.52 show plots of the measured local splash fractions, Sauter mean drop diameters and Rosin-Rammler parameters. Note that the water that falls back onto the slat after splashing, shown in Figure B.48(b$_1$ to d$_1$) is not taken into account when splashing is determined.

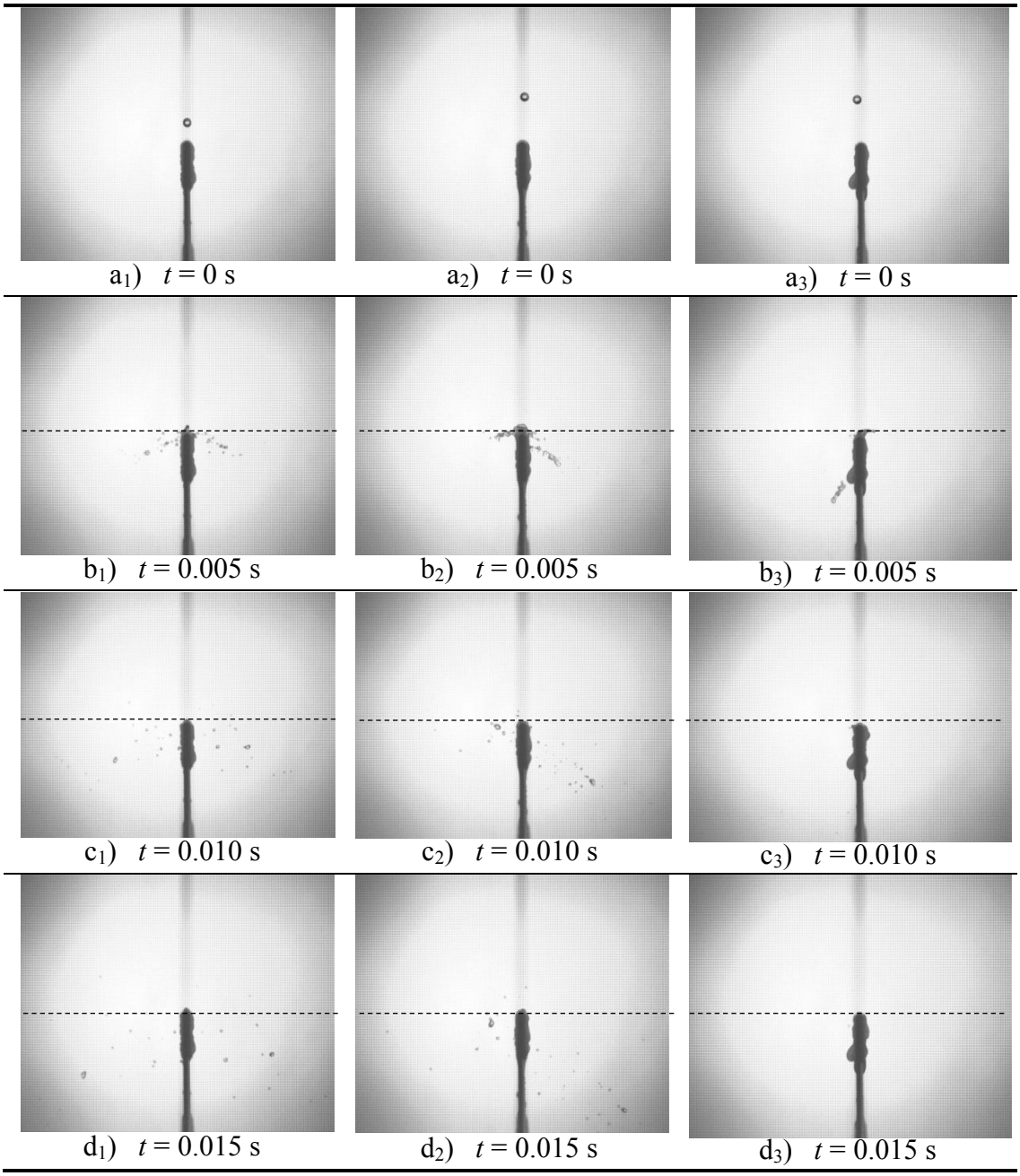

Figure B.45: Splash photographs (H_d = 470 mm, W = 3 mm, $d_i \approx$ 2.89 mm, $\delta = 1.00 \pm 0.15$ mm).

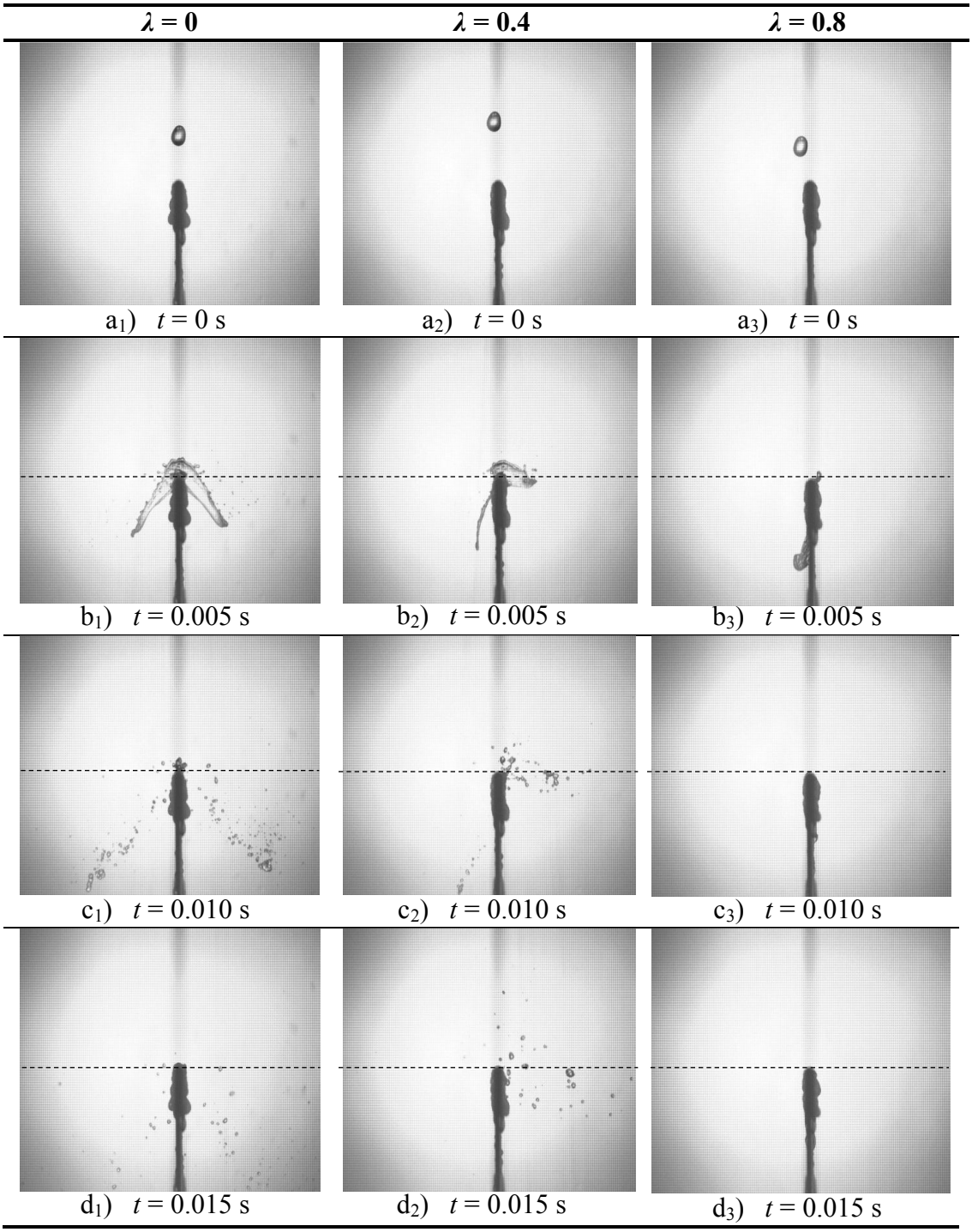

Figure B.46: Splash photographs (H_d = 470 mm, W = 3 mm, $d_i \approx$ 5.48 mm, δ = 1.00 ± 0.14 mm).

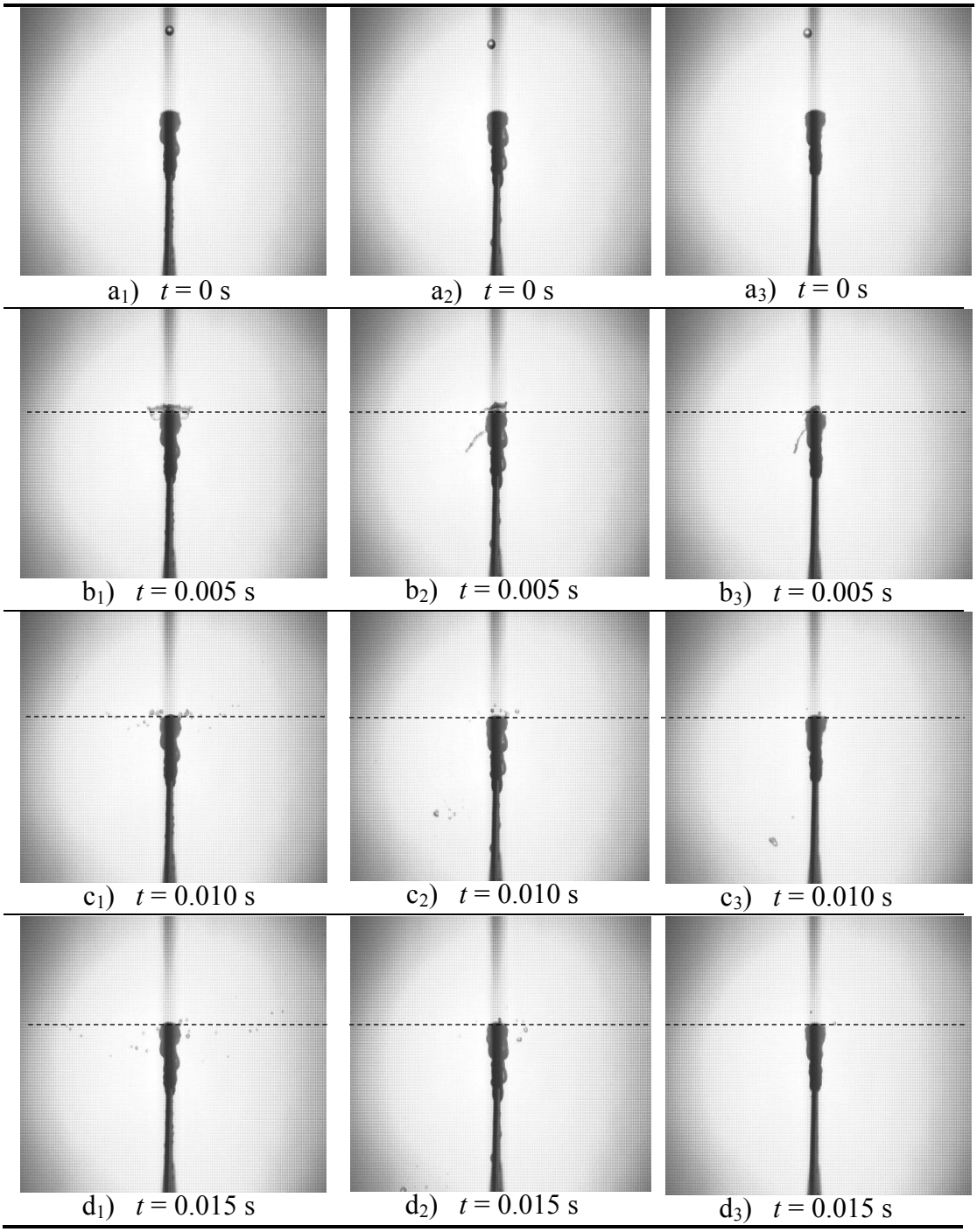

Figure B.47: Splash photographs (H_d = 470 mm, W = 6 mm, $d_i \approx$ 2.89 mm, $\delta = 0.85 \pm 0.2$ mm).

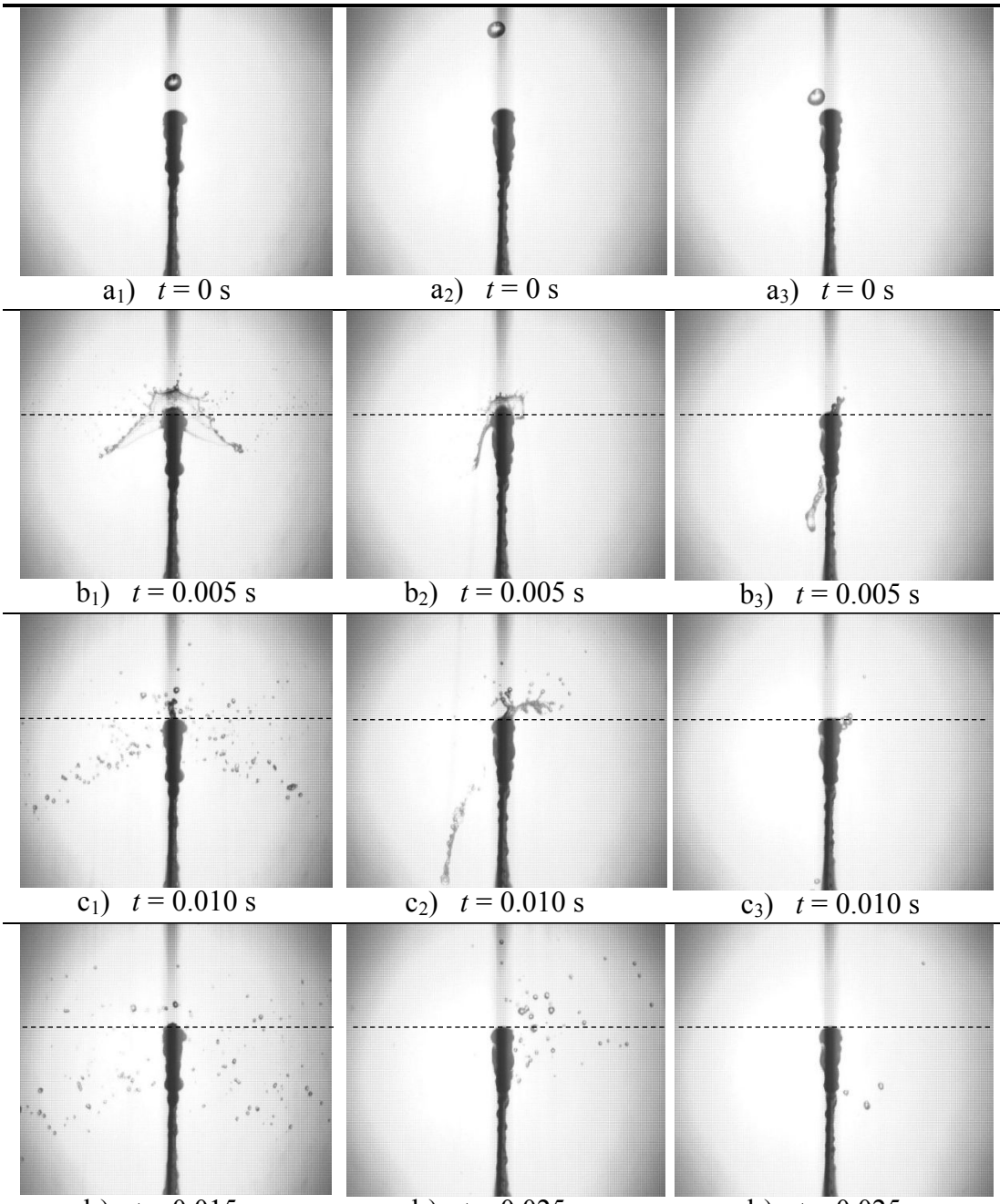

Figure B.48: Splash photographs (H_d = 470 mm, W = 6 mm, $d_i \approx$ 5.48 mm, $\delta = 0.85 \pm 0.25$ mm).

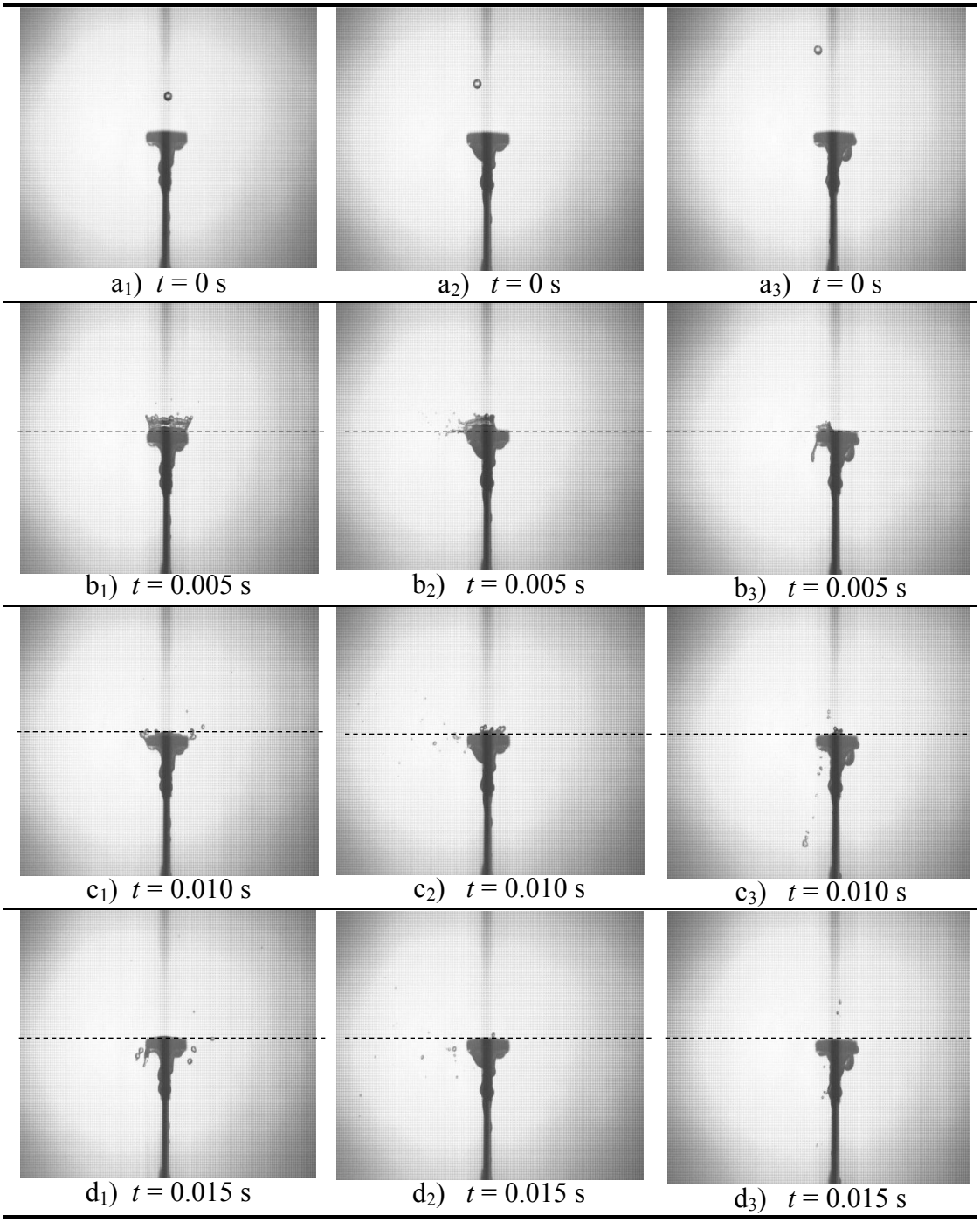

Figure B.49: Splash photographs (H_d = 470 mm, W = 12 mm, $d_i \approx$ 2.89 mm, $\delta = 0.78 \pm 0.1$ mm).

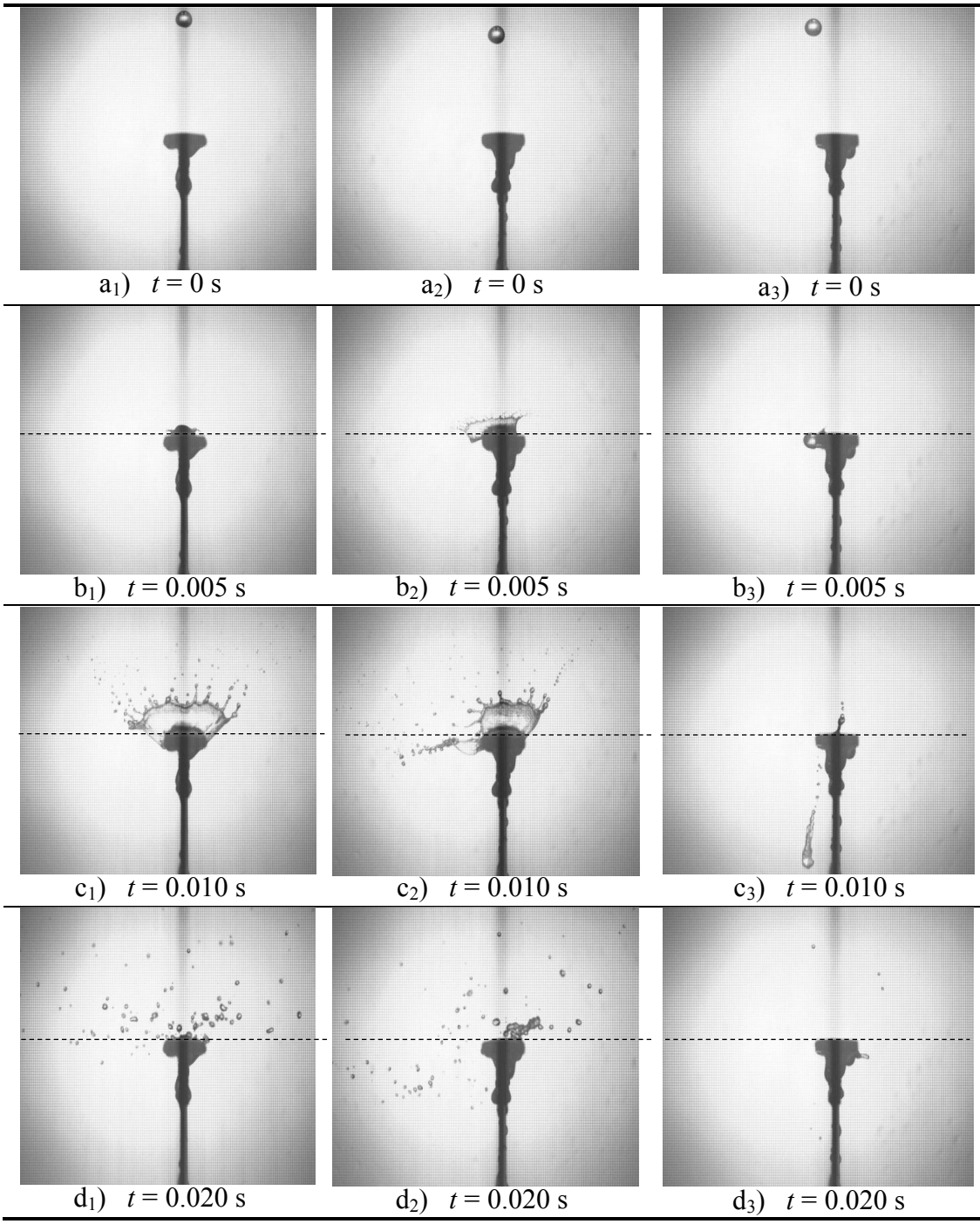

Figure B.50: Splash photographs (H_d = 470 mm, W = 12 mm, $d_i \approx$ 5.48 mm, $\delta = 0.78 \pm 0.1$ mm).

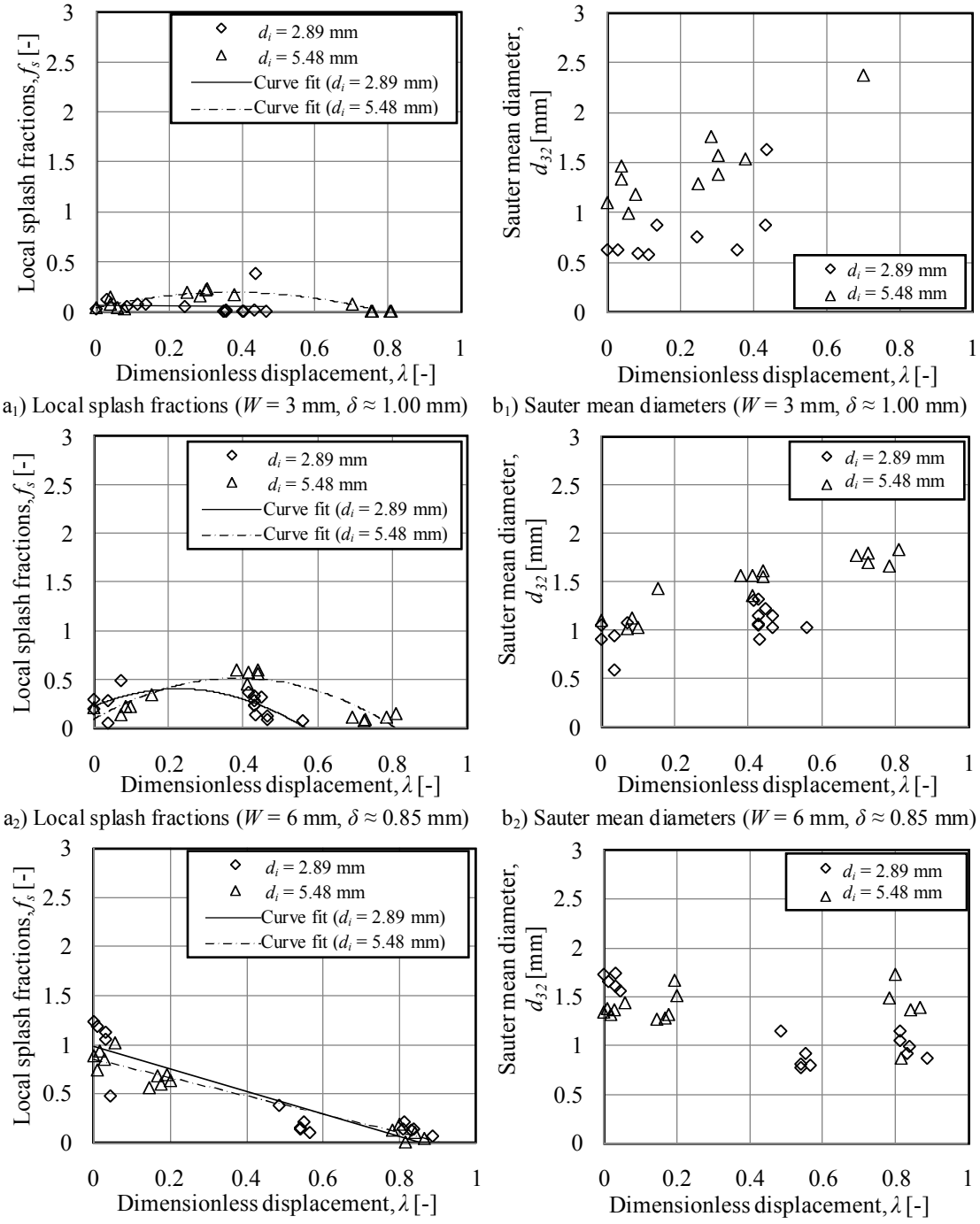

a$_1$) Local splash fractions (W = 3 mm, $\delta \approx$ 1.00 mm) b$_1$) Sauter mean diameters (W = 3 mm, $\delta \approx$ 1.00 mm)

a$_2$) Local splash fractions (W = 6 mm, $\delta \approx$ 0.85 mm) b$_2$) Sauter mean diameters (W = 6 mm, $\delta \approx$ 0.85 mm)

a$_3$) Local splash fractions (W = 12 mm, $\delta \approx$ 0.78 mm) b$_3$) Sauter mean diameters (W = 12 mm, $\delta \approx$ 0.78 mm)

Figure B.51: Measured splash fractions and Sauter mean drop sizes (H_d = 470 mm, $d_i \approx$ 2.89 mm and $d_i \approx$ 5.48 mm).

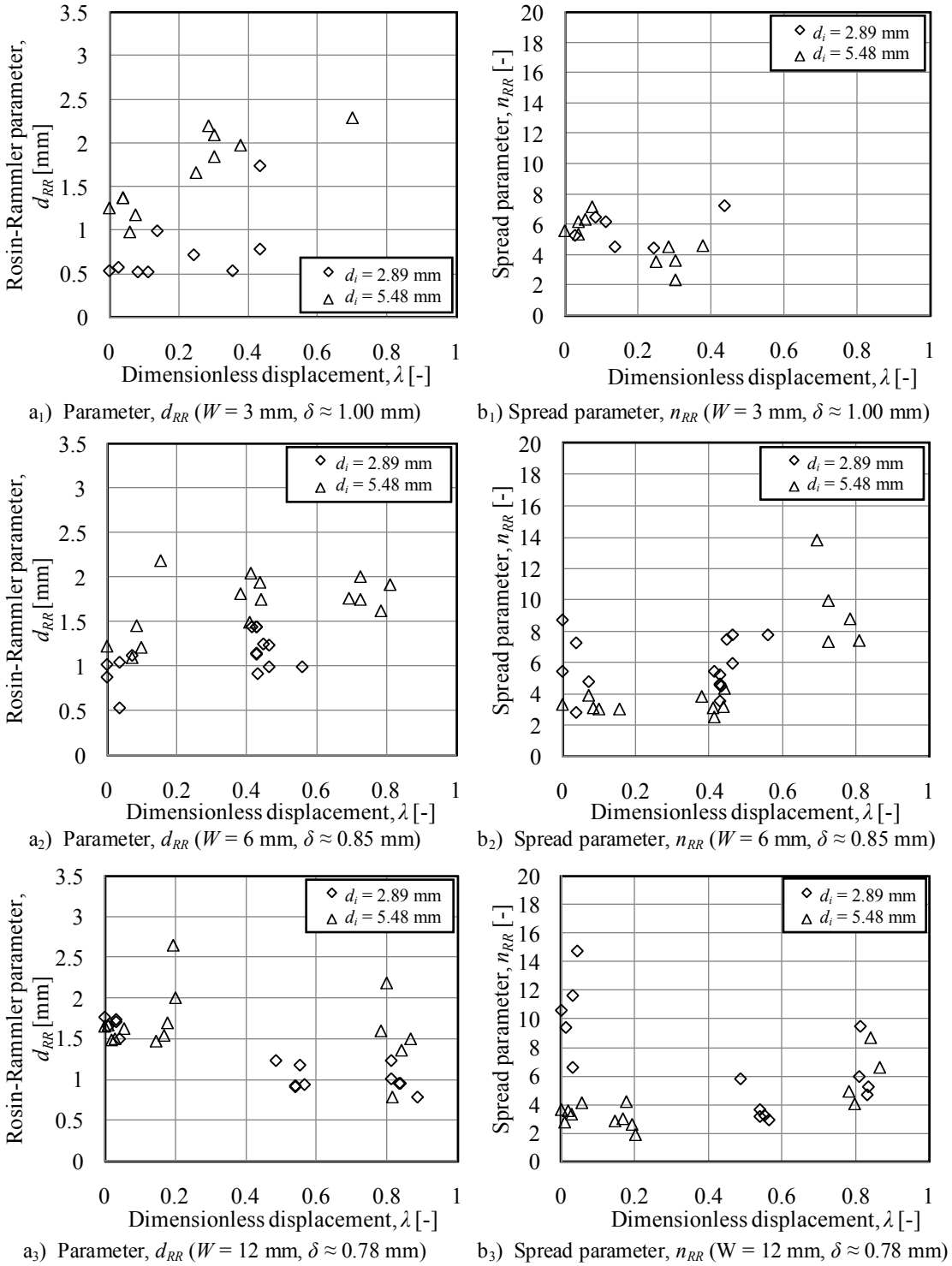

a$_1$) Parameter, d_{RR} (W = 3 mm, $\delta \approx$ 1.00 mm) b$_1$) Spread parameter, n_{RR} (W = 3 mm, $\delta \approx$ 1.00 mm)

a$_2$) Parameter, d_{RR} (W = 6 mm, $\delta \approx$ 0.85 mm) b$_2$) Spread parameter, n_{RR} (W = 6 mm, $\delta \approx$ 0.85 mm)

a$_3$) Parameter, d_{RR} (W = 12 mm, $\delta \approx$ 0.78 mm) b$_3$) Spread parameter, n_{RR} (W = 12 mm, $\delta \approx$ 0.78 mm)

Figure B.52: Rosin-Rammler parameters (H_d = 470 mm, d_i = 2.89 mm and d_i = 5.48 mm).

B.3.6 Splash results (H_d = 970 mm, d_i = 2.89 mm and d_i = 5.48 mm)

This section presents the splash results when a relatively small (d_i = 2.89 mm) and large drop (d_i = 5.48 mm), respectively, falls H_d = 970 mm before impinging onto different slats. Figures B.53 to B.58 show sequential photographs of drop impingements at different locations over the width of a slat for different drop size (d_i = 2.89 mm and d_i = 5.48 mm) and slat width (W = 3, W = 6 and W = 12 mm) combinations while the film thickness on each slat is constant. Figures B.59 and B.60 show plots of the measured local splash fractions, Sauter mean drop diameters and Rosin-Rammler parameters.

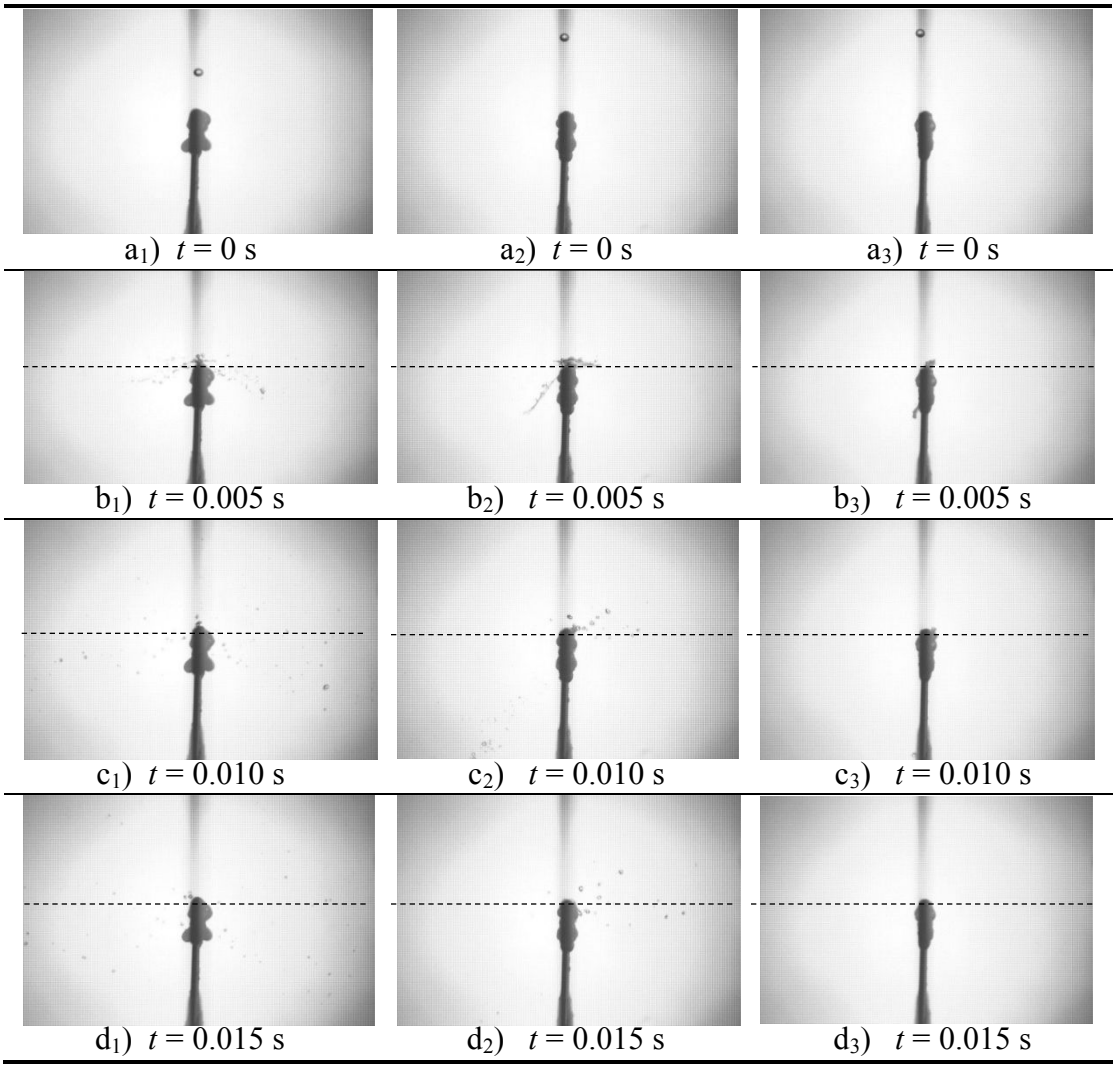

Figure B.53: Splash photographs (H_d = 970 mm, W = 3 mm, $d_i \approx$ 2.89 mm, δ = 1.00 ± 0.2 mm).

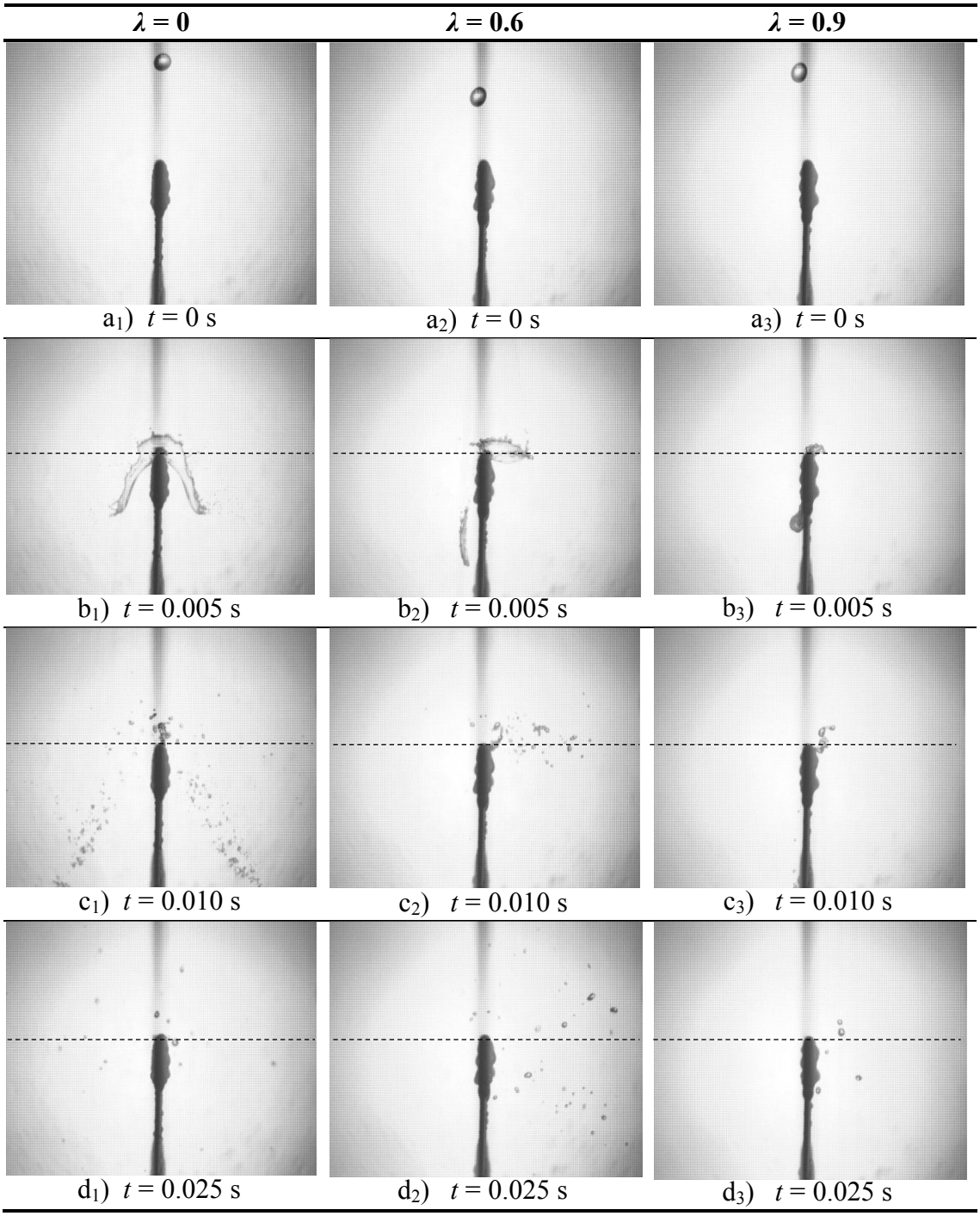

Figure B.54: Splash photographs (H_d = 970 mm, W = 3 mm, $d_i \approx$ 5.48 mm, δ = 1.00 ± 0.2 mm).

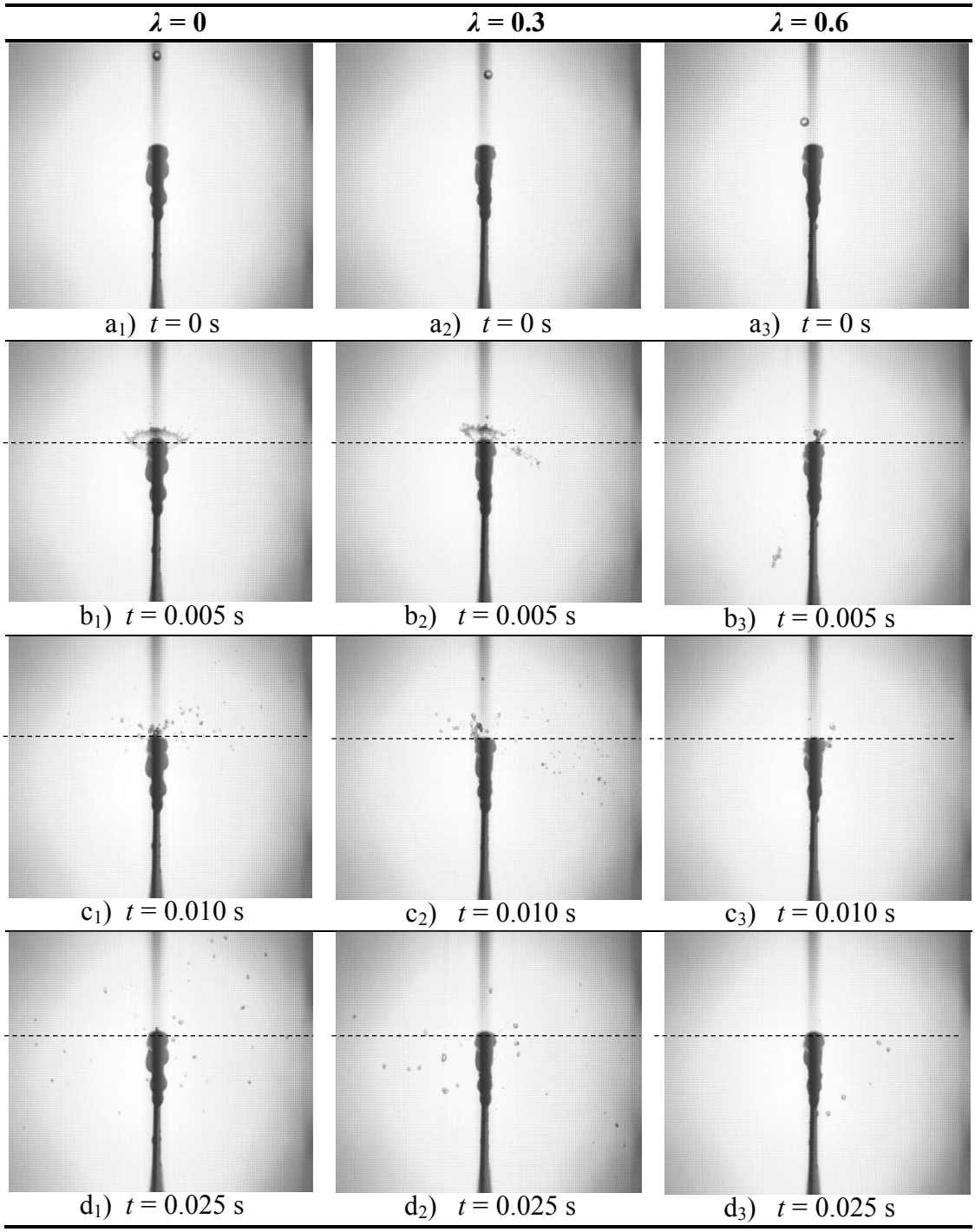

Figure B.55: Splash photographs (H_d = 970 mm, W = 6 mm, $d_i \approx$ 2.89 mm, $\delta = 0.85 \pm 0.1$ mm).

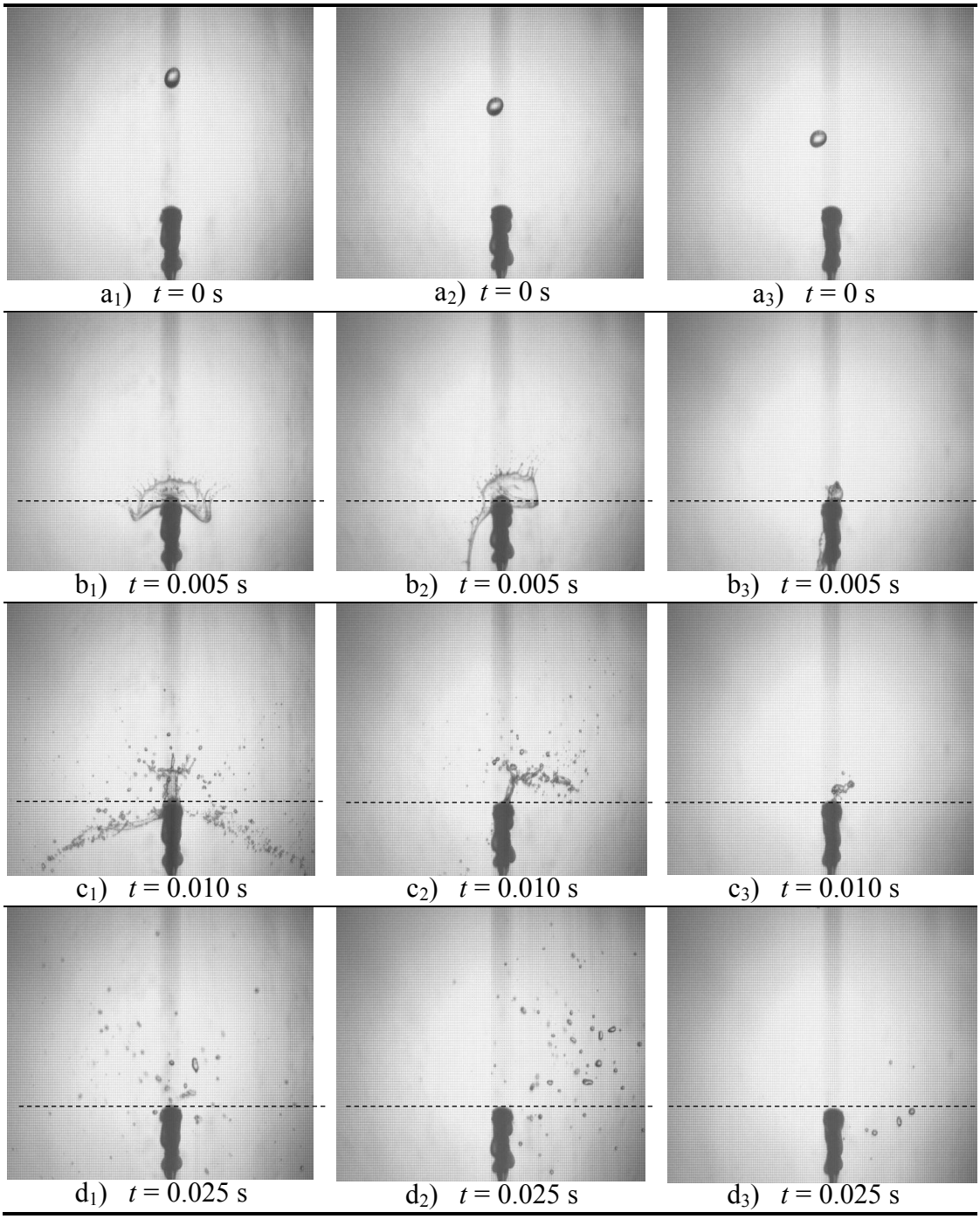

Figure B.56: Splash photographs (H_d = 970 mm, W = 6 mm, $d_i \approx$ 5.48 mm, $\delta = 0.85 \pm 0.2$ mm).

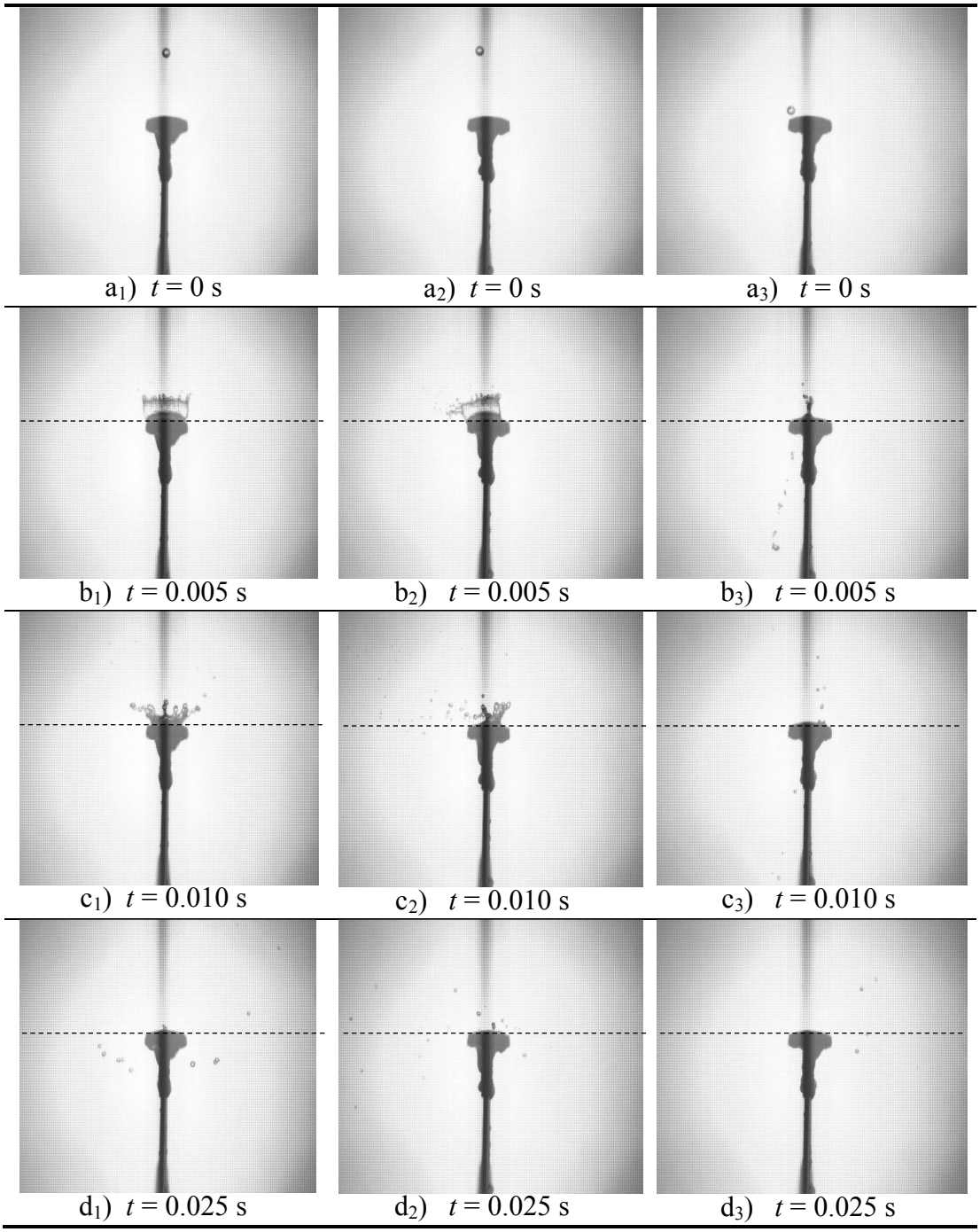

Figure B.57: Splash photographs (H_d = 970 mm, W = 12 mm, $d_i \approx$ 2.89 mm, $\delta = 0.78 \pm 0.24$ mm).

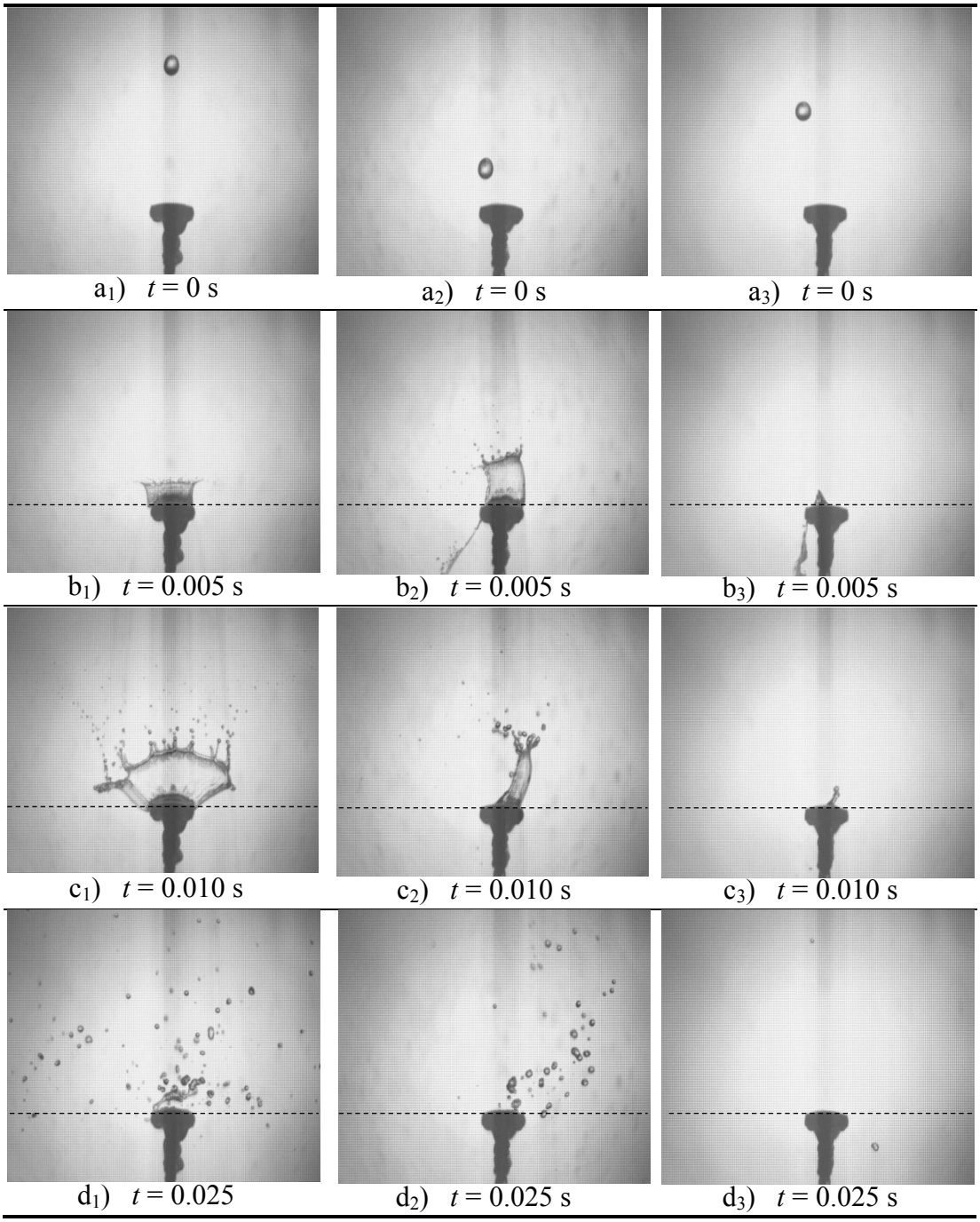

Figure B.58: Splash photographs (H_d = 970 mm, W = 12 mm, $d_i \approx$ 5.48 mm, $\delta = 0.78 \pm 0.14$ mm).

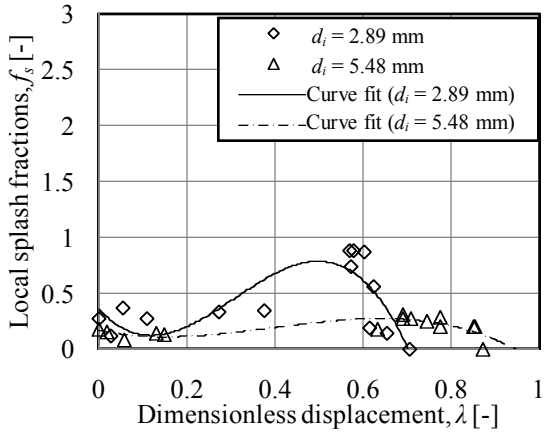

a$_1$) Local splash fractions (W = 3 mm, $\delta \approx$ 1.00 mm)

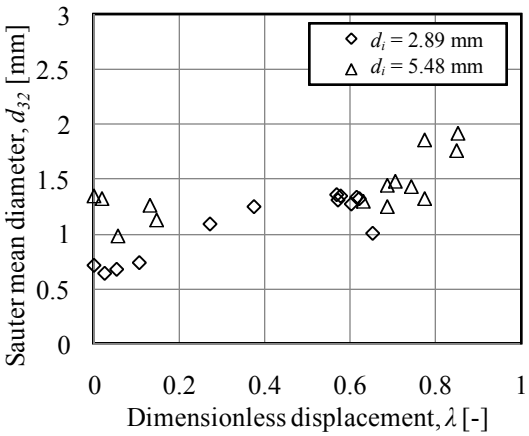

b$_1$) Sauter mean diameters (W = 3 mm, $\delta \approx$ 1.00 mm)

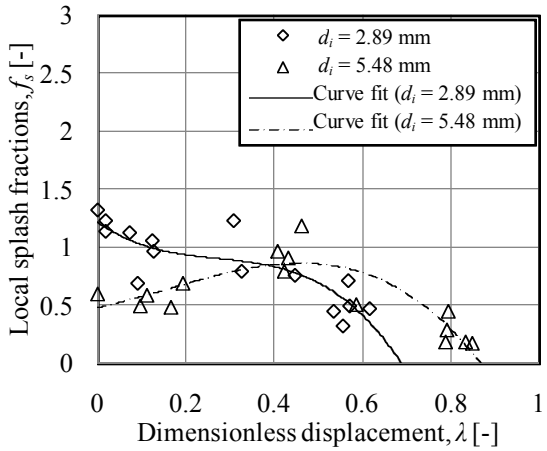

a$_2$) Local splash fractions (W = 6 mm, $\delta \approx$ 0.85 mm)

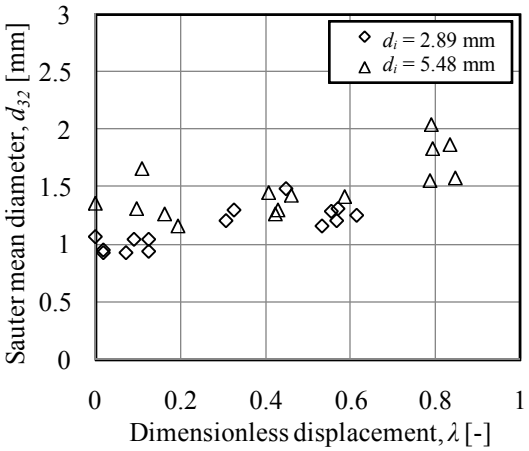

b$_2$) Sauter mean diameters (W = 6 mm, $\delta \approx$ 0.85 mm)

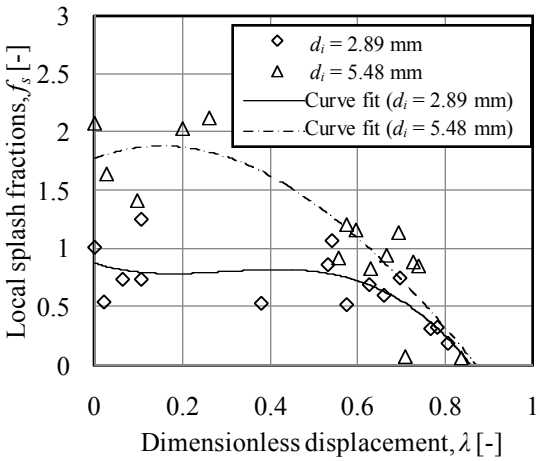

a$_3$) Local splash fractions (W = 12 mm, $\delta \approx$ 0.78 mm)

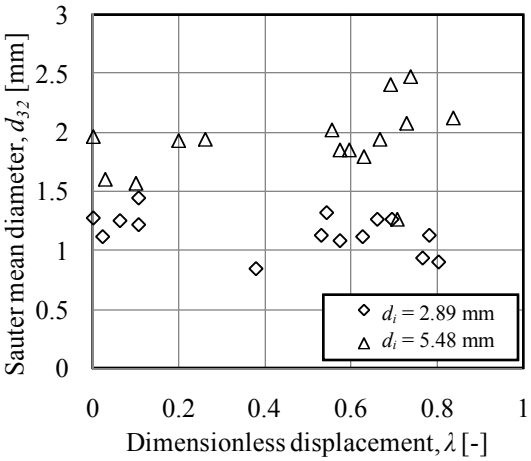

b$_3$) Sauter mean diameters (W = 12 mm, $\delta \approx$ 0.78 mm)

Figure B.59: Splash fractions and drop sizes (H_d = 970 mm, $d_i \approx$ 2.89 mm and $d_i \approx$ 5.48 mm).

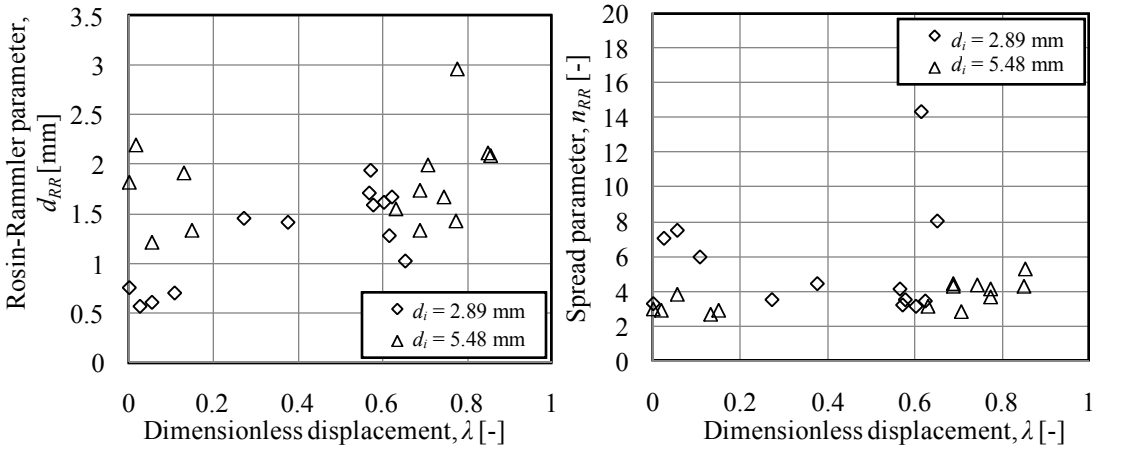

a$_1$) Parameter, d_{RR} (W = 3 mm, $\delta \approx$ 1.00 mm) b$_1$) Spread parameter, n_{RR} (W = 3 mm, $\delta \approx$ 1.00 mm)

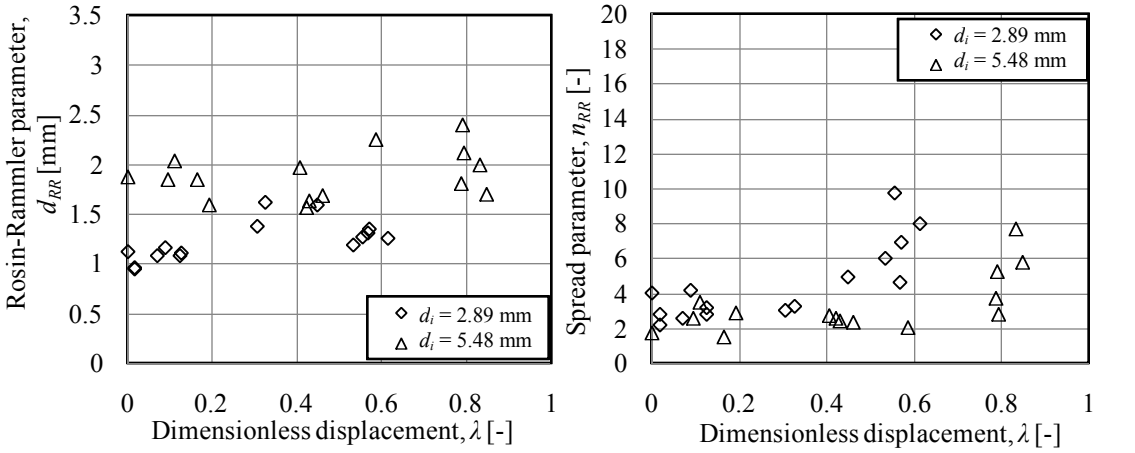

a$_2$) Parameter, d_{RR} (W = 6 mm, $\delta \approx$ 0.85 mm) b$_2$) Spread parameter, n_{RR} (W = 6 mm, $\delta \approx$ 0.85 mm)

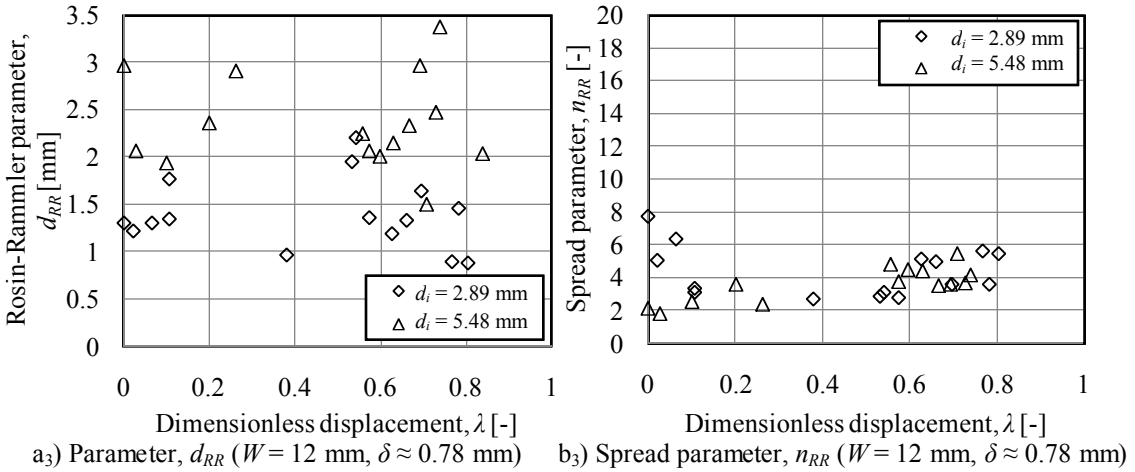

a$_3$) Parameter, d_{RR} (W = 12 mm, $\delta \approx$ 0.78 mm) b$_3$) Spread parameter, n_{RR} (W = 12 mm, $\delta \approx$ 0.78 mm)

Figure B.60: Rosin-Rammler parameters (H_d = 970 mm, $d_i \approx$ 2.89 mm and $d_i \approx$ 5.48 mm).

B.4 Data correlation

In order to predict the contribution of splashing to the overall performance enhancement of an installed splash grid in a rain zone, the amount of splashing and also the size distribution of the splash drops must be known. The experimental results in this chapter show that variables such as slat width, film thickness on the slat, drop diameter and impingement velocity have a significant influence on the splash mass as well as on the size distribution of the splash drops.

The average splash fractions are obtained by fitting curves through the local splash fraction plots (shown in the previous section) before integrating the curve fit equations in terms of the dimensionless displacement parameter, while the average Rosin-Rammler parameters are obtained by averaging the measured values for each test case. Table B.2 lists the average splash fractions and Rosin-Rammler parameters for all the test cases presented in the previous section.

Table B.2: Measured average splash data.

H_d [mm]	d_i [mm]	δ [mm]	W [mm]	We [-]	δ/W [-]	d_i/W [-]	$\bar{f}_s$ [-]	$\bar{n}_{RR}$ [-]	$\bar{d}_{RR}$ [mm]
250	2.89	1.00	3	186.34	0.333	0.963	0	-	-
250	4.00	0.43	3	261.99	0.143	1.333	0.059	5.957	1.123
250	4.00	0.78	3	261.99	0.260	1.333	0.010	9.228	1.189
250	4.00	1.30	3	261.99	0.433	1.333	0.035	12.301	2.241
250	5.48	1.00	3	362.90	0.333	1.827	0	-	-
250	2.89	0.85	6	186.34	0.142	0.482	0	-	-
250	4.00	0.85	6	261.99	0.142	0.667	0	-	-
250	5.48	0.85	6	362. 90	0.142	0.913	0.198	6.610	1.867
250	2.89	0.78	12	186.34	0.065	0.241	0	-	-
250	4.00	0.36	12	261.99	0.030	0.333	0.165	5.331	1.370
250	4.00	1.00	12	261.99	0.083	0.333	0.119	6.487	1.527
250	4.00	1.75	12	261.99	0.146	0.333	0.028	5.274	1.236
250	5.48	0.78	12	362.90	0.065	0.457	0.463	7.241	2.178
470	2.89	1.00	3	338.61	0.333	0.963	0.026	5.676	0.768
470	4.00	0.35	3	480.98	0.117	1.333	0.126	5.353	1.096
470	4.00	0.95	3	480.98	0.317	1.333	0.181	5.008	1.664

H_d [mm]	d_i [mm]	δ [mm]	W [mm]	We [-]	δ/W [-]	d_i/W [-]	$\bar{f}_s$ [-]	$\bar{n}_{RR}$ [-]	$\bar{d}_{RR}$ [mm]
470	4.00	1.40	3	480.98	0.467	1.333	0.118	10.742	2.488
470	5.48	1.00	3	670.63	0.333	1.827	0.108	4.923	1.654
470	2.89	0.85	6	338.61	0.142	0.482	0.166	5.716	1.104
470	4.00	0.25	6	480.98	0.042	0.667	0.208	4.507	0.987
470	4.00	0.85	6	480.98	0.142	0.667	0.598	5.033	1.668
470	4.00	1.45	6	480.98	0.242	0.667	0.499	5.742	1.757
470	5.48	0.85	6	670.63	0.142	0.913	0.288	5.378	1.683
470	2.89	0.78	12	338.61	0.065	0.241	0.420	6.919	1.231
470	4.00	0.30	12	480.98	0.025	0.333	0.477	4.242	1.113
470	4.00	0.75	12	480.98	0.063	0.333	0.547	5.410	1.639
470	4.00	1.95	12	480.98	0.163	0.333	0.326	6.526	1.911
470	5.48	0.78	12	670.63	0.065	0.457	0.389	4.004	1.646
970	2.89	1.00	3	655.03	0.333	0.963	0.301	5.498	1.255
970	4.00	0.11	3	951.98	0.037	1.333	0.117	3.737	0.699
970	4.00	0.85	3	951.98	0.333	1.333	0.450	3.647	1.520
970	4.00	1.32	3	951.98	0.440	1.333	0.487	4.549	1.739
970	5.48	1.00	3	1345.43	0.333	1.827	0.165	3.688	1.809
970	2.89	0.85	6	655.03	0.142	0.482	0.540	4.564	1.229
970	4.00	0.50	6	951.98	0.083	0.667	0.492	3.590	1.161
970	4.00	0.84	6	951.98	0.142	0.667	0.506	4.616	1.390
970	4.00	1.43	6	951.98	0.238	0.667	0.652	4.108	2.018
970	5.48	0.85	6	1345.43	0.142	0.913	0.570	3.312	1.887
970	2.89	0.78	12	655.03	0.065	0.241	0.597	4.372	1.384
970	4.00	0.21	12	951.98	0.018	0.333	0.733	3.686	1.221
970	4.00	0.95	12	951.98	0.079	0.333	0.895	3.902	1.722
970	4.00	1.75	12	951.98	0.146	0.333	1.170	5.627	2.130
970	5.48	0.78	12	1345.43	0.065	0.457	1.158	3.597	2.357

B.4.1 Average splash fraction

The average splash fractions are correlated in this section for the three individual slats (W = 3 mm, W = 6 mm and W = 12 mm) by means of the following procedure:

1) The average splash fractions for a constant water film thickness on each slat are plotted against Weber number (Figures B.61) for each of the three initial drop sizes (d_i = 2.89, 4.00 and 5.48 mm) tested in Section B.3 and a correlation is obtained (Equation B.3) for the average splash fraction in terms of the dimensionless variables $We_n = We/We_{ref}$ and $d_n = d_i/W$.
2) The average splash fractions for an initial drop with a constant diameter of d_i = 4 mm are then plotted against the film thickness to slat width ratio on each slat for three different drop fall distances that correspond to three different Weber numbers (Figures B.63a). Due to the fact that the average splash fraction measurements at the three drop fall distances are not at corresponding film thickness a function (Equation B.5) is used to interpolate the data (Figures B.63a).
3) The interpolation function (Equation B.5) is used to generate data points for the average splash fractions for a d_i = 4 mm in diameter initial drop at five different water film thicknesses on each slat and the data is plotted in terms of the Weber number (Figures B.63b).
4) The effect of film thickness on the average splash fraction (Figure B.63b) is incorporated into the final equations that give the average splash fraction on each slat in terms of the dimensionless variables $We_n = We/We_{ref}$, $d_n = d_i/W$ and $\delta_n = \delta/W$ (Equations B.7, B.8 and B.9).

Figure B.61 shows a plot of the measured (Table B.2) and correlated average splash fractions for different drop sizes on each of the three slats, covered by a water film of constant thickness. The curve fit correlation shown in Figure B.61 has the following form.

$$\bar{f}_{s,d} = \alpha_d \tanh[\beta_d(We_n + \gamma)] \tag{B.3}$$

where

$$We_n = We/We_{ref} \tag{B.4}$$

The values of α_d and β_d (Equation B.3) depend on the initial drop diameter and are expressed as functions of the initial drop diameter to slat width ratio (d_i/W). Figure B.62 shows plots of α_d and β_d in terms of the initial drop diameter to slat width ratio for each slat, together with curve fits that represent the data. The parameter γ is constant for the W = 3 mm and W = 6 mm wide slats (γ = -0.018), but for the W = 12 mm wide slat it is later shown that it becomes a function of the film thickness on the slat.

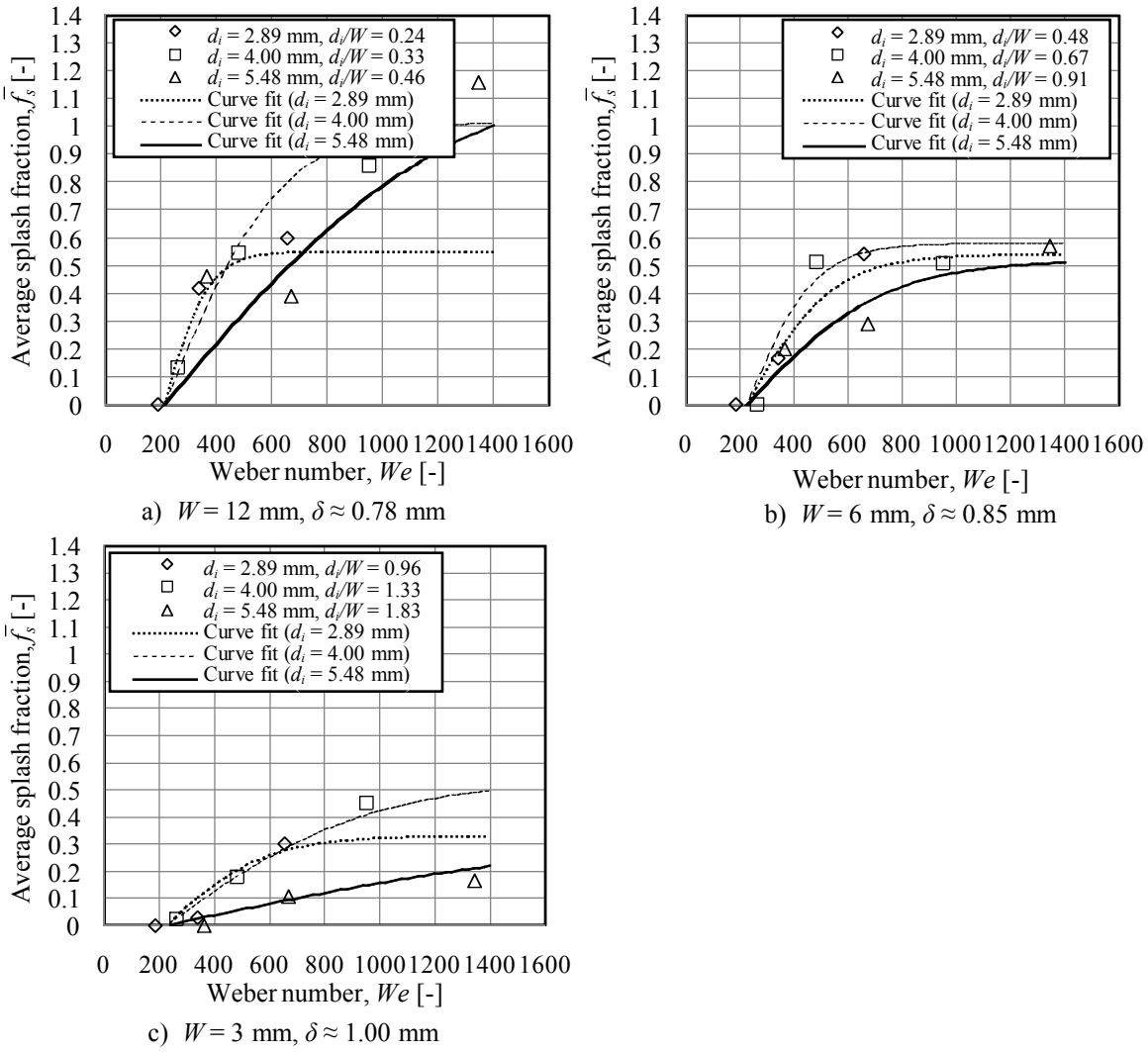

a) W = 12 mm, $\delta \approx$ 0.78 mm

b) W = 6 mm, $\delta \approx$ 0.85 mm

c) W = 3 mm, $\delta \approx$ 1.00 mm

Figure B.61: Measured average splash fractions for drops of different diameters impinging onto slats covered by water films of constant thickness (Equation B.3).

The relationship between the average splash fraction and the film thickness to slat width ratio (δ/W) is determined by keeping the drop diameter constant at d_i = 4 mm and by varying the film thickness on each slat as well as the drop fall distance that corresponds to a change in Weber number. The relevant measured data is obtained from Table B.2 and plotted in Figure B.63(a). Figure B.63(a) also shows interpolation lines that are used to interpolate the average splash fractions for all three Weber numbers (for the three fall distances) because the measured data for the three fall distances aren't measured at corresponding film thicknesses. Equation (B.5) shows the form of the interpolation equation in which the coefficients a, b and c are adjusted to obtain an accurate curve through the data at each Weber number as shown in

Figure B.63(a). The sole purpose of Equation (B.5) at this point is to generate data points for the average splash fraction of a d_i = 4 mm in diameter initial drop at five different film thicknesses on each slat as shown in Figure B.63(b)

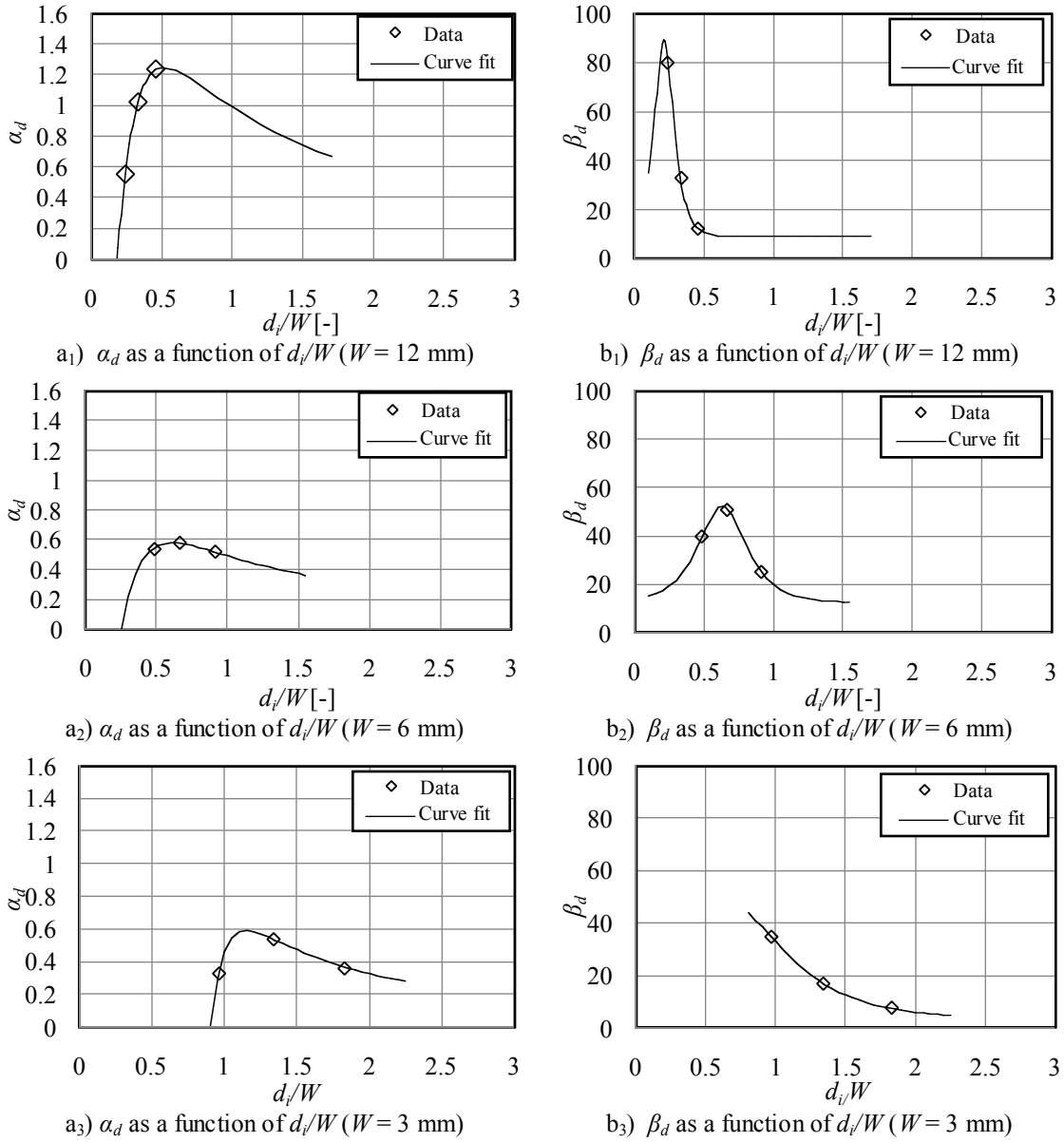

a$_1$) α_d as a function of d_i/W (W = 12 mm)

b$_1$) β_d as a function of d_i/W (W = 12 mm)

a$_2$) α_d as a function of d_i/W (W = 6 mm)

b$_2$) β_d as a function of d_i/W (W = 6 mm)

a$_3$) α_d as a function of d_i/W (W = 3 mm)

b$_3$) β_d as a function of d_i/W (W = 3 mm)

Figure B.62: Average splash fraction correlation parameters α_d and β_d.

$$\bar{f}_{s,\delta} = a\bar{f}_{s,d} \sin\left(\frac{\pi}{b\frac{\delta}{W} + c}\right) \tag{B.5}$$

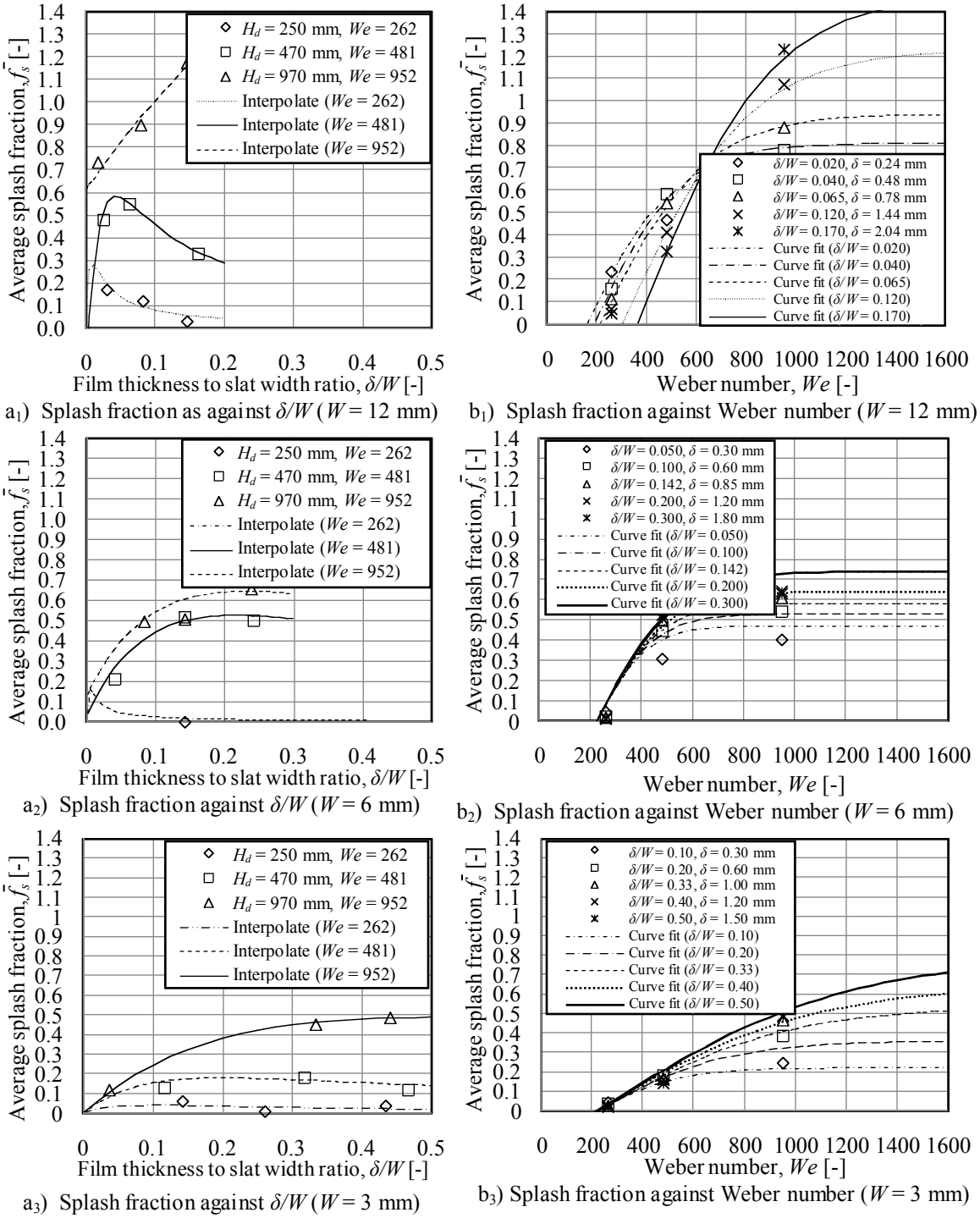

a$_1$) Splash fraction as against δ/W (W = 12 mm)

b$_1$) Splash fraction against Weber number (W = 12 mm)

a$_2$) Splash fraction against δ/W (W = 6 mm)

b$_2$) Splash fraction against Weber number (W = 6 mm)

a$_3$) Splash fraction against δ/W (W = 3 mm)

b$_3$) Splash fraction against Weber number (W = 3 mm)

Figure B.63: Average splash fractions ($d_i \approx 4$ mm) for different water film thicknesses on each slat.

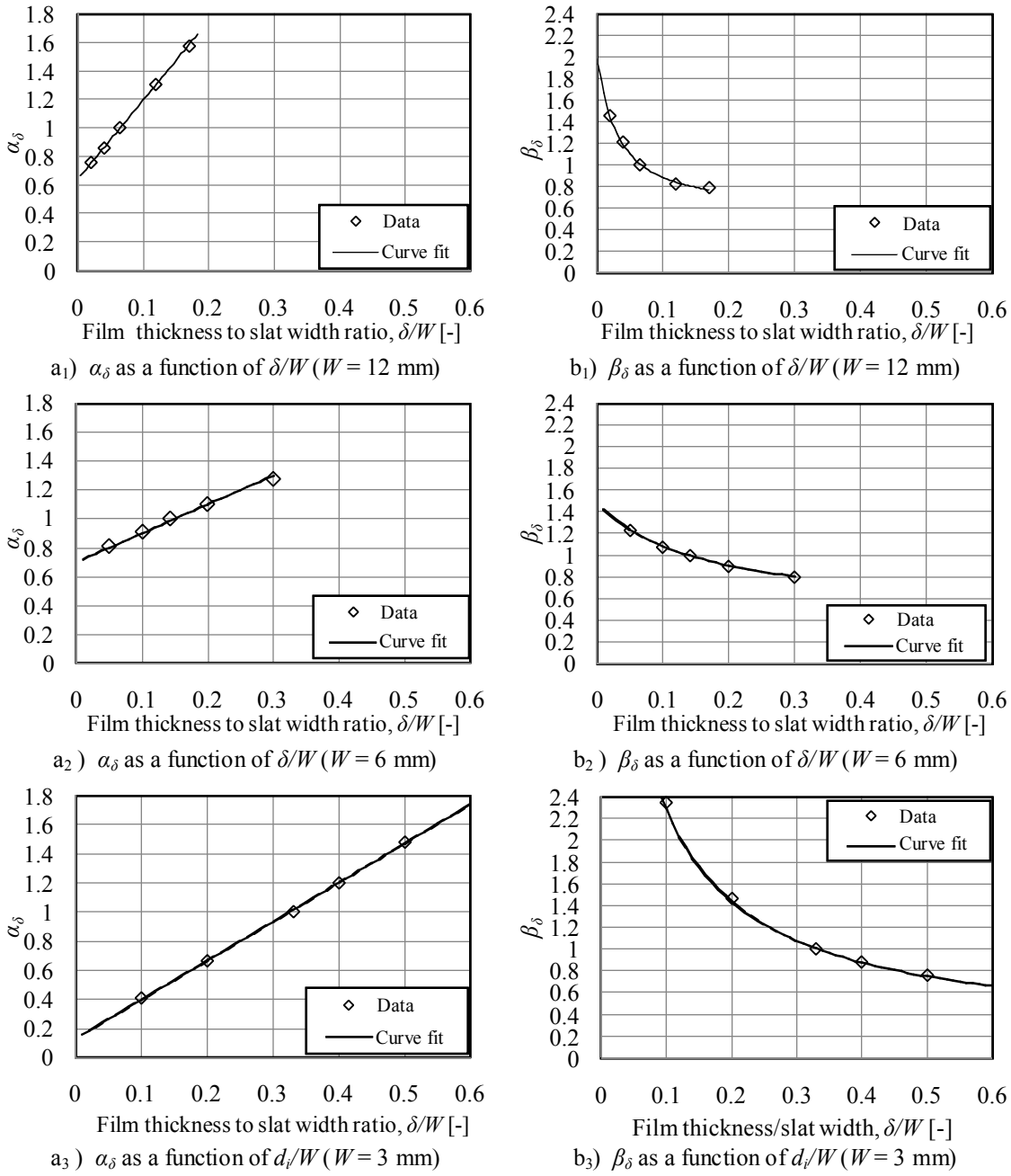

a$_1$) α_δ as a function of δ/W (W = 12 mm)

b$_1$) β_δ as a function of δ/W (W = 12 mm)

a$_2$) α_δ as a function of δ/W (W = 6 mm)

b$_2$) β_δ as a function of δ/W (W = 6 mm)

a$_3$) α_δ as a function of d_i/W (W = 3 mm)

b$_3$) β_δ as a function of d_i/W (W = 3 mm)

Figure B.64: Splash fraction correlation parameters α_δ and β_δ.

The data points shown in Figure B.63(b) are correlated by expanding Equation (B.3) to include the effect of film thickness in the following way

$$\bar{f}_s = \alpha_d \alpha_\delta \tanh[\beta_d \beta_\delta (We_n + \gamma)] \quad \text{(B.6)}$$

where the coefficients α_d and β_d are already determined and presented in Figure B.62 and the coefficients α_δ and β_δ, which can be seen as correction coefficients on the previous two coefficients for film thickness, are presented in Figure B.64.

The parameter γ becomes a function of the film thickness for the W = 12 mm wide slat as mentioned earlier and is plotted in Figure B.65. The reason for this dependency on film thickness can be seen in the plot shown Figure B.63(b_1) where the curves move to the right as the film thickness increases. This is not the case for the W = 3 mm and W = 6 mm wide slats as shown in the plots presented in Figure B.63(b_2 and b_3).

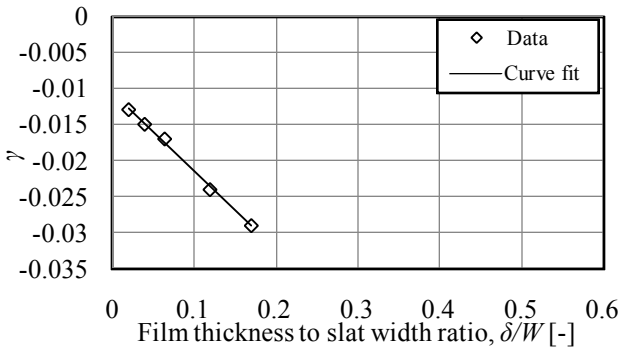

Figure B.65: Splash fraction correlation parameter, γ (W = 12 mm).

The equations for predicting the average splash fractions of drops impinging on W = 3, W = 6 or W = 12 mm slats covered by thin layers of water are finally given by the following three equations

$$\bar{f}_{s,12} = \frac{6.94\delta_n + 0.8}{\csc[\pi/(3d_n + 0.45)]}\tanh\left[\frac{(We_n - 0.11\delta_n - 0.01)\{\mathrm{sech}(16d_n - 3.3) + 0.11\}}{0.02\cos\{\pi/(15\delta_n + 2.5)\}}\right] \tag{B.7}$$

$$\bar{f}_{s,6} = \frac{1.16\delta_n + 0.41}{\csc[\pi/(2.8d_n + 0.3)]}\tanh\left[\frac{(We_n - 0.018)\{\mathrm{sech}(6.5d_n - 4.1) + 0.31\}}{0.05\cos\{\pi/(3.5\delta_n + 2.6)\}}\right] \tag{B.8}$$

$$\bar{f}_{s,3} = \frac{1.58\delta_n + 0.077}{\csc[\pi/(4d_n - 2.6)]}\tanh\left[\frac{(We_n - 0.018)\{\mathrm{sech}(2.6d_n - 1.6) + 0.08\}}{0.09\cos\{\pi/(\delta_n + 2.05)\}}\right] \tag{B.9}$$

where

$$d_n = \frac{d_i}{W} \quad \text{and} \quad \delta_n = \frac{\delta}{W}$$

and d_i > 2 mm and We > 250. The Weber number (We), reference Weber number (We_{ref}) and normalized Weber number (We_n) are respectively given by Equations (2.49e), (2.57) and (B.4).

B.4.2 Average Rosin-Rammler parameter, $\bar{d}_{RR}$

The average Rosin-Rammler parameter $\bar{d}_{RR}$ is correlated for three individual slats (W = 3 mm, W = 6 mm and W = 12 mm) in this section and combined into a single equation by means of the following procedure:

1) The measured average parameter $\bar{d}_{RR}$ (Table B.2) for a constant water film thickness on each slat is plotted against the Weber number (Figure B.66) for the three initial drop sizes (d_i = 2.89, 4.00 and 5.48 mm) tested in Section B.3 and a correlation is obtained (Equation B.10) for $\bar{d}_{RR}$ in terms of the dimensionless variables $We_n = We/We_{ref}$ and $d_n = d_i/W$.
2) The parameter $\bar{d}_{RR}$ for an initial drop with a constant diameter of d_i = 4 mm is then plotted against the film thickness to slat width ratio on each slat for different drop fall distances that correspond to different Weber numbers (Figure B.68a). Due to the fact that the $\bar{d}_{RR}$ measurements at the three drop fall distances are not at corresponding film thicknesses a function (Equation B.11) is used to interpolate the data (Figure B.68a).
3) The interpolation function (Equation B.11) is used to generate data points of $\bar{d}_{RR}$, for a d_i = 4 mm in diameter initial drop, at five different water film thicknesses on each slat before this data is plotted in terms of the Weber number (Figure B.68b).
4) The effect of film thickness on $\bar{d}_{RR}$ is incorporated into the equation (Equation B.12) for each slat that now gives $\bar{d}_{RR}$ in terms of the dimensionless variables $We_n = We/We_{ref}$, $d_n = d_i/W$ and $\delta_n = \delta/W$.
5) The final equation for $\bar{d}_{RR}$ (Equation B.13) is obtained by combining the equations for each slat to give $\bar{d}_{RR}$ in terms of the dimensionless variables $We_n = We/We_{ref}$, $d_n = d_i/W$, $\delta_n = \delta/W$ and W/d_m.

Figure B.66 shows a plot of the measured (Table B.2) and correlated average Rosin-Rammler parameter $\bar{d}_{RR}$ for different initial drop sizes on three different slats, each covered by a water film of constant thickness. The curve fit correlation shown in Figure B.66 has the following form.

$$\bar{d}_{RR,d} = \alpha_d We_n^{\beta} \tag{B.10}$$

where α_d is a function of the drop diameter to slat width ratio as presented in Figure B.67 and $\beta = 0.09$.

Figure B.68 (a) shows the relationship between $\bar{d}_{RR}$ and the film thickness to slat width ratio for each slat when the initial drop falls from different heights and has a constant diameter of $d_i = 4$ mm.

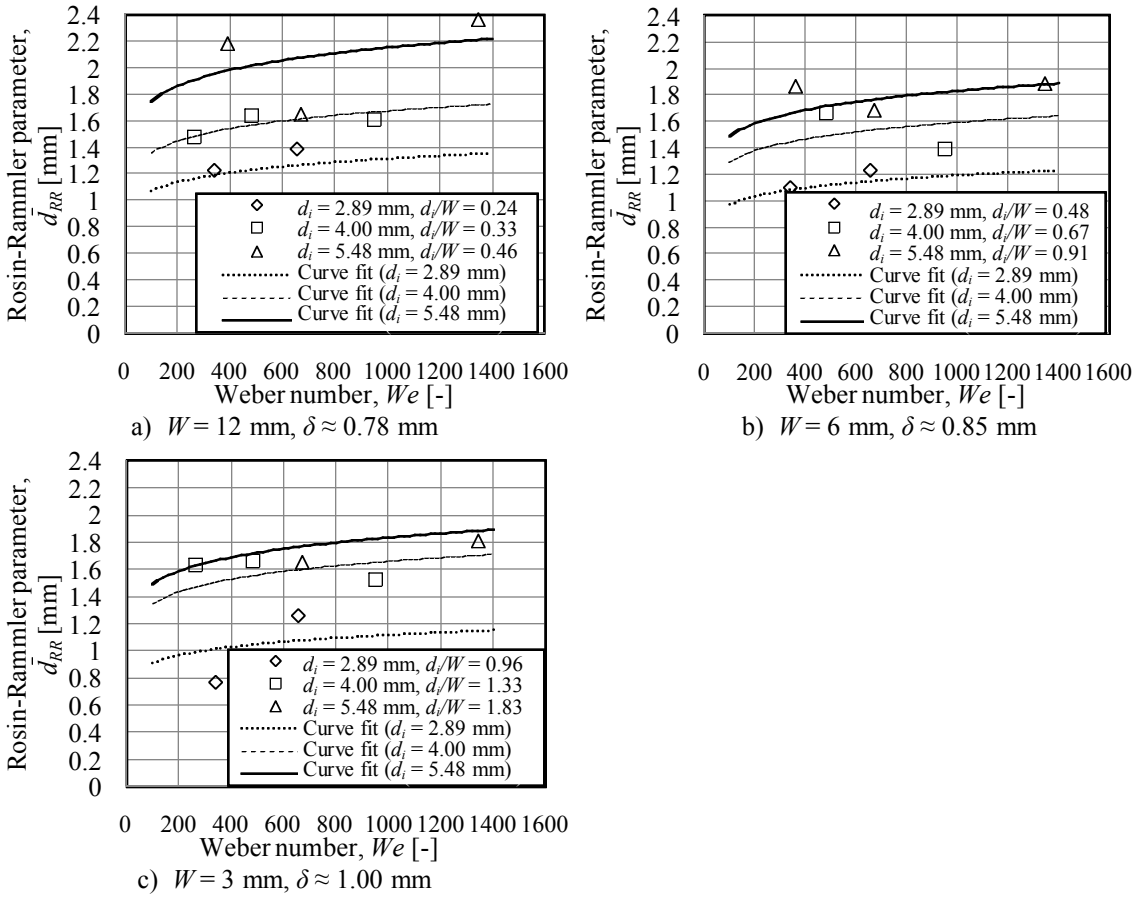

Figure B.66: Measured average Rosin-Rammler parameters, $\bar{d}_{RR}$, for drops of different diameters impinging onto slats covered by water films of constant thickness (Equation B.10).

The plotted data in Figure B.68 (a) is interpolated by

$$\bar{d}_{RR,\delta} = a\bar{d}_{RR,d} \sin\left(\frac{\pi}{b\frac{\delta}{W} + c}\right) \tag{B.11}$$

which is used to generate the data points presented in Figure B.68(b) for $\bar{d}_{RR}$ in terms of the Weber number at five different film thicknesses on each slat.

Equation (B.10) is now expanded for each slat to include the effect of film thickness by correlating the data presented in Figure B.68(b) and an equation of the following form is obtained for each slat

$$\bar{d}_{RR} = 2.04\alpha_W \tanh(1.8d_n - \beta_W) We_n{}^{0.09} \delta_n{}^{\gamma_W} \tag{B.12}$$

where the values of α_W, β_W and γ_W depend on the slat width. In order to obtain a single equation for $\bar{d}_{RR}$ the variables α_W, β_W and γ_W are expressed as functions of the slat width to maximum stable drop diameter ratio as presented in Figure B.69.

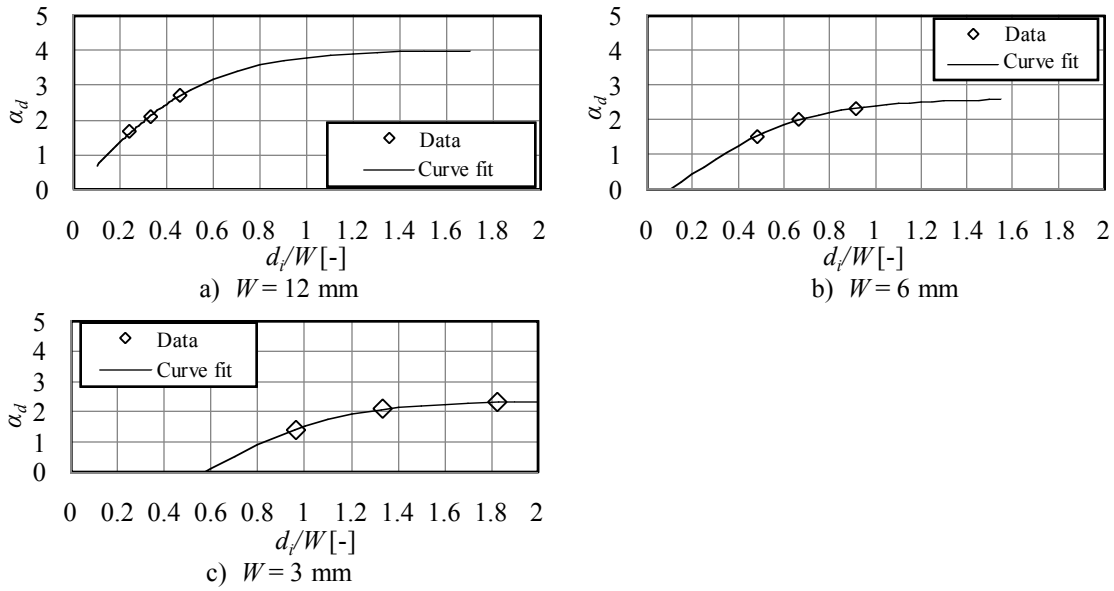

Figure B.67: $\bar{d}_{RR}$ correlation parameter α_d.

The final equation for the average Rosin-Rammler parameter $\bar{d}_{RR}$ is be given by

$$\bar{d}_{RR} = 3.86\delta_n{}^{R} We_n{}^{0.09} \tanh\left[1.8d_n - 5.39/exp\left(6.03\frac{W}{d_m}\right)\right] exp\left(0.66\frac{W}{d_m}\right) \tag{B.13}$$

where

$$R = 0.28\left(\frac{W}{d_m}\right)^{-0.56} \quad \text{and} \quad d_n = \frac{d_i}{W} \quad \text{and} \quad \delta_n = \frac{\delta}{W}$$

The Weber number (We), reference Weber number (We_{ref}) and normalized Weber number (We_n) are respectively given by Equations (2.49e), (2.57) and (B.4).

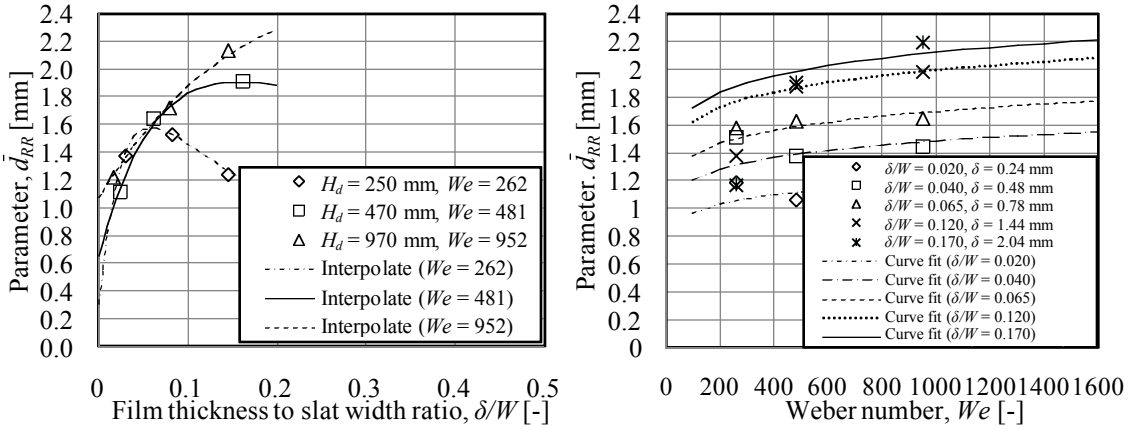

a$_1$) $\bar{d}_{RR}$ as a function of δ/W (W = 12 mm)

b$_1$) $\bar{d}_{RR}$ as a function of Weber number (W = 12 mm)

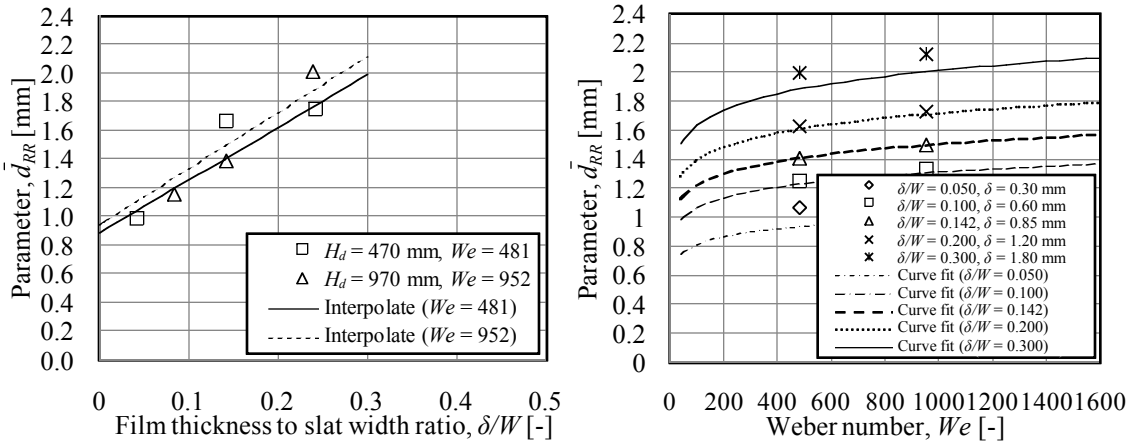

a$_2$) $\bar{d}_{RR}$ as a function of δ/W (W = 6 mm)

b$_2$) $\bar{d}_{RR}$ as a function of Weber number (W = 6 mm)

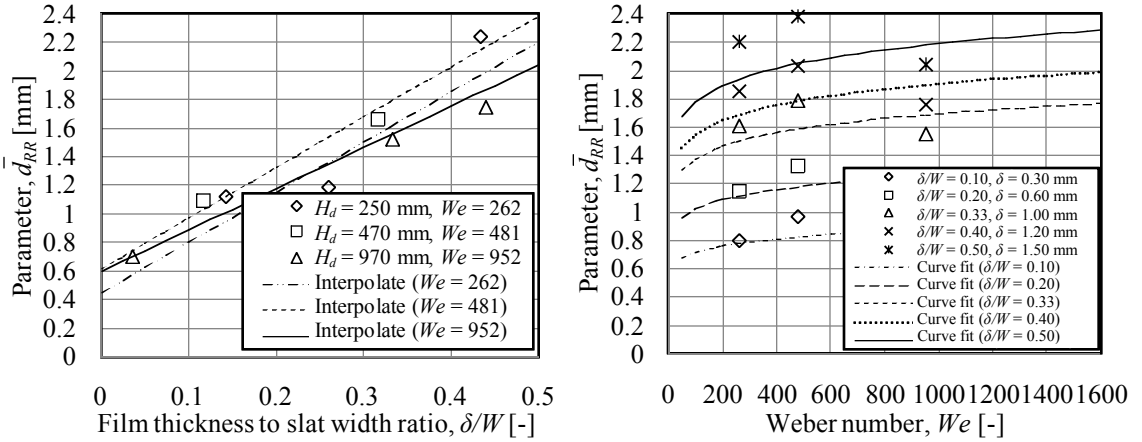

a$_3$) $\bar{d}_{RR}$ as a function of δ/W (W = 3 mm)

b$_3$) $\bar{d}_{RR}$ as a function of Weber number (W = 3 mm)

Figure B.68: Average Rosin-Rammler parameter, $\bar{d}_{RR}$ ($d_i \approx 4$ mm), for different water film thicknesses on each slat.

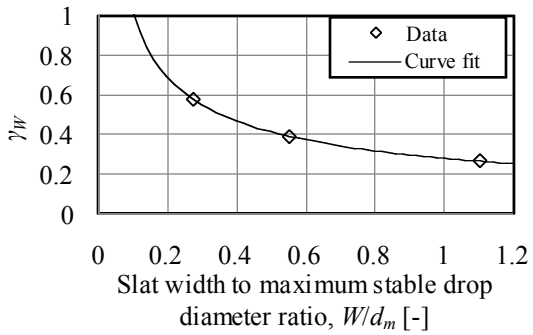

a) γ_W as a function of W/d_m

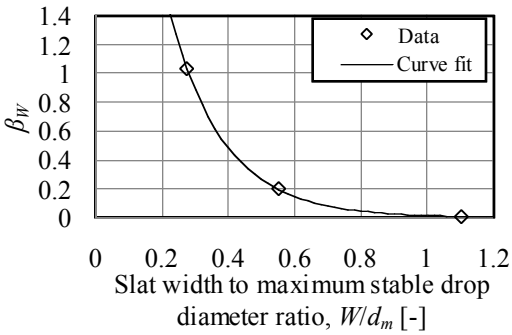

b) β_W as a function of W/d_m

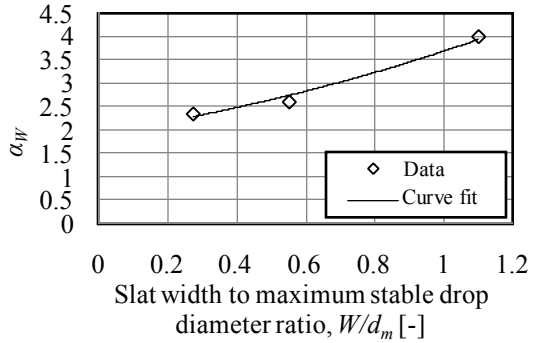

c) α_W as a function of W/d_m

Figure B.69: $\bar{d}_{RR}$ correlation parameters α_W, β_W and γ_W.

B.4.3 Average spread parameter, $\bar{n}_{RR}$

The average spread parameter ($\bar{n}_{RR}$) is correlated for three individual slats (W = 3 mm, W = 6 mm and W = 12 mm) in this section and combined into a single equation by means of the following procedure:

1) The average spread parameters for a constant water film thickness on each slat are plotted against Weber number (Figure B.70) for each of the three initial drop sizes (d_i = 2.89, 4.00 and 5.48 mm) tested in Section B.3 and a correlation is obtained (Equation B.14) for the average spread parameter in terms of the dimensionless variable $We_n = We/We_{ref}$.
2) The spread parameter $\bar{n}_{RR}$ for an initial drop with a constant diameter of d_i = 4 mm is then plotted against the film thickness to slat width ratio on each slat for different drop fall distances that correspond to different Weber numbers (Figure B.71a). Due to the fact that the $\bar{n}_{RR}$ measurements at the different drop fall distances are not at corresponding film thicknesses a function (Equation B.15) is used to interpolate the data (Figure B.71a).
3) The interpolation function (Equation B.15) is used to generate data points for the average spread parameter $\bar{n}_{RR}$, for a d_i = 4 mm in diameter initial drop, at

different water film thicknesses on each slat and the data is plotted against Weber number (Figure B.71b).

4) The effect of film thickness on $\bar{n}_{RR}$ is incorporated into the equation for each slat that now gives $\bar{n}_{RR}$ in terms of the dimensionless variables $We_n = We/We_{ref}$ and $\delta_n = \delta/W$ (Equation B.16).
5) The final equation for $\bar{n}_{RR}$ (Equation B.17) is obtained by combining the equations for each slat to give $\bar{n}_{RR}$ in terms of the dimensionless variables $We_n = We/We_{ref}$, $\delta_n = \delta/W$ and W/d_m.

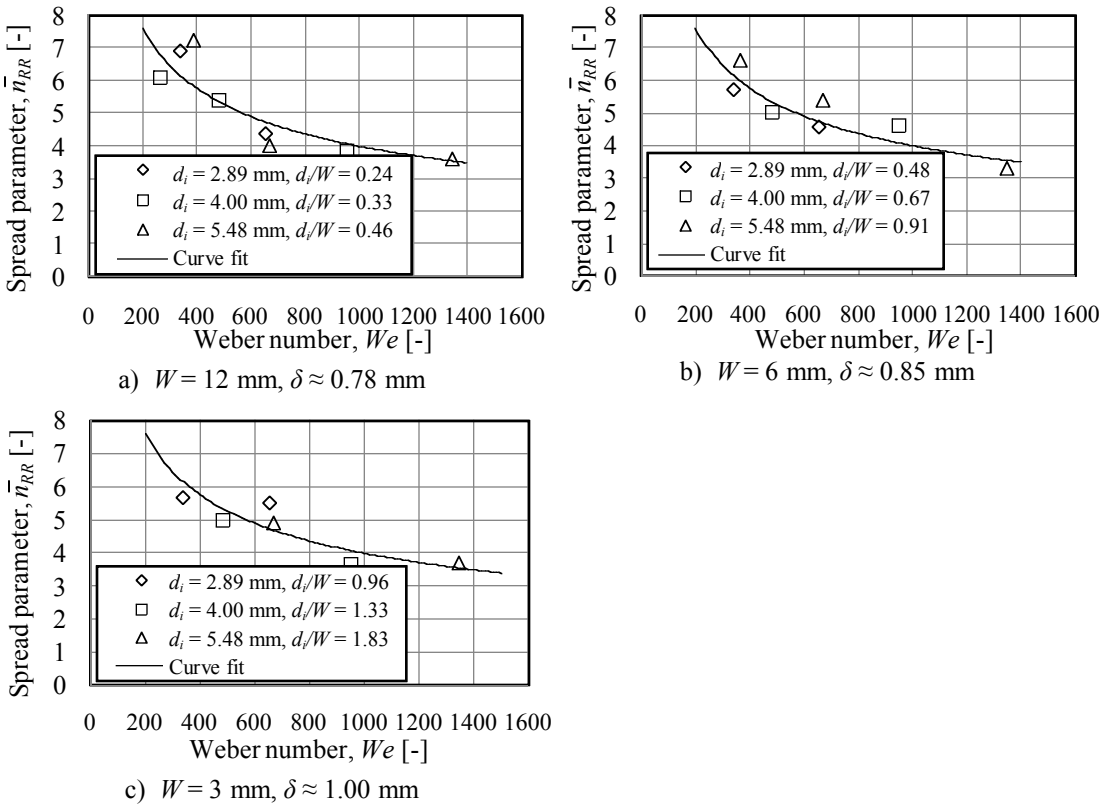

a) W = 12 mm, $\delta \approx$ 0.78 mm

b) W = 6 mm, $\delta \approx$ 0.85 mm

c) W = 3 mm, $\delta \approx$ 1.00 mm

Figure B.70: Measured average spread parameters, $\bar{n}_{RR}$, for drops of different diameters impinging onto slats covered by water films of constant thickness (Equation B.14).

Figure B.70 shows a plot of the measured (Table B.2) and correlated average spread parameter $\bar{n}_{RR}$ for different initial drop sizes on three different slats, each covered by a water film of constant thickness. The curve fit correlation shown in Figure B.70 is given by

$$\bar{n}_{RR,d} = 1.45 We_n^{-0.4} \quad \text{(B.14)}$$

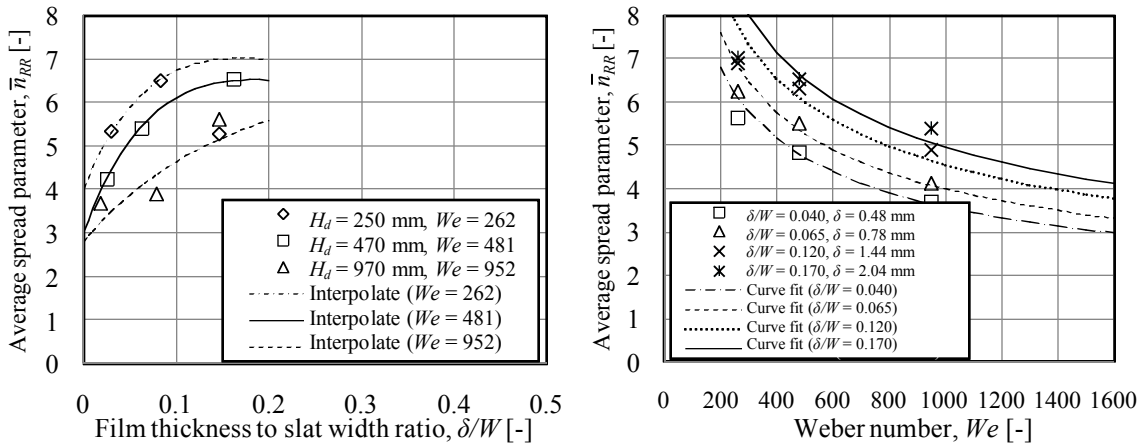

a$_1$) $\bar{n}_{RR}$ as a function of δ/W (W = 12 mm)

b$_1$) $\bar{n}_{RR}$ as a function of We (W = 12 mm)

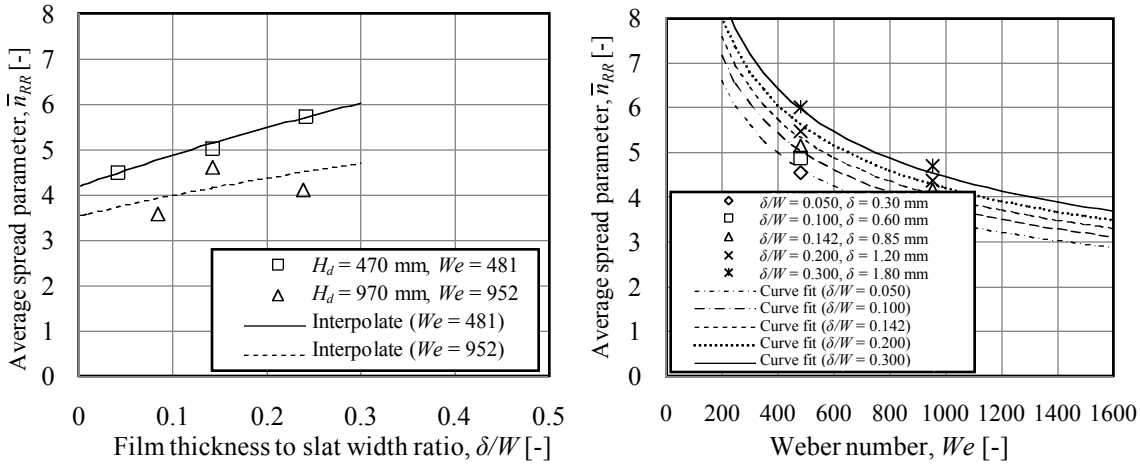

a$_2$) $\bar{n}_{RR}$ as a function of δ/W (W = 6 mm)

b$_2$) $\bar{n}_{RR}$ as a function of We (W = 6 mm)

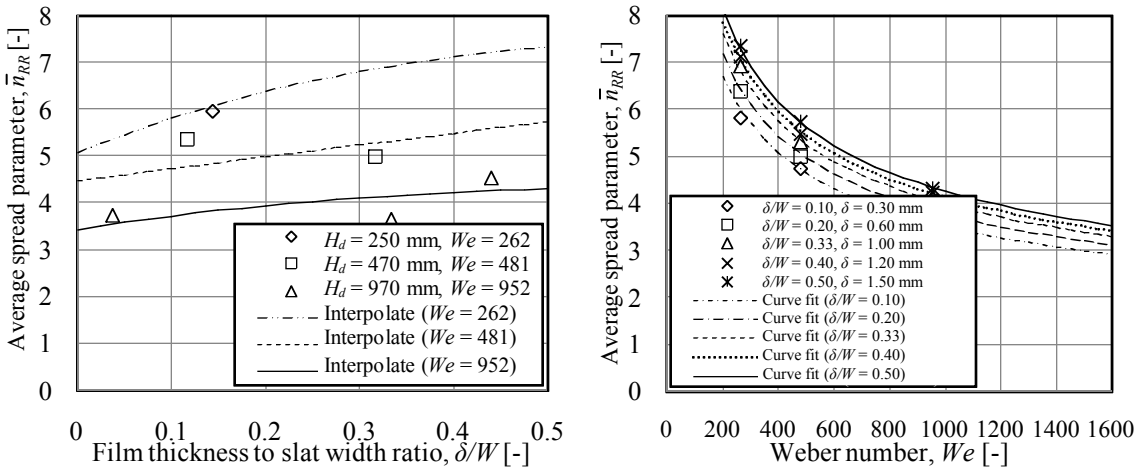

a$_3$) $\bar{n}_{RR}$ as a function of δ/W (W = 3 mm)

b$_3$) $\bar{n}_{RR}$ as a function of We (W = 3 mm)

Figure B.71: Average spread parameters, $\bar{n}_{RR}$ ($d_i \approx 4$ mm) for different water film thicknesses on each slat.

Figure B.71(a) shows the relationship between $\bar{n}_{RR}$ and the film thickness to slat width ratio for each slat when the initial drop falls from different heights and has a constant diameter of d_i = 4 mm.

The data in Figure B.71(a) is interpolated by an equation of the following form where the parameters a, b and c are adjusted until an accurate fit for the data is obtained.

$$\bar{n}_{RR,\delta} = a\bar{n}_{RR,d} \sin\left(\frac{\pi}{b\frac{\delta}{W} + c}\right) \tag{B.15}$$

Equation (B.15) is used to generate the data points shown in Figure B.71(b) where the average spread parameters for a d_i = 4 mm in diameter initial drop are plotted in terms of the Weber number for different film thicknesses on each slat.

Equation (B.14) is now expanded for each slat to include the effect of film thickness by correlating the data presented in Figure B.71(b) and an equation of the following form is obtained for each slat

$$\bar{n}_{RR} = \alpha_W \frac{{\delta_n}^{\beta_W}}{{We_n}^{0.4}} \tag{B.16}$$

where the values of α_W and β_W depend on the slat width. In order to obtain a single equation for $\bar{n}_{RR}$ the variables α_W and β_W are expressed as functions of the slat width to maximum stable drop diameter ratio as presented in Figure B.72.

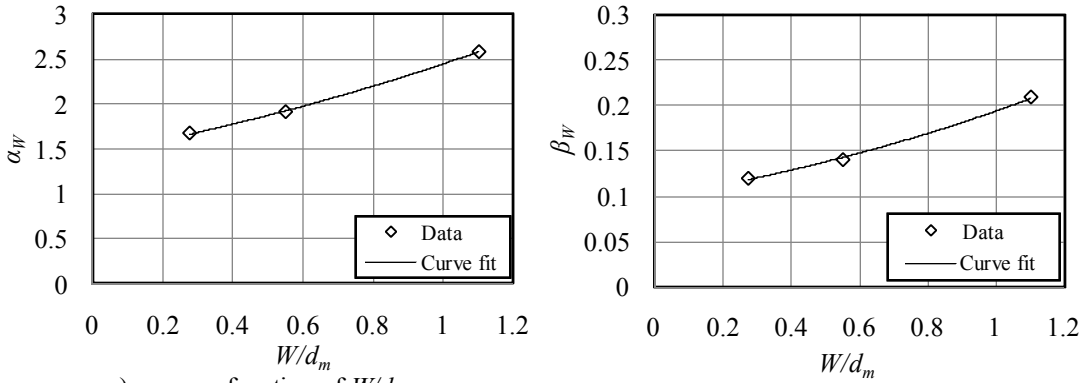

a) α_W as a function of W/d_m

b) β_W as a function of W/d_m

Figure B.72: $\bar{n}_{RR}$ correlation parameters α_W and β_W.

The final equation for predicting the average spread parameter is given by

$$\bar{n}_{RR} = 1.44exp\left(0.53\frac{W}{d_m}\right)\frac{\delta_n^{\,0.1exp\left(0.69\frac{W}{d_m}\right)}}{We_n^{\,0.4}} \tag{B.17}$$

The Weber number (We), reference Weber number (We_{ref}) and normalized Weber number (We_n) are respectively given by Equations (2.49e), (2.57) and (B.4).

B.5 Discussion

Drop splashing on slats is investigated in this appendix for different drop fall distance (H_d = 250 mm, H_d = 470 mm and H_d = 970 mm), initial drop size ($d_i \approx$ 2.89 mm, $d_i \approx$ 4.00 mm and $d_i \approx$ 5.48 mm), slat width (W = 3 mm, W = 6 mm and W = 12 mm) and water film thickness (δ < 2 mm) combinations.

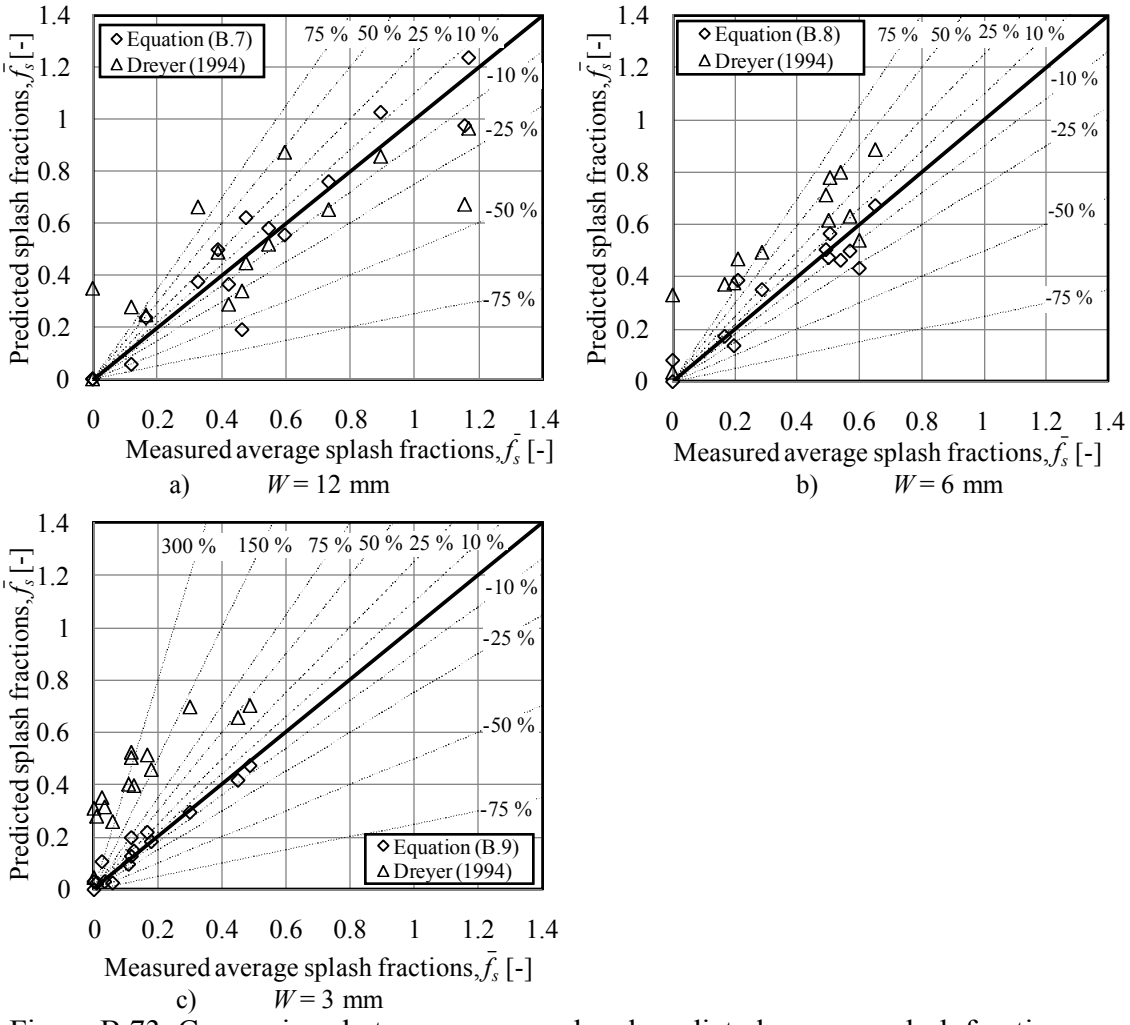

Figure B.73: Comparison between measured and predicted average splash fractions.

Visual insight into drop splashing on the slats is given by means of sequential photographs taken at different time steps during drop impingements to show the splash drop formation. Drop size distribution data and splash fraction data are extracted from these photographs by means of the software program described in Appendix F. For each test case the local splash fractions and drop distributions are measured for drop impingements at different locations over the slat width and the average values are determined from this data.

Average splash fraction data for three different slat widths (W = 3 mm, W = 6 mm and W = 12 mm) are correlated by Equations (B.7) to (B.9) that can be interpolated to determine the splash fractions at intermediate slat widths. Figure B.73 shows a comparison between the predicted average splash fractions [using Equations (B.7) to (B.9) and the Dreyer (1994) equations] and the measured data. The figure shows the measured drop splashing to be much less, especially for W = 3 mm, than the values predicted by Dreyer and in many cases drop splashing can be assumed negligible. Dreyer never measured drop splashing for slat widths below W = 5 mm, but used extrapolated results to predict the splash fractions on these slats, which may explain his over prediction.

Splash drop distributions are expressed by the Rosin-Rammler function and Figure B.74 shows how Equations (B.13) and (B.17) and the equations by Dreyer (1994) for predicting the average Rosin-Rammler parameters $\bar{d}_{RR}$ and $\bar{n}_{RR}$ compare to the measured results.

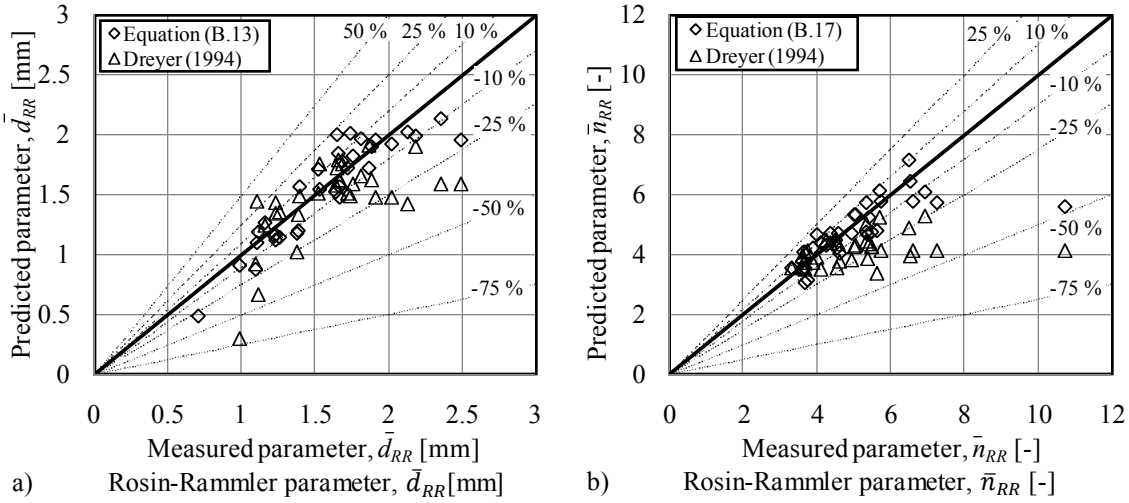

Figure B.74: Comparison between measured and predicted Rosin-Rammler parameters.

Figure B.74 shows that Dreyer (1994) under predicts the Rosin-Rammler parameters. Equations (B.13) and (B.17) predict the Rosin-Rammler parameters $\bar{d}_{RR}$ and $\bar{n}_{RR}$

higher than Dreyer (1994) for the measured cases by 10% and 16% on average respectively. Dreyer measured splash drop size distribution when the initial drops impinged in the middle of a W = 25 mm wide slat where the smallest splash drops generally form and assumed that the splash drop size distribution is independent of the slat width and impingement location. The measured results in this appendix show that the splash drop sizes are indeed a function of the slat width and drop sizes generally tend to increase with increasing displacement between the drop and slat centres.

The measurement uncertainties associated with the measurement results of this section are discussed in Appendix L.

C

SPLASH DROP MOTION, TEMPERATURE CHANGE AND INTERACTION AFTER DROP IMPINGEMENT

C.1 Introduction

In this appendix simplified equations are obtained from a numerical model to determine the splash drop trajectories and temperature changes as they travel through the air above the splash grid. With the simplified model for describing drop trajectories the number of splash drops returning to the grid and the number of splash drops that coalesce with other falling drops upon collision can be estimated.

C.2 Splash drop trajectories in counter flowing air after drop impingement

Drop splashing on the slats of a grid in upward flowing air is numerically investigated in this section. A free-body diagram for a splash drop in upward flowing air is shown in Figure C.1.

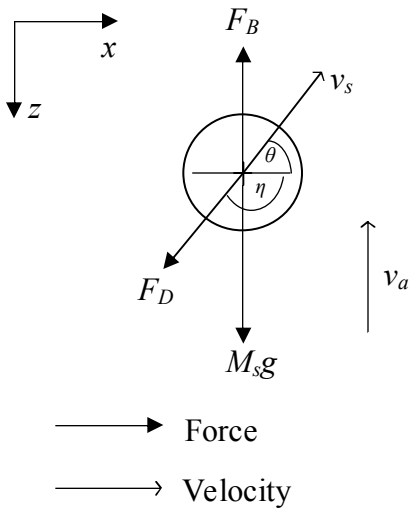

Figure C.1: Free-body diagram for a splash drop.

From Newton's second law the following expression can be obtained to describe the dynamics of a splash drop when external forces act on it.

$$\boldsymbol{F_R} = M_s \frac{\partial \boldsymbol{v_s}}{\partial t} + \boldsymbol{v_s} \frac{\partial M_s}{\partial t} \approx M_s \frac{\partial \boldsymbol{v_s}}{\partial t} \tag{C.1}$$

The resultant force acting on a splash drop is given by

$$\boldsymbol{F_R} = F_D \cos\eta\, \mathbf{i} + [M_s g + F_D \sin\eta - F_B]\mathbf{k} \tag{C.2}$$

and when this equation is substituted back into Equation (C.1) the following equation for the time derivative of the splash drop velocity is obtained.

$$\frac{\partial \boldsymbol{v_s}}{\partial t} = \frac{1}{M_s}(\boldsymbol{F_R}) = \frac{1}{M_s}(F_D \cos\eta\, \mathbf{i} + [M_s g + F_D \sin\eta - F_B]\mathbf{k}) \tag{C.3}$$

Equation (C.3) is numerically integrated by following an Euler approach where the drop trajectory is divided into equal time increments (Δt) to yield Equation (C.4) for drop velocity. Equation (C.4) expresses the drop velocity after each time increment ($t + \Delta t$) in terms of the velocity and the time derivative of the velocity at the current time step (t).

$$v_{s,x}^{t+\Delta t}\mathbf{i} + v_{s,z}^{t+\Delta t}\mathbf{k} = \left(v_{s,x}^{t} + \frac{1}{M_s}F_D \cos\eta\, \Delta t\right)\mathbf{i} + \left(v_{s,z}^{t} + \frac{1}{M_s}[M_s g + F_D \sin\eta - F_B]\Delta t\right)\mathbf{k} \tag{C.4}$$

where

$$F_D = \frac{\pi}{8} C_D \rho_{av} {d_s}^2 \left[{v_{s,x}^t}^2 + \left(v_{s,z}^t - v_a\right)^2\right] \tag{C.5}$$

$$F_B = \frac{\pi}{6} \rho_{av} {d_s}^3 g \tag{C.6}$$

$$\eta = 180° + \tan^{-1}\left(\frac{v_{s,z}^t - v_a}{v_{s,x}^t}\right) \tag{C.7}$$

The trajectory angle at any time is given by

$$\theta = \tan^{-1}\frac{v_{s,z}^t}{v_{s,x}^t} \tag{C.8}$$

The initial velocity of the splash drop is given by Dreyer (1994)

$$\left(\frac{v_{s,i}}{v_{dm,T}}\right) = 1.925 \times 10^{-2} + \left[\frac{7.372 \times 10^{-3}}{(d_s/d_m) - 0.01}\right] \tag{2.64}$$

The trajectory of the splash drop can be obtained by numerically integrating the velocity of the drop with respect to time by again following an Eulerian approach to yield

$$s_{s,x}^{t+\Delta t}\mathbf{i} + s_{s,z}^{t+\Delta t}\mathbf{k} = \left(s_{s,x}^{t} + v_{s,x}^{t}\Delta t\right)\mathbf{i} + \left(s_{s,z}^{t} + v_{s,z}^{t}\Delta t\right)\mathbf{k} \tag{C.9}$$

Figure C.2 shows the drop trajectories of splash drops in upward flowing air for an initial upward splash angle θ_s = -50° and in Figure C.3 the drop trajectories for the same drops are shown, but with an initial upward splash angle of θ_s = -70°.

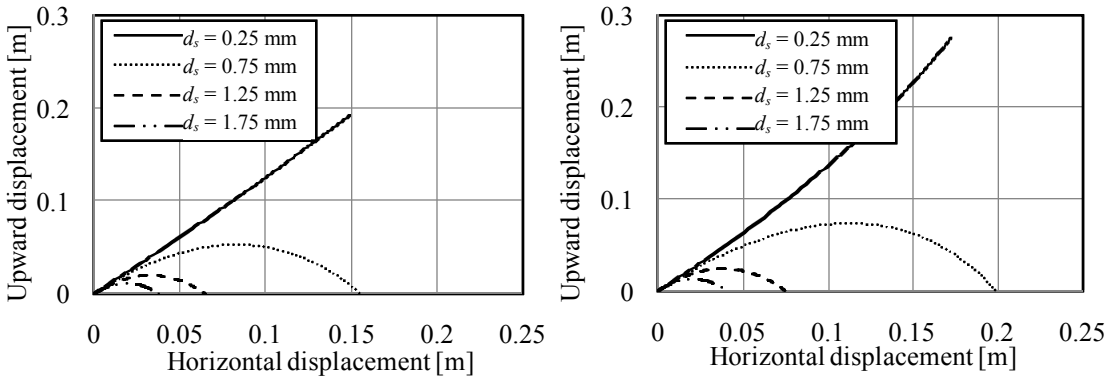

a) v_a = -1 m/s b) v_a = -2 m/s

Figure C.2: Splash drop trajectories in counter flowing air, θ_s = -50°.

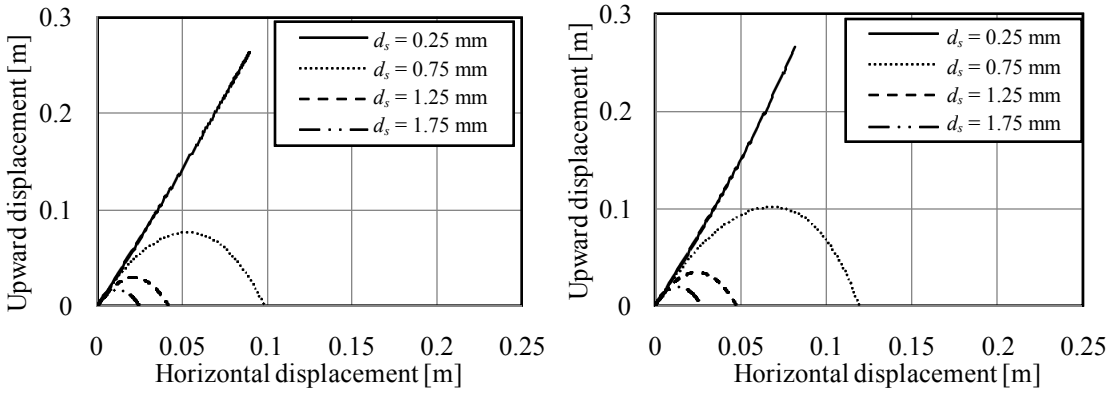

a) v_a = -1 m/s b) v_a = -2 m/s

Figure C.3: Splash drop trajectories in counter flowing air, θ_s = -70°.

C.3 Fraction of splash drops returning to grid after drop impingement

It can be seen from the previous section that a splash drop of a certain diameter and splash angle that experiences a certain upward air velocity will have a certain splash radius, shown in the Figure C.4, which is defined as twice the horizontal distance from the splash origin at which the returning splash drop passes the grid. If the splash diameter (D_s) is known, the fraction (grid fraction) of the splash drops that return to the grid after splashing can be estimated by determining the fraction of the splash circle over which it is assumed that the drops will become part of the grid surface water. A splash drop is assumed to become part of the grid surface water when the horizontal distance between the splash drop and slat centre as the splash drop passes the grid level on its way down, is equal or smaller than $(W + d_s)/2$.

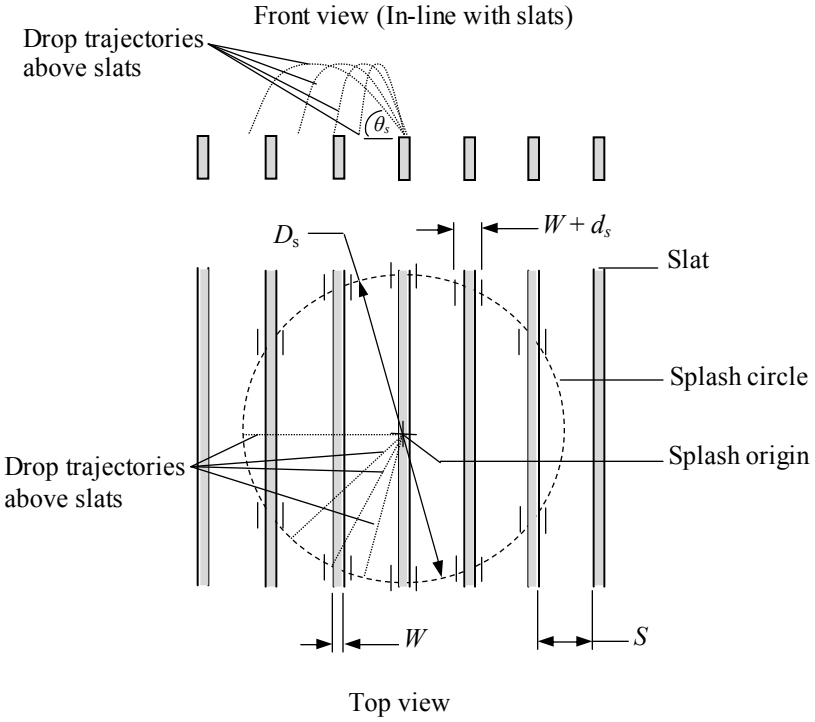

Figure C.4: Diagram showing the grid fraction variables.

The grid fraction is approximated from the geometry shown in Figure C.4 and is given by

$$f_G = \frac{2(D_s + W + S)(W + d_s)}{\pi D_s (W + S)} \tag{C.10}$$

where the splash diameter is given by

$$D_s = exp(0.0225\theta_s - 1.3981d_s - 0.1191v_a + 0.8497) \quad \text{(C.11)}$$

with the initial splash angel (θ_s) in degrees, the splash drop diameter (d_s) in mm, the upward air velocity (v_a) in m/s and the splash diameter (D_s) in m.

Figure C.5 shows the grid fractions (W = 3 mm, S = 10 mm) of splash drops at splash angles of -50° and -70° respectively.

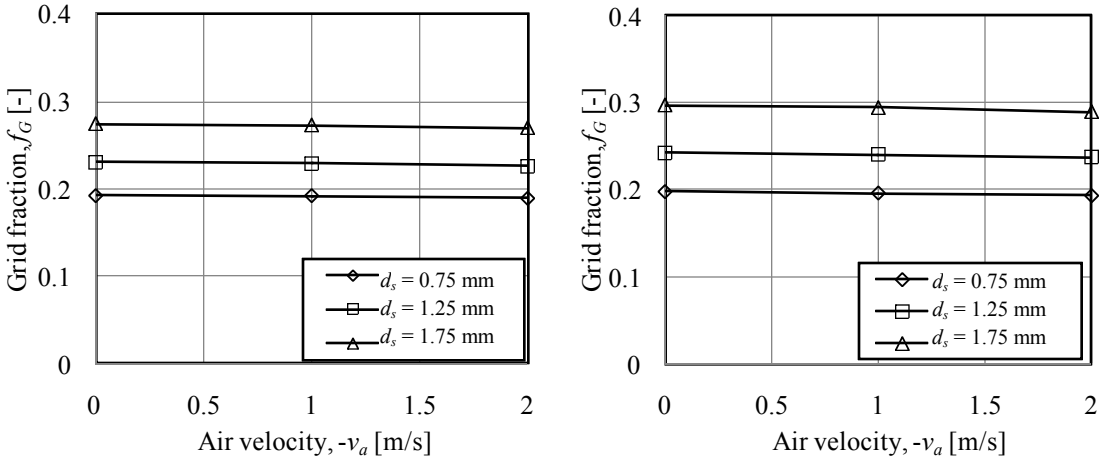

a) θ_s = -50° b) θ_s = -70°

Figure C.5: Estimated grid factions (W = 3 mm, S = 10 mm).

C.4 Splash drop interaction after drop impingement

Due to the relatively high rain densities in the rain zones of wet-cooling towers and the high relative velocities between up-splashing drops and the falling drops in the rain shower a significant amount of drop collisions above an installed splash grid are expected. This needs to be accounted for in order to predict the drop distribution and water temperature change accurately below such a grid.

Assuming that the drops of the rain shower fall in straight trajectories and that the splash drops leave the slat at a certain initial angle (θ_s) and velocity, collisions ($\dot{n}_{coll}$) between the splash drops and shower drops are due to the relative motion in the vertical as well as in the horizontal directions as illustrated (Figure C.6).

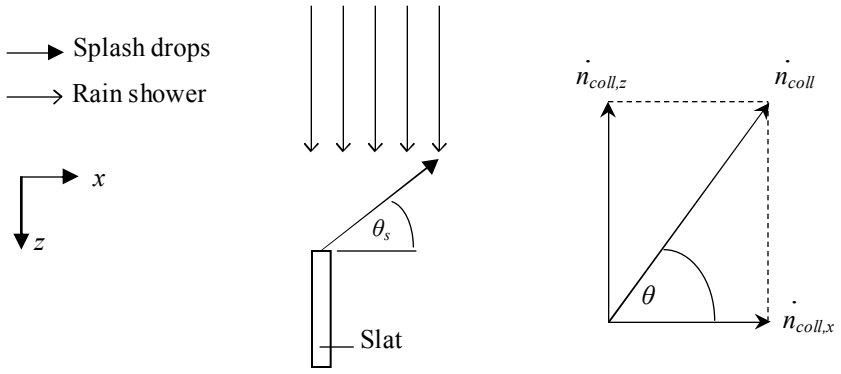

Figure C.6: Rain zone and splash drop interaction.

In order to simplify the drop collision calculation, it is assumed that the horizontal splash drop velocity is constant for the time the splash drop travels above the slat and for the vertical drop velocity averages are used, based upon the results obtained from the numerical model. The average upward vertical splash drop velocity is given by

$$\bar{v}_{s,z-} = -exp(-0.01\theta_s - 0.6783d_s + 0.0162v_a - 0.7627) \quad \text{(C.12)}$$

and the average vertical downward velocity is given by

$$\bar{v}_{s,z+} = exp(-0.0094\theta_s - 0.5659d_s + 0.0581v_a - 0.9099) \quad \text{(C.13)}$$

with the average horizontal velocity given by

$$\bar{v}_{s,x} = exp(0.0332\theta_s - 0.4898d_s + 0.0462v_a + 1.5912) \quad \text{(C.14)}$$

The maximum height that a splash drop can reach above a slat is given by

$$s_{s,zmax} = -exp(-0.0192\theta_s - 1.5252d_s - 0.1417v_a - 2.9320) \quad \text{(C.15)}$$

with the initial splash angle (θ_s) in degrees, the splash drop diameter (d_s) in mm and the upward air velocity (v_a) in m/s.

The vertical upward component of the collision rate between a number of splash drops (n_s) of a certain diameter (d_s) and a number of downward moving drops (n_l) of a certain diameter (d_l) is obtained by substituting the relevant values into Equation (3.1) to get

$$\dot{n}_{coll,z-} = \frac{\pi}{4}(d_l + d_s)^2 \left| v_{dl} - \bar{v}_{s,z-} \right| n_l n_s A_{fr} \left| s_{s,zmax} \right| \tag{C.16}$$

where

$$n_s = \frac{\dot{n}_s}{A_{fr}\left|\bar{v}_{s,z-}\right|} \quad \text{with} \quad \dot{n}_s = \frac{m_s}{\rho_w\left(\pi {d_s}^3/6\right)} \tag{C.17}$$

and

$$n_l = \frac{\dot{n}_l}{A_{fr} v_{dl}} \quad \text{with} \quad \dot{n}_l = \frac{m_l}{\rho_w\left(\pi {d_l}^3/6\right)} \tag{C.18}$$

The vertical downward component of the collision is expressed by

$$\dot{n}_{coll,z+} = \frac{\pi}{4}(d_l + d_s)^2 \left| v_{dl} - \bar{v}_{s,z+} \right| n_l n_s A_{fr} \left| s_{s,zmax} \right| \tag{C.19}$$

where

$$n_s = \frac{\dot{n}_s}{A_{fr}\left|\bar{v}_{s,z+}\right|} \quad \text{with} \quad \dot{n}_s = \frac{m_s}{\rho_w\left(\pi {d_s}^3/6\right)} \tag{C.20}$$

The total collision rate in the vertical direction can now be given by

$$\dot{n}_{coll,z} = \dot{n}_{coll,z-} + \dot{n}_{coll,z+} \tag{C.21}$$

The horizontal collision rate component is expressed by

$$\dot{n}_{coll,x} = \frac{\pi}{4}(d_l + d_s)^2 \bar{v}_{s,x} n_l n_s A_{fr} \left| s_{s,zmax} \right| \tag{C.22}$$

where

$$n_s = \frac{\dot{n}_s}{A_{fr}\left|\bar{v}_{s,x}\right|} \quad \text{with} \quad \dot{n}_s = \frac{m_s}{\rho_w\left(\pi {d_s}^3/6\right)} \tag{C.23}$$

The total collision rate between the two drop sizes can now be given by

$$\dot{n}_{coll} = \sqrt{{\dot{n}_{coll,z}}^2 + {\dot{n}_{coll,x}}^2} \tag{C.24}$$

with the number of collisions that lead to coalescence of the two drops given by

$$\dot{n}_{coal} = \eta_{coal}\dot{n}_{coll} \tag{C.25}$$

where the coalescence efficiency can be expressed in terms of the critical impact parameter

$$\eta_{coal} = x_c{}^2 \tag{3.6}$$

C.5 Temperature change of splash drops after drop impingement

When drops impinge onto the surface of a splash grid, it leads to the formation of a large number of relatively small splash drops of which the Sauter mean drop diameters are generally smaller than d_s = 3 mm (Appendix B). These drops return to the splash grid or pass the grid on their way down (in about 0.01 to 0.03 seconds) and due to their large numbers a significant amount of cooling is expected to take place in this cloud of small drops above a splash grid. The temperature change of these drops must be accounted for and are therefore investigated numerically. Figure C.7 show the control volume used when determining the temperature change of a drop from the first law of thermodynamics.

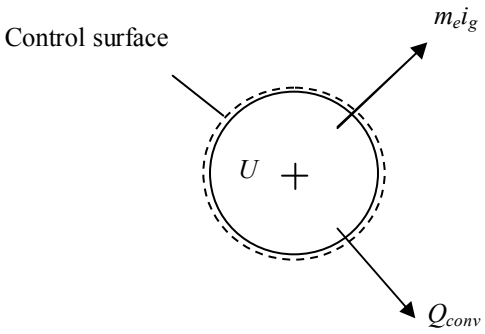

Figure C.7: Control volume of a drop when calculating temperature change.

The rate at which the internal energy of the splash drop changes is given by

$$\frac{\partial U}{\partial t} = -Q_{conv} - m_e i_g \tag{C.26}$$

The rate of the internal energy change of the splash drop can be expressed in terms of splash drop temperature by

$$\frac{\partial U}{\partial t} = \frac{\partial (M_s c_v T_s)}{\partial t} = M_s T_s \frac{\partial c_v}{\partial t} + M_s c_v \frac{\partial T_s}{\partial t} + c_v T_s \frac{\partial M_s}{\partial t} \tag{C.27}$$

and if it is assumed that $c_p = c_v$ for water and that $dc_v/dt \approx 0$ the following equation for drop temperature change is obtained.

$$\frac{\partial T_s}{\partial t} = \frac{-m_e i_{fgw} - Q_{conv}}{M_s c_{pw}} = \frac{-h_c A_s (T_s - T_\infty) - h_D A_s (\rho_{vs} - \rho_{v\infty}) i_{fg}}{M_s c_{pw}} \tag{C.28}$$

The heat- and mass transfer coefficients are determined from the definitions of the Nusselt and Sherwood numbers and available correlations by Ranz and Marshall (1952) for Nusselt and Sherwood numbers, given in Equations (2.40).

Equation (C.28) is in integrated numerically by using an Eulerian approach to give the temperature of the drop as

$$T_s^{t+\Delta t} = T_s^t + \left.\frac{dT_s}{dt}\right|^t \Delta t \tag{C.29}$$

From the numerically integrated results a curve fit is done and an equation is obtained to approximate the temperature change of a splash drop for the time it remains above the grid that is given by

$$\begin{aligned}\Delta T_s = -exp\big(&-0.0031\theta_s - 2.0422 d_s - 0.2974 v_a + 0.01113 T_{s,i} - 0.0099 T_{wb} \\ &- 0.0036 T_a - 4.9405 \cdot 10^{-7} P_{atm} - 28.4274\big)\end{aligned} \tag{C.30}$$

with the initial splash angle (θ_s) in degrees, the splash drop diameter (d_s) in mm, the upward air velocity (v_a) in m/s, temperature (T_a, T_{wb} and $T_{s,i}$) in Kelvin and atmospheric pressure (P_{atm}) in Pa.

Figure C.8 shows how Equation (C.30) compares to the results obtained from the numerical model.

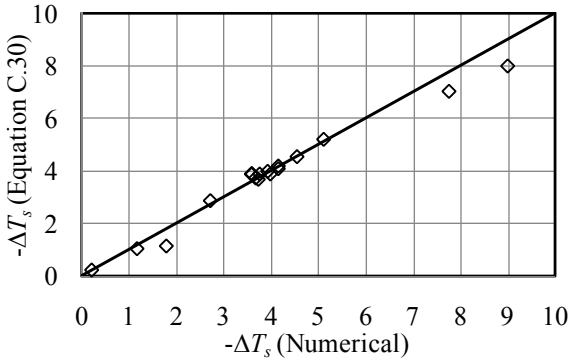

Figure C.8: Comparison between numerically predicted splash drop temperature change and Equation (C.30).

D

DROP STRADDLING AFTER IMPINGEMENT ON NARROW SLATS COVERED BY A THIN LAYER OF WATER

D.1 Introduction

Installation of splash grids below the fill in natural draught wet-cooling towers (NDWCTs) can enhance rain zone and therefore cooling tower performance due to the break-up of larger drops into smaller ones, herewith increasing the interfacial surface area between the water and the air and the residence time of drops in the rain zone. Splashing, straddling and dripping are the three mechanisms of drop break-up when drops impinge onto the surfaces of splash grids. In this appendix straddling is investigated and is defined as the break-up of drops after impingement on a slat due to a combination of deflection and cutting, resulting in straddled drops with downward trajectories as shown in Figures D.1 and D.2.

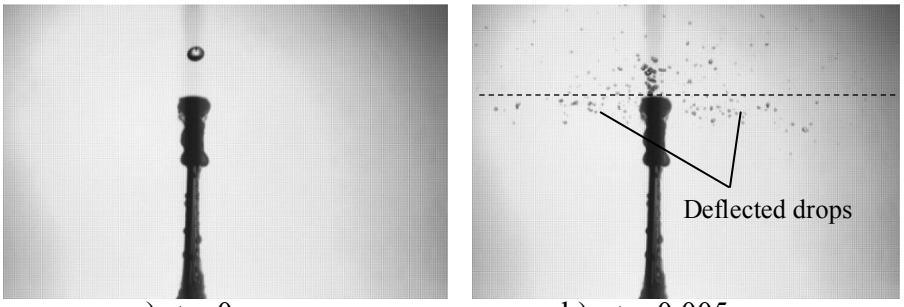

a) $t = 0$ s b) $t = 0.005$ s

Figure D.1: Deflective drop break-up.

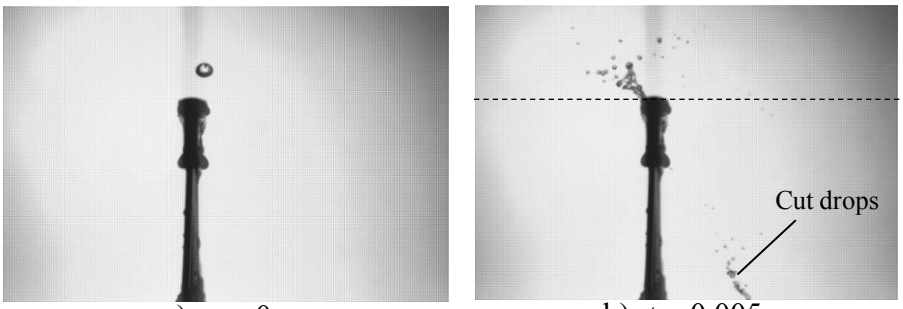

a) $t = 0$ s b) $t = 0.005$ s

Figure D.2: Cutting drop break-up.

Deflective break-up happens when the initial drop is close enough to the edge of the slat when it impinges so that there is not enough water between the drop and slat edge to cause enough horizontal resistance for crown formation and resultant upward moving splash drops. The resultant drops are rather deflected in the horizontal direction away from the slat and the drops are generally much smaller than the initial drop (Figure D.1).

Cutting happens when part of the initial drop is not directly above the slat and therefore gets sheared from the initial drop to form drops that are relatively large in relation to the deflected drops (Figure D.2).

Sequential photographs of drop impingements at locations where drop break-up is mainly due to cutting are presented in this appendix. These photographs are used in conjunction with the photographs of corresponding cases in Appendix B to quantify the average straddle fractions and straddle drop sizes for different impingement locations over the width of the slat. Results are presented for different initial drop size, drop fall distance, slat width and water film thickness combinations before the data is compared to the simplified model of Dreyer (1994).

D.2 Experimental setup

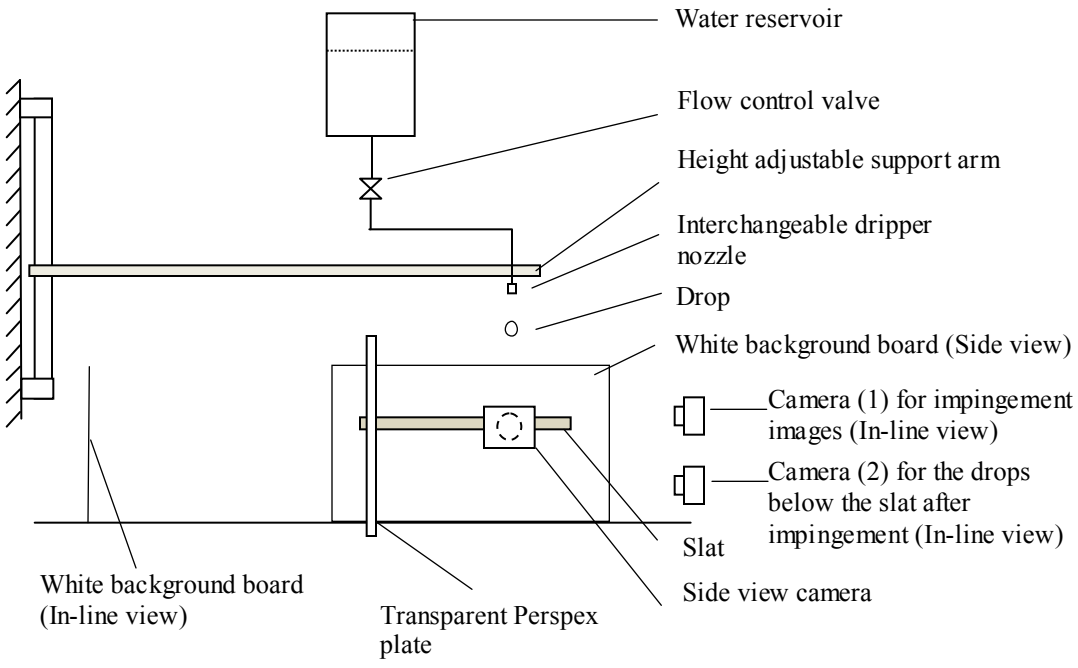

Figure D.3: Schematic of experimental setup for straddle experiments.

Figure D.3 and D.4 show a similar experimental setup to the one described in Appendix B that is used to investigate straddling. Sequential photographs of a drop impingement are taken by two cameras from the front, in-line with the slat. Camera (1) captures the drop impingement at slat level and is used to determine the impingement location and to capture the deflected drops, while Camera (2) captures the cut drops a distance below the slat when the cutting process is completed. The vertical pitch between the two cameras lenses is 80 mm for all the experiments except where it is stated that the pitch is increased to 160 mm. A camera capturing the slat from the side is used to determine the film thickness on the slat just before the drop impinges according to the method described in Appendix B (Section B.1).

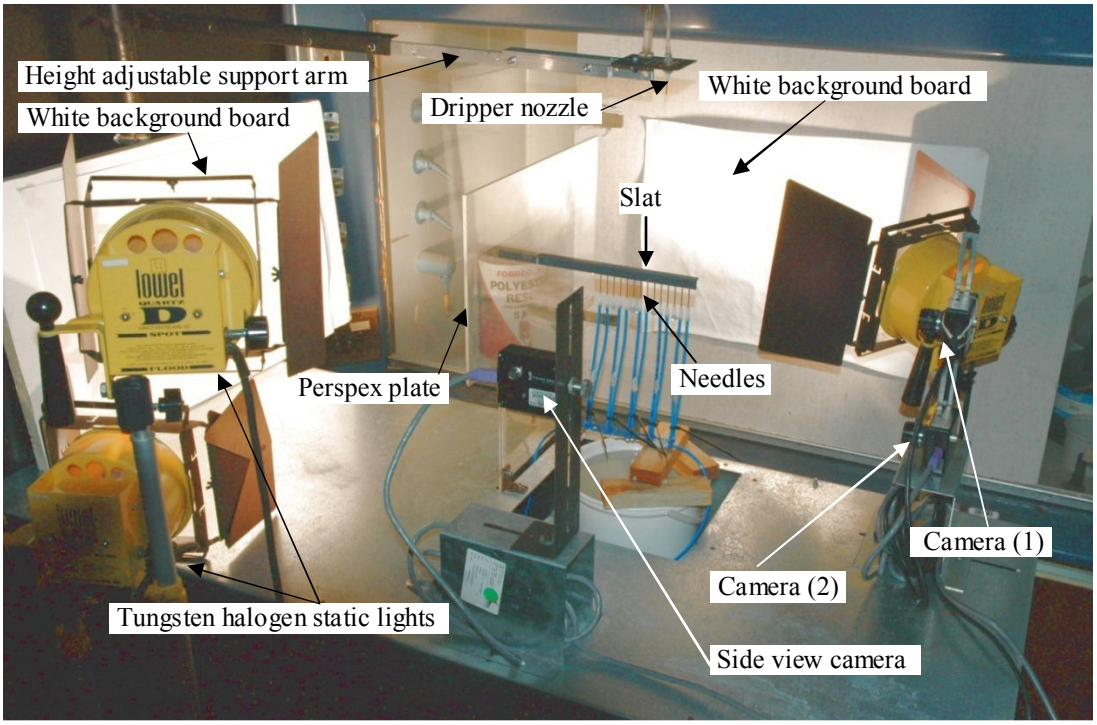

Figure D.4: Photograph of experimental setup for straddle experiments.

D.3 Experimental results

This section presents sequential photographs of drop impingements on slats for cases where the drop break-up is mainly due to cutting, together with plots of the locally measured straddle fractions and straddle drop size distributions. Table D.1 shows a summary of the experiments done in terms of the test variables, also giving the sections where the data can be found.

Table D.1: Summary of straddle experiments.

Section	Initial drop diameter, d_i [mm]	Slat width, W [mm]	Film thickness on slat, δ [mm]	Drop fall distance, H_d [mm]
D.3.1	4	3, 6, 12	$0 < \delta < 2$	250
D.3.2	4	3, 6, 12	$0 < \delta < 2$	470
D.3.3	4	3, 6, 12	$0 < \delta < 2$	970
D.3.4	2.89, 5.48	3, 6, 12	$0.78 \leq \delta \leq 1.00$	250
D.3.5	2.89, 5.48	3, 6, 12	$0.78 \leq \delta \leq 1.00$	470
D.3.6	2.89, 5.48	3, 6, 12	$0.78 \leq \delta \leq 1.00$	970

The straddle mass data is presented by the local straddle mass fraction given by

$$f_c = \frac{M_c}{M_i} \tag{2.66}$$

The average straddle fraction is given by

$$\bar{f_c} = \int_0^1 f_c(\lambda)\, \partial\lambda \tag{D.1}$$

where the dimensionless displacement, λ is defined as

$$\lambda = \frac{2x}{W + d_i} \tag{B.2}$$

and x is the horizontal displacement between the drop and slat centres and W and d_i are the slat width and initial drop diameter respectively, as shown in Figure B.5.

D.3.1 Straddle results (H_d = 250 mm, $d_i \approx$ 4 mm)

This section presents the straddle results when a d_i = 4 mm in diameter drop falls H_d = 250 mm before it impinges onto different film covered slats. Figures D.5 to D.11 show sequential photographs of the drop impingements, where break-up is mainly due to cutting, for different slat width (W = 3, W = 6 and W = 12 mm) and film thickness combinations. Figure D.12 shows plots of the measured local straddle fractions and Sauter mean drop diameters for each slat.

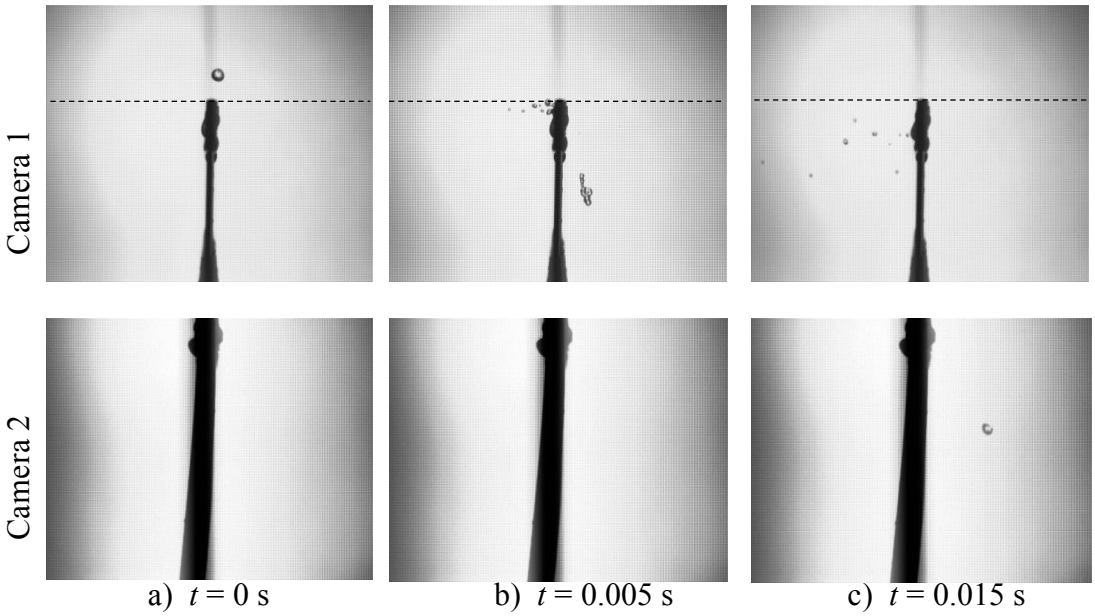

Figure D.5: Straddle photographs (H_d = 250 mm, W = 3 mm, $\delta \approx 0.43$ mm, $\lambda \approx 0.4$, $d_i \approx 4$ mm).

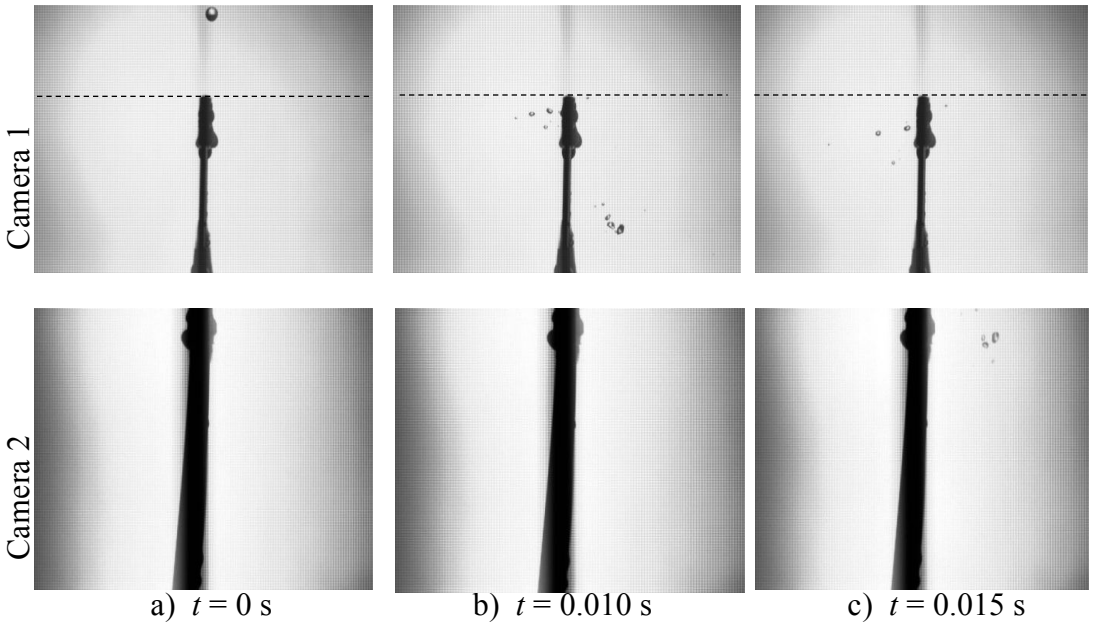

Figure D.6: Straddle photographs (H_d = 250 mm, W = 3 mm, $\delta \approx 0.78$ mm, $\lambda \approx 0.3$, $d_i \approx 4$ mm).

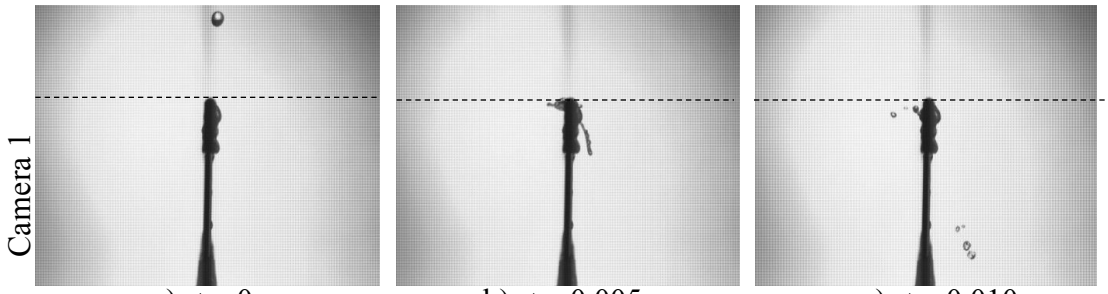

a) $t = 0$ s b) $t = 0.005$ s c) $t = 0.010$ s

Figure D.7: Straddle photographs (H_d = 250 mm, W = 3 mm, $\delta \approx 1.30$ mm, $\lambda \approx 0.5$, $d_i \approx 4$ mm).

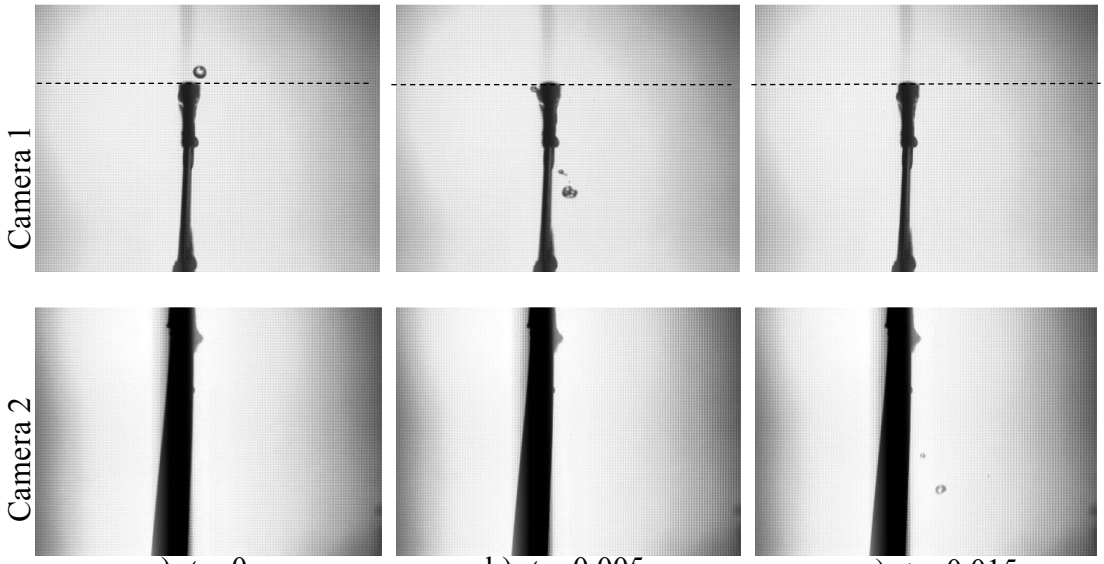

a) $t = 0$ s b) $t = 0.005$ s c) $t = 0.015$ s

Figure D.8: Straddle photographs (H_d = 250 mm, W = 6 mm, $\delta \approx 0.85$ mm, $\lambda \approx 0.6$, $d_i \approx 4$ mm).

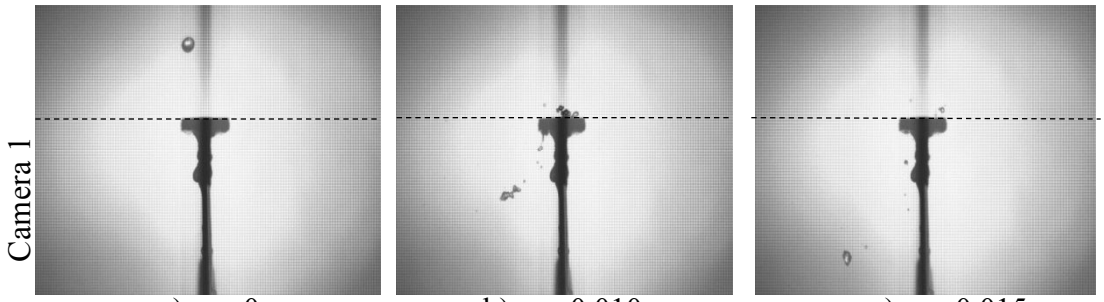

a) $t = 0$ s b) $t = 0.010$ s c) $t = 0.015$ s

Figure D.9: Straddle photographs (H_d = 250 mm, W = 12 mm, $\delta \approx 0.36$ mm, $\lambda \approx 0.6$, $d_i \approx 4$ mm).

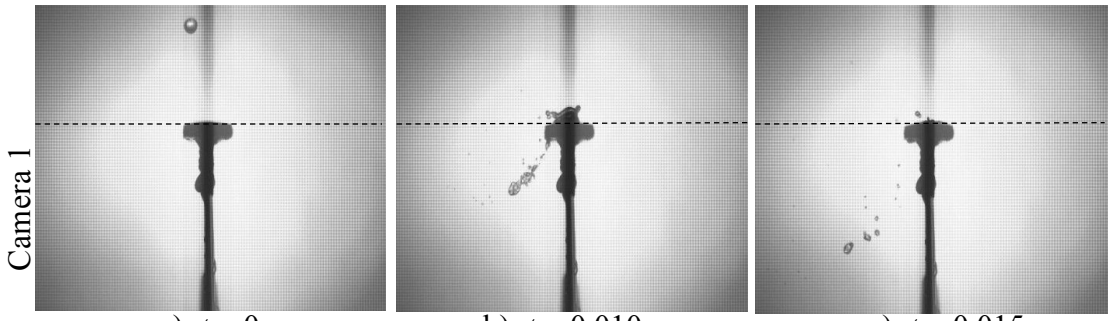

a) $t = 0$ s b) $t = 0.010$ s c) $t = 0.015$ s

Figure D.10: Straddle photographs ($H_d = 250$ mm, $W = 12$ mm, $\delta \approx 1.00$ mm, $\lambda \approx 0.6$, $d_i \approx 4$ mm).

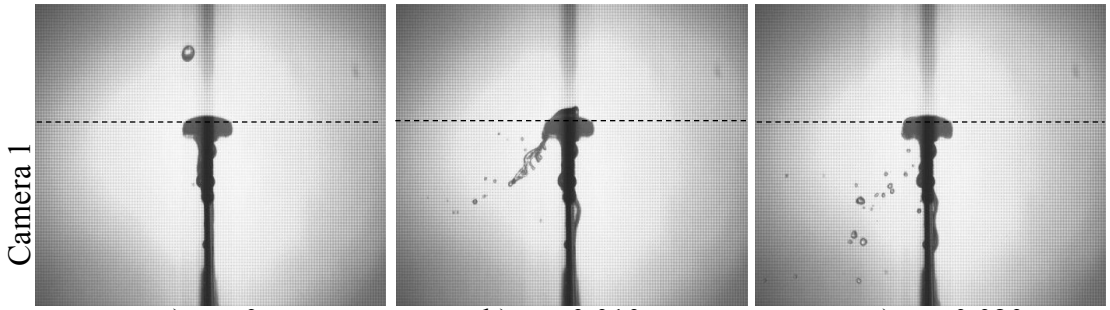

a) $t = 0$ s b) $t = 0.010$ s c) $t = 0.020$ s

Figure D.11: Straddle photographs ($H_d = 250$ mm, $W = 12$ mm, $\delta \approx 1.75$ mm, $\lambda \approx 0.7$, $d_i \approx 4$ mm).

Figure D.12 shows an increase in the straddle fraction with increasing displacement between the drop and slat centre up to a point where the initial drop only grazes the slat. The number of straddle drops (not shown) decreases with increasing horizontal displacement between the initial drop centre and the slat centre and becomes one when the drop grazes the slat.

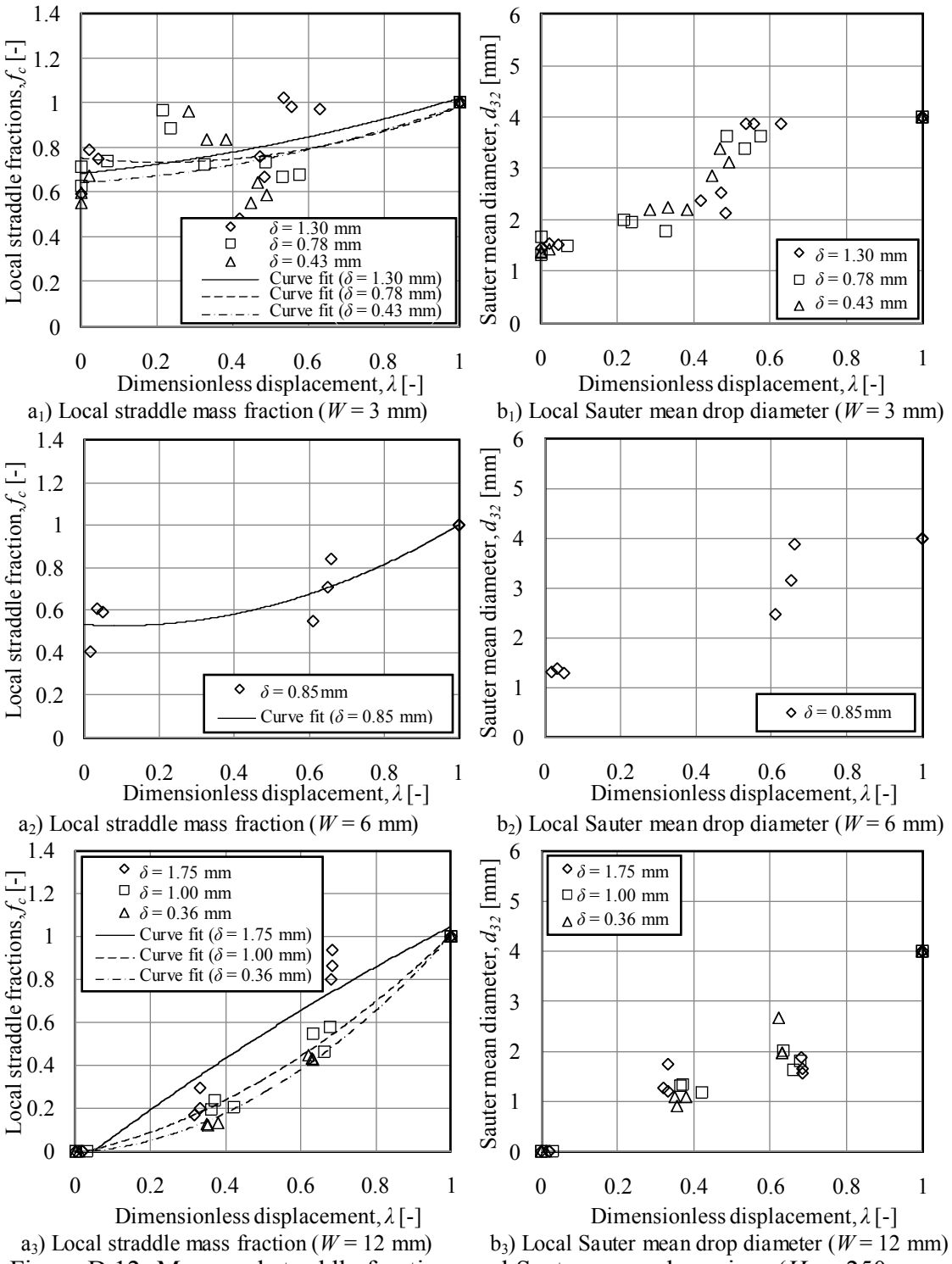

a$_1$) Local straddle mass fraction (W = 3 mm)
b$_1$) Local Sauter mean drop diameter (W = 3 mm)
a$_2$) Local straddle mass fraction (W = 6 mm)
b$_2$) Local Sauter mean drop diameter (W = 6 mm)
a$_3$) Local straddle mass fraction (W = 12 mm)
b$_3$) Local Sauter mean drop diameter (W = 12 mm)

Figure D.12: Measured straddle fractions and Sauter mean drop sizes (H_d = 250 mm, $d_i \approx$ 4.00 mm).

D.3.2 Straddle results (H_d = 470 mm, $d_i \approx$ 4 mm)

This section presents the straddle results when a d_i = 4 mm in diameter drop falls H_d = 470 mm before it impinges onto different film covered slats. Figures D.13 to D.22 show sequential photographs of the drop impingements, where break-up is mainly due to cutting, for different slat width (W = 3, W = 6 and W = 12 mm) and film thickness combinations. Figure D.23 shows plots of the measured local straddle fractions and Sauter mean drop diameters for each slat.

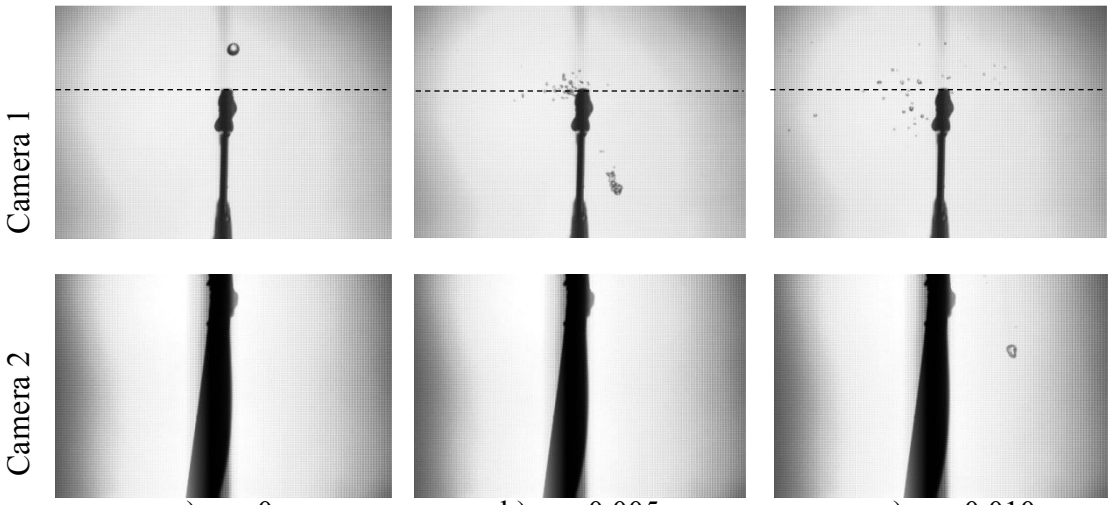

a) t = 0 s b) t = 0.005 s c) t = 0.010s

Figure D.13: Straddle photographs (H_d = 470 mm, W = 3 mm, $\delta \approx$ 0.35 mm, $\lambda \approx$ 0.5, $d_i \approx$ 4 mm).

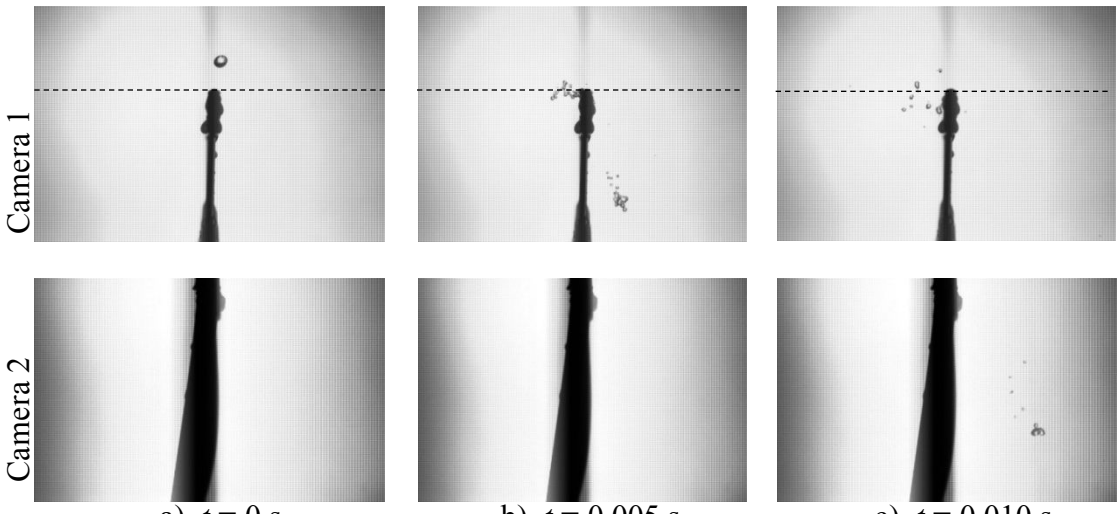

a) t = 0 s b) t = 0.005 s c) t = 0.010 s

Figure D.14: Straddle photographs (H_d = 470 mm, W = 3 mm, $\delta \approx$ 0.95 mm, $\lambda \approx$ 0.5, $d_i \approx$ 4 mm).

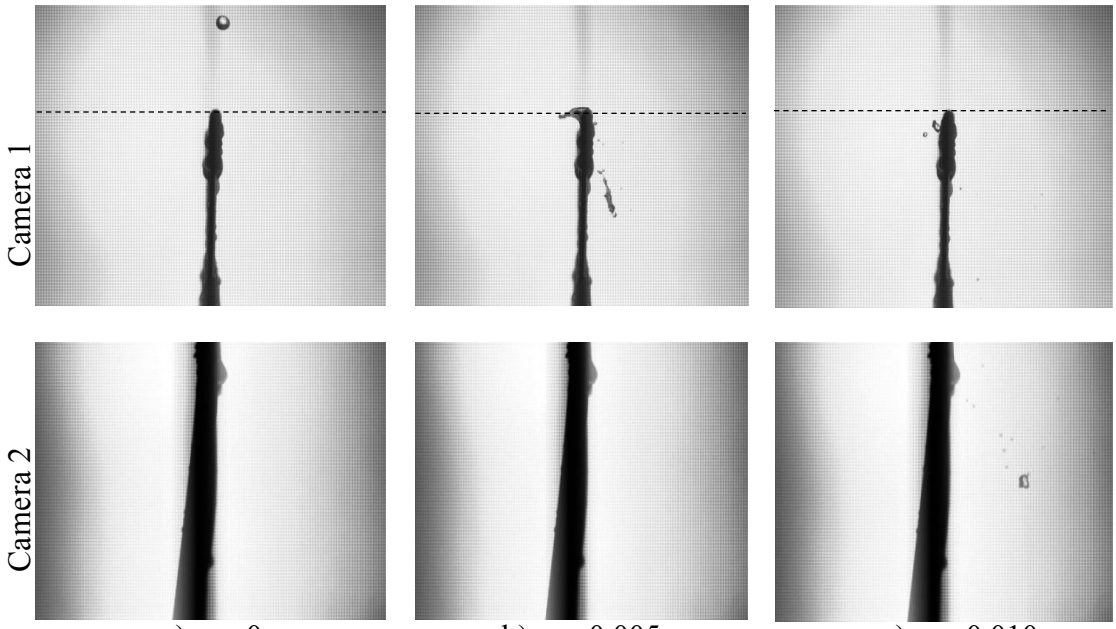

a) $t = 0$ s b) $t = 0.005$ s c) $t = 0.010$ s

Figure D.15: Straddle photographs ($H_d = 470$ mm, $W = 3$ mm, $\delta \approx 1.40$ mm, $\lambda \approx 0.5$, $d_i \approx 4$ mm).

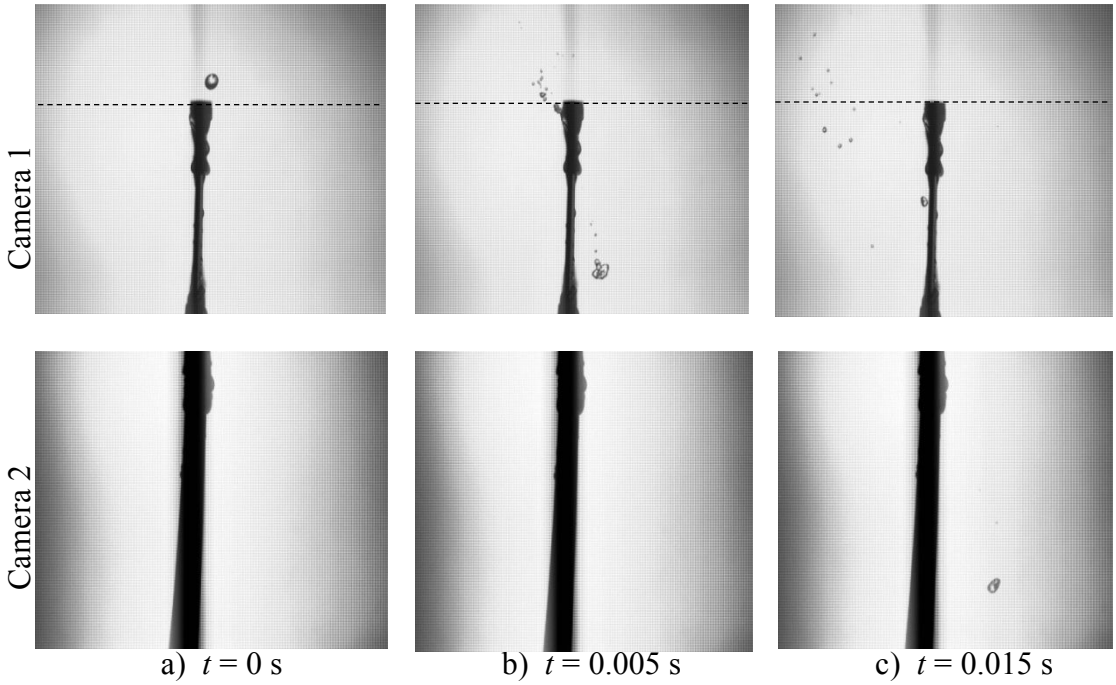

a) $t = 0$ s b) $t = 0.005$ s c) $t = 0.015$ s

Figure D.16: Straddle photographs ($H_d = 470$ mm, $W = 6$ mm, $\delta \approx 0.25$ mm, $\lambda \approx 0.5$, $d_i \approx 4$ mm).

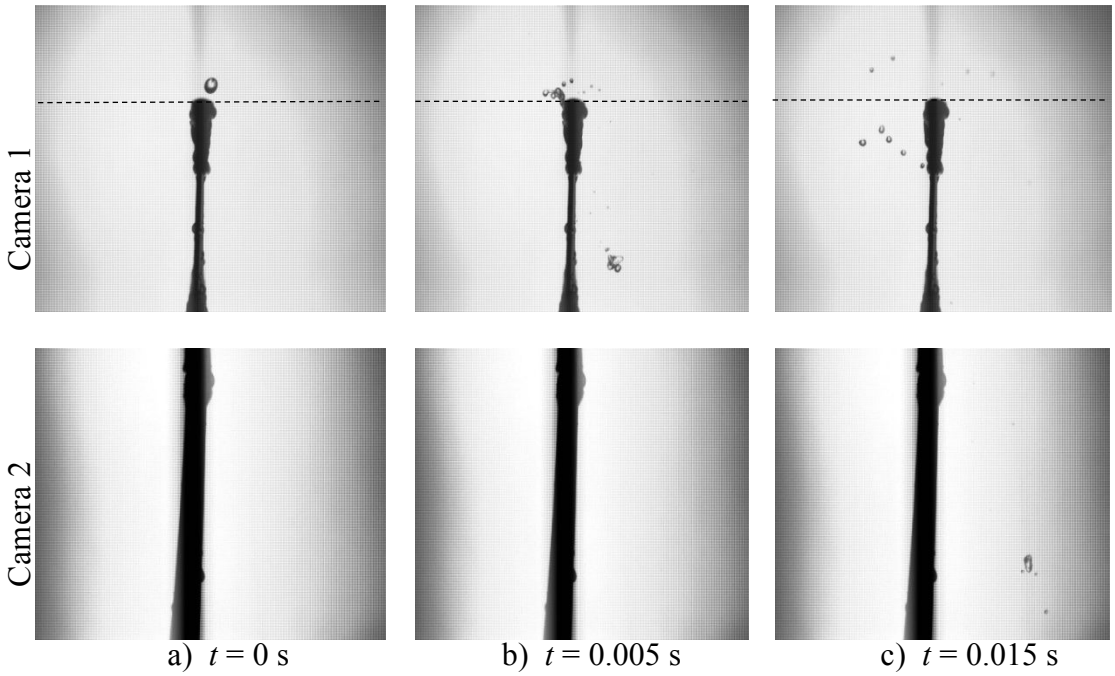

Figure D.17: Straddle photographs (H_d = 470 mm, W = 6 mm, $\delta \approx 0.85$ mm, $\lambda \approx 0.5$, $d_i \approx 4$ mm).

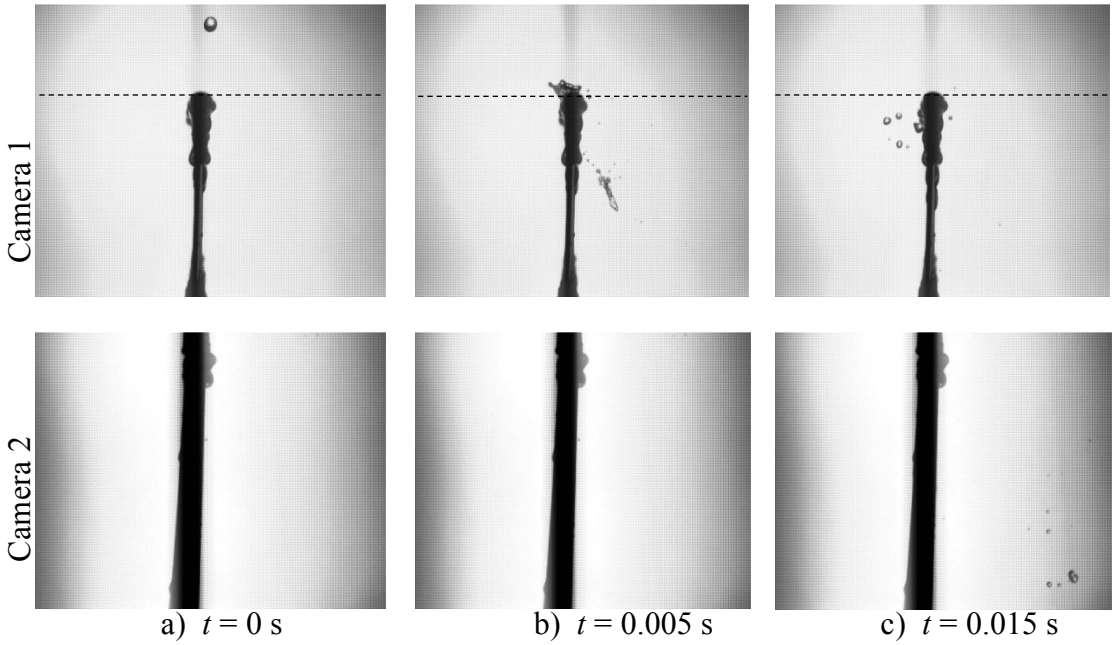

Figure D.18: Straddle photographs (H_d = 470 mm, W = 6 mm, $\delta \approx 1.45$ mm, $\lambda \approx 0.5$, $d_i \approx 4$ mm).

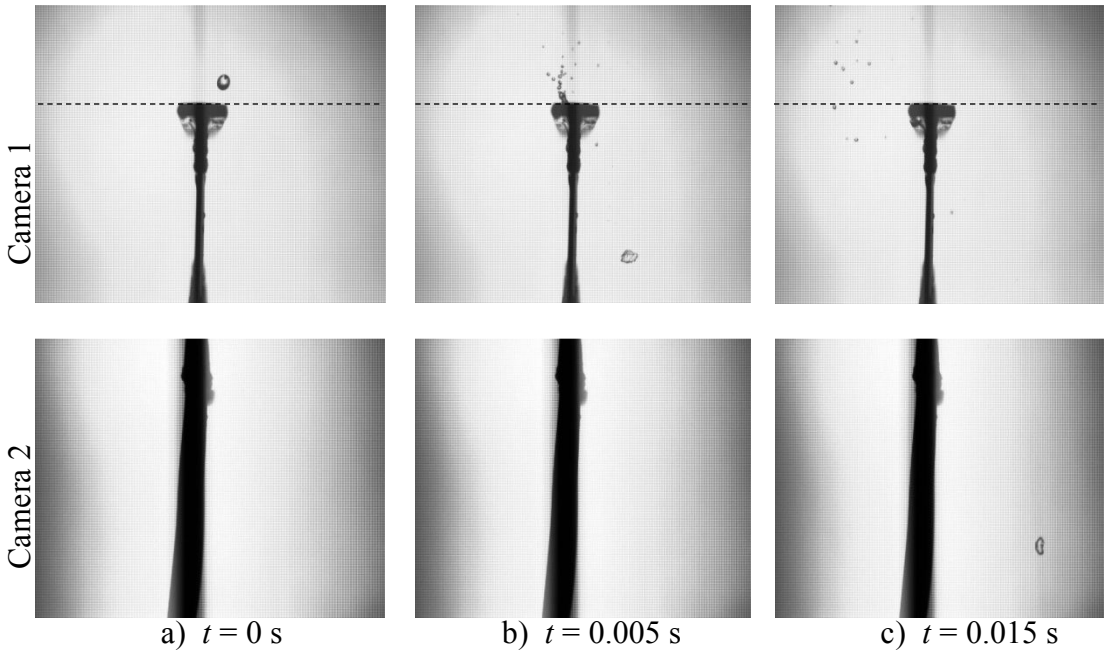

a) $t = 0$ s b) $t = 0.005$ s c) $t = 0.015$ s

Figure D.19: Straddle photographs (H_d = 470 mm, W = 12 mm, $\delta \approx 0.30$ mm, $\lambda \approx 0.75$, $d_i \approx 4$ mm).

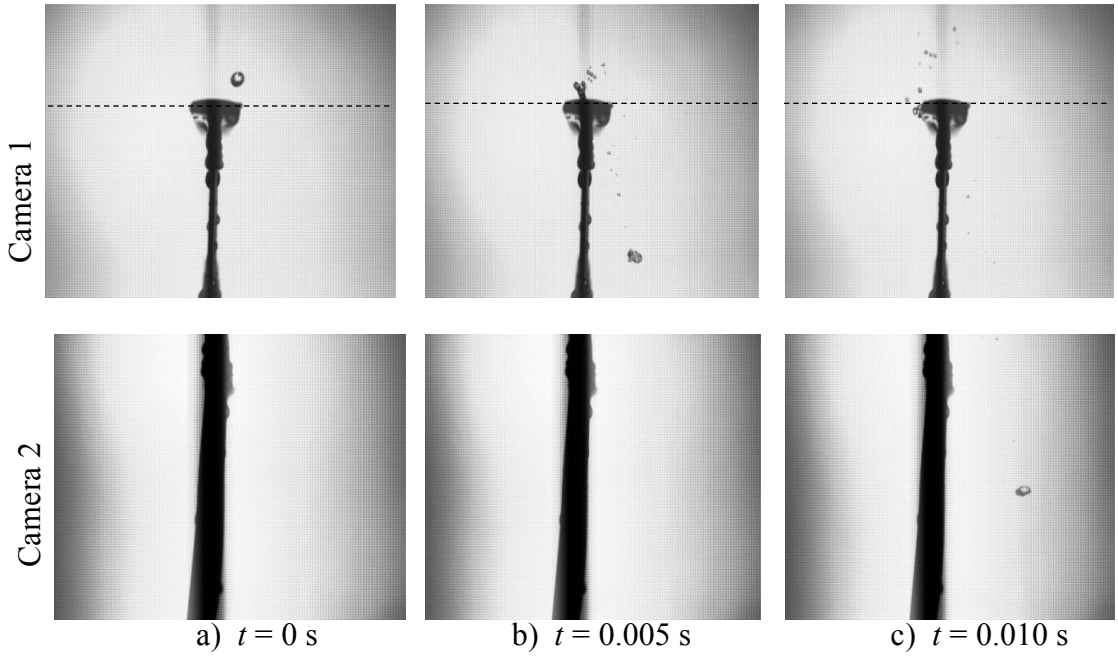

a) $t = 0$ s b) $t = 0.005$ s c) $t = 0.010$ s

Figure D.20: Straddle photographs (H_d = 470 mm, W = 12 mm, $\delta \approx 0.75$ mm, $\lambda \approx 0.75$, $d_i \approx 4$ mm).

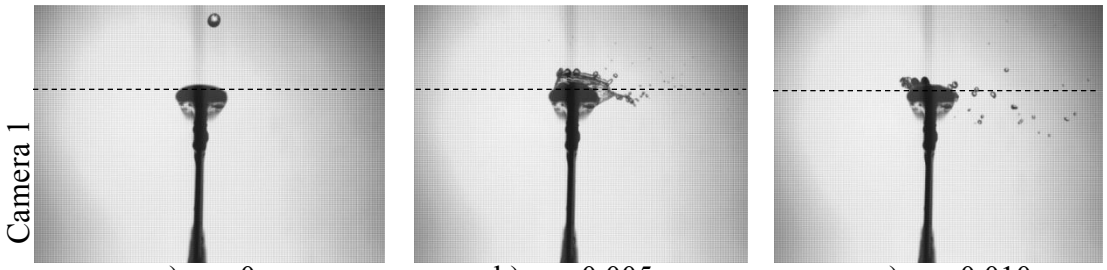

a) $t = 0$ s b) $t = 0.005$ s c) $t = 0.010$ s

Figure D.21: Straddle photographs (H_d = 470 mm, W = 12 mm, $\delta \approx 1.95$ mm, $\lambda \approx 0.40$, $d_i \approx 4$ mm).

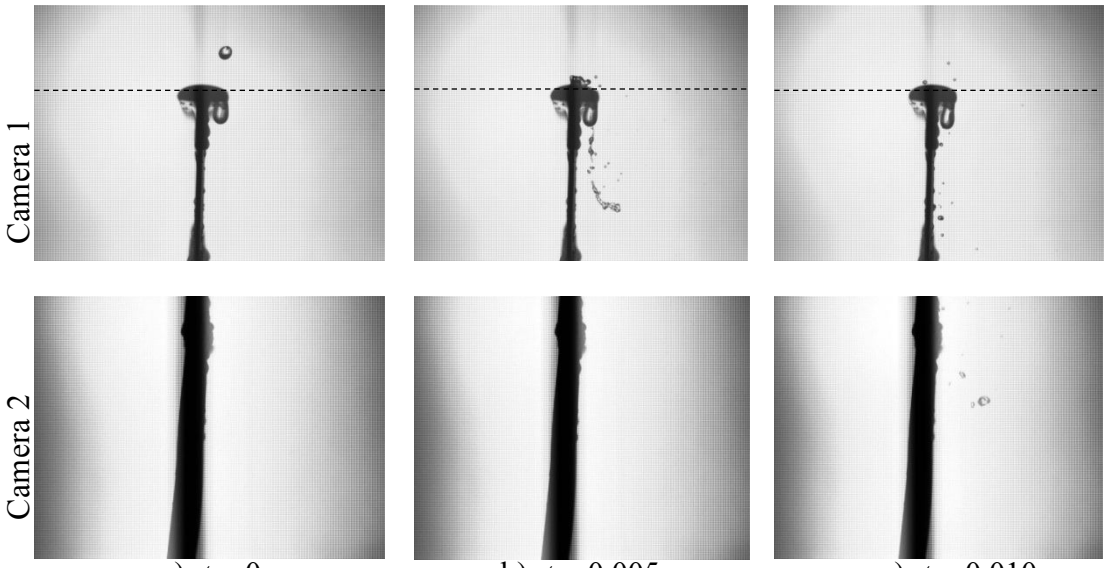

a) $t = 0$ s b) $t = 0.005$ s c) $t = 0.010$ s

Figure D.22: Straddle photographs (H_d = 470 mm, W = 12 mm, $\delta \approx 1.95$ mm, $\lambda \approx 0.85$, $d_i \approx 4$ mm).

Figure D.23 presents the local straddle fractions and Sauter mean drop diameters in terms of the dimensionless displacement parameter and it can be seen when Figures D.12 and D.23 are compared that the results are very similar for the two different drop fall distances.

The straddle results seems to be relatively insensitive to the fall distance of the $d_i = 4$ mm in diameter drop up to a fall distance of $H_d = 0.47$ m. This may be due to the fact that the straddled part of the original drop is isolated from the rest of the drop before the impulse due to the impact onto the slat can propagate far enough through the drop, especially for larger horizontal displacements between the drop and slat centre.

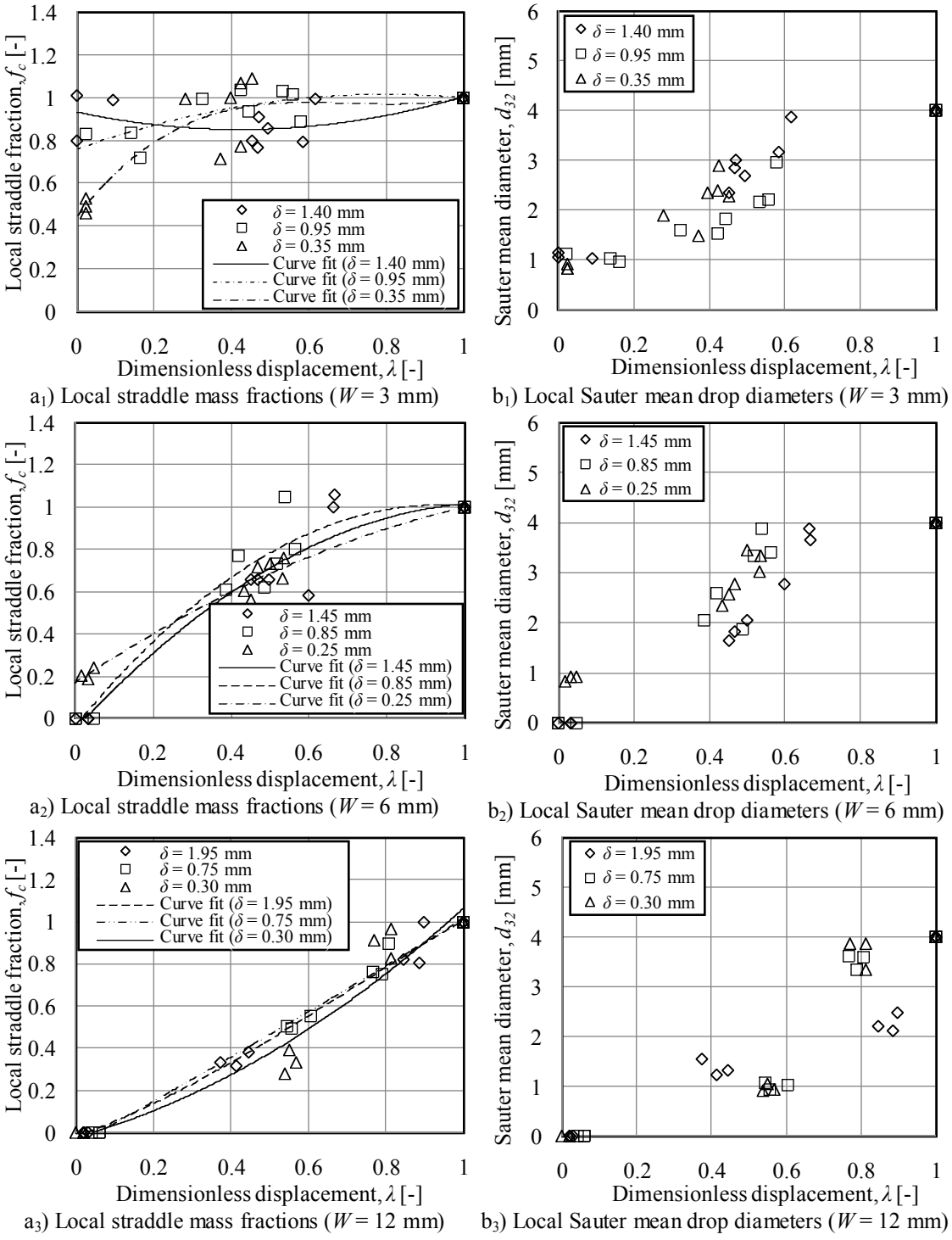

a$_1$) Local straddle mass fractions (W = 3 mm)
b$_1$) Local Sauter mean drop diameters (W = 3 mm)
a$_2$) Local straddle mass fractions (W = 6 mm)
b$_2$) Local Sauter mean drop diameters (W = 6 mm)
a$_3$) Local straddle mass fractions (W = 12 mm)
b$_3$) Local Sauter mean drop diameters (W = 12 mm)

Figure D.23: Measured straddle fractions and Sauter mean drop sizes (H_d = 470 mm, $d_i \approx$ 4.00 mm).

D.3.3 Straddle results (H_d = 970 mm, $d_i \approx$ 4 mm)

This section presents the straddle results when a d_i = 4 mm in diameter drop falls H_d = 970 mm before it impinges onto different film covered slats. Figures D.24 to D.32 show sequential photographs of the drop impingements, where break-up is mainly due to cutting, for different slat width (W = 3, W = 6 and W = 12 mm) and film thickness combinations. Figure D.33 shows plots of the measured local straddle fractions and Sauter mean drop diameters for each slat.

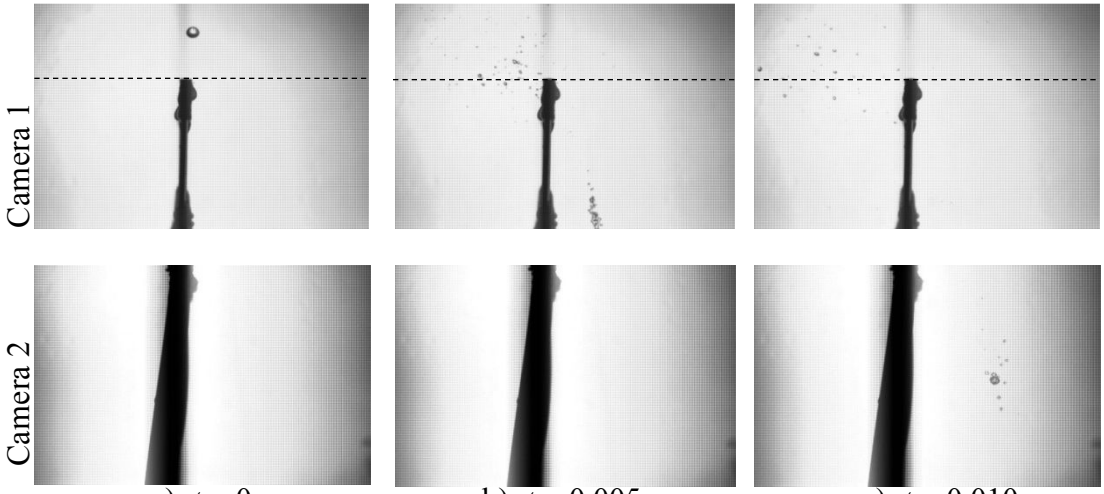

a) t = 0 s b) t = 0.005 s c) t = 0.010 s

Figure D.24: Straddle photographs (H_d = 970 mm, W = 3 mm, $\delta \approx$ 0.11 mm, $\lambda \approx$ 0.5, $d_i \approx$ 4 mm).

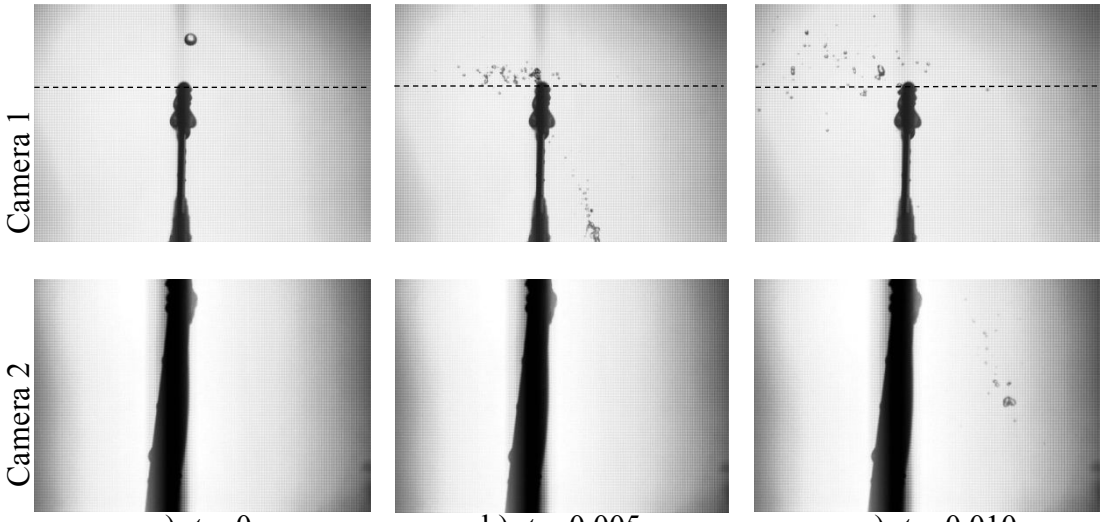

a) t = 0 s b) t = 0.005 s c) t = 0.010 s

Figure D.25: Straddle photographs (H_d = 970 mm, W = 3 mm, $\delta \approx$ 1.00 mm, $\lambda \approx$ 0.5, $d_i \approx$ 4 mm).

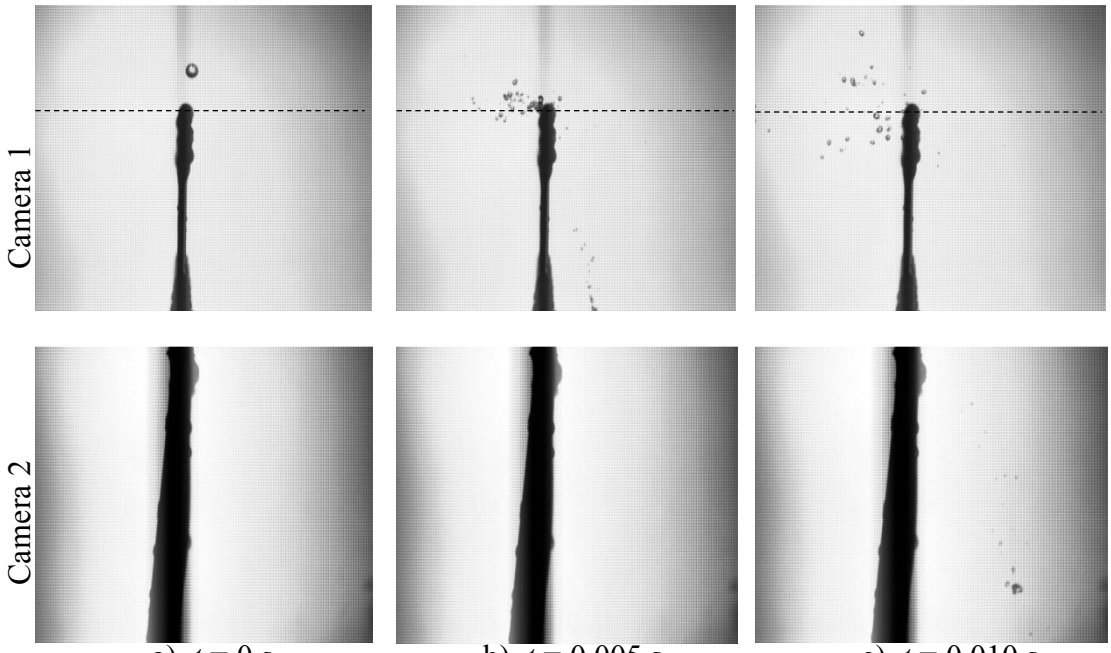

a) $t = 0$ s b) $t = 0.005$ s c) $t = 0.010$ s

Figure D.26: Straddle photographs ($H_d = 970$ mm, $W = 3$ mm, $\delta \approx 1.32$ mm, $\lambda \approx 0.5$, $d_i \approx 4$ mm).

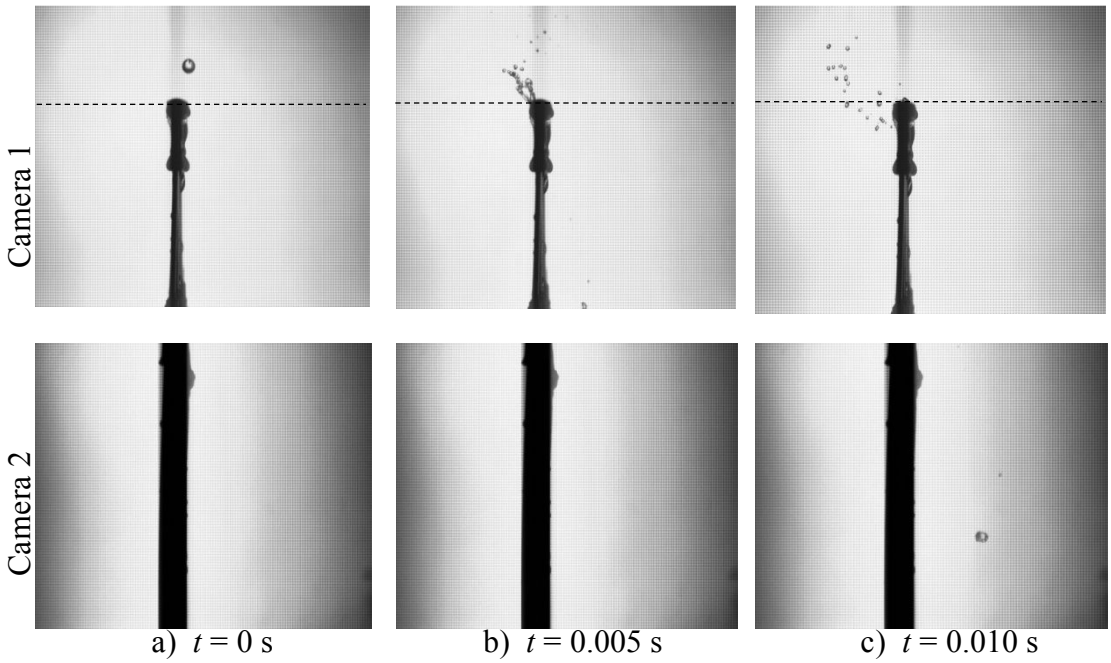

a) $t = 0$ s b) $t = 0.005$ s c) $t = 0.010$ s

Figure D.27: Straddle photographs ($H_d = 970$ mm, $W = 6$ mm, $\delta \approx 0.50$ mm, $\lambda \approx 0.5$, $d_i \approx 4$ mm).

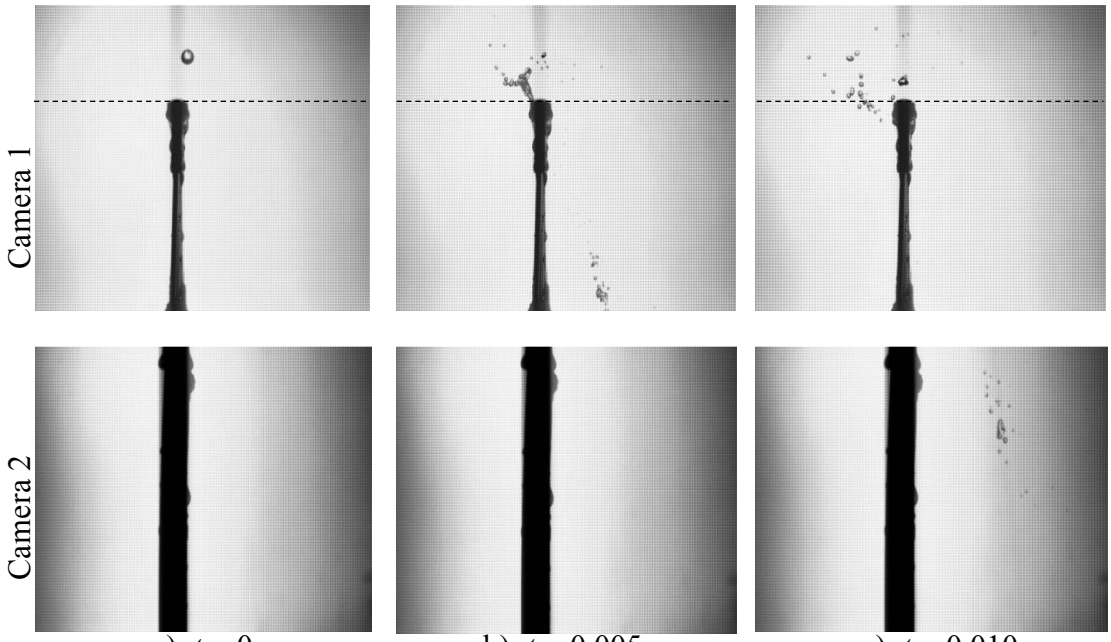

a) $t = 0$ s b) $t = 0.005$ s c) $t = 0.010$ s

Figure D.28: Straddle photographs ($H_d = 970$ mm, $W = 6$ mm, $\delta \approx 0.85$ mm, $\lambda \approx 0.5$, $d_i \approx 4$ mm).

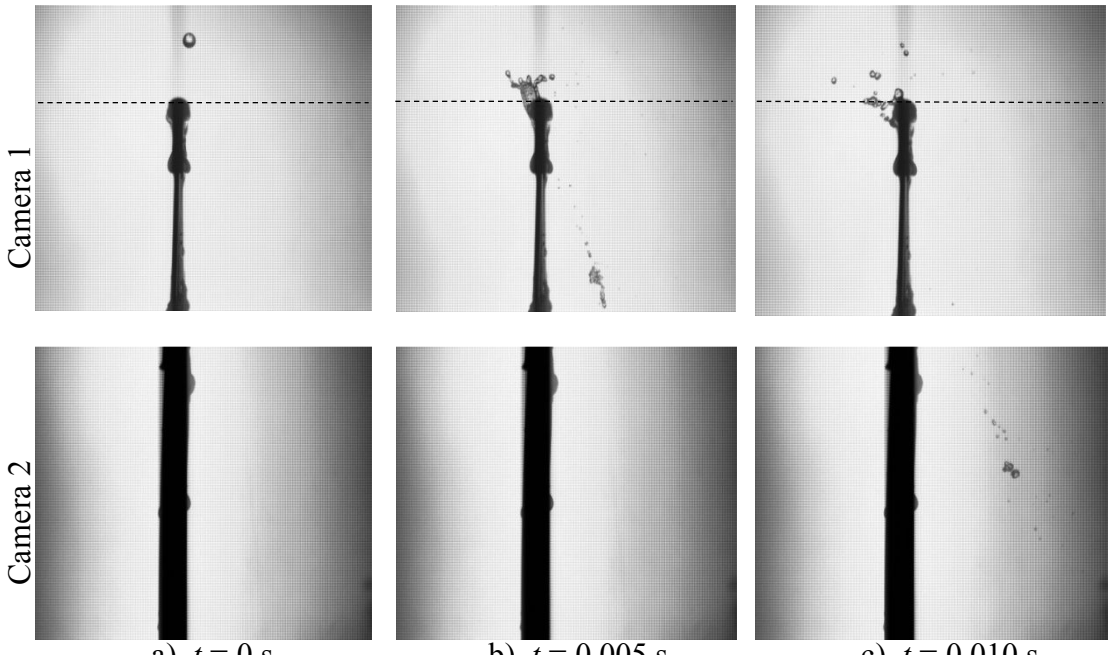

a) $t = 0$ s b) $t = 0.005$ s c) $t = 0.010$ s

Figure D.29: Straddle photographs ($H_d = 970$ mm, $W = 6$ mm, $\delta \approx 1.43$ mm, $\lambda \approx 0.5$, $d_i \approx 4$ mm).

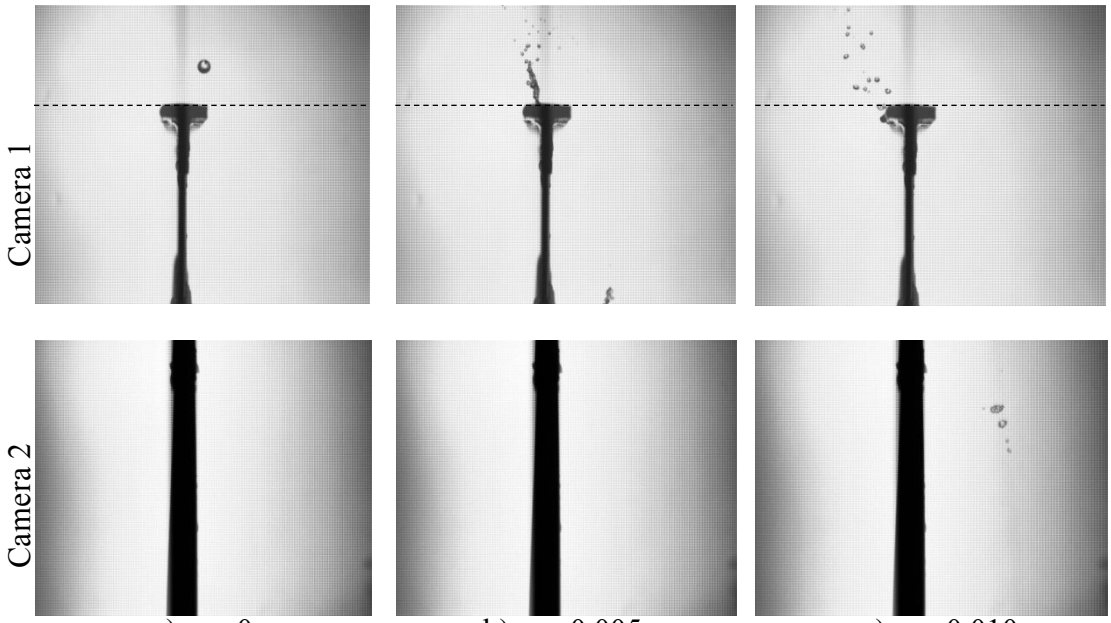

a) $t = 0$ s b) $t = 0.005$ s c) $t = 0.010$ s

Figure D.30: Straddle photographs ($H_d = 970$ mm, $W = 12$ mm, $\delta \approx 0.21$ mm, $\lambda \approx 0.7$, $d_i \approx 4$ mm).

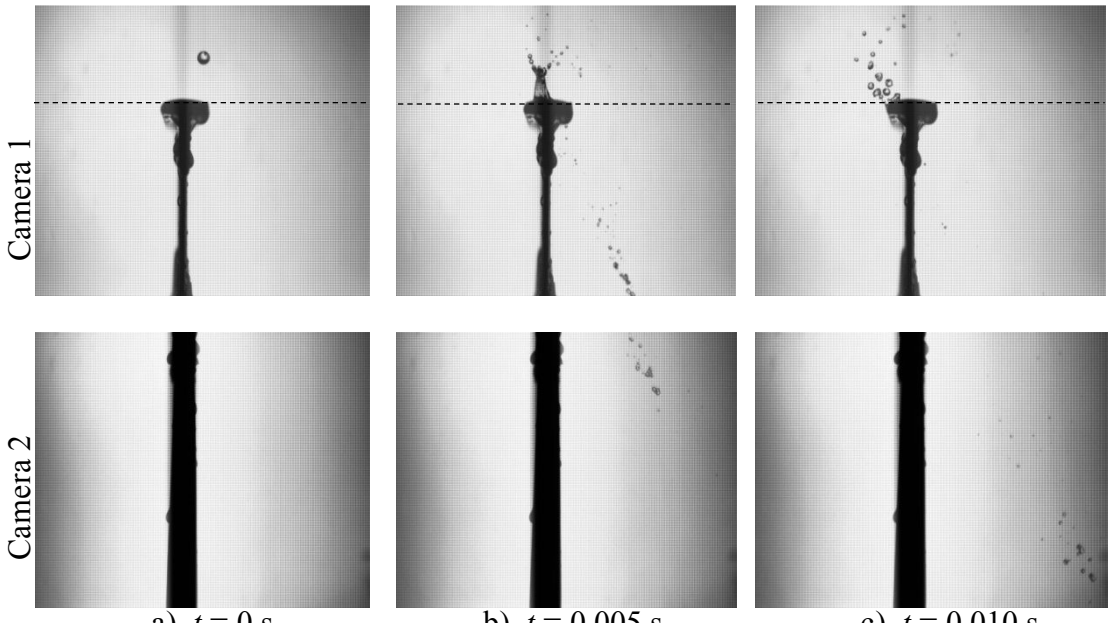

a) $t = 0$ s b) $t = 0.005$ s c) $t = 0.010$ s

Figure D.31: Straddle photographs ($H_d = 970$ mm, $W = 12$ mm, $\delta \approx 0.95$ mm, $\lambda \approx 0.7$, $d_i \approx 4$ mm).

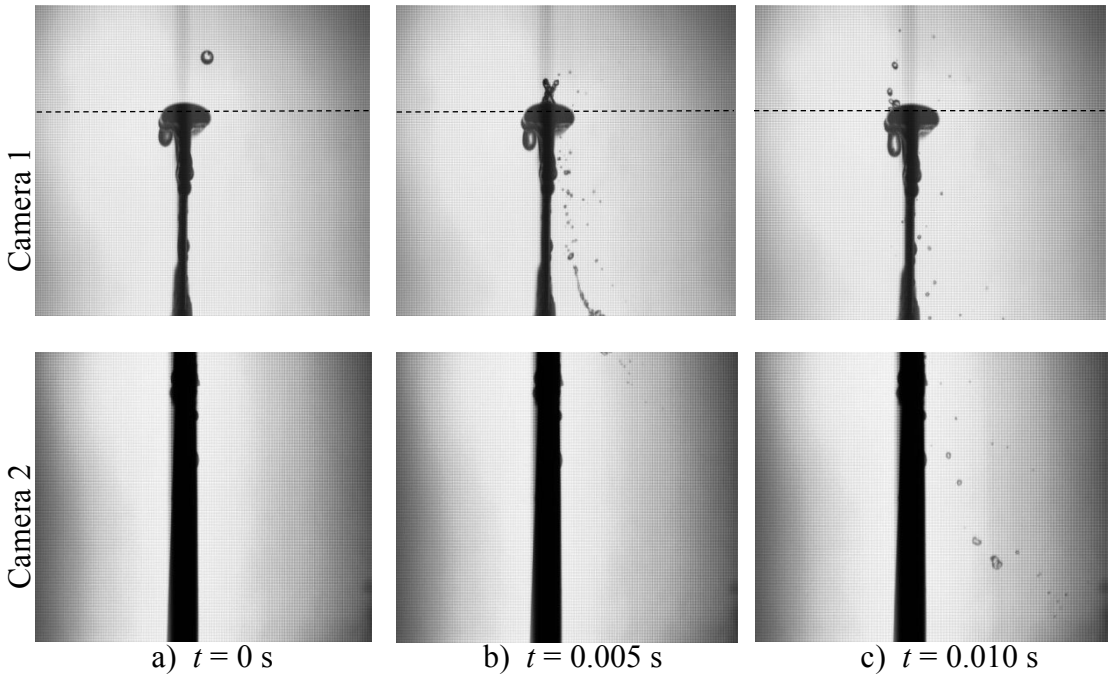

Figure D.32: Straddle photographs (H_d = 970 mm, W = 12 mm, $\delta \approx 1.75$ mm, $\lambda \approx 0.8$, $d_i \approx 4$ mm).

Figure D.33 again shows similar straddle trends when a d_i = 4 mm in diameter drop impinges from a falling height of H_d = 970 mm, compared to the previous falling heights of H_d = 250 mm and H_d = 470 mm. The results also show that straddle fractions and Sauter mean drop sizes for a d_i = 4 mm in diameter impinging drop are not significantly influenced by the water film thicknesses on the slats. Straddle Sauter mean drop sizes do however show a rapid increase with displacement at $\lambda \approx 0.5$ on the narrower slats, while this increase happens more gradually with displacement on the W = 12 mm slat.

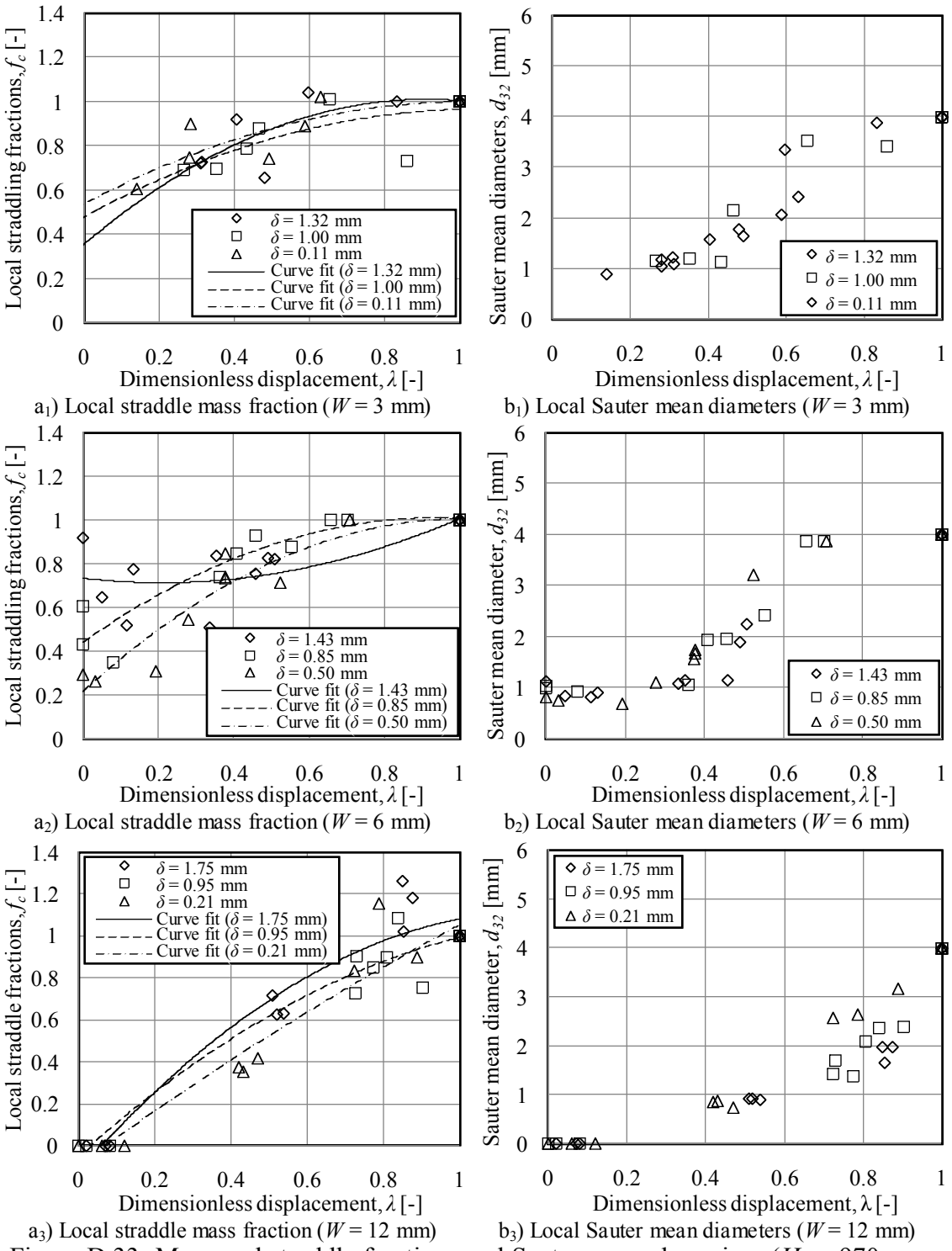

a$_1$) Local straddle mass fraction (W = 3 mm) b$_1$) Local Sauter mean diameters (W = 3 mm)

a$_2$) Local straddle mass fraction (W = 6 mm) b$_2$) Local Sauter mean diameters (W = 6 mm)

a$_3$) Local straddle mass fraction (W = 12 mm) b$_3$) Local Sauter mean diameters (W = 12 mm)

Figure D.33: Measured straddle fractions and Sauter mean drop sizes (H_d = 970 mm, $d_i \approx$ 4.00 mm).

D.3.4 Straddle results (H_d = 250 mm, $d_i \approx$ 2.89 mm and $d_i \approx$ 5.48 mm)

This section presents the straddle results when a relatively small (d_i = 2.89 mm) and large drop (d_i = 5.48 mm), respectively, falls H_d = 250 mm before impinging onto different slats. Figures D.34 to D.40 show sequential photographs of drop impingements for different drop size (d_i = 2.89 mm and d_i = 5.48 mm) and slat width (W = 3, W = 6 and W = 12 mm) combinations while the film thickness on each slat is constant. For each of these cases the drop break-up is mainly due to cutting. Figure D.41 shows plots of the measured local straddle fractions and Sauter mean drop diameters.

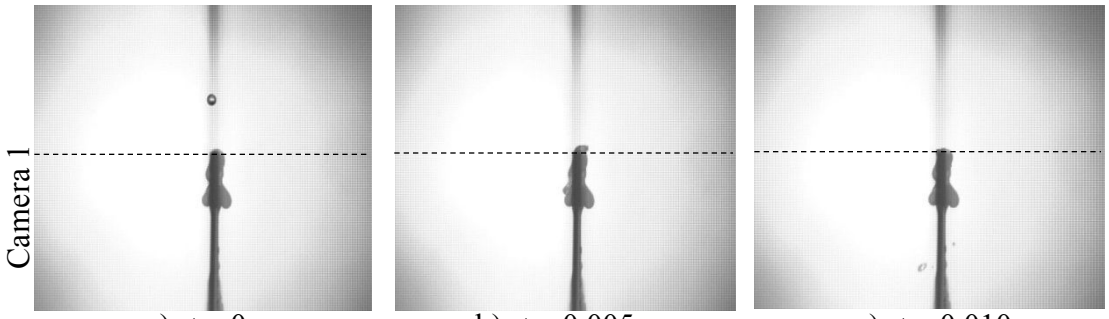

a) t = 0 s b) t = 0.005 s c) t = 0.010 s

Figure D.34: Straddle photographs (H_d = 250 mm, W = 3 mm, $\delta \approx$ 1.00 mm, $d_i \approx$ 2.89 mm, $\lambda \approx$ 0.5).

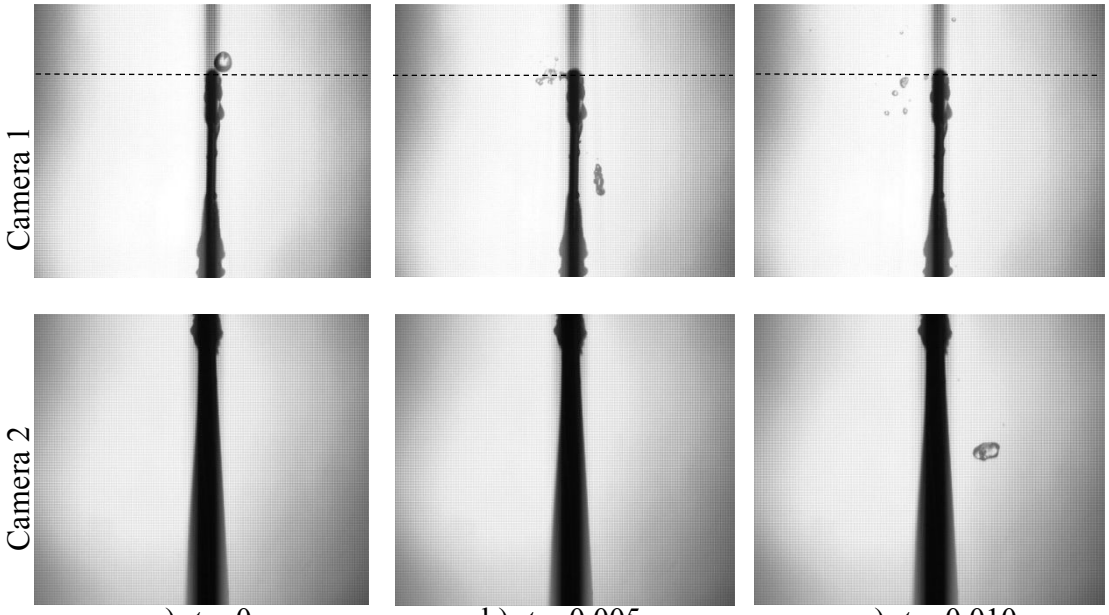

a) t = 0 s b) t = 0.005 s c) t = 0.010 s

Figure D.35: Straddle photographs (H_d = 250 mm, W = 3 mm, $\delta \approx$ 1.00 mm, $d_i \approx$ 5.48 mm, $\lambda \approx$ 0.5).

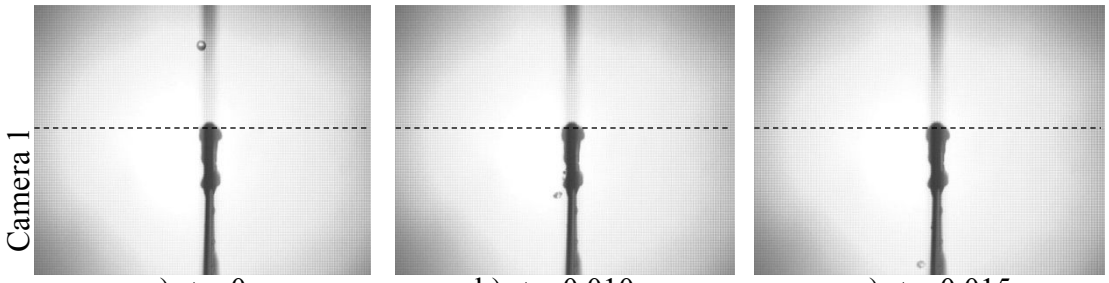

a) $t = 0$ s b) $t = 0.010$ s c) $t = 0.015$ s

Figure D.36: Straddle photographs (H_d = 250 mm, W = 6 mm, $\delta \approx 0.85$ mm, $d_i \approx 2.89$ mm, $\lambda \approx 0.6$).

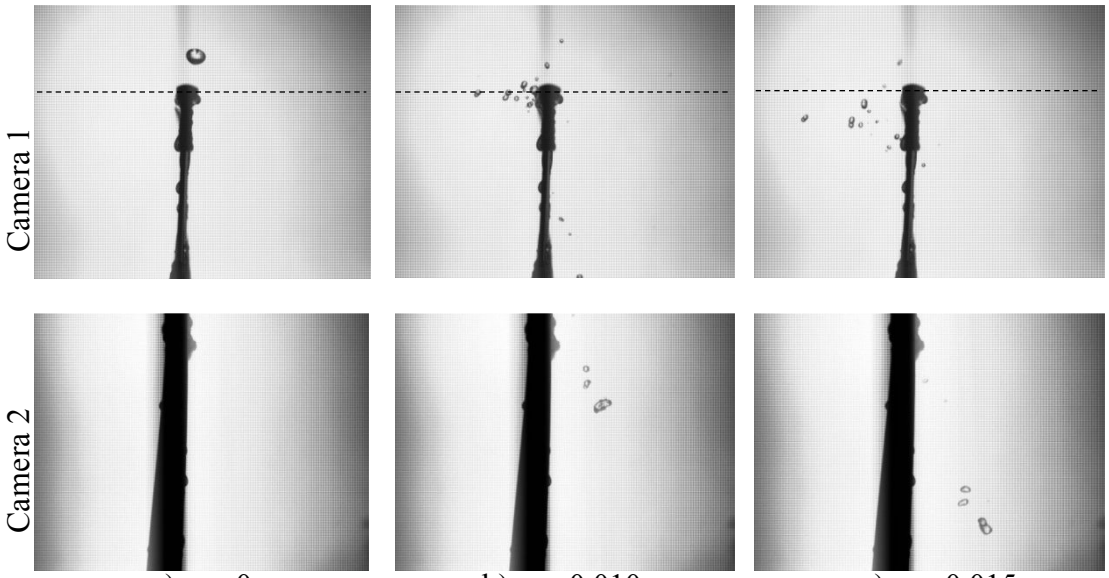

a) $t = 0$ s b) $t = 0.010$ s c) $t = 0.015$ s

Figure D. 37: Straddle photographs (H_d = 250 mm, W = 6 mm, $\delta \approx 0.85$ mm, $d_i \approx 5.48$ mm, $\lambda \approx 0.5$).

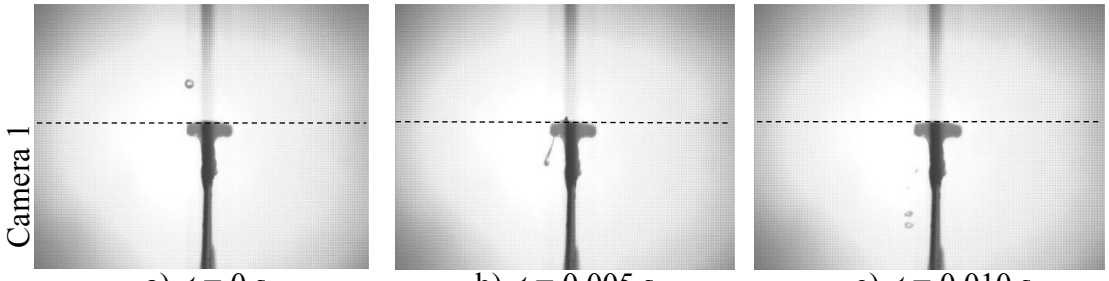

a) $t = 0$ s b) $t = 0.005$ s c) $t = 0.010$ s

Figure D.38: Straddle photographs (H_d = 250 mm, W = 12 mm, $\delta \approx 0.78$ mm, $d_i \approx 2.89$ mm, $\lambda \approx 0.8$).

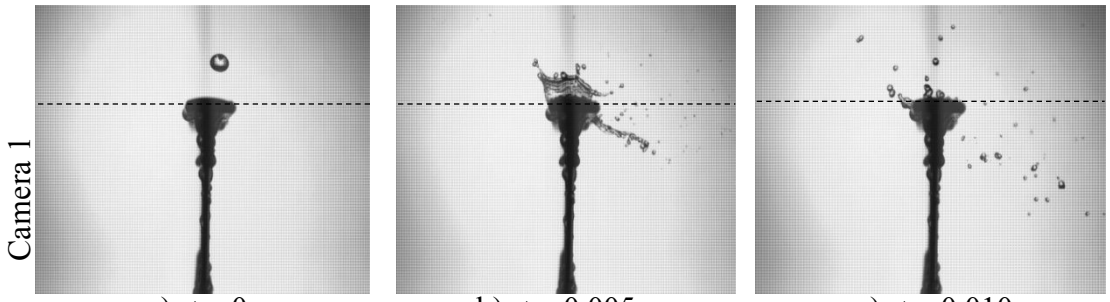

a) $t = 0$ s b) $t = 0.005$ s c) $t = 0.010$ s

Figure D.39: Straddle photographs (H_d = 250 mm, W = 12 mm, $\delta \approx 0.78$ mm, $d_i \approx 5.48$ mm, $\lambda \approx 0.4$).

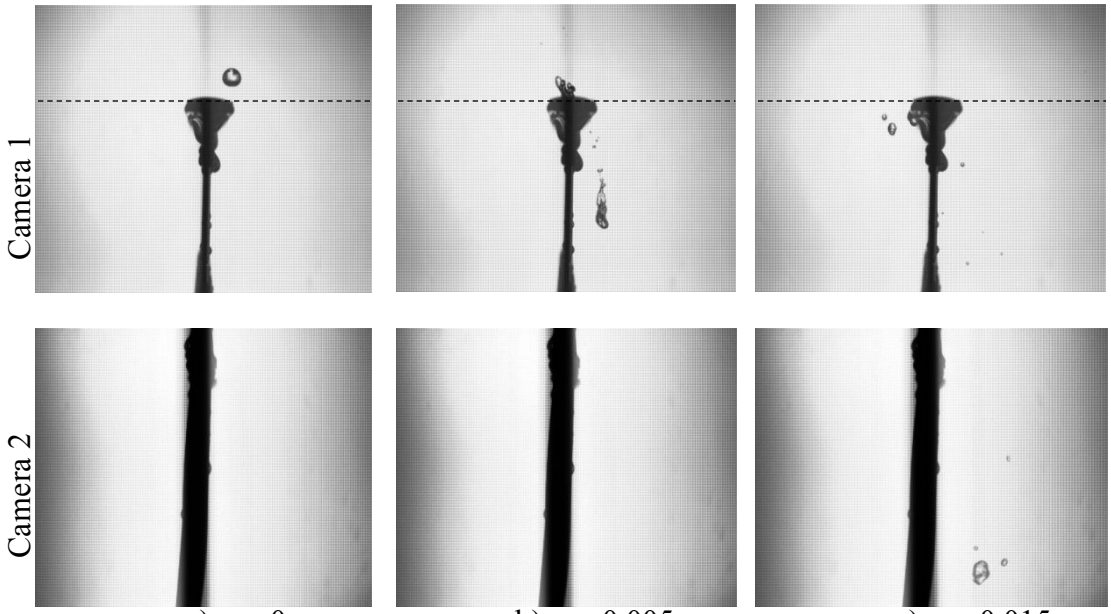

a) $t = 0$ s b) $t = 0.005$ s c) $t = 0.015$ s

Figure D.40: Straddle photographs (H_d = 250 mm, W = 12 mm, $\delta \approx 0.78$ mm, $d_i \approx 5.48$ mm, $\lambda \approx 0.8$).

The results presented in this section show that drop break-up on a W = 3 mm wide slat for the current drop fall distance (H_d = 250 mm) is dominated by straddling, while its effect becomes less on the W = 12 mm wide slat. The average straddle fractions for a d_i = 2.89 mm and d_i = 5.48 mm in diameter drop impinging onto a W = 3 mm wide slat are approximately $\bar{f}_c \approx 0.5$ and $\bar{f}_c \approx 1$ respectively, with a significant portion of the smaller drop (d_i = 2.89 mm) that becomes part of the surface water after impingement. Straddling is significant on the W = 12 mm wide slat although splashing plays a much bigger part compared to a W = 3 mm wide slat. Significant deflection (Figure D.39) is observed on the W = 12 mm wide slat which leads to the formation of relatively small drops.

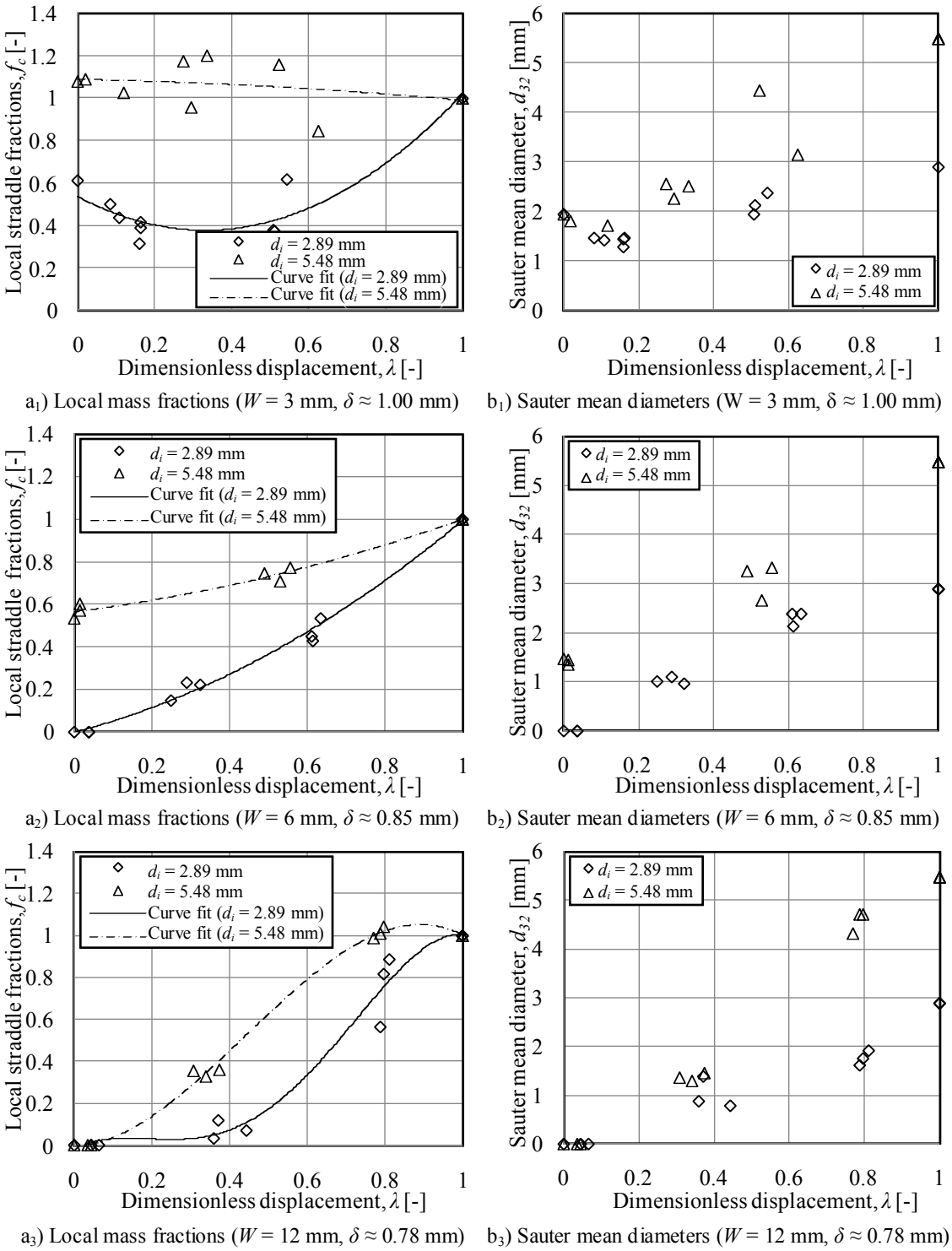

a$_1$) Local mass fractions (W = 3 mm, $\delta \approx$ 1.00 mm)

b$_1$) Sauter mean diameters (W = 3 mm, $\delta \approx$ 1.00 mm)

a$_2$) Local mass fractions (W = 6 mm, $\delta \approx$ 0.85 mm)

b$_2$) Sauter mean diameters (W = 6 mm, $\delta \approx$ 0.85 mm)

a$_3$) Local mass fractions (W = 12 mm, $\delta \approx$ 0.78 mm)

b$_3$) Sauter mean diameters (W = 12 mm, $\delta \approx$ 0.78 mm)

Figure D.41: Measured straddle fractions and Sauter mean drop sizes (H_d = 250 mm, $d_i \approx$ 2.89 mm and $d_i \approx$ 5.48 mm).

D.3.5 Straddle results (H_d = 470 mm, $d_i \approx$ 2.89 mm and $d_i \approx$ 5.48 mm)

This section presents the straddle results when a relatively small (d_i = 2.89 mm) and large drop (d_i = 5.48 mm), respectively, falls H_d = 470 mm before impinging onto different slats.

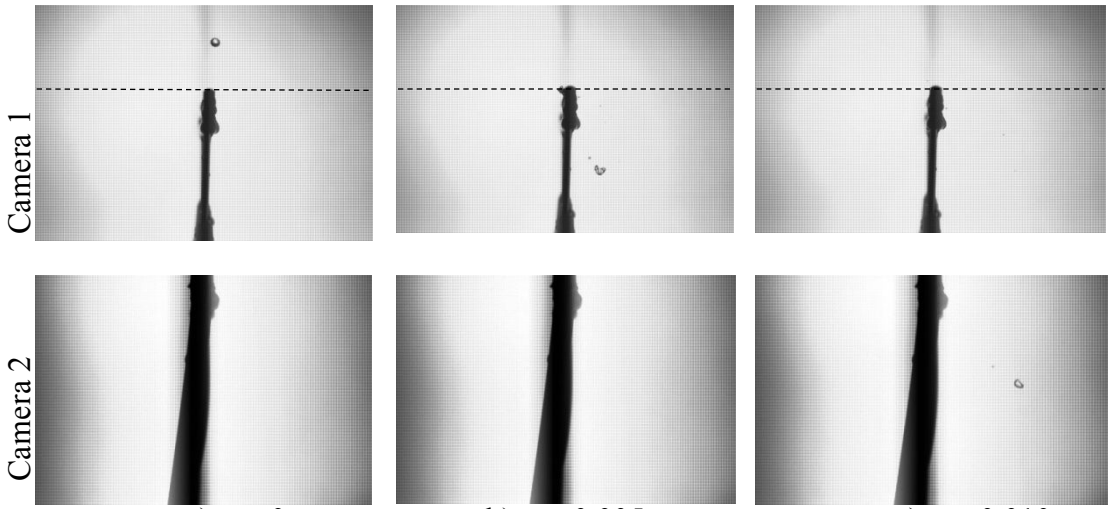

a) t = 0 s b) t = 0.005 s c) t = 0.010 s

Figure D.42: Straddle photographs (H_d = 470 mm, W = 3 mm, $\delta \approx$ 1.00 mm, $d_i \approx$ 2.89 mm, $\lambda \approx$ 0.5).

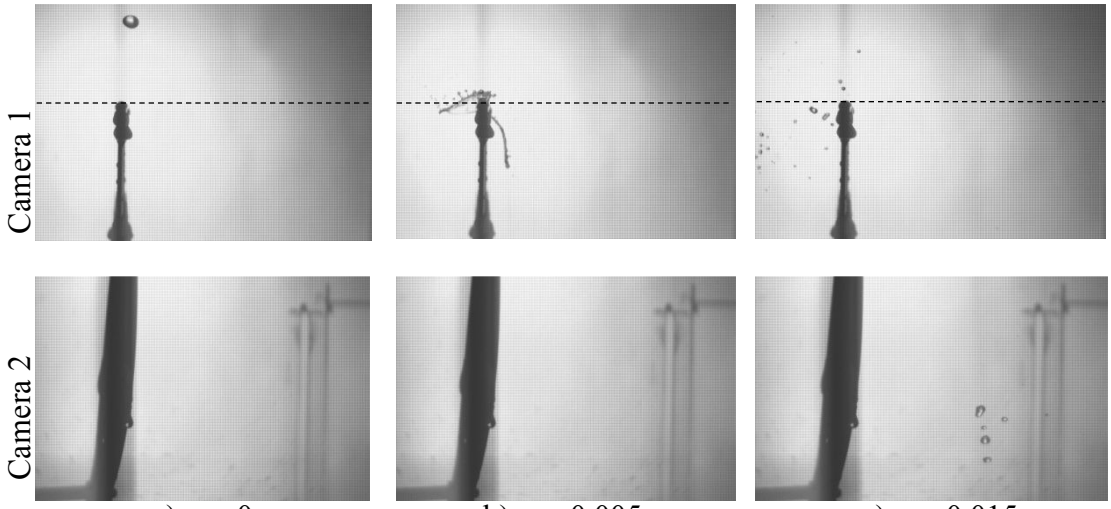

a) t = 0 s b) t = 0.005 s c) t = 0.015 s

Figure D.43: Straddle photographs (H_d = 470 mm, W = 3 mm, $\delta \approx$ 1.00 mm, $d_i \approx$ 5.48 mm, $\lambda \approx$ 0.4).

Figures D.42 to D.47 show sequential photographs of drop impingements for different drop size (d_i = 2.89 mm and d_i = 5.48 mm) and slat width (W = 3, W = 6 and

W = 12 mm) combinations while the film thickness on each slat is constant. For each of these cases the drop break-up is mainly due to cutting. Figure D.48 shows plots of the measured local straddle fractions and Sauter mean drop diameters.

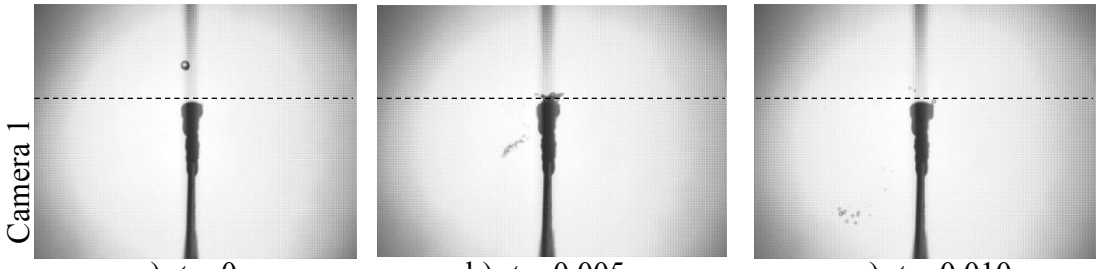

a) t = 0 s b) t = 0.005 s c) t = 0.010 s

Figure D.44: Straddle photographs (H_d = 470 mm, W = 6 mm, $\delta \approx$ 0.85 mm, $d_i \approx$ 2.89 mm, $\lambda \approx$ 0.5).

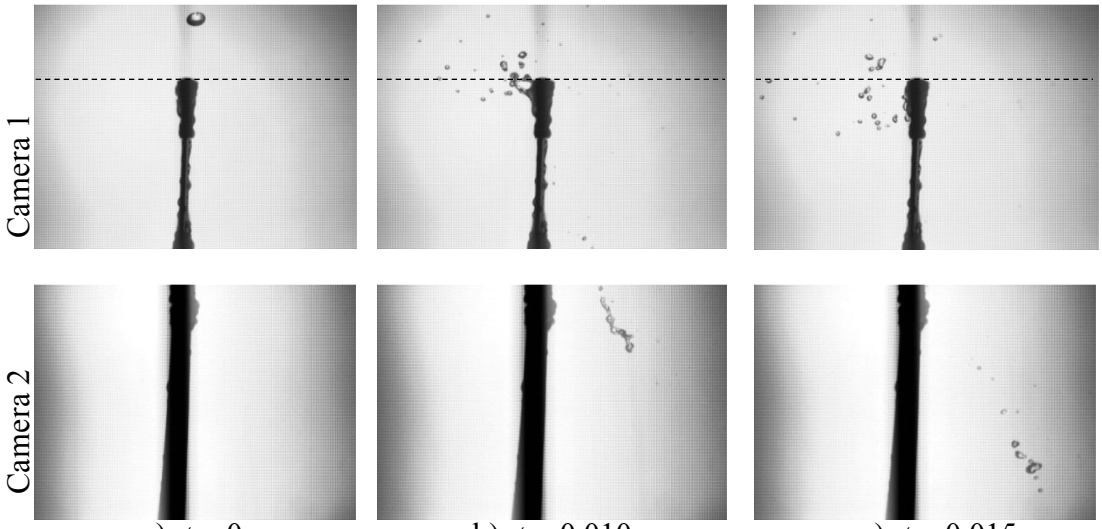

a) t = 0 s b) t = 0.010 s c) t = 0.015 s

Figure D.45: Straddle photographs (H_d = 470 mm, W = 6 mm, $\delta \approx$ 0.85 mm, $d_i \approx$ 5.48 mm, $\lambda \approx$ 0.5).

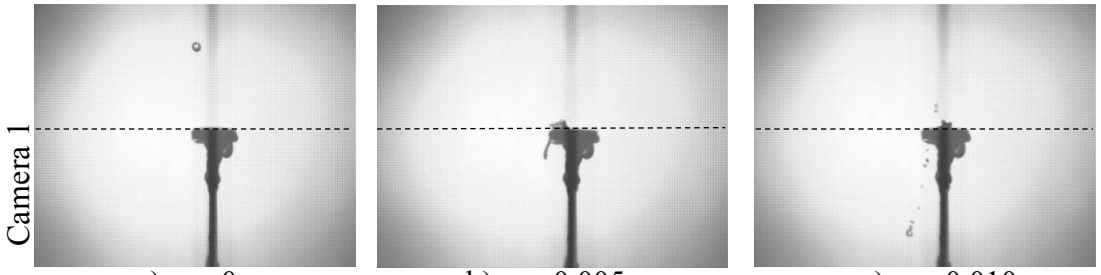

a) t = 0 s b) t = 0.005 s c) t = 0.010 s

Figure D.46: Straddle photographs (H_d = 470 mm, W = 12 mm, $\delta \approx$ 0.78 mm, $d_i \approx$ 2.89 mm, $\lambda \approx$ 0.8).

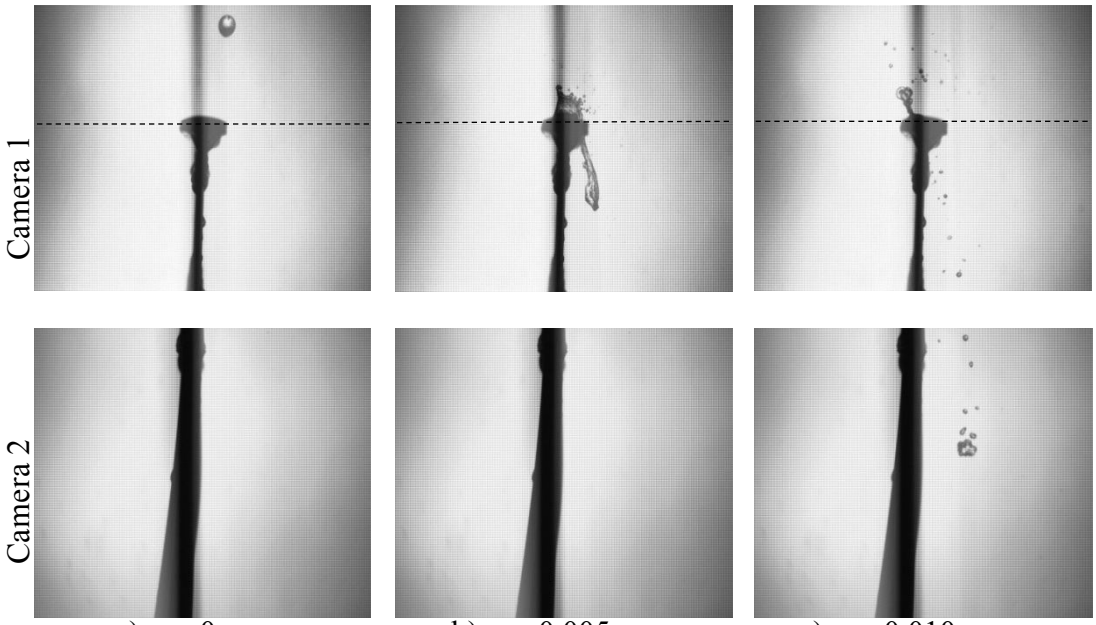

a) $t = 0$ s b) $t = 0.005$ s c) $t = 0.010$ s

Figure D.47: Straddle photographs (H_d = 470 mm, W = 12 mm, $\delta \approx 0.78$ mm, $d_i \approx 5.48$ mm, $\lambda \approx 0.8$).

For the results presented in Figure D.43 the vertical pitch between camera 1 and 2 is increased to 160 mm and the distance between the drop and the camera lenses is also increased.

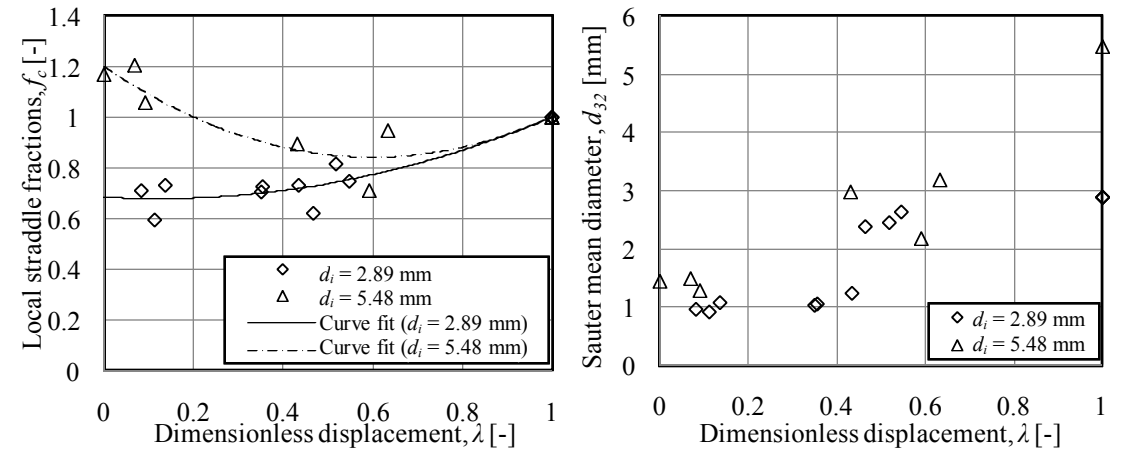

a$_1$) Local mass fractions (W = 3 mm, $\delta \approx$ 1.00 mm) b$_1$) Sauter mean diameters (W = 3 mm, $\delta \approx$ 1.00 mm)

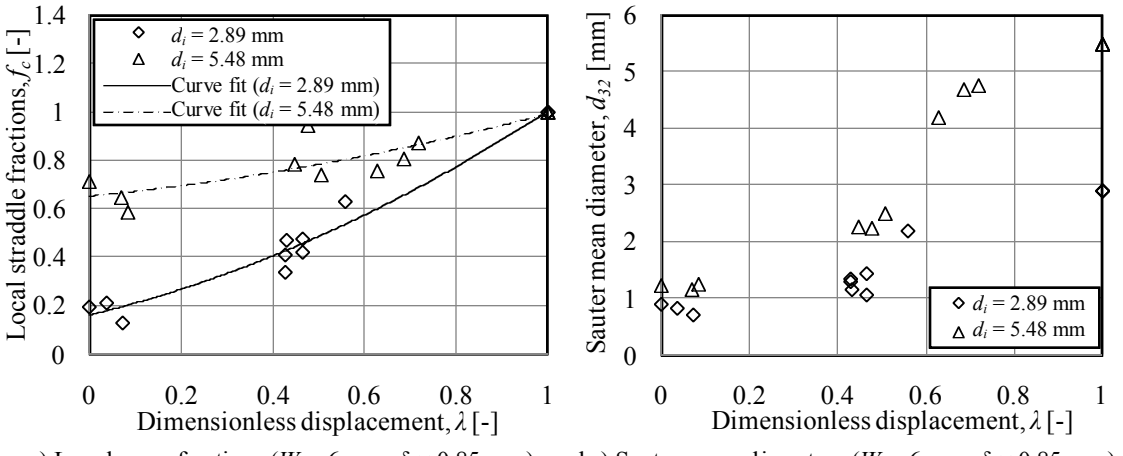

a$_2$) Local mass fractions (W = 6 mm, $\delta \approx$ 0.85 mm) b$_2$) Sauter mean diameters (W = 6 mm, $\delta \approx$ 0.85 mm)

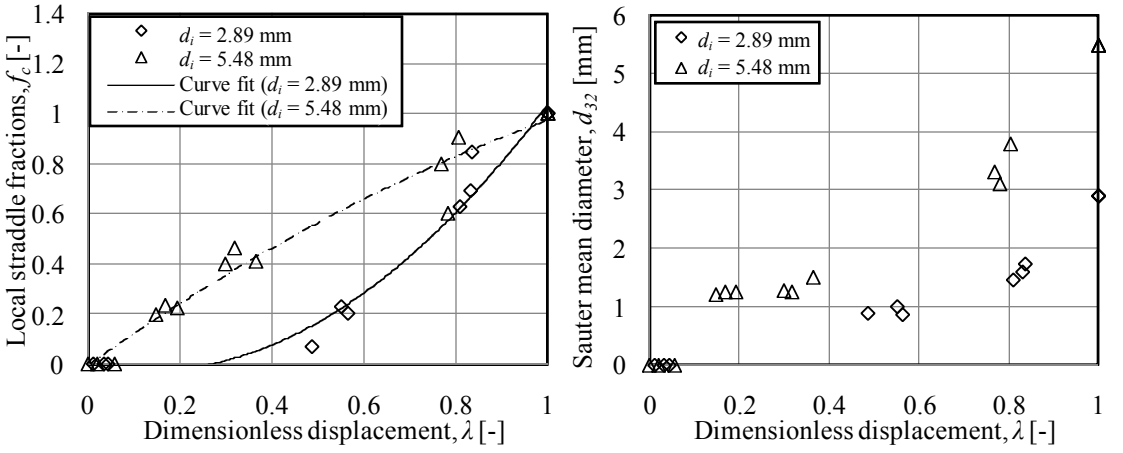

a$_3$) Local mass fractions (W = 12 mm, $\delta \approx$ 0.78 mm) b$_3$) Sauter mean diameters (W = 12 mm, $\delta \approx$ 0.78 mm)

Figure D.48: Measured straddle fractions and Sauter mean drop sizes (H_d = 470 mm, $d_i \approx$ 2.89 mm and $d_i \approx$ 5.48 mm).

D.3.6 Straddle results (H_d = 970 mm, $d_i \approx$ 2.89 mm and $d_i \approx$ 5.48 mm)

This section presents the straddle results when a relatively small (d_i = 2.89 mm) and large drop (d_i = 5.48 mm), respectively, falls H_d = 970 mm before impinging onto different slats. Figures D.49 to D.54 show sequential photographs of drop impingements for different drop size (d_i = 2.89 mm and d_i = 5.48 mm) and slat width (W = 3, W = 6 and W = 12 mm) combinations while the film thickness on each slat is constant. For each of these cases the drop break-up is mainly due to cutting. Figure D.55 shows plots of the measured local straddle fractions and Sauter mean drop diameters.

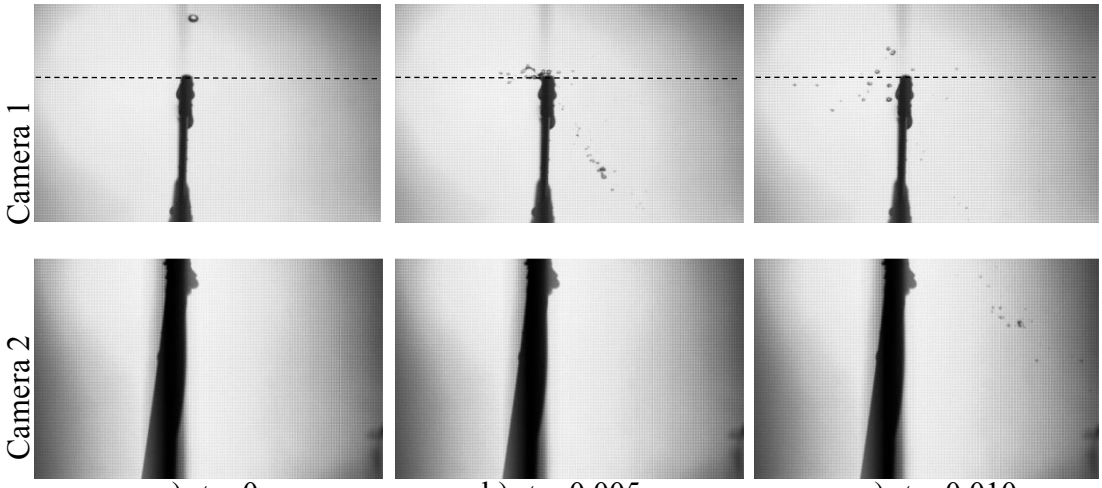

a) t = 0 s b) t = 0.005 s c) t = 0.010 s

Figure D.49: Straddle photographs (H_d = 970 mm, W = 3 mm, $\delta \approx$ 1.00 mm, $d_i \approx$ 2.89 mm, $\lambda \approx$ 0.6).

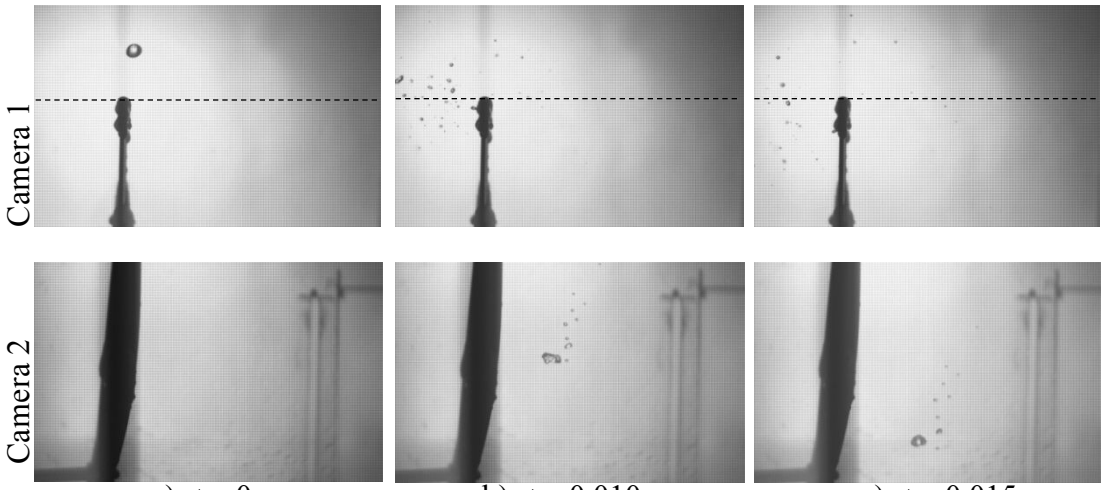

a) t = 0 s b) t = 0.010 s c) t = 0.015 s

Figure D.50: Straddle photographs (H_d = 970 mm, W = 3 mm, $\delta \approx$ 1.00 mm, $d_i \approx$ 5.48 mm, $\lambda \approx$ 0.5).

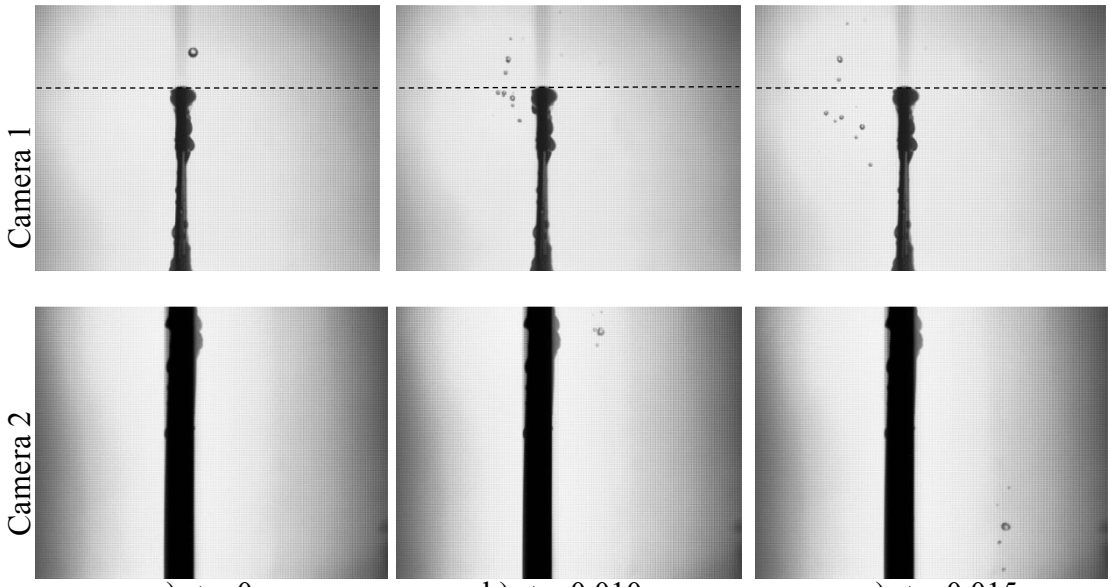

a) $t = 0$ s b) $t = 0.010$ s c) $t = 0.015$ s

Figure D.51: Straddle photographs (H_d = 970 mm, W = 6 mm, $\delta \approx 0.85$ mm, $d_i \approx 2.89$ mm, $\lambda \approx 0.5$).

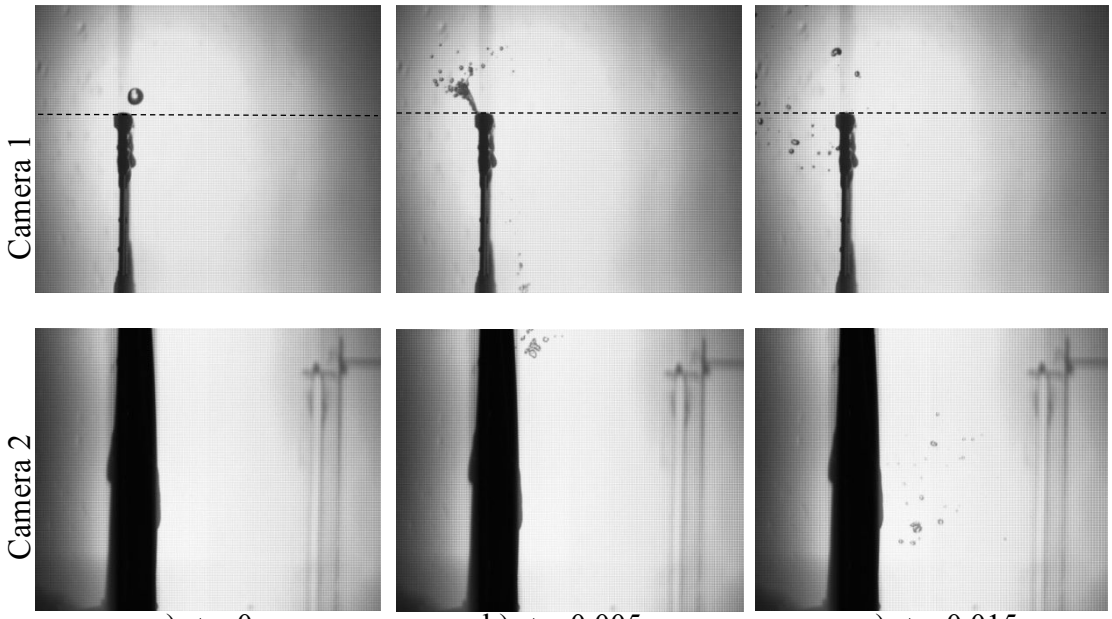

a) $t = 0$ s b) $t = 0.005$ s c) $t = 0.015$ s

Figure D.52: Straddle photographs (H_d = 970 mm, W = 6 mm, $\delta \approx 0.85$ mm, $d_i \approx 5.48$ mm, $\lambda \approx 0.5$).

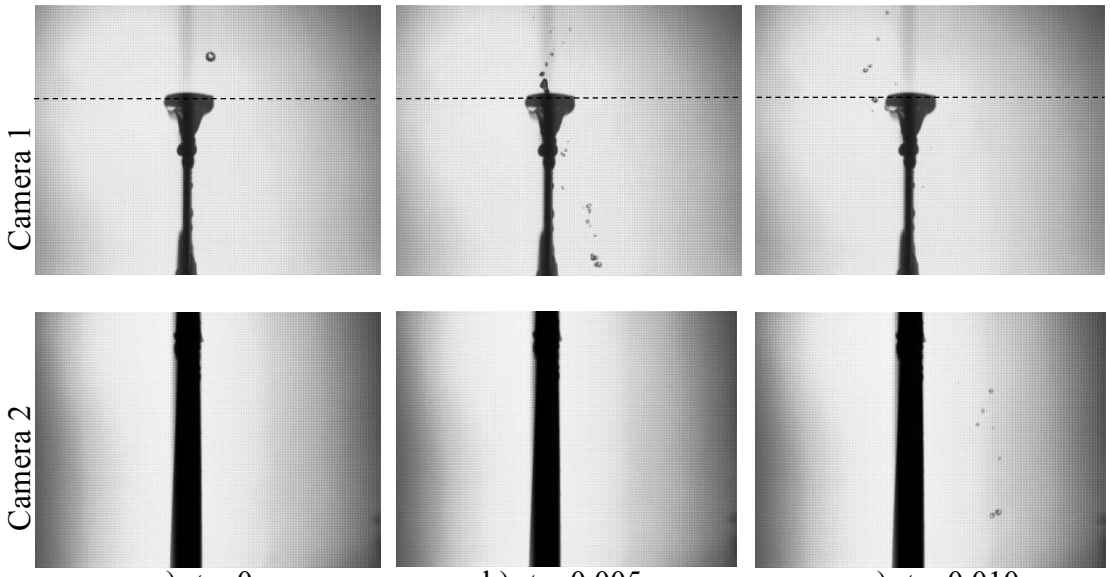

Figure D.53: Straddle photographs (H_d = 970 mm, W = 12 mm, $\delta \approx 0.78$ mm, $d_i \approx 2.89$ mm, $\lambda \approx 0.8$).

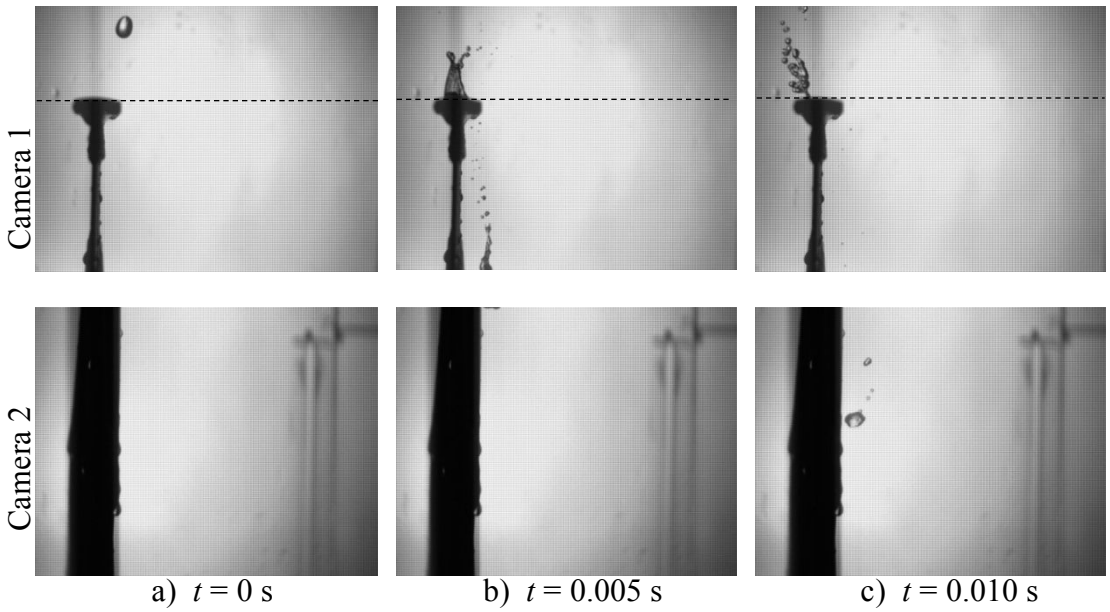

Figure D.54: Straddle photographs (H_d = 970 mm, W = 12 mm, $\delta \approx 0.78$ mm, $d_i \approx 5.48$ mm, $\lambda \approx 0.8$).

The vertical pitch between the cameras 1 and 2 is increased to 160 mm for the photographs presented in Figures D.50, D.52 and D.54. The distance between the falling drop and the camera lens is also increased for these cases.

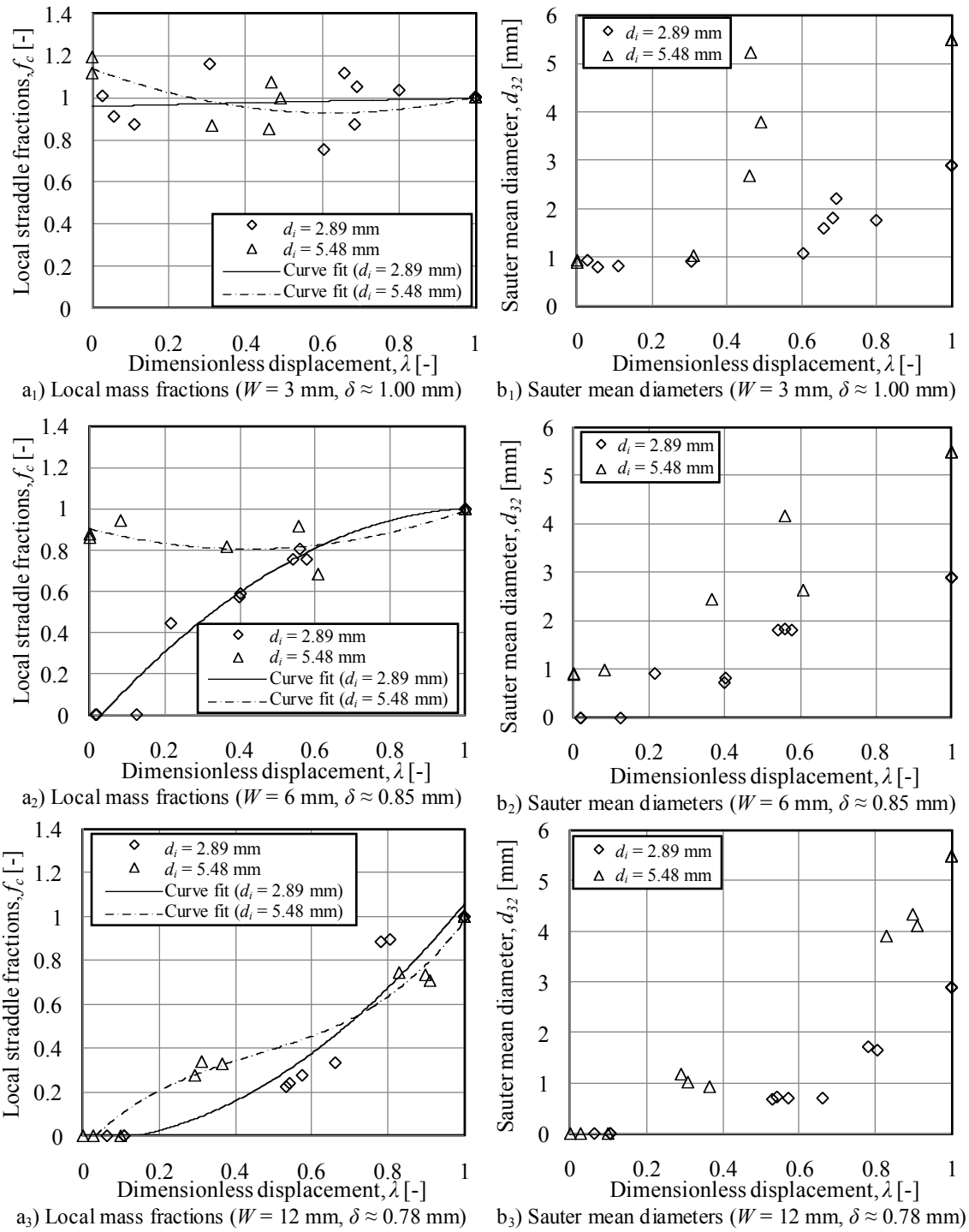

a$_1$) Local mass fractions (W = 3 mm, $\delta \approx$ 1.00 mm)

b$_1$) Sauter mean diameters (W = 3 mm, $\delta \approx$ 1.00 mm)

a$_2$) Local mass fractions (W = 6 mm, $\delta \approx$ 0.85 mm)

b$_2$) Sauter mean diameters (W = 6 mm, $\delta \approx$ 0.85 mm)

a$_3$) Local mass fractions (W = 12 mm, $\delta \approx$ 0.78 mm)

b$_3$) Sauter mean diameters (W = 12 mm, $\delta \approx$ 0.78 mm)

Figure D.55: Measured straddle fractions and Sauter mean drop sizes (H_d = 970 mm, $d_i \approx$ 2.89 mm and $d_i \approx$ 5.48 mm).

D.4 Data correlation

The straddle fraction and drop distribution must be known in order to predict the straddle component of drop break-up when a drop impinges onto a slat. Equations for the average straddle fractions and straddle drop size distributions are obtained in this section by correlating the measured data presented in Table D.2. The average straddle fractions (Table D.2) are obtained through the integration of the curve fit equations for the local straddle fractions shown in Figures D.12, D.23, D.33, D.41, D.48 and D.55. The cumulative mass distribution of the straddled drops is expressed in terms of a power function (Equation D.2) of which the power for every test case is determined (Section D.4.2) and is also given in Table D.2.

$$R(d) = \left(\frac{d}{d_i}\right)^{n_{RT}} \tag{D.2}$$

Table D.2: Measured average straddling data.

H_d [mm]	d_i [mm]	δ [mm]	W [mm]	We [-]	δ/W [-]	d_i/W [-]	$\bar{f}_c$ [-]	n_{RT} [-]	d_{32} [mm]
250	2.89	1.00	3	186.34	0.333	0.963	0.541	3.37	2.16
250	4.00	0.43	3	261.99	0.143	1.333	0.774	2.41	2.60
250	4.00	0.78	3	261.99	0.260	1.333	0.801	2.45	2.62
250	4.00	1.30	3	261.99	0.433	1.333	0.824	2.41	2.60
250	5.48	1.00	3	362.90	0.333	1.827	1.048	1.92	2.96
250	2.89	0.85	6	186.34	0.142	0.482	0.408	3.60	2.21
250	4.00	0.85	6	261.99	0.142	0.667	0.672	2.34	2.55
250	5.48	0.85	6	362. 90	0.142	0.913	0.748	1.84	2.85
250	2.89	0.78	12	186.34	0.065	0.241	0.341	2.58	1.92
250	4.00	0.36	12	261.99	0.030	0.333	0.347	2.29	2.51
250	4.00	1.00	12	261.99	0.083	0.333	0.391	1.82	2.13
250	4.00	1.75	12	261.99	0.146	0.333	0.528	1.65	1.95
250	5.48	0.78	12	362.90	0.065	0.457	0.549	2.05	3.12
470	2.89	1.00	3	338.61	0.333	0.963	0.772	2.11	1.71
470	4.00	0.35	3	480.98	0.117	1.333	0.889	1.90	2.20
470	4.00	0.95	3	480.98	0.317	1.333	0.946	1.58	1.87
470	4.00	1.40	3	480.98	0.467	1.333	0.891	1.74	2.04
470	5.48	1.00	3	670.63	0.333	1.827	0.933	1.47	2.29

H_d [mm]	d_i [mm]	δ [mm]	W [mm]	We [-]	δ/W [-]	d_i/W [-]	$\bar{f}_c$ [-]	n_{RT} [-]	d_{32} [mm]
470	2.89	0.85	6	338.61	0.142	0.482	0.518	2.14	1.73
470	4.00	0.25	6	480.98	0.042	0.667	0.651	2.77	2.80
470	4.00	0.85	6	480.98	0.142	0.667	0.683	2.88	2.85
470	4.00	1.45	6	480.98	0.242	0.667	0.638	2.26	2.49
470	5.48	0.85	6	670.63	0.142	0.913	0.797	1.29	1.94
470	2.89	0.78	12	338.61	0.065	0.241	0.286	1.93	1.60
470	4.00	0.30	12	480.98	0.025	0.333	0.425	1.78	2.09
470	4.00	0.75	12	480.98	0.063	0.333	0.469	1.64	1.93
470	4.00	1.95	12	480.98	0.163	0.333	0.459	1.65	1.95
470	5.48	0.78	12	670.63	0.065	0.457	0.539	1.62	2.53
970	2.89	1.00	3	655.03	0.333	0.963	0.978	1.47	1.27
970	4.00	0.11	3	951.98	0.037	1.333	0.842	1.46	1.72
970	4.00	1.00	3	951.98	0.333	1.333	0.795	1.54	1.82
970	4.00	1.32	3	951.98	0.440	1.333	0.809	1.64	1.94
970	5.48	1.00	3	1345.43	0.333	1.827	0.981	1.21	1.78
970	2.89	0.85	6	655.03	0.142	0.482	0.628	2.17	1.74
970	4.00	0.50	6	951.98	0.083	0.667	0.742	1.91	2.21
970	4.00	0.85	6	951.98	0.142	0.667	0.832	1.62	1.91
970	4.00	1.43	6	951.98	0.238	0.667	0.792	1.42	1.67
970	5.48	0.85	6	1345.43	0.142	0.913	0.855	1.47	2.28
970	2.89	0.78	12	655.03	0.065	0.241	0.342	1.81	1.53
970	4.00	0.21	12	951.98	0.018	0.333	0.509	1.57	1.85
970	4.00	0.95	12	951.98	0.079	0.333	0.568	1.26	1.46
970	4.00	1.75	12	951.98	0.146	0.333	0.623	1.36	1.59
970	5.48	0.78	12	1345.43	0.065	0.457	0.419	1.48	2.29

D.4.1 Average straddle fraction

The average straddle fraction ($\bar{f}_c$) is correlated for three individual slats (W = 3 mm, W = 6 mm and W = 12 mm) in this section and combined into a single equation by means of the following procedure:

1) The average straddle fractions for a d_i = 4 mm in diameter initial drop are plotted in terms of the film thicknesses on each slat to show that the influence of film thickness is negligible (Figure D.56).
2) The average straddle fractions of the three initial drops (d_i = 2.89, 4.00 and 5.48 mm) are plotted in terms of Weber number for each of the three slats (Figure D.57) before the average straddle fractions for each slat are correlated (Equations D.3) in terms of $We_n = We/We_{ref}$ and d_i/d_m.
3) The final equation (Equation D.5) for predicting the average straddle fraction is obtained by combining the individual equations for each slat to give the average straddle fraction in terms of $We_n = We/We_{ref}$, d_i/d_m and W/d_m.

Figure D.56 shows the influence of film thickness on the straddle fraction when a d_i = 4 mm in diameter drop impinges onto W = 3, W = 6 or W = 12 mm wide slats covered by water films of different thicknesses. The figure shows that the film thickness on the slat has a negligible influence on the average straddle fraction.

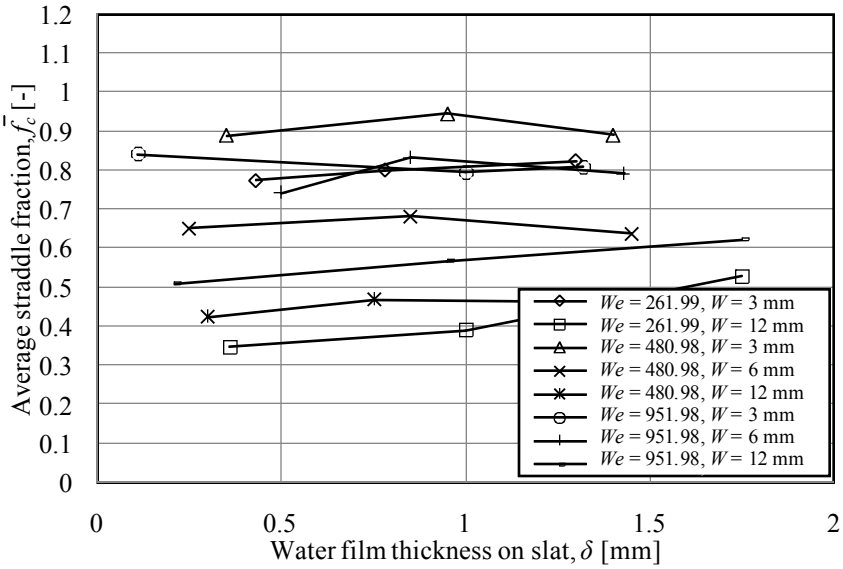

Figure D.56: Relationship between the straddle fractions and the water film thickness on different slats ($d_i \approx 4$ mm).

Figure D.57 presents the average straddle fractions of three different initial drops in terms of the Weber numbers just before impingement on each of the slats. Straddle

fractions are assumed to be zero when the Weber number is zero because the surface forces will pull a drop with zero velocity into the water film and the drop will leave the slat in the form drip drops below the slat rather than straddled drops.

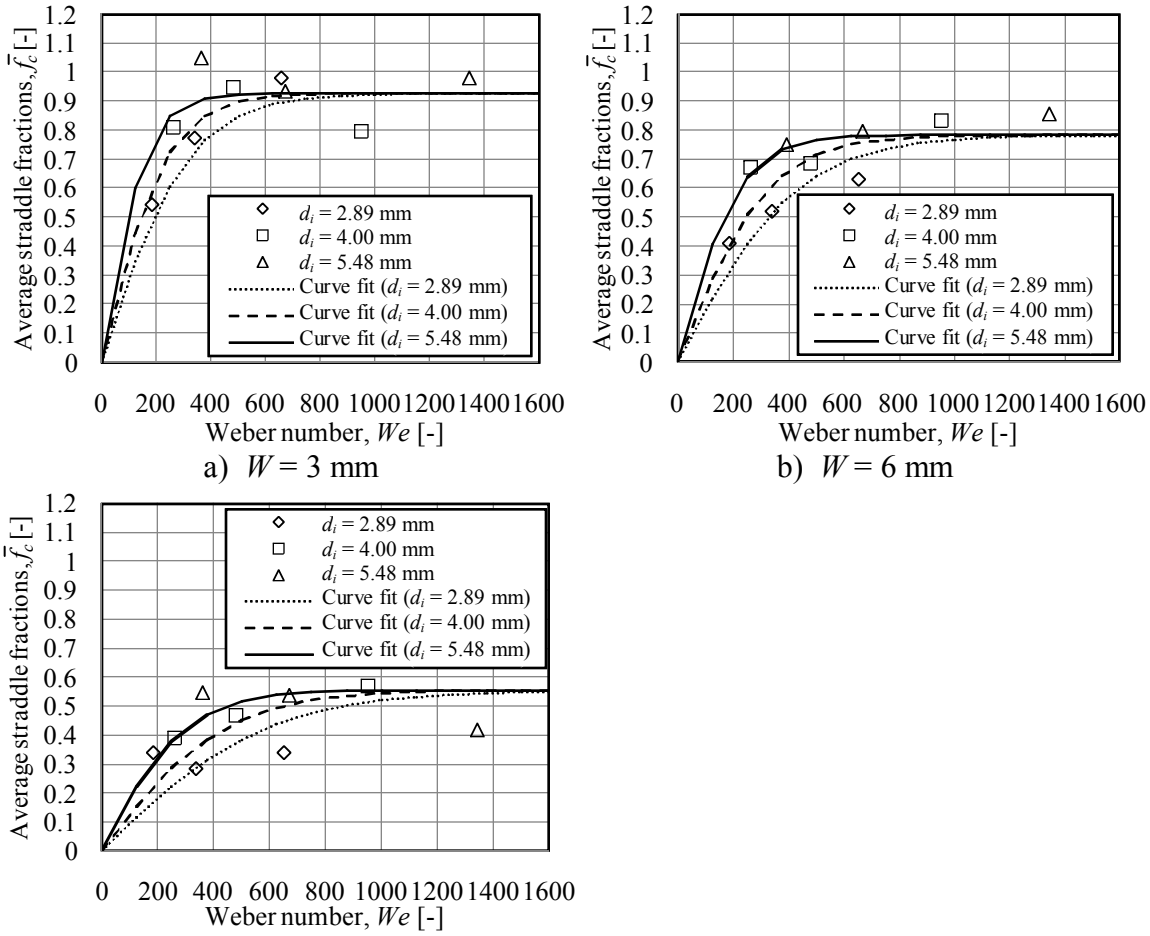

a) W = 3 mm

b) W = 6 mm

c) W = 12 mm

Figure D.57: Measured average straddle fractions for drops of different diameters impinging onto different slats.

Figure D.57 shows that for a certain slat width the average straddle fraction is a function of the initial drop diameter as well as the Weber number and equations for predicting the average straddle fraction on each slat are given by

$$\bar{f}_{c,3} = 0.927 \tanh(18.3\alpha_d We_n) \quad \text{(D.3a)}$$

$$\bar{f}_{c,6} = 0.782 \tanh(13.5\alpha_d We_n) \quad \text{(D.3b)}$$

$$\bar{f}_{c,12} = 0.556 \tanh(9.9\alpha_d We_n) \quad \text{(D.3c)}$$

where

$$\alpha_d = exp\left(2.87\frac{d_i}{d_m}\right) \tag{D.3d}$$

From Equations (D.3) it is evident that the final equation for predicting the average straddle faction must have the following form

$$\bar{f_c} = \alpha_W \tanh\left(\beta_W \alpha_d \frac{We}{We_{ref}}\right) \tag{D.4}$$

where the parameters α_W and β_W are obtained in terms of the slat width to maximum stable drop diameter ratio (W/d_m) as shown in Figure D.58. The parameter α_d is expressed as a function of the initial drop diameter to maximum stable drop diameter ratio (d_i/d_m) and is also shown in Figure D.58.

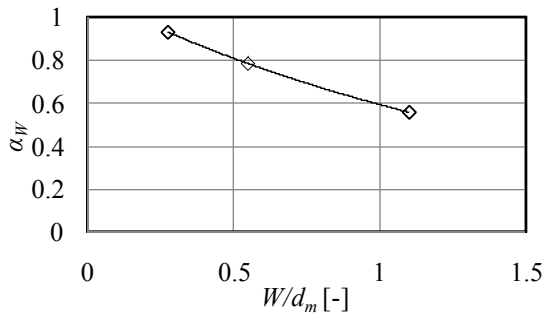

a) Straddle coefficient, α_W

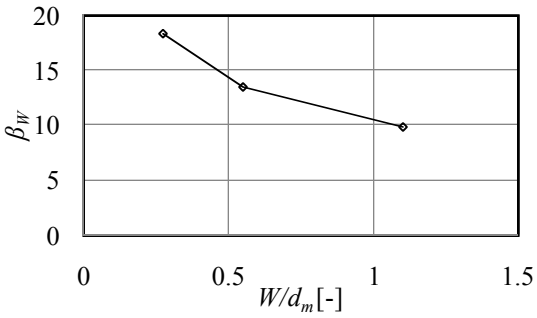

b) Straddle coefficient, β_W

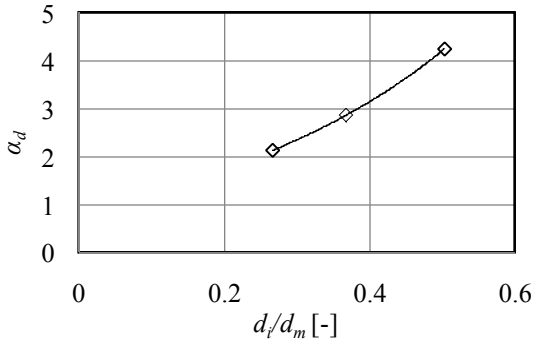

c) Straddling coefficient, α_d

Figure D.58: Average straddle fraction correlation parameters.

The final equation for predicting the average straddle fraction is given by

$$\bar{f_c} = 1.1exp\left(-0.62\frac{W}{d_m}\right)\tanh\left[10.3\left(\frac{W}{d_m}\right)^{-0.4} exp\left(2.87\frac{d_i}{d_m}\right)We_n\right] \tag{D.5}$$

The Weber number (We), reference Weber number (We_{ref}) and normalized Weber number (We_n) are respectively given by Equations (2.49e), (2.57) and (B.4). The maximum stable drop diameter (d_m) is given by Equation (2.48).

D.4.2 Straddle drop distribution

The cumulative mass distribution of the straddled drops is expressed by a power function (Equation D.2) and the parameter (n_{RT}) is correlated in this section by means of the following procedure:

1) The parameter n_{RT} for a d_i = 4 mm in diameter initial drop is plotted in terms of the film thicknesses on the different slats (W = 3, 6 and 12 mm) to show the negligible influence of film thickness on the parameter (Figure D.59).
2) The parameter n_{RT} for the three initial drops (d_i = 2.89, 4.00 and 5.48 mm) are plotted in terms of Weber number for each of the three slats (Figure D.57) before the parameter is correlated in terms of $We_n = We/We_{ref}$.

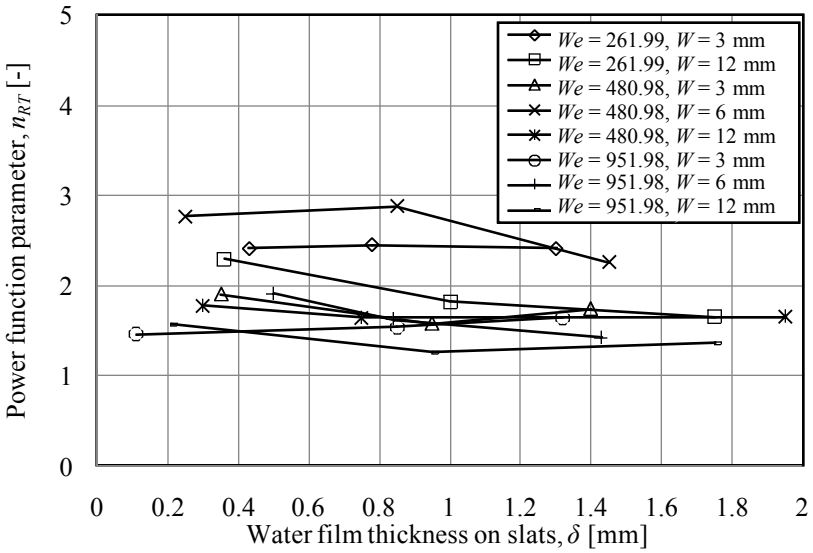

Figure D.59: Relationship between n_{RT} and water film thickness on different slats ($d_i \approx 4$ mm).

The cumulative mass distribution of the straddled drops for each test case is expressed with a power function (Equation D.2) for which the parameter n_{RT} is chosen so that the Sauter mean drop diameter of the predicted straddle drop distribution equals the representative Sauter mean drop diameter determined from the measured data. The representative Sauter mean drop diameter for each test case is calculated by determining the number of drops equal to the local Sauter mean drop diameter at eleven locations from $x = 0$ to $x = (W + d_i)/2$ before calculating the collective Sauter mean drop diameter of all these drops. The number of drops at each

location is determined from the local straddle mass and Sauter mean drop diameter data, which in turn is calculated from curve fits made through the local straddle fraction and Sauter mean drop diameter data presented in Section D.3. Table D.2 presents the representative Sauter mean drop diameters and the parameter n_{RT} for each test case.

Figure D.59 presents the parameter n_{RT} for a d_i = 4 mm in diameter initial drop in terms of the film thicknesses on the different slats and shows that the film thickness on a slat has no significant effect on this parameter.

Figure D.60 presents the parameter n_{RT} in terms of the initial drop Weber number just before impingement for different initial drop size (d_i = 2.89 mm, 4.00 mm and 5.48 mm) and slat width (W = 3 mm, 6 mm and 12 mm) combinations. This data shows n_{RT} is a function of Weber number only that is given by Equation (D.6).

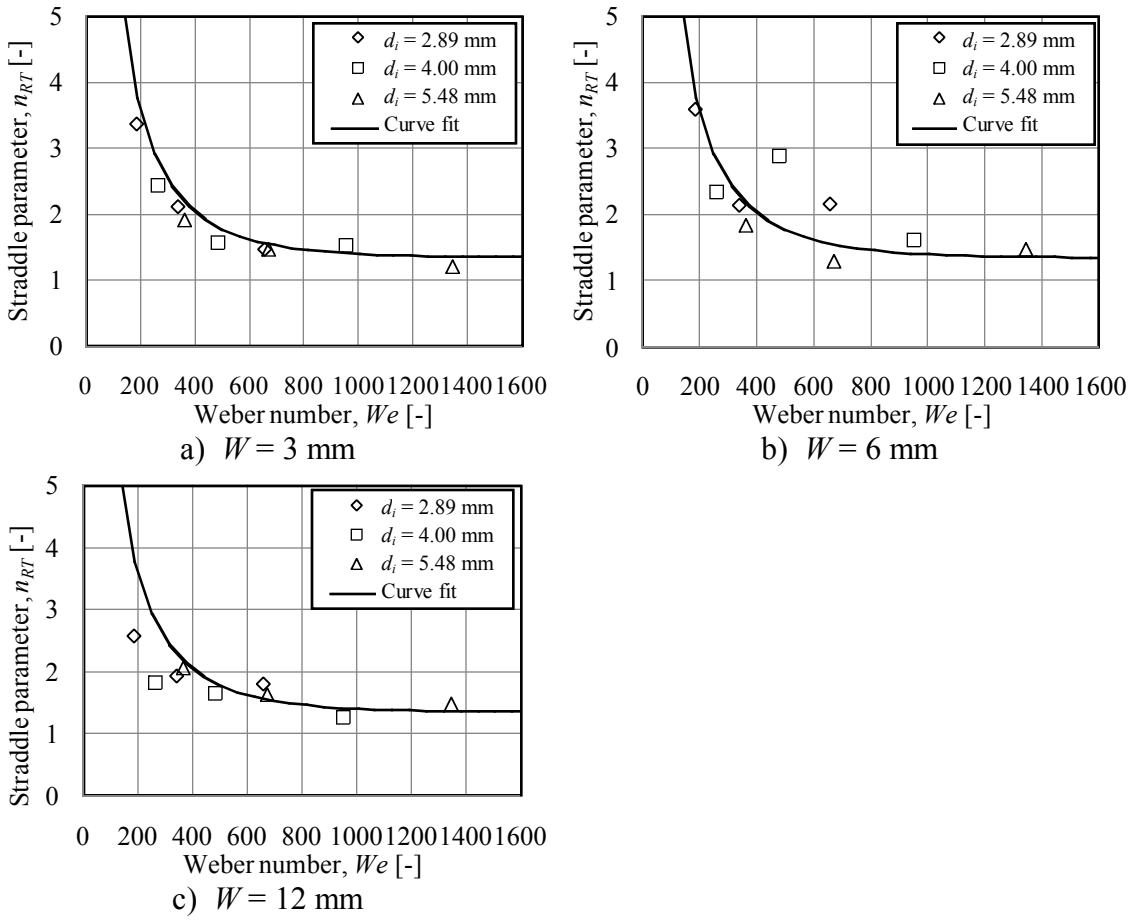

a) W = 3 mm

b) W = 6 mm

c) W = 12 mm

Figure D.60: Straddle distribution parameter n_{RT} for different slats.

$$n_{RT} = 1.35 \coth(25We_n) \tag{D.6}$$

The Weber number (We), reference Weber number (We_{ref}) and normalized Weber number (We_n) are respectively given by Equations (2.49e), (2.57) and (B.4).

D.5 Discussion

In this appendix straddling, defined as the break-up of drops after impingement on a slat due to a combination of deflection and cutting, is experimentally investigated and quantified in terms of the fraction of the original drop that straddles a slat after impingement as well as the distribution of the drops that form due to straddling. Figure D.61 shows a comparison between Equation (D.5), developed for predicting the average straddle fraction, and the measured data and also shows how this equation compares to the simplified analytical model used by Dreyer (1994), that is given by Equation (2.67).

Dreyer's model (Equation 2.67) generally under predicts the measured straddle fractions significantly due to the following possible reasons:

1) Dreyer assumed that the drop can be presented by a sphere just before impingement and that the part of the drop not directly above the slat is the part cut from the initial drop. Photographs presented in Appendices B and D show that significant drop flattening and deformation takes place upon impingement before any straddling happens, which means that the slat effectively cuts a larger portion of the initial drop.
2) The drop deflection when the drop is close to the edge of a slat before impingement, but still completely above the slat, is ignored and Dreyer assumed nothing happens in these cases.
3) The straddle fraction's dependency on the Weber number is ignored and Dreyer assumed that the initial drop velocity doesn't influence the straddle fraction.

The distribution of the straddled drops is expressed in terms of a power function (Equation D.2) of which the parameter n_{RT} is correlated from the measured data (Table D.2). Figure D.62 shows a comparison between the measured and predicted (Equation D.6) n_{RT} values.

A complete model for predicting the drop break-up due to straddling is developed in this appendix that can be used in conjunction with the splash model developed in Appendix B to determine the drop break-up due to splash grids in a rain zone.

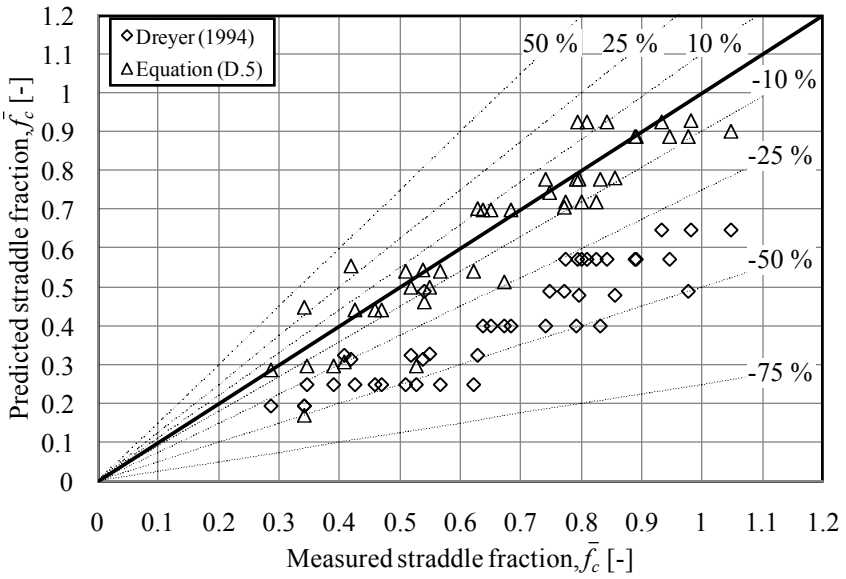

Figure D.61: Comparison between the measured and predicted average straddle fractions.

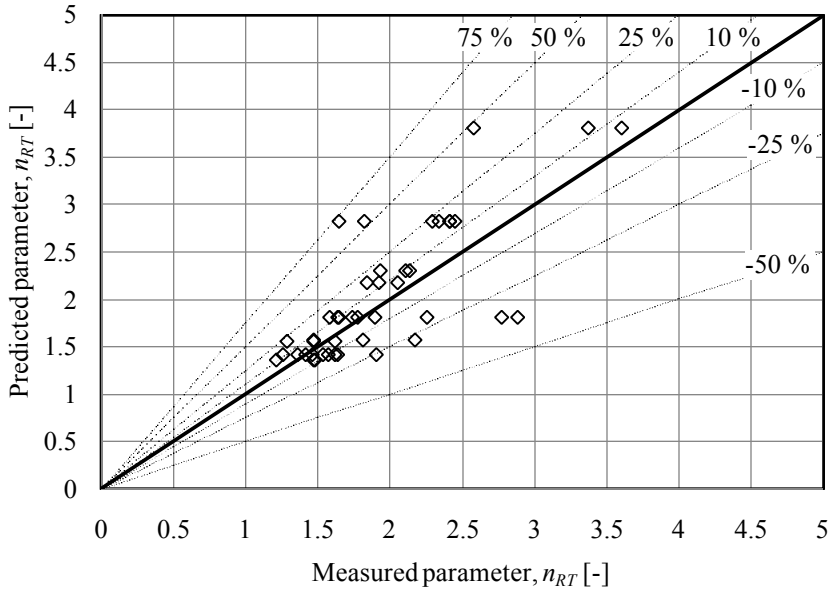

Figure D.62: Comparison between Equation (D.6) and the measured parameter, n_{RT}.

The measurement uncertainties associated with the measurement results of this section are discussed in Appendix L.

E

A THEORETICAL APPROACH FOR PREDICTING DRIP DROP SIZES BELOW SLATS WITH DIFFERENT BOTTOM PROFILES

E.1 Introduction

Drops generally break up when they impinge onto the surfaces of splash grids due to the mechanisms of splashing and straddling. Small drops or drops that are low in kinetic energy can however become part of the surface water that runs down the grid surface and leaves the grid in the form relatively large drip drops. Drip drops are characterised by a large primary drop, followed by smaller satellite drops that form in the final stages of detachment from the bottom of the grid.

A simplified analytical model for predicting the drip drop sizes below slats with different bottom profiles is derived in this appendix and the results compared to the measured results of Dreyer (1994) and Terblanche (2008).

E.2 Estimation of primary drip drop diameters for different slat bottom profiles

The assumption is made in the derivation of the analytical model that the drip drops are attached to the lowest point of the slats as they grow in size and that the momentum effect of the water running down the grid surface has no significant effect on the maximum size of the drops before they detach from the slat bottom.

Surface tension- , buoyancy- and gravitational forces acting on a suspended drop are balanced to find an expression for the diameter of the primary drip drop at low liquid flow rates (negligible momentum effects) that is given by

$$d_p = 1.2407 \sqrt[3]{\frac{\sigma S_P}{g(\rho_w - \rho_{av})}} \tag{E.1}$$

where S_P is a characteristic length defined as the length of the line where the slat, water and air intersect.

Figure E.1(a) shows a diagram of a drop suspended below a narrow, flat bottomed slat, just before the drop detaches and also after detachment. The characteristic length

S_p is determined by assuming that the characteristic length component in-line with the slat equals the primary drip drop diameter and the characteristic length component perpendicular to the slat equals the width of the slat (W). Equation (E.2) gives the approximated characteristic length for this case.

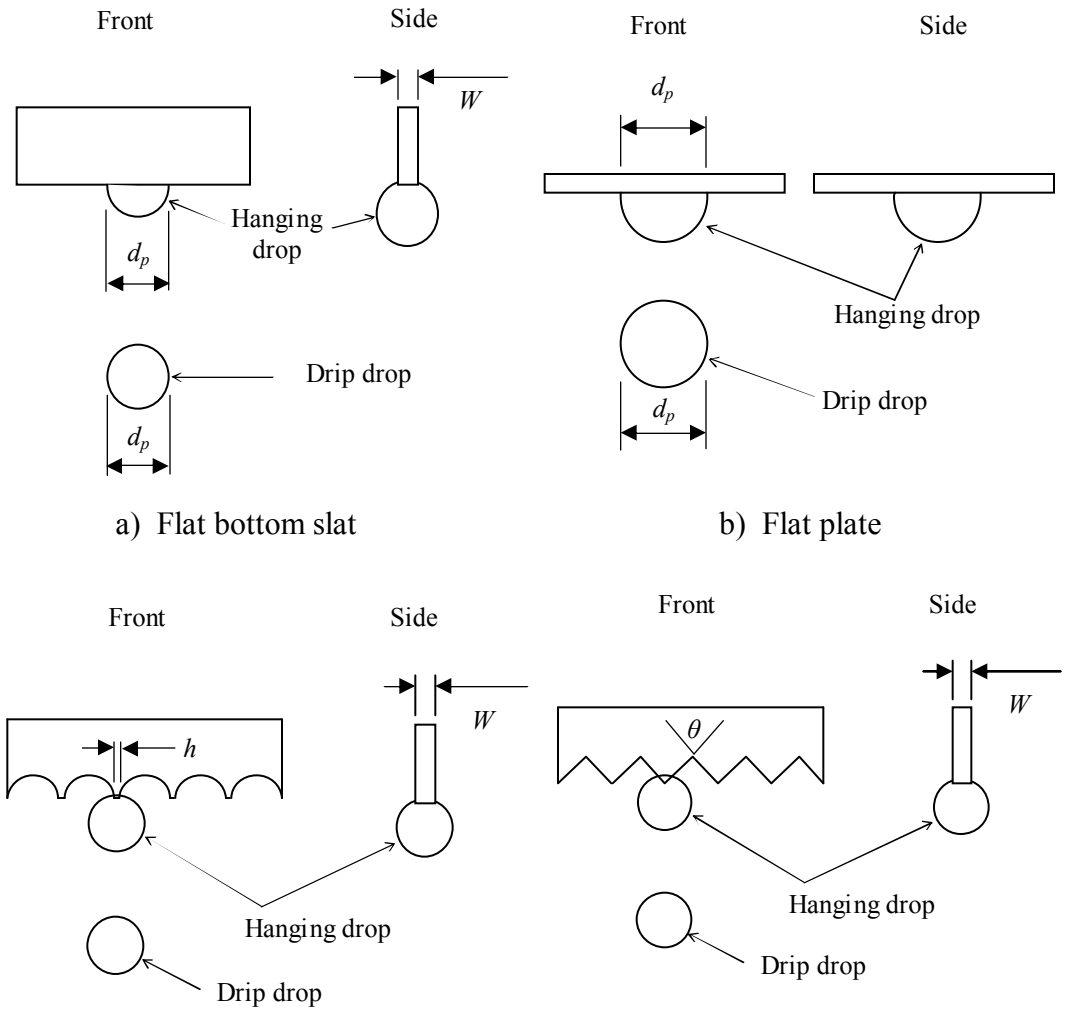

Figure E.1: Dripping diagrams for different slat bottom profiles.

Figure E.1(b) shows a diagram of a drop suspended below a horizontal flat plate just before it detaches and also after detachment. In order to determine the primary drip drop diameter in this case the maximum diameter of the water hemisphere suspended below the plate before detachment is assumed to equal the primary drip drop

diameter. The characteristic length S_p, taken as the circumference of the circle with diameter d_p, is given by Equation (E.3).

Table E.1: Interpenetrating line length S_P for different slat geometries.

Slat geometry		Characteristic length, S_p	
Narrow slat	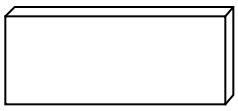	$S_P = 2(d_p + W), \quad W \leq 4.5\ mm$	(E.2)
Flat plate	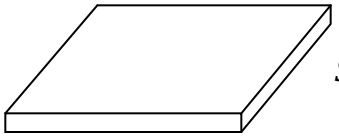	$S_P = \pi d_p, \quad W \geq 4.5\ mm$	(E.3)
Sharp round tooth slat	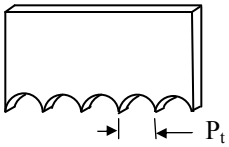	$S_P = 2W, \quad W \leq 4.5\ mm$ $P_t > 1.35 d_{p,flat\ plate}$	(E.4)
Flat round tooth slat	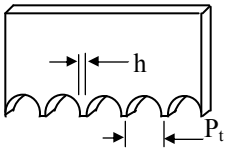	$S_p = 2(h + W), \quad W \leq 4.5\ mm$	(E.5)
Saw tooth slat	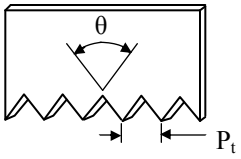	$S_P = 0.637 d_p \theta + 2W, W \leq 4.5\ mm$ $P_t > 1.35 d_{p,flat\ plate}$, $\tan\frac{\theta}{2} > 0.5$	(E.6)
Angled slat	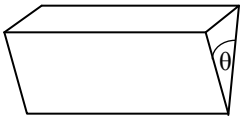	$S_P = 0.363 d_p \theta + 2d_p$	(E.7)

Figure E.1(c) shows a diagram of a drop suspended below a slat with a round tooth profile on the bottom, just before it detaches and also after detachment. The

characteristic length can be estimated by Equation (E.4) if the teeth are perfectly sharp and by Equation (E.5) if not.

Figure E.1(d) shows a diagram of a drop suspended below a slat with a saw tooth profile on the bottom just before it detaches and also after detachment. An equation for predicting the characteristic length (S_P) is obtained by firstly realising that for $\theta = 0$ radials the characteristic length equals $S_P = 2W$ and for $\theta = \pi$ radials the characteristic length equals $S_P = 2(d_p + W)$. Equation (E.6) is then obtained by assuming that the variation of S_P with θ is linear.

A slat with a sharp edge at the bottom (without teeth) is the last slat profile considered in this section. Equation (E.7) is obtained by realising that $S_P = 2d_p$ for $\theta = 0$ radials and $S_P = \pi d_p$ for $\theta = \pi$ radials and by assuming the variation of S_P with θ is linear.

E.3 Conclusions

In this appendix a theoretical equation for predicting the primary drip drop diameter is derived by balancing the surface tension- , gravitational- and buoyancy forces acting on a drop suspended below a slat. Equation (E.1) is obtained to estimate the primary drip drop diameters below slats with different bottom profiles and is expressed in terms of a characteristic length that is a function of the bottom profile of the slat. Table E.1 lists equations for predicting the characteristic length (S_P) of some slat profiles.

Table E.2: Comparison between measured and predicted primary drip drop diameters.

Slat type	Researcher	W [mm]	P_t [mm]	h [mm]	θ [rad]	d_p [mm]	d_p (predicted) [mm]
Flat plate	Dreyer (1994)	30	-	-	-	7.66	6.69
Angled slat	Dreyer (1994)	-	-	-	0.79	6.61	5.70
Flat plate	Dreyer (1994)	10	-	-	-	7.31	6.90
Angled slat	Dreyer (1994)	-	-	-	0.33	6.47	5.50
Narrow slat	Terblanche (2008)	3	-	-	-	6.88	6.46
Saw tooth	Terblanche (2008)	3	12	-	0.79	5.13	4.94
Round tooth	Terblanche (2008)	3	15	1	-	4.63	4.85
Round tooth (sandblasted)	Terblanche (2008)	3	15	1	-	5.35	4.85

Table E.2 and Figure E.2 show a comparison between the primary drip drop diameters measured by Dreyer (1994) and Terblanche (2008) and the values predicted by Equation (E.1), based on the slat classification listed in Table E.1.

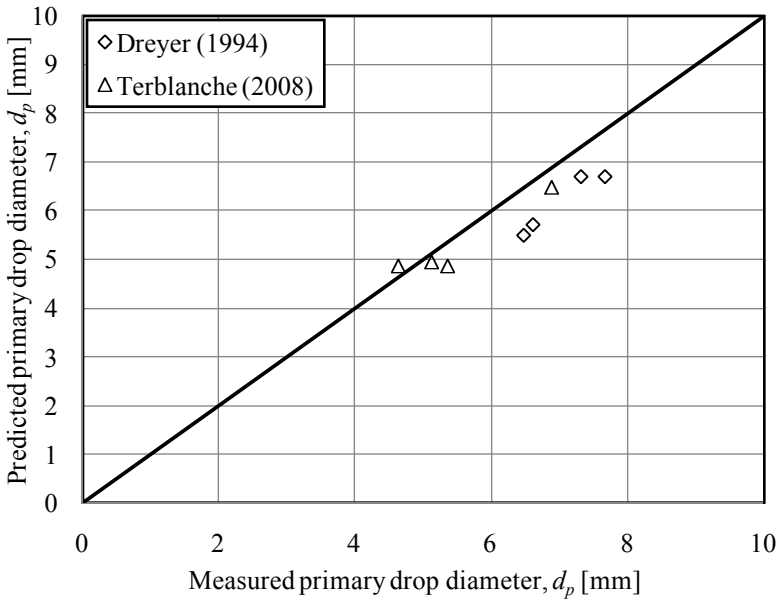

Figure E.2: Comparison between predicted primary drip drop sizes and those in literature.

The drip drop model does not take any surface characteristics of the slat material into account, but does predict a good representative primary drop diameter between a relatively smooth PVC surface and a sandblasted PVC surface (Table E.2) in the case of a slat with a round tooth profile.

F

HIGH SPEED CAMERA IMAGE PROCESSING

The image processing procedure for extracting drop data from the images taken with high speed video cameras is explained in this appendix. The first part of this procedure creates a noise free image on which the drops are clearly highlighted and the second part counts the drops and determines their sizes.

Figure F.1 shows a flow chart of the first part of the algorithm that highlights the drops in the in the high speed video camera images.

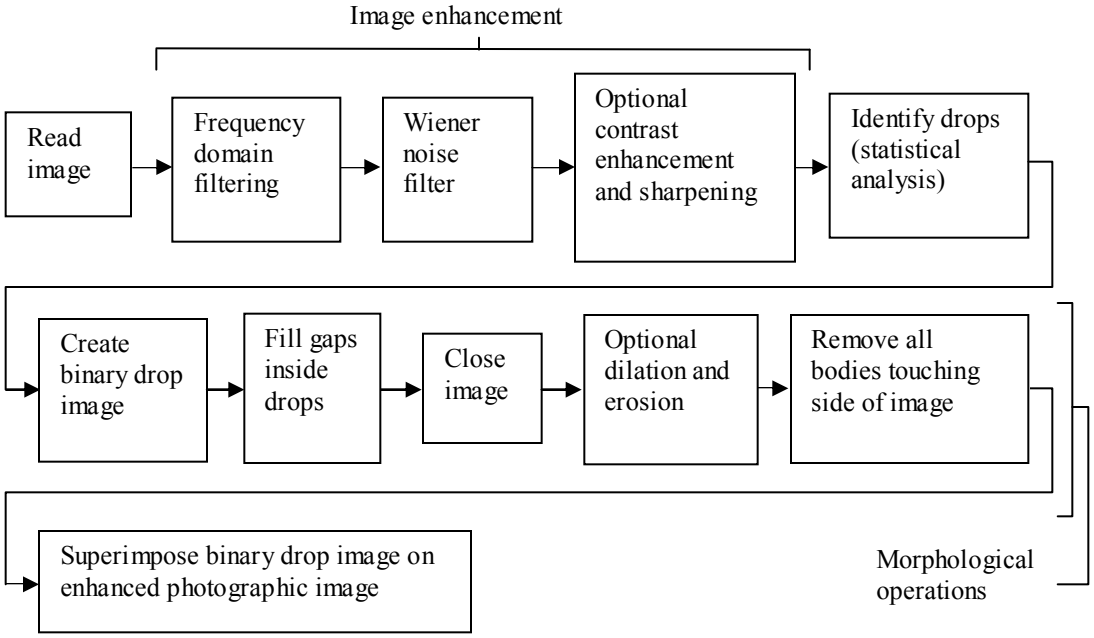

Figure F.1: Image processing algorithm.

The original images are generally very noisy and this makes drop identification difficult (Figure F.2). The noise is mainly periodic and can be filtered out in the frequency domain by constructing a filter on the Fourier transform image (Figure F.3) of the photograph before converting the image back to the spatial domain. The value of the constructed filter is taken as the median value of the Fourier spectrum image. A Wiener filter is used in addition to the constructed filter (Figure F.3b) as well as

optional contrast enhancement and image sharpening procedures to obtain the enhanced image shown in Figure F.4 that contains very little noise.

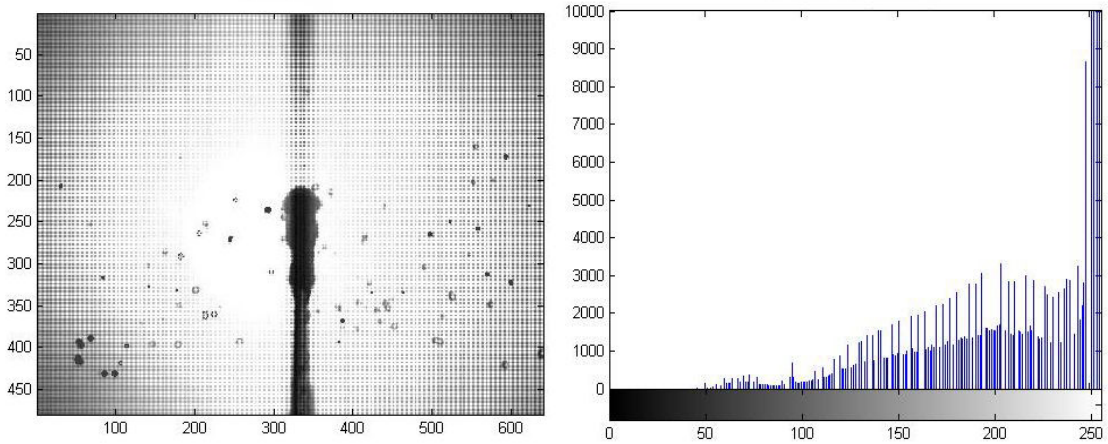

a) Original image b) Histogram of original image

Figure F.2: Program view of original image.

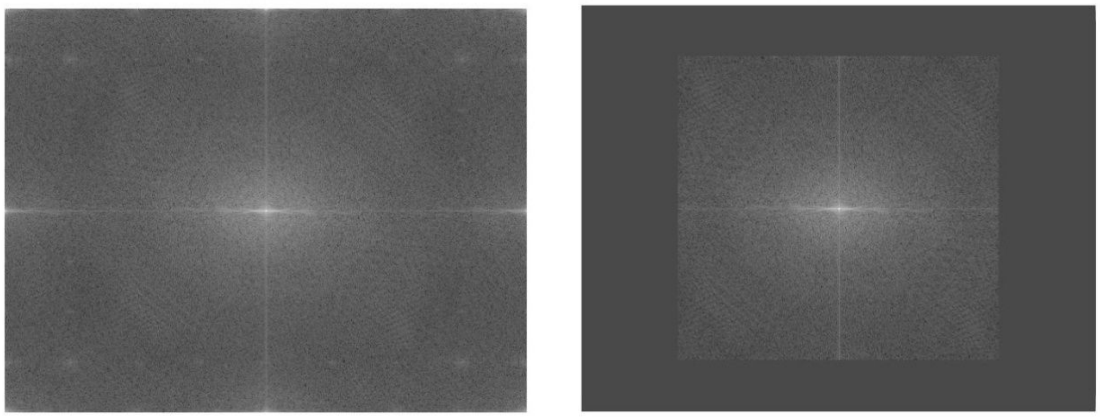

a) Fourier spectrum of original image b) Constructed filter on Fourier spectrum

Figure F.3: Fourier spectrums.

Drop identification in the enhanced image (Figure F.4) is done according to a statistical method based on colour that are applied to equally sized sub-regions in the photograph of which the sub-region size is defined by the user. A pixel in this region is considered to be part of a drop when its colour falls outside a user-defined number of standard deviations from the mean colour value to the black side of the spectrum. For the example shown in this appendix an experimentally determined value of 1.6 standard deviations is used (1.6σ). The user must also provide a minimum colour range inside the sub-region in order to prevent the algorithm from identifying drops

in an area with no drops where the colour variation is relatively small. For this example an experimentally determined minimum colour range of 55 is specified.

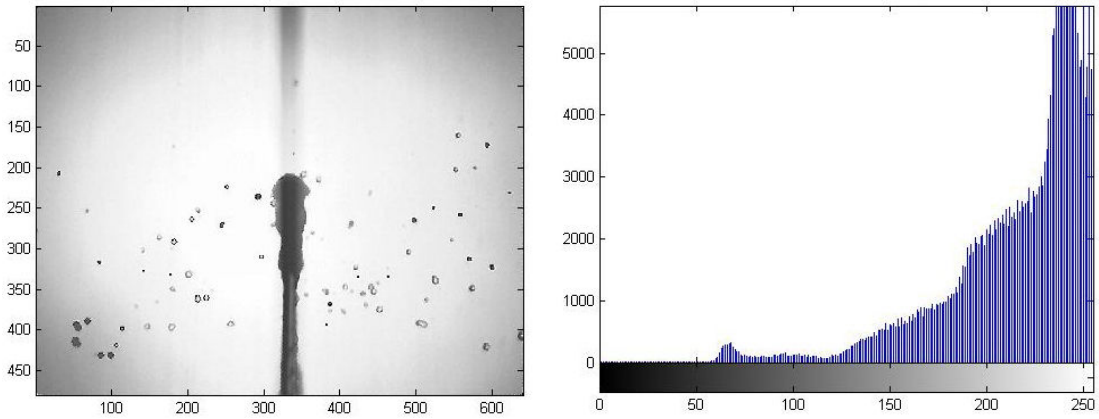

a) Enhanced image b) Histogram of enhanced image

Figure F.4: Enhanced image after filtering.

Figure F.5 shows a binary image of the identified drops and also shows how the image was subdivided into smaller regions for the analysis.

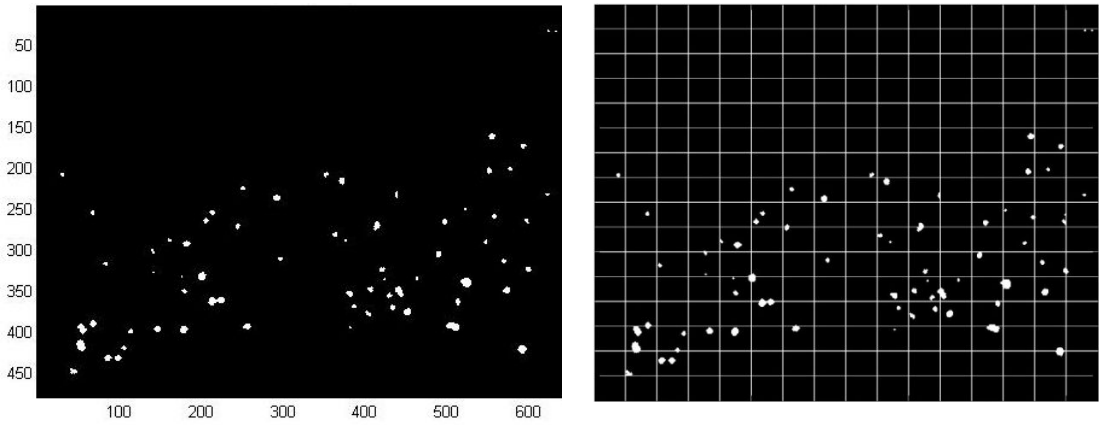

a) Binary image of drops b) Sub-regions for statistical analysis

Figure F.5: Binary images containing drops.

Figure F.6 shows the highlighted drop image where the binary drop image (Figure F.5a) is superimposed on the enhanced image (Figure F.4a). The highlighted images are also visually inspected to make sure that the drops are accurately highlighted and if necessary any further improvements are done manually.

In the second part of the algorithm the drops in the highlighted image are counted by the software program and their projected frontal areas (A_{pr}) determined by counting

the number of pixels comprising each drop before multiplying this number with a calibration value. The equivalent spherical drop diameter for each drop is determined from Equation (F.1).

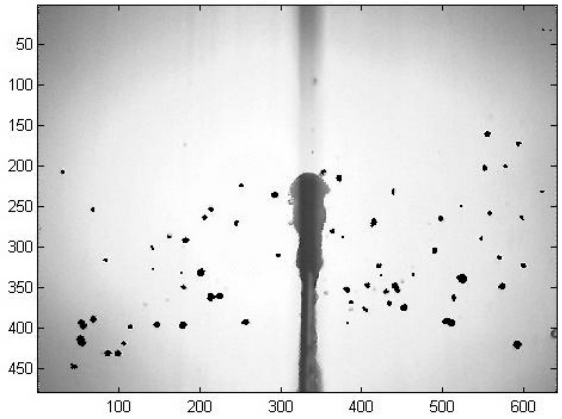

Figure F.6: Image with highlighted drops.

$$d_d = \sqrt{4A_{pr}/\pi} \tag{F.1}$$

The Sauter mean diameter of the drops is determined from

$$d_{32} = \frac{\sum nd^3}{\sum n\, d^2} \tag{F.2}$$

G

DROP INTERACTION IN A RAIN ZONE WITH NO AIR FLOW

G.1 Introduction

The change in drop distribution with rain zone height due to drop collisions and aerodynamic break-up is investigated in this appendix. Drop distributions are measured H_{rz} = 0.26 m and H_{rz} = 7.05 to 7.65 m below different fill and grid configurations before the two measurements below each configuration are compared.

G.2 Apparatus for drop interaction experiments

Figure G.1 shows the experimental setup for the rain zone drop interaction measurements. A 300 mm x 300 mm height adjustable spray frame is built according to the specification of the spray frame used in the counter flow cooling tower test facility of the University of Stellenbosch. Drop size measurements below this spray frame are taken by means of photographs at two different elevations by keeping the photographic measuring equipment in a fixed position while adjusting the spray frame to a high (Position 1) and low position (Position 2).

The photographic measurement technique and equipment of Terblanche *et al.* (2009) is used for drop size measurements which makes use of a Nikon D70S digital SLR camera inside a PVC pipe housing, that is inserted below the mini spray frame (also splash grid or trickle fill). Backlighting is provided by means of three 1000 W tungsten halogen static lights that illuminate a sandblasted glass background plate to ensure that the drops in the photographs have well defined dark edges.

Drop data is extracted from the drop images by means of a software program (Terblanche, 2008) developed for this purpose that includes drop location and the number of pixels contained in each drop. The projected frontal area of each drop is determined by multiplying the number of pixels contained in each drop with a calibration value and the equivalent spherical drop diameter is determined from

$$d_d = \sqrt{4A_{pr}/\pi} \tag{F.1}$$

Each measurement presented for position 2 in this appendix is the sum of the drops contained in 3 images, while 7 to 8 images are used for position 1 because of the lower drop densities at this height.

Water is supplied to the spray frame via a wall mounted valve and all measurements are done at a water mass velocity of G_w = 2.84 kg/m^{2}s where the flow measurement is done by means of a flow meter. Measurements are also done with a trickle fill installed below the spray frame, a trickle fill together with a splash grid below the spray frame and with only a slat grid below the spray frame.

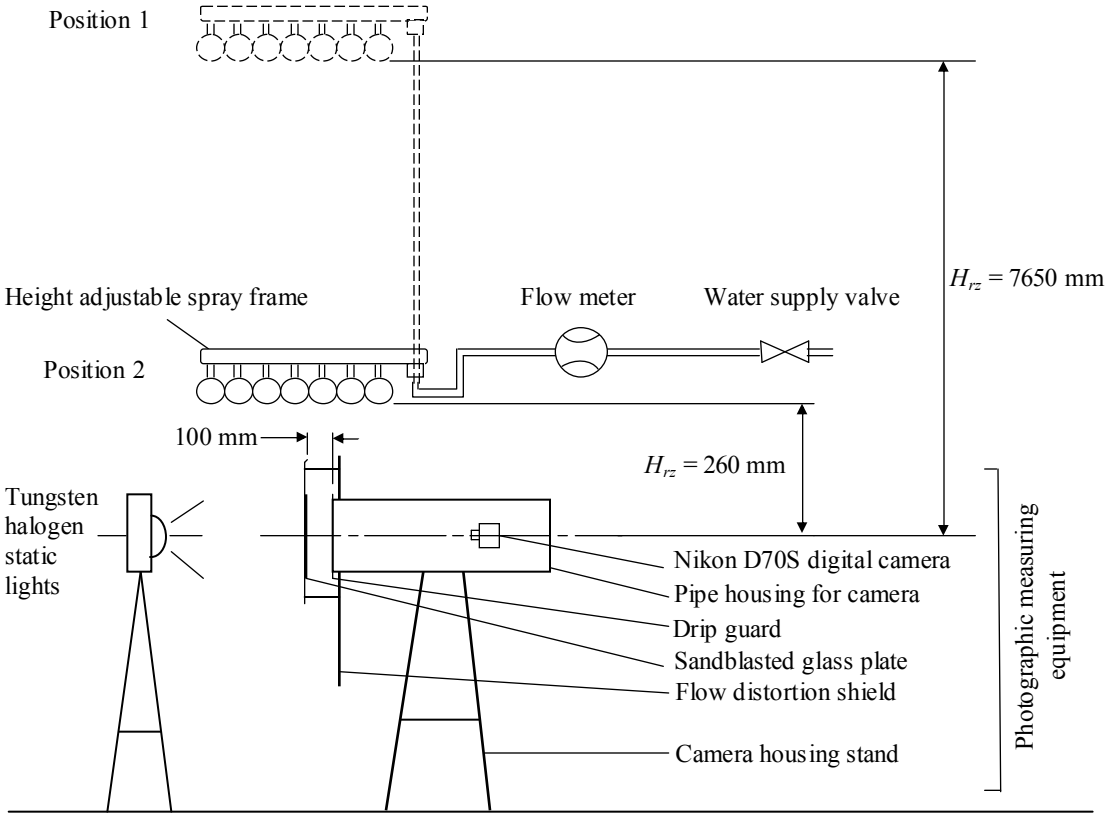

Figure G.1: Experimental setup for rain zone drop interaction measurements in still air.

G.3 Drop size distributions measured below the spray frame

This section presents the drop distributions measured H_{rz} = 260 mm (Position 2) and H_{rz} = 7650 mm (Position 1) below the spray frame. The spray frame produces a relatively small Sauter mean drop diameter (d_{32} = 2.325 mm) with an approximate outlet water velocity through the sprayers of 6 m/s. The interaction between the drops over the 7390 mm (= 7650 – 260 mm) fall distance is negligible due to the relatively

uniform distribution of small drops with small velocity differences between the drops. Figure G.2 presents the measured drop- and mass distributions below the spray frame, together with drop distribution photographs. The Sauter mean drop diameter stays relatively constant and only changes from d_{32} = 2.325 mm (H_{rz} = 260 mm) to d_{32} = 2.434 mm (H_{rz} = 7650 mm).

a) Photograph (H_{rz} = 260 mm)

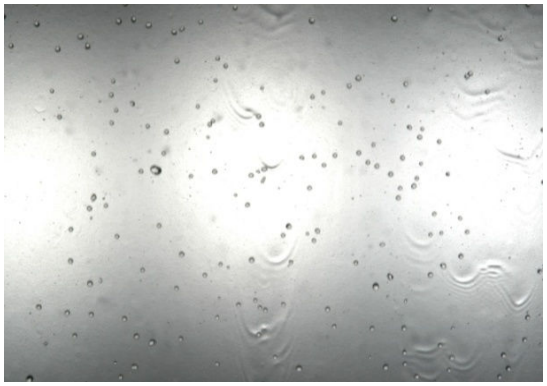

b) Photograph (H_{rz} = 7650 mm)

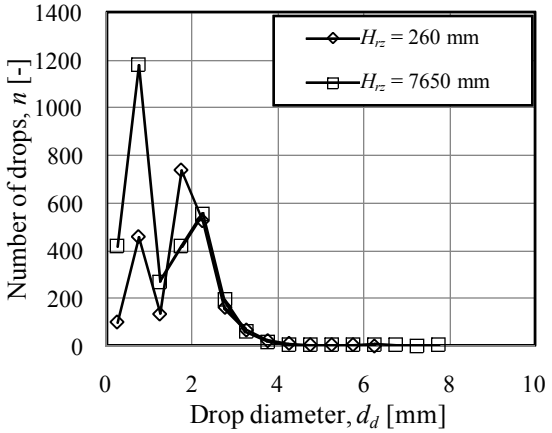

c) Drop distribution

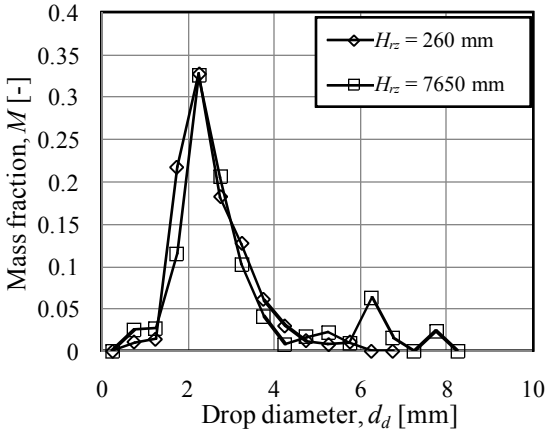

d) Mass distribution

Figure G.2: Drop distribution at different elevations below a mini spray frame (G_w = 2.84 kg/m^{2}s, G_a = 0).

G.4 Drop size distributions measured below a trickle fill installed below the spray frame

This section presents the drop distributions measured H_{rz} = 260 mm (Position 2) and H_{rz} = 7650 mm (Position 1) below a trickle fill. The trickle fill is installed below the spray frame (Section G.3) with insulation wool is inserted between the spray frame and the trickle fill to reduce the velocity of the water into the fill and to spread the water evenly onto the fill. This makes the results comparable to the drop size

measurements of Terblanche *et al.* (2009) below a trickle fill where the water from the distribution system was dripped onto the fill. Figure G.3 presents the measured drop- and mass distributions below the spray frame, together with drop distribution photographs.

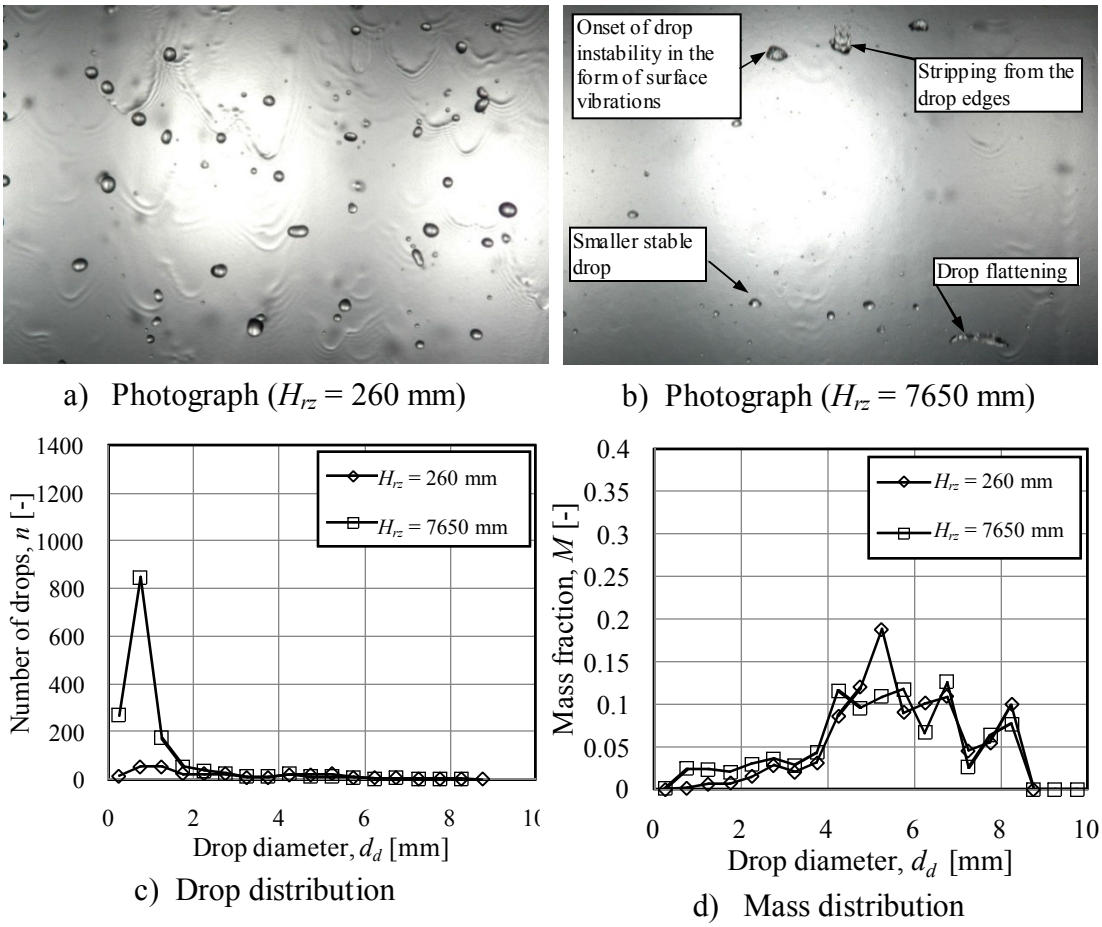

a) Photograph (H_{rz} = 260 mm)

b) Photograph (H_{rz} = 7650 mm)

c) Drop distribution

d) Mass distribution

Figure G.3: Drop distribution at different elevations below a trickle fill (G_w = 2.84 kg/m^{2}s, G_a = 0).

Figure G.3 shows a significant increase in the number of smaller drops between H_{rz} = 260 mm and H_{rz} = 7650 mm due to the break-up of the large drops. These large drops that drip from below the fill become unstable due to increased aerodynamic forces acting on them as they reach higher velocities [Figure G.3(b)]. The onset of these instabilities can be linked to a Weber number based on air density which is approximately $We_c \approx 10$ (Section 2.3). The Sauter mean drop diameter changes from d_{32} = 5.092 mm (H_{rz} = 260 mm) to d_{32} = 4.021 mm (H_{rz} = 7650 mm).

G.5 Drop size distributions measured below a slat grid installed below a trickle fill

This section presents the drop distributions measured H_{rz} = 260 mm (Position 2) and H_{rz} = 7050 mm (Position 1) below a slat grid (Figure H.9) that is installed H_{FG} = 600 mm below a trickle fill. The trickle fill is again installed below the spray frame (Section G.3) with insulation wool inserted between the fill and the spray frame to reduce the water velocity into the fill and to spread the water evenly onto the fill. Due to restriction in the height of the setup the maximum fall height (below the grid) of the drops for this experiment is only H_{rz} = 7050 mm. Figure G.4 presents the measured drop- and mass distributions below the slat grid, together with drop distribution photographs. The Sauter mean drop diameter changes from d_{32} = 3.060 mm (H_{rz} = 260 mm) to d_{32} = 3.603 mm (H_{rz} = 7050 mm).

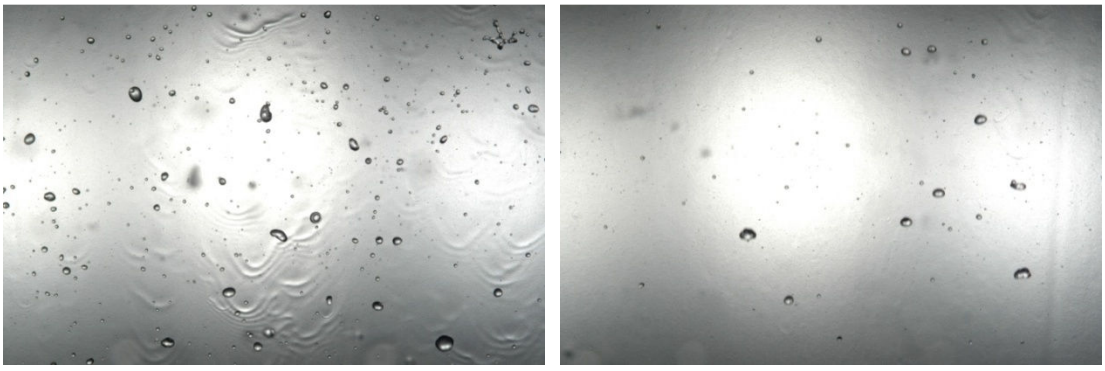

a) Photograph (H_{rz} = 260 mm) b) Photograph (H_{rz} = 7050 mm)

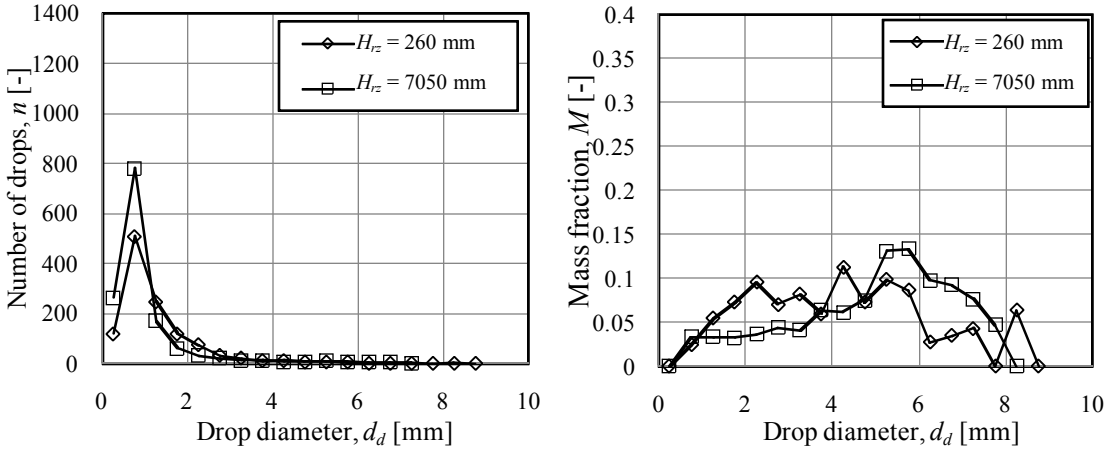

c) Drop distribution d) Mass distribution

Figure G.4: Drop distribution at different elevations below a slat grid installed below a trickle fill (G_w = 2.84 kg/m^{2}s, G_a = 0, H_{FG} = 600 mm).

In this case there is a slight increase in the Sauter mean drop diameter between H_{rz} = 260 mm and H_{rz} = 7050 mm. Figure G.4 shows a relative large number of drops below the grid (H_{rz} = 260 mm) with diameters ranging between d_d = 1 and 3 mm, that formed due to drop break-up (splashing, straddling and dripping) on the grid. A large part of these and other slower moving drops are swept up by the faster moving drops as the fall distance increases. This may explain the increase in drops with diameters ranging from between d_d = 5 to 7 mm. Larger drops will still break-up as they did in Section G.4, but due to a reduction in the number of these large drops by the grid (compare the numbers in Figures G.3d and G.4d) this effect is not as significant as in Section G.4. Larger drops, ranging from d_d = 5 to 8 mm in diameter, are still present at H_{rz} = 7050 mm (Figure G.4) and the reason for this might be that these drops formed through the coalescence of smaller drops and haven't reached the critical Weber number yet.

G.6 Drop size distributions measured below a slat grid installed below the spray frame

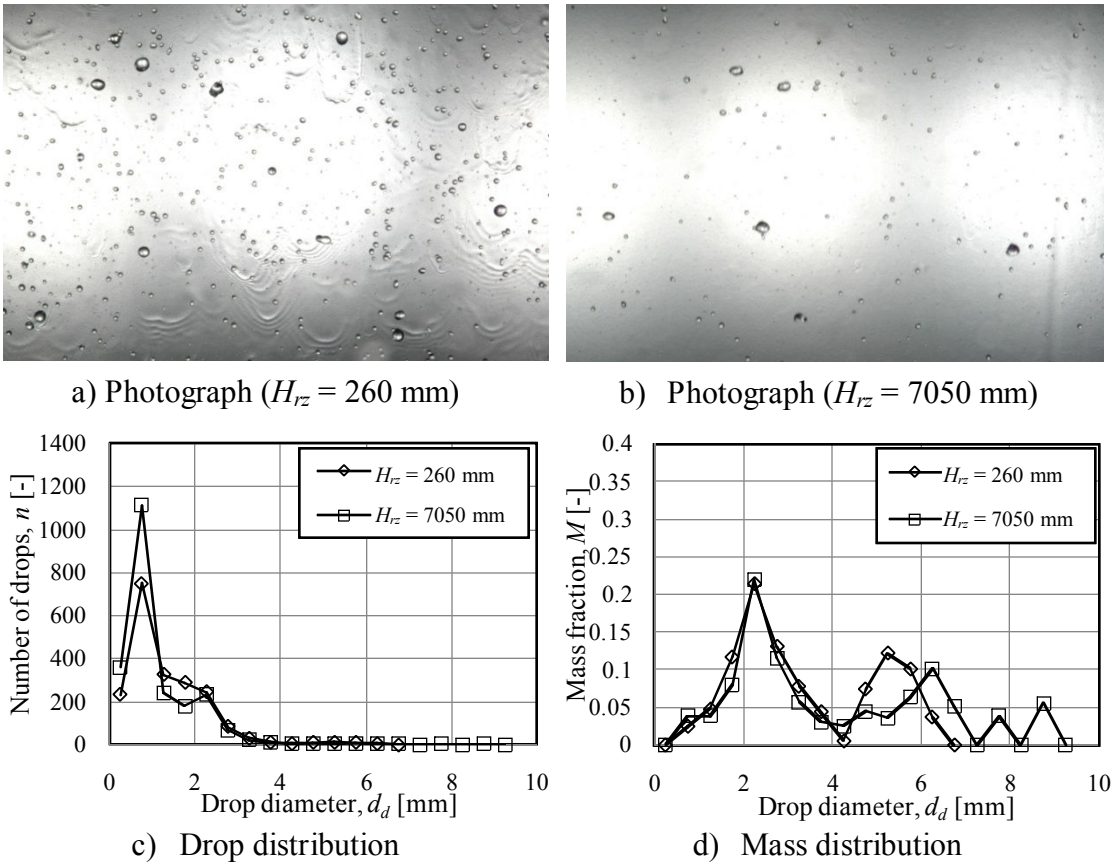

a) Photograph (H_{rz} = 260 mm) b) Photograph (H_{rz} = 7050 mm)

c) Drop distribution d) Mass distribution

Figure G.5: Drop distribution at different elevations below a slat grid installed below the spray frame (G_w = 2.84 kg/m^{2}s, G_a = 0, H_{FG} = 600 mm).

This section presents the drop distributions measured H_{rz} = 260 mm (Position 2) and H_{rz} = 7050 mm (Position 1) below a slat grid (Figure H.9) that is installed H_{FG} = 600 mm below a spray frame (Section G.3). Figure G.5 presents the measured drop- and mass distributions below the slat grid, together with drop distribution photographs. The Sauter mean drop diameter changes from d_{32} = 2.616 mm (H_{rz} = 260 mm) to d_{32} = 2.737 mm (H_{rz} = 7050 mm).

G.7 Conclusions

When a drop distribution below a drop generating device like a spray frame contains small drops of relatively uniform sizes, little to no interaction between these drops are expected due to the small velocity differences between these drops (Section G.3). If significant interaction does take place it is expected that there would be a slight increase in the Sauter mean drop diameter due to drop collisions. Since the distribution doesn't contain any large drops, aerodynamic drop break-up is expected be negligible.

If the initial drop distribution contains predominantly larger (Section G.4) drops, like below a trickle fill (d_{32} = 5 to 6 mm), a significant number of these drops are expected to undergo aerodynamic drop break-up (Figure G.6). This may easily lead to a reduction in the Sauter mean drop diameter over a H_{rz} = 7 to 10 m fall distance (still air) of 1 mm. Larger drops will still sweep up the smaller drops, but the aerodynamic break-up of the predominantly larger drops is dominant.

Figure G.6: Drops breaking up due to aerodynamic forces.

Significant drop size reduction may be achieved by installing a splash grid below a trickle fill. This break-up introduces large velocity differences between drops that lead to an increased number of collisions between the drops in the free fall zone below such a grid. The Sauter mean drop diameter can easily increase by 0.6 mm below such a splash grid over a fall distance of H_{rz} = 6.8 m in still air (Section G.5).

The measurement uncertainties associated with the measurement results of this section are discussed in Appendix L.

H

DROP SIZE MEASUREMENTS BELOW DIFFERENT SPLASH GRID CONFIGURATIONS IN A RAIN ZONE WITH NO AIR FLOW

H.1 Introduction

This appendix presents the drop size measurement results below different splash grid configurations (installed below the cross flow test facility spray frame) in the form of drop distribution, mass distribution and Sauter mean drop diameter plots.

H.2 Description of experimental setup

The photographic measurement technique and equipment of Terblanche (2008), as described in Section G.2, is used to measure drop size distribution data below the cross flow spray frame as well as under different grid configurations installed below the spray frame. Each measurement presented in this appendix is the sum of the drops contained in three images from which the drop distribution, mass distribution and Sauter mean drop diameters are determined.

H.3 Drop size distribution data measured below the cross flow spray frame

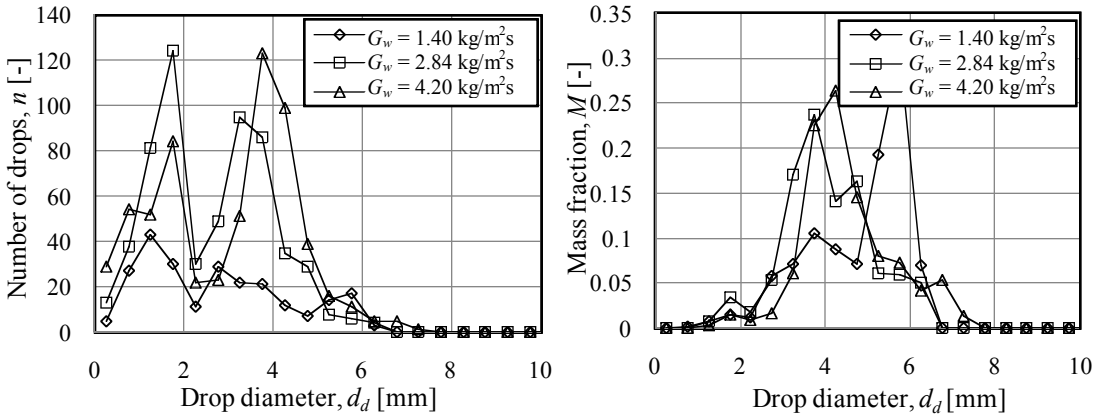

(a) Drop distribution (b) Mass distribution

Figure H.1: Drop size data measured below the cross flow spray frame (G_a = 0).

Drop size distribution measurements are taken H_{rz} = 260 mm below the spray frame of the cross flow test facility at three different water mass velocities and the results are presented in this section as a drop distribution (Figure H.1a), a mass distribution (Figure H.1b) and a Sauter mean drop diameter plot (Figure H.2).

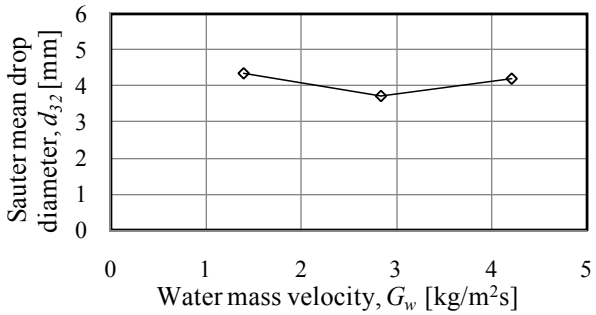

Figure H.2: Sauter mean drop diameters below the cross flow spray frame (G_a = 0).

H.4 Drop size distribution data measured below a PVC grid consisting of narrow slats

One and two layers of a PVC grid (with a vertical grid spacing of H_{GG} = 100 mm) consisting of narrow slats (Figure H.3), as used by Terblanche *et al.* (2009), is placed at various distances (H_{FG}) below the cross flow spray frame and drop size measurements are taken (H_{rz} = 260 mm) below the lowest grid at a water mass velocity of G_w = 2.84 kg/m^{2}s. Figure H.4 presents the measured drop size distribution and mass distribution plots and Figure H.5 presents the measured Sauter mean drop diameters.

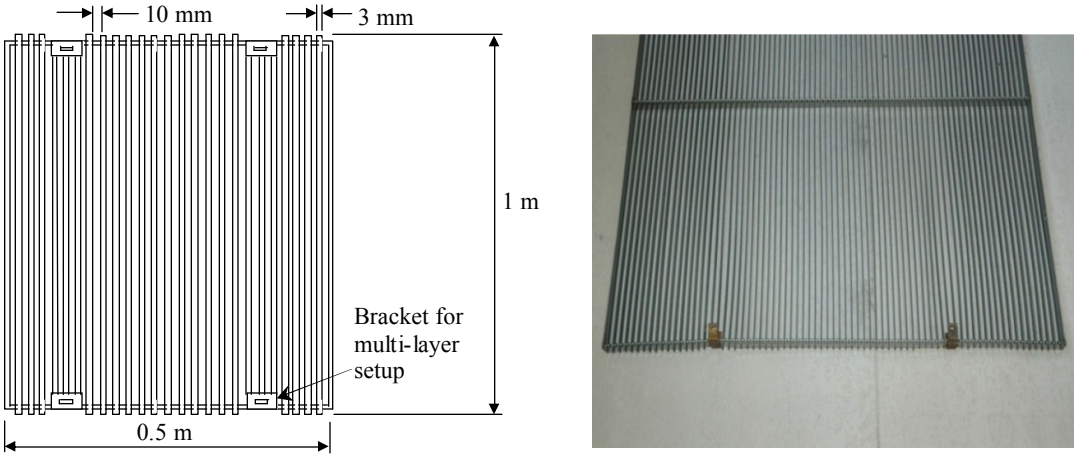

a) Diagram of slat grid

b) Photograph of grid

Figure H.3: Splash grid comprising evenly spaced, horizontal slats.

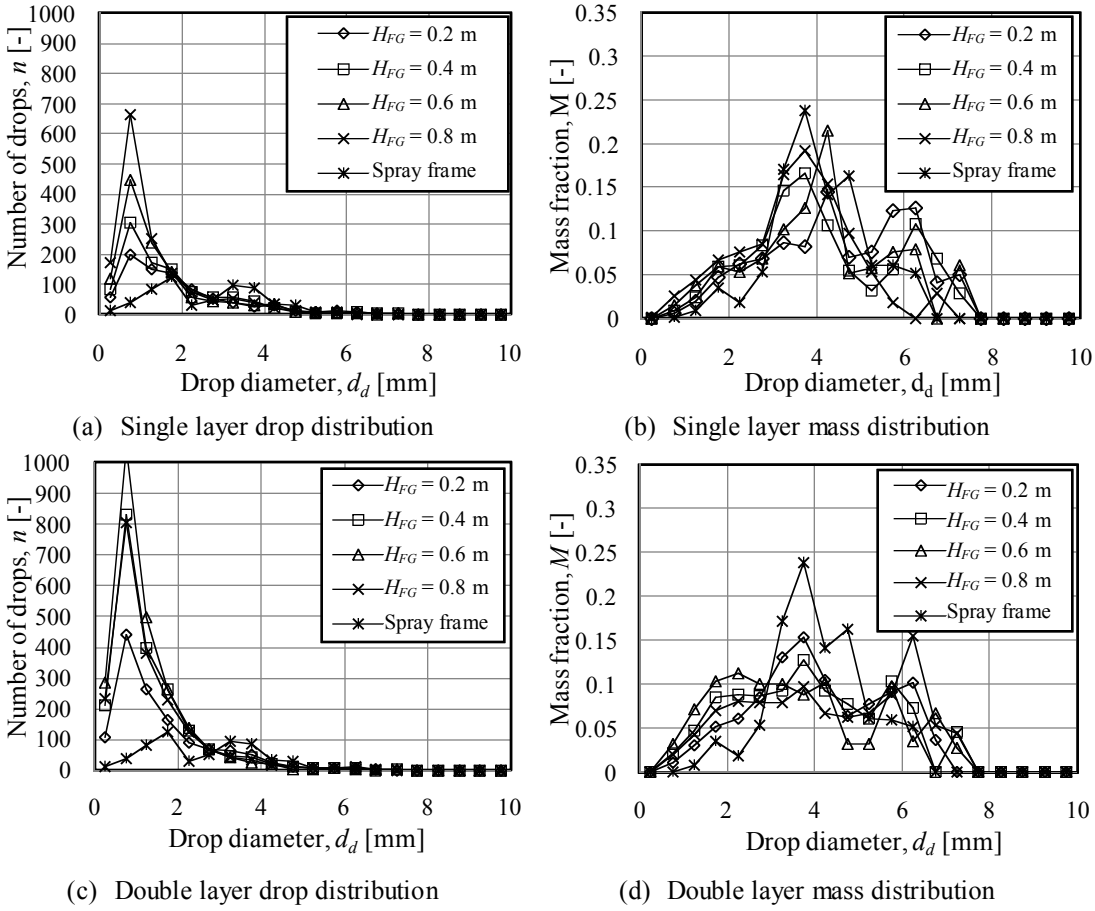

(a) Single layer drop distribution

(b) Single layer mass distribution

(c) Double layer drop distribution

(d) Double layer mass distribution

Figure H.4: Drop size data measured below PVC slat grids installed below the cross flow spray frame (G_w = 2.84 kg/m^{2}s, G_a = 0).

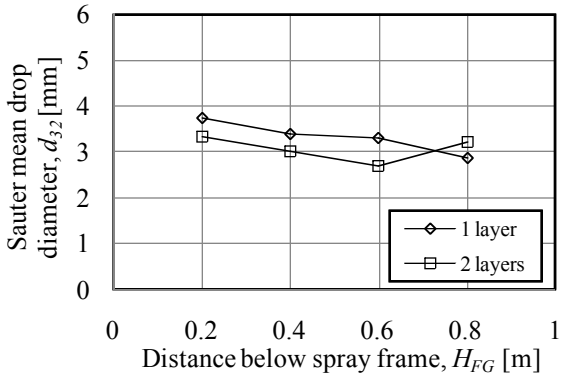

Figure H.5: Sauter mean drop diameters below the PVC slat grid installed below the cross flow spray frame (G_w = 2.84 kg/m^{2}s, G_a = 0).

Figure H.4 shows that the largest drop produced below the grid is larger than the largest drop in the initial distribution below the spray frame even though there is a reduction in the overall Sauter mean drop diameter. The increase in the largest drop size may be due to the accumulation and coalescence of water drops on the grid surface that leaves the grid in the form of drip drops when they grow too big. The number of these larger drops generally decreases as the distance between the spray frame and the slat grid is increased, becoming negligible when a single grid is placed H_{FG} = 0.8 m below the spray frame.

H.5 Drop size data measured below a commercial splash grid

Drop size measurements are taken below one, two and three layers of a commercial splash grid (Figure H.6) respectively in this section. The grids are installed below the cross flow spray frame, where the two and three layers are installed in the staggered configurations shown in Figures H.6(b) and H.6(c) with zero spacing between the individual layers.

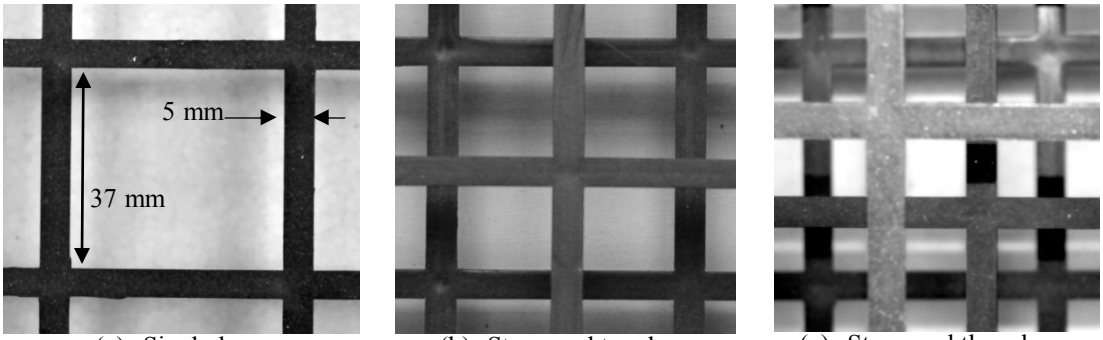

(a) Single layer (b) Staggered two layers (c) Staggered three layers

Figure H.6: Commercial splash grid.

Figure H.7 presents the measured drop distribution and mass distributions plots and Figure H.8 presents the measured Sauter mean drop diameters below the commercial grid. The measurements are taken H_{rz} = 260 mm below the lowest grid in each case at a water mass velocity of G_w = 2.84 kg/m^{2}s. Figure H.7 show a significant increase in the number of drops with diameters greater than d_d = 5.5 mm compared to the slat grid in the previous section. Significant dripping happens below the T-sections which may explain the presence of these drops and they seem to increase as further layers of the commercial splash grid are added.

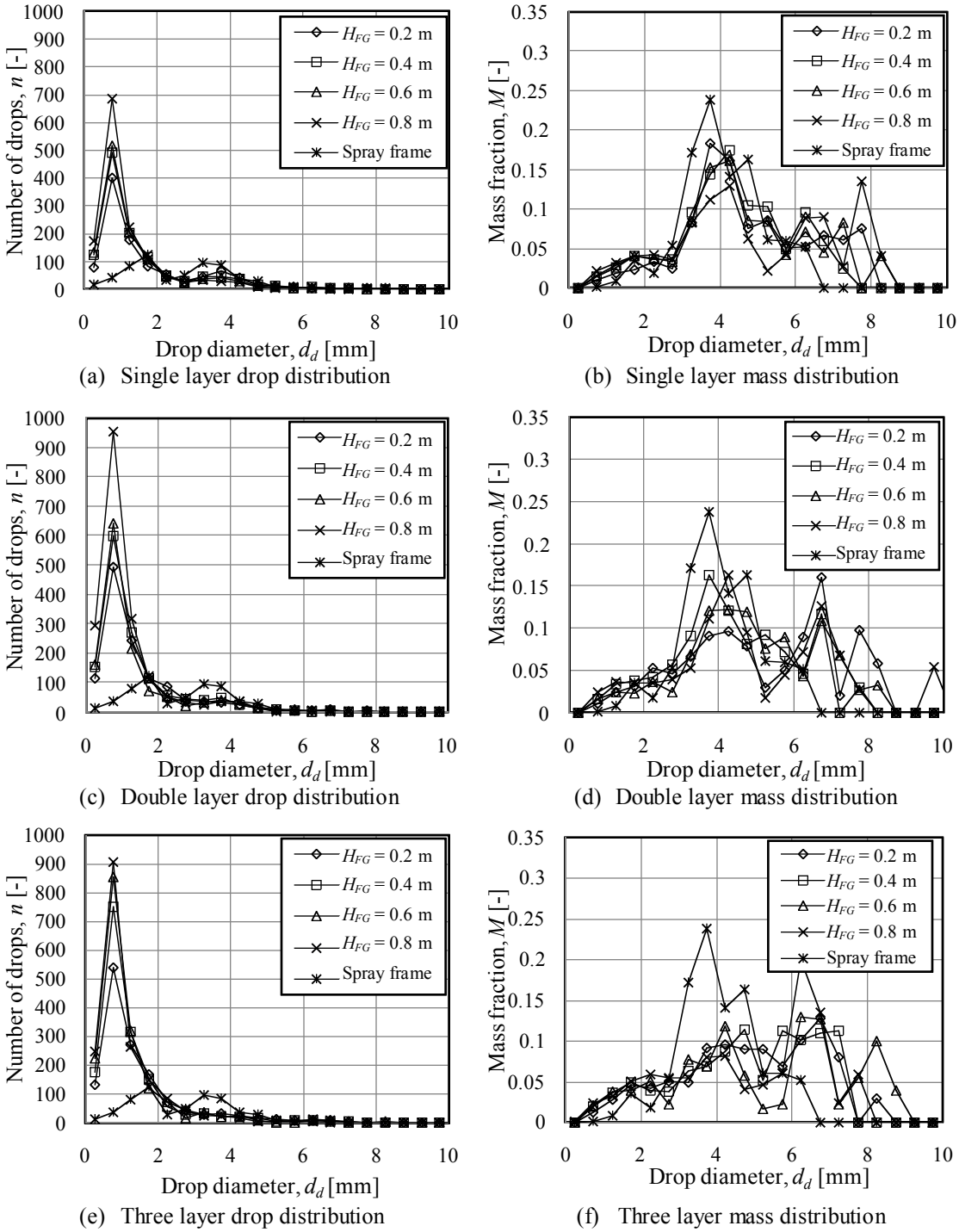

Figure H.7: Drop size data measured below a commercial grid installed below the cross flow spray frame (G_w = 2.84 kg/m^{2}s, G_a = 0).

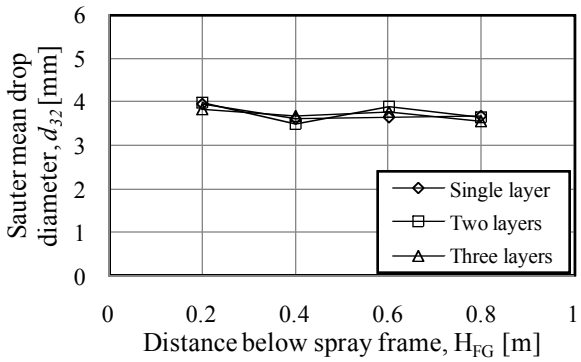

Figure H.8: Sauter mean drop diameters below the commercial grid installed below the cross flow spray frame (G_w = 2.84 kg/m^{2}s, G_a = 0).

H.6 Drop size measurements below a PVC grid with a toothed bottom profile

Drop size measurements are taken below a grid of the same layout as shown in Figure H.3 consisting of the slats shown in Figure H.9 and the results are presented as drop distribution, mass distribution and Sauter mean drop diameter plots. One two and three layers of this grid are respectively installed at different heights below the cross flow spray with a vertical grid spacing of H_{GG} = 42 mm for the multi layer setups. For each case the drop size measurements are taken H_{rz} = 260 mm below the lowest grid. Figure H.10 presents the measured drop size distributions and mass distributions and Figure H.11 presents the measured Sauter mean drop diameters below the grid.

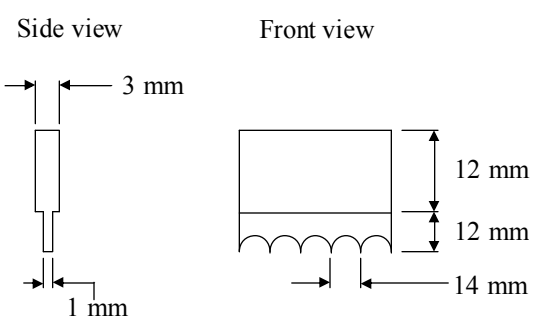

(a) Slat dimensions

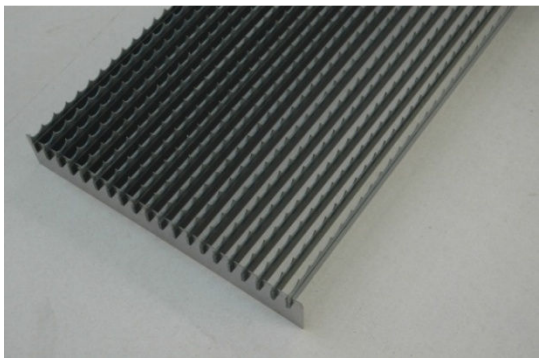

(b) Photograph of test sample

Figure H.9: PVC slats with round tooth profile and shoulder.

The teeth at the bottom of the slats causes a definite reduction in the number of drops with diameters in the region of d_d = 6 mm as seen when comparing Figures H.4 and H.10, especially as the distance between the spray frame and the grid (H_{FG}) decreases.

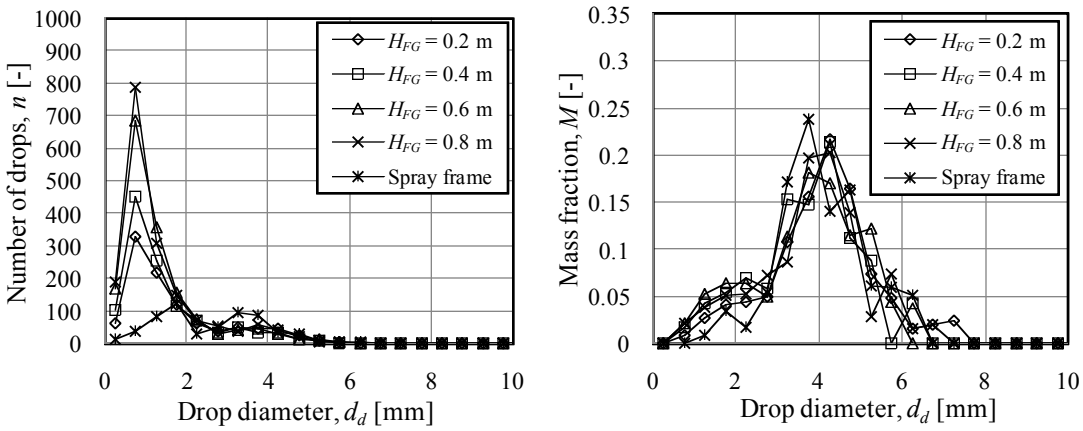

(a) Single layer drop distribution

(b) Single layer mass distribution

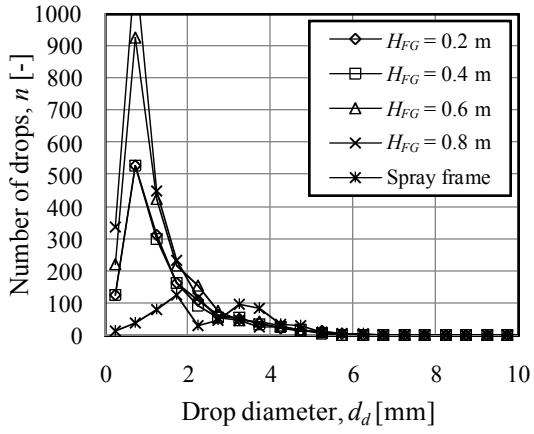

(c) Double layer drop distribution

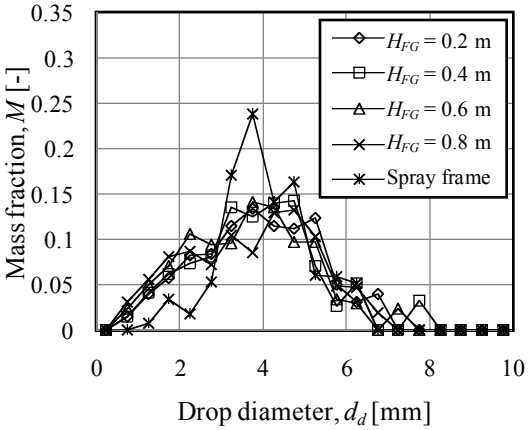

(d) Double layer mass distribution

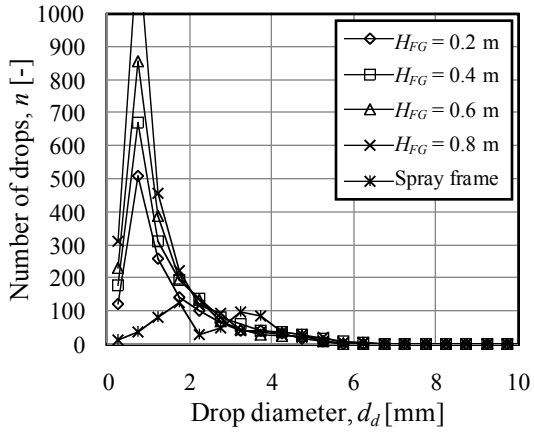

(e) Three layer drop distribution

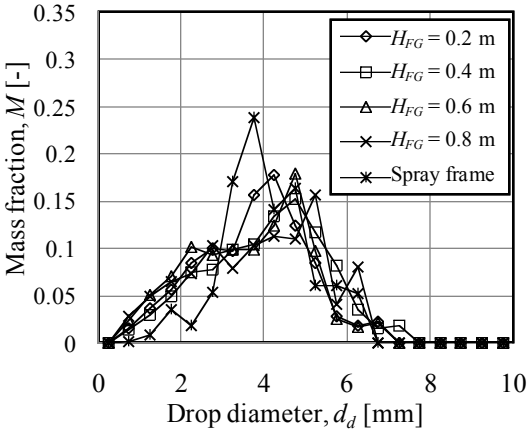

(f) Three layer mass distribution

Figure H.10: Drop size data measured below a PVC grid, with a tooth profile on the slat bottoms, installed below the cross flow spray frame (G_w = 2.84 kg/m^{2}s, G_a = 0).

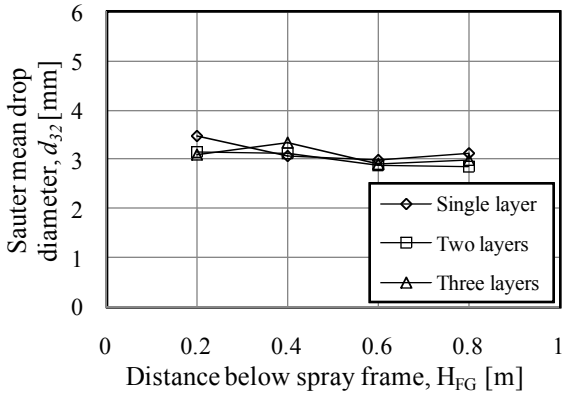

Figure H.11: Sauter mean drop diameters below the PVC grid, with a tooth profile on the slat bottom, installed below the cross flow spray frame (G_w = 2.84 kg/m^{2}s, G_a = 0).

H.7 Conclusions

Significant drop size reduction is achieved by installing splash grids below the spray frame although the drops produced by the spray frame is significantly smaller (d_{32} = 3.72 to 4.35 mm) than the d_{32} = 5 to 6 mm produced below some commercial fills (Terblanche *et al.*, 2009). The best drop size reduction is achieved with the PVC grids (Section H.4 and H.6) with a smallest measured Sauter mean drop diameter of d_{32} = 2.68 mm. Very little drop size reduction is measured under the commercial splash grid for the arrangements used and a reason for this might be the dripping at the T-sections below these grids that causes the formation of larger drops (d_d > 5.5 mm) or simply the fact that a larger number of drops fall through the grid openings than what is expected below a fill, because of the spray frame arrangement.

A toothed profile at the bottom of the PVC slats (Section H.6) decreases the number of larger drops ($d_d \approx$ 6 mm) below the grid caused by dripping. The effect of teeth on the Sauter mean drop diameter below the grid is however not very significant and when the distance between the fill and grid exceeds H_{FG} = 0.6 to 0.8 m there is no difference between the drop distributions below a grid with teeth and an equivalent grid without teeth (compare Sections H.4 and H.6).

Due to an accumulation effect on the grid surface, shown in Figure H.12, that may lead to the formation of larger drops it often happens that larger drops are observed below the grids than below the spray frame. When improving the rain zone the aim is to reduce the drop size for faster cooling and longer residence times of drops in the rain zone, but due to the relative long time this small percentage of surface water (which can be the cause of larger drops) spends on the slat surface they may quite possibly cool down enough as not impact the performance of the rain zone

negatively. This accumulation can however be counteracted by increasing the distance between the grid and fill and also by reducing the slat height.

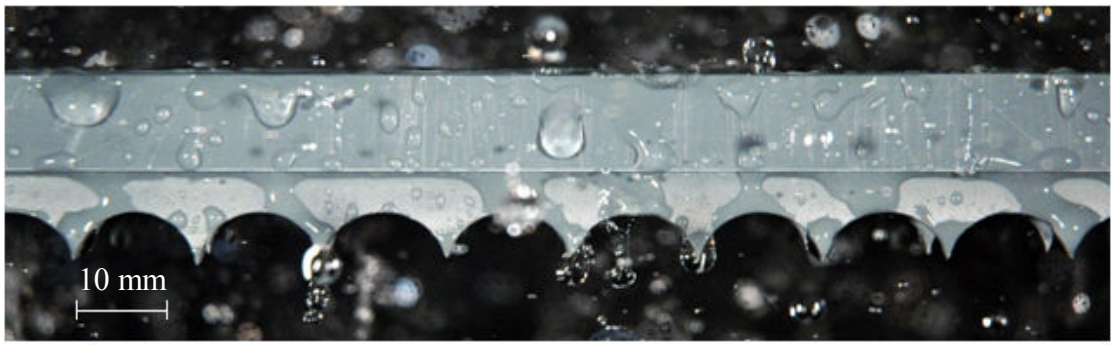

Figure H.12: Water accumulation on a PVC slat.

The measurement uncertainties associated with the measurement results of this section are discussed in Appendix L.

I

ANALYTICAL SOLUTION FOR DROP VELOCITY AND TRAJECTORY

I.1 Introduction

In this appendix the derivations for the analytical solutions of motion for a falling drop are presented and the results compared with numerical results obtained from an Eulerian model.

I.2 Analytical solution for drop velocity

Figure I.1 shows the free-body diagram with velocity and force vectors for a falling drop.

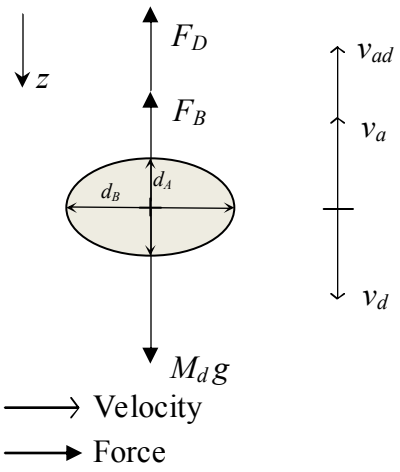

Figure I.1: Free body diagram of a falling, deformable drop.

From Newton's second law of motion the following expression for a drop that deforms due to the dynamic forces acting on its forward stagnation point can be obtained.

$$\frac{\partial v_d}{\partial t} = \frac{1}{M_d}\left(K_1 - K_2 E^{-\frac{2}{3}} C_D {v_d}^2\right) \tag{I.1}$$

where

$$K_1 = \rho_d V_d g - \rho_{av} V_d g \quad \text{and} \quad K_2 = \frac{1}{2}\rho_{av} A_{f,sphere} \quad \text{and} \quad A_f = A_{f,sphere} E^{-\frac{2}{3}}$$

The aspect ratio is given by Dreyer (1994)

$$E = \frac{d_A}{d_B} = 1 - \left(\frac{v_d}{v_T}\right)^2 (1 - E_T) \tag{2.15}$$

Equation (I.1) can be expressed in terms of the drop Reynolds number by making the following substitution

$$\frac{\partial v_d}{\partial t} = \frac{\mu_{av}}{\rho_{av} d_d} \cdot \frac{\partial Re}{\partial t} \tag{I.2}$$

to yield

$$\frac{\partial Re}{\partial t} = \alpha - \beta C_D E^{-\frac{2}{3}} Re^2 \tag{I.3}$$

where

$$\alpha = \frac{6\rho_{av} K_1}{\pi \rho_d \mu_{av} {d_d}^2} \quad \text{and} \quad \beta = \frac{6\mu_{av} K_2}{\pi \rho_d \rho_{av} {d_d}^4}$$

Equation (I.3) is solved by making the following substitution

$$C_D E^{-\frac{2}{3}} Re^2 = C_{D,T} E_T{}^{-\frac{2}{3}} {Re_T}^2 \left(\frac{C_D}{C_{D,T}}\right)\left(\frac{E}{E_T}\right)^{-\frac{2}{3}}\left(\frac{Re}{Re_T}\right)^2 = C_{D,T} E_T{}^{-\frac{2}{3}} {Re_T}^2 f\left(\frac{Re}{Re_T}\right) \tag{I.4}$$

where the aspect ratio at terminal velocity is given by Dreyer (1994)

$$E_T = (1 + 0.148 Eo^{0.85})^{-1} \tag{2.20}$$

and

$$Eo = \frac{g {d_d}^2 (\rho_d - \rho_{av})}{\sigma_d} \tag{2.16}$$

The drag coefficient of the deforming drop at terminal velocity is obtained from the following ratio by Dreyer (1994)

$$\frac{C_{D,T}}{C_{D,sphere,T}} = 1 - 0.17185(1 - E_T) + 6.692(1 - E_T)^2 - 6.605(1 - E_T)^3 \tag{I.5}$$

where the drag coefficient for a sphere is given by Turton and Levenspiel (1986)

$$C_{D,sphere} = 24\frac{(1+0.173Re^{0.657})}{Re} + \frac{0.413}{(1+16300Re^{-1.09})} \tag{2.7}$$

The terminal velocity of the deforming drop is given by

$$v_{d,T} = \left(\frac{K_1}{K_2 E_T{}^{-\frac{2}{3}} C_{D,T}}\right)^{0.5} \tag{I.6}$$

The function $f(Re/Re_T)$ in Equation (I.4) is plotted in Figure I.2(a) and an example of a three interval curve fit over the Reynolds range is shown in Figure I.2(b).

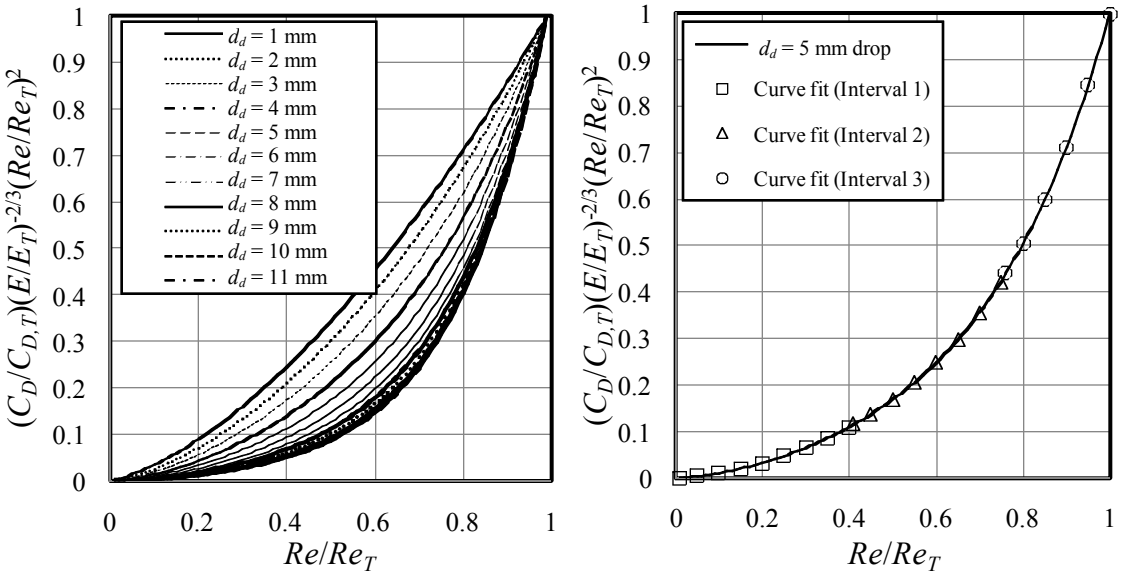

a) $f(Re/Re_T)$ for different drop diameters

b) Curve fit for d_d = 5 mm drop

Figure I.2: $f(Re/Re_T)$ for different drop diameters.

The curves of Figure I.2(a) can be described by fourth order polynomials, but this would make integration difficult and therefore the range is divided into three intervals ($0 < Re/Re_T < 0.4$, $0.4 < Re/Re_T < 0.75$, $0.75 < Re/Re_T < 1$) that can be described by second order polynomials (Figure I.2b).

Equation (I.3) can now be integrated by making the following substitution

$$z = \frac{Re}{Re_T} \tag{I.7}$$

The integral of Equation (I.3) can be expressed in the following form

$$\int_{t_i}^{t} \partial t = Re_T \int_{z_i}^{z} \frac{\partial z}{a_\alpha z^2 + a_\beta z + a_\gamma} \tag{I.8}$$

and the square below the line on the right hand side of Equation (I.8) is completed to give the integral equation in the following form.

$$\int_{t_i}^{t} \partial t = \frac{Re_T}{a_\alpha} \int_{z_i}^{z} \frac{\partial z}{\left(z + \frac{a_\beta}{2a_\alpha}\right)^2 + \left[\frac{a_\gamma}{a_\alpha} - \left(\frac{a_\beta}{2a_\alpha}\right)^2\right]} \tag{I.9}$$

The integral for Equation (I.9) can now be determined according to the following relation as given by Stewart (1999)

$$\int \frac{\partial u}{a^2 + u^2} = \frac{1}{a} tan^{-1} \frac{u}{a} + C \tag{I.10}$$

and the following equation is obtained after integration

$$t - t_i = \frac{2Re_T}{\varphi} \left[tan^{-1}\left(\frac{2a_\alpha z + a_\beta}{\varphi}\right) - tan^{-1}\left(\frac{2a_\alpha z_i + a_\beta}{\varphi}\right)\right] \tag{I.11a}$$

where

$$\varphi = \left(4a_\gamma a_\alpha - a_\beta{}^2\right)^{\frac{1}{2}} \tag{I.11b}$$

Equation (I.12) shows the times at z = 0.4 and z = 0.75 as determined by Equation (I.11) if it is assumed that a drop starts from rest (z_i = 0, t_i = 0).

$$t_{z=0.4} = \frac{2Re_T}{\phi_1} \left[tan^{-1}\left(\frac{0.8a_{\alpha 1} + a_{\beta 1}}{\phi_1}\right) - tan^{-1}\left(\frac{a_{\beta 1}}{\phi_1}\right)\right] \tag{I.12a}$$

$$t_{z=0.75} = \frac{2Re_T}{\varphi_2} \left[tan^{-1}\left(\frac{1.5a_{\alpha 2} + b_{\beta 2}}{\varphi_2}\right) - tan^{-1}\left(\frac{0.8a_{\alpha 2} + a_{\beta 2}}{\varphi_2}\right)\right] + t_{z=0.4} \tag{I.12b}$$

The velocity of the drop can be obtained by manipulation of Equation (I.11) and back substitution of z to yield the following relation for drop velocity as a function of time

$$v_d(t) = \frac{\mu_{av} Re_T}{2a_\alpha \rho_{av} d_d} \left[\varphi tan\left\{\frac{\varphi}{2Re_T}(t - t_i) + tan^{-1}\left(\frac{2a_\alpha z_i + a_\beta}{\varphi}\right)\right\} - a_\beta\right] - v_a \tag{I.13}$$

From Equation (I.13) the drop velocity for the three intervals (denoted with subscripts: 1, 2 and 3) of z can be determined in the following manner ($z_i = 0$, $t_i = 0$).

$$v_d(t) = \frac{\mu_{av} Re_T}{2a_{\alpha 1}\rho_{av} d_d}\left[\varphi_1 tan\left\{\frac{\varphi_1}{2Re_T}t + tan^{-1}\left(\frac{a_{\beta 1}}{\varphi_1}\right)\right\} - a_{\beta 1}\right] - v_a \qquad \text{(I.14a)}$$

$$for \quad 0 < z < 0.4$$

$$v_d(t) = \frac{\mu_{av} Re_T}{2a_{\alpha 2}\rho_{av} d_d}\left[\varphi_2 tan\left\{\frac{\varphi_2}{2Re_T}(t - t_{z=0.4}) + tan^{-1}\left(\frac{0.8a_{\alpha 2} + a_{\beta 2}}{\varphi_2}\right)\right\} - a_{\beta 2}\right] - v_a \qquad \text{(I.14b)}$$

$$for \quad 0.4 < z < 0.75$$

$$v_d(t) = \frac{\mu_{av} Re_T}{2a_{\alpha 3}\rho_{av} d_d}\left[\varphi_3 tan\left\{\frac{\varphi_3}{2Re_T}(t - t_{z=0.75}) + tan^{-1}\left(\frac{1.5a_{\alpha 3} + a_{\beta 3}}{\varphi_3}\right)\right\} - a_{\beta 3}\right] - v_a \qquad \text{(I.14c)}$$

$$for \quad 0.75 < z < 1$$

I.3 Analytical solution for drop trajectory

The path length of the drop can be obtained by integrating the velocity equation with respect to time

$$\int_{s_i}^{s} \partial s = \int_{t_i}^{t} v_d(t)\,\partial t \qquad \text{(I.15)}$$

where the right hand side integral can be expressed by

$$\int_{t_i}^{t} v_d(t)\,\partial t = \frac{\mu_{av} Re_T}{2a_\alpha \rho_{av} d_d}\left[\int_{t_i}^{t} \varphi tan\left\{\frac{\varphi}{2Re_T}(t - t_i) + tan^{-1}\left(\frac{2a_\alpha z_i + a_\beta}{\varphi}\right)\right\}\partial t - \int_{t_i}^{t} a_\beta \partial t\right] - \int_{t_i}^{t} v_a \partial t \qquad \text{(I.16)}$$

The first integral term on the right in Equation (I.16) can be simplified by doing the following substitution

$$u = \frac{\varphi}{2Re_T}(t - t_i) + tan^{-1}\left(\frac{2a_\alpha z_i + a_\beta}{\varphi}\right) \qquad \text{(I.17)}$$

The derivative of u yields the following

$$\partial u = \frac{\varphi}{2Re_T}\partial t \tag{I.18}$$

and therefore

$$\int_{t_i}^{t} \varphi tan\left[\frac{\varphi}{2Re_T}(t - t_i) + tan^{-1}\left(\frac{2a_\alpha z_i + a_\beta}{\varphi}\right)\right]\partial t = 2Re_T \int_{u_i}^{u} \tan u \, \partial u \tag{I.19}$$

The equation on the right can be integrated by noting that

$$2Re_T \int_{u_i}^{u} \tan u \, \partial u = 2Re_T \int_{u_i}^{u} \frac{\sin u}{\cos u}\partial u \tag{I.20}$$

and doing the substitution

$$a = \cos u \tag{I.21}$$

The derivative of Equation (I.21) yields the following

$$\partial a = -\sin u \, \partial u \tag{I.22}$$

and by substituting Equation (I.21) and (I.22) back into Equation (I.20) the following can be obtained

$$2Re_T \int_{u_i}^{u} \frac{\sin u}{\cos u}\partial u = -2Re_T \int_{a_i}^{a} \frac{\partial a}{a} = -2Re_T \, ln(a)\Big|_{a_i}^{a} = -2\,Re_T ln(\cos u)\Big|_{u_i}^{u} \tag{I.23}$$

After back substitution of u and integration of the other terms in Equation (I.16) the following equation for path length of a falling drop is obtained

$$s_d(t) = -\frac{\mu_{av} Re_T}{2a_\alpha \rho_{av} d_d}\left[2Re_T \, ln\left[\frac{cos\left\{\frac{\varphi}{2Re_T}(t - t_i) + tan^{-1}\left(\frac{2a_\alpha z_i + a_\beta}{\varphi}\right)\right\}}{cos\left\{tan^{-1}\left(\frac{2a_\alpha z_i + a_\beta}{\varphi}\right)\right\}}\right] + a_\beta(t - t_i)\right] - v_a(t - t_i) + s_i \tag{I.24}$$

From Equation (I.24) the drop trajectory for the three intervals (denoted with subscripts: 1, 2 and 3) of z can now be determined in the following manner ($z_i = 0$, $t_i = 0$, $s_i = 0$)

$$s_d(t) = -\frac{\mu_{av} Re_T}{2a_{\alpha 1}\rho_{av} d_d}\left(2Re_T\ ln\left[\frac{cos\left\{\frac{\varphi_1}{2Re_T}t + tan^{-1}\left(\frac{a_{\beta 1}}{\varphi_1}\right)\right\}}{cos\left\{tan^{-1}\left(\frac{a_{\beta 1}}{\varphi_1}\right)\right\}}\right] + a_{\beta 1}t\right) - v_a t \tag{I.25a}$$

$for\ 0 < z < 0.4$

$$s_d(t) = -\frac{\mu_{av} Re_T}{2a_{\alpha 2}\rho_{av} d_d}\left(2Re_T\ ln\left[\frac{cos\left\{\frac{\varphi_2}{2Re_T}(t - t_{z=0.4}) + tan^{-1}\left(\frac{0.8a_{\alpha 2} + a_{\beta 2}}{\phi_2}\right)\right\}}{cos\left\{tan^{-1}\left(\frac{0.8a_{\alpha 2} + a_{\beta 2}}{\varphi_2}\right)\right\}}\right] + a_{\beta 2}(t - t_{z=0.4})\right) - v_a(t - t_{z=0.4}) + s_{d,z=0.4} \tag{I.25b}$$

$for\ 0.4 < z < 0.75$

$$s_d(t) = -\frac{\mu_{av} Re_T}{2a_{\alpha 3}\rho_{av} d_d}\left(2Re_T\ ln\left[\frac{cos\left\{\frac{\varphi_3}{2Re_T}(t - t_{z=0.75}) + tan^{-1}\left(\frac{1.5a_{\alpha 3} + a_{\beta 3}}{\varphi_3}\right)\right\}}{cos\left\{tan^{-1}\left(\frac{1.5a_{\alpha 3} + a_{\beta 3}}{\varphi_3}\right)\right\}}\right] + a_{\beta 3}(t - t_{z=0.75})\right) - v_a(t - t_{z=0.75}) + s_{d,z=0.75} \tag{I.25c}$$

$for\ 0.75 < z < 1$

The coefficients used in the above Equations (I.13) and (I.24) are listed in Table I.1 where d_d is in mm.

Table I.1: *a*-Coefficients for Equations (I.13) and (I.24).

Coefficient	Interval 1 $0 \le Re/Re_T < 0.4$	Interval 2 $0.4 \le Re/Re_T < 0.75$	Interval 3 $0.75 \le Re/Re_T < 1$
a_α	$\gamma \cdot (0.0008d_d^3 - 0.01062d_d^2 - 0.03273d_d + 0.90347)$	$\gamma \cdot (-0.01292d_d^2 + 0.26246d_d + 0.33407)$	$\gamma \cdot (-0.03493d_d^2 + 0.98159d_d - 0.25258)$

Coefficient	Interval 1 $0 \leq Re/Re_T < 0.4$	Interval 2 $0.4 \leq Re/Re_T < 0.75$	Interval 3 $0.75 \leq Re/Re_T < 1$
a_β	$\gamma \cdot (-0.11679 \ln(d_d) + 0.25530)$	$\gamma \cdot (0.01618 d_d^2 - 0.36115 d_d + 0.76871)$	$\gamma \cdot (0.04952 d_d^2 - 1.45015 d_d + 1.65403)$
a_γ	$\gamma \cdot (0.00174 \ln(d_d) - 0.00333) + \alpha$	$\gamma \cdot (0.03330 d_d - 0.03469) + \alpha$	$\gamma \cdot (-0.01457 d_d^2 + 0.46780 d_d - 0.40086) + \alpha$
γ	$-\beta Re_T^2 C_{D,T} E_T^{-2/3}$	$-\beta Re_T^2 C_{D,T} E_T^{-2/3}$	$-\beta Re_T^2 C_{D,T} E_T^{-2/3}$

I.4 Comparison between analytical and numerical results

Figure I.3 shows a comparison between the velocity and trajectory results obtained with a numerical model and the results obtained with Equations (I.13) and (I.24) for drops of different diameters, falling in still air.

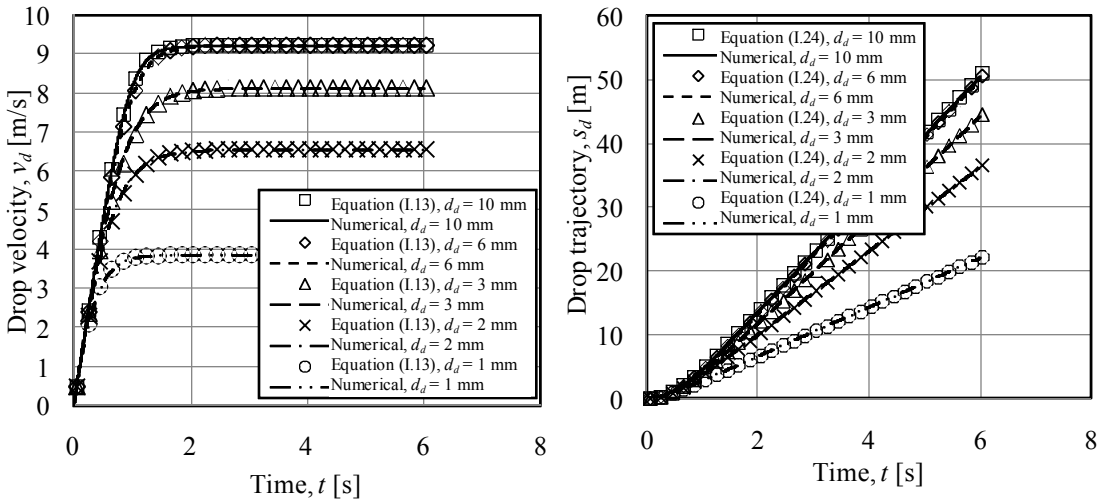

a) Velocity of drops in still air

b) Trajectory of drops in still air

Figure I.3: Comparison between analytical Equations (I.13) and (I.24) and numerical results.

J

ANALYTICAL SOLUTION FOR DROP TEMPERATURE CHANGE

J.1 Introduction

In this appendix an analytical equation for determining the drop temperature is derived and the results compared to numerical results obtained with an Eulerian model.

J.2 Analytical solution for drop temperature

The control volume of the drop is shown in Figure J.1

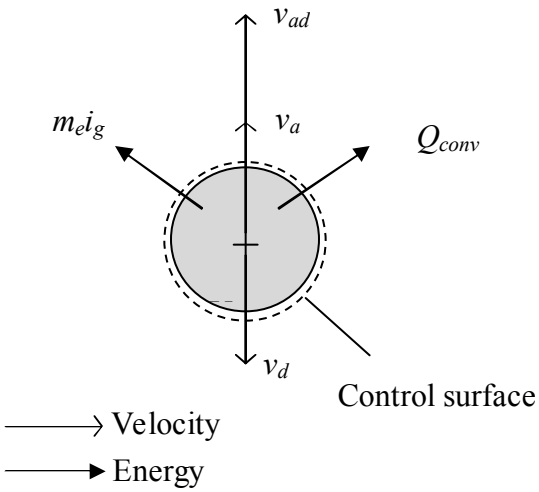

Figure J.1: Control volume for a cooling drop.

From the first law of thermodynamics the following equation for the rate at which the internal energy of the drop changes can be obtained.

$$\frac{\partial U}{\partial t} = -Q_{conv} - m_e i_g \qquad \text{(C.26)}$$

The rate of internal energy change can also be expressed in terms of drop temperature by

$$\frac{\partial U}{\partial t} = \frac{\partial (M_d c_v T_d)}{\partial t} = M_d T_d \frac{\partial c_v}{\partial t} + M_d c_v \frac{\partial T_d}{\partial t} + c_v T_d \frac{\partial M_d}{\partial t} \tag{C.27}$$

The following equation can now be obtained by assuming $\partial c_v/\partial t \approx 0$ and that $c_p \approx c_v$ for water.

$$\frac{\partial U}{\partial t} = M_d c_p \frac{\partial T_d}{\partial t} + c_p T_d \frac{\partial M_d}{\partial t} \tag{J.1}$$

By equating Equations (C.26) and (C.27) and realising that $m_e = -\partial M_d/\partial t$ the following equation for the rate of temperature change of a falling drop can be obtained.

$$\frac{\partial T_d}{\partial t} = \frac{-m_e i_{fgw} - Q_{conv}}{M_d c_{pw}} \tag{J.2}$$

The convection heat transfer rate is given by

$$Q_{conv} = h_c A_s (T_d - T_\infty) \tag{J.3}$$

The heat transfer coefficient h_c can be obtained from the definition of Nusselt number (Equation J.4) and the correlation (Equation 2.40) of Ranz and Marshall (1952).

$$Nu_d = \frac{h_c d_d}{k_{av}} \tag{J.4}$$

$$Nu_d = 2 + 0.6 Re^{\frac{1}{2}} Pr^{\frac{1}{3}} \qquad for \qquad 2 \leq Re \leq 800 \tag{2.40}$$

The evaporation rate can be obtained from equation (J.5) or (J.6).

$$m_e = h_D A_S (\rho_{vsw} - \rho_{v\infty}) \tag{J.5}$$

$$m_e = h_d A_S (\omega_{sw} - \omega_\infty) \tag{J.6}$$

The mass transfer coefficient h_D can be obtained from the definition of Sherwood number (Equation J.7) and the correlation (Equation 2.40) of Ranz and Marshall (1952).

$$Sh_d = \frac{h_D d_d}{D_{AB}} \tag{J.7}$$

$$Sh_d = 2 + 0.6 Re^{\frac{1}{2}} Sc^{\frac{1}{3}} \qquad for \qquad 2 \leq Re \leq 800 \tag{2.40}$$

By combining Equations (J.2), (J.3) and (J.5) the following equation for drop temperature can be obtained.

$$M_d \frac{\partial T_d}{\partial t} = -A_s \left[\frac{h_D i_{fgw}}{c_{pw}} (\rho_{vsw} - \rho_{v\alpha}) + \frac{h_c}{c_{pw}} (T_d - T_\infty) \right] \tag{J.8}$$

By dividing right through with h_D and rearranging the following equation can be obtained if it is assumed that the Nusselt and Sherwood numbers are approximately equal

$$h_D \partial t = - \frac{M_d \partial T_d}{A_s \left[\frac{i_{fgw}}{c_{pw}} (\rho_{vsw} - \rho_{v\infty}) + L_v (T_d - T_\infty) \right]} \tag{J.9}$$

where

$$L_v = \frac{h_c}{h_D c_{pw}} \approx \frac{k_{av}}{D_{AB} c_{pw}} \tag{J.10}$$

The diffusion coefficient for binary mixtures can be determined by Fuller and Giddings (1965)

$$D_{AB} = \frac{10^{-3} T^{1.75} [(M_a + M_v)/M_a M_v]^{1/2}}{P \left[(\sum v)_a{}^{1/3} + (\sum v)_v{}^{1/3} \right]^2} \tag{J.11}$$

where T is in Kelvin, P is in atmospheres and D_{AB} is in cm^2/s. The molecular weights M_a and M_v for air and water vapour are respectively 28.850 g/mol and 18.015g/mol. The diffusion volumes $(\sum v)_a$ and $(\sum v)_v$ for air and water vapour are respectively 19.7 and 13.1.

In order to solve the left-hand side of Equation (J.9) the h_D must be expressed as a function of time as given by

$$\int_{t_i}^{t} h_D \partial t = \int_{t_i}^{t} \frac{D_{AB} Sh_d}{d_d} \partial t = \int_{t_i}^{t} \left(\frac{D_{AB}}{d_d} \right) \left[2 + 0.6 Re(t)^{\frac{1}{2}} Sc^{\frac{1}{3}} \right] \partial t \tag{J.12}$$

It is assumed that the diffusion coefficient, drop diameter and Schmidt number are weak functions of time and are determined at the initial film temperature between the drop and the air. The integral of Equation (J.12) can now be given by

$$\int_{t_i}^{t} \left(\frac{D_{AB}}{d_d} \right) \left[2 + 0.6 Re(t)^{\frac{1}{2}} Sc^{\frac{1}{3}} \right] \partial t = \left(\frac{D_{AB}}{d_d} \right) \left[2(t - t_i) + 0.6 Sc^{\frac{1}{3}} \int_{t_i}^{t} Re(t)^{\frac{1}{2}} \partial t \right] \tag{J.13}$$

In order to simplify integration on the right-hand side of Equation (J.13) a three interval linear approximation is made so that

$$Re(t)^{\frac{1}{2}} \approx Re_T^{\frac{1}{2}} f\left[\frac{Re}{Re_T}(t)\right] = Re_T^{\frac{1}{2}}\left[h_\alpha z(t) + h_\beta\right] \tag{J.14a}$$

where from Appendix I

$$z(t) = \frac{1}{2a_\alpha}\left[\varphi tan\left\{\frac{\varphi}{2Re_T}(t - t_i) + tan^{-1}\left(\frac{2a_\alpha z_i + a_\beta}{\varphi}\right)\right\} - a_\beta\right] \tag{J.14b}$$

with

$$\varphi = \left(4a_\gamma a_\alpha - a_\beta{}^2\right)^{\frac{1}{2}} \tag{I.11b}$$

in order to express the following integral.

$$\int_{t_i}^{t} Re(t)^{\frac{1}{2}}\,\partial t \approx Re_T^{\frac{1}{2}}\left[\frac{h_\alpha}{2a_\alpha}\int_{t_i}^{t}\varphi\tan\left\{\frac{\varphi}{2Re_T}(t - t_i) + tan^{-1}\left(\frac{2a_\alpha z_i + a_\beta}{\varphi}\right)\right\}\partial t + \left(h_\beta - \frac{h_\alpha a_\beta}{2a_\alpha}\right)\int_{t_i}^{t}\partial t\right] \tag{J.15}$$

To solve the first term in the right-hand side of Equation (J.15) the following substitution can be made

$$u = \frac{\varphi}{2Re_T}(t - t_i) + tan^{-1}\left(\frac{2a_\alpha z_i + a_\beta}{\varphi}\right) \tag{J.16}$$

with its time derivative given by

$$\frac{\partial u}{\partial t} = \frac{\varphi}{2Re_T} \tag{J.17}$$

to yield

$$\int_{t_i}^{t} Re(t)^{\frac{1}{2}}\partial t \approx Re_T^{\frac{1}{2}}\left[\frac{h_\alpha Re_T}{a_\alpha}\int_{u_i}^{u}\frac{\sin u}{\cos u}\partial u + \left(h_\beta - \frac{h_\alpha a_\beta}{2a_\alpha}\right)\int_{t_i}^{t}\partial t\right] \tag{J.18}$$

By making the following substitution

$$w = \cos u \tag{J.19}$$

and

$$\frac{\partial w}{\partial u} = -\sin u \tag{J.20}$$

Equation (J.18) can be solved to yield the following equation.

$$\int_{t_i}^{t} Re(t)^{\frac{1}{2}}\,\partial t = -Re_T^{\frac{1}{2}}\left(\frac{h_\alpha Re_T}{a_\alpha} ln\left[\frac{\cos\left\{\frac{\varphi}{2Re_T}(t-t_i)+\tan^{-1}\left(\frac{2a_\alpha z_i + a_\beta}{\varphi}\right)\right\}}{\cos\left[\tan^{-1}\left(\frac{2a_\alpha z_i + a_\beta}{\varphi}\right)\right]}\right] + \left(\frac{h_\alpha a_\beta}{2a_\alpha} - h_\beta\right)(t-t_i)\right) \tag{J.21}$$

The integral in the right-hand side of Equation (J.13) is now obtained.

In order to determine the integral on the right hand side of Equation (J.9) a simplified second order polynomial is needed to approximate the saturated water vapour density. Equation (A.9) gives the saturated vapour density as a function of temperature, but this equation would make integration difficult due to its order and a simplified second order equation applicable to a smaller temperature range is therefore used to calculate the saturated vapour density at the drop surface and is given by

$$\rho_{vs} = 3.7435604 \cdot 10^{-5}T^2 - 2.0915734136 \cdot 10^{-2}T + 2.930789793493$$
$$285.15 \leq T \leq 323.15 \tag{J.22}$$

The deviation percentages between Equations (A.9) and (J.22) are shown in Figure J.2.

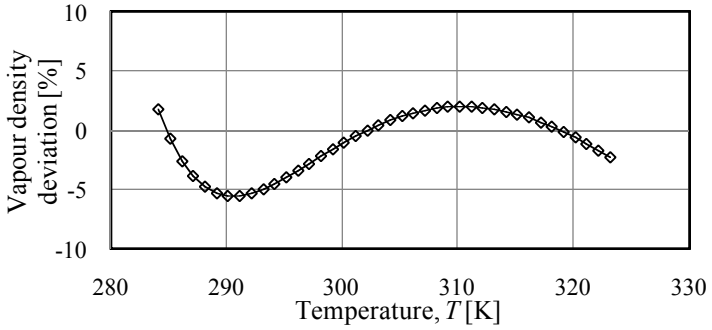

Figure J.2: Deviation between Equations (A.9) and (J.22).

By using Equation (J.22) the integral for the right-hand side of Equation (J.9) can be expressed by

$$-\int_{T_{d,i}}^{T_d} \frac{M_d \partial T_d}{A_s\left[\frac{i_{fgw}}{c_{pw}}(\rho_{vsw} - \rho_{v\infty}) + L_v(T_d - T_\infty)\right]} = -\int_{T_{d,i}}^{T_d} \frac{\partial T_d}{c_\alpha {T_d}^2 + c_\beta T_d + c_\gamma} \tag{J.23}$$

where

$$c_\alpha = 3.7435604 \cdot 10^{-5} \frac{i_{fgw} A_s}{M_d c_{pw}} \tag{J.24}$$

$$c_\beta = -\frac{A_s}{M_d}\left(2.0915734136 \cdot 10^{-2} \frac{i_{fgw}}{c_{pw}} - L_v\right) \tag{J.25}$$

$$c_\gamma = \frac{A_s}{M_d}\left[\frac{i_{fgw}}{c_{pw}}(2.930789793493 - \rho_{v\infty}) - L_v T_\infty\right] \tag{J.26}$$

By completing the square below the line, the right-hand side of Equation (J.23) can be expressed by

$$-\int_{T_{d,i}}^{T_d} \frac{\partial T_d}{c_\alpha {T_d}^2 + c_\beta T_d + c_\gamma} = -\frac{1}{c_\alpha}\int_{T_{d,i}}^{T_d} \frac{\partial T_d}{\left(T + \frac{c_\beta}{2c_\alpha}\right)^2 + \left[\frac{c_\gamma}{c_\alpha} - \left(\frac{c_\beta}{2c_\alpha}\right)^2\right]} \tag{J.27}$$

The integral can be obtained from the relation (Equation I.10) by Stewart (1999) to yield the following

$$\frac{1}{c_\alpha}\int_{T_{d,i}}^{T_d} \frac{\partial T_d}{\left(T_d + \frac{c_\beta}{2c_\alpha}\right)^2 + \left[\frac{c_\gamma}{c_\alpha} - \left(\frac{c_\beta}{2c_\alpha}\right)^2\right]} = \frac{2}{\psi}\left[\tan^{-1}\left(\frac{2c_\alpha T_d + c_\beta}{\psi}\right) - \tan^{-1}\left(\frac{2c_\alpha T_{d,i} + c_\beta}{\psi}\right)\right] \tag{J.28}$$

where

$$\psi = \left(4c_\alpha c_\gamma - {c_\beta}^2\right)^{\frac{1}{2}} \tag{J.29}$$

The equation for the temperature of a falling drop can be obtained by combining Equations (J.9) (J.13) (J.21) (J.23) and (J.28) and is given by

$$T_d(t) = \frac{1}{2c_\alpha}\left[\psi \tan\left\{-\frac{\psi}{2}k_5 + \tan^{-1}\left(\frac{2c_\alpha T_{d,i} + c_\beta}{\psi}\right)\right\} - c_\beta\right] \tag{J.30}$$

where

$$k_1 = \frac{\varphi}{2Re_T} \tag{J.31}$$

$$k_2 = \tan^{-1}\left(\frac{2a_\alpha z_i + a_\beta}{\varphi}\right) \tag{J.32}$$

$$k_3 = k_1(t - t_i) + k_2 \tag{J.33}$$

$$k_4 = \frac{h_\alpha a_\beta}{2a_\alpha} - h_\beta \tag{J.34}$$

$$k_5 = \frac{D_{AB}}{d_d}\left[2(t - t_i) - 0.6Sc^{\frac{1}{3}}Re_T^{\frac{1}{2}}\left\{\frac{h_\alpha Re_T}{a_\alpha} ln\left(\frac{\cos k_3}{\cos k_2}\right) + k_4(t - t_i)\right\}\right] \tag{J.35}$$

The a-coefficients for the three different intervals of z in Equation (J.30) are presented in Table I.1 with the h-coefficients presented in Table J.1.

Table J.1: h-Coefficients for Equation (J.30).

Coefficient	Interval 1 $0 \leq z \leq 0.4$	Interval 2 $0.4 \leq z < 0.75$	Interval 3 $0.75 \leq z < 1$
h_α	1.10383	0.66114	0.53381
h_β	0.19051	0.37518	0.46754

Equation (J.30) is compared to a numerical model and the results presented in Figure J.3. The curves are determined at P_{atm} = 101325, $T_{d,i}$ = 323 K, T_a = 298 K, T_{wb} = 295.76 K , z_i = 0 and still air.

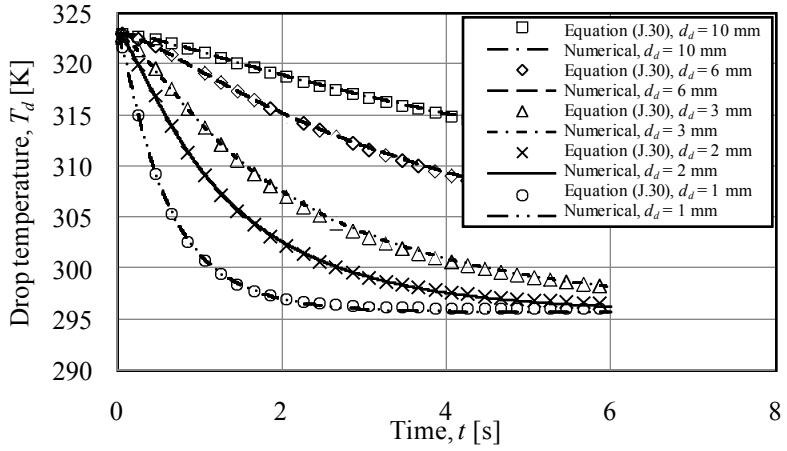

Figure J.3: Comparison between Equation (J.30) and a numerical model.

K

CROSS FLOW RAIN ZONE PERFORMANCE TESTS

K.1 Introduction

The measured performance results for a cross flow rain zone with and without installed splash grids are presented in this appendix. The results are presented in terms of the measured inlet and outlet air- and water temperatures for different combinations of air- and water mass velocities, as well as the Merkel numbers for each case determined according to the Merkel, Poppe and *e*-NTU methods respectively.

K.2 Description of experimental equipment

Figure K.1 shows the layout of the cross flow rain zone test facility. Air is drawn, with a centrifugal fan, through a rounded inlet of 4 m^2 (2 m x 2 m) before passing through the cross flow test section, a drift eliminator, mixers, a screen and flow measurement nozzles. Wet- and dry bulb air temperatures are measured at various heights before and after the cross flow test section and the air flow rate through the test facility is determined by measuring the pressure difference over three flow measurement nozzles. Water is pumped from an underground reservoir to the cross flow spray frame where water is distributed evenly over a 3.1 m^2 (2 m x 1.55 m) area in the form of drops of various sizes with a Sauter mean drop diameter that ranges from d_{32} = 3.7 mm to d_{32} = 4.2 mm for water mass velocities between G_w = 1.40 kg/m^2s and G_w = 4.20 kg/m^2s (Section H.3). These drops pass through the test section, as they accelerate under gravity, and are collected in the pond below the test section from where the water is pumped back to the underground reservoir. The water flow rate is measured by means of an electromagnetic flow meter and as a control measurement the flow rate is also determined by measuring the pressure difference over an orifice plate. The inlet water temperature is measured by means of three T-type thermocouples located on the spray frame manifold below the water filter and the outlet water temperature is measured above the pond and a control measurement is done in the pond. The pond temperature is measured by means of three floating T-type thermocouples just below the water surface and the rain zone outlet temperature is measured by means of 8 T-type thermocouples that are located above the pond in specially designed pipe housings.

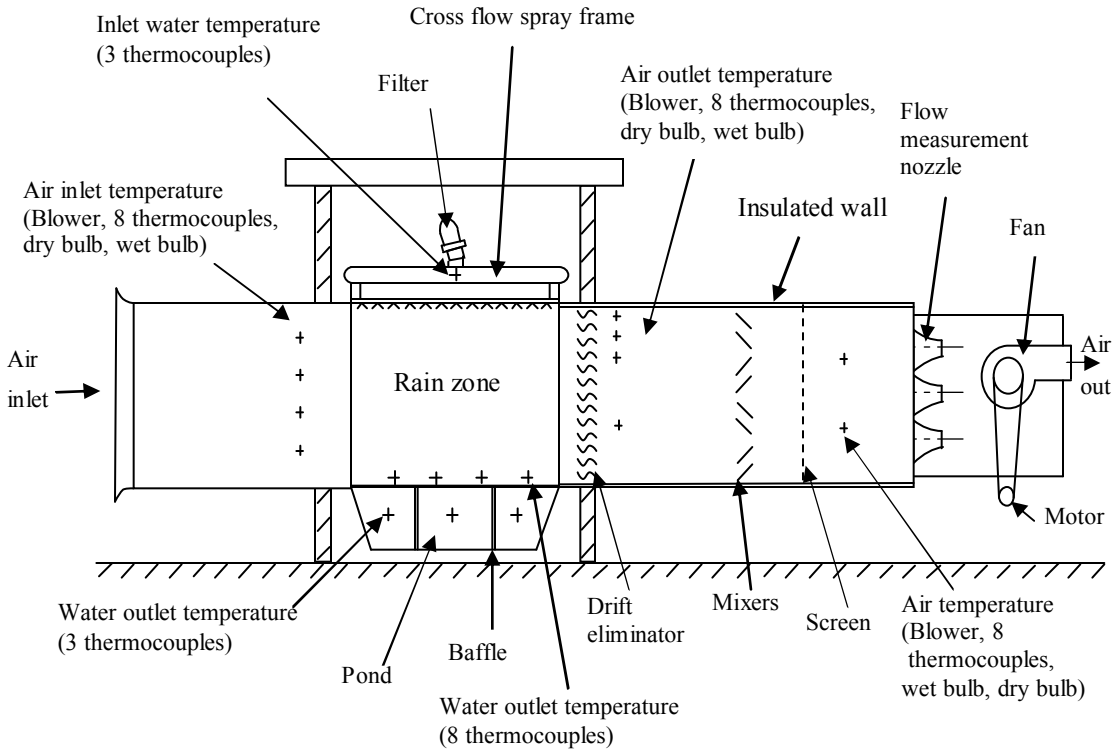

Figure K.1: Cross flow rain zone test facility (Not to scale).

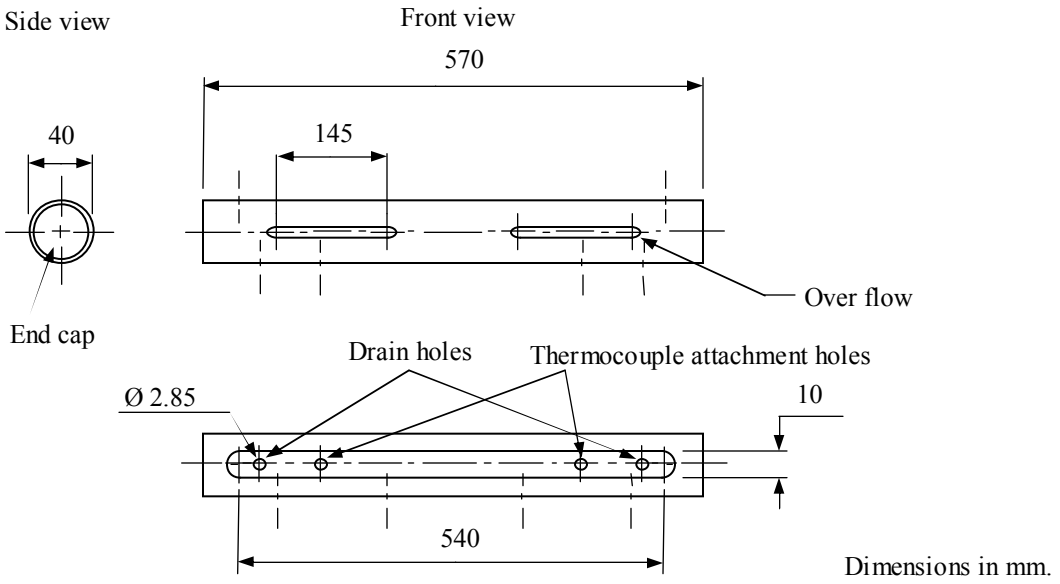

Figure K.2: Thermocouple pipe housing for cross flow water outlet temperature measurement.

The pipe housing, shown in Figure K.2, is positioned with the over flow openings in the down- stream air direction while the two thermocouples are fastened at the two attachment holes. Water from the rain zone enters the housing through an opening on top and the water can drain through the drain holes at low rain zone mass velocities or through the over flow openings at higher water mass velocities.

K.3 Measured cross flow rain zone performance results

The measured performance results for a cross flow rain zone with and without installed splash grids are presented in this section. For each rain zone setup the inlet and outlet water- and air temperatures (wet- and dry bulb) are measured for a combination of three water mass velocities ($G_w \approx 1.40$, 2.84 and 4.20 kg/m^{2}s) and four air mass velocities ($G_a \approx 1.22$, 1.71, 2.28 and 2.85 kg/m^{2}s). All measurements are carried out three times.

K.3.1 Pure rain zone

The measured performance results for a pure cross flow rain zone with no grids are presented in Tables K.1 to K.3.

Table K.1: Performance measurements for a pure cross flow rain zone (Test #1).

G_w [kg/m^{2}s]	G_a [kg/m^{2}s]	T_{ai} [° C]	T_{wbi} [° C]	T_{ao} [° C]	T_{wbo} [° C]	T_{wi} [° C]	T_{wo} [° C]	Me_M [m^{-1}]	Me_e [m^{-1}]	Me_P [m^{-1}]
1.404	1.209	13.697	11.187	17.315	17.498	48.525	43.864	0.0526	0.0531	0.0570
1.384	1.712	13.113	10.880	15.206	15.030	48.110	43.312	0.0548	0.0550	0.0593
1.375	2.294	13.668	11.102	14.483	13.911	47.755	42.673	0.0595	0.0597	0.0644
1.364	2.720	14.058	11.274	14.504	13.467	47.366	42.387	0.0593	0.0594	0.0641
2.846	1.186	13.512	11.164	21.774	21.860	47.080	42.881	0.0534	0.0550	0.0580
2.831	1.712	14.072	11.424	19.164	19.276	46.645	42.267	0.0562	0.0572	0.0609
2.826	2.294	13.817	11.341	17.433	17.409	46.326	41.624	0.0612	0.0620	0.0663
2.826	2.711	14.168	11.513	16.637	16.553	46.107	41.353	0.0625	0.0631	0.0676
4.183	1.199	14.035	11.607	23.761	23.710	45.673	42.435	0.0446	0.0464	0.0485
4.146	1.723	14.671	11.961	20.742	20.735	44.926	41.417	0.0500	0.0516	0.0541
4.127	2.227	15.441	12.461	19.323	19.373	44.315	40.737	0.0525	0.0538	0.0568
4.136	2.708	15.430	12.584	18.418	18.287	44.012	40.263	0.0560	0.0571	0.0605

Table K.2: Performance measurements for a pure cross flow rain zone (Test #2).

G_w [kg/m^{2}s]	G_a [kg/m^{2}s]	T_{ai} [° C]	T_{wbi} [° C]	T_{ao} [° C]	T_{wbo} [° C]	T_{wi} [° C]	T_{wo} [° C]	Me_M [m^{-1}]	Me_e [m^{-1}]	Me_P [m^{-1}]
1.384	1.251	16.236	13.208	18.244	17.402	43.471	40.050	0.0518	0.0524	0.0558
1.402	1.728	16.604	13.427	17.734	16.397	43.350	39.882	0.0526	0.0530	0.0566
1.394	2.324	16.883	13.624	17.428	15.665	43.192	39.418	0.0583	0.0586	0.0627
1.394	2.729	17.317	13.761	17.682	15.527	43.040	39.263	0.0588	0.0590	0.0633
2.817	1.240	17.544	13.694	21.636	21.316	42.890	39.620	0.0542	0.0560	0.0585
2.799	1.720	17.552	13.970	20.315	19.547	42.646	39.144	0.0585	0.0598	0.0631

G_w [kg/m^{2}s]	G_a [kg/m^{2}s]	T_{ai} [° C]	T_{wbi} [° C]	T_{ao} [° C]	T_{wbo} [° C]	T_{wi} [° C]	T_{wo} [° C]	Me_M [m^{-1}]	Me_e [m^{-1}]	Me_P [m^{-1}]
2.804	2.333	17.924	14.153	19.863	18.413	42.356	38.649	0.0628	0.0638	0.0677
2.807	2.711	17.929	14.193	19.497	17.846	42.071	38.410	0.0627	0.0635	0.0675
4.185	1.217	17.768	14.116	22.974	22.798	41.706	39.148	0.0463	0.0478	0.0500
4.169	1.696	18.473	14.460	21.824	21.224	41.439	38.650	0.0508	0.0528	0.0548
4.049	2.296	18.253	14.320	20.700	19.378	41.024	38.146	0.0526	0.0541	0.0567
4.033	2.700	18.445	14.241	20.561	18.670	40.841	37.769	0.0568	0.0581	0.0611

Table K.3: Performance measurementsfor a pure cross flow rain zone (Test #3).

G_w [kg/m^{2}s]	G_a [kg/m^{2}s]	T_{ai} [° C]	T_{wbi} [° C]	T_{ao} [° C]	T_{wbo} [° C]	T_{wi} [° C]	T_{wo} [° C]	Me_M [m^{-1}]	Me_e [m^{-1}]	Me_P [m^{-1}]
1.447	1.232	18.367	14.472	20.092	18.199	40.490	37.504	0.0558	0.0568	0.0600
1.412	1.689	18.486	14.282	19.260	16.707	40.283	37.294	0.0557	0.0562	0.0597
1.406	2.292	18.754	14.331	19.250	16.116	40.194	37.005	0.0598	0.0602	0.0641
1.399	2.696	19.443	14.468	19.696	15.937	40.065	36.864	0.0605	0.0608	0.0649
2.851	1.222	18.598	14.272	21.681	20.516	39.920	37.134	0.0562	0.0585	0.0606
2.835	1.663	18.908	14.339	21.149	19.200	39.672	36.733	0.0594	0.0611	0.0639
2.818	2.288	19.496	14.461	20.972	18.171	39.454	36.374	0.0626	0.0638	0.0671
2.787	2.707	20.398	14.707	21.425	17.711	39.158	36.039	0.0647	0.0657	0.0694
4.185	1.219	19.600	14.516	23.312	21.807	38.854	36.700	0.0471	0.0484	0.0507
4.190	1.709	20.674	14.776	22.968	20.377	38.744	36.371	0.0517	0.0537	0.0555
4.196	2.272	20.954	14.781	22.473	19.197	38.431	35.964	0.0540	0.0557	0.0580
4.180	2.690	21.287	14.949	22.465	18.686	38.316	35.677	0.0585	0.0600	0.0627

K.3.2 Rain zone with a single layer of slat grid

The measured performance results for a cross flow rain zone with one layer of horizontal slat grid (Figure H.3), installed H_{FG} = 0.645 m below the spray frame, are presented in Tables K.4 to K.6.

Table K.4: Performance measurements for a cross flow rain zone with one layer of horizontal slat grid (H_{FG} = 0.645 m, Test #1).

G_w [kg/m^{2}s]	G_a [kg/m^{2}s]	T_{ai} [° C]	T_{wbi} [° C]	T_{ao} [° C]	T_{wbo} [° C]	T_{wi} [° C]	T_{wo} [° C]	Me_M [m^{-1}]	Me_e [m^{-1}]	Me_P [m^{-1}]
1.404	1.244	14.368	13.040	22.427	22.362	49.231	42.075	0.0875	0.0882	0.0952
1.398	1.727	14.102	12.917	19.899	19.922	48.647	41.292	0.0920	0.0923	0.0998
1.393	2.274	13.964	12.927	18.503	18.542	48.245	40.569	0.0984	0.0984	0.1067
1.381	2.691	13.938	12.875	17.569	17.658	48.020	40.013	0.1046	0.1045	0.1133
2.824	1.181	14.101	12.934	27.029	26.934	47.579	41.732	0.0811	0.0836	0.0886
2.795	1.707	14.025	12.850	24.291	24.240	47.199	40.990	0.0857	0.0873	0.0932
2.781	2.267	14.013	12.850	22.107	22.164	46.666	39.991	0.0950	0.0961	0.1031
2.820	2.697	13.978	12.794	20.488	20.550	45.366	38.996	0.0960	0.0970	0.1040
4.165	1.206	14.084	12.844	28.110	28.158	44.125	39.819	0.0733	0.0761	0.0799
4.110	1.715	14.117	12.918	24.820	24.944	43.467	38.878	0.0785	0.0816	0.0852
4.090	2.272	14.080	12.851	22.728	22.896	43.062	37.953	0.0894	0.0919	0.0968
4.101	2.681	14.026	12.859	21.146	21.273	42.214	37.352	0.0873	0.0894	0.0944

Table K.5: Performance measurements for a cross flow rain zone with one layer of horizontal slat grid (H_{FG} = 0.645 m, Test #2).

G_w [kg/m^{2}s]	G_a [kg/m^{2}s]	T_{ai} [° C]	T_{wbi} [° C]	T_{ao} [° C]	T_{wbo} [° C]	T_{wi} [° C]	T_{wo} [° C]	Me_M [m^{-1}]	Me_e [m^{-1}]	Me_P [m^{-1}]
1.388	1.222	14.032	12.855	19.544	19.654	41.178	36.365	0.0902	0.0918	0.0972
1.384	1.673	13.920	12.844	18.002	18.129	41.056	35.981	0.0951	0.0961	0.1023
1.384	2.326	13.960	12.895	16.576	16.831	40.914	35.580	0.1005	0.1011	0.1081
1.380	2.714	13.858	12.766	15.817	16.003	40.603	35.132	0.1049	0.1053	0.1128
2.852	1.207	13.892	12.794	23.193	23.094	40.325	36.163	0.0869	0.0909	0.0940
2.835	1.712	14.012	12.799	21.218	21.306	40.026	35.563	0.0925	0.0953	0.0998
2.806	2.269	13.938	12.731	19.510	19.669	39.711	34.822	0.1030	0.1051	0.1109
2.794	2.706	13.878	12.770	18.418	18.586	39.236	34.508	0.1006	0.1022	0.1082
4.140	1.249	14.088	12.858	24.852	24.821	38.642	35.351	0.0776	0.0799	0.0840
4.152	1.707	14.045	12.822	22.413	22.464	38.314	34.749	0.0834	0.0869	0.0900
4.144	2.237	14.061	12.809	20.683	20.787	37.955	34.050	0.0926	0.0962	0.0998
4.133	2.693	14.062	12.792	19.481	19.652	37.606	33.721	0.0923	0.0951	0.0992

Table K.6: Performance measurements for a cross flow rain zone with one layer of horizontal slat grid (H_{FG} = 0.645 m, Test #3).

G_w [kg/m^{2}s]	G_a [kg/m^{2}s]	T_{ai} [° C]	T_{wbi} [° C]	T_{ao} [° C]	T_{wbo} [° C]	T_{wi} [° C]	T_{wo} [° C]	Me_M [m^{-1}]	Me_e [m^{-1}]	Me_P [m^{-1}]
1.393	1.199	13.932	12.867	18.446	18.570	37.068	33.279	0.0909	0.0929	0.0975
1.431	1.630	13.921	12.799	17.037	17.171	36.945	32.839	0.0989	0.1005	0.1061
1.425	2.289	13.968	12.841	16.016	16.195	36.864	32.473	0.1060	0.1070	0.1136
1.430	2.727	13.809	12.716	15.455	15.656	36.610	32.097	0.1104	0.1112	0.1182
2.742	1.283	13.761	12.728	21.223	21.217	36.602	33.118	0.0908	0.0948	0.0977
2.799	1.714	13.478	12.617	19.505	19.563	36.325	32.593	0.0973	0.1008	0.1045
2.792	2.295	13.501	12.650	18.337	18.441	36.150	32.107	0.1057	0.1084	0.1134
2.784	2.688	13.562	12.541	17.389	17.529	35.896	31.832	0.1065	0.1087	0.1142
4.147	1.211	13.767	12.690	23.382	23.397	35.423	32.744	0.0775	0.0794	0.0836
4.147	1.697	13.913	12.825	20.963	20.999	34.996	32.068	0.0850	0.0880	0.0914
4.186	2.262	13.866	12.761	19.606	19.669	34.964	31.672	0.0947	0.0989	0.1017
4.163	2.701	13.810	12.721	18.393	18.490	34.642	31.379	0.0938	0.0971	0.1005

K.3.3 Rain zone with two layers of slat grid

The measured performance results for a cross flow rain zone with two layers of horizontal slat grids (Figure H.3), installed below the spray frame (H_{FG} = 0.6 m, H_{GG} = 0.6 m), are presented in Tables K.7 to K.9.

Table K.7: Performance measurements for a cross flow rain zone with two layers of horizontal slat grids installed (H_{FG} = 0.6 m, H_{GG} = 0.6 m, Test #1).

G_w [kg/m^{2}s]	G_a [kg/m^{2}s]	T_{ai} [° C]	T_{wbi} [° C]	T_{ao} [° C]	T_{wbo} [° C]	T_{wi} [° C]	T_{wo} [° C]	Me_M [m^{-1}]	Me_e [m^{-1}]	Me_P [m^{-1}]
1.401	1.220	12.933	9.547	23.445	23.523	49.543	39.987	0.123	0.124	0.134
1.388	1.747	12.923	9.543	20.252	20.435	49.219	38.872	0.136	0.136	0.148
1.370	2.242	12.876	9.492	18.154	18.252	48.319	37.865	0.143	0.143	0.156

G_w [kg/m^{2}s]	G_a [kg/m^{2}s]	T_{ai} [° C]	T_{wbi} [° C]	T_{ao} [° C]	T_{wbo} [° C]	T_{wi} [° C]	T_{wo} [° C]	Me_M [m^{-1}]	Me_e [m^{-1}]	Me_P [m^{-1}]
1.434	2.775	12.746	9.334	16.902	17.016	47.762	37.355	0.145	0.145	0.158
2.843	1.239	12.885	9.523	28.716	28.806	46.999	39.579	0.113	0.116	0.123
2.819	1.724	12.801	9.528	25.467	25.532	46.403	38.319	0.125	0.127	0.136
2.826	2.282	12.711	9.528	22.383	22.588	46.074	37.573	0.132	0.133	0.144
2.804	2.749	12.638	9.550	20.402	20.552	45.921	37.199	0.135	0.136	0.147
4.211	1.197	12.688	9.633	30.226	30.260	44.716	39.153	0.097	0.100	0.107
4.171	1.717	12.640	9.581	27.513	27.605	44.144	37.803	0.111	0.116	0.122
4.171	2.284	12.666	9.577	24.250	24.497	43.482	36.601	0.124	0.128	0.135
4.128	2.714	12.719	9.588	22.216	22.480	42.770	36.027	0.123	0.126	0.133

Table K.8: Performance measurements for a cross flow rain zone with two layers of horizontal slat grids installed (H_{FG} = 0.6 m, H_{GG} = 0.6 m, Test #2).

G_w [kg/m^{2}s]	G_a [kg/m^{2}s]	T_{ai} [° C]	T_{wbi} [° C]	T_{ao} [° C]	T_{wbo} [° C]	T_{wi} [° C]	T_{wo} [° C]	Me_M [m^{-1}]	Me_e [m^{-1}]	Me_P [m^{-1}]
1.413	1.218	12.585	9.507	20.750	20.912	41.486	34.522	0.136	0.138	0.146
1.403	1.744	12.617	9.529	18.018	18.198	41.389	33.842	0.146	0.148	0.158
1.391	2.273	12.548	9.454	16.501	16.662	40.983	33.309	0.150	0.151	0.162
1.384	2.801	12.466	9.412	15.233	15.224	40.709	32.998	0.152	0.152	0.163
2.808	1.265	12.504	9.409	24.591	24.559	39.955	34.438	0.122	0.128	0.132
2.816	1.684	12.494	9.443	22.330	22.483	39.074	33.094	0.138	0.143	0.149
2.800	2.254	12.496	9.490	19.330	19.542	38.303	32.201	0.143	0.147	0.154
2.788	2.771	12.386	9.359	17.520	17.701	37.793	31.719	0.143	0.146	0.154
4.207	1.245	12.371	9.392	24.795	24.846	36.544	32.686	0.107	0.109	0.116
4.208	1.773	12.380	9.479	22.534	22.637	35.963	31.512	0.125	0.130	0.135
4.192	2.248	12.280	9.358	20.130	20.280	34.942	30.438	0.131	0.137	0.141
4.173	2.774	12.285	9.343	18.528	18.690	34.700	30.100	0.132	0.137	0.141

Table K.9: Performance measurements for a cross flow rain zone with two layers of horizontal slat grids installed (H_{FG} = 0.6 m, H_{GG} = 0.6 m, Test #3).

G_w [kg/m^{2}s]	G_a [kg/m^{2}s]	T_{ai} [° C]	T_{wbi} [° C]	T_{ao} [° C]	T_{wbo} [° C]	T_{wi} [° C]	T_{wo} [° C]	Me_M [m^{-1}]	Me_e [m^{-1}]	Me_P [m^{-1}]
1.407	1.216	12.234	9.302	17.474	17.477	33.354	28.779	0.140	0.144	0.150
1.397	1.716	12.182	9.277	15.601	15.703	33.020	28.035	0.154	0.157	0.165
1.397	2.330	12.096	9.238	14.147	14.216	33.002	27.823	0.158	0.160	0.169
1.388	2.813	12.122	9.299	13.509	13.500	32.928	27.627	0.162	0.163	0.173
2.824	1.207	12.122	9.258	20.648	20.626	32.898	29.046	0.131	0.135	0.141
2.796	1.731	12.196	9.319	18.703	18.748	32.640	28.284	0.147	0.154	0.158
2.813	2.332	11.985	9.234	16.335	16.485	32.244	27.872	0.145	0.150	0.155
2.790	2.792	12.025	9.242	15.359	15.488	31.973	27.473	0.150	0.154	0.160
4.169	1.233	11.935	9.221	21.310	21.393	31.290	28.529	0.105	0.106	0.113
4.151	1.729	12.023	9.216	19.573	19.590	30.338	27.142	0.128	0.131	0.137
4.142	2.331	12.132	9.171	17.545	17.607	29.822	26.420	0.136	0.141	0.145
4.139	2.793	12.083	9.112	16.474	16.610	29.505	26.078	0.136	0.143	0.145

K.3.4 Rain zone with two layers of commercial splash grid

The measured performance results for a cross flow rain zone with two layers of horizontal commercial splash grids (Figure H.6a), installed below the spray frame (H_{FG} = 0.6 m, H_{GG} = 0.6 m), are presented in Tables K.10 to K.12.

Table K.10: Performance measurements for a cross flow rain zone with two layers of horizontal commercial grids installed (H_{FG} = 0.6 m, H_{GG} = 0.6 m, Test #1).

G_w [kg/m^{2}s]	G_a [kg/m^{2}s]	T_{ai} [° C]	T_{wbi} [° C]	T_{ao} [° C]	T_{wbo} [° C]	T_{wi} [° C]	T_{wo} [° C]	Me_M [m^{-1}]	Me_e [m^{-1}]	Me_P [m^{-1}]
1.349	1.211	12.907	11.626	23.341	23.512	50.972	42.122	0.103	0.103	0.112
1.400	1.709	12.856	11.596	21.441	21.643	51.029	41.010	0.119	0.119	0.130
1.391	2.278	12.745	11.574	19.853	20.052	50.968	40.583	0.123	0.123	0.134
1.381	2.772	12.777	11.523	18.062	18.247	50.884	40.335	0.125	0.125	0.136
2.781	1.200	12.829	11.503	30.319	30.418	50.674	43.065	0.093	0.095	0.102
2.689	1.755	12.836	11.498	24.930	25.130	47.758	40.047	0.108	0.110	0.118
2.800	2.243	12.748	11.424	22.641	22.754	46.055	38.686	0.111	0.113	0.121
2.780	2.747	12.631	11.301	20.455	20.720	44.713	37.390	0.118	0.119	0.128
4.175	1.215	12.615	11.298	28.948	28.960	43.521	38.809	0.085	0.088	0.093
4.133	1.716	12.520	11.247	26.366	26.546	43.028	37.571	0.100	0.104	0.109
4.179	2.254	12.339	11.127	23.579	23.712	42.185	36.785	0.100	0.103	0.108
4.194	2.695	12.495	11.182	22.114	22.334	41.549	35.880	0.109	0.112	0.118

Table K.11: Performance measurements for a cross flow rain zone with two layers of horizontal commercial grids installed (H_{FG} = 0.6 m, H_{GG} = 0.6 m, Test #2).

G_w [kg/m^{2}s]	G_a [kg/m^{2}s]	T_{ai} [° C]	T_{wbi} [° C]	T_{ao} [° C]	T_{wbo} [° C]	T_{wi} [° C]	T_{wo} [° C]	Me_M [m^{-1}]	Me_e [m^{-1}]	Me_P [m^{-1}]
1.428	1.233	12.388	11.115	19.978	20.113	39.936	34.369	0.115	0.117	0.124
1.426	1.757	12.285	11.058	18.004	18.183	39.413	32.935	0.141	0.143	0.152
1.422	2.272	12.386	10.997	16.284	16.475	38.807	32.852	0.129	0.130	0.139
1.398	2.786	12.432	10.980	15.739	15.775	38.555	32.048	0.145	0.146	0.156
2.804	1.218	12.443	10.988	23.738	23.711	38.491	34.043	0.105	0.110	0.113
2.810	1.718	12.438	10.858	20.652	20.760	37.719	32.784	0.120	0.125	0.130
2.811	2.284	12.308	10.845	18.767	18.917	36.895	31.941	0.124	0.127	0.133
2.784	2.768	12.583	10.965	17.533	17.728	36.111	31.012	0.134	0.137	0.144
4.200	1.200	12.708	10.962	23.560	23.535	35.109	32.052	0.091	0.093	0.098
4.168	1.681	12.731	10.986	22.047	22.153	34.921	31.256	0.110	0.113	0.118
4.172	2.258	12.548	10.821	19.565	19.750	34.259	30.571	0.110	0.115	0.118
4.167	2.767	12.382	10.772	18.410	18.626	34.136	30.147	0.119	0.123	0.127

Table K.12: Performance measurements for a cross flow rain zone with two layers of horizontal commercial grids installed (H_{FG} = 0.6 m, H_{GG} = 0.6 m, Test #3).

G_w [kg/m^{2}s]	G_a [kg/m^{2}s]	T_{ai} [° C]	T_{wbi} [° C]	T_{ao} [° C]	T_{wbo} [° C]	T_{wi} [° C]	T_{wo} [° C]	Me_M [m^{-1}]	Me_e [m^{-1}]	Me_P [m^{-1}]
1.342	1.236	12.161	10.692	17.017	17.169	33.174	29.148	0.124	0.128	0.133
1.422	1.701	12.074	10.600	15.621	15.801	32.910	28.761	0.128	0.131	0.137
1.422	2.298	11.909	10.513	14.644	14.822	32.889	28.294	0.142	0.144	0.152

G_w [kg/m^{2}s]	G_a [kg/m^{2}s]	T_{ai} [° C]	T_{wbi} [° C]	T_{ao} [° C]	T_{wbo} [° C]	T_{wi} [° C]	T_{wo} [° C]	Me_M [m^{-1}]	Me_e [m^{-1}]	Me_P [m^{-1}]
1.420	2.797	12.323	10.657	14.004	14.103	32.403	28.010	0.139	0.140	0.148
2.829	1.211	12.205	10.688	20.098	20.008	32.311	29.100	0.112	0.116	0.121
2.824	1.718	12.070	10.642	18.381	18.517	32.173	28.444	0.130	0.136	0.139
2.806	2.302	11.936	10.558	16.881	17.063	31.981	28.307	0.123	0.127	0.132
2.788	2.786	12.140	10.644	16.036	16.245	31.871	27.855	0.137	0.140	0.146
4.152	1.229	12.118	10.602	21.723	21.638	31.668	29.204	0.090	0.092	0.097
4.137	1.695	12.081	10.580	19.985	20.129	31.290	28.400	0.107	0.110	0.115
4.141	2.287	12.378	10.708	17.962	18.114	30.687	27.692	0.113	0.117	0.121
4.123	2.781	11.988	10.499	16.826	16.979	30.383	27.251	0.118	0.123	0.126

K.4 Conclusions

The rain zone performance measurement results presented in Section K.3 show the installation of splash grids can significantly enhance rain zone performance.

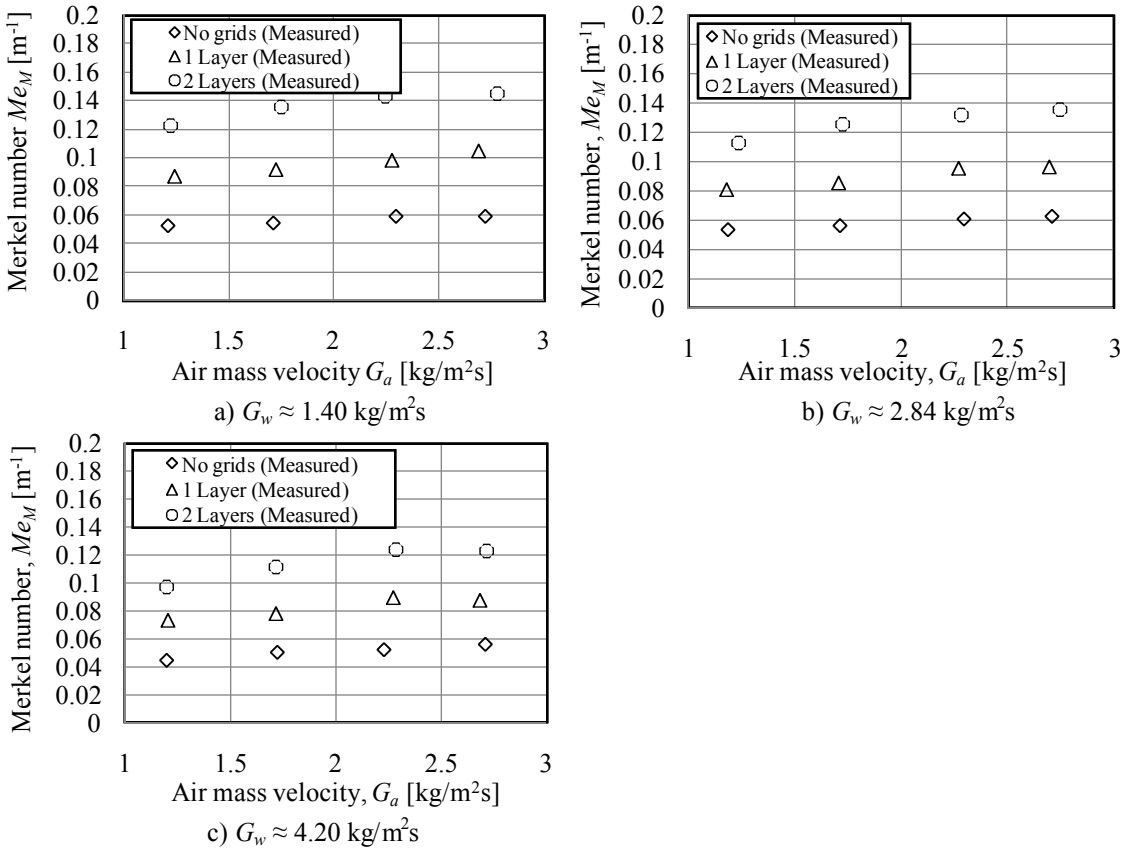

Figure K.3: Comparison between the Merkel transfer characteristics for a pure cross flow rain zone and a rain zone with one and two layers of horizontal slat grids (Section H.4) respectively.

Figure K.3 shows a comparison between the Merkel transfer characteristics (Merkel method), obtained from Sections K.3.1 to K.3.3 (Tests #1), for a pure cross flow rain zone and a rain zone with one and two layers of horizontal slat grid respectively.

Figure K.4 shows the measured Merkel transfer characteristics, obtained from Section K.3.4, for the cross flow rain zone when two layers of commercial grid are installed. When comparing Figures K.3 and K.4 it can be seen that the results are similar for two grid layers due to similar grid porosities of the two grid types.

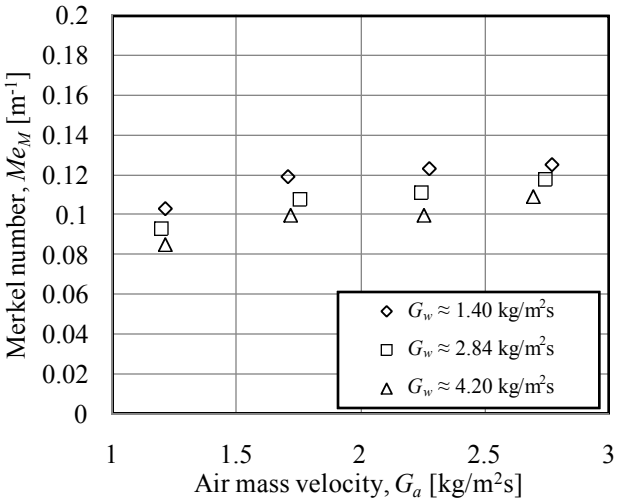

Figure K.4: Merkel transfer characteristics for a cross flow rain zone with two layers of commercial splash grid (Section H.5).

L

DROP SIZE MEASUREMENT UNCERTAINTY ANALYSIS

L.1 Introduction

In this appendix the measurement uncertainties associated with the high speed camera drop size measurement technique used in Appendices B and D and the drop size measurement technique used in Appendices G and H are investigated.

L.2 Measurement uncertainty

In the drop size measurement technique used in Appendices B and D the splash or straddled drops that are present in a certain volume above or below the slat after drop impingement are photographed in order to determine their size distributions. The measurement uncertainties associated with this technique are due to the resolution of the camera and the depth of field variation in the photographed volume.

Figure L.1 illustrates a simple example where the length of a line is measured by means of a photographic procedure where the line is photographed and the pixels comprising the line on the photograph are counted and multiplied by a calibration value. Each pixel presents an area of $2l$ x $2l$ and by counting the number of pixels the measured line length ($L_{measured}$) is determined while the actual line length (L_{actual}) is anywhere between L-l and L+l with equal probability.

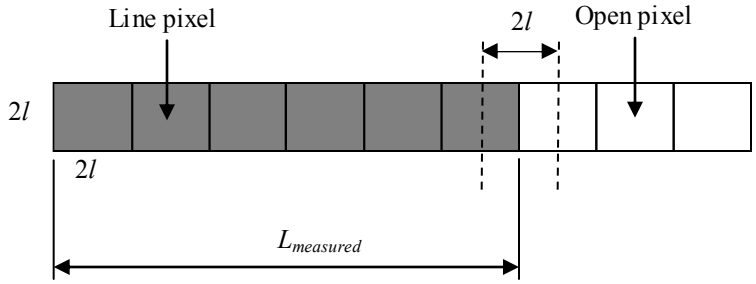

Figure L.1: Photographic line measurement illustration.

The basic model for the measurement error due to resolution is given by

$$\varepsilon_{res} = L_{measured} - L_{actual} \tag{L.1}$$

with a uniform error probability distribution as shown in Figure L.2.

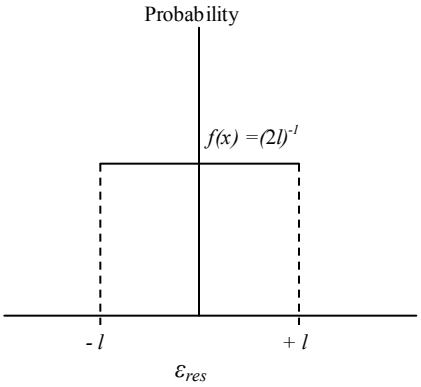

Figure L.2: Uniform probability distribution of measurement errors due to camera resolution.

The measurement error uncertainty with a 100 % containment probability is given by

$$u = l \tag{L.2}$$

The measurement uncertainty equals the error uncertainty and is given by Equation (L.3) for a camera resolution of $2l$ = 0.161 mm/pixel (Appendices B and D).

$$u_{res} = 0.081\ mm \tag{L.3}$$

Due to field depth variation all drop diameter measurements (d) are between $0.96d_d \leq d \leq 1.04d_d$ and a drop has an equal probability to be at any location over the depth of the field. The error probability is therefore uniformly distributed between $-0.04d_d \leq \varepsilon_{field} \leq 0.04d_d$ (similar to resolution uncertainty) and the measurement uncertainty with a 100 % containment probability is given by

$$u_{field} = 0.04d_d \tag{L.4}$$

The combined measurement uncertainty is given by

$$u_{measure} = \sqrt{{u_{res}}^2 + {u_{field}}^2} \tag{L.5}$$

Figure L.3(a) shows the measurement uncertainties for different drop diameters as measured in Appendices B and D.

Figure L.3(b) shows the measurement uncertainties for Appendices G and H where drops are photographed as they fall through an opening between the camera housing and a sandblasted glass background plate. In this case the camera resolution is

$2l$ = 0.0682 mm/pixel and the drop diameter measurements are all between $0.9d_d \leq d \leq 1.1d_d$. The field depth in this case is not constant but becomes a weak function of the drop diameter. This happens because drops will always be at least their own radius away from the background plate or the camera housing as they pass through the opening. This effect contributes to a change in the upper and lower measurement boundaries of less than 1% of the drop diameter and is therefore considered negligible.

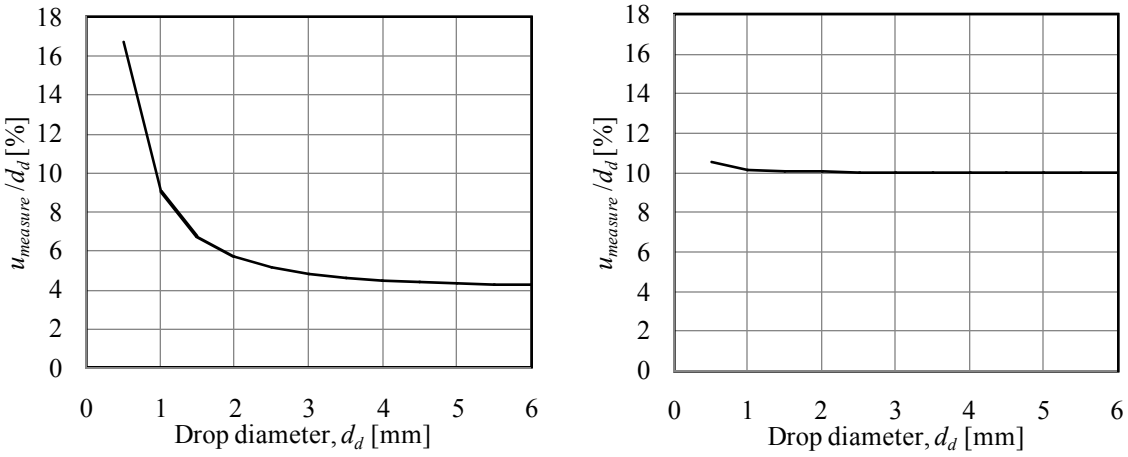

a) Appendices B and D

b) Appendices G and H

Figure L.3: Measurement uncertainties for different drop diameters.

L.3 Conclusion

The previous section shows the measurement uncertainties for the two drop size measurement techniques used in this project. The results show that the uncertainty in drop size measurement is generally less than 10 % of the drop diameter.

The sensitivity of the rain zone Merkel number ($\partial Me/\partial d_{32}$) and loss coefficient ($\partial K_{rz}/\partial d_{32}$) can be obtained from Figure 4.16. The respective sensitivities are multiplied by the measurement uncertainty of the Sauter mean drop diameter in order to obtain the uncertainty of the predicted parameters. Drop size measurement uncertainties contributes to an uncertainty in predicted Merkel number of less than 0.2 % and an uncertainty in the predicted loss coefficient of less than 0.1 % when the rain zone Sauter mean drop diameter is d_{32} = 2 mm. The reader is referred to Van der Merwe (2007) for a detailed analysis on wet-cooling tower performance uncertainties.